Inflaton and Dark Matter Phenomenology Via Reheating and Its Observational Signatures

A Thesis Submitted By-

Rajesh Mondal

Submitted To-

Indian Institute of Technology Guwahati
in partial fulfillment of the requirements for the degree of
Doctor of Philosophy in Physics

Supervised By-

Prof. Debaprasad Maity

Indian Institute of Technology Guwahati
Department of Physics
Guwahati-781039, Assam, India

Declaration

The work presented in this thesis, entitled " **Inflaton and Dark Matter Phenomenology Via Reheating and Its Observational Signatures** ", has been carried out by me under the supervision of Prof. Debaprasad Maity at the Department of Physics, Indian Institute of Technology Guwahati, India. I hereby declare that the content of this thesis is original and has not been submitted elsewhere for any other degree or diploma. All work included in this thesis is my own unless otherwise referenced.

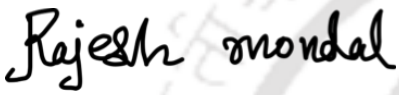

.....

(Signature)

Rajesh Mondal
Roll No.-206121024
Department of Physics
Indian Institute of Technology Guwahati
Guwahati-781039, Assam, India
Date:10/12/2025

Certification

It is certified that the work contained in the thesis entitled " **Inflaton and Dark Matter Phenomenology Via Reheating and Its Observational Signatures**" by Rajesh Mondal (roll number-206121024), a Ph.D. student of the Department of Physics, IIT Guwahati, was carried out under my supervision. The material of this thesis is original and has not been submitted elsewhere for any other degree or diploma.

Debaprasad Maity

.....

(Signature of the supervisor)

10/12/25

Prof. Debaprasad Maity
Department of Physics
Indian Institute of Technology Guwahati
Guwahati-781039, Assam, India
Date:10/12/2025

Acknowledgments

First and foremost, I would like to express my heartfelt thanks to my Ph.D. advisor, Prof. Debaprasad Maity, for his expert guidance on my research, unwavering support, and the patience and kindness he showed throughout my doctoral journey. Most importantly, his expertise, insights, and constructive criticism have been invaluable in shaping my work and helping me overcome obstacles.

I would like to extend my gratitude to my doctoral committee members, Prof. Arunansu Sil, Dr. Debasish Borah, and Dr. Sayan Chakrabarti, for their encouragement and insightful comments, which helped enhance both my presentation skills and my understanding of my research. I also thank all the faculty members and non-teaching staff of the Physics Department for their support.

I express my deep gratitude to my collaborator, Dr. Md. Riajul Haque, whose valuable guidance and insight have greatly contributed to my learning. At the outset of my PhD journey, I received immense help from him, for which I am truly thankful.

I would like to express my gratitude to my senior and current Ph.D. group mates-Dr. Mousumi Maitra, Dr. Rajesh Karmakar, Dr. Banashree Baishya, Dr. Sourav Pal, Gargi Sen, Ayan Chakraborty, Subhasis Maity, Jitumani Kalita, and Sitesh Panda-for all the enriching discussions we have shared. I would especially like to thank our group mate, Ayan Chakraborty, for all the stimulating discussions on physics and for always lending a helping hand whenever needed.

I would also like to extend my sincere thanks to my department seniors, Dr. Pritam Das, Dr. Suruj Jyoti Das, Dr. Swrup Kranti Sarkar, Dr. Dipankar Pradhan, Dr. Soumen Manna, and Dr. Sahabub Jahedi, for our engaging academic and non-academic discussions. I will always cherish the support and companionship of my friends Niloy, Abhik, Sourav, Indrajit, Nayan, Sanjib, Ankan, Amit, Dipendu Haldar, Dipendu Bhandari, Dipankar, and Shubhankar. I especially want to thank Niloy, Abhik, and Nayan for their help and fruitful discussions whenever I needed. I am especially grateful to Niloy, who treated me like a brother when I was hospitalized for a minor surgery.

I want to thank my hostel mates Pracharya, Aminul, Kaushik, Junaid, Selim, Abdurrahman, Saifuddin, Sachin, Abid, and Manoj for all the great times and fun we had together. I also want to thank my school friends Jishan, Abdullah, and Sahinur, with whom I can disturb over phone calls anytime and share anything without hesitation. I would like to express my gratitude to my school's physics teacher, Mr. Ayub Ali, who made physics both easy and interesting for me. I also want to thank my college physics teacher, Dr. Md Injamamul Haque. I considered myself extremely fortunate to have had him as my teacher.

I would like to express my heartfelt gratitude to my mother, my first teacher. Her deep passion for learning and unwavering love continue to inspire me. Without her guidance and support, I wouldn't have come this far. I also want to thank my father, whose dedication I can never fully express in words. I am also deeply thankful to my sister, Runa, for her constant support and encouragement. I am grateful to my grandparents, who have showered me with love and affection since my childhood. I also want to thank all of my family members who believe in me and have always encouraged me to reach great heights.

Finally, I want to thank Almighty God for everything (Alhamdulillah).

Abstract

We are currently in the era of precision cosmology, which offers us a unique opportunity to investigate beyond the Standard Model (SM) of physics. Toward this endeavor, the inflaton and Dark Matter (DM) are assumed to be natural new physics candidates. It is believed that reheating takes place right after inflation, during which all the SM particles are produced. Interestingly, reheating not only explains the cosmic origin of visible matter but also provides a mechanism for the production of other cosmological relics, such as DM. Furthermore, reheating can also affect the observational predictions of the preceding phase of inflation. Thus, reheating offers a promising playground for the phenomenological study of inflation and DM within a unified framework, which has been studied extensively in this thesis.

We first studied the dynamics of reheating for a general inflaton equation of state (EoS), considering both gravitational and non-gravitational interactions between the inflaton and radiation. We showed that, depending on the EoS and the nature of the inflaton's decay products (radiation), thermal effects can play a significant role in the reheating process. We have constrained key microphysical parameter, namely the non-gravitational inflaton coupling, in terms of the inflaton EoS, the reheating temperature, and the CMB spectral index $n_{\rm s}$. Furthermore, we analyzed the implications of the reheating dynamics for the DM phenomenology, considering both thermal and non-thermal production of DM. The non-trivial expansion and thermal history during reheating significantly impact the viable DM parameter space, potentially enlarging the regions accessible to future experiments. This opens a promising, indirect window to probe the early Universe in laboratory settings.

Then, we explored the impact of the latest observation of Planck and BICEP/Keck data on the inflaton phenomenology. Due to the lack of direct experimental probes, both the inflationary and post-inflationary parameters, like inflationary e-folding number, reheating temperature, inflaton couplings, etc, remain largely unconstrained. Using the latest constraints on CMB from Planck+BICEP/Keck, we derived detailed phenomenological constraints on inflationary and post-inflationary parameters.

Finally, we propose a novel reheating scenario governed by the right-handed neutrinos (RHNs) in the well-known Type-I seesaw framework embedded in the SM. Our scenario represents the most minimal possible framework, as it does not introduce any new interactions beyond the SM, except for gravity. We call this scenario gravitational neutrino reheating, abbreviated as νGRe. Interestingly, νGRe not only offers successful reheating but also solves the well-known neutrino mass and baryon asymmetry problems. This νGRe constrains a large class of inflation models, RHN masses, and predicts a non-vanishing lightest active neutrino mass.

Overall, this thesis demonstrates how reheating serves as a unifying bridge between inflation, dark matter, and particle physics, allowing these seemingly disparate sectors to be constrained within a single framework. By combining theoretical modeling with state-of-the-art cosmological observations, it shows how precision cosmology can indirectly probe physics at energy scales far beyond the reach of terrestrial

experiments, offering a powerful window into the fundamental physics of the early Universe.

Nomenclature

Throughout this thesis, we use natural units $\hbar = c = k_{\rm B} = 1$. In this unit, the reduced Planck mass is given by $M_{\rm p} = \frac{1}{\sqrt{8\pi G}} = 2.4 \times 10^{18}$ GeV.

Minkowski metric is given by $\eta_{\mu\nu} = \text{diag}[1, -1, -1, -1]$.

Spatial vectors are written in boldface.

Table of Contents

CHAPTER 1

Introduction and Motivation

1.1 Introduction and Motivation

The question of the origin of the cosmos has fascinated humanity for millennia. In recent decades, our understanding of the universe's cosmic history has advanced significantly due to precise measurements of cosmological observables. For instance, detailed observations of the temperature anisotropies in the cosmic microwave background (CMB) [1–4] have revealed that the universe is homogeneous and isotropic on large scales, but with tiny temperature fluctuations. CMB measurements have also revealed that the universe has negligible spatial curvature, and the power spectrum of primordial curvature perturbations is nearly scale-invariant. The standard cosmological ΛCDM model fails to explain all these phenomena. All these observations strongly support the idea that the early universe underwent a period of rapid exponential expansion known as *cosmic inflation* [5–9]. The theory of cosmic inflation not only explains the observed flatness, homogeneity, and isotropy of the Universe but also provides a mechanism for generating the initial density fluctuations that later grow into galaxies and large-scale structures. Inflation is believed to have occurred at an enormous energy scale (may be as high as $\sim 10^{15}$ GeV, with the duration $\sim 10^{-34}$ seconds (s)). However, inflation also dilutes any pre-existing matter and radiation, leaving behind a cold and nearly empty Universe. In contrast, the remarkable agreement between the observed light element abundances and the predictions of Big Bang nucleosynthesis (BBN) [10] strongly suggests that the Universe was filled with a hot, dense plasma of relativistic particles in thermal equilibrium at a temperature of around 1 MeV (time scale ~ 1 s). Thus, the early evolution of our observable universe was shaped by two key phases: inflation and BBN. However, connecting these two important epochs remains a significant challenge, as there exists a vast gap in both energy and time scales that is poorly understood and largely unconstrained by current observations. Collider experiments can probe intermediate phenomena like electroweak symmetry breaking ($E_{\rm EW} \sim 100$ GeV) and QCD phase transitions ($E_{\rm qcd} \sim 100$ MeV), but they cannot cover the vast energy range between inflation and BBN. Most of the information about the complex dynamics following inflation gets erased before the BBN. Therefore, current cosmological experiments are unable to probe the period between inflation and BBN.

From a theoretical perspective, these two phases can be connected through the theory of *post-inflationary reheating*. After the end of inflation, the Universe is cold, dark, and dominated by a homogeneous inflaton field. It is, therefore, essential to understand how the universe transitioned from this cold, inflaton-dominated state to a hot, thermalized, radiation-dominated phase. The natural expectation is that, after inflation, the inflaton must transfer its energy to the Standard Model (SM) degrees of freedom

(DOFs), which subsequently thermalize and give rise to a radiation-dominated Universe. This transition period, from the end of inflation to the onset of radiation domination, is known as the reheating phase, and the process of energy transfer itself is called reheating. Interestingly, reheating not only explains the cosmic origin of radiation but also provides a mechanism for the production of other cosmological relics, such as DM, gravitational waves (GWs), and even the matter-antimatter asymmetry of the Universe. Despite its crucial role in early universe cosmology, reheating still lacks direct observational evidence. If it occurred in the early universe, its signatures might survive in cosmological observables, for example, in GWs, DM relic, and the anisotropies of CMB.

Reheating influences cosmology in at least two significant ways:

- **Expansion history:** It affects the expansion history since the equation of state during reheating differs from that during inflation, and the radiation-dominated eras. As a result, the post-inflationary expansion history, which is still poorly constrained, directly affects the predictions for CMB observables such as spectral index (n_s) and tensor-to-scalar ratio (r), etc. Furthermore, this modified expansion history significantly impacts the evolution of primordial GWs, which are pivotal for understanding the early universe.

- **Thermal history:** It affects the thermal history because the entropy of the SM sector is generated during reheating. Consequently, the thermal evolution during this phase differs from that of the standard radiation era. This non-trivial thermal and expansion history can significantly impact DM production and the generation of the matter-antimatter asymmetry.

Considering the important role of reheating in shaping both the expansion and thermal history of the universe, gaining a deeper understanding of its dynamics is essential to enhance our understanding of the early universe. The primary objective of this thesis is to systematically study the dynamics of the reheating phase and the cosmological implications of reheating in connection with inflationary and DM physics. In addition, we try to constrain and decode the signatures of reheating via primordial GWs and baryogenesis. The physics after the end of inflation is expected to play a significant role in every aspect of the late-time universe. Over the years, endeavors toward understanding this phase have gained significant interest due to its rich new physics content [11–23]. In this thesis, we take a small step toward understanding the reheating phase, exploring its implications through new physics that could shed light on key aspects of the early universe.

This thesis is organized into five chapters. In Chapter 2, we provide a brief overview of both standard and non-standard cosmology. After outlining the successes and limitations of standard cosmology, we discuss the motivation for non-standard inflationary cosmology. We then examine the conditions required for inflation and show how it can be realized within the framework of a single-field inflation model. The necessity of the post-inflationary reheating phase is discussed next, along with a detailed treatment of perturbative reheating. We further derive the key predictions of single-field inflationary models in terms of cosmological perturbations, both scalar and tensor, and establish their connection to inflationary and CMB parameters. Subsequently, we revisit the compelling evidence for the existence of DM and discuss the freeze-out and freeze-in production mechanisms of DM. Finally, we delve into baryogenesis via leptogenesis, analyzing how the decay of right-handed neutrinos can account for the matter-antimatter asymmetry observed in the universe today. The remaining Chapters 3-5 are based on our original works.
In Chapter 3, we study the dynamics of perturbative reheating for the general inflaton EoS. We show that,

depending on the EoS and decay products (radiation) of the inflaton, the thermal effects play a significant role in the reheating process compared to the scenario without thermal effects. In this context, we constrain the inflaton's coupling with the inflaton EoS and reheating temperature for both scenarios. Secondly, we analyze the implications of these reheating dynamics for DM phenomenology, considering both thermal and non-thermal production mechanisms of DM.

In Chapter 4, we focus primarily on constraining the inflationary and post-inflationary reheating parameters in light of the latest Planck+BICEP/$Keck$ observation. Additionally, we incorporate various theoretical bounds to further constrain these parameters.

In Chapter 5, we propose a novel reheating framework that addresses both reheating and the matter-antimatter asymmetry in the most minimal way. We also apply this framework to the generation of DM.

Finally, in Chapter 6, we conclude with a summary of the findings and discuss potential future directions for research.

List of publications/preprints

The work presented in this thesis is based on the following publications, listed in chronological order:

1. MD Riajul Haque, Debaprasad Maity, and **Rajesh Mondal**, *"WIMPs, FIMPs, and Inflaton phenomenology via reheating, CMB and ΔN_{eff}"*. JHEP 09 (2023) 012, arxiv: 2301.01641 [hep-ph]

2. Ayan Chakraborty, Md Riajul Haque, Debaprasad Maity, and **Rajesh Mondal** *"Inflaton phenomenology via reheating in light of primordial gravitational waves and the latest BICEP/Keck data"*, Phys. Rev. D 108, 023515 (2023), arXiv: 2304.13637 [astro-ph.CO].

3. Md Riajul Haque, Debaprasad Maity, and **Rajesh Mondal**, *"Gravitational neutrino reheating"*, Phys. Rev. D 109, 063543 (2024), arxiv: 2311.07684 [hep-ph].

4. Md Riajul Haque, Debaprasad Maity, and **Rajesh Mondal**, *"Thermal and nonthermal dark matter with gravitational neutrino reheating"*, Phys. Rev. D 111, 063546 (2025), arXiv: 2408.12450 [hep-ph].

In addition to the work presented in this thesis, I have also contributed to the following works:

1. **Rajesh Mondal**, Sourav Mondal, and Toshifumi Yamada, *"Freeze-in and freeze-out production of higgs portal majorana fermionic dark matter during and after reheating"*, arXiv: 2503.20738 [hep-ph].

2. Ayan Chakraborty, **Rajesh Mondal**, Sourav Mondal *"Constraining Reheating Temperature, Inflaton-SM Coupling and Dark Matter Mass in Light of ACT DR6 Observations"*. arXiv: 2505.13387 [hep-ph]

3. Ayan Chakraborty, Debaprasad Maity, **Rajesh Mondal** *"Nonminimal infrared gravitational reheating in light of ACT"*. arXiv: 2506.02141 [astro-ph.CO]

CHAPTER 2

Standard and Non-standard Cosmology

2.1 FLRW Cosmology

The Friedmann-Lemaitre-Robertson-Walker (FLRW) cosmology is the cornerstone of modern cosmology, built upon the assumption that the universe is homogeneous and isotropic on large scales. This high degree of symmetry allows the spacetime metric to be written in a simple form as [24–27],

$$ds^2 = dt^2 - a^2(t)\left[\frac{dr^2}{1-\mathcal{K}\,r^2} + r^2(d\theta^2 + \sin^2\theta\, d\phi^2)\right], \tag{2.1}$$

where t is cosmic time, $\mathcal{K}$ denotes the spatial curvature (0 for flat, +1 for closed, and -1 for open universe) of the metric. The scale factor $a(t)$ describes the universe's expansion and its evolution governed by the Einstein equations [28–30],

$$R_{\mu\nu} - \frac{1}{2}g_{\mu\nu}R = 8\pi G\, T_{\mu\nu} - \Lambda g_{\mu\nu}, \tag{2.2}$$

where $R_{\mu\nu}$ is the Ricci tensor, R is the Ricci scalar, and $g_{\mu\nu}$ is the component of the metric tensor, which are related by the following equations,

$$R_{\mu\nu} = \partial_\alpha \Gamma^\alpha_{\mu\nu} - \partial_\mu \Gamma^\alpha_{\alpha\nu} + \Gamma^\alpha_{\alpha\beta}\Gamma^\beta_{\mu\nu} - \Gamma^\alpha_{\mu\beta}\Gamma^\beta_{\alpha\nu}, \quad R = g^{\mu\nu}R_{\mu\nu}. \tag{2.3}$$

To be consistent with the symmetries of the FLRW metric, which assumes spatial homogeneity and isotropy, the energy-momentum tensor $T_{\mu\nu}$ must take the form of a perfect fluid. This requires that it be diagonal and free from anisotropic stress [26]

$$T^\mu_{\ \nu} = \mathrm{diag}(\rho, -P, -P, -P), \tag{2.4}$$

where ρ is the energy density and P is the isotropic pressure. Any off-diagonal components or anisotropic stress terms would break the isotropy of the spatial slices and thus be incompatible with the FLRW metric.

Using the FLRW metric and the stress-energy tensor in Eq. 2.2, the Einstein equations reduce to two ordinary differential equations-known as the Friedmann equation, that govern the dynamics of the expanding universe,

$$H^2 = \left(\frac{\dot{a}}{a}\right)^2 = \frac{8\pi G}{3}\rho - \frac{\mathcal{K}}{a^2} + \frac{\Lambda}{3}, \quad \frac{\ddot{a}}{a} = -\frac{4\pi G}{3}(\rho + 3P) + \frac{\Lambda}{3}, \tag{2.5}$$

where $H = \dot{a}/a$ is the Hubble parameter. In the early universe, it is a good approximation to neglect the cosmological constant term Λ, since the dynamic is dominated by radiation or matter. Furthermore, current

observations suggest that the universe is spatially flat ($\mathcal{K} = 0$). Under these assumptions, the Friedmann equations simplify to,

$$H^2 = \frac{\rho}{3M_{\rm p}^2}, \quad \frac{\ddot{a}}{a} = -\frac{1}{6M_{\rm p}^2}(\rho + 3P), \tag{2.6}$$

where $M_{\rm p} = 1/\sqrt{8\pi G} = 2.4 \times 10^{18}$ GeV is the reduced Planck mass. The covariance conservation of the stress-energy tensor, $\nabla^\mu T_{\mu\nu} = 0$, leads to the continuity equation

$$\dot{\rho} + 3H(\rho + P) = 0. \tag{2.7}$$

This equation describes how the energy density of the cosmic fluid evolves with time, depending on the pressure P. To proceed, we define the equation of state (EoS) parameter $w \equiv P/\rho$, which allows us to rewrite the equation as

$$\dot{\rho} + 3H(1 + w)\rho = 0. \tag{2.8}$$

Solving this differential equation gives the scaling behavior of the energy density with the scale factor $a(t)$:

$$\rho(a) \propto a^{-3(1+w)}. \tag{2.9}$$

Different values of w correspond to different dominant components of the universe:

- **For radiation**, , $w = 1/3$, which implies $\rho_r \propto a^{-4}$.
- **For pressureless matter (dust)**, $w = 0$, which implies $\rho_{\rm m} \propto a^{-3}$.
- **For a cosmological constant or vacuum energy**, $w = -1$, which implies $\rho_\Lambda = \text{const.}$

To understand how the universe expands in time, we solve the Friedmann Eq. 2.6 using Eq. 2.9,

$$a(t) \propto \begin{cases} t^{\frac{2}{3(1+w)}}, & \text{for } w \neq -1, \\ e^{Ht}, & \text{for } w = -1. \end{cases} \tag{2.10}$$

$$H(t) \propto \begin{cases} \frac{1}{t}, & \text{for } w \neq -1, \\ \text{const}, & \text{for } w = -1. \end{cases} \tag{2.11}$$

Based on a wide range of cosmological observations, such as the CMB [31], large-scale structures [32], and supernova measurements [33], it is now well established that the current universe is dominated by a cosmological constant (ΛD). As we look back in time, we find that the universe evolved from a matter-dominated (MD) universe to the current cosmological constant-dominated universe, and the MD universe was preceded by a radiation-dominated (RD) universe (see Fig. 2.1). The Table 2.1 summarises the solutions for a flat universe during RD, MD, and ΛD domination. Although the present universe is dominated by the cosmological constant, it still contains significant contributions from radiation, DM, and baryonic matter. In terms of the density parameter (Ω_i), the Friedmann Eq. 2.6 can be written as,

Table 2.1: Evolution of energy density, Hubble parameter, and the scale factor with time:

	w	$\rho(a)$	$H(a)$	$a(t)$
RD	$\frac{1}{3}$	a^{-4}	a^{-2}	$t^{1/2}$
MD	0	a^{-3}	$a^{-3/2}$	$a^{3/2}$
ΛD	-1	a^0	a^0	e^{Ht}

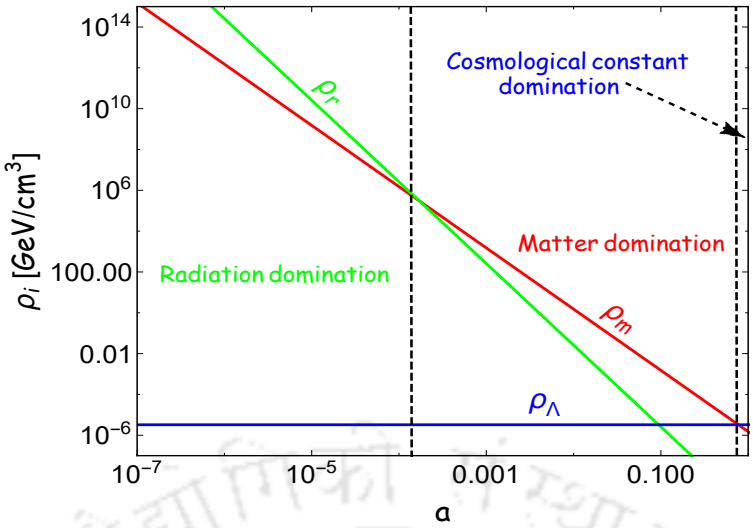

Figure 2.1: Evolution of the energy densities of radiation (green), matter (red), and dark energy (blue) in the Universe with respect to the scale factor a.

$$H^2(a) = H_0^2 \left[\Omega_{r,0} \left(\frac{a}{a_0}\right)^{-4} + \Omega_{\mathrm{m},0} \left(\frac{a}{a_0}\right)^{-3} + \Omega_{\Lambda,0} \left(\frac{a}{a_0}\right)^{0} + \Omega_{\mathscr{K},0} \left(\frac{a}{a_0}\right)^{-2} \right], \tag{2.12}$$

where $a_0\,(H_0)$ is the present-day scale factor (Hubble parameter), $\Omega_{i,0} = \rho_{i,0}/\rho_{\mathrm{crit},0}$ denotes the present-day density parameter of component i and $\rho_{\mathrm{crit},0} = 3M_{\mathrm{p}}^2 H_0^2 = 4\times10^{-6}$ GeV/cm^3 [31] is the critical energy density today. As per the latest observations, the present-day values of these density parameters are approximately [31],

$$\Omega_{r,0} \simeq 9.2\times10^{-5}, \quad \Omega_{\mathrm{m},0} \simeq 0.315 \quad \Omega_{\Lambda,0} \simeq 0.685, \quad \Omega_{\mathscr{K},0} \simeq -0.0007 \pm 0.0019 \tag{2.13}$$

FLRW cosmology successfully describes the evolution of the universe from an early hot, dense phase (the Big Bang) to its current accelerating expansion. It provides a robust framework for interpreting a wide range of cosmological observations, such as the CMB, large-scale structure, and Hubble expansion. However, despite its success, it leaves several fundamental questions unresolved-such as the horizon problem, flatness problem, and monopole problem. These shortcomings indicate the need for new physics in the very early universe, which led to the development of the inflationary paradigm- an accelerated expansion phase that precedes the standard hot Big Bang evolution.

2.2 Shortcomings of standard cosmology and motivation for inflation

In this section, we briefly review the above-mentioned shortcomings of standard cosmology.

- **Horizon problem:** The CMB, a remnant of the early universe emitted approximately 380,000 years after the Big Bang, now exhibits an almost perfectly uniform temperature of $T_0 = 2.725 \pm 0.01$K. This uniformity suggests that all regions of the observable universe were in causal contact at the time of CMB decoupling. However, standard cosmology predicts that the universe at that epoch consisted of nearly 10^4 causally disconnected patches. The physical separation between these regions was so large that they could not have exchanged any signals or energy by the time the CMB was released. If that is the case, why do we observe such a uniform CMB temperature across the sky, as shown in

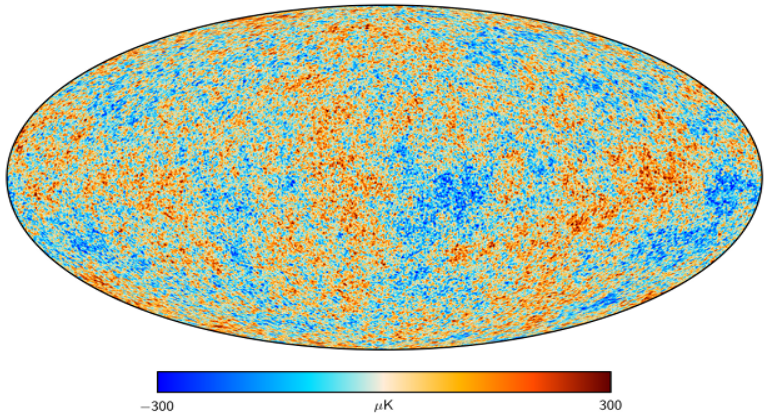

Figure 2.2: Full sky CMB temperature map. [Source figure [35]]

Fig. 2.2? This contradiction between the theory and observations is known as the horizon problem [6, 34]. To understand the horizon problem more rigorously, we introduce the concept of the particle horizon ($R_{\rm ph}$), which is the maximum distance traveled by the photon from the beginning of the universe up to a scale factor a

$$R_{\rm ph} = a \int_0^a (aH)^{-1} d(\ln a). \tag{2.14}$$

Here, the quantity $(aH)^{-1}$ is known as co-moving Hubble radius, and if the universe is dominated by a component with EoS w, then the comoving Hubble radius evolves as $(aH)^{-1} \sim a^{\frac{1}{2}(1+3w)}$. Under such a scenario, the particle horizon scales roughly as

$$R_{\rm ph} \sim H^{-1}. \tag{2.15}$$

Therefore, the ratio of any physical length scale ($\lambda_{\rm phl} = a\,\lambda$) to the particle horizon becomes

$$\frac{\lambda_{\rm phl}}{H^{-1}} = a\,\lambda H = \dot{a}\,\lambda, \tag{2.16}$$

which decreases with time in the standard Big Bang cosmology, since $\ddot{a} < 0$ (2.6). This implies that, by the time of last scattering, many regions of the universe were outside the particle horizon, meaning they could not have been in causal contact with each other. To quantify this, we can relate the present-day particle horizon $R_{\rm ph,0}$ to the particle horizon at the time of last scattering $R_{\rm ph,ls}$,

$$R_{\rm ph,0} = R_{\rm ph,ls} \frac{H_{\rm ls}}{H_0}. \tag{2.17}$$

Here, $H_{\rm ls}$ and H_0 represent the Hubble parameter at the time of last scattering and at the present time, respectively. During the MD universe, the Hubble parameter scales as $H \propto a^{-3/2} \sim T_{\rm rad}^{3/2}$, where $T_{\rm rad}$ is the temperature of the universe. Since $T_{\rm rad} \propto a^{-1}$, we have the following relation for the particle horizons,

$$\frac{R_{\rm ph,0}}{R_{\rm ph,ls}} = \frac{H_{\rm ls}}{H_0} \simeq \left(\frac{a_0}{a_{\rm ls}}\right)^{\frac{3}{2}} \simeq \left(\frac{T_{\rm ls}}{T_0}\right)^{3/2}. \tag{2.18}$$

Substituting the value of the bath temperature at the time of last scattering, $T_{\rm ls} = 0.23\,\text{eV}$ and the present-day CMB temperature, $T_0 = 2.725\,\text{K}$, we get,

$$\frac{R_{\rm ph,0}}{R_{\rm ph,ls}} \sim 10^4. \tag{2.19}$$

So, at the time of last scattering, there were roughly 10^4 causally disconnected regions in the universe. Today, these regions lie within the same Hubble volume, but the uniformity observed in the CMB suggests that these regions must have interacted in the past. This apparent contradiction forms the horizon problem.

- **Flatness problem:** Another fundamental puzzle of standard cosmology is the flatness problem, which concerns the extreme fine-tuning required for the spatial curvature of the universe to be close to zero today.

  The curvature density parameter can be written as

$$\Omega_{\mathcal{K}} = -\frac{\mathcal{K}}{a^2 H^2}. \tag{2.20}$$

  Current CMB observations constrain the spatial curvature to be extremely small, $|\Omega_{\mathcal{K},0}| < 0.001$ [31]. In a RD universe, $H \propto a^{-2} \Rightarrow |\Omega_{\mathcal{K}}| \propto a^2$,while in a MD universe, $H \propto a^{-3/2}$, leading to $|\Omega_{\mathcal{K}}| \propto a$. In both cases, $|\Omega_{\mathcal{K}}|$ grows with time. Therefore, for the universe to be as flat as it is today, the initial value of $\Omega_{\mathcal{K}}$ must have been exceedingly small-implying an incredible level of fine-tuning in the early universe.

  The degree of fine-tuning required at some early epoch (a_i) can be estimated as [35],

$$\left|\frac{\Omega_{\mathcal{K},i}}{\Omega_{\mathcal{K},0}}\right| = \left(\frac{a_0 H_0}{a_i H_i}\right)^2 = \left(\frac{a_0}{a_i}\right)^2 \left(\frac{H_0}{H_{\rm eq}}\right)^2 \left(\frac{H_{\rm eq}}{H_i}\right)^2 = \left(\frac{a_{\rm eq}}{a_0}\right)\left(\frac{a_i}{a_{\rm eq}}\right)^2 \simeq \left(\frac{T_{\rm eq}}{T_i}\right)\left(\frac{T_0}{T_i}\right). \tag{2.21}$$

  Where we have assumed the universe evolved from an early RD era ($a_i < a < a_{\rm eq}$) to a MD era ($a_{\rm eq} < a < a_0$). Here, $a_{\rm eq}(T_{\rm eq})$ represents the scale factor (temperature) at the matter-radiation equality. Similarly, $H_{\rm eq}$ represents the Hubble parameter at the matter-radiation equality. At the epoch of BBN, when the temperature $T(a_i) = T_{\rm BBN} \sim 1$ MeV, the required fine-tuning is,

$$\left|\frac{\Omega_{\mathcal{K},\rm BBN}}{\Omega_{\mathcal{K},0}}\right| \simeq 10^{-16}. \tag{2.22}$$

  At the Grand Unified Theory (GUT) scale, $T(a_i) = T_{\rm GUT} \sim 10^{16}$ GeV, the tuning becomes even more severe,

$$\left|\frac{\Omega_{\mathcal{K},\rm GUT}}{\Omega_{\mathcal{K},0}}\right| \simeq 10^{-54}. \tag{2.23}$$

  Such extreme sensitivity to initial conditions means that unless the early universe was extraordinarily flat, it would have either recollapsed too quickly or expanded too rapidly for structure formation to occur. This unexplained fine-tuning is what constitutes the flatness problem

- **Monopole Problem:** Many GUTs predict the formation of heavy, stable magnetic monopoles during early-universe phase transitions at temperatures around $T_{\rm rad} \sim 10^{16}$ GeV. In standard cosmology, these relics would be abundantly produced and persist to the present day, contributing a large energy density. However, no monopoles have been observed today, and their predicted abundance would overclose the universe, contradicting current observations. This discrepancy is known as the monopole problem. It suggests that standard cosmology cannot account for the dilution of such relics and motivates the need for an early period of accelerated expansion-inflation to dilute their density to unobservable levels.

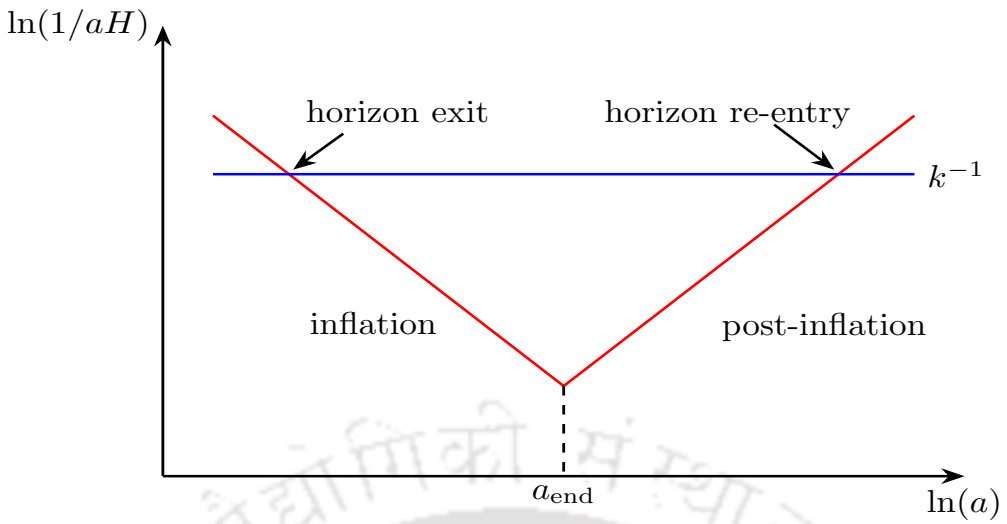

Figure 2.3: A visual diagram of the solution of the horizon problem. The Evolution of the comoving Hubble radius (red solid line) during and after inflation. Comoving scale k exits the horizon during inflation, and later re-enters the horizon after inflation.

2.3 Introduction to inflation and possible solution of shortcomings of standard cosmology

From the above discussion, all cosmological puzzles arise due to the growing Hubble sphere during the standard RD universe, where $\ddot{a} < 0$. To address the unresolved puzzles of standard cosmology, Alan Guth introduced [34] the concept of an inflationary epoch- a brief period of accelerated exponential expansion ($\ddot{a} > 0$) preceding the conventional RD phase. A key feature of this phase is the shrinking comoving Hubble radius, $(aH)^{-1}$, which decreased over time, as expressed by the condition $\frac{d}{dt}(aH)^{-1} < 0$. As a result, it is plausible that the entire observable universe was within the Hubble radius and in causal contact at the onset of inflation. Inflation stretches initially small, causally connected regions to super-Hubble scales. After inflation ends, the universe enters a decelerated expansion phase, during which the comoving Hubble radius grows, allowing those super-Hubble modes to eventually reenter the horizon. This behavior is illustrated in Fig. 2.3, where we show the evolution of the comoving Hubble radius (red line) and the horizon crossing of comoving modes during inflation (blue line), followed by their reentry in the later universe. Therefore, inflation naturally solves the horizon problem [6, 34]; the observed large-scale homogeneity of the CMB can be attributed to causal physics before inflation stretched those regions apart.

We can also estimate the duration of inflation required to resolve the horizon problem. At the very least, the comoving Hubble radius today must be smaller than the comoving Hubble radius at the onset of inflation,

$$(a_0 H_0)^{-1} < (a_{\rm I} H_{\rm I})^{-1}, \tag{2.24}$$

where $a_{\rm I}$ and $H_{\rm I}$ denote the scale factor and the Hubble parameter at the onset of inflation. Assuming that the universe transitions to a RD phase immediately after inflation ends, followed by MD phase, the ratio of the comoving Hubble radius between the end of inflation and today is given by,

$$\frac{a_{\rm end} H_{\rm end}}{a_0 H_0} = \left(\frac{a_{\rm eq}}{a_{\rm end}}\right)^{\frac{1}{2}} \left(\frac{a_0}{a_{\rm end}}\right)^{\frac{1}{2}} \simeq \frac{T_{\rm end}}{\sqrt{T_{\rm eq} T_0}} \simeq 10^{26}, \quad [\text{taking } T_{\rm end} \sim 10^{15} \text{ GeV}]. \tag{2.25}$$

where $a_{\rm end}$ is the scale factor at the end of inflation, and for numerical estimation taking temperature at the end of inflation $T_{\rm end} \sim 10^{15}$ GeV. Combining Eqs. 2.24 and 2.25, we get

$$(a_{\rm I} H_{\rm I})^{-1} > (a_0 H_0)^{-1} \simeq 10^{26} (a_{\rm end} H_{\rm end})^{-1} \tag{2.26}$$

Assuming a nearly constant Hubble parameter during inflation, $H \approx$ const, so from the above equation

$$\frac{a_{\rm end}}{a_{\rm I}} > 10^{26} \Rightarrow N = \ln\left(\frac{a_{\rm end}}{a_{\rm I}}\right) > 60\,, \tag{2.27}$$

here, N is the e-folding number. Therefore, to solve the horizon problem, inflation must last for at least 60 e-folds [27, 36].

Inflation also provides a natural solution to the flatness problem by exponentially diluting any initial spatial curvature. We see that during inflation, the scale factor "a" grows exponentially while $H \approx$ const. Therefore from Eq. 2.20,

$$\left|\frac{\Omega_{\mathcal{K},\rm end}}{\Omega_{\mathcal{K},\rm I}}\right| \sim e^{-2N}\,. \tag{2.28}$$

Assuming an initial curvature of order unity, i.e, $|\Omega_{\mathcal{K},\rm I} \sim \mathcal{O}(1)|$ to be unity, then $\Omega_{\mathcal{K},\rm end} \sim 10^{-52}$ at the end of inflation. Thus, the extreme fine-tuning required in standard cosmology is dynamically achieved through inflation.

Similarly, inflation also resolves the monopole problem. If the GUT phase transition occurred before or during the inflationary epoch, any monopoles produced would have been stretched exponentially and diluted by the rapidly expanding spacetime. Their number density $n_{\rm M}$ would decrease as

$$n_{\rm M} \propto a^{-3} \sim e^{-3N},$$

which, for $N > 60$, leads to a suppression factor of $\sim 10^{-78}$. This renders the monopole abundance negligibly small, making them effectively unobservable in the current universe.

2.4 Condition for inflation

The primary condition for inflation is that the universe undergoes accelerated expansion, which $\ddot{a} > 0$. Recall the second Friedmann equation 2.6,

$$\frac{\ddot{a}}{a} = -\frac{1}{6M_{\rm p}^2}(\rho + 3P)\,. \tag{2.29}$$

The condition $\ddot{a} > 0$, implies that inflation can occur only if the total energy density and pressure satisfy,

$$\rho + 3p < 0 \Leftrightarrow P < -\frac{1}{3}\rho \Leftrightarrow w < -\frac{1}{3}\,. \tag{2.30}$$

This condition is equivalent to a violation of the strong energy condition (SEC), and inflation requires the negative pressure. We will see in the next section that this condition is achieved by introducing a scalar field (the inflaton) with a potential energy dominating over its kinetic energy.

In addition to these general conditions, for inflation to be sustained over a sufficient duration (i.e., to yield enough e-folds), the dynamics of the inflaton field must satisfy the so-called Hubble slow-roll conditions,

$$\epsilon_{\rm H} = -\frac{\dot{H}}{H^2} \ll 1\,, \quad \eta_{\rm H} = \frac{d\ln\epsilon_{\rm H}}{dN} = \frac{\dot{\epsilon}_{\rm H}}{H\epsilon_{\rm H}} \ll 1\,. \tag{2.31}$$

The time derivative of the comoving Hubble radius can be written as

$$\frac{d}{dt}(aH)^{-1} = -\frac{\ddot{a}}{\dot{a}^2} = -\left(\frac{\dot{a}}{a^2 H} + \frac{\dot{H}}{aH^2}\right) = -\frac{1}{a}\left(1 + \frac{\dot{H}}{H^2}\right) = -\frac{1}{a}(1-\epsilon_{\rm H}). \tag{2.32}$$

Therefore, for the shrinking Hubble sphere, $\epsilon_{\rm H} < 1$. To achieve sufficiently many e-folds of inflation, we need $\epsilon_{\rm H} \ll 1$ for long time, and the parameter $\eta_{\rm H}$, which quantifies the fractional change of $\epsilon_{\rm H}$ per Hubble time, should also satisfy $\eta_{\rm H} \ll 1$.

2.5 Dynamics of single field inflation

A minimal and well-motivated way to realize inflation is through a scalar field ϕ, known as the inflaton, which is considered minimally coupled to gravity. The action for such a system in natural units ($\hbar = c = 1$) is given by

$$S = \int d^4x\sqrt{-g}\left[-\frac{M_{\rm p}^2}{2}R + \frac{1}{2}g^{\mu\nu}\partial_\mu\phi\partial_\nu\phi - V(\phi)\right] + S_{\rm matter}, \tag{2.33}$$

where $\sqrt{-g} = a^3(t)$ in the FLRW background, R is the Ricci scalar, and $V(\phi)$ is the inflaton potential responsible for driving inflation. The matter action term $S_{\rm matter}$ encodes the full content of the matter sector, including the SM, DM, and any interactions between the inflaton and other fields (SM, DM). Using the Euler-Lagrange equation, the equation of motion (EoM) for the scalar field is obtained as [1],

$$\ddot{\phi} + 3H\dot{\phi} - \frac{\nabla^2\phi}{a^2} + \frac{dV(\phi)}{d\phi} = 0. \tag{2.34}$$

The energy-momentum tensor associated with the scalar field is defined as the functional derivative of the scalar field action with respect to the metric $g_{\mu\nu}$,

$$T_{\mu\nu} = \frac{-2}{\sqrt{-g}}\frac{\delta S}{\delta g^{\mu\nu}} = \partial_\mu\phi\partial_\nu\phi - g_{\mu\nu}\mathscr{L}. \tag{2.35}$$

The energy-momentum tensor derived from the action leads to the following expressions for the energy density and pressure,

$$\rho_\phi = T_{00} = \frac{1}{2}\dot{\phi}^2 + V(\phi) + \frac{(\nabla\phi)^2}{2a^2}, \quad P_\phi = \frac{T_i^i}{3} = \frac{1}{2}\dot{\phi}^2 - V(\phi) - \frac{(\nabla\phi)^2}{6a^2}. \tag{2.36}$$

Under the assumptions of isotropy and homogeneity for the background universe, we decompose the field into a homogeneous background component and perturbations,

$$\phi(\mathbf{x},t) = \bar{\phi}(t) + \delta\phi(\mathbf{x},t), \tag{2.37}$$

where $\bar{\phi}(t)$ is the homogeneous background field and $\delta\phi(\mathbf{x},t)$ represents small spatial fluctuations. This homogeneous background field can be interpreted as a Bose-Einstein condensate, which can be treated quite as a classical background field. As a result, the homogeneous component $\bar{\phi}(t)$ behaves like a classical field. For the purpose of studying inflationary dynamics, we are primarily interested in the evolution of this classical background field. Therefore, for simplicity, we will denote it as $\phi(t)$ from now on. Since the field is homogeneous, spatial gradient terms vanish, and the EoM of the scalar field reduces to

[1] Here we assume the inflaton is not coupled to other fields

$$\ddot{\phi} + 3H\dot{\phi} + V'(\phi) = 0\,, \tag{2.38}$$

where $V'(\phi) = dV(\phi)/d\phi$. Similarly, the energy density and pressure can be written as

$$\rho_\phi = \frac{1}{2}\dot{\phi}^2 + V(\phi)\,, \quad P_\phi = \frac{1}{2}\dot{\phi}^2 - V(\phi)\,. \tag{2.39}$$

From the above equation, the Friedmann equations can be written as,

$$H^2 = \left(\frac{\dot{a}}{a}\right)^2 = \frac{1}{3M_{\rm p}^2}\left(\frac{1}{2}\dot{\phi}^2 + V(\phi)\right), \tag{2.40}$$

$$H^2 + \dot{H} = \frac{\ddot{a}}{a} = -\frac{1}{3M_{\rm p}^2}(\dot{\phi}^2 - V(\phi))\,. \tag{2.41}$$

Inflation occurs when the potential energy dominates over the kinetic energy, $V(\phi) \gg \dot{\phi}^2/2$, so that the pressure becomes sufficiently negative, leading to $\ddot{a} > 0$. This condition is naturally realized when the scalar field rolls slowly down a flat potential, a regime known as the slow-roll regime. Combining two Friedmann Eqs. 2.40 and 2.41, we have

$$\dot{H} = -\frac{1}{2M_{\rm p}^2}\dot{\phi}^2\,. \tag{2.42}$$

Therefore the Hubble slow-roll parameter $\epsilon_{\rm H}$ can be written as

$$\epsilon_{\rm H} = \frac{1}{2}\frac{\dot{\phi}^2}{M_{\rm p}^2 H^2}\,. \tag{2.43}$$

The slow-roll condition $\epsilon_{\rm H} \ll 1$ suggests that the kinetic energy has a very small contribution to the total energy density, and using the slow-roll approximation, from Eq. 2.40, the Hubble parameter can be written as

$$H \simeq \frac{V(\phi)}{3M_{\rm p}^2}\,. \tag{2.44}$$

In order to persist inflation to be long-lasting, the second slow-roll Hubble parameter $\eta_H \ll 1$, and it can be written as

$$\eta_H = \frac{\dot{\epsilon}_{\rm H}}{H\epsilon_{\rm H}} = \frac{2\ddot{\phi}}{H\dot{\phi}} - \frac{2\dot{H}}{H^2} = 2\left(\epsilon_H - \frac{\ddot{\phi}}{H\dot{\phi}}\right). \tag{2.45}$$

The condition $\eta_H \ll 1$ also indicates that the acceleration of the scalar field has to be small, therefore $\ddot{\phi} \ll H\dot{\phi}$. As a result, from the EoM 2.38,

$$3H\dot{\phi} \simeq -V'(\phi)\,. \tag{2.46}$$

Combining Eqs. 2.44 and 2.46, the slow-roll parameter can be written as

$$\begin{aligned} \epsilon_{\rm H} = \epsilon_{\rm H} &= -\frac{\dot{H}}{H^2} \simeq \frac{M_p^2}{2}\left(\frac{V'(\phi)}{V(\phi)}\right)^2 = \epsilon_{\rm V}\,, \\ \eta_{\rm H} &= \frac{\dot{\epsilon}_{\rm H}}{H\epsilon_{\rm H}} \simeq 4\epsilon_{\rm V} - 2\eta_{\rm V}\,, \end{aligned} \tag{2.47}$$

where $\epsilon_{\rm V}$ and $\eta_{\rm V}$ are called the potential-slow roll parameters, which are defined as

$$\epsilon_{\rm V} \equiv \frac{M_p^2}{2}\left(\frac{V'(\phi)}{V(\phi)}\right)^2, \quad \eta_{\rm V} \equiv M_p^2\left(\frac{V''(\phi)}{V(\phi)}\right). \tag{2.48}$$

Whether a given potential can lead to slow-roll inflation or not, we need to check these slow-roll parameters are small, $\epsilon_{\rm V} \ll 1, |\eta_{\rm V}| \ll 1$.

The efficiency of inflation in solving the flatness and horizon problems of the standard Big Bang cosmology depends on how long the accelerated expansion lasts. This is quantified by the number of e-folds N, which measures the logarithmic growth of the scale factor during inflation,

$$N \equiv \int_{a_{\rm I}}^{a_{end}} d\ln a \tag{2.49}$$

where $a_{\rm I}$ and $a_{\rm end}$ are the scale factors at the onset and end of inflation, respectively. In terms of the slow-roll parameter above equation can be written as,

$$N(\phi) = \int_{\phi_I}^{\phi_{\rm end}} \frac{H}{\dot{\phi}} d\phi \simeq \frac{1}{M_{\rm p}^2} \int_{\phi_{\rm end}}^{\phi_I} \frac{1}{\sqrt{2\epsilon_{\rm V}}} \frac{1}{M_{\rm p}} d\phi, \tag{2.50}$$

where ϕ_I is the initial field value at the beginning of inflation, and ϕ_{end} is the field value at the end of inflation where $\epsilon_V(\phi_{end}) \simeq 1$. To solve the horizon and flatness problems, we require that the total number of inflationary e-folds exceeds about 50. The precise value depends on the energy scale of inflation and on the details of reheating history after inflation, which we have discussed in Chapter 3 and 4.

2.6 End of slow-roll inflation and beginning of reheating

In the previous section, we discussed how inflation can dynamically drive the universe toward a homogeneous and isotropic state, consistent with observations. This phase of accelerated expansion must eventually end to allow the standard hot Big Bang evolution to proceed. From Eq. 2.32, it is clear that accelerated expansion will cease, i.e., $\ddot{a} = 0$, when the slow-roll parameters $\epsilon_{\rm H} = \epsilon_{\rm V} = 1$. Therefore, when the slow-roll parameters reach unity, the universe exits the inflationary phase and transitions into the deceleration phase. This transition is often referred to as the "graceful exit" problem. A well-known example where inflation fails to end gracefully is the Old inflation scenario proposed by Alan Guth [34], where the inflaton field becomes trapped in a metastable false vacuum. The transition to the true vacuum proceeds via bubble nucleation, but this leads to an inhomogeneous universe due to collisions between expanding bubbles, thereby spoiling the success of inflation. In contrast, Chaotic inflation models [37, 38] naturally provide a graceful exit. For example, in inflationary scenarios with power-law potentials ($V(\phi) \propto \phi^{2n}$), the inflaton field rolls down to the minimum of its potential and begins to oscillate coherently after the inflation (see left plot in Fig. 2.4). Further, in the right plot of Fig. 2.4, we have shown that the slow-roll parameter $\epsilon_{\rm V}$ evolves from a very small value to unity at the end of inflation. The general solution of the inflaton field for a power law potential during the oscillation can be written as [39, 40]

$$\phi(t) = \phi_0(t)\mathscr{P}(t), \tag{2.51}$$

where $\phi_0(t)$ represents the time-dependent amplitude of the oscillation, and $\mathscr{P}(t)$ captures the oscillatory behavior of the inflaton. For the detailed solution of $\phi_0(t)$ and periodic function $\mathscr{P}(t)$, see the Appendix-A.

Once inflation ends and the inflaton field begins to oscillate about the minimum of its potential, the universe enters a crucial transition phase known as *reheating*. During inflation, the exponential expansion dilutes all pre-existing matter and radiation, rendering the universe extremely cold and devoid of particles, dominated solely by the homogeneous inflaton field. However, for the hot Big Bang phase of standard cosmology to commence, the universe must be repopulated with a thermal bath of particles. This is

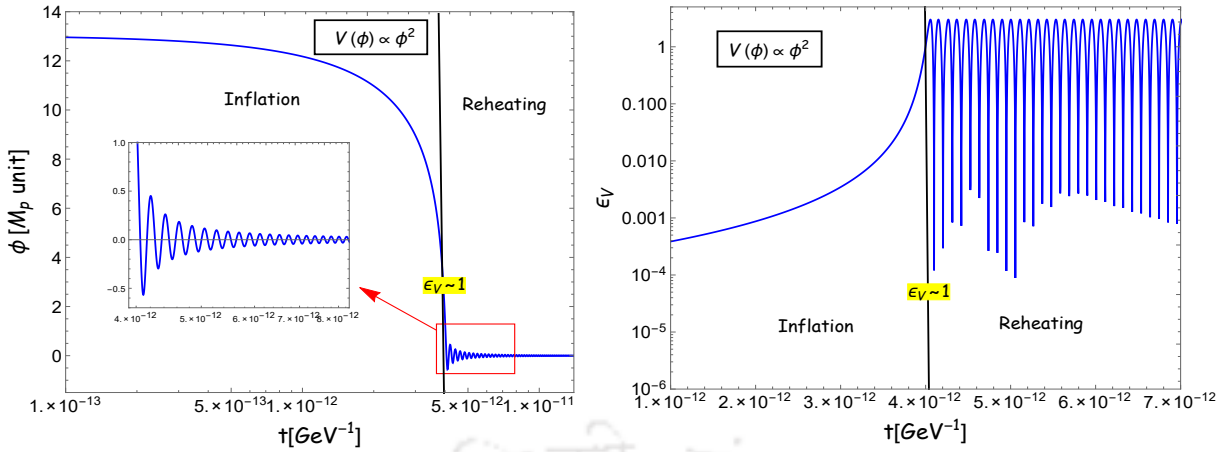

Figure 2.4: ***Left plot***: The general behaviour of the inflaton field ϕ with cosmic time t. ***Right plot***: The evolution of slow-roll parameter ϵ_V with cosmic time t. Both vertical dashed line corresponds to the end of inflation when $\epsilon_V(\phi_{\rm end}) \simeq 1$. Here, we have taken the α-attractor E-model potential with $n = \alpha = 1$.

precisely the role played by reheating. In this phase, the energy stored in the coherent oscillations of the inflaton field is transferred to SM and beyond-the-standard-model (BSM) particles via perturbative decays and/or non-perturbative processes such as parametric resonance. These processes lead to efficient particle production, interactions, and eventual thermalization, thereby giving rise to a radiation-dominated universe with a temperature referred to as the *reheating temperature* $T_{\rm re}$. This temperature is a key parameter in reheating models, influencing both cosmological history and observational signatures.

The precise nature of reheating, including how efficiently the inflaton decays into other particles, depends sensitively on the inflaton's couplings to other fields and the shape of the potential near its minimum. Depending on the strength of these couplings, the inflaton may decay through either perturbative [41, 42] or non-perturbative mechanisms [43–45], leading to reheating durations that can be either short or long. These behaviors are expected to leave imprints on various cosmological observables, such as the CMB anisotropies, GWs, and DM generation, etc, which will be discussed throughout this thesis. In this thesis, we will primarily focus on the perturbative decay of the inflaton, a process referred to as *perturbative reheating*.

2.7 Perturbative framework of reheating

In the simplest scenario, reheating proceeds via perturbative decay of the inflaton into light degrees of freedom. This approach assumes that the inflaton decays gradually as it oscillates around the minimum of its potential, producing relativistic particles which eventually thermalize to form the radiation bath.

To track the evolution of the energy densities during reheating, one uses a set of coupled Boltzmann equations that describe the transfer of energy from the inflaton field ϕ to the radiation bath. Starting from the inflaton EoM Eq. 2.52, and including a decay term, we have

$$\ddot{\phi} + 3H\dot{\phi} + V'(\phi) = -\Gamma_\phi \dot{\phi},, \tag{2.52}$$

where Γ_ϕ is the perturbative decay rate of the inflaton. Multiplying both sides by $\dot{\phi}$, the above equation can be written as

$$\frac{d}{dt}\left(\frac{1}{2}\dot{\phi}^2 + V(\phi)\right) + 3H\dot{\phi}^2 = -\Gamma_\phi \dot{\phi}^2 . \tag{2.53}$$

Replace $\dot{\phi}^2 = \rho_\phi + P_\phi$ from the Eq. 2.39, we have

$$\frac{d\rho_\phi}{dt} + 3H(\rho_\phi + P_\phi) = -\Gamma_\phi(\rho_\phi + P_\phi). \tag{2.54}$$

If $w_\phi = P_\phi/\rho_\phi$ is the average EoS parameter of the inflaton, then the above equation becomes,

$$\frac{d\rho_\phi}{dt} + 3H(1+w_\phi)\rho_\phi = -\Gamma_\phi(1+w_\phi)\rho_\phi. \tag{2.55}$$

The average EoS w_ϕ depends on the shape of the inflation potential around its minimum. For a potential of the form $V(\phi) \propto \phi^{2n}$ around the potential minimum, we can easily determine the average EoS w_ϕ during the oscillatory reheating phase. Assuming that the oscillation time scale is much shorter than both the inflaton decay and Hubble expansion time scales, multiplying Eq. 2.38 by ϕ and taking the average over one oscillation of each term in Eq. 2.38, we get [46, 47],

$$\langle \dot{\phi}^2 \rangle \simeq \langle \phi V'(\phi) \rangle. \tag{2.56}$$

Using the above equation, the energy density and pressure can be written as [46, 47]

$$\begin{aligned} \rho_\phi &= \frac{1}{2}\langle \dot{\phi}^2 \rangle + \langle V(\phi) \rangle \simeq (n+1)\langle V(\phi) \rangle, \\ P_\phi &= \frac{1}{2}\langle \dot{\phi}^2 \rangle - \langle V(\phi) \rangle \simeq (n-1)\langle V(\phi) \rangle. \end{aligned} \tag{2.57}$$

Now, the average EoS w_ϕ can be written as [46, 47]

$$w_\phi = \frac{n-1}{n+1}. \tag{2.58}$$

The energy lost by the inflaton field through its decay is converted into radiation. The evolution of the radiation energy density ρ_r is governed by the corresponding Boltzmann equation is,

$$\frac{d\rho_r}{dt} + 4H\rho_r = \Gamma_\phi(1+w_\phi)\rho_\phi. \tag{2.59}$$

The Hubble parameter H is determined by the total energy density via the Friedmann equation,

$$H^2 = \frac{1}{3M_{\rm p}^2}(\rho_\phi + \rho_r). \tag{2.60}$$

Finally, the dynamics of reheating are governed by the following coupled Boltzmann equations (BEQs),

$$\dot{\rho}_\phi + 3H(1+w_\phi)\rho_\phi = -\Gamma_\phi(1+w_\phi)\rho_\phi, \tag{2.61a}$$

$$\dot{\rho}_r + 4H\rho_r = \Gamma_\phi(1+w_\phi)\rho_\phi, \tag{2.61b}$$

$$H^2 = \frac{\rho_\phi + \rho_r}{3M_{\rm p}^2}. \tag{2.61c}$$

Initially, the universe is dominated by the oscillating inflaton field ($\rho_\phi \gg \rho_r$). As the inflaton decays, its energy density ρ_ϕ decreases while the radiation energy density ρ_r increases. The efficiency of energy transfer from the inflaton to the radiation depends on the decay width of the inflaton Γ_ϕ and the inflaton EoS during reheating. In general, the decay rate of the inflaton is time-dependent; it depends on both the EoS and the interaction of the inflaton with its decay products [18]. Additionally, depending on the spin of the decay products, statistical effects play an important role in the reheating process [48]. In this thesis,

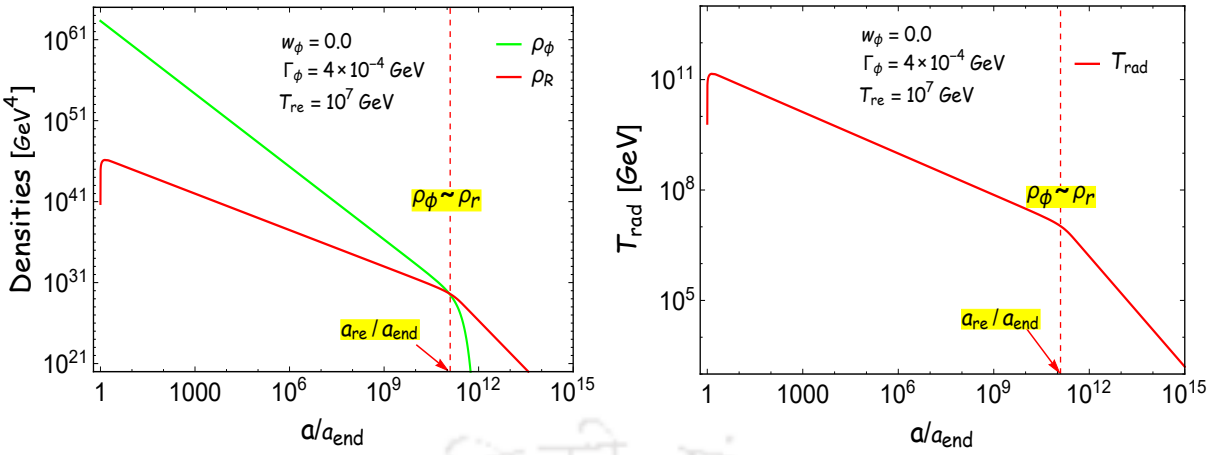

Figure 2.5: ***Left plot***: The evolution of the energy density of the inflaton (green) and radiation (red) with respect to the scale factor a. ***Right plot***: The evolution of the bath temperature $T_{\rm rad}$ with respect to the scale factor a. The vertical red dashed line in both plots corresponds to the end of reheating ($\rho_\phi \sim \rho_r$).

we incorporate all of these factors to study the dynamics of reheating in detail. Now, for a qualitative understanding of the dynamics of reheating, we will solve the coupled BEQs in Eq. 2.61 by assuming that Γ_ϕ is constant. The starting point of reheating is the endpoint of inflation $a_{\rm end}$ where $\epsilon_{\rm V}(\phi_{\rm end}) \simeq 1$. Using this condition, we can derive the initial condition for the inflaton energy density $\rho_\phi^{\rm end}$. By combining Eqs.2.39, 2.40, and 2.43, we get,

$$\rho_\phi^{\rm end} = V(\phi_{\rm end})\left(1+\frac{\epsilon_{\rm V}(\phi_{\rm end})}{3-\epsilon_{\rm V}(\phi_{\rm end})}\right) \simeq \frac{3}{2}V(\phi_{\rm end}). \tag{2.62}$$

Since raditions are produced from inflaton, the initial radiation energy density $\rho_r(a_{\rm end}) = 0$. Assuming during reheating $H \gg \Gamma_\phi$ and $\rho_\phi \gg \rho_r$, the analytical solution of Eq. 2.61 during reheating can be found,

$$\begin{aligned}
\rho_\phi(a) &\simeq \rho_\phi^{\rm end}\left(\frac{a}{a_{\rm end}}\right)^{-3(1+w_\phi)}, \\
H(a) &\simeq H_{\rm end}\left(\frac{a}{a_{\rm end}}\right)^{-3(1+w_\phi)/2}, \\
\rho_r(a) &\simeq \frac{2(1+w_\phi)\Gamma_\phi\,\rho_\phi^{\rm end}}{(5-3w_\phi)H_{\rm end}}\left(\left(\frac{a}{a_{\rm end}}\right)^{-\frac{3}{2}(1+w_\phi)} - \left(\frac{a}{a_{\rm end}}\right)^{-4}\right),
\end{aligned} \tag{2.63}$$

where $H_{\rm end} = \rho_\phi^{\rm end}/(3M_{\rm p}^2)$ Hubble parameter value at the end of inflation. From the above solution, it is evident that the production of radiation energy density depends not only on the inflaton decay width but also on the inflaton EoS. Depending on the EoS, the evolution of the radiation energy density will vary, which, in turn, affects the evolution of the bath temperature during the reheating phase. To define the bath temperature, we assume that the radiation produced by the inflaton decay thermalizes instantaneously, thereby creating a thermal bath. The temperature of this thermal bath can then be determined using the Stefan-Boltzmann relation, which connects the energy density of radiation to its temperature,

$$\rho_r = \frac{\pi^2}{30}g_{\star r}(T_{\rm rad})T_{\rm rad}^4. \tag{2.64}$$

where $g_{\star r}(T_{\rm rad})$ is the effective number of relativistic degrees of freedom associated with the thermal bath. Using the expression of energy density of radiation from Eq. 2.63, the evolution of bath temperature can

be written as,

$$T_{\rm rad}(a) \simeq \left(\frac{60(1+w_\phi)\Gamma_\phi \rho_\phi^{\rm end}}{(5-3w_\phi)\pi^2 g_{\star r} H_{\rm end}}\right)^{1/4} \left(\left(\frac{a}{a_{\rm end}}\right)^{-\frac{3}{2}(1+w_\phi)} - \left(\frac{a}{a_{\rm end}}\right)^{-4}\right)^{1/4}. \tag{2.65}$$

The schematic evolution of the energy density (left plot) and the bath temperature (right plot) is shown in Fig. 2.5. Initially, the bath temperature is zero; it quickly reaches its maximum at the very beginning of reheating, and then gradually decreases as the universe expands. In order to get a standard RD universe, the reheating phase must end. Reheating ends when the energy density of radiation overtakes that of the inflaton, i.e, $\rho_\phi(a_{\rm re}) \simeq \rho_r(a_{\rm re})$, marking the onset of a radiation-dominated universe. This condition is also equivalent to the $H(a_{\rm re}) \simeq \Gamma_\phi$ condition [49]. Therefore, we can determine the reheating temperature $T_{\rm re}$ from this condition as,

$$\Gamma_\phi = H \simeq \frac{2\rho_r(a_{\rm re})^{\frac{1}{2}}}{\sqrt{3}M_{\rm p}} \simeq \sqrt{\frac{\pi^2 g_{\star r}^{\rm re}}{45}}\frac{T_{\rm re}^2}{M_{\rm p}}, \tag{2.66}$$

where $g_{\star r}^{\rm re} = g_{\star r}(T_{\rm re})$ is the relativistic SM degrees of freedom at the end of reheating $a_{\rm re}$, and we have taken $g_{\star r}^{\rm re} = 100$ throughout the thesis. Now, we can express the reheating temperature in terms of the decay width as,

$$T_{\rm re} = \left(\frac{45}{\pi^2 g_{\star r}^{\rm re}}\right)^{\frac{1}{4}} \sqrt{\Gamma_\phi M_{\rm p}}\,. \tag{2.67}$$

For $w_\phi < \frac{1}{3}$, reheating is never completed if $\Gamma_\phi \simeq H(a_{\rm re})$ condition is not satisfied but this is not necessary for $w_\phi > \frac{1}{3}$. This is because, when $w_\phi > \frac{1}{3}$, the inflaton energy density ρ_ϕ is decays faster than radiation density ρ_r (see Eq. 2.63), so we will definitely get a point where $\rho_\phi(a_{\rm re}) \simeq \rho_r(a_{\rm re})$ is satisfied. We have encountered this type of scenario in our work. Therefore, throughout this thesis, we used $\rho_\phi(a_{\rm re}) \simeq \rho_r(a_{\rm re})$ condition for ending the reheating, and we have calculated the reheating temperature using Eq. 2.64,

$$T_{\rm re} = \left(\frac{30}{\pi^2 g_{\star r}^{\rm re}}\right)^{1/4} \rho_{\rm r}^{1/4}(a_{\rm re}), \tag{2.68}$$

In the absence of direct experimental evidence for the reheating phase, the reheating temperature remains largely unconstrained. However, a conservative range often quoted in the literature is [4, 50–54]

$$T_{\rm BBN} \simeq 4\ \ {\rm MeV} \lesssim T_{\rm re} \lesssim 10^{15}\ {\rm GeV}, \tag{2.69}$$

where the lower bound is imposed to ensure that the reheating phase completes before the onset of BBN, thereby preserving the successful predictions of primordial element abundances, and the upper bound is set by the maximum energy scale allowed by inflation. In this thesis, we aim to place tighter, indirect constraints on $T_{\rm re}$ using a combination of observational and theoretical inputs. From the observational perspective, we consider the latest constraints on the inflationary observables (n_s, r) based on the combined data from Planck [4, 31] and BICEP/Keck 2018 (BK18) [54, 55]. On the theoretical side, we explore the impact of reheating on various cosmological relics, such as DM, the matter-antimatter asymmetry, and primordial gravitational waves, all of which can encode valuable information about the reheating dynamics.

2.8 Cosmological Perturbations from Inflation

Although the inflationary scenario was initially proposed to address various puzzles related to the homogeneous and isotropic background of the universe, it was soon recognized that it also provides a natural mechanism for generating primordial perturbations. During inflation, quantum fluctuations of the

inflaton field give rise to tiny inhomogeneities that are widely believed to seed the large-scale structure observed in the Universe today. Up to this point, we have assumed a spatially homogeneous inflaton field $\bar{\phi}(t) = \phi(t)$ in a background described by the FLRW metric. However, quantum effects inevitably generate small deviations $\delta\phi(\mathbf{x}, t)$ from homogeneity, which can be treated perturbatively as long as these deviations remain small $\delta\phi(\mathbf{x}, t) \ll \phi(t)$. These fluctuations cause inflation to end at slightly different times in different regions of space, resulting in small inhomogeneities in the energy density, $\delta\rho(\mathbf{x})$. These primordial density perturbations eventually lead to the temperature anisotropies observed in the Cosmic Microwave Background (CMB):

$$\delta\phi(\mathbf{x}, t) \to \delta\rho(\mathbf{x}, t) \to \Delta T(\mathbf{x}). \tag{2.70}$$

In the following sections, we will study the dynamics of these perturbations within the standard inflationary framework, drawing from foundational works [36, 56–59]. Observations of the CMB reveal that the temperature anisotropies are of order $\Delta T/T \sim \mathcal{O}(10^{-5})$, indicating that the universe at recombination was nearly homogeneous and that linear perturbation theory is sufficient to describe these deviations. Expanding Einstein's equations to first order, the evolution of these perturbations is governed by

$$\delta G_{\mu\nu} = 8\pi G\, \delta T_{\mu\nu}. \tag{2.71}$$

This equation shows that we can separately analyze perturbations in both the metric and the matter fields within a consistent perturbative framework.

2.8.1 Metric Perturbations

In General Relativity, energy and momentum are the sources of spacetime curvature. Therefore, fluctuations in the matter field, such as those described by $\delta\phi(\mathbf{x}, t)$, must induce corresponding perturbations in the metric. In this section, we outline the formalism for analyzing such perturbations on the homogeneous background. The most general form of a perturbed FLRW metric can be written as [58],

$$\mathrm{d}s^2 = (1 + 2\Phi)\,\mathrm{d}t^2 - 2a(t)B_i\,\mathrm{d}t\mathrm{d}x^i - a^2(t)\left(\delta_{ij} + h_{ij}\right)\mathrm{d}x^i\,\mathrm{d}x^j, \tag{2.72}$$

where Φ, B_i, and h_{ij} represent the scalar, vector, and tensor perturbations, respectively.

Under spatial rotations, the 10 independent components of $\delta g_{\mu\nu}(\mathbf{x})$ decompose into:

$$\delta g_{\mu\nu} \equiv \left(\delta g_{00}, \delta g_{0i}, \delta g_{ij}\right), \tag{2.73}$$

with the following degrees of freedom:
Scalar perturbations: 4 degrees of freedom, including $\delta g_{00} \equiv \Phi$, scalar parts of δg_{0i} (B) and δg_{ij} (Ψ, E)
Vector perturbations: 4 divergence-less components such as $\hat{B}_i$ and $\hat{E}_i$,

$$\delta g_{0i} \equiv B_i = \underbrace{\partial_i B}_{\text{scalar}} + \underbrace{\hat{B}_i}_{\text{vector}}, \quad \text{with} \quad \partial^i \hat{B}_i = 0\,. \tag{2.74}$$

Tensor perturbations: 2 transverse, traceless degrees of freedom,

$$h_{ij} = \underbrace{2\Psi\,\delta_{ij} + 2\left(\partial_i\partial_j E - \frac{1}{3}\delta_{ij}\nabla^2 E\right)}_{\text{scalar}} + \underbrace{\left(\partial_i \hat{E}_j + \partial_j \hat{E}_i\right)}_{\text{vector}} + \underbrace{2\hat{h}_{ij}}_{\text{tensor}}, \tag{2.75}$$

with the constraints $\partial^i \hat{E}_i = \partial^i \hat{h}_{ij} = \hat{h}^i_i = 0$. This scalar-vector-tensor (SVT) decomposition is particularly useful in linear theory, where each class of perturbation evolves independently according to the linearized Einstein equations. It is convenient to perform this decomposition in Fourier space,

$$X_{\boldsymbol{k}} = \int \mathrm{d}^3\boldsymbol{x}\, X(t,\boldsymbol{x}) e^{-i\boldsymbol{k}\cdot\boldsymbol{x}}, \quad X \in \delta\phi, \delta g_{\mu\nu}, \ldots. \tag{2.76}$$

Importantly, vector perturbations $(\hat{B}_i, \hat{E}_i)$ do not possess growing modes in an expanding universe and typically decay over time [60]. This is consistent with the fact that the gravity sector supports only two propagating degrees of freedom (scalar and tensor). As such, we will neglect the vector modes in our subsequent analysis.

The metric perturbation defined in Eq. 2.72 is not unique; it depends on the choice of gauge, meaning that the perturbations are sensitive to the coordinate system. To proceed, let us examine how the perturbation variables transform under infinitesimal coordinate transformations. Consider the following transformations,

$$t \to t + \alpha, \quad x^i \to x^i + \beta^{,i}, \quad \text{where } \beta^{,i} = \partial^i \beta. \tag{2.77}$$

Under this transformation, the metric perturbations transform as:

$$\Phi \to \Phi - \dot{\alpha}, \qquad B \to B + \frac{\alpha}{a} + \frac{\dot{\beta}}{a}, \qquad \Psi \to \Psi + H\alpha, \qquad E \to E + \frac{\beta}{a^2}, \qquad \hat{h}_{ij} \to \hat{h}_{ij}. \tag{2.78}$$

These transformation laws reveal that most of the perturbation variables are gauge-dependent and do not represent physical observables. Only, $\hat{h}_{ij}$ is manifestly gauge-invariant and corresponds to primordial gravitational waves. However, these transformation properties help us to define the different gauge-invariant perturbation variables through specific combinations of the perturbation variables. One such example is the curvature perturbation, which directly relates to observables in the CMB, which we discuss later. Before defining the physical perturbations, let us first discuss the perturbation of the energy-momentum tensor for the inflaton.

2.8.2 Matter Perturbations

In Eq. 2.4, we defined the energy-momentum tensor for a homogeneous and isotropic universe as follows,

$$\bar{T}_{\mu\nu} = (\bar{\rho} + \bar{P})\bar{u}_\mu \bar{u}_\nu - \bar{P}\,\bar{g}_{\mu\nu}, \tag{2.79}$$

where the co-moving 4-velocity $\bar{u}_\mu = (1,0)$. Here, overbars are used to represent the background values. In the perturbed universe, the energy-momentum tensor can be written as,

$$T_{\mu\nu} = \bar{T}_{\mu\nu} + \delta T_{\mu\nu} \tag{2.80}$$

In order to write perturbations of the stress-energy tensor, at first, we mention the perturbations of the density and pressure as,

$$\delta\rho(t,\boldsymbol{x}) \equiv \rho(t,\boldsymbol{x}) - \bar{\rho}(t) \tag{2.81}$$

$$\delta P(t,\boldsymbol{x}) \equiv P(t,\boldsymbol{x}) - \bar{P}(t) \tag{2.82}$$

Using, the perturbed metric in Eq. 2.72, the perturbed 4-velocity is given by,

$$u_\mu \equiv (1-\Phi, v_i), \quad u^\mu \equiv \left(1+\Phi, -\frac{1}{a^2}v^i - \frac{1}{a}B^i\right), \tag{2.83}$$

where $v^i = dx^i/dt$ is the coordinate velocity. On deriving the above equation, we use the normalization condition $u_\mu u^\mu = 1$. With these prescriptions, perturbed components of the stress-energy tensor can be written as

$$\delta T^0_0 = \delta\rho\,, \tag{2.84}$$
$$\delta T^0_i = (\bar{\rho}+\bar{P})v_i = q_i\,, \tag{2.85}$$
$$\delta T^i_j = -\delta^i_j \delta P + \pi^i_j\,, \tag{2.86}$$
$$\tag{2.87}$$

where q_i is defined as the momentum density, and π^i_j is the anisotropic stress, which is a gauge-invariant quantity. However, pressure and momentum densities are gauge-dependent. Similarly considering general coordinate transformations (gauge transformations in Eq. 2.77) ($t \to t+\alpha,\ x^i \to x^i + \beta^{,i}$), above quantities transform as

$$\delta\rho \to \delta\rho - \dot{\bar{\rho}}\alpha \tag{2.88}$$
$$\delta P \to \delta P - \dot{\bar{P}}\alpha \tag{2.89}$$
$$q_i \to q_i + (\bar{\rho}+\bar{P})\dot{\beta}_{,i}\,. \tag{2.90}$$

2.8.3 Scalar Perturbations: Generation of primordial curvature fluctuations

Scalar perturbations are the most significant for structure formation and CMB anisotropies. These arise from fluctuations in both the inflaton field $\delta\phi$ and the spacetime curvature. Since general relativity is a gauge theory, it is crucial to identify combinations of these perturbations that are gauge-invariant and physically meaningful. One such quantity is the comoving curvature perturbation $\mathscr{R}$, and it is defined as [36, 58]

$$\mathscr{R} = \Psi - \frac{H}{\bar{\rho}+\bar{P}}\,q\,, \tag{2.91}$$

where the scalar part of the 3-momentum density (q_i) is identified as q which can be written as,

$$T^0_i = q_i = \partial_i q + \hat{q}_i\,. \tag{2.92}$$

It is evident that $\mathscr{R}$ is invariant under general coordinate transformations. In the case of a homogeneous inflaton field, the momentum density can be expressed as $T^0_i = -\dot{\bar{\phi}}\partial_i\delta\phi$. Hence, the comoving curvature perturbation takes the following form,

$$\mathscr{R} = \Psi + \frac{H}{\dot{\bar{\phi}}}\delta\phi\,. \tag{2.93}$$

To proceed, it is helpful to assume a particular gauge choice, such as the comoving gauge ($\delta\phi = 0$). In this gauge, the perturbations are expressed as

$$\delta\phi = \quad \delta g_{ij} = a^2\left[(1-2\mathscr{R})\delta_{ij} + h_{ij}\right], \quad \partial_i h_{ij} = h^i_i = 0\,. \tag{2.94}$$

This gauge choice is applicable since in this gauge, the inflaton field remains unperturbed, and $\mathscr{R}$ acts as a gauge-invariant quantity. All other scalar perturbations (Φ, B) can be expressed in terms of $\mathscr{R}(t,\boldsymbol{x})$, as described in Ref. [58]. Notably, Ψ measures the three-curvature of the spatial section, given by $R^{(3)} = \frac{1}{3}\nabla^2\Psi$. Therefore, in the gauge defined in Eq. 2.94, the quadratic action for the comoving curvature perturbation $\mathscr{R}$ can be written as [58],

$$S = \frac{1}{2}\int d^4x\, a^3 \frac{\dot{\phi}^2}{H^2}\left[\dot{\mathscr{R}}^2 - \frac{1}{a^2}(\partial_i\mathscr{R})^2\right]. \tag{2.95}$$

To study the quantum evolution of perturbations, we define the Mukhanov-Sasaki variable v, which is related to $\mathscr{R}$ as

$$v = z\mathscr{R}, \qquad \text{where } z = a\frac{\dot{\phi}}{H}. \tag{2.96}$$

This reformulation casts the scalar perturbations into the form of a canonical scalar field in a curved spacetime, allowing standard quantization procedures.

In conformal time τ, defined via $d\tau = dt/a(t)$, the action for scalar perturbations becomes:

$$S = \frac{1}{2}\int d\tau d^3x \left[(v')^2 - (\nabla v)^2 + \frac{z''}{z}v^2\right], \tag{2.97}$$

where the prime denotes differentiation with respect to conformal time τ. Varying this action leads to the Mukhanov-Sasaki equation [61],

$$v_{\boldsymbol{k}}'' + \left(k^2 - \frac{z''}{z}\right)v_{\boldsymbol{k}} = 0\,. \tag{2.98}$$

where $v_{\boldsymbol{k}}$ is the Fourier transform of $v(\boldsymbol{x},\tau)$

$$v_{\boldsymbol{k}}(\tau) = \int \frac{\mathrm{d}^3\boldsymbol{x}}{(2\pi)^{3/2}}\, v(\tau,\boldsymbol{x})\, e^{-i\,\boldsymbol{k}\cdot\boldsymbol{x}}. \tag{2.99}$$

Furthermore, the Fourier mode $v_{\boldsymbol{k}}$ can be written as

$$v_{\boldsymbol{k}}(\tau) = v_k(\tau)\hat{a}_{\boldsymbol{k}} + v_k^{\star}(\tau)\hat{a}^{\dagger}_{-\boldsymbol{k}}, \tag{2.100}$$

where the creation and annihilation operators $\hat{a}^{\dagger}_{-\boldsymbol{k}}$ and $\hat{a}_{\boldsymbol{k}}$ are obey the following canonical commutation relation,

$$[\hat{a}_{\boldsymbol{k}}, \hat{a}^{\dagger}_{-\boldsymbol{k}'}] = \delta(\boldsymbol{k} - \boldsymbol{k}')\,. \tag{2.101}$$

The mode function $v_k(\tau)$ and its complex conjugate $v_k^{\star}(\tau)$ are two linearly independent solutions of Eq. 2.98, so they also satisfy the Mukhanov-Sasaki equation,

$$v_k'' + \left(k^2 - \frac{z''}{z}\right)v_k = 0\,. \tag{2.102}$$

This equation governs the mode evolution of scalar perturbations. The term z''/z acts like a time-dependent effective mass. Deep inside the horizon ($k^2 \gg z''/z$), the modes oscillate as in flat space,

$$v_k(\tau) \simeq \frac{1}{\sqrt{2k}}e^{-ik\tau} \tag{2.103}$$

This defines the Bunch-Davies vacuum, the standard choice for initial conditions. We can solve Eq. 2.102 in a more general way [36, 58] in terms of slow-roll parameters. Callling $z = a\dot{\phi}/H \implies z^2 = 2\epsilon M_{\rm p}^2 a^2$ and after differentiation with conformal time,

$$\frac{z'}{z} = (aH)\left(1 + \frac{\eta_H}{2}\right), \frac{z''}{z} = (aH)^2\left(2 - \epsilon_{\rm H} + \frac{3}{2}\eta_{\rm H}\right). \tag{2.104}$$

keeping only the first order in the slow-roll parameter. Again, from the definition of the slow-roll parameter $\epsilon_{\rm H} = -\dot{H}/H^2$, one can write

$$\frac{1}{d\tau}\left(\frac{a}{aH}\right) = \epsilon_{\rm H} - 1\,. \tag{2.105}$$

Integrating the above equation and then expanding to first order in the slow-roll parameter, we have

$$aH = -\frac{1}{\tau}(1+\epsilon)\,. \tag{2.106}$$

Using the above equation in Eq. 2.104, we have

$$\frac{z''}{z} = \frac{1}{\tau^2}\left(2+3\epsilon_{\rm H}+\frac{3}{2}\eta_{\rm H}\right) = \frac{1}{\tau^2}\left(\nu_{\rm s}^2-\frac{1}{4}\right), \tag{2.107}$$

where $\nu_{\rm s} = \frac{3}{2}+\epsilon_{\rm H}+\frac{\eta_{\rm H}}{2}$. Now, the Mukhanov-Sasaki equation 2.102 can be written as [36, 58],

$$v_k'' + \left(k^2 - \frac{\nu_{\rm s}^2-\frac{1}{4}}{\tau^2}\right)v_k = 0. \tag{2.108}$$

The general solution of the above equation can be written in terms of the Hankel function

$$v_k(\tau) = \sqrt{-\tau}\,X(k)H_k^{(1)}(-k\tau) + \sqrt{-\tau}\,Y(k)H_k^{(2)}(-k\tau) \tag{2.109}$$

with $H_k^{(1)}(x)$ and $H_k^{(2)}(x)$ the Hankel functions of the first and second kind, $X(k)$ and $Y(k)$ are the integration constants. We impose Bunch-Davies boundary conditions at early times for each mode $-k\tau \gg 1$, corresponding to modes well within the horizon, and obtain the later evolution:

$$v_k(\tau) = \frac{\sqrt{\pi}}{2}e^{i(\nu_{\rm s}+1/2)\pi/2}\sqrt{-\tau}H_{\nu_{\rm s}}^{(1)}(-k\tau) \implies \lim_{-k\tau\to 0} v_k(\tau) \propto \frac{1}{\sqrt{2k}}(-k\tau)^{1/2-\nu_{\rm s}} \tag{2.110}$$

As the universe expands and the comoving Hubble radius $1/(aH)$ shrinks during inflation, each mode v_k eventually crosses the horizon ($k = aH$). Once outside the horizon ($k^2 \ll z''/z$), the mode freezes out and $\mathscr{R}_k = v_k/z$ becomes approximately constant.

The two-point correlation function of the curvature perturbation defines the power spectrum. The power spectrum of the comoving curvature perturbation is defined as,

$$\langle \mathscr{R}(\boldsymbol{k})\mathscr{R}(\boldsymbol{k}')\rangle = \langle 0|\mathscr{R}(\boldsymbol{k})\mathscr{R}(\boldsymbol{k}')|0\rangle = (2\pi)^3\delta^3(\boldsymbol{k}+\boldsymbol{k}')\frac{2\pi^2}{k^3}\mathscr{P}_{\mathscr{R}}(k), \tag{2.111}$$

where the vacuum state $|0\rangle$ is defined as $\hat{a}_{\boldsymbol{k}}|0\rangle = 0$, for all $\boldsymbol{k}$. Using the solution of v_k in Eq. 2.110, the dimensionless curvature power spectrum $\mathscr{P}_{\mathscr{R}}(k)$ can be written is,

$$\mathscr{P}_{\mathscr{R}}(k) = \frac{k^3}{2\pi^2}|\mathscr{R}(k)|^2 = \frac{H^2}{8\pi^2 M_{\rm p}^2\epsilon_{\rm H}}\left(\frac{k}{aH}\right)^{3-2\nu_{\rm s}}. \tag{2.112}$$

The power spectrum of the curvature perturbation is nearly independent of the scale k. There is still a mild scale dependence coming from the small evolution of the Hubble rate during inflation. The spectral index $n_{\rm s}$ characterizes the scale dependence of the power spectrum and is defined by

$$n_{\rm s}-1 \equiv \frac{d\ln\mathscr{P}_{\mathscr{R}}(k)}{d\ln k} = 3-2\nu_{\rm s} = -6\epsilon_V+2\eta_V, \tag{2.113}$$

A nearly scale-invariant spectrum ($n_{\rm s}\approx 1$) is one of the key predictions of inflation and is strongly supported by current CMB observations. The curvature power spectrum is usually parametrized considering the exit of the CMB pivot scale $k_\star = aH$,

$$\mathscr{P}_{\mathscr{R}}(k) = A_{\rm s}\left(\frac{k}{k_\star}\right)^{n_{\rm s}-1}, \tag{2.114}$$

where $A_{\rm s}$ is called the amplitude of the power spectrum, and it is

$$A_{\rm s} = \frac{H_k^2}{8\pi^2 M_{\rm p}^2\epsilon_{{\rm H}_k}} = \frac{V_k}{24\pi^2 M_{\rm p}^4\epsilon_{\rm V}(\phi_k)}. \tag{2.115}$$

The last expression is derived using Eq. 2.44, where the quantities with a subscript k are evaluated at the pivot scale horizon crossing.

2.8.4 Tensor Perturbations: Generation of primordial gravitational waves

In addition to scalar perturbations, inflation generically predicts the generation of tensor perturbations-fluctuations in the spacetime metric that correspond to primordial gravitational waves. These tensor modes are transverse, traceless perturbations of the spatial metric:

$$ds^2 = dt^2 - a^2(t)\left(\delta_{ij} + h_{ij}\right)dx^i dx^j = a^2(\tau)(d\tau^2 - \left(\delta_{ij} + h_{ij}\right)dx^i dx^j), \tag{2.116}$$

where h_{ij} satisfy the transverse, traceless property, $\partial^i h_{ij} = 0$, $h^i_i = 0$. Being gauge-invariant by construction, tensor perturbations are simpler to analyze than scalar modes. The quadratic action for tensor perturbations is obtained by expanding the Einstein-Hilbert action to the second order in [62]

$$S = \frac{M_{\rm p}^2}{8}\int \mathrm{d}\tau\, \mathrm{d}^3\boldsymbol{x}\, a^2(\tau)\left[(h'_{ij})^2 - (\nabla h_{ij})^2\right]. \tag{2.117}$$

Decomposing the tensor field into Fourier modes and polarization states [57–59, 63, 64],

$$h_{ij}(\tau,\boldsymbol{x}) = \sum_{s=+,\times}\int \frac{\mathrm{d}^3\boldsymbol{k}}{(2\pi)^{3/2}}\epsilon^s_{ij}(\boldsymbol{k})h_{\boldsymbol{k},s}(\tau)e^{i\boldsymbol{k}\cdot\boldsymbol{x}}, \tag{2.118}$$

where polarization tensors $\epsilon^s_{ij}(\boldsymbol{k})$ is normalized as as $\epsilon^s_{ij}(\boldsymbol{k})\epsilon^{s',ij}(\boldsymbol{k}) = 2\delta^{ss'}$ and they also satisfy the traceless condition $\epsilon^{s,i}_{i}(\boldsymbol{k}) = 0$ and the transverse condition $k^j\epsilon^s_{ij}(\boldsymbol{k}) = 0$. The modes function $h_{\boldsymbol{k},s}$ corresponds to the two polarization states of the gravitational waves (+ and ×). Using the above decomposition in Eq. 2.117, the EoM of the mode function can be calculated as

$$h''_{\boldsymbol{k},s} + 2\frac{a'}{a}h'_{\boldsymbol{k},s} + k^2 h_{\boldsymbol{k},s} = 0. \tag{2.119}$$

Again, the Fourier mode $h_{\boldsymbol{k},s}$ can be written as,

$$h_{\boldsymbol{k},s}(\tau) = h_k(\tau)\hat{a}_{\boldsymbol{k},s} + h^\star_k(\tau)\hat{a}^\dagger_{-\boldsymbol{k},s}, \tag{2.120}$$

where the creation and annihilation operators $\hat{a}^\dagger_{-\boldsymbol{k},s}$ and $\hat{a}_{\boldsymbol{k},s}$ are obey the following canonical commutation relation,

$$[\hat{a}_{\boldsymbol{k},s}, \hat{a}^\dagger_{-\boldsymbol{k}',s'}] = \delta_{ss'}\,\delta(\boldsymbol{k} - \boldsymbol{k}'). \tag{2.121}$$

The mode functions $h_k(\tau)$ and $h^\star_k(\tau)$ are linear independent solutions of Eq. 2.119. Like scalar perturbation, we can also write the EoM of h_k in terms of Mukhanov-Sasaki variable v_k as $h_k = \frac{\sqrt{2}}{M_{\rm p}}\frac{v_k}{a}$. The Mukhanov-Sasaki variable v_k satisfies the equation,

$$v''_k + \left(k^2 - \frac{a''}{a}\right)v_k = 0. \tag{2.122}$$

This equation closely resembles the Mukhanov-Sasaki equation 2.102 for scalar modes, with [36, 58]

$$\frac{a''}{a} \simeq \frac{\nu_{\rm t}^2 - \frac{1}{4}}{\tau^2}, \quad \text{where} \quad \nu_{\rm t} = \frac{3}{2} + \epsilon_H. \tag{2.123}$$

On superhorizon scales ($k \gg aH$), the tensor mode function freezes out, and we can compute the power spectrum of tensor perturbations in like same manner as we did for the scalar perturbations.

$$\mathscr{P}_{\rm t}(k) = 2\cdot\frac{k^3}{2\pi^2}|h_k|^2 = \frac{2H^2}{\pi^2 M_{\rm p}^2}\left(\frac{k}{aH}\right)^{3-2\nu_{\rm t}}, \tag{2.124}$$

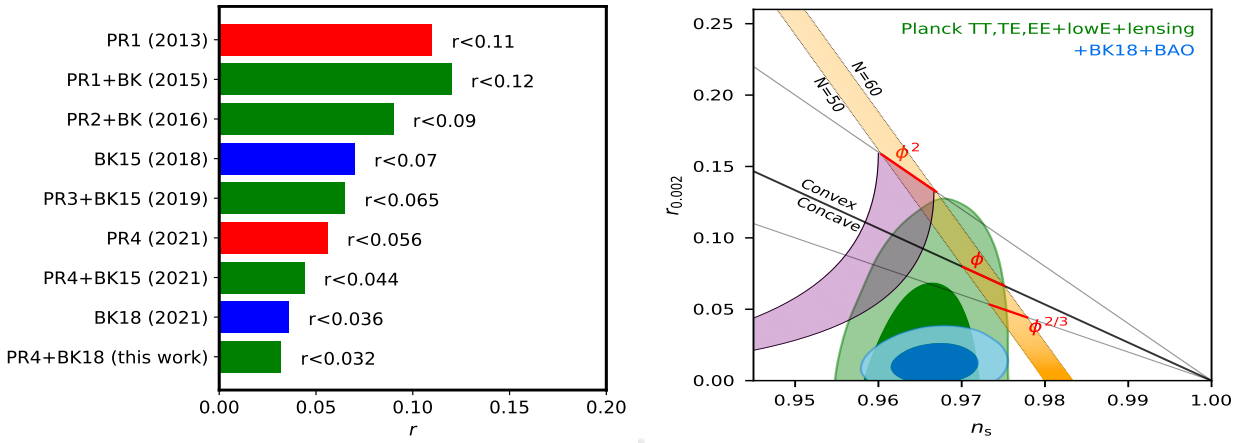

Figure 2.6: **Left plot:** Historical progression of constraints on the tensor-to-scalar ratio r. Shown are results from various data combinations: Planck PR1 [1], Planck PR1+BK [65], Planck PR2+BK [2], BK15 [66], Planck PR3+BK15 [31], Planck PR4 [67], Planck PR4+BK15 [67], BK18 [54], Planck PR4+BK18 [55]. [Source figure [55]]. ***Right plot*:** Constraints on the spectral index n_s and the tensor-to-scalar ratio r in the r-n_s plane are shown from Planck 2018 data alone (green), and from the combined analysis including Planck, BICEP/Keck 2018 (BK18), and Baryon Acoustic Oscillation (BAO) data (cyan). The inclusion of BK18 and BAO significantly tightens the bounds on both n_s and r. [Source figure BICEP/Keck website].

where the factor of 2 accounts for the two polarization states. Similar to the scalar case, the tensor power spectrum is nearly scale-invariant, and its tilt is given by:

$$n_{\rm t} \equiv \frac{d\ln {\rm P}_{\rm t}(k)}{d\ln k} = 3 - 2\nu_{\rm t} = -2\epsilon_{\rm H} = -2\epsilon_{\rm V}. \tag{2.125}$$

As for comoving curvature perturbations, we parametrized the initial tensor power spectrum at the horizon crossing of the CMB pivot scale,

$$\mathscr{P}_t(k) = A_{\rm t}\left(\frac{k}{k_\star}\right)^{n_{\rm t}}, \tag{2.126}$$

where $n_{\rm t}$ is called the tensor spectral index, and the amplitude of the tensor power spectrum $A_{\rm t}$ is

$$A_{\rm t} = \frac{2H_k^2}{\pi^2 M_{\rm p}^2} = \frac{2V_k}{3\pi^2 M_{\rm p}^4}. \tag{2.127}$$

A key observable that links scalar and tensor perturbations is the tensor-to-scalar ratio (r) defined as,

$$r \equiv \frac{A_{\rm t}}{A_{\rm s}} = 16\epsilon_V(\phi_k), \tag{2.128}$$

This ratio not only encodes the strength of tensor modes relative to scalar perturbations but also serves as a direct probe of the energy scale of inflation. In particular, combining the Eqs. 2.127 and 2.128, the Hubble scale during inflation is related to r and $A_{\rm s}$ by

$$H_k = \frac{\pi M_{\rm p}\sqrt{rA_{\rm s}}}{\sqrt{2}}. \tag{2.129}$$

Hence, measuring r constrains the inflationary energy scale. In recent years, significant progress has been made in constraining r (see right plot of Fig. 2.6). The latest results from Planck 2018, in combination with BICEP/Keck 2018 (BK18), provide a stringent upper bound [54],

$$r_{0.05} < 0.035 \text{ at } 95\% \text{ C.L.} \tag{2.130}$$

Furthermore, Planck 2018 [4, 31] also measures the amplitude and spectral tilt of the scalar curvature power spectrum at the pivot scale $k_\star/a_0 = 0.05\,\mathrm{Mpc}^{-1}$,

$$A_\mathrm{s} = (2.101 \pm 0.034) \times 10^{-9}, \quad n_\mathrm{s} = 0.9649 \pm 0.0042 \quad \text{at } 68\%\ \text{C.L.} \tag{2.131}$$

The scalar spectral index n_s characterizes the scale dependence of the scalar perturbations. The fact that $n_\mathrm{s} < 1$ implies a slight red tilt, consistent with the predictions of standard slow-roll inflation. Using Eq. 2.129 and the observational upper limit on r, we can place an upper bound on the Hubble parameter during inflation,

$$H_k < 2 \times 10^{-5} M_\mathrm{p} = 4.8 \times 10^{13}\,\mathrm{GeV}. \tag{2.132}$$

This corresponds to the maximum allowed energy scale of inflation under current constraints, making r a powerful window into the early universe.

2.9 Inflationary models and inflationary parameters

So far, we have not specified the explicit form of the inflaton potential. Since the inception of inflationary theory, various models have been proposed [68], some of which have already been ruled out either due to incompatibility with CMB observations or the inability to end inflation properly. Among the broad landscape of single-field inflationary models, these can generally be classified into three types based on the trajectory of the inflaton and the shape of its potential. The first category comprises the large-field models, where the inflaton field starts with a large initial value, typically exceeding the Planck scale ($\phi_i > M_P$), and undergoes slow-roll evolution down to the potential minimum. In this thesis, we consider several representative models within this class, including the α-attractor models (both E- and T-type) [69–72] and the minimal plateau model [15, 73]. The second class includes the small-field models [74], characterized by a sub-Planckian initial value ($\phi_i < M_\mathrm{p}$), where the inflaton slowly rolls away from a local maximum or inflection point toward a minimum at larger field values. These models often face more difficulty in satisfying current CMB constraints on the scalar spectral index n_s and the tensor-to-scalar ratio r. The third class consists of hybrid inflation models [75, 76], in which inflation ends not due to the dynamics of the inflaton field alone but through its coupling to a second scalar field (ψ). The end of inflation is triggered by a phase transition initiated by this auxiliary field (ψ), which drives the system toward a stable minimum. We illustrate the typical potential shapes corresponding to large-field (left), small-field (middle), and hybrid-field models (right) in Fig. 2.7.

Next, we will discuss a few slow-roll inflationary models that we have used in this thesis and derive the relation between the inflationary parameters and the CMB parameters.

2.9.1 α-attractor E-model

The α-attractor E-model [69–72] is a well-motivated class of inflationary potentials inspired by supergravity and conformal field theory [77–79]. The typical form of the α-attractor model is given by[69–72],

$$V(\phi) = \Lambda^4 \left(1 - e^{-\sqrt{\frac{2}{3\alpha}}\frac{\phi}{M_p}}\right)^{2n}, \tag{2.133}$$

Here, Λ represents the potential scale, which can be determined from the CMB measurements [18]. The parameters n and α control the shape of the potential. Specifically, the parameter n governs the

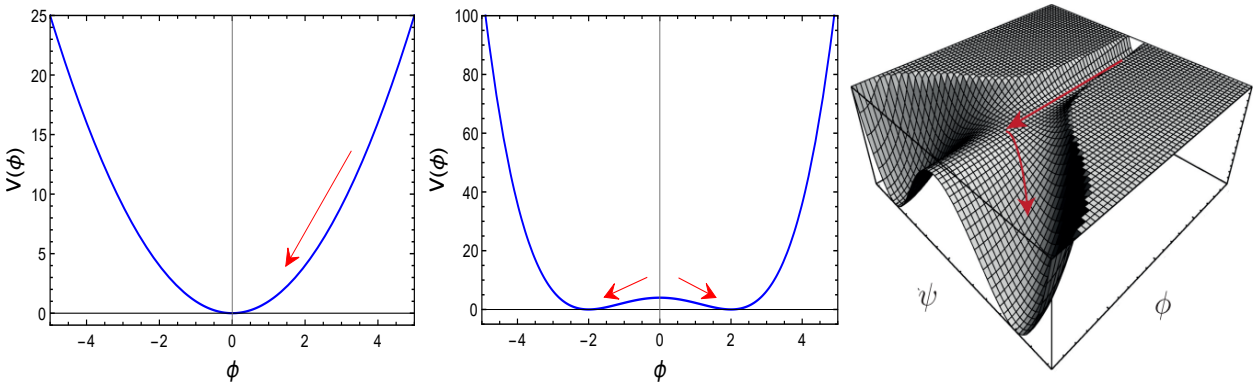

Figure 2.7: Schematic diagram of large field model (left), small field model (middle), and hybrid field model (right).

steepness of the potential near its minimum, and this steepness is related to the EoS of the inflaton field, $w_\phi = (n-1)/(n+1)$. The parameter α, on the other hand, controls the curvature of the scalar field manifold, influencing the overall shape of the potential. Different choices of n and α thereby affect inflationary predictions such as the scalar spectral index n_s and the tensor-to-scalar ratio r. For $n = 1$ and $\alpha = 1$, the potential simplifies to the Starobinsky potential [80], which is a widely studied model in inflationary cosmology. Like the Starobinsky potential, the E-model exhibits a similar plateau region at large field values for all values of n.

From the definition of slow-roll parameters (see Eq. 2.48), the expression of the slow-roll parameter for the E-model can be written as,

$$\begin{aligned}\epsilon_V(\phi) &= \frac{M_p^2}{2}\left(\frac{V'(\phi)}{V(\phi)}\right)^2 = \frac{4n^2}{3\alpha}\frac{1}{\left(e^{\sqrt{\frac{2}{3\alpha}}\frac{\phi}{M_p}}-1\right)^2},\\ \eta_V(\phi) &= \frac{M_p^2}{2}\frac{V''(\phi)}{V(\phi)} = \frac{4n}{3\alpha}\frac{\left(2n - e^{\sqrt{\frac{2}{3\alpha}}\frac{\phi}{M_p}}\right)}{\left(e^{\sqrt{\frac{2}{3\alpha}}\frac{\phi}{M_p}}-1\right)^2}.\end{aligned} \tag{2.134}$$

We can write the scalar spectral index n_s and the tensor-to-scalar ratio r in terms slow-roll parameters for a particular pivot scale $k_\star$ (from Eq. 2.113, 2.128),

$$\begin{aligned}n_s &= 1 - 6\epsilon_V(\phi_k) + 2\eta_V(\phi_k) = 1 - \frac{8n}{3\alpha}\frac{\left(n + e^{\sqrt{\frac{2}{3\alpha}}\frac{\phi_k}{M_p}}\right)}{\left(e^{\sqrt{\frac{2}{3\alpha}}\frac{\phi_k}{M_p}}-1\right)^2},\\ r &= 16\epsilon_V(\phi_k) = \frac{64n^2}{3\alpha}\frac{1}{\left(e^{\sqrt{\frac{2}{3\alpha}}\frac{\phi_k}{M_p}}-1\right)^2}.\end{aligned} \tag{2.135}$$

After solving the above equation, we can write the field value ϕ_k at the horizon crossing, and the quantity

r in terms of n_s, α, n,

$$\begin{aligned}\phi_k &= \sqrt{\frac{3\alpha}{2}}\, M_p \ln\left[1+\frac{4n+\sqrt{16n^2+24\alpha n(1-n_s)(1+n)}}{3\alpha(1-n_s)}\right],\\ r &= \frac{192\,\alpha\, n^2(1-n_s)^2}{\left(4n+\sqrt{16n^2+24\alpha n(1-n_s)(1+n)}\right)^2}.\end{aligned} \tag{2.136}$$

The inflationary e-folding number (N_k) between the exit of the horizon of the scale $k_\star$ at ϕ_k, and the end of inflation at $\phi_{\rm end}$, can be calculated in the slow-roll approximation,

$$N_k = \int_{a_k}^{a_{\rm end}} d(\ln a) = \frac{1}{M_p}\int_{\phi_k}^{\phi_{\rm end}} \frac{d\phi}{\sqrt{2\epsilon}} = \frac{3\alpha}{4}\left(e^{\sqrt{\frac{2}{3\alpha}}\cdot\frac{\phi_k}{M_{\rm p}}} - e^{\sqrt{\frac{2}{3\alpha}}\cdot\frac{\phi_{\rm end}}{M_{\rm p}}} - \sqrt{\frac{2}{3\alpha}}\,\frac{(\phi_k-\phi_{\rm end})}{M_{\rm p}}\right). \tag{2.137}$$

Here ϕ_k and $\phi_{\rm end}$ represent the values of the inflaton field at the point of horizon crossing and at the end of the inflation, respectively. The value of $\phi_{\rm end}$ is determined by the condition $\epsilon_{\rm V}(\phi_{\rm end}) = 1$, marking the end of inflation. Using this condition, the field value and the potential at the end of inflation can be expressed as follows,

$$\phi_{\rm end} = \frac{\sqrt{3\alpha}}{2n} M_p \ln\left(\frac{2n+\sqrt{3\alpha}}{\sqrt{3\alpha}}\right) \quad , \quad V(\phi_{\rm end}) = \Lambda^4\left(\frac{2n}{2n+\sqrt{3\alpha}}\right)^{2n}. \tag{2.138}$$

To find the potential scale Λ, we use the following relation (Eq. 2.127),

$$V(\phi_k) = \frac{3\pi^2 A_s M_{\rm p}^4}{2} r = \Lambda^4\left(1-e^{-\sqrt{\frac{2}{3\alpha}}\frac{\phi_k}{M_{\rm p}}}\right)^{2n}. \tag{2.139}$$

Using the expression of ϕ_k and r, we obtain,

$$\Lambda = M_{\rm p}\left(\frac{3\pi^2 r A_s}{2}\right)^{1/4}\left[\frac{2n(2n+1)+\sqrt{4n^2+6\alpha(1+n)(1-n_s)}}{4n(1+n)}\right]^{n/2}. \tag{2.140}$$

Finally, using this expression of Λ in Eq. 2.138, we can determine the initial condition for reheating,

$$\rho_\phi^{\rm end} \simeq \frac{3}{2}V(\phi_{\rm end}) = \frac{3}{2}\Lambda^4\left(\frac{2n}{2n+\sqrt{3\alpha}}\right)^{2n}. \tag{2.141}$$

2.9.2 α-attractor T-model

Another class of α-attractor models that we consider is the α-attractor T-model. Its potential is given by [69–72],

$$V(\phi) = \Lambda^4 \tanh^{2n}\left(\frac{\phi}{\sqrt{6\,\alpha}\,M_{\rm p}}\right). \tag{2.142}$$

To compute the inflationary parameters, we will follow the same procedure as in the E-model. Using the definition of slow-roll parameters, the expression of the slow-roll parameters for the T-model can be written as,

$$\begin{aligned}\epsilon_{\rm V}(\phi) &= \frac{M_{\rm p}^2}{2}\left(\frac{V'(\phi)}{V(\phi)}\right)^2 = \frac{4n^2}{3\,\alpha}\,{\rm csch}^2\left(\sqrt{\frac{2}{3\alpha}}\,\frac{\phi}{M_{\rm p}}\right),\\ \eta_{\rm V}(\phi) &= \frac{M_{\rm p}^2}{2}\frac{V''(\phi)}{V(\phi)} = \frac{4n}{3\,\alpha}\,{\rm csch}^2\left(\sqrt{\frac{2}{3\alpha}}\,\frac{\phi}{M_{\rm p}}\right)\left[\cosh\left(\sqrt{\frac{2}{3\alpha}}\,\frac{\phi}{M_{\rm p}}\right)-2n\right].\end{aligned} \tag{2.143}$$

At the end of inflation $\epsilon_V(\phi_{\rm end}) \simeq 1$, from the above equation, $\phi_{\rm end}$ for T-model can be written as,

$$\phi_{\rm end} = \sqrt{\frac{3\alpha}{2}}\, M_{\rm p}\, \text{arcsinh}\left(\frac{2n}{\sqrt{3\alpha}}\right) = \sqrt{\frac{3\alpha}{8}}\, M_{\rm p}\, \ln\left(1 + \frac{4n\left(2n+\sqrt{4n^2+3\alpha}\right)}{3\alpha}\right). \tag{2.144}$$

The inflationary e-folding number (N_k) between the exit of the horizon of the scale k at ϕ_k, and the end of inflation at $\phi_{\rm end}$, can be calculated in the slow-roll approximation,

$$N_k = \frac{1}{M_{\rm p}}\int_{\phi_k}^{\phi_{\rm end}} \frac{d\phi}{\sqrt{2\epsilon}} = -\frac{3\alpha}{4n}\left(\cosh\left(\sqrt{\frac{2}{3\alpha}}\frac{\phi_{\rm end}}{M_{\rm p}}\right) - \cosh\left(\sqrt{\frac{2}{3\alpha}}\frac{\phi_k}{M_{\rm p}}\right)\right). \tag{2.145}$$

Again, ϕ_k can be computed in terms of $n_{\rm s}$ using the relation $n_{\rm s} = 1 - 6\epsilon(\phi_k) + 2\eta(\phi_{\rm end})$,

$$\phi_k = \sqrt{6\alpha}\, M_{\rm p}\, \text{arctanh}\left[\frac{2\sqrt{n(1+n)}}{\sqrt{4n^2+3\alpha(1-n_{\rm s}) + \sqrt{(3\alpha(1-n_{\rm s}))^2 + 8n^2(2+3\alpha(1-n_{\rm s}))}}}\right]. \tag{2.146}$$

Utilizing ϕ_k we can compute tensor-to-scalar ratio $r = 16\epsilon(\phi_k)$ (defined Eq. 2.128)

$$r = \frac{64n^2}{3\alpha}\,\text{csch}^2\left(\sqrt{\frac{2}{3\alpha}}\frac{\phi_k}{M_{\rm p}}\right) = \begin{cases} \frac{n(4-3(-1+n_{\rm s})\alpha) - \sqrt{9(-1+n_{\rm s})^2\alpha^2 + 8n^2(2+3\alpha-3n_{\rm s}\alpha)}}{8n(-1+n^2)}, & \text{for } n \neq 1, \\ \frac{\left(-4-3(n_{\rm s}-1)\alpha + \sqrt{(4-3(n_{\rm s}-1)\alpha)^2}\right)^2}{32\left(4-3(n_{\rm s}-1)\alpha+\sqrt{(4-3(n_{\rm s}-1)\alpha)^2}\right)} & \text{for } n = 1. \end{cases} \tag{2.147}$$

The amplitude of the primordial curvature power spectrum $A_{\rm s}$ and r is related to the inflaton potential at the horizon crossing via the relation 2.127,

$$V(\phi_k) = \frac{3\pi^2 A_{\rm s} M_{\rm p}^4}{2} r = \Lambda^4 \tanh^{2n}\left(\frac{\phi_k}{\sqrt{6\alpha}\, M_{\rm p}}\right). \tag{2.148}$$

Using ϕ_k in the above equation, and inverting this equation, the scale Λ can be written as

$$\Lambda = M_{\rm p}\left(\frac{3\pi^2 A_{\rm s} r}{2}\right)^{1/4}\left(\frac{4n^2+3\alpha(1-n_{\rm s}) + \sqrt{9\alpha^2(1-n_{\rm s})^2 + 8n^2(2+3\alpha(1-3n_{\rm s}))}}{4n(n+1)}\right)^{n/4}. \tag{2.149}$$

2.9.3 Minimal plateau model

The Minimal plateau Model is another well-studied model of inflation that is particularly known for its simplicity and ability to accommodate a wide range of observational data, including the CMB measurements. This model is characterized by a potential that approaches a plateau at large field values, which leads to a period of slow-roll inflation. The form of the minimal plateau model is given by [15, 17, 73]

$$V(\phi) = \Lambda^4 \frac{\phi^{2n}}{\phi^{2n} + \phi_*^{2n}}. \tag{2.150}$$

where Λ is the potential scale, can be fixed in terms of CMB observables ($n_{\rm s}$,r). A new mass scale ϕ_* is introduced to control the shape of the potential. Here, one important point is to note that ϕ_* is measured in $M_{\rm p}$ units. The expressions of the slow-roll parameters are

$$\epsilon_V(\phi) = \frac{2n^2 M_{\rm p}^2 \phi_*^{4n}}{\phi^2(\phi^{2n} + \phi_*^{2n})^2}. \tag{2.151}$$

$$\eta_V(\phi) = 2nM_p^2 \frac{\phi_*^{2n}}{\phi^2} \frac{\left[(n-1)\phi_*^{2n} + (n+1)\phi^{2n}\right]}{(\phi_*^{2n} + \phi^{2n})^2}. \tag{2.152}$$

The e-folding number can be derived as,

$$N_k = \frac{1}{M_p^2} \int_{\phi_{end}}^{\phi_k} \frac{V(\phi)}{V'(\phi)} d\phi = \frac{1}{2nM_p^2} \left[\frac{\phi_k^2 - \phi_{end}^2}{2} + \frac{\phi_k^{2n+2} - \phi_{end}^{2n+2}}{(2n+2)\phi_*^{2n}} \right]. \tag{2.153}$$

The above expression simplifies under the approximation $\phi_k \gg \phi_{end}$, which holds well for $\phi_* \lesssim \mathcal{O}(1)$. Neglecting the quadratic term, we get,

$$N_k \simeq \frac{1}{2nM_p^2} \frac{\phi_k^{2n+2}}{(2n+2)\phi_*^{2n}}. \tag{2.154}$$

Since in our work we are also interested in $\phi_* > 1$, we adopt the exact form for numerical solution. Without any approximation, the n_s and r can be written as,

$$n_s = 1 - 2nM_p^2 \frac{\left[(2n+2)\phi_*^{2n} + 2(2n+1)\phi_k^{2n}\right]\phi_k^{2n}}{\left[\phi_k^{2n} + \phi_*^{2n}\right]^2 \phi_k^2}, \quad r = \frac{32n^2 M_p^2 \phi_*^{4n}}{\phi_k^2 \left(\phi_k^{2n} + \phi_*^{2n}\right)^2}. \tag{2.155}$$

Now, we will consider another approximation $\phi_k >> \phi_*$, and it is also good approximation within $\phi_* < \mathcal{O}(1)$. Under this condition, we can analytically compute N_k and r in terms of n_s. By combining the Eqs. 2.154 and 2.155, we have

$$N_k \simeq \frac{2(2n+1)}{(2n+2)(1-n_s)}, \quad r \simeq 16n^2 \left(\frac{\phi_*}{M_p}\right)^{\frac{4n}{(2n+2)}} \left(\frac{(1-n_s)(2n+2)}{4n(2n+1)}\right)^{\frac{(2n+1)}{2(2n+2)}}. \tag{2.156}$$

Now, from Eq. 2.154, the field value at the horizon crossing with this approximation can be written as,

$$\phi_k \simeq \left(\frac{4n(2n+1)M_p^2}{1-n_s}\right)^{\frac{1}{2n+2}} \phi_*^{\frac{n}{n+1}}. \tag{2.157}$$

Utilizing the above expression ϕ_k, we can calculate the scale Λ for this model,

$$\Lambda = M_p \left(\frac{3\pi^2 A_s r}{2}\right)^{1/4} \left[1 + \left(\frac{(1-n_s)}{4n(2n+1)}\left(\frac{\phi_*}{M_p}\right)^2\right)^{\frac{2n}{2n+2}}\right]^{1/4}. \tag{2.158}$$

However, it is important to note that the analytical expressions for the inflationary parameters (N_k, ϕ_k, Λ) in this minimal model are approximate and not exact expressions. The precise values of these parameters can only be obtained through numerical computation. Therefore, for our analysis, we determined all of these parameters numerically.

In this thesis, we dedicate a whole chapter (Chapter 4) to examining the validity of all these models in light of the latest Planck and BICEP/*Keck* observations.

2.10 Dark Matter

One of the most profound mysteries in modern cosmology and particle physics is the nature of DM. Although it does not emit, absorb, or reflect light, its existence is firmly established through its gravitational influence on visible matter, radiation, and the large-scale structure of the universe. DM constitutes about 27% of the total energy density of the universe, far exceeding the contribution from ordinary baryonic

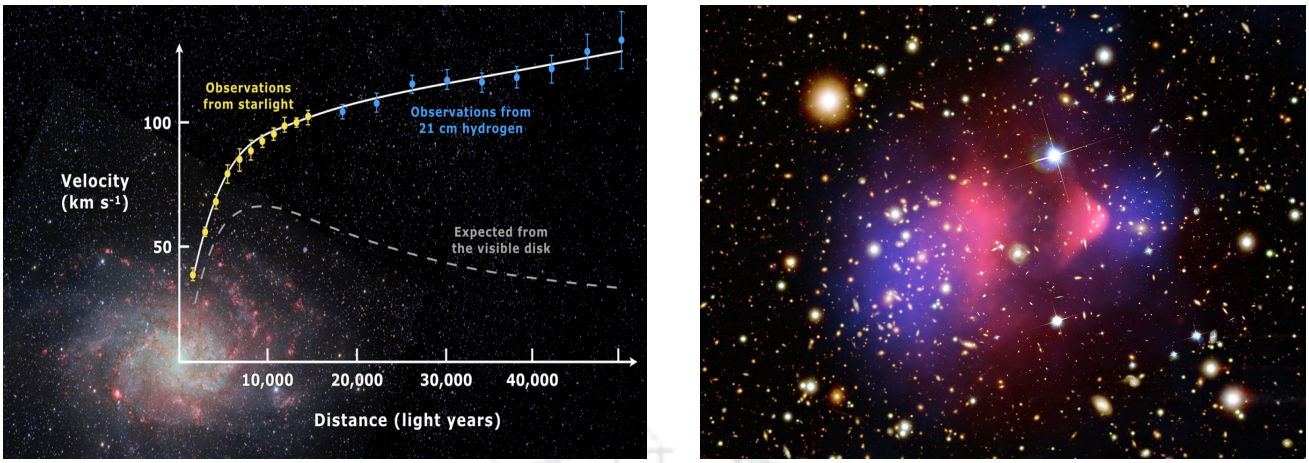

Figure 2.8: ***Left plot***: Rotation curve of galaxy Messier 33 [81] [Image courtesy: wikipedia]. ***Right plot***: Composite image of the Bullet Cluster. The background shows visible light from Magellan and Hubble Space Telescope images. The pink overlay represents X-ray emission from the colliding clusters, observed by the Chandra Telescope. The blue overlay shows the mass distribution of the clusters, calculated from gravitational lensing effects.[Image courtesy: ESA website]

matter, which accounts for merely 5%. The rest is attributed to dark energy (about 68%), responsible for the observed accelerated expansion of the universe.

The SM of particle physics, despite its tremendous success in explaining the known fundamental particles and their interactions, fails to provide a suitable DM candidate. This indicates the necessity for new physics beyond the SM. The search for the identity of DM has, therefore, become one of the central questions at the interface of cosmology, astrophysics, and high-energy particle physics.

DM plays a pivotal role in shaping the universe. It acts as the cosmic scaffolding on which galaxies and large-scale structures form and evolve. Without DM, the observed structure formation, from galaxies to galaxy clusters, cannot be explained within the framework of the standard cosmological model (ΛCDM). Moreover, precise measurements of the CMB, large-scale structure, gravitational lensing, and the dynamics of galaxies and clusters all independently point toward the presence of a non-luminous and non-baryonic matter component.

Despite its gravitational dominance, DM interacts very weakly with electromagnetic radiation or ordinary matter. This elusive behavior has made its direct detection extremely challenging, but it also helps constrain the properties that any viable DM candidate must satisfy. Understanding DM requires us to explore both its cosmological implications and its possible microscopic origin, motivating a diverse array of theoretical models and experimental searches.

In what follows, we begin by reviewing the key observational evidence supporting the existence of DM, followed by a discussion on the criteria a particle must fulfill to qualify as a DM candidate, and then proceed to explore various theoretical frameworks and production mechanisms.

2.10.1 Observational evidence for DM

The existence of DM is inferred from several independent and complementary observations :

- **Galactic Rotation Curves :** The first compelling evidence for DM emerged from studies of the

rotation curves of spiral galaxies [82]. According to Newtonian mechanics, the orbital velocity $v(r)$ of stars and gas at a distance r from the galactic center should decrease with r, roughly following $v(r) \propto 1/\sqrt{r}$. Contrary to this expectation, observations show that the rotation curves tend to remain flat or even rise slightly at large radii (see left Fig. 2.8). Such flat rotation curves, first systematically studied by Vera Rubin and collaborators [83, 84] in the 1970s, are now observed in many spiral galaxies. This behavior cannot be explained by the visible matter alone. The discrepancy is naturally resolved by postulating the existence of an extended DM halo surrounding galaxies, contributing the additional gravitational pull required to sustain the high orbital velocities.

- **Gravitational Lensing :** Gravitational lensing offers compelling evidence for the existence of DM. According to General Relativity, massive objects curve the surrounding spacetime, bending the path of light- a phenomenon known as gravitational lensing. When light from distant galaxies passes through an intervening massive object, such as a galaxy or galaxy cluster, its path is distorted due to the gravitational influence of the mass. As a result, a characteristic distortion pattern of light is observed by detectors. A striking example of gravitational lensing is the Bullet Cluster [85], formed by the collision of two galaxy clusters, which is shown in the right Fig. 2.8. X-ray observations (shown in pink) reveal the distribution of hot gas, which contains most of the baryonic matter. However, gravitational lensing maps (shown in blue) indicate that the majority of the total mass lies in regions spatially offset from the gas. This spatial separation demonstrates that the dominant matter component is DM, which does not interact strongly either with itself or with baryonic matter, as it passed through the collision largely unaffected. These features cannot be explained by modified gravity alone if the hot gas is assumed to be the most massive component; instead, DM is required to account for the observations.

- **CMB :** Measurements of the CMB temperature anisotropies by experiments such as WMAP [86] and Planck [1] provide strong constraints on the cosmological parameters. The angular power spectrum of these anisotropies is sensitive to the matter content of the universe. The best-fit cosmological model requires DM to constitute about 26.8% of the total energy density of the universe today, significantly more than five times the contribution from baryonic matter. [31].

- **Structure Formation :** The CMB shows that the early universe had tiny energy density fluctuations, $\delta\rho/\rho \sim 10^{-5}$. However, these small inhomogeneities grew into the vast cosmic structures we observe today- galaxies, clusters, and stars. This structure formation cannot be explained by baryonic matter alone, as its interaction with radiation delayed gravitational collapse in the early universe. In contrast, DM, which interacts only gravitationally, was free to collapse into dense halos much earlier, providing the gravitational wells that later attracted baryonic matter after recombination. Importantly, DM must be non-relativistic (cold) during structure formation. If it were relativistic, as in the case of neutrinos, its large thermal velocities would prevent clustering on small scales, washing out the formation of halos. The presence of cold DM is essential; without it, the onset of galaxy formation would occur much later than what observations indicate [87]. Furthermore, numerical simulations like the Millennium simulation [88] confirm that cold DM is essential to reproduce the observed distribution and growth of cosmic structures. Without a cold DM component, the observed cosmic web and clustering pattern would be impossible to explain.

To qualify as a viable DM candidate, a particle or field must satisfy the following conditions [89]:

1. **Neutrality:** It must be electrically neutral to avoid electromagnetic interactions.
2. **Stability:** Its lifetime must be at least comparable to the age of the universe, $\tau \gtrsim 10^{17}$ s.
3. **Cold nature:** It should be non-relativistic at the time of structure formation to support the growth of cosmic structures.
4. **Weak interactions:** It must have sufficiently weak couplings with SM particles to evade current experimental limits.
5. **Correct relic abundance:** It should yield a relic density consistent with observations, $\Omega_{\rm DM}h^2 \simeq 0.12$, as reported by Planck 2018 [31].

These requirements have guided extensive theoretical and experimental searches for DM, motivating numerous particle physics models beyond the SM, including *Weakly interacting massive particles* (WIMPs), axions, sterile neutrinos, and *Feebly interacting massive particles* (FIMPs) produced via non-thermal mechanisms, and non-particle objects like Primordial Black Holes (PBHs).

2.10.2 Dark Matter Production

A complete and realistic DM model must not only comply with all known particle physics and astrophysical constraints but also provide a viable mechanism for generating the DM abundance observed today, $\Omega_{\rm DM}h^2 \simeq 0.12$. This requires a consistent understanding of how DM particles were produced in the early universe and how their number density evolved over time. Broadly speaking, DM production mechanisms are classified into two main categories: *thermal* and *non-thermal* production. In thermal production scenarios, DM particles were once in thermal equilibrium with the SM plasma and decoupled as the universe expanded and cooled. The classic example is the freeze-out mechanism, which is characteristic of WIMPs. In contrast, non-thermal production refers to scenarios where dark matter was never in equilibrium with the SM bath; instead, it was gradually produced through suppressed interactions or from decays of other heavier particles. A well-known example of this is the freeze-in mechanism, relevant for FIMPs. In the following sections, we discuss these mechanisms in detail.

2.10.2.1 Freeze-Out Mechanism: WIMPs

A well-motivated and extensively studied scenario for DM production in the early universe is the thermal freeze-out mechanism. In this framework, DM particles were initially in thermal equilibrium with the SM plasma in the early universe and later decoupled as the universe expanded and cooled. This mechanism is naturally realized in a class of candidates known as WIMPs [90–92].

To understand the evolution history and eventual abundance of DM in the universe, we must track the evolution of its number density in the expanding background. This evolution is governed by the Boltzmann equation, which describes how the phase space distribution function of a particle species evolves due to both cosmic expansion and particle interactions. Let us consider a generic DM particle (say X) with phase space distribution function $f_{\rm X}(t, \boldsymbol{p})$, where $\boldsymbol{p}$ is the spatial momentum vector. In a homogeneous and isotropic universe described by the FLRW metric, the Boltzmann equation for $f_{\rm X}$ takes the form [26]

$$\frac{\partial f_{\rm X}}{\partial t} - H|\vec{p}|\frac{\partial f_{\rm X}}{\partial |\vec{p}|} = C[f_{\rm X}],, \tag{2.159}$$

where H is the Hubble expansion rate and $C[f_X]$ denotes the collision term, accounting for interactions such as annihilation, production, or decay of X particles. To follow the evolution of the total number density, we integrate the distribution function over momentum space. The number density n_X is given by

$$n_X(t) = g_X \int \frac{d^3\mathbf{p}_X}{(2\pi)^3} f_{\mathbf{X}}(t,\vec{p}),, \tag{2.160}$$

where g_X is the number of internal degrees of freedom of the DM particle. Taking the time derivative and using the Boltzmann equation 2.159, the evolution equation of n_X becomes

$$\frac{dn_X}{dt} + 3Hn_X = \int \frac{d^3\mathbf{p}_X}{(2\pi)^3} C[f_X]. \tag{2.161}$$

Here, the $3Hn_X$ term accounts for dilution due to the expansion of the universe, while the collision term $C[f_X]$ encodes the net effect of interactions that change the number of X particles.

To make further progress, we need to specify the nature of DM interactions in the early universe. We consider a scenario in which a DM particle X and its antiparticle $\bar{X}$ can annihilate into a pair of SM particles Y and $\bar{Y}$, and conversely, the reverse process $Y\bar{Y} \to X\bar{X}$ is also possible. This interaction governs the thermal production and eventual freeze-out of DM in the early universe.

We begin with the collision term in the Boltzmann equation, which governs the evolution of the distribution function f_X of the DM particle due to interactions like $X\bar{X} \leftrightarrow Y\bar{Y}$. The general expression for the collision term is given by:

$$\begin{aligned} C[f_X] = \int & \frac{d^3\mathbf{p}_Y}{(2\pi)^3 2E_Y} \frac{d^3\mathbf{p}_{\bar{Y}}}{(2\pi)^3 2E_{\bar{Y}}} \frac{d^3\mathbf{p}_{\bar{X}}}{(2\pi)^3 2E_{\bar{X}}} (2\pi)^4 \delta^4(p_X + p_{\bar{X}} - p_Y - p_{\bar{Y}}) \\ & \left[|\mathcal{M}_{X\bar{X}\to Y\bar{Y}}|^2 f_X f_{\bar{X}} (1 \pm f_Y)(1 \pm f_{\bar{Y}}) - |\mathcal{M}_{Y\bar{Y}\to X\bar{X}}|^2 f_Y f_{\bar{Y}} (1 \pm f_X)(1 \pm f_{\bar{X}}) \right], \end{aligned} \tag{2.162}$$

where $E_{X,Y}$ corresponds to the energy of the particles. To simplify this expression, we make the following assumptions,

1. No CP violation: By CPT symmetry, the squared matrix elements $\mathcal{M}$ are equal for forward and backward reactions:

$$|\mathcal{M}_{X\bar{X}\to Y\bar{Y}}|^2 = |\mathcal{M}_{Y\bar{Y}\to X\bar{X}}|^2 = |\mathcal{M}|^2. \tag{2.163}$$

2. Negligible quantum statistical effects: At the early universe, $1 \pm f \approx 1$, so Bose enhancement and Pauli blocking can be neglected.

3. The SM particles are assumed to be in thermal equilibrium with zero chemical potential ($\mu = 0$). Under these assumption, the distribution functions for bot Y and $\bar{Y}$ follow Maxwell-Boltzmann (MB) statistics,

$$f_Y = f_Y^{\rm eq} = \exp(-E_Y/T_{\rm rad}), \quad f_{\bar{Y}} = f_{\bar{Y}}^{\rm eq} = \exp(-E_{\bar{Y}}/T_{\rm rad}). \tag{2.164}$$

Substituting the above into the collision term and integrating over energy conservation, we obtain the simplified form,

$$C[f_X] = \int \frac{d^3\mathbf{p}_Y}{(2\pi)^3 2E_Y} \frac{d^3\mathbf{p}_{\bar{Y}}}{(2\pi)^3 2E_{\bar{Y}}} \frac{d^3\mathbf{p}_{\bar{X}}}{(2\pi)^3 2E_{\bar{X}}} (2\pi)^4 \delta^4(p_X + p_{\bar{X}} - p_Y - p_{\bar{Y}}) |\mathcal{M}|^2 \left[f_Y^{\rm eq} f_{\bar{Y}}^{\rm eq} - f_X f_{\bar{X}} \right] \tag{2.165}$$

Furthermore, the DM distribution function f_X is also assumed to follow MB distribution,

$$f_X = \exp[-(E_X + \mu_X)/T_{\rm rad}], \tag{2.166}$$

where μ_X is the chemical potential of the DM. After integrating both sides with factor $\int g_X \frac{d^3\mathbf{p}_X}{(2\pi)^3}$, we have

$$n_X = \exp(\mu_X/T_{\rm rad})\, n_X^{\rm eq}, \tag{2.167}$$

where $n_X^{\rm eq}$ be the equilibrium number density which is defined as

$$n_X^{\rm eq} = \int g_X \frac{d^3\mathbf{p}_X}{(2\pi)^3} \exp(-E_X/T_{\rm rad}) = \frac{g_X\, T_{\rm rad}^3}{2\pi^2} \left(\frac{m_X}{T_{\rm rad}}\right)^2 K_2\left(\frac{m_X}{T_{\rm rad}}\right), \tag{2.168}$$

where, K_2 is the modified Bessel function of the second kind of order 2 and m_X is the DM mass. Using the Eqs. 2.166 and 2.167, the term $f_X\, f_{\bar{X}}$ can be written as,

$$f_X\, f_{\bar{X}} = \exp[-(E_X + E_{\bar{X}})/T_{\rm rad}]\, \frac{n_X}{n_X^{\rm eq}}\, \frac{n_{\bar{X}}}{n_{\bar{X}}^{\rm eq}} = \exp[-(E_Y + E_{\bar{Y}})/T_{\rm rad}]\, \frac{n_X^2}{\left(n_X^{\rm eq}\right)^2}. \tag{2.169}$$

where we used the energy conservation condition $E_X + E_{\bar{X}} = E_Y + E_{\bar{Y}}$, and finally, we assume that there is no asymmetry between particles and anti-particles, i.e, $n_X = n_{\bar{X}}$. Using the Eq. 2.169, the collision term 2.170 can be written as,

$$C[f_X] = \int \frac{d^3\boldsymbol{p}_Y}{(2\pi)^3 2E_Y} \frac{d^3\boldsymbol{p}_{\bar{Y}}}{(2\pi)^3 2E_{\bar{Y}}} \frac{d^3\boldsymbol{p}_{\bar{X}}}{(2\pi)^3 2E_{\bar{X}}} (2\pi)^4 \delta^4(p_X + p_{\bar{X}} - p_Y - p_{\bar{Y}}) |\mathrm{M}|^2 \left[1 - \frac{n_X^2}{\left(n_X^{\rm eq}\right)^2}\right] \exp[-(E_Y + E_{\bar{Y}})/T_{\rm rad}] \tag{2.170}$$

Incorporating the above form of the collision term, the right-hand side of Eq. 2.161 simplifies to,

$$\int \frac{d^3\mathbf{p}_X}{(2\pi)^3} C[f_{\rm X}] = -\langle\sigma v\rangle \left[n_X^2 - \left(n_X^{\rm eq}\right)^2\right], \tag{2.171}$$

where $\langle\sigma v\rangle$ is the thermally averaged annihilation cross section times the relative velocity of DM and can be expressed as [26],

$$\begin{aligned}
\langle\sigma v\rangle &= \frac{1}{\left(n_X^{\rm eq}\right)^2} \int \frac{d^3\boldsymbol{p}_X}{(2\pi)^3 2E_X} \frac{d^3\boldsymbol{p}_{\bar{X}}}{(2\pi)^3 2E_{\bar{X}}} \frac{d^3\boldsymbol{p}_Y}{(2\pi)^3 2E_Y} \frac{d^3\boldsymbol{p}_{\bar{Y}}}{(2\pi)^3 2E_{\bar{Y}}} (2\pi)^4 \delta^4(p_X + p_{\bar{X}} - p_Y - p_{\bar{Y}}) |\mathscr{M}|^2 \exp[-(E_Y + E_{\bar{Y}})/T_{\rm rad}], \\
&= \frac{1}{\left(n_X^{\rm eq}\right)^2} \int \frac{d^3\mathbf{p}_X}{(2\pi)^3 2E_X} \frac{d^3\mathbf{p}_{\bar{X}}}{(2\pi)^3 2E_{\bar{X}}} (\sigma v) \exp[-(E_Y + E_{\bar{Y}})/T_{\rm rad}], \\
&= \frac{g_X^2}{\left(n_X^{\rm eq}\right)^2} \frac{T_{\rm rad}}{32\pi^4} \int_{4m_X^2}^{\infty} \sqrt{q}\,(q - 4m_X^2)\sigma(q) K_1\left(\frac{\sqrt{q}}{T_{\rm rad}}\right) dq,
\end{aligned} \tag{2.172}$$

where K_1 is the first-order modified Bessel function of the second kind, and $\sqrt{q} = (E_X + E_{\bar{X}})$ is the total initial energy in the center-of-mass (CM) frame . The final expression follows from the standard formalism for thermally averaged cross sections as developed in [93, 94]. Finally, the Boltzmann evolution equation of DM number density can be written as,

$$\frac{dn_X}{dt} + 3Hn_X = -\langle\sigma v\rangle \left[n_X^2 - \left(n_X^{\rm eq}\right)^2\right]. \tag{2.173}$$

To track the evolution in an expanding universe, it is convenient to recast the Boltzmann equation in terms of the comoving DM yield $Y_X = n_X/s$, where s is the entropy density. Since the entropy is conserved in the standard cosmology, the Boltzmann equation can be rewritten in terms of the yield as,

$$\frac{dY}{dx} = -\frac{\langle\sigma v\rangle\, s}{xH} \left(Y^2 - Y_{\rm eq}^2\right), \tag{2.174}$$

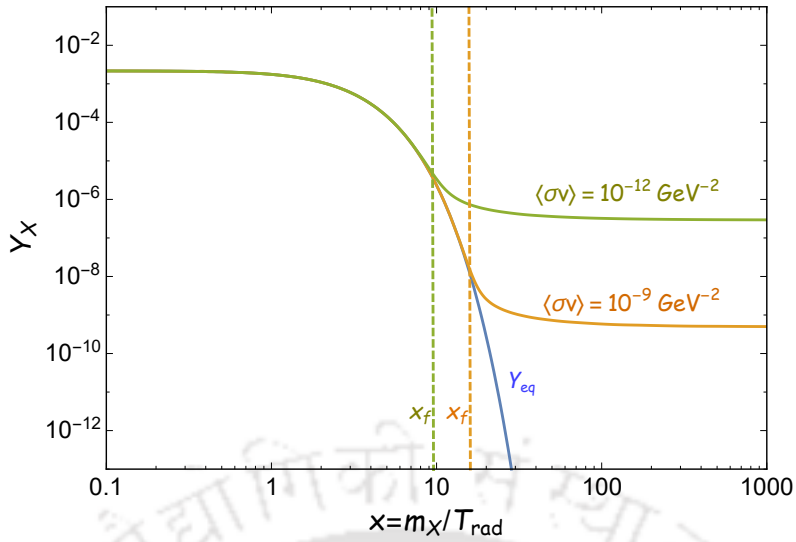

Figure 2.9: The evolution of the DM yield Y_X as a function of $x = m_X/T_{\rm rad}$ for two different values of the thermally averaged annihilation cross section: $\langle\sigma v\rangle = 10^{-12}\,\text{GeV}^{-2}$ (green) and $10^{-7}\,\text{GeV}^{-2}$ (orange). These curves represent the numerical solution of Eq. 2.174 for a purely RD universe. The blue curve corresponds to the equilibrium yield $Y_{\rm eq}$. The two vertical dashed lines mark the respective freeze-out points x_f for the two cross-section values.

where $x = m_X/T_{\rm rad}$, $s = \frac{2\pi^2}{45} g_{\star s} T_{\rm rad}^3$ and $H = \sqrt{\frac{\pi^2 g_{\star r}}{90}} \frac{T_{\rm rad}^2}{M_{\rm p}}$ in the RD era. $g_{\star r}\,(g_{\star s})$ denote the number of relativistic degrees of freedom contributing to the SM energy (entropy) density. During the early high-temperature phase,$Y_X \simeq Y_{\rm eq}$, as annihilations maintain the equilibrium. However, as the universe expands and cools, the equilibrium number density decreases rapidly. At some point, known as the freeze-out temperature T_f, the annihilation rate becomes too slow compared to the expansion rate of the universe, and the actual number density deviates from its equilibrium value and eventually freezes to a constant value. The freeze-out temperature T_f is determined by the condition,

$$n_X^{\rm eq}(x_f)\langle\sigma v\rangle = H(x_f). \tag{2.175}$$

After freeze-out, the annihilation term becomes negligible, and the yield Y asymptotically approaches a constant value Y_∞ which determines the present-day DM abundance. We show in Fig. 2.9 the numerical solution of DM yield as a function of x by taking $\langle\sigma v\rangle$ constant. Unfortunately, even for constant $\langle\sigma v\rangle$, there are no pure analytic solutions to Eq. 2.174. But, a semi-analytic solution is possible when $x \gg 1$, the equilibrium density is Boltzmann suppressed and $Y_X \gg Y_{\rm eq}$, so Eq. 2.174 becomes,

$$\frac{dY_X}{dx} = -\frac{2\pi g_{\star s}}{15}\sqrt{\frac{10}{g_{\star r}}}\frac{\langle\sigma v\rangle m_X M_{\rm p}}{x^2} Y_X^2. \tag{2.176}$$

Neglecting the temperature dependence of these degrees of freedom, Eq. 2.176 admits an approximate solution:

$$Y_X(\infty) \simeq \frac{15}{2\pi g_{\star s}}\sqrt{\frac{g_{\star r}}{10}}\frac{x_f}{\langle\sigma v\rangle m_X M_{\rm p}}. \tag{2.177}$$

After freeze-out, the comoving yield Y_X becomes approximately constant, and the relic abundance of DM observed today can be expressed as

$$\Omega_X h^2 = \frac{m_X s_0 Y_X(\infty)}{\rho_{\rm crit}/h^2} \approx 2.755\times 10^8 \left(\frac{m_X}{\text{GeV}}\right) Y_X(\infty), \tag{2.178}$$

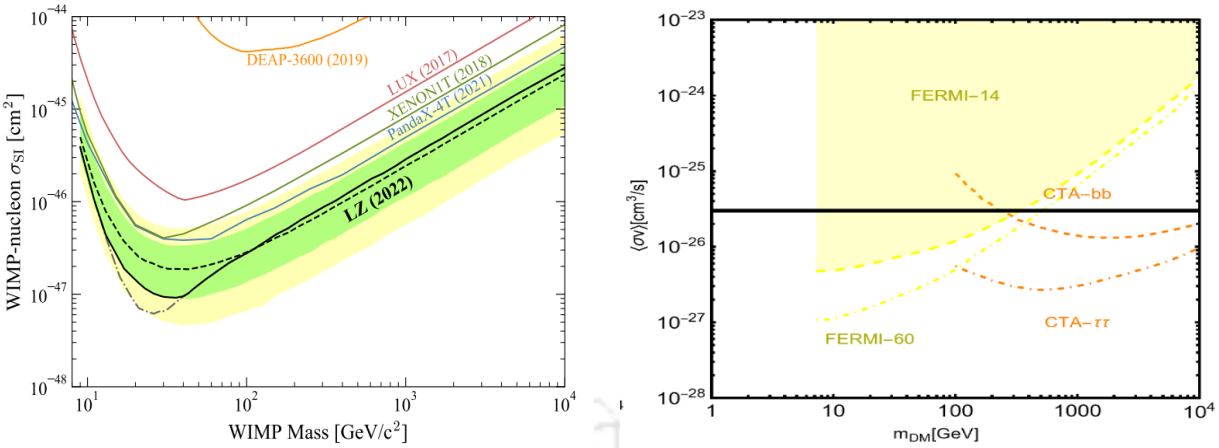

Figure 2.10: Sensitivity curve for different direct detection (left) and indirect detection (right) experiments. Figure taken from [95, 96]

where $s_0 \approx 2891\,\mathrm{cm}^{-3}$ is the present-day entropy density, and $\rho_{\mathrm{crit}}/h^2 \approx 1.05 \times 10^{-5}\,\mathrm{GeV/cm}^3$ is the critical energy density of the universe. For a typical annihilation cross-section of order $\langle\sigma v\rangle \sim 3 \times 10^{-26}\,\mathrm{cm}^3/\mathrm{s} = 10^{-9}\,\mathrm{GeV}^{-2}$, which corresponds to a weak-scale interaction, one finds that the relic abundance matches the observed value $\Omega_X h^2 \approx 0.12$. This coincidence is often referred to as the "WIMP miracle" [91, 97], which has motivated a wide range of searches for WIMP DM in direct detection [98–104] and indirect detection [105–109] experiments. However, despite significant progress and sensitivity improvements, no conclusive experimental signal of WIMPs has been observed so far. The null results from these searches have placed stringent bounds on the parameter space of conventional WIMP models. This is illustrated in Figure 2.10, where the left panel shows exclusion limits from direct detection experiments, and the right panel displays constraints from indirect searches. In light of these persistent null results, attention has increasingly shifted toward alternative DM production mechanisms, such as the freeze-in mechanism, where DM interacts feebly with SM. These particles are referred to as FIMPs [110].

It is also important to note that the freeze-out scenario discussed above assumes a standard RD universe, and this is known as the standard freeze-out scenario. However, deviations from this assumption, such as those arising from a non-standard cosmological history (an extended reheating phase), can significantly alter the dynamics of freeze-out. Moreover, such non-standard scenarios can also open new pathways for non-thermal DM production, where DM is generated from the decay of the inflaton or from the thermal bath. All these possibilities have been explored in detail in this thesis.

2.10.2.2 Freeze-in Mechanism: FIMPs

In contrast to the freeze-out mechanism, where DM particles were once in thermal equilibrium with the SM bath, the freeze-in scenario assumes that DM has extremely feeble interactions with the SM particles and therefore never reaches thermal equilibrium. In this case, the DM particles are gradually produced from the thermal bath through processes such as annihilations or decays of SM particles, and the DM abundance accumulates slowly over time. This scenario is particularly appealing in situations where the DM interactions are so weak that even in the early universe the production rate was not sufficient to establish equilibrium. The particles responsible for freeze-in production are often termed *Feebly interacting massive particles* (FIMPs) [110–114].

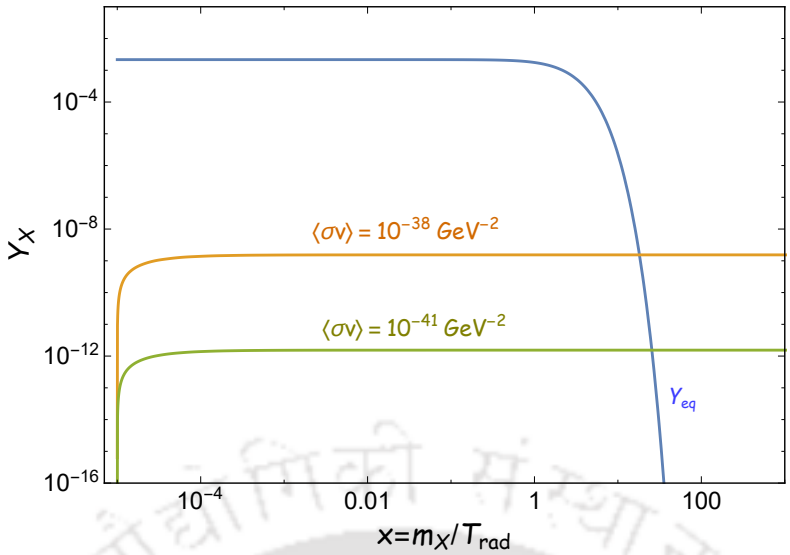

Figure 2.11: The evolution of the DM yield Y_X as a function of $x = m_X/T_{\rm rad}$ for freeze-in with two different values of $\langle\sigma v\rangle$: $\langle\sigma v\rangle = 10^{-38}\,\text{GeV}^{-2}$ (orange) and $10^{-41}\,\text{GeV}^{-2}$ (green).

To describe the evolution of the DM number density in this framework, we consider the Boltzmann equation with the assumption that X is produced via annihilation of SM particles, for example through the process $Y\bar{Y} \to X\bar{X}$. Since X was never abundant enough to reach thermal equilibrium, we can neglect the back-reaction term involving n_X in the collision integral. The Boltzmann equation then simplifies to (from Eq. 2.161)

$$\frac{dn_X}{dt} + 3Hn_X = \langle\sigma v\rangle (n_X^{\rm eq})^2 = \langle\Gamma_X\rangle\, n_{\rm eq}\,, \tag{2.179}$$

where $\langle\Gamma_X\rangle = \langle\sigma v\rangle\, n_{\rm eq}$ is called thermal average production rate of X.

In Fig. 2.11, we show the evolution of the DM yield for the freeze-in scenario in a purely RD background. This solution is obtained by numerically solving Eq. 2.179 with a constant $\langle\sigma v\rangle$, where DM production occurs exclusively through interactions with the thermal bath. From the figure, it is clear that DM could not reach thermal equilibrium due to its extremely weak interactions with the bath.

In more general scenarios, DM may also be produced from the decay of heavy particles, which could be either part of the thermal plasma or completely decoupled from it. If the decaying particles are thermal bath particles, the production rate is still governed by the thermal average $\langle\sigma v\rangle$ multiplied by their equilibrium number density. However, in the case of non-thermal particle decay, such as from the decay of the inflaton field during reheating, the decaying particle is not in thermal equilibrium. In such cases, the production rate is governed by the decay width $\Gamma_{\phi\to XX}$, and the relevant number density is that of the heavy decaying field n_ϕ, rather than $n_X^{\rm eq}$.

The freeze-in mechanism has gained significant attention, especially in light of the absence of experimental signals for WIMPs. Since it involves such tiny couplings, it is more challenging to test directly, but it remains a theoretically robust and cosmologically consistent alternative to thermal freeze-out. In this thesis, we will explore both freeze-out and freeze-in production of DM during the phase of reheating after inflation. Understanding how reheating affects this DM production mechanism and the DM parameter space is one of the central objectives of my thesis.

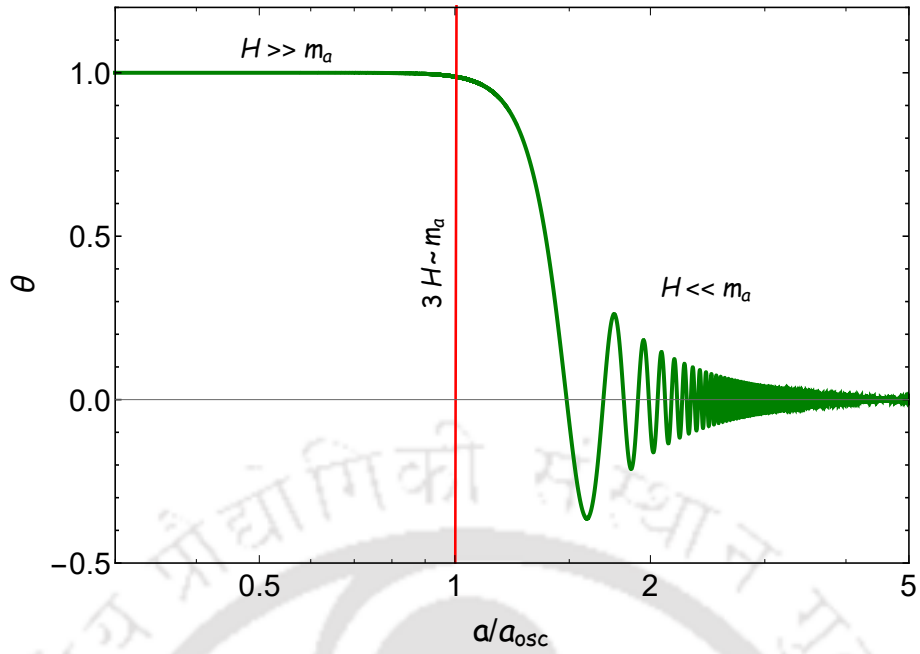

Figure 2.12: The evolution of the misalignment angle θ as a function of the scale factor a. The red vertical line corresponds to oscillation condition $3H(t_{\rm osc}) \sim m_{\mathfrak{a}}$.

2.10.2.3 Misalignment Mechanism

A well-established example of a non-thermal DM production mechanism is the vacuum misalignment [115–117], often applied to axions and axion-like fields. In particular, the QCD axion, originally proposed to solve the strong CP problem, can also naturally account for the observed DM abundance through this mechanism. To describe this mechanism, consider a pseudo-scalar field $\mathfrak{a}$ governed by the Lagrangian [118, 119],

$$\mathscr{L} = \frac{1}{2}\partial^{\mu}\mathfrak{a}\,\partial_{\mu}\mathfrak{a} - V(\mathfrak{a}). \tag{2.180}$$

where $\mathfrak{a}$ is a periodic field with $\mathfrak{a} = \mathfrak{a} + 2\pi f$. For the case of axion, f is called the axion decay constant. The potential for such a field typically takes the form

$$V(\mathfrak{a}) = \Lambda_{\mathfrak{a}}^4\left[1 - \cos\left(\frac{\mathfrak{a}}{f}\right)\right], \tag{2.181}$$

where $\Lambda_{\mathfrak{a}}$ is the confinement scale (e.g., $\Lambda_{\rm QCD}$ for the QCD axion). The vacuum expectation value is set such that the potential minimum lies at $\mathfrak{a} = 0$. Expand around the minimum $V(\mathfrak{a}) \simeq \frac{1}{2}\Lambda_{\mathfrak{a}}^4\left(\frac{\mathfrak{a}}{f}\right)^2$ and the mass $m_{\mathfrak{a}} = \frac{\Lambda_{\mathfrak{a}}^2}{f^2}$. Therefore, the EOM of the homogeneous field $\mathfrak{a}$ can be derived as

$$\ddot{\mathfrak{a}} + 3H\dot{\mathfrak{a}} + m_{\mathfrak{a}}^2\mathfrak{a} = 0. \tag{2.182}$$

At early times, when the Hubble friction is large ($H \gg m_{\mathfrak{a}}$), the large Hubble friction term suppresses the field's motion, effectively freezing it at some initial value $\mathfrak{a}_i$, often parametrized as a dimensionless misalignment angle $\theta_i = \mathfrak{a}_i/f$, which is assumed to be of order unity. This is the essence of the vacuum misalignment: the field starts away from the minimum of its potential due to random initial conditions after spontaneous symmetry breaking. As the universe expands and cold, $H(t)$ drops below the axion mass $m_{\mathfrak{a}}$, the field begins to oscillate about the minimum when the condition $3H(t_{\rm osc}) \sim m_{\mathfrak{a}}$ is satisfied. The dynamics of these oscillations are depicted in Fig. 2.12, where we numerically solve Eq. 2.182 for a RD

universe. These coherent oscillations behave like pressureless dust, with an energy density that redshifts as $\rho_{\mathfrak{a}} \propto a^{-3}$, just like cold DM. The averaged energy density stored in the field at the onset of oscillation is [118],

$$\rho_{\mathfrak{a}}(t_{\rm osc}) \simeq \frac{1}{2} m_{\mathfrak{a}}^2 f^2 \theta_i^2, \tag{2.183}$$

and assuming oscillation occurs during a standard RD universe, the relic abundance today can be estimated as [118]

$$\Omega_{\mathfrak{a}} h^2 \simeq 0.12 \left(\frac{\theta_i}{1.0}\right)^2 \left(\frac{f}{10^{16}\,\text{GeV}}\right)^2 \left(\frac{m_{\mathfrak{a}}}{5\times 10^{-19}\,\text{eV}}\right)^{1/2}. \tag{2.184}$$

For a suitable choice of the axion mass $m_{\mathfrak{a}}$ and decay constant f, the misalignment mechanism can successfully account for the observed DM relic abundance. For instance, choosing $m_{\mathfrak{a}} = 10^{-18}\,\text{eV}$ and $f = 10^{16}\,\text{GeV}$ yields the correct abundance. However, in the case of the QCD axion, the decay constant and the mass are not independent parameters; they are related through non-perturbative QCD dynamics. This interdependence makes it particularly compelling-if the axion constitutes the dominant DM component, the relic density requirement allows one to tightly constrain the decay constant. We have explored the production of the QCD axion during the reheating epoch in detail in Chapter 5.

2.11 Baryogenesis via leptogenesis

The Dirac equation predicts the existence of both particle and antiparticle states with equal probabilities. However, our observable Universe is overwhelmingly composed of matter, with a conspicuous absence of antimatter. This observed imbalance between matter and antimatter is referred to as the baryon asymmetry of the Universe (BAU). It can be quantitatively described in two ways: (i) the ratio of net baryon number density to photon number density $\eta_B = (n_B - n_{\bar{B}})/n_\gamma$, (ii) ratio of net baryon number density to entropy density $Y_{\rm B} = (n_B - n_{\bar{B}})/s$. Both CMB [31] and BBN [120] observations provide strong evidence for a small but non-zero baryon asymmetry. The most recent measurements come from the Planck satellite [31, 121], which yields the following values,

$$\eta_{\rm B} \simeq (6.12 \pm 0.04)\times 10^{-10}, Y_{\rm B} \simeq (8.7 \pm 0.08)\times 10^{-11} \tag{2.185}$$

Since the universe is expected to originate in a matter-antimatter symmetric manner, and any pre-existing asymmetry would have been diluted by the exponential expansion during inflation, the presence of such an asymmetry demands a dynamical origin. This necessity leads to the framework of *baryogenesis* [122–124], the process through which an initially symmetric state evolves into a baryon-asymmetric one. For any successful dynamical mechanism of baryon asymmetry generation, three essential conditions must be satisfied-first articulated by Andrei Sakharov in 1967 [125]: (i) baryon number (B) violation, to generate an imbalance; (ii) C and CP violation, to excess matter over antimatter; and (iii) a departure from thermal equilibrium, to prevent the washout of the generated asymmetry. While the SM does include processes that violate B (via non-perturbative sphaleron transitions) and CP (through the CKM matrix), these effects are far too weak to account for the observed baryon asymmetry. Furthermore, the electroweak phase transition [126] in the SM is a smooth crossover rather than a first-order transition, failing to provide the necessary out-of-equilibrium dynamics. As a result, extensions of the SM are required to implement a successful baryogenesis mechanism. One such well-motivated and compelling framework is *leptogenesis* [127–129], which provides a mechanism for generating the observed baryon asymmetry of the universe. A natural and widely-studied realization of leptogenesis utilizes the Type-I seesaw mechanism [130–132]. In this

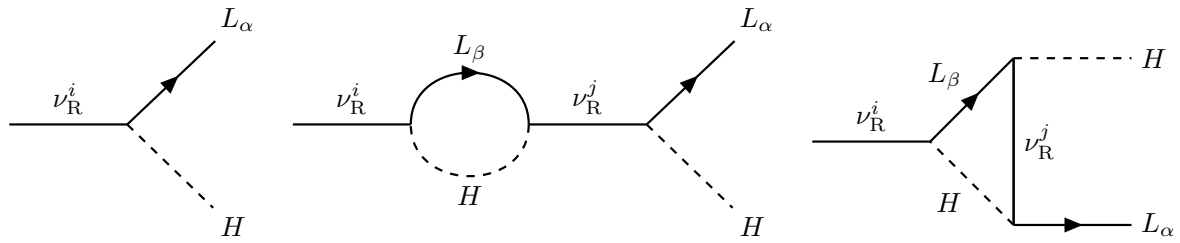

Figure 2.13: Tree-level diagram (left) and one-loop level diagrams, including the self-energy (middle) and vertex correction diagram (right), for CP asymmetry generation in the decay of RHNs.

mechanism, heavy right-handed neutrinos (RHNs), which are introduced as SM gauge singlets, play a dual role: their Yukawa interactions generate light neutrino masses via the seesaw mechanism, while their CP-violating decays can be the source of a lepton asymmetry, which is subsequently converted into the baryon asymmetry via SM sphaleron processes. The relevant interactions can be described by the Lagrangian,

$$\mathscr{L} = -\frac{1}{2} M_i \overline{\nu_R^{ci}} \nu_R^i - y_{\alpha i} \bar{L}_\alpha \tilde{H} \nu_R^i + h.c., \tag{2.186}$$

where ν_R^i $(i = 1,2,3)$ are the RHNs with Majorana mass M_i, $L_\alpha (\alpha = e,\mu,\tau)$ are the left-handed lepton doublets, $\tilde{H} = i\sigma_2 H^*$ is the conjugate Higgs doublet, and $y_{\alpha i}$ are the neutrino Yukawa couplings. The first term represents the Majorana mass for the RHNs, and the second term gives rise to Yukawa interactions responsible for neutrino mass generation.

In its simplest form, leptogenesis proceeds via the out-of-equilibrium, CP-violating decays of the heavy RHNs into leptons and Higgs bosons. Since the ν_R^i are Majorana fermions, their mass term M_i violates lepton number by two units. As a result, the first Sakharov condition is satisfied. This violation arises because the RHNs are assigned a lepton number of $+1$, while their charge conjugates carry a lepton number of -1. The left-handed lepton doublet and anti-lepton doublet are assigned lepton numbers $+1$ and -1, respectively. The Higgs doublet carries a lepton number of 0. The interference between the tree-level and one-loop decay amplitudes generates a CP asymmetry in the lepton sector, quantified by a parameter ε_i, defined as the difference in decay rates between $\nu_R^i \to L_\alpha H$ and $\nu_R^i \to \bar{L}_\alpha H^\dagger$. The CP asymmetry parameter ε_i associated with the decay of the i^{th} heavy neutrino is defined as [128, 133, 134]:

$$\varepsilon_i = \frac{\sum_\alpha \left[\Gamma(\nu_R^i \to L_\alpha H) - \Gamma(\nu_R^i \to \bar{L}_\alpha \bar{H})\right]}{\sum_\alpha \left[\Gamma(\nu_R^i \to L_\alpha H) + \Gamma(\nu_R^i \to \bar{L}_\alpha \bar{H})\right]}. \tag{2.187}$$

At tree level, the decay rates for both channels, $\Gamma(\nu_R^i \to L_\alpha H)$ and $\Gamma(\nu_R^i \to \bar{L}_\alpha \bar{H})$ are equal. The tree-level decay rate is given by,

$$\Gamma(\nu_R^i \to L_\alpha H) = \Gamma(\nu_R^i \to \bar{L}_\alpha \bar{H})) = \frac{(y^\dagger y)_{ii}}{16\pi} M_i \,. \tag{2.188}$$

Hence, at this tree level, the difference between the decay rates vanishes and $\varepsilon_i = 0$. However, CP asymmetry arises at the one-loop level due to the interference between the tree-level diagram and one-loop diagrams, such as the self-energy diagram [133] and the vertex correction diagram [128]. The relevant tree-level and loop-level diagrams are shown in Fig. 2.13. After performing the loop calculation and summing over all lepton families, the total CP-asymmetry generated by the decay ν_R^i can be written as [134],

$$\varepsilon_i = \frac{1}{8\pi (y^\dagger y)_{ii}} \sum_{j \neq i} \text{Im}\left[\left(y^\dagger y\right)_{ij}^2\right] f\left(\frac{M_j^2}{M_i^2}\right), \tag{2.189}$$

where the loop function $f(x = M_j/M_i)$ receives contributions from both vertex and self-energy corrections and is given by

$$\begin{aligned} f(x) &= \sqrt{x}\left[\frac{1}{1-x} + 1 - (1+x)\ln\left(\frac{1+x}{x}\right)\right] \\ &\simeq -\frac{3}{2\sqrt{x}} - \frac{5}{6x\sqrt{x}} + \mathcal{O}\left(\frac{1}{x^2\sqrt{x}}\right) \quad \text{for} \quad x \gg 1\,. \end{aligned} \tag{2.190}$$

The CP asymmetry ϵ_i is non-zero due to the complex nature of the Yukawa couplings, thereby fulfilling the second Sakharov condition. If the decay of $\nu_{\rm R}^i$ occurs out of thermal equilibrium-i.e., their decay rate is slower than the Hubble expansion rate-then the third Sakharov condition is also satisfied. Therefore, by extending the SM with RHNs, all three Sakharov conditions can be simultaneously satisfied, paving the way for leptogenesis.

In a scenario where the RHN masses are hierarchical, i.e., $M_1 \ll M_2, M_3$, the dominant CP asymmetry arises from the decay of the lightest RHN $\nu_{\rm R}^1$. This is because $\nu_{\rm R}^1$ stays in thermal equilibrium for a much longer time than the other two heavy RHNs. Consequently, the CP asymmetries generated by $\nu_{\rm R}^2$ and $\nu_{\rm R}^3$ are expected to be erased by the lepton number-violating interactions of $\nu_{\rm R}^1$. As a result, the CP asymmetry generated by $\nu_{\rm R}^1$ becomes the primary contributor to the leptogenesis process. In the hierarchical limit $x \gg 1$ (i.e., $M_j \gg M_1$), the total CP asymmetry ε_1 simplifies to,

$$\varepsilon_1 \simeq -\frac{3}{16\pi (y^\dagger y)_{11}}\left(\text{Im}\left[\left(y^\dagger y\right)^2_{12}\right]\frac{M_1}{M_2} + \text{Im}\left[\left(y^\dagger y\right)^2_{13}\right]\frac{M_1}{M_3}\right). \tag{2.191}$$

This expression can be further simplified by assuming that the dominant contribution comes from the largest entry in the Yukawa matrix and invoking the seesaw relation to connect the Yukawa couplings to the light neutrino mass scale. Under these assumptions, the CP asymmetry can be approximately expressed as [135, 136],

$$\varepsilon_1 \simeq -\frac{3\,\delta_{\rm eff}}{16\pi}\frac{m_{\nu,\rm max}\,M_1}{v^2}\,, \tag{2.192}$$

where $v = 174$ GeV is the Higgs vacuum expectation value (vev), $m_{\nu,\rm max} = 0.05$ eV is the mass of the heaviest light neutrino, and $\delta_{\rm eff}$ is an effective CP-violating parameter that encapsulates the complex phases in the Yukawa matrix, typically taking values in the range $0 \le \delta_{\rm eff} \le 1$ [136]. See the Appendix-B for the derivation of Eq. 2.192.

The lepton asymmetry generated from the decay of the lightest RHN $\nu_{\rm R}^1$ is subsequently converted into a baryon asymmetry through non-perturbative electroweak sphaleron processes [137, 138], which are active at temperatures above the electroweak scale ($T_{\rm rad} \gtrsim 160$ GeV). These processes violate $B+L$ but conserve $B-L$, and therefore have the unique ability to convert a lepton asymmetry into a baryon asymmetry. In the framework of leptogenesis, the decay of the lightest RHN $\nu_{\rm R}^1$ generates a lepton asymmetry, which is equivalent to a non-zero $B-L$ asymmetry since the initial B asymmetry is absent. This $B-L$ asymmetry is then partially converted into a baryon asymmetry $Y_{\rm B}$ by sphaleron transitions. The conversion is quantified by the relation [137, 138]

$$Y_{\rm B} = a_{\rm sph} Y_{\rm B-L} = \frac{8N_f + 4N_H}{22N_f + 13N_H} Y_{\rm B-L} = \frac{28}{79} Y_{\rm B-L}\,, \tag{2.193}$$

where $N_f = 3$ is the number of fermion generations, and $N_H = 1$ is the number of Higgs doublets in the SM.

A well-motivated and extensively studied scenario is thermal leptogenesis [139], in which the RHNs are initially produced from the thermal bath in the early Universe. In this setup, scattering processes involving SM particles populate the RHNs while they remain in thermal equilibrium. As the Universe expands and

cools, the RHNs begin to decouple and eventually decay out of equilibrium when the temperature drops below their mass scale, $T_{\rm rad} \sim M_i$. Since their equilibrium number density becomes Boltzmann suppressed at these temperatures, any net lepton asymmetry generated during the decay survives, provided that the decay occurs out of equilibrium. The same neutrino Yukawa couplings are responsible for both the thermal production and decay of the RHNs. For successful baryogenesis, this scenario typically requires the RHN mass to be $M_i > 10^{10}$ GeV, a bound known as the Davidson-Ibarra bound [139]. Consequently, this bound implies that the reheating temperature must be larger than this value to achieve the correct baryon asymmetry [139].

In contrast, in this thesis, we will primarily focus on a simpler but equally compelling alternative: non-thermal leptogenesis [140, 141], motivated by the post-inflationary reheating paradigm. In this scenario, RHNs are not generated from the thermal bath but are instead produced directly through non-thermal processes, such as the decay/scattering of the inflaton field. This mechanism was originally proposed in [140], where it was shown that heavy RHNs can be sourced from inflaton decays and then decay themselves, generating a lepton asymmetry without ever reaching thermal equilibrium.

In this thesis, we consider a scenario where RHNs are produced from the inflaton through 2-2 scattering processes mediated by gravitational interactions. A characteristic feature of our non-thermal leptogenesis setup is that the mass of all RHNs satisfies $M > T_{\rm rad}^{\rm max}$, where $T_{\rm rad}^{\rm max}$ is the maximum bath temperature during reheating. Under this condition, thermal scatterings in the bath are insufficient to produce RHNs after inflation, and the dominant production mechanism is non-thermal. The lepton asymmetry is then generated when the RHNs decay, typically once the Hubble rate becomes comparable to their dacay rate, i.e., $H \sim \Gamma_\nu$. Since the RHNs are never in equilibrium, the analysis simplifies considerably, and the freeze-out and washout effects are typically negligible.

CHAPTER 3

Dynamics of Reheating and Dark Matter Production

In cosmology, the reheating era is probably the least understood epoch of cosmic history. It is, however, of enormous importance for both cosmology and particle physics. It is the phase that bridges the two important paradigms of cosmology, namely, inflation and the standard hot Big Bang. While inflation sets the nearly uniform initial conditions across all the causally disconnected patches of the exponentially expanded universe, the subsequent phase fills the spaces with visible hot matter homogeneously distributed through the process called reheating [49, 142–144]. The endpoint of the reheating is when the standard radiation-dominated universe begins, which sets the proper initial conditions for BBN. From these chronological cosmological events, it is obvious that the present state of our universe must be non-trivially dependent on the process of reheating. Investigation of this phase is still an ongoing effort since its theoretical inception proposed in [49, 142–144]. Since there is no way to directly probe this phase with the present experimental techniques, understanding reheating relies on exploring the various physical processes that could have occurred during this phase, and looking for indirect observables that could potentially be detected in future experiments. One key aspect of reheating is its modification of the universe's expansion history prior to the onset of the hot Big Bang [10, 50, 145]. This altered expansion history could leave imprints on observable cosmological scales, such as those observed in the CMB. Therefore, future experiments might be able to indirectly constrain the reheating phase through these observable effects [11, 146, 147]. Furthermore, the underlying dynamics of reheating and the decay of the inflaton into various daughter fields-are believed to have deep connections with fundamental cosmological phenomena, including the production of dark matter [15, 17, 18], the generation of matter-antimatter asymmetry [148–152], and even the propagation and generation of primordial gravitational waves [23, 153]. The study of reheating thus holds the potential to address several fundamental questions in cosmology and particle physics, paving the way for a deeper understanding of the universe's early evolution.

Therefore, the dynamics of reheating are rich and will have important observational signatures. In this chapter, we have two main objectives: firstly, to study the dynamics of reheating through various possible inflaton decay channels; and second, to explore how these dynamics affect DM production, thereby placing constraints on the associated DM parameter space.

To study the reheating dynamics, we consider the decay of the inflaton into radiation through various interaction channels, namely: (i) decay into bosonic radiation (s) via $g_1^r \phi s^2$ and $g_2^r \phi^2 s^2$ interactions, (ii) decay into fermionic radiation (f) via the Yukawa-type interaction $h^r \phi f \bar{f}$, and (iii) inflaton decaying into

all fundamental fields through minimal s-channel graviton ($h_{\mu\nu}$) exchange interaction, $(1/M_P)(h_{\mu\nu}T^{\mu\nu}_{\phi} + h_{\mu\nu}T^{\mu\nu}_{s/f})$ [154, 155]. Further, we also include the thermal effect, such as Bose-enhancement, Pauli-Blocking effect, on the reheating process. To this end, we would like to point out that in the context of gravity-mediated decay, the effect of non-minimal Ricci curvature (R) coupling $\zeta\phi^2 R$ has been considered in the reference [156]. However, the contribution of such a term has been shown to be negligible for dimensionless coupling $\zeta < 1$ and hence will be ignored in this thesis.

Our second objective is to study the DM production during reheating by considering different production processes via gravitational scattering, thermal bath scattering, and direct inflaton decay. From the phenomenological perspective, DM is assumed to be an integral part of the visible standard model components in the quantum field theoretic framework [90–92] . In this framework, it is just the DM mass and the cross-section that are shown to be sufficient to explain the current abundance of DM. However, a large number of attempts over the years to detect such particles appeared to go in vain [102, 157–160]. This motivates the need to go beyond conventional theoretical frameworks in order to gain deeper insights into the nature and origin of DM [161–164]. Towards this endeavor recent proposal of graviton mediated DM production [165–173] has been shown to have some promising universal features, and it cannot be ignored in any DM studies. Interestingly, such gravitational production has been observed to set a limit on the maximum possible value of the DM mass [174, 175]. Further, we will see how universal gravitational DM production during the initial phase of the reheating phase plays an important role in constraining the DM parameters. In the standard DM literature, two primary DM production mechanisms-WIMPs and FIMPs-have been studied in the context of the early universe. Most of the DM phenomenological studies were confined to the early radiation-dominated universe. DM physics during reheating has gained significant interest only recently [16–18, 41, 47, 176–183]. We aim to explore these two mechanisms in the context of a non-trivial reheating phase. We propose a unified framework in which the inflaton plays a central role in the model-building of DM, examining the interplay between reheating dynamics and the production of DM. *Apart from understanding the very nature of DM, these studies actually open up the possibilities of looking for the signature of reheating and, most importantly, the nature of inflaton through the physics of DM.*

3.1 Dynamics of Reheating and constraining its parameter spaces

In this section, we provide a detailed analysis of the dynamics of reheating, focusing on the decay of the inflaton into radiation via various channels. We incorporate important thermal effects-such as Bose enhancement and Pauli blocking-which significantly influence the efficiency and nature of the reheating process. Furthermore, we explore and constrain the reheating parameter space by connecting it with both the inflationary and CMB parameters. In the next section, we extend our analysis to the production of DM during the reheating phase and explore different possible production mechanisms and their observable possibilities in a unified framework.

This section is organized as follows: In sub-section 3.1.1, we will discuss the basic setup for the perturbative reheating processes for different decay channels and their connection with the inflationary parameters. As mentioned earlier, in sub-section 3.1.2 we include the effect of finite temperature corrections in the decay widths for various decay channels. In sub-section-2.9.1, we relate reheating and inflationary parameters through the CMB. In sub-section 3.1.4, we discuss in detail the reheating dynamics due to two different bosonic decay channels. We identify the parameter regions with respect to the inflaton EoS, where

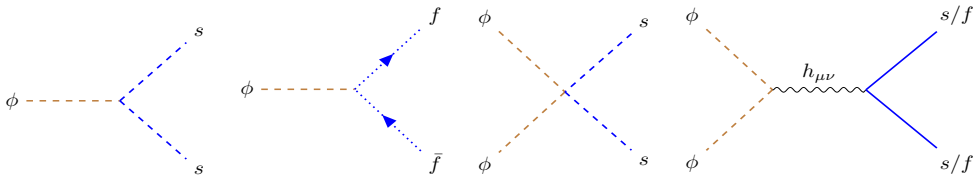

Figure 3.1: Fynmann diagram for all possible interactions between inflaton (ϕ) and radiation (R=s,f)

reheating can be successfully achieved depending upon the strength of the different decay channels under consideration. We further discuss the possible constraints on those inflaton coupling parameters with respect to the CMB observations. In section 3.1.5, we discuss in detail the fermionic reheating scenario where the reheating occurs due to the inflaton decaying into fermionic radiation. Similar to the bosonic reheating scenario, we constrain the inflaton-fermion coupling parameter in light of CMB observables.

3.1.1 Perturbative reheating: general set up

After the end of inflation, the inflaton field starts to oscillate with a decaying amplitude, initiating the reheating phase. During this phase, the inflaton field transfers its energy into massless fields termed as radiation ($R = s, f$) through various perturbative decay channels: $g_1^r \phi s^2$, $g_2^r \phi^2 s^2$ and $h^r \phi \bar{f} f$, where we assume explicit coupling between inflation and daughter fields. In addition, there exists universal gravitational coupling between inflaton and daughter field through s-channel graviton ($h_{\mu\nu}$) exchange interaction, $(1/M_P^2) h_{\mu\nu} T^{\mu\nu}$, which has been shown to influence the reheating dynamics [175, 184]. In this thesis, we have also incorporated such universal contributions. Therefore, we have the following general interaction Lagrangian,

$$\mathscr{L}_{int} \supset -\frac{h_{\mu\nu}}{M_P}(T_\phi^{\mu\nu} + T_s^{\mu\nu}) - g_1^r \phi s^2 - g_2^r \phi^2 s^2 - h^r \phi \bar{f} f, \tag{3.1}$$

where g_1^r is the coupling parameter for the trilinear interaction with mass dimension unity, and g_2^r is the dimensionless coupling parameter for the quartic interaction. h^r is the Yukawa coupling. In Fig. 5.9, we have shown the Feynman diagram for all possible interactions between inflation (ϕ), and radiation ($R = (s, f)$). We consider inflaton coupled with scalar (s) and fermion (f) as massless radiation for the case of bosonic and fermionic reheating, respectively. Compared to the direct decay with free coupling parameters, decay due to gravitational interaction is universal and hence will always be present. Setting all the direct inflaton coupling to zero implies purely gravitational scattering, named as gravitational reheating (GRe), which has been studied in detail in [175, 184].

3.1.2 Finite temperature decay widths and Boltzmann equation

The standard assumption of any reheating studies is that radiation is always thermalized among its constituents throughout the entire process. Hence, inflaton decay products must encounter a finite temperature thermal bath which will modify the decay width [146, 185–187]. Such finite temperature effect has already been discussed in [188, 189] for the special cases with a matter-dominated reheating phase. In this thesis, we aim to generalize those studies for the arbitrary inflaton EoS (EoS) w_ϕ, which has not been studied earlier. For the bosonic decay of the inflaton, the thermal effect introduces Bose enhancement factor into the decay width, which makes bosonic reheating efficient compared to the zero

temperature one. On the other hand, for fermionic decay of the inflaton, the thermal bath induces an additional Pauli blocking factor into the decay width, which makes fermionic reheating less efficient compared to the zero-temperature one. Including the finite temperature effect, we list the following decay widths [1] for various decay/scattering channels as [47, 48, 147, 188, 190]

$$\Gamma_{s/f} = \begin{cases} \Gamma_{\phi\to ss} & = \frac{(g_1^r)^2}{8\pi m_\phi(t)}(1+2f_s(m_\phi/2T_{\rm rad})), \quad \text{for } g_1^r\,\phi s^2 \\ \Gamma_{\phi\phi\to ss} & = \frac{(g_2^r)^2\rho_\phi(t)}{8\pi m_\phi^3(t)}(1+2f_s(m_\phi/T_{\rm rad})), \quad \text{for } g_2^r\,\phi^2 s^2 \\ \Gamma_{\phi\to \bar f f} & = \frac{(h^r)^2}{8\pi} m_\phi(t)(1-2f_f(m_\phi/2T_{\rm rad})), \quad \text{for } h^r\phi\bar f f \end{cases} \tag{3.2}$$

$$\Gamma^{\rm gr}_{\phi\phi\to ss} = \frac{\rho_\phi m_\phi}{1024\pi M_p^4}(1+2f_s(m_\phi/T_{\rm rad})), \quad \text{for } \phi\phi \xrightarrow{h_{\mu\nu}} ss \tag{3.3}$$

$$\Gamma^{\rm gr}_{\phi\phi\to \bar f f} = \frac{\rho_\phi m_f^2}{4096\pi M_p^4 m_\phi}(1-2f_f(m_\phi/T_{\rm rad})), \quad \text{for } \phi\phi \xrightarrow{h_{\mu\nu}} \bar f f \tag{3.4}$$

where $f_{f/s}(z) = \frac{1}{e^z \pm 1}$ are the equilibrium Fermi-Dirac (f)(+) and Bose-Einstein (s)(−) distribution function. In these expressions, we ignore the effect of thermal mass correction due to self-interaction. $m_\phi(t)$ corresponds to time-dependent inflaton mass defined as $m_\phi^2(t) = \partial^2 V(\phi)/\partial\phi^2$ for a generic inflaton potential $V(\phi)$. It is obvious from the expression that when the temperature of the radiation bath is greater than the inflaton mass, i.e. ($T_{\rm rad} > m_\phi(t)$), the Bose-enhancement or Pauli-blocking is effective. Due to the Bose enhancement, the decay rate is enhanced for the Bosons, and due to Pauli blocking, the decay rate is suppressed for the Fermions.

Since the radiation particles are massless, the total decay width for the gravitational sector is mainly associated with the scalar particles. For fermionic particles, the decay width for gravitational interaction $\propto m_f^2$ [168, 190], and that is the reason for not taking the contribution from the fermionic particles in the thermal bath for gravitational production. In addition, in the case of vector boson production, we need to introduce the mass term to break the conformal invariance; thus, massless vector boson production is impossible. Therefore, the total gravitational scattering rate to radiation production will be simply $\Gamma^{\rm gr}_{\phi\phi\to RR} = \Gamma^{\rm gr}_{\phi\phi\to \rm s\,s}$. One important point is to note that we consider only one type of scalar particle in the radiation bath, and all other particles are assumed to be fermions or vector bosons, so their gravitational production is unimportant. It has already been established that for the inflaton EoS $w_\phi \gtrsim 0.65$, the gravitational scattering can alone reheat the universe (see, for instance, reference [184]). Therefore, for our analysis, we have considered the explicit coupling-dependent interaction alongside the universal gravitational interaction, and performed a comprehensive analysis to determine the complete parameter space for successful reheating. As part of this, we performed a detailed comparative study to delineate the regions where each interaction channel becomes dominant, providing a clearer understanding of their respective roles in the reheating dynamics. We study the detailed dynamics of reheating by solving the

[1] In this chapter, we have not included the effect of zero-mode inflaton oscillations [47] in the decay width formula. Incorporating these oscillations modifies the decay width by an overall constant factor, without altering its time dependence (for detailed computation, see Appendix-C). Therefore, the physical analysis presented here remains unchanged.

following Boltzmann equations [41, 191]

$$\dot{\rho}_\phi + 3H(1+w_\phi)\rho_\phi + (\Gamma_{s/f} + \Gamma^{\rm gr}_{\phi\phi\to RR})(1+w_\phi)\rho_\phi = 0\,, \tag{3.5a}$$

$$\dot{\rho}^r_{s/f} + 4H\rho^r_{s/f} - \Gamma_{s/f}(1+w_\phi)\rho_\phi = 0\,, \tag{3.5b}$$

$$\dot{\rho}^r_{\rm gr} + 4H\rho^r_{\rm gr} - \Gamma^{\rm gr}_{\phi\phi\to RR}(1+w_\phi)\rho_\phi = 0\,, \tag{3.5c}$$

$$H^2 = \frac{\rho_\phi + \rho^r_{s/f} + \rho^r_{\rm gr}}{3M_{\rm p}^2}\,. \tag{3.5d}$$

Where ρ_ϕ is the inflaton energy density, and $\rho^r_{s/f}$ corresponds to the radiation energy density from direct inflaton decay to either scalar (s) or fermion (f) via the coupling parameters (g^r_i, h^r) respectively. $\rho^r_{\rm gr}$ is the radiation energy density produced through universal gravitational scattering. For solving this set of equations numerically, we define dimensionless comoving variables $\Phi = \rho_\phi A^{3(1+w_\phi)}/(m^{\rm end}_\phi)^4$, and $R_{\rm rad} = \rho_{\rm rad}A^4/(m^{\rm end}_\phi)^4$. Where $\rho_{\rm rad}$ is the radiation produced from either direct decay or gravitational scattering from the inflaton. The normalized scale factor is defined as $A = a/a_{\rm end}$, with $a_{\rm end}$ as the scale factor at the end of inflation, and the Hubble expansion parameter $H = \dot{A}/A$. At the end of inflation i.e., $A = 1$, $\rho_\phi = 3V(\phi_{\rm end})/2$, and the energy densities of all the other components are set to be, $\rho^r_{s/f/{\rm gr}} = 0$. Hence, the appropriate initial condition for the above set of Boltzmann equations is,

$$\Phi(A=1) = \frac{3}{2}\frac{V(\phi_{\rm end})}{(m^{\rm end}_\phi)^4}\;\;;\;\; R_s(A=1) = R_f(A=1) = R_{\rm gr}(A=1) = 0\,. \tag{3.6}$$

Where $m^{\rm end}_\phi$ is the value of the inflaton mass at the end of inflation, which we define in the next subsection.

3.1.3 Relating reheating and inflationary parameters through CMB ($n_{\rm s}, r$)

To connect the inflationary and reheating parameters, we need to consider the inflationary potential. In this chapter, we consider the well-known α-attractor E-model [69–72] inflation potential. The E-model α-attractor potential is given by,

$$V(\phi) = \Lambda^4\left(1 - e^{-\sqrt{\frac{2}{3\alpha}}\frac{\phi}{M_p}}\right)^{2n}\,, \tag{3.7}$$

where Λ is the potential scale determined from the CMB measurements [18], (see Eq. 2.140) and the parameter (α, n) controls the shape of the potential. In this chapter, we have taken $\alpha = 1$, although our analysis is not very sensitive [2] within the allowed range of α values from Planck+BICEP/$Keck$ combined results [192, 193].

After the end of the inflation, the inflaton field oscillates around its minima, and the reheating phase begins. At the minimum of the potential, we expand the inflaton potential (Eq. 5.6) in the limit $\phi \ll M_p$ as

$$V(\phi) \simeq \Lambda^4\xi^{2n}\phi^{2n}, \tag{3.8}$$

where $\xi = \sqrt{2/(3\,\alpha\, M_{\rm p}^2)}$. The field-dependent mass becomes,

$$m^2_\phi = V''(\phi_0) = 2n(2n-1)\Lambda^4\xi^{2n}\phi_0^{2n-2} \simeq 2n(2n-1)\Lambda^4\xi^2\left(\frac{V(\phi_0)}{\Lambda^4}\right)^{1-\frac{1}{n}}. \tag{3.9}$$

[2] Except the prediction of $n_{\rm s}$ (Fig. 3.5, upper pannel of Fig. 3.6), this prediction is sensitive to α, and also sensitive to the choice of potential model. These aspects will be discussed in detail in Chapter 4.

Using the envelope approximation at any instant of time, the envelope value of the field ϕ_0 must satisfy $V(\phi_0) \simeq \rho_\phi(t)$ [47]. Under this approximation, the inflaton mass can be written as

$$m_\phi^2(t) = 2n(2n-1)\xi^2 \Lambda^{4/n} \rho_\phi(t)^{\frac{n-1}{n}}. \tag{3.10}$$

The inflaton mass at the end of inflation can be written as,

$$(m_\phi^{\rm end})^2 \simeq 2n(2n-1)\Lambda^4 \xi^2 \left(\frac{\rho_\phi^{\rm end}}{\Lambda^4}\right)^{1-\frac{1}{n}}, \tag{3.11}$$

where $\rho_\phi^{\rm end}$ is the energy density of the inflaton at the end of inflation, and it will be $\rho_\phi^{\rm end} = 3M_{\rm p}^2 H_{\rm end}^2 \simeq \frac{3}{2}V(\phi_{\rm end})$. It is the initial condition of ρ_ϕ, which is required to solve the Eqs. 3.5. For the details expression of $V(\phi_{\rm end})$, see 2.9.1.

Through the background dynamics and entropy conservation, we can connect the inflationary parameters defined above with the reheating parameters. The reheating period is effectively described by very few parameters, viz. reheating temperature ($T_{\rm re}$), reheating e-folding number ($N_{\rm re}$), and the inflation EoS w_ϕ. In general, the end of reheating is marked at the point when the condition $\rho_\phi(A_{\rm re}) = \rho^r_{\rm tot}(A_{\rm re})$ is satisfied, where $\rho^r_{\rm tot}$ is the total radiation density constituted of all massless daughter fields. The reheating temperature $T_{\rm re}$ can be expressed in terms of the radiation temperature $T_{\rm rad}$ as

$$T_{\rm re} = T_{\rm rad}(A_{\rm re}) = \left(\frac{30}{\pi^2 g^{\rm re}_{\star r}}\right)^{\frac{1}{4}} \left(\rho^r_{\rm tot}(A_{\rm re})\right)^{\frac{1}{4}}. \tag{3.12}$$

Here, $g^{\rm re}_{\star r}$ is the effective number of relativistic degrees of freedom at the end of reheating, and we take $g^{\rm re}_{\star r} = 100$ throughout the thesis. From the above equation, we can get the one-to-one correspondence between the coupling constant (g^r_i, h^r) and reheating temperature $T_{\rm re}$, where $i = 1, 2$ correspond to two different inflaton-Boson couplings described earlier. One can further obtain a constraint relation between reheating temperature $T_{\rm re}$ and the present CMB temperature (T_0) by considering a physical assumption that from the end of reheating to the present time, the co-moving entropy density of the universe is conserved. This condition leads to [11],

$$T_{\rm re} = \left(\frac{43}{11 g^{\rm re}_{\star r}}\right)^{\frac{1}{3}} \left(\frac{a_0 T_0}{k_\star}\right) H_k \, e^{-(N_k + N_{\rm re})}. \tag{3.13}$$

Where $k_\star/a_0 = 0.05$ Mpc^{-1} is the CMB pivot scale, the present CMB temperature $T_0 = 2.725$ K, $a_0 = 1$ is the present day scale factor, and $N_{\rm re} = \ln A_{\rm re}$ is the reheating e-folding number. Combining the above two Eqs. 3.13 and 3.12, we can directly relate the reheating temperature $T_{\rm re}$ to the CMB spectral index $n_{\rm s}$, as both H_k and N_k depend on $n_{\rm s}$. Therefore, we can essentially obtain an indirect connection between the coupling constant (g^r_i, h^r) and the spectral index $n_{\rm s}$, which parameterizes the anisotropies in the CMB fluctuations.

3.1.4 Bosonic Reheating: Dynamics and constraints

A. Dynamics: probing different decay channels

During reheating, if the dominant decay channel of the inflaton is through massless Bosons, we call it Bosonic reheating. For our phenomenological purpose, we discuss two different non-gravitational bosonic channels $\phi \to ss$ and $\phi\phi \to ss$ of inflaton along with the gravitational scattering process $\phi\phi \to h_{\mu\nu} \to ss$.

The total radiation component will be composed of all these thermalized decay products produced from different decay channels. Most of the studies on reheating were done at zero temperature, except for a few very special cases [188, 194]. Therefore, a more realistic consideration would be to take into account finite temperature corrections due to radiation baths. We compare the results with the zero temperature case in all the figures to quantify such effects. The detailed analytic calculation for both zero and finite temperature cases and the description of the dynamics are given in Addenda-A.

We solve the Boltzmann equations for the general inflaton EoS w_ϕ and scan the entire inflaton-scalar coupling (g_i^r) parameter space[3] and figure out one of our most significant results shown in Fig. 3.2. The parameter space (g_i^r, w_ϕ) can be generically divided into four regions marked in different colors: i) Light-cyan region is where reheating is entirely controlled by the gravity-mediated decay channel (gravitational reheating), ii) Yellow region is controlled by mostly inflaton-Boson coupling, iii) Light-red region is where successful reheating cannot be achieved as reheating temperature $T_{\rm re} < T_{\rm BBN}$, and iv) Pink region where initial parametric resonance will be important. In this thesis, we ignore such an effect and defer it to our future study. The system has two competing effects due to direct and gravity-mediated inflaton decay. Based on their relative dominance, we observe three distinct regions of coupling g_i^r where reheating evolution will be different: 1) **Case-I**: Entire reheating dynamics will be dominated by direct inflaton decay, 2) **Case-II**: Both the decay processes will partially dominate the reheating dynamics, 3) **Case-III**: Entire reheating dynamics will be dominated by gravity mediated decay (gravitational reheating [184]). These three cases immediately suggest the existence of two critical coupling values for every individual inflaton-scalar radiation coupling g_i^r, which set the phase boundaries among those three cases in (g_i^r, w_ϕ) plane. If the coupling $g_i^r > \mathscr{G}_{ci}^{1,th} \simeq \mathscr{G}_{ci}^{1}$, the reheating evolution will be according to case-I. Where, $\mathscr{G}_{ci}^{1}$ is computed without thermal effect, for it turned to be same for both with and without thermal effect (see detailed derivation in the Addenda-A). The critical coupling strength $\mathscr{G}_{ci}^{1}$ is found to be,

$$\mathscr{G}_{ci}^{1,th} = \begin{cases} \left[\dfrac{3(5+3w_\phi)(H_{\rm end}m_\phi^{\rm end})^2}{128M_p^2(1+15w_\phi)}\dfrac{\left[\left(\frac{9+15w_\phi}{8}\right)^{\frac{-8}{1+15w_\phi}}-\left(\frac{9+15w_\phi}{8}\right)^{\frac{-9-15w_\phi}{1+15w_\phi}}\right]}{\left[\left(\frac{8}{3(1-w_\phi)}\right)^{\frac{3(w_\phi-1)}{(5+3w_\phi)}}-\left(\frac{8}{3(1-w_\phi)}\right)^{\frac{-8}{5+3w_\phi}}\right]}\right]^{1/2} & \text{for } g_1^r\phi s^2, \\ \left[\dfrac{(9w_\phi-1)(m_\phi^{\rm end})^4}{64M_p^4(1+15w_\phi)}\dfrac{\left[\left(\frac{9+15w_\phi}{8}\right)^{\frac{-8}{1+15w_\phi}}-\left(\frac{9+15w_\phi}{8}\right)^{\frac{-9-15w_\phi}{1+15w_\phi}}\right]}{\left[\left(\frac{9(1-w_\phi)}{8}\right)^{\frac{9(w_\phi-1)}{1-9w_\phi}}-\left(\frac{9(1-w_\phi)}{8}\right)^{\frac{-8}{1-9w_\phi}}\right]}\right]^{1/2} & \text{for } g_2^r\phi^2 s^2. \end{cases} \tag{3.14}$$

If we lower the couplings g_i^r below $\mathscr{G}_{ci}^{1,th}$, the gravitational scattering starts to reveal its presence in the early phase of the reheating process, and the complete takeover happens if the non-gravitational coupling strength is lower than a new critical coupling which we denoted as $\mathscr{G}_{ci}^{2,th}$. Therefore, if coupling strength in between $\mathscr{G}_{ci}^{2,th} < g_i^r < \mathscr{G}_{ci}^{1,th}$, the reheating evolution will be according to case-II. The expressions of $\mathscr{G}_{ci}^{2,th}$ for different interaction are calculated as,

$$\mathscr{G}_{ci}^{2,th} = \begin{cases} \left[\left(\dfrac{9(1+w_\phi)H_{\rm end}^3 m_\phi^{\rm end}}{512\pi(1+15w_\phi)}\right)\left(\dfrac{4\pi\epsilon^{1/4}(m_\phi^{\rm end})^2(3w_\phi+1)}{3(1+w_\phi)M_p^2H_{\rm end}}\right)^{4/3}(A_{\rm re}^{\rm gr})^{-2-6w_\phi}\right]^{3/8} & \text{for } g_1^r\phi s^2 \\ \left[\left(\dfrac{9(1+w_\phi)H_{\rm end}^3 m_\phi^{\rm end}}{512\pi(1+15w_\phi)}\right)\left(\dfrac{8\pi\epsilon^{1/4}(m_\phi^{\rm end})^4(5w_\phi-1)}{9(1+w_\phi)M_p^4H_{\rm end}^3}\right)^{4/3}(A_{\rm re}^{\rm gr})^{2-10w_\phi}\right]^{3/8} & \text{for } g_2^r\phi^2 s^2, \end{cases} \tag{3.15}$$

[3] In Addenda-E, we have shown the regions (Fig. 3.19) where the self-resonance [13, 14] effect is important.

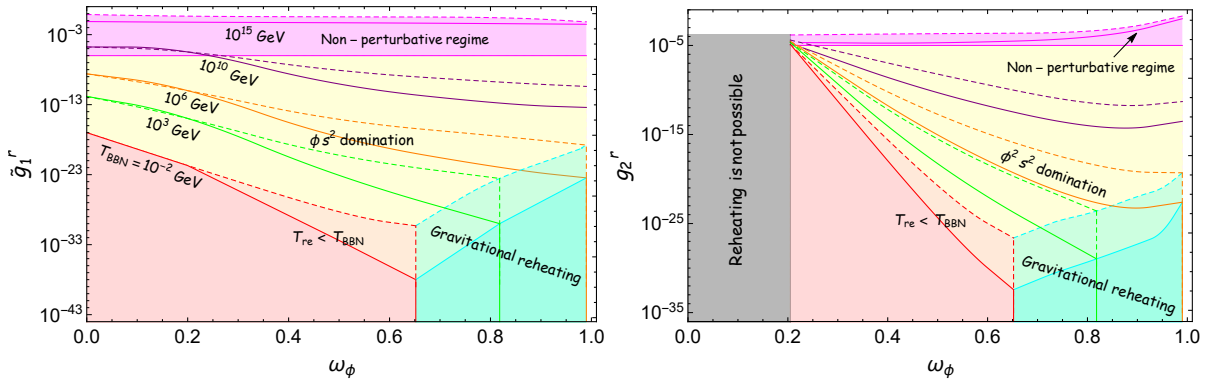

Figure 3.2: We have plotted the Variation of the dimensionless bosonic coupling $\tilde{g}_1^r = g_1^r/m_\phi^{\rm end}$ (for ϕs^2 left figure) and g_2^r (for $\phi^2 s^2$ right figure) as a function of w_ϕ. Dashed and solid lines correspond to without and with the thermal effect being taken into account in the decay process respectively. The yellow and pink shaded regions indicate the explicitly coupling-dominated region where the decay channel controls the reheating temperature. The light-cyan region corresponds to gravitational reheating. The light-red region corresponds to $T_{\rm re} < T_{\rm BBN} \simeq 10$ MeV. The light-gray region corresponds to the no reheating region where the inflaton energy density falls faster than the radiation energy density, and successful reheating is not possible. The pink region corresponds to the non-perturbative regime where bounds on the coupling are, $\tilde{g}_1^r \geq \left(V_{end}^{1/2} m_\phi^{\rm end}/(24 M_p \phi_{end}^2)\right)^{1/2}$ and $g_2^r \geq (V_{end}^{1/8}/\phi_{\rm end})\left(V_{end}^{1/2}(m_\phi^{\rm end})^3/(\sqrt{2} M_p \phi_{end}^4)\right)^{1/4}$ are obtained from resonance condition of Mathieu equation for scalar field [45, 143, 144].

where, $A_{\rm re}^{\rm gr}$ is the scale factor defined at reheating end for the gravitational reheating scenario (see, for this instance, Eq. 3.28).

Finally, as pointed out just above, if $g_i^r < \mathscr{G}_{ci}^{2,th}$, the reheating evolution will be according to case-III, which we call gravitational reheating. We will now dwell on these three cases and discuss their thermal histories in detail:

Case-I: Coupling strength $g_i^r > \mathscr{G}_{ci}^{1,th}$: In this regime, direct decay of inflaton into radiation controls the entire reheating process. In the left panel of Fig. 3.4, we showed the evolution of the different energy components with the coupling parameter. Since the radiation bath of temperature $T_{\rm rad}$ is produced from the decay products of a homogeneous inflaton background, the typical energy of the bath particles will be of the order of the inflaton mass m_ϕ. And, hence, for the condition $T_{\rm rad} > m_\phi(t)$, the thermal effect will be dominant. For any reheating dynamics, there exist two important energy scales of importance, and those are the maximum radiation temperature ($T_{\rm rad}^{\rm max}$) and the reheating temperature ($T_{\rm re}$). Given the inflation model under consideration, we have two free parameters, namely, the inflaton EoS (w_ϕ) and the inflaton-Boson coupling (g_i^r), where "i" stands for two different bosonic decay channels mentioned earlier. Depending upon the evolution of ($T_{\rm rad}, m_\phi$), and consequently the behavior of thermal effect, we have observed rich reheating histories. In the following section, we lay bare the detailed discussions on those for different cases in different temperature regimes.

When $T_{\rm rad}^{\rm max} > m_\phi^{\rm end}$: This is the situation which typically occurs for large values of inflaton-scalar coupling, mostly in the pink region of Fig. 3.2. Since the maximum radiation temperature $T_{\rm rad}^{\rm max}$ is greater than the inflaton mass $m_\phi^{\rm end}$ defined at the end of inflation, the thermal effect influences the reheating dynamics significantly. Details of this finite temperature effect will be further controlled by the parameters (w_ϕ, g_i^r) and the time-dependent inflaton mass $m_\phi(t)$. We will first discuss the situation when $T_{\rm rad} > m_\phi(t)$ throughout the entire period of reheating. With this condition, the finite temperature decay widths can be

approximated as,

$$\Gamma_\phi = \begin{cases} \Gamma_{\phi\to ss} = \dfrac{4(g_1^r)^2 T_{\rm rad}}{8\pi m_\phi^2(t)}\,, \\ \Gamma_{\phi\phi\to ss} = \dfrac{2(g_2^r)^2}{8\pi}\dfrac{\rho_\phi(t) T_{\rm rad}}{m_\phi^4(t)}\,, \end{cases} \tag{3.16}$$

With the aforementioned decay width, one can estimate the behaviour of the radiation energy density,

$$\rho_s^r(A) = \begin{cases} \left[\dfrac{3M_p^2(1+w_\phi)H_{\rm end}}{4\pi\epsilon^{1/4}(1+3w_\phi)(m_\phi^{\rm end})^2 A^3}(g_1^r)^2\left(A^{\frac{3(1+3w_\phi)}{2}}-1\right)\right]^{4/3} & \text{for } g_1^r\phi s^2\,, \\ \left[\dfrac{9M_p^4(1+w_\phi)H_{\rm end}^3}{8\pi\epsilon^{1/4}(5w_\phi-1)(m_\phi^{\rm end})^4 A^3}(g_2^r)^2\left(A^{\frac{3(-1+5w_\phi)}{2}}-1\right)\right]^{4/3} & \text{for } g_2^r\phi^2 s^2\,. \end{cases} \tag{3.17}$$

Using the relation Eq. 3.12, the reheating temperatures are estimated for two different decay channels as,

$$T_{\rm re} = \begin{cases} \left[\dfrac{3M_p^2(1+w_\phi)H_{\rm end}}{4\pi\epsilon(1+3w_\phi)(m_\phi^{\rm end})^2}(g_1^r)^2 A_{\rm re}^{-\frac{3}{2}(1-3w_\phi)}\right]^{1/3} & \text{for } g_1^r\phi s^2\,, \\ \left[\dfrac{9M_p^4(1+w_\phi)H_{\rm end}^3}{8\pi\epsilon(5w_\phi-1)(m_\phi^{\rm end})^4}(g_2^r)^2 A_{\rm re}^{\frac{-3(3-5w_\phi)}{2}}\right]^{1/3} & \text{for } g_2^r\phi^2 s^2\,, \end{cases} \tag{3.18}$$

where $\epsilon = (\pi^2/30)g_{\star r}^{\rm re}$, and $A_{\rm re}$ is the normalized scale factor at the end of reheating

$$A_{\rm re} = \begin{cases} \left(\dfrac{4\pi(1+3w_\phi)(m_\phi^{\rm end})^2}{(1+w_\phi)(g_1^r)^2(\frac{\epsilon}{3})^{1/4}}\left(\dfrac{H_{\rm end}}{M_p}\right)^{1/2}\right)^{\frac{4}{3(1+9w_\phi)}} & \text{for } g_1^r\phi s^2\,, \\ \left(\dfrac{8\pi(27\epsilon)^{1/4}(5w_\phi-1)}{9(1+w_\phi)M_p^{5/2}H_{end}^{3/2}}(m_\phi^{\rm end})^4\right)^{\frac{4}{3(13w_\phi-3)}} & \text{for } g_2^r\phi^2 s^2\,, \end{cases} \tag{3.19}$$

For detailed solutions and derivations, see Addenda-A.2.

Table 3.1: The evolution of bath temperature for bosonic reheating:

	$T_{\rm rad} \ll m_\phi(t)$ (Without thermal effect)		$T_{\rm rad} \gg m_\phi(t)$ (With thermal effect)	
Channel	Non-gravitational	Gravitational	Non-gravitational	Gravitational
$\phi \to ss$	$A^{-\frac{3(1-w_\phi)}{8}}$	A^{-1}	$A^{-\frac{(1-3w_\phi)}{2}}$	A^{-1}
$\phi\phi \to ss$	$A^{-\frac{9(1-w_\phi)}{8}}$	A^{-1}	$A^{-\frac{(3-5w_\phi)}{2}}$	A^{-1}

Now, we would like to point out an interesting fact associated with the maximum radiation temperature $T_{\rm rad}^{\rm max}$, which generically satisfies $T_{\rm rad}^{\rm max} \gg T_{\rm re}$. We observed the existence of a critical value of $w_\phi^t = (1/3, 3/5)$ for two different bosonic decay channels $\phi \to ss$ and $\phi\phi \to ss$ (see, for instance, Eqs. 3.17). If $w_\phi < w_\phi^t$, the maximum radiation temperature ($T_{\rm rad}^{\rm max}$) satisfies the usual condition mentioned above,

$$T_{\rm rad}^{\rm max} \simeq T_s^{r,\rm max} = \begin{cases} \left[\dfrac{3M_p^2(1+w_\phi)H_{\rm end}}{4\pi\epsilon(1+3w_\phi)(m_\phi^{\rm end})^2}(g_1^r)^2\left\{\left(\dfrac{2}{1-3w_\phi}\right)^{\frac{3w_\phi-1}{3+9w_\phi}} - \left(\dfrac{2}{1-3w_\phi}\right)^{\frac{-2}{3+9w_\phi}}\right\}\right]^{1/3} & \text{for } g_1^r\phi s^2\,, \\ \left[\dfrac{9M_p^4(1+w_\phi)H_{\rm end}^3}{8\pi\epsilon(5w_\phi-1)(m_\phi^{\rm end})^4}(g_2^r)^2\left\{\left(\dfrac{2}{3-5w_\phi}\right)^{\frac{5w_\phi-3}{5w_\phi-1}} - \left(\dfrac{2}{3-5w_\phi}\right)^{\frac{-2}{5w_\phi-1}}\right\}\right]^{1/3} & \text{for } g_2^r\phi^2 s^2\,. \end{cases} \tag{3.20}$$

Where $T_{\rm s}^{\rm r,\,max}$ indicates the maximum radiation temperature due to the direct inflaton decay channel (see Addenda-A.2). Surprising result emerges, however, for $w_\phi > w_\phi^t$ case, for which the evolution of radiation and background conspire in such a manner that at the end of reheating maximum radiation temperature becomes equal to the reheating temperature, $T_{\rm rad}^{\rm max} \simeq T_{\rm re}$ (for better visualization, see the left most plot

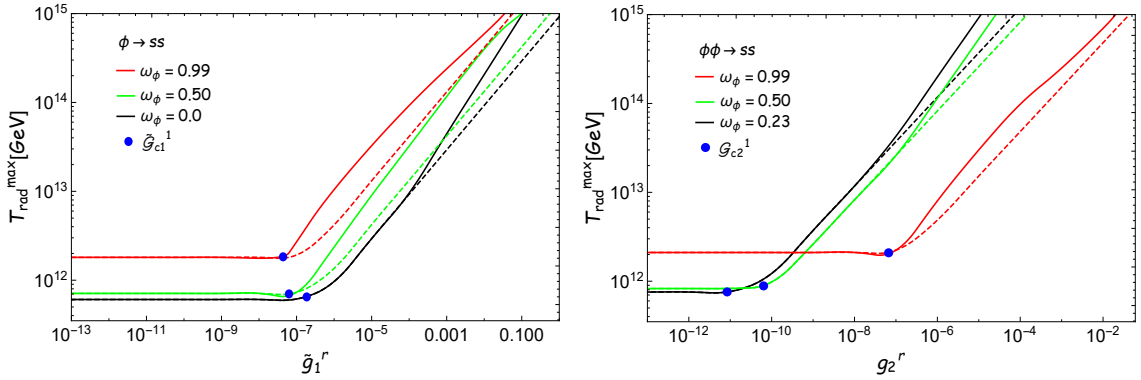

Figure 3.3: Variation of maximum radiation temperature $T_{\rm rad}^{\rm max}$ as function of dimensionless coupling parameter $\tilde{g}_1^r = \frac{g}{m_\phi^{\rm end}}, g_2^r$, for three different inflaton EoS $w_\phi = 0.0(0.23), 0.50, 0.99$ for the $\phi \to ss$ (left-most), and $\phi\phi \to ss$ (right-most) model.

of Fig. 3.4). Such behavior has been observed before considering the phenomenological expression of the decay rate as a function of temperature [195]. The implication of this specific case could be interesting to study.

It is observed that in this region the ratio $T_{\rm rad}/m_\phi(t)$ varies as $A^{9w_\phi-1}(A^{11w_\phi-3})$ for $\phi \to ss$ ($\phi\phi \to ss$). This behavior suggests the existence of a critical value $w_\phi^c = 1/9$ for the decay channel $\phi \to ss$ and $w_\phi^c = 3/11$ for the decay channel $\phi\phi \to ss$, above which $T_{\rm rad} > m_\phi(t)$ condition is always maintained. But, when EoS lies within $0 \le w_\phi < w_\phi^c$, the initially high radiation temperature ensures that thermal corrections significantly influence the dynamics at early times. Nevertheless, these finite-temperature effects gradually diminish and may become negligible at some intermediate scale factor A_c during reheating, which depends on the inflaton EoS w_ϕ as follows,

$$A_c = \begin{cases} (A_{\rm max})^{\frac{1-3w_\phi}{1-9w_\phi}} \left(\frac{m_\phi^{\rm end}}{(\rho_s^{r,\rm max}/\epsilon)^{1/4}}\right)^{-\frac{2}{(1-9w_\phi)}} & \text{for} \quad g_1^r \phi s^2, \\ (A_{\rm max})^{\frac{3-5w_\phi}{3-11w_\phi}} \left(\frac{m_\phi^{\rm end}}{(\rho_s^{r,\rm max}/\epsilon)^{1/4}}\right)^{-\frac{2}{3(1-11w_\phi)}} & \text{for} \quad g_2^r \phi^2 s^2, \end{cases} \tag{3.21}$$

where $A_{\rm max}$ and $\rho_s^{r,\rm max}$ are defined in Eqs. 3.130, 3.129. After this crossover occurs, the radiation energy density subsequently evolves according to the zero-temperature solution given in Eq. 3.114. In the DM studies, we will see such an intermediate scale will have non-trivial dependence on its abundance. We find the associated reheating temperature as

$$T_{\rm re} = \begin{cases} \left(\frac{6M_p^2(1+w_\phi)H_{\rm end}}{8\pi\epsilon(5+3w_\phi)m_\phi^{\rm end}}(g_1^r)^2\right)^{1/4} A_{re}^{-\frac{3}{8}(1-w_\phi)} & \text{for } g_1^r \phi s^2, \\ \left(\frac{9M_p^4(1+w_\phi)H_{\rm end}^3}{4\pi\epsilon(9w_\phi-1)(m_\phi^{\rm end})^3}(g_2^r)^2\right)^{1/4} A_{re}^{\frac{9(w_\phi-1)}{8}} & \text{for } g_2^r \phi^2 s^2, \end{cases} \tag{3.22}$$

where

$$A_{\rm re} = \begin{cases} \left(\frac{4\pi(5+3w_\phi)H_{\rm end}m_\phi^{\rm end}}{(1+w_\phi)(g_1^r)^2}\right)^{\frac{2}{3+9w_\phi}} & \text{for } g_1^r \phi s^2, \\ \left(\frac{4\pi(9w_\phi-1)(m_\phi^{\rm end})^3}{3(1+w_\phi)M_p^2 H_{\rm end}(g_2^r)^2}\right)^{\frac{2}{3(5w_\phi-1)}} & \text{for } g_2^r \phi^2 s^2. \end{cases} \tag{3.23}$$

In reheating model building, the gravitational contribution to the radiation sector is universally present along with the non-gravitational one. Therefore, it is natural to expect that the $T_{\rm rad}^{\rm max}$ for a given reheating model can not assume an arbitrarily low value. In fact, due to the universal gravitational contribution, there exists a lower limit on $T_{\rm rad}^{\rm max}$, which is $T_{\rm gr}^{r,\rm max} \simeq (10^{11} - 10^{12})$ GeV [175, 184]. The small variations are due to different values of EoS w_ϕ. Therefore, the minimum possible value of $T_{\rm rad}^{\rm max}$ simply turns out as $T_{\rm gr}^{r,\rm max}$. In the following discussion, we now consider the regime where $T_{\rm rad}^{\rm max} > T_{\rm gr}^{r,\rm max}$ but less than $m_\phi^{\rm end}$.

When $T_{\rm gr}^{r,\rm max} < T_{\rm rad}^{\rm max} < m_\phi^{\rm end}$: The parameter region (see Fig. 3.2) wherein this condition is satisfied belongs to the yellow region. However, for this case, initially $T_{\rm rad}^{\rm max} < m_\phi^{\rm end}$, and hence there is no thermal effect initially, and the ratio $T_{\rm rad}/m_\phi \propto A^{-(3-27w_\phi)/8}$ ($A^{-(9-33w_\phi)/8}$) for $\phi \to ss$ ($\phi\phi \to ss$) respectively. Thus, for $w_\phi < w_\phi^c$ (defined before), the finite temperature effect will never be significant. Consequently, the reheating dynamics will be the same as that of the zero temperature, and details of such dynamics are described in the Addenda-A (for example, the radiation energy density evolves following Eq. 3.114). However, if the inflaton EoS satisfies the condition $w_\phi > w_\phi^c$, the finite temperature effect ($T_{\rm rad} > m_\phi$) is expected to occur at some intermediate radiation temperature $T_c = T_{\rm rad}(A_c)$ with the scale factor A_c during reheating. We have

$$A_c = \begin{cases} (A_{\rm max})^{\frac{1-w_\phi}{1-9w_\phi}} \left(\frac{m_\phi^{\rm end}}{(\rho_s^{r,\rm max}/\epsilon)^{1/4}}\right)^{-\frac{8}{3(1-9w_\phi)}} & \text{for} \quad g_1^r \phi s^2, \\ (A_{\rm max})^{\frac{3(1-w_\phi)}{3-11w_\phi}} \left(\frac{m_\phi^{\rm end}}{(\rho_s^{r,\rm max}/\epsilon)^{1/4}}\right)^{-\frac{8}{3(1-11w_\phi)}} & \text{for} \quad g_2^r \phi^2 s^2, \end{cases} \tag{3.24}$$

where $A_{\rm max}$ and $\rho_s^{r,\rm max}$ are defined in Eqs. 3.117, 3.118. After this crossover happens, the radiation energy density simply follows the Eq. 3.17. In the DM studies, we will see that such an intermediate scale will have non-trivial dependence on its abundance.

For case-I, the above two temperature regimes will be possible. To this end, we point out another important scenario that warrants detailed discussion-namely, the case when $T_{\rm rad}^{\rm max} = T_{\rm gr}^{\rm r,max}$, which indicates that the initial phase of reheating must be dominated by the graviton-mediated inflaton decay. This situation arises only if the non-gravitational inflaton coupling satisfies $g_i^r < \mathscr{G}_{ci}^{1,th}$. This condition, therefore, belongs to the other two cases of coupling ranges mentioned before.

Case-II: Coupling strength in between $\mathscr{G}_{ci}^{2,th} < g_i^r < \mathscr{G}_{ci}^{1,th}$: In this coupling range, gravitational interaction drives the dynamics of reheating at the beginning. The gravitational production is nearly instantaneous and happens just at the beginning of reheating. In fact, this case is true for the entire range of coupling with $g_i^r < \mathscr{G}_{ci}^{1,th}$, and $T_{\rm rad}^{\rm max} = T_{\rm gr}^{\rm r,max}$ condition always holds. However, since the non-gravitational bosonic coupling is non-zero, during the reheating process gravitational coupling, non-gravitational coupling, and thermal effect of the produced radiation undergo interesting interplay among themselves. Let us illustrate the following two different possibilities of thermal history in this context,

- The thermal effect may start dominating the early phase when gravity-mediated decay controls the reheating. During this phase the ratio behaves $T_{\rm rad}/m_\phi(A) \propto A^{3w_\phi - 1}$. Hence, for $w_\phi > 1/3$, it is clear from this ratio that the thermal effect cannot be ignored. And we found a particular value of scale factor $A_{\rm c}^{\rm g}$, after which Bose enhancement starts affecting the dynamics,

$$A_{\rm c}^{\rm g} = \left[A_{\rm max}\left(\frac{m_\phi^{\rm end}}{(\rho_{\rm gr}^{r,\rm max}/\epsilon)^{1/4}}\right)\right]^{\frac{1}{1+3w_\phi}}, \tag{3.25}$$

  where, $A_{\rm max}$ is the scale factor at which $T_{\rm rad} = T_{\rm rad}^{\rm max} = T_{\rm gr}^{r,\rm max}$, and maximum radiation energy density ($\rho_{\rm gr}^{r,\rm max}$) is obtained from gravitational decay (see, for instance, the last expression of Eq. 3.117 and

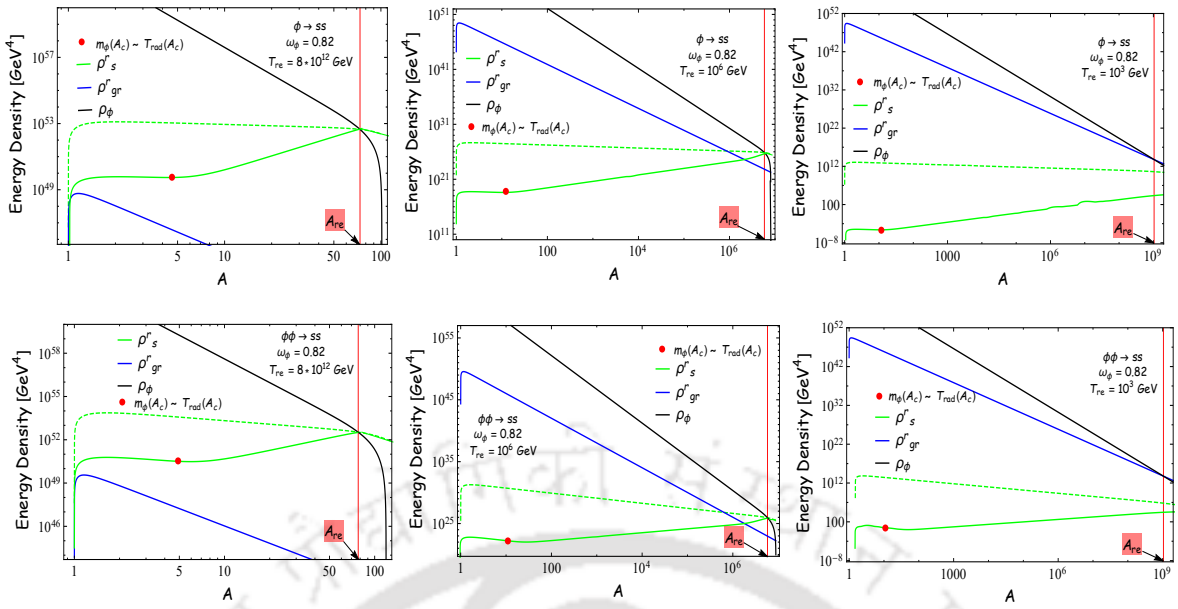

Figure 3.4: Evolution of inflaton and radiation energy density as a function of normalized scale factor $A = a/a_{\rm end}$ for both $\phi \to ss$ and $\phi\phi \to ss$ with and without thermal effect (solid line for with thermal effect and dashed line for without thermal effect). **Left panel:** Coupling is in the range of $g^r_i > \mathscr{G}^{1,th}_{ci}$. **Middle panel:** Coupling is in the range of $\mathscr{G}^{2,th}_{ci}/\mathscr{G}^2_{ci} < g^r_i < \mathscr{G}^{1,th}_{ci}$. **Right panel:** Coupling is in the range of $g^r_i < \mathscr{G}^{2,th}_{ci}/\mathscr{G}^2_{ci}$. For all these cases, we have considered the inflaton EoS $w_\phi = 0.82$.

Eq. 3.119). After this point, the radiation energy density simply varies as A^{-4}. However, as reheating proceeds towards the end, there is another crossover from gravitational decay domination to non-gravitational decay domination, which will happen at the value of scale factor, defined as

$$A_{\rm gr\to ngr} = \begin{cases} \left(\dfrac{2M_p^2(1+w_\phi)H_{\rm end}}{8\pi(1+3w_\phi)(m_\phi^{\rm end})^2(\mathscr{C}(w_\phi))^3}(g^r_1)^2\right)^{\frac{-2}{3(1+3w_\phi)}} & \text{For } g^r_1\,\phi\, s^2\,, \\ \left(\dfrac{4(3M_p^2H_{\rm end}^2)^2M_p^2(1+w_\phi)H_{\rm end}}{8\pi(5w_\phi-1)(m_\phi^{\rm end})^4(\mathscr{C}(w_\phi))^2}(g^r_2)^2\right)^{\frac{2}{3(1+5w_\phi)}} & \text{For } g^r_2\,\phi^2\, s^2\,, \end{cases} \tag{3.26}$$

where $\mathscr{C}(w_\phi) = \left(\dfrac{9(1+w_\phi)H^3_{\rm end}}{1024\pi(1+3w_\phi)\epsilon M_p^2}\right)^{1/3}$. The reheating temperature assumes the same form as Eq. 3.19. For better visualization of the evolution of different energy components see the middle panel of Fig. 3.4. In summary, the reheating dynamics can be read off as follows: at the beginning gravitational sector dominates the porcess with radiation temperature varies as $T_{\rm rad} \propto A^{-1} \to$ as reheating proceeds the thermal effect starts to play its role but with the same temperature evolution $T_{\rm rad} \propto A^{-1} \to$ non-gravitational coupling takes over the process, and the radiation temperatures vary as $T_{\rm rad} \propto A^{-\frac{1}{2}+\frac{3w_\phi}{2}}\left(A^{-\frac{3-5w_\phi}{2}}\right)$ for the decay process $\phi \to ss$ ($\phi\phi \to ss$)).

- There may be a situation where the thermal effect will be important only during non-gravitational production. For this case, reheating proceeds from gravity-mediated decay to explicit inflaton decay

Table 3.2: Bosonic reheating: Bounds on the inflationary parameters

Parameter	$\phi \to ss$					$\phi \to ss$			
	$w_\phi = 0.0$	$w_\phi = 0.20$	$w_\phi = 0.50$	$w_\phi = 0.82$	$w_\phi = 0.99$	$w_\phi = 0.23$	$w_\phi = 0.50$	$w_\phi = 0.82$	$w_\phi = 0.99$
$n_s^{\min}$	0.95520	0.96220	0.96473	0.96455	0.96440	0.96294	0.96473	0.96455	0.96440
$n_s^{\max}$	0.96540	0.96505	0.96722	0.96855	0.96809	0.96506	0.96722	0.96855	0.96809
N_k	42.42-55.69	51.31-55.78	55.71-60.16	55.83-66.35	56.04-68.86	52.42-55.78	60.16-55.71	66.35-55.83	68.86-56.04

domination, and the transition occurs at the scale factor,

$$A_{\rm gr\to ngr} = \begin{cases} \left(\frac{\rho_{gr}^{r,max}}{\rho_s^{r,max}} \frac{\left(\frac{9+15w_\phi}{8}\right)^{\frac{8}{1+15w_\phi}}}{\left(\frac{8}{3(1-w_\phi)}\right)^{\frac{3(w_\phi-1)}{5+3w_\phi}}} \right)^{\frac{2}{5+3w_\phi}} & \text{for } g_1^r \phi s^2\,, \\ \left(\frac{\rho_{gr}^{r,max}}{\rho_s^{r,max}} \frac{\left(\frac{9+15w_\phi}{8}\right)^{\frac{8}{1+15w_\phi}}}{\left(\frac{9(1-w_\phi)}{8}\right)^{\frac{9(w_\phi-1)}{1-9w_\phi}}} \right)^{\frac{2}{9w_\phi-1}} & \text{for } g_2^r \phi^2 s^2\,, \end{cases} \tag{3.27}$$

where $\rho_{\rm gr}^{r,\max}$ and $\rho_s^{r,\max}$ are defined in Eqs. 3.118, 3.119. Once the reheating process starts to be dominated by the explicit inflaton coupling, the scale factor beyond which the thermal effect starts working is given by Eq. 3.24. Finally, the decay channel defines the reheating temperature (see, for instance, Eq. 3.19). In summary, dynamics can be described as follows: reheating proceeds through gravity-mediated decay with no finite temperature effect ($T_{\rm rad} \propto A^{-1}$) → non-gravitational decay dominates the phase with negligible thermal effect with radiation temperature varies as $T_{\rm rad} \propto A^{-\frac{3}{8}(1-w_\phi)} \left(A^{-\frac{9}{8}(1-w_\phi)}\right)$ for decay process $\phi \to ss$ ($\phi\phi \to ss$)) → non-gravitational coupling domination with significant thermal effect $\left(T_{\rm rad} \propto A^{-\frac{1}{2}+\frac{3w_\phi}{2}} \left(A^{-\frac{3-5w_\phi}{2}}\right)\right)$ for $\phi \to ss$ ($\phi\phi \to ss$)).

Case III: when $g_i^r < \mathscr{G}_{ci}^2$: The bath temperature always falls as A^{-1}, and thermal effect is observed to play no role throughout. The gravity-mediated decay of inflaton controls the entire dynamics of reheating, and the scenario is termed as gravitational reheating (GRe), and that will occur only for $w_\phi \gtrsim 0.65$ (see the light-cyan region of Fig. 3.2). The reheating temperature is defined when $\rho_\phi = \rho_{\rm gr}^r$, and the condiction gives

$$T_{\rm re}^{\rm gr} = \left(\frac{9H_{\rm end}^3 m_\phi^{\rm end}(1+w_\phi)}{512\epsilon\pi(1+15w_\phi)(A_{\rm re}^{\rm gr})^4} \right)^{1/4}, A_{\rm re}^{\rm gr} = \left(\frac{512\pi M_p^2(1+15w_\phi)}{3H_{\rm end} m_\phi^{\rm end}(1+w_\phi)} \right)^{\frac{1}{3w_\phi-1}}, \tag{3.28}$$

where $A_{\rm re}^{\rm gr}$ is the normalized scale factor at the end of gravitational reheating. In the right panel of Fig. 3.4, we have shown the dynamical behaviour of different energy components, and in Table-3.1, showing the evolution of the bath temperature with A for non-gravitational reheating and gravitational reheating.

In the subsequent section, we will focus on the possible constraints on the inflaton coupling strengths depending on the CMB ($n_{\rm s}$) and reheating parameter $T_{\rm re}$.

B. Constraining reheating temperature and bosonic coupling parameters with CMB

For illustration, we consider five different values of the inflaton EoS $w_\phi = (0.0, 0.20, 0.50, 0.82, 0.99)$. For each w_ϕ, we have plotted : (i) $T_{\rm re}$ vs $n_{\rm s}$, (ii) g_i^r vs $n_{\rm s}$, (iii) g_i^r vs $T_{\rm re}$. We compare the results with and without the thermal effect for all cases.

i) Reheating temperature ($T_{\rm re}$) in terms inflationary (CMB) parameter ($\mathbf{n_s}$): From the Fig. 3.5 we observe that the variation of reheating temperature in terms of the scalar spectral index ($n_{\rm s}$) for a given EoS w_ϕ is insensitive to the finite temperature correction in the inflaton decay width. More generally, it can be said

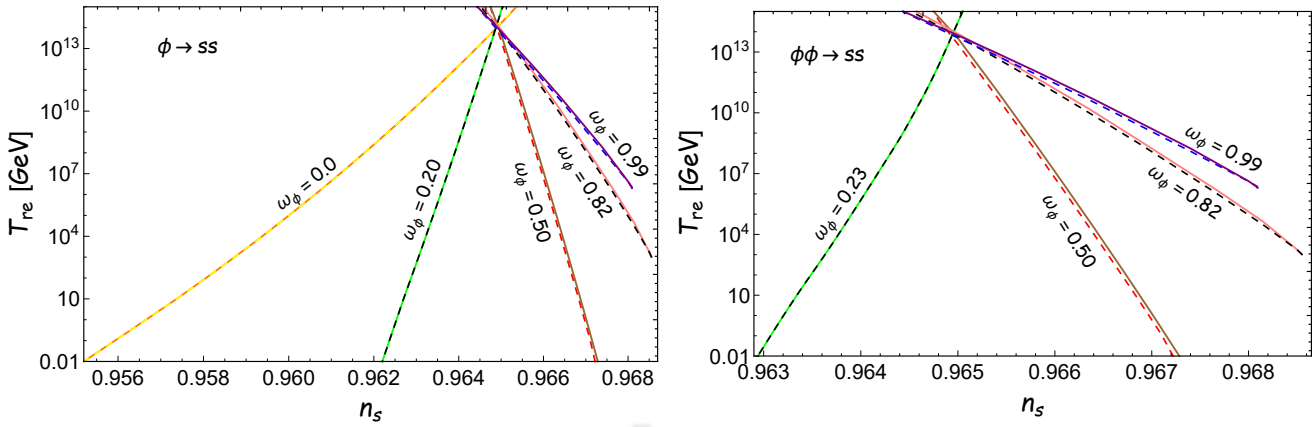

Figure 3.5: Variation of reheating temperature $T_{\rm re}$ as a function of spectral index $n_{\rm s}$ for $\alpha-$attractor E-model ($\alpha = 1$) with $w_\phi = (0, 0.200.50, 0.82, 0.99)$. The plot is on the left side for the bosonic reheating with $\phi \to ss$ process and on the right side for the process $\phi\phi \to ss$. The solid lines are for considering the thermal effect, and the dashed lines are for without the thermal effect.

that the dependence of $T_{\rm re}$ on $n_{\rm s}$ is insensitive to the specific mechanism through which radiation (entropy) is produced during reheating from inflaton decay. The likely reason for this is that $T_{\rm re}$ is connected to $n_{\rm s}$ through the entropy conservation relation (Eq. 3.13), which contains the term $N_{\rm re}$. The relation between $T_{\rm re}$ and $N_{\rm re}$ can be written as,

$$N_{\rm re} = \ln A_{\rm re} = \frac{1}{3(1+w_\phi)} \ln\left(\frac{90}{\pi^2 g^{\rm re}_{\star r}} \frac{M_{\rm p}^2 H_{\rm end}^2}{T_{\rm re}^4}\right) \tag{3.29}$$

Using this expression, the entropy conservation relation can be further rewritten as,

$$T_{\rm re} = \left(\frac{11 g^{\rm re}_{\star r}}{43}\right)^{\frac{1+w_\phi}{1-3w_\phi}} \left(\frac{k_\star/a_0}{T_0 H_k}\right)^{\frac{3(1+w_\phi)}{1-3w_\phi}} \left(\frac{90 M_{\rm p}^2 H_{\rm end}^2}{\pi^2 g^{\rm re}_{\star r}}\right)^{\frac{1}{1-3w_\phi}} e^{\frac{3(1+w_\phi)}{1-3w_\phi} N_k} \tag{3.30}$$

It is evident from the above expression that this equation does not contain any terms explicitly tied to the details of the inflaton-to-radiation transfer process. This explains why the variation of $T_{\rm re}$ with $n_{\rm s}$ is unaffected by the specific inflaton-radiation interaction channel. However, the expression remains sensitive to the background expansion history, i.e, the inflaton EoS w_ϕ. The generic feature is that for $w_\phi < 1/3$, (see Fig. 3.5), $T_{\rm re}$ increases with increasing $n_{\rm s}$, and as a consequence the reheating e-folding number $N_{\rm re}$ decreases with $n_{\rm s}$. This indicates the existence of a maximum scalar spectral index n_s^{max} corresponding to the maximum reheating temperature $T_{\rm re}^{\rm max} = 10^{15}$ GeV, and that is called instantaneous reheating. Similarly, the minimum reheating temperature $T_{\rm re} = T_{\rm BBN} \sim 10$ MeV [10, 50, 145], corresponds to a minimum allowed spectral index $n_{\rm s}^{\rm min}$ for a given the inflaton EoS w_ϕ. On the other hand, for $w_\phi > 1/3$, one finds the opposite feature: maximum $T_{\rm re}$ corresponds to the minimum spectral index $n_{\rm s}^{\rm min}$ and vice versa. When the reheating phase is dominated by purely gravitational interaction, the minimum possible reheating temperature fixes the maximum possible value of $n_{\rm s}$ for the EoS $w_\phi \geq 0.65$. For example, as shown in the Fig. 3.5, for $w_\phi = (0.82, 0.99)$, we obtain $T_{re}^{min} \simeq (10^3, 10^6)$ GeV, respectively. In Table 3.2, we have given the possible bounds on the inflationary parameters such as spectral index $n_{\rm s}$, and inflationary e-folding number N_k, assuming $\alpha = 1$, for various values of w_ϕ. These bounds remain unchanged for both cases-with and without thermal effects. Furthermore, we observe that the two reheating processes, $\phi \to s\,s$ and $\phi\phi \to s\,s$, yield the same bounds. This is because the dependence of the reheating temperature $T_{\rm re}$ on

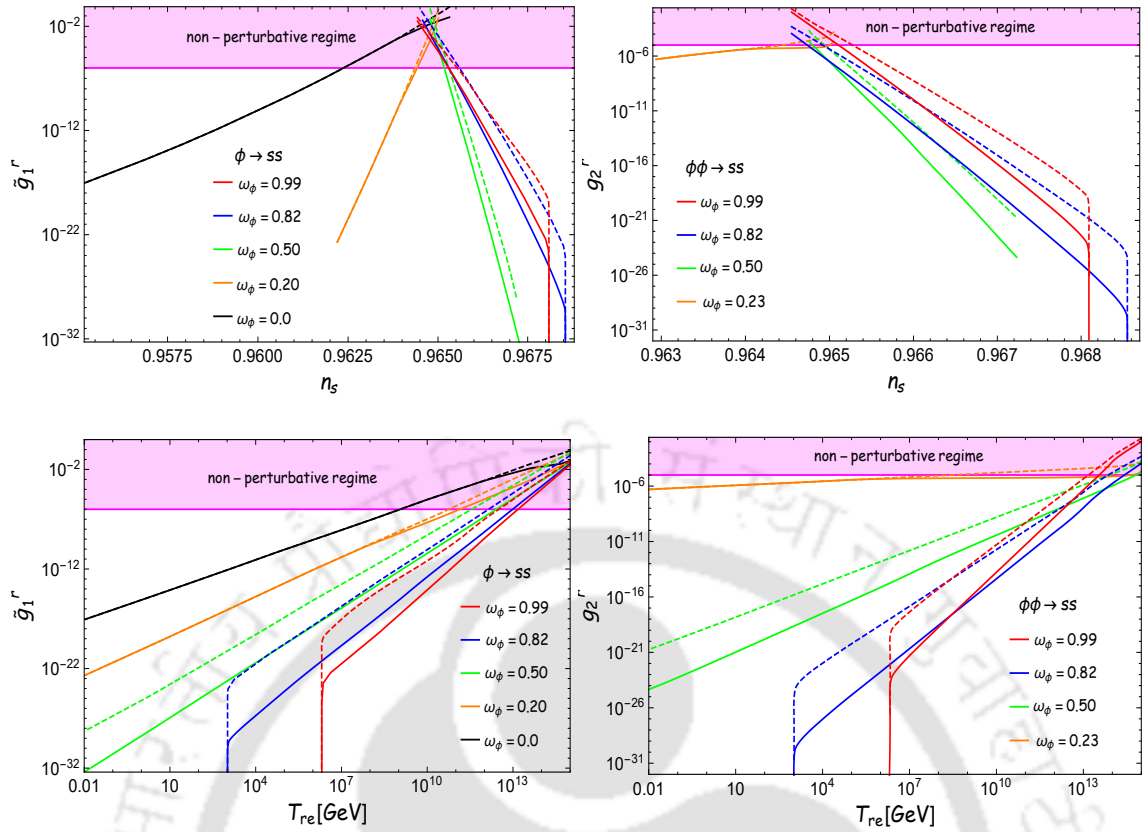

Figure 3.6: **Upper panel :** Variation of dimensionless coupling parameters with respect to the spectral index n_s for $w_\phi = 0.0$ (black), 0.20 (orange), 0.50 (green), 0.82 (red), 0.99 (blue). The dashed lines are for without the thermal feedback effect, and the solid lines are for with the thermal feedback effect. The purple-shaded region corresponds to the non-perturbative regime. **Lower panel :** Variation of dimensionless coupling parameters as a function of reheating temperature T_{re}. The description of this plot is the same as the upper panel.

n_s is largely insensitive to the specific reheating channel. In this chapter, we have restricted our analysis to the case $\alpha = 1$, while in the next chapter, we will extend the study to varying α values and derive the corresponding bounds on inflationary and reheating parameters.

(ii) Constraining inflaton couplings with bosonic radiation (g_1^r, g_2^r): One of the most important findings of our present analysis is illustrated in Fig. 3.2. The figure depicts different regions in the parameter space of (g_i^r, w_ϕ), where the effect of different inflaton decay channels on the reheating process can be understood. At this point, let us reiterate different regions again: i) the light-cyan region is where reheating is entirely controlled by the gravity-mediated decay channel (gravitational reheating), ii) the yellow region is controlled by mostly inflaton-scalar coupling, iii) the light-red region is where successful reheating cannot be achieved as reheating temperature $T_{re} < T_{BBN}$, and iv) pink region where initial parametric resonance will be important. Furthermore, in the right panel of Fig. 3.2, there is a light-gray region where reheating is not possible for the decay process $\phi\phi \to ss$. For this process, if the thermal effect is subdominant at the beginning ($m_\phi^{end} < T_{rad}^{max}$ limit), the ratio between inflaton and radiation energy density varies as $\frac{\rho_\phi}{\rho_s^r} \propto A^{\frac{3}{2}(1-5w_\phi)}$ (see, for instance, Eqs. 3.105 and 3.114), and hence if $w_\phi < 1/5$, the universe will always be inflaton dominated irrespective of the value of inflaton-scalar coupling g_2^r. In addition to that, if the thermal effect starts dominating from the beginning ($m_\phi^{end} > T_{rad}^{max}$ limit), the ratio varies as

$\frac{\rho_\phi}{\rho_s^r} \propto A^{(3-13w_\phi)}$ (see, for instance, Eqs. 3.105 and 3.114) which implies that if $w_\phi < 3/13 \sim 0.23$ achieving radiation domination is not possible. However, for extremely large coupling, parametric resonance may have some effect.

From Fig. 3.2, a generic feature can be observed, and that is related to the monotonic decrease of g_i^r with w_ϕ for a fixed reheating temperature $T_{\rm re}$. The reason behind this behavior can be understood as follows: with increasing w_ϕ, inflaton energy density dilutes faster, and hence to achieve the reheating condition $\rho_\phi = \rho_s^r$, one needs to lower the coupling. Furthermore, $m_\phi(t)$ decays faster with increasing w_ϕ, and for both types of bosonic decay channels ($\phi \to ss$ and $\phi\phi \to ss$), the production rate goes as $\propto 1/m_\phi(t)$, which will boost up the production. As a result, to keep reheating temperature fixed, one needs to lower the value of g_i^r again.

Due to the very nature of the bosonic particles, the finite temperature correction in the decay width enhances the particle production rate from the inflaton condensate. As discussed, this physical fact is imprinted in the reheating dynamics and is further reflected in the parameter plot shown in Fig. 3.6. Finite temperature correction naturally increases the effective decay width of the inflaton to scalar radiation, and consequently, one needs to lower the values of the dimensionless coupling parameters $\tilde{g}_1^r = g_1^r/m_\phi^{\rm end}$ and g_2^r as compared to their zero temperature case to have successful reheating. This can be observed in Fig. 3.6 both with respect to reheating temperature ($T_{\rm re}$) (lower panel) and CMB spectral index $n_{\rm s}$ (upper panel). Note that the variation of the coupling is sensitive to $n_{\rm s}$, as the relation between $T_{\rm re}$ and the coupling differs across reheating scenarios, as evident from the expressions of $T_{\rm re}$ Eqs. 3.19, 3.22, 3.28, and the bottom panel of Fig. 3.6. Since the coupling parameter encapsulates the microphysical details of the inflaton-radiation interaction, its dependence is expected to manifest in both $n_{\rm s}$ and $T_{\rm re}$.

The maximum limiting value of the coupling parameters will naturally be set by the maximum possible reheating temperature $T_{\rm re}^{\rm max} \simeq 10^{15}$ GeV, where all the lines converge (see Fig. 3.6). If the reheating dynamics are controlled directly by the inflaton-radiation coupling, the minimum possible value of the coupling will be set by the minimum reheating temperature. However, such a limit on the inflaton coupling is observed to be dependent on the finite temperature correction, which will be discussed in detail. When the radiation temperature $T_{\rm rad} \gg m_\phi(t)$, the thermal effect significantly influences the radiation dynamics and consequently affects the possible constraints on the coupling parameter as compared to the zero temperature case. Notably, the impact of finite-temperature corrections becomes more pronounced with increasing values of the inflaton EoS w_ϕ. For $w_\phi = 0$, the effective mass of the inflaton $m_\phi(\sim 10^{13}\,{\rm GeV})$ remains constant; as a result, the thermal effect manifests (see left panel of Fig. 3.6) itself only very near and above the reheating temperature $\sim 10^{13}$ GeV (or for $n_{\rm s} > 0.9645$). On the other hand, for $w_\phi > 0$, the rate of decrease of effective inflaton mass $m_\phi \propto \partial_\phi^2 V$ increases with increasing w_ϕ such that the condition $T_{\rm rad} > m_\phi(t)$ becomes easier to satisfy even at a lower temperature. For example, for $w_\phi = 0.20$, the above condition begins to satisfy (see left Fig. 3.6) when $n_{\rm s} > 0.9639 (T \sim 10^8)$ GeV, and accordingly, the finite temperature effect (solid line) manifest itself after $T_{\rm re} \sim 10^8$ GeV. For $w_\phi = 0.50, 0.82, 0.99$, the condition $T_{\rm rad} > m_\phi(t)$ can be observed to be satisfied throughout the whole range of reheating temperature.

To this end, we would like to elaborate on the finite temperature effect for low reheating temperatures. The author in the reference [194] claims that the thermal effect will be insignificant at low reheating temperatures. However, generically such an effect depends on the evolution of the ratio $m_\phi/T_{\rm rad}$. And we found that the finite temperature effect can be significant at low reheating temperature for the higher EoS $w_\phi = (0.20, 0.50, 0.82, 0.99)$ (see solid and dotted lines in Fig. 3.6), for which inflaton mass undergoes non-trivial evolution. As can be seen from the second row of Fig. 3.6, for the higher w_ϕ, the finite temperature

effect becomes more prominent at lower reheating temperature mainly because the inflaton mass can become significantly smaller during the course of reheating. Moreover, for higher EoS ($w = 0.82, 0.99$), the gravitational reheating has been observed to give a lower limit of the reheating temperature ($10^3, 10^6$ GeV), which is again found to be directly corresponding to the specific inflationary scalar spectral index n_s. The spectral indices associated with those temperatures are $n_s = 0.96855$ and 0.9681 for $w = 0.82$ and 0.99, respectively. When n_s reaches these values, the coupling parameter tends towards zero, i.e., gravitational scattering solely controls the reheating dynamics.

3.1.5 Fermionic Reheating: dynamics and constraints

A. Dynamics

During reheating, if the dominant decay channel of the inflaton is through massless fermions, we call it fermionic reheating. For this purpose, we consider the inflaton decaying only into massless fermions through the standard Yukawa decay channel $\phi \to \bar{f} f$ along with the gravitational scattering process $\phi\phi \to h_{\mu\nu} \to ss$. Instantaneous thermalization of those different components are assumed throughout. To study the evolution of the radiation energy density, we took the finite temperature effect arising due to Pauli blocking (see, for instance, Addenda-B for details calculation). Similar to bosonic reheating, for the fermionic case, we identified distinct regions in (h^r, w_ϕ) plane depending upon different physical processes involved in controlling the reheating dynamics (see Fig. 3.7). For this case, we have plotted separately with and without the finite temperature effect and observed the quantitative change in parameter space[4] due to the finite temperature effect where reheating would be successful. The parameter space (h^r, w_ϕ) is again divided into four regions marked in different colors: i) Light-cyan region is where reheating is entirely controlled by the gravity-mediated decay channel (gravitational reheating), ii) Yellow region is controlled by mostly inflaton-Fermion coupling, iii) Light-red region is where successful reheating cannot be achieved as reheating temperature $T_{re} < T_{BBN}$, and iv) Pink region signifies initial parametric resonance domination which we ignored in this thesis. As we discussed for bosonic reheating, based on whether gravitational or non-gravitational sectors dominate the dynamics, we have a fermionic critical coupling $\mathscr{H}_c$ which sets a boundary for two distinct scenarios:

1) Case-I: The entire reheating dynamics is dominated by the Yukawa coupling. For this case, the fermionic coupling parameter is in the range $h^r > \mathscr{H}_c$. The critical coupling $\mathscr{H}_c$ is identified by equating the maximum energy densities from non-gravitational and gravitational sector $\rho_f^{r,\max} = \rho_{gr}^{r,\max}$. One can find the expression for the critical coupling for fermionic reheating as

$$\mathscr{H}_c = \left[\frac{3(5-9w_\phi)H_{end}^2}{128 M_p^2 (1+15w_\phi)} \frac{\left[\left(\frac{9+15w_\phi}{8}\right)^{-\frac{8}{1+15w_\phi}} - \left(\frac{9+15w_\phi}{8}\right)^{-\frac{9+15w_\phi}{1+15w_\phi}} \right]}{\left[\left(\frac{8}{3(1+3w_\phi)}\right)^{-\frac{3(1+3w_\phi)}{5-9w_\phi}} - \left(\frac{8}{3(1+3w_\phi)}\right)^{-\frac{8}{5-9w_\phi}} \right]} \right]^{1/2} . \tag{3.31}$$

The maximum energy densities for both gravitational and non-gravitational sectors appear at the initial stage of reheating, and as the radiation bath associated with gravity mediated process dilutes faster than the non-gravitational one, for $h^r > \mathscr{H}_c$ reheating dynamics always have explicit fermionic coupling domination.

2) Case-II: For this case coupling parameter satisfies $h^r < \mathscr{H}_c$ and both sectors partially dominates the

[4] In Addenda-E, we have shown the regions (Fig. 3.20) where the self-resonance effect is important.

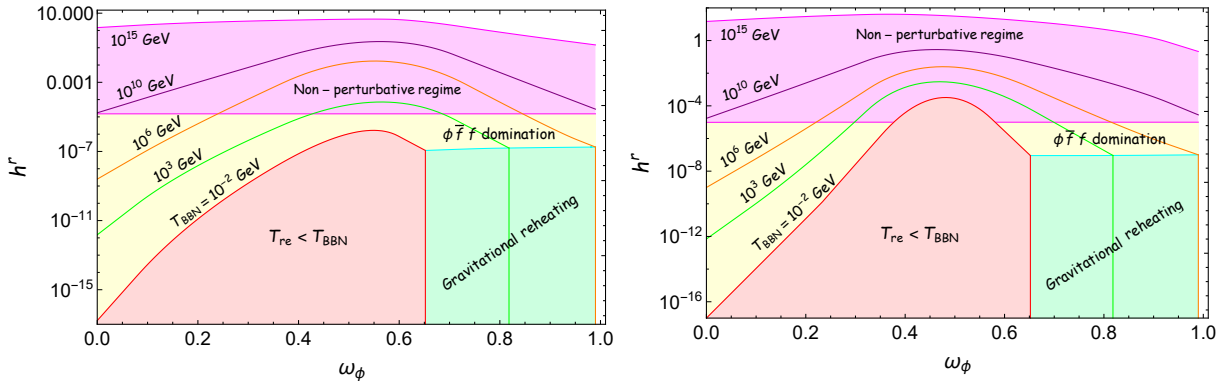

Figure 3.7: The description of this plot is the same as Fig. 3.2, the main difference is that we have shown the results in (h^r, w_ϕ) plane for the fermionic decay channel $\phi \to \bar{f} f$. On the left panel, we have plotted for without thermal effect, whereas on the right, the results are for with thermal effect. The pink-shaded region corresponds to the non-perturbative regime where bounds on the coupling $h^r \geq \left(V_{end}^{1/2}(m_\phi^{\rm end})^3/\sqrt{2}M_p\phi_{end}^4\right)^{1/4}$ are obtained from the resonance condition of the Mathieu equation for the fermion field [194, 196, 197].

reheating phase. However, when EoS w_ϕ lies above 0.65, gravity-mediated decay controls the reheating phase termed as gravitational reheating. In our succeeding discussion, we will discuss these two cases in detail:

Case-I: Coupling strength $h^r > \mathscr{H}_c$: In this coupling regime, non-gravitational decay of inflaton into fermionic radiation controls the entire reheating process. In order to give analytical estimation and compare our result with the zero temperature scenario, we consider two separate regimes of the maximum radiation temperature (see Fig. 3.8 for its depiction), and those are as follows:

When $T_{\rm rad}^{\rm max} > m_\phi^{\rm end}$: If the maximum radiation temperature is greater than m_ϕ^{end}, the coupling parameter associated with this region entirely lies in the pink region of Fig. 3.7 (non-perturbative resonance-dominated region). Due to strong inflaton-Fermion coupling, the gravitational channel is naturally subdominant throughout the reheating, and the thermal effect is non-negligible from early stage of reheating. However, its effectiveness through out the reheating process will depend on how $T_{\rm rad}/m_\phi$ evolves. Since $T_{\rm rad} > m_\phi$ at the initial stage, decay width can be approximated as,

$$\Gamma_{\phi\to\bar{f}f} = \frac{(h^r)^2}{8\pi}\frac{m_\phi^2(t)}{4T_{\rm rad}}. \tag{3.32}$$

With the aforementioned decay width, one can estimate the behavior of radiation energy density,

$$\rho_f^r(A) = \left[\frac{\zeta(w_\phi)(h^r)^2\epsilon^{1/4}M_P^2}{A^5}(m_\phi^{\rm end})^2 H_{\rm end}\left(A^{\frac{7-15w_\phi}{2}}-1\right)\right]^{4/5}, \quad \text{where } \zeta(w_\phi) = \frac{15(1+w_\phi)}{64\pi(7-15w_\phi)}. \tag{3.33}$$

The above equation suggests that the evolution of the radiation component is entirely different in two different regimes

- $w_\phi > 7/15$: Most of the production occurs at the initial reheating stage, and temperature decreases with the scale factor as A^{-1}. Since the ratio $T_{\rm rad}/m_\phi$ behaves as $A^{3w_\phi-1}$, $T_{\rm rad}$ always remains greater than m_ϕ, and hence the finite temperature effect will be significant till the end of reheating. The

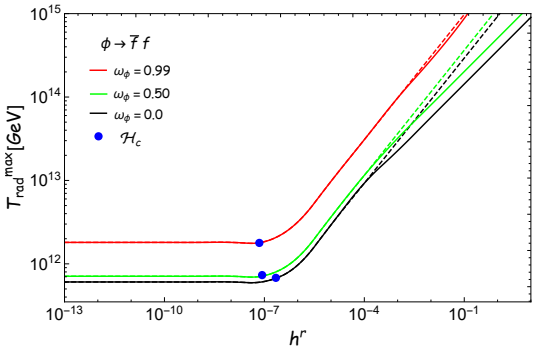

Figure 3.8: The description of this plot is the same as Fig. 3.3, the main difference is that here we have shown results for the fermionic reheating.

reheating temperature for this case assumes the following form,

$$T_{\rm re} = \left[\frac{\zeta(w_\phi)(h^r)^2 M_P^2}{\epsilon}(m_\phi^{\rm end})^2 H_{\rm end} A_{re}^{-5}\right]^{1/5}, A_{\rm re} = \left[\frac{\zeta(w_\phi) h^2 \epsilon^{1/4} M_p^2 (m_\phi^{\rm end})^2 H_{\rm end}}{(3M_p^2 H_{\rm end}^2)^{5/4}}\right]^{\frac{5(1-3w_\phi)}{4}}. \tag{3.34}$$

- $0 \le w_\phi < 7/15$: For this case, the ratio $T_{\rm rad}/m_\phi \propto A^{\frac{3}{10}(5w_\phi-1)}$ induces two different evolution history with regard to the finite temperature effect. It turns out that when EoS stays within $0 \le w_\phi < 1/5$, due to initial high radiation temperature thermal correction will have a significant effect. As the reheating progresses, such effect diminishes with the complete takeover by the zero temperature dynamics at a certain value of scale factor, which depends on the inflaton EoS as follows,

$$A_c = \left(\frac{\zeta(w_\phi)(h^r)^2 M_p^2 H_{\rm end}}{\epsilon (m_\phi^{\rm end})^3}\right)^{2/(3-15w_\phi)}. \tag{3.35}$$

After this intermediate scale factor, the dynamics is governed by the zero temperature decay channel following the Eq. 3.135 (see without thermal effect section of Addenda-B for details calculation) till the end of reheating and eventually equating $\rho_\phi = \rho_f^r$, we find the associated reheating temperature as,

$$T_{\rm re} = \left(\frac{6M_p^2(1+w_\phi) m_\phi^{\rm end} H_{\rm end}}{8\pi\epsilon(5-9w_\phi)}(h^r)^2\right)^{1/4} A_{\rm re}^{\frac{-3(1+3w_\phi}{8}}, A_{\rm re} = \left(\frac{8\pi(5-9w_\phi)H_{\rm end}}{2(1+w_\phi)m_\phi^{\rm end}}(h^r)^2\right)^{\frac{2}{3-3w_\phi}}. \tag{3.36}$$

On the other hand when w_ϕ is in between $1/5 < w_\phi < 7/15$, the thermal effect will be non-negligible throughout the entire reheating history, and we have the associated reheating temperature

$$T_{\rm re} = \left(\frac{\zeta(w_\phi)(h^r M_P)^2}{\epsilon}(m_\phi^{\rm end})^2 H_{\rm end}\right)^{1/5} A_{re}^{\frac{-3-15w_\phi}{10}}, A_{\rm re} = \left[\frac{\zeta(w_\phi)\epsilon^{\frac{1}{4}}(h^r M_p m_\phi^{\rm end})^2 H_{\rm end}}{(3M_p^2 H_{\rm end}^2)^{5/4}}\right]^{-\frac{4}{3(3+5w_\phi)}}. \tag{3.37}$$

When $T_{\rm gr}^{r,\max} < T_{\rm rad}^{\max} < m_\phi^{\rm end}$: For this case, the coupling parameter mostly lies in the pink region of Fig. 3.7. Similar to the previous case, whole reheating dynamics are governed by non-gravitational coupling. Since $T_{\rm rad} < m_\phi$ at the initial stage, the thermal effect is minimal. As reheating progresses, depending on the ratio $\frac{T_{\rm rad}}{m_\phi}$, the thermal effect may state dominating the dynamics. Thus initially, the radiation component evolves as

$$\rho_f^r(A) = \frac{6M_p^2(1+w_\phi)m_\phi^{\rm end}H_{\rm end}}{8\pi(5-9w_\phi)A^4}(h^r)^2(A^{\frac{5-9w_\phi}{2}}-1). \tag{3.38}$$

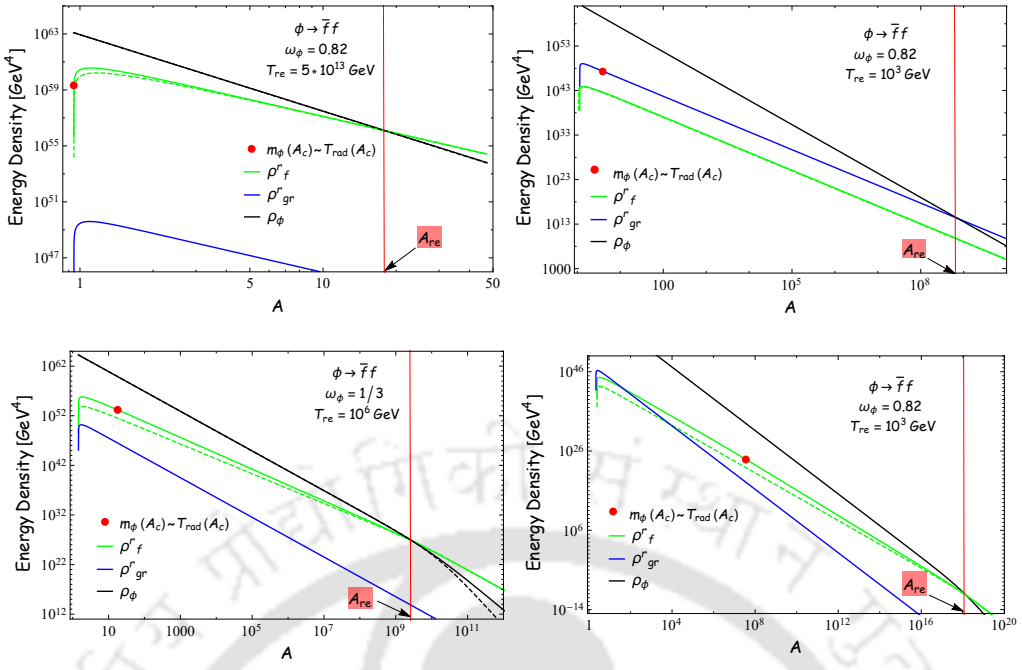

Figure 3.9: Evolution of inflaton and radiation energy density as a function of normalized scale factor A for $\phi \to \bar{f} f$ decay channel with and without thermal effect (solid line for with thermal effect and dashed line for without thermal effect). **Left panel:** Coupling is in the range of $h^r > \mathscr{H}_c$. **Right panel:** Coupling is in the range of $h^r < \mathscr{H}_c$. We have considered two distinct values of $w_\phi = (0.82, 1/3)$ for these two cases.

The aforementioned equation clearly suggests that the radiation component behaves differently for $w_\phi < 5/9$ and $w_\phi > 5/9$. Let us discuss these two cases,

- $w_\phi > 5/9$: Maximum production happens initially, and the bath temperature falls as A^{-1}. For this case, $T_{\rm rad}/m_\phi \propto A^{3w_\phi - 1}$ and hence finite temperature effect will be important near the final stage of reheating, and the reheating temperature can be expressed as,

$$T_{\rm re} = \left(\frac{6M_p^2(1+w_\phi)m_\phi^{\rm end}H_{\rm end}}{8\pi\epsilon(9w_\phi - 5)}(h^r)^2\right)^{1/4} A_{\rm re}^{-1} \quad ; \quad A_{\rm re} = \left(\frac{8\pi(9w_\phi - 5)H_{\rm end}}{2h^2(1+w_\phi)m_\phi^{\rm end}}\right)^{\frac{-1}{1-3w_\phi}} \tag{3.39}$$

- $0 \le w_\phi < 5/9$: For this case, $T_{\rm rad}/m_\phi \propto A^{-3/8(1-5w_\phi)}$ implies two different evolution histories depending on the value of equation state greater or less than 0.2. For $0 \le w_\phi < 0.2$, the thermal correction will be subdominant, and the reheating temperature can be simply read off from Eq. 3.36. Whereas for EoS $w_\phi > 0.2$, the thermal effect will start to dominate at some intermediate time within the reheating phase, which we call the crossover point,

$$A_c = \left(\frac{6M_p^2(1+w_\phi)m_\phi^{\rm end}H_{\rm end}}{8\pi\epsilon(5 - 9w_\phi)}(h^r)^2\right)^{\frac{-2}{3(1-5w_\phi)}}, \tag{3.40}$$

and reheating temperature is given by Eq. 3.37.

Table 3.3: The temperature evolution for fermionic reheating

Channel	$T_{\rm rad} \ll m_\phi(t)$ (Without thermal effect)		$T_{\rm rad} \gg m_\phi(t)$ (With thermal effect)	
	Non-gravitational	Gravitational	Non-gravitational	Gravitational
$\phi \to \bar{f} f$	$A^{-\frac{3(1+3w_\phi)}{8}}(A^{-1})\text{for}\, w_\phi < \frac{5}{9}(> \frac{5}{9})$	A^{-1}	$A^{-\frac{3(1+5w_\phi)}{10}}(A^{-1})\text{for}\, w_\phi < \frac{7}{15}(> \frac{7}{15})$	A^{-1}

Case-II: Coupling strength $h^r < \mathscr{H}_c$:

In this coupling regime, the maximum temperature is always controlled by the gravitational sector $T_{\rm rad}^{\rm max} = T_{\rm gr}^{\rm r,max}$. This condition generally satisfies within the entire allowed region shown in Fig. 3.7 except the parametric resonance dominated region shaded in pink. Evolution of the different energy densities in two different regimes $h^r > \mathscr{H}_c$ and $h^r < \mathscr{H}_c$ with two distinct values of inflaton EoS $w_\phi(1/3, 0.82)$ are shown in Fig. 3.9. Depending on the inflaton EoS, here also we have the following three different scenarios.

- $w_\phi > 0.65$: For this case, the gravitational sector governs the entire reheating phase, and we termed this as gravitational reheating. The parameter space where this condition is met is shaded in light cyan in both the Figs. 3.7. The reheating temperature can be followed from Eq. 3.28, which depends only on the reheating EoS.

- $5/9 < w_\phi < 0.65$: This case turned out to be within the light red shaded region in the (h, w_ϕ) plane of Fig. 3.7. As the figure suggests, reheating temperature evolved into below BBN temperature, which does not support the standard cosmological constraints.

- $0 \le w_\phi < 5/9$: In this case, the competition between two sectors of production, along with the finite temperature effect, leads to two different physically distinguishable reheating dynamics. In the (w_ϕ, h) plane, the condition under consideration lies in the light yellow region of Fig. 3.7. Here we have two different possibilities depending on how the thermal effect plays its role during the reheating history. As discussed for the bosonic reheating case
  1) The thermal effect starts to influence the reheating dynamics in its early stage ($T_{\rm rad} > m_\phi$) during the gravitational decay of inflaton. For this case, the behavior of the radiation component during non-gravitational sector domination is simply followed by Eq. 3.33, and we have reheating temperature as in Eq. 3.37.
  2) The thermal effect starts dominance during the later stage of reheating when it is governed by non-gravitational inflaton decay. The scale factor associated with the point where the thermal effect starts to influence the dynamics can be the same as the Eq. 3.40, and reheating temperature is given by Eq. 3.37.

B. Constraining reheating temperature and fermionic coupling parameter with CMB

Similar to the bosonic reheating case, to illustrate our results in terms of inflationary parameter $n_{\rm s}$ and to see how the coupling strength behaves as a function of reheating reheating temperature $T_{\rm re}$, we have taken five different sample values of $w_\phi = (0, 0.2, 0.5, 0.82, 0.99)$ and compare the results for with and without thermal effect.

i) Reheating temperature ($T_{\rm re}$) in terms inflationary (CMB) parameter ($n_{\rm s}$): As we earlier discussed, the dependence of the reheating temperature $T_{\rm re}$ on $n_{\rm s}$ is largely insensitive to the specific reheating channel. Therefore, the qualitative relation between the reheating temperature and the inflationary parameters for fermionic reheating remains similar to that of the bosonic reheating case as discussed

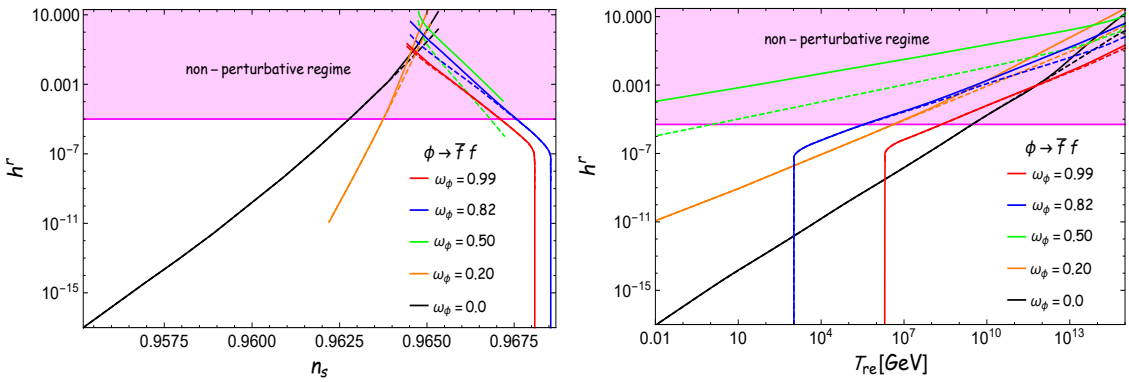

Figure 3.10: The description of the plot is the same as Fig. (3.6), the only difference is that here we have plotted for fermionic reheating.

earlier. As a result, bounds on the inflationary parameters remain the same as bosonic reheating (see, for instance, Table-3.2). This can be easily read off from the left plot of Fig. 3.5. In addition, Fig. 3.5, further indicates that the thermal feedback on the decay process does not affect the reheating temperature variation with n_s.

(ii) Constraining inflaton couplings with fermionic radiation (h^r): For the fermionic reheating, the parameter space in Fig. 3.7 illustrates different regions in (w_ϕ, h^r) plane, where the effect of different inflaton decay channels on the reheating process can be read off. We have given two plots with and without finite temperature effects for clear depiction.

An interesting distinction can be observed as compared to the scalar reheating case is that for fermionic reheating inflaton-fermion coupling h^r does not vary monotonically with respect to w_ϕ given a fixed reheating temperature. There exists a critical value of $w_\phi \simeq 7/15(5/9)$ for with (without) thermal effect, below which one requires a higher h^r value for a higher equation state for a fixed reheating temperature. And this can be understood from the behavior of fermion production rate $\propto \Gamma_{\phi\to\bar{f}f}\rho_\phi \propto (h^r)^2 m_\phi(t)\rho_\phi$. With increasing w_ϕ, the effective mass of the inflaton decreases faster with time; hence, to achieve a fixed reheating temperature, h^r needs to be enhanced. However, this simple physical argument is no longer tenable after $w_\phi \geq 7/15$ (5/9) for with (without) thermal effect. For such cases, most of the production happens initially, and the radiation energy density simply dilutes as A^{-4}, which is slower than that of the inflaton energy density. In such a situation with increasing w_ϕ and fixed reheating temperature, we need a lower value of h^r to satisfy the reheating condition $\rho_\phi = \rho_f^r$.

Due to its intrinsic nature, the finite temperature fermion bath diminishes its own production rate from the inflaton condensate. Consequently, for successful reheating, one needs higher values of the dimensionless coupling parameters h^r as compared to the zero temperature case. This can be clearly observed from Fig. 3.10, and such behavior is opposite to that of the bosonic reheating case. The qualitative behavior of the fermionic coupling in terms of the spectral index and reheating temperature is the same as that of the bosonic reheating case. For example, for $w_\phi = 0$ the coupling parameter h^r with thermal effect begins to affect only at very high temperatures at around $\sim 10^{13}$ GeV, and in terms of the spectral index, the deviation is visible for $n_s > 0.9645$. On the other hand, since the effective mass of the inflaton varies as A^{-3w_ϕ} (see, for instance, Eq. 3.111), for $w_\phi > 0$, $m_\phi(t)$ decrease faster with increasing w_ϕ and the $T_{\rm rad} > m_\phi(t)$ condition becomes easier to fulfill even at a lower radiation temperature. As a result,

for $w_\phi = 0.2$, the thermal effect starts dominating even at smaller radiation temperature $T_{\rm rad} \geq 10^8$ GeV when $n_{\rm s} > 0.9639$. The situation changes significantly for $w_\phi > 5/9$. In this regime, the maximum radiation production occurs at the onset of reheating. Consequently, thermal effects become relevant only if the condition $T_{\rm rad}^{\rm max} > m_\phi^{\rm end}$ is satisfied at the beginning of reheating. For low reheating temperatures, this condition is not met, and thermal corrections play no role-hence, the variation of the coupling closely follows that of the scenario without thermal effects. However, at higher reheating temperatures where $T_{\rm rad}^{\rm max} > m_\phi^{\rm end}$ becomes possible, thermal effects begin to influence the dynamics. This behavior is evident in Fig. 3.10, where for $w_\phi = (0.82, , 0.99)$, a clear deviation between the results with and without thermal effects emerges precisely when $T_{\rm rad}^{\rm max} \sim m_\phi^{\rm end}$.

3.2 Unifying dark sector: FIMPs and WIMPs during reheating and Observational constraints

In the previous section, we discussed in detail the dynamics of reheating, where the inflaton decays only into radiation. In the present discussion, we add additional DM components and discuss the impact of reheating on DM phenomenology. Discussion on DM will be considered in three parts. In the first part, we discuss the production of DM exclusively from the inflaton through non-gravitational and gravitational interactions. We mainly point out the constraints on the inflaton-DM coupling and DM mass from both theory and observation. Since it is produced solely from the inflaton decay, we call it FIMP-like DM. In the second part, we discuss the production from the thermal bath assuming an effective radiation to DM annihilation cross-section $\langle\sigma v\rangle$, added with the universal gravitational production discussed in the first section. For this case, we will have both the freeze-in and freeze-out production scenarios depending upon the strength of $\langle\sigma v\rangle$. The DM produced due to thermal freeze-out from the radiation bath will be generally called WIMPs. On the other hand, DM produced by the scattering process from the radiation bath via the Freeze-in mechanism will be called FIMPs. In the third part, we discuss the experimental constraints on various reheating and DM scenarios.

This section is organized as follows: we begin by discussing the constraints on light DM from the extra relativistic degrees of freedom, $\Delta N_{\rm eff}$, during BBN. In Subsection 3.2.2, we explore the freeze-in production of DM from inflaton decay and the associated constraints. In Subsection 3.2.3, we examine both freeze-in and freeze-out production of DM from the radiation bath. Subsections 3.2.4 and 3.2.5 are dedicated to analyzing theoretical and experimental bounds that further constrain the parameter space. Finally, we summarize the main findings of this chapter in Section 3.3.

3.2.1 Constraining light DM through $\Delta N_{\rm eff}$ during BBN :

In this short section, we would like to point out the BBN bound on the additional light degrees of freedom. We use this bound to constrain the DM parameter space of both FIMP and WIMP scenarios that were relativistic at the time of BBN. If the DM is relativistic at the time of BBN, it would inevitably modify the background expansion and may jeopardize the formation of the light elements, which is tightly constrained by the BBN observation. The total effective number of relativistic degrees of freedom is defined as $N_{\rm eff} = N_{\rm eff}^{\rm SM} + \Delta N_{\rm eff}$. At the time of BBN, if the active neutrinos are the only relativistic without any new particle, $N_{\rm eff} = N_{\rm eff}^{\rm SM} = 3.046$ ($\Delta N_{\rm eff} = 0$). BBN observation gives the bound of $\Delta N_{\rm eff} \leq 0.5$ at 95% [198–201] confidence level. A general expression of $\Delta N_{\rm eff}$ can be written as [202]

$$\Delta N_{\rm eff} = \left(\frac{\text{extra radiation energy density}(\rho_{DM})}{\text{energy density of single SM neutrino species}(\rho_\nu)}\right)_{T=T_{\rm BBN}} = \left(\frac{43}{7}\right)\left(\frac{\rho_{DM}}{\rho_{\rm rad}}\right)_{T=T_{\rm BBN}} \tag{3.41}$$

We will be discussing two production mechanisms. For FIMP like DM, we intend to separately discuss its production from the direct inflaton decay and radiation bath. For inflaton decaying into DM, production freezes during reheating or at the end of reheating, depending on the decay channels and DM mass. On the other hand, for DM from the thermal bath, its production rate crucially depends on the radiation production rate. Therefore, in this case, also freeze-in occurs mostly during or at the end of reheating, depending on DM mass. Overall, for the freeze-in mechanism, we, therefore, can always express

$$\Delta N_{\rm eff} = \left(\frac{43}{7}\right)\left(\frac{\rho_{DM}}{\rho_{\rm rad}}\right)_{T=T_{\rm BBN}} = \left(\frac{43}{7}\right)\left(\frac{\rho_{DM}}{\rho_{\rm rad}}\right)_{T=T_{\rm re}}. \tag{3.42}$$

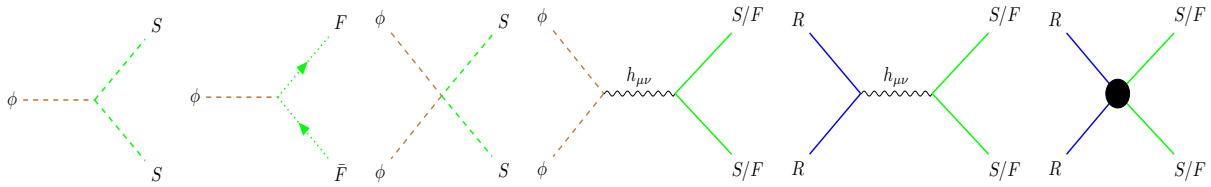

Figure 3.11: Fynmann diagram for DM production. The solid black circle corresponds to effective vertex representing $2 \to 2$ scattering process between the bath particle (R) and DM (S,F).

If the DM is relativistic after Freeze-in, both radiation ($\rho_{\rm rad}$) and relativistic DM energy density (ρ_{DM}) fall as a^{-4}. The ratio $\rho_{DM}/\rho_{\rm rad}$, therefore, stays constant between reheating and BBN. Hence, the above equality Eq. 3.42, holds true generically for any FIMP scenario.
For WIMP, on the other hand, the situation becomes very different but simpler. For such cases, till it freezes out, DM remains in equilibrium with the thermal bath. Therefore, any relativistic DM being in the thermal bath at the time of BBN always behaves like an additional degree of freedom. Therefore, $\Delta N_{\rm eff}$ naturally transforms into [202, 203]

$$\Delta N_{\rm eff} = \frac{4}{7} j_{\rm x} = \begin{cases} 0.571 & \text{scalar DM} \\ 1.14 & \text{fermionic DM} \end{cases} \tag{3.43}$$

Where $j_{\rm x}$ is the DM's intrinsic number of degrees of freedom, WIMPs mass lighter than $T_{\rm BBN} \sim 10$ MeV always behaves like dark radiation at the time of BBN. Hence, Therefore, all the WIMPs of mass $m_{\rm x} \leq 10$ MeV violate the BBN bound of $\Delta N_{\rm eff}$ (see Eq. (3.43)).

3.2.2 Freeze-in production of DM from inflaton decay and constraints

Similar to massless radiation production, we will now discuss DM production during reheating, considering various decay channels for both scalar and fermion DM. As discussed in the introduction, we considered two categories of production channels: (i) DM production from inflaton through gravitational scattering and (ii) production through explicit coupling-dependent decay channel.
The governing equation for the DM number density ($n_{\rm x}$) produced from direct inflaton decay takes the following form

$$\dot{n}_{\rm x} + 3Hn_{\rm x} = \frac{\Gamma^{\phi}_{\rm x}\rho_{\phi}}{\langle E_{\rm x}\rangle^{\phi}} \tag{3.44}$$

where $\Gamma^{\phi}_{\rm x}$ is the inflaton decay width to DM and $\langle E_{\rm x}\rangle^{\phi}$ the average energy of the DM particles.

A. Freeze-in production via gravitational interaction

Gravitational freeze-in production of DM is universal in nature and hence will always be present in any inflationary scenario. In this work, we have considered scalar (S) and Fermion (F) DM (see Fig. 3.11 for relevant Feynman diagrams for gravitational scatting from inflaton). The decay rates associated with the gravitational production are [167, 168]

$$\Gamma^{\phi}_{\rm x} = \begin{cases} \frac{\rho_{\phi} m_{\phi}}{1024\pi M_p^4}\left(1+\frac{m_{\rm x}^2}{2m_{\phi}^2}\right)^2\sqrt{1-\frac{m_{\rm x}^2}{m_{\phi}^2}} & \text{for} \quad h_{\mu\nu}(T^{\mu\nu}_S + T^{\mu\nu}_{\phi}) \\ \frac{\rho_{\phi} m_f^2}{4096\pi M_p^4 m_{\phi}}\left(1-\frac{m_{\rm x}^2}{m_{\phi}^2}\right)^{3/2} & \text{for} \quad h_{\mu\nu}(T^{\mu\nu}_F + T^{\mu\nu}_{\phi}). \end{cases} \tag{3.45}$$

Since, DM are feebly coupled with the radiation bath, the thermal correction to the decay width will be unimportant. Using the above equations in Eq. 3.44, we have obtained the following solutions for the number density,

$$n_{\rm x}^{\rm g}(A)=\begin{cases}\frac{3H_{\rm end}^3}{512\pi(1+3w_\phi)A^3}\left(1-A^{-\frac{3(1+3w_\phi)}{2}}\right) & \text{for}\quad h_{\mu\nu}(T_S^{\mu\nu}+T_\phi^{\mu\nu})\\ \frac{3H_{\rm end}^3}{2048\pi(1-w_\phi)A^3}\left(\frac{m_{\rm x}}{m_\phi^{\rm end}}\right)^2\left(1-A^{-\frac{3(1-w_\phi)}{2}}\right) & \text{for}\quad h_{\mu\nu}(T_F^{\mu\nu}+T_\phi^{\mu\nu}).\end{cases} \tag{3.46}$$

Therefore, the gravitational contribution to the DM abundance can be calculated using the expression [5]

$$\Omega_{\rm x}h^2=\frac{m_{\rm x}n_x(A_{re})}{\epsilon T_{\rm re}^3T_{\rm now}}\Omega_rh^2 \tag{3.47}$$

Substituting the expressions $n_{\rm x}(A_{\rm re})$ from Eq. 3.46, we obtain

$$\Omega_{\rm x}^{\rm g}h^2=\begin{cases}\Omega_rh^2\frac{3m_{\rm x}H_{\rm end}^3}{512\pi\epsilon(1+3w_\phi)T_{\rm now}}\left(\frac{\epsilon}{3M_p^2H_{\rm end}^2}\right)^{1/1+w_\phi}T_{\rm re}^{\frac{1-3w_\phi}{1+w_\phi}} & \text{for}\quad h_{\mu\nu}(T_S^{\mu\nu}+T_\phi^{\mu\nu})\\ \Omega_rh^2\frac{3m_x^3H_{\rm end}^3}{2048\pi\epsilon(1-w_\phi)\mathscr{M}_\phi^2T_{\rm now}}\left(\frac{\epsilon}{3M_p^2H_{\rm end}^2}\right)^{\frac{1+2w_\phi}{1+w_\phi}}T_{\rm re}^{\frac{1-3w_\phi}{1+w_\phi}} & \text{for}\quad h_{\mu\nu}(T_F^{\mu\nu}+T_\phi^{\mu\nu}).\end{cases} \tag{3.48}$$

Where the suffix "g" stands for production due to the gravitational scattering process. $\Omega_rh^2\simeq4.3\times10^{-5}$ is the present value of the radiation abundance. It is clear from the expression above that gravitational DM abundance depends on $H_{\rm end}, w_\phi, T_{\rm re}$, and DM mass $m_{\rm x}$. Given an inflation model, inflationary parameters $H_{\rm end}$ are fixed by CMB observation once we fix w_ϕ and $T_{\rm re}$. Therefore, $w_\phi, T_{\rm re}$ and DM mass $m_{\rm x}$ are the only free parameters. Therefore, the present DM abundance can completely fix the DM mass once a particular inflaton EoS w_ϕ and $T_{\rm re}$ is assumed. We will later observe that the aforesaid mass will set a maximum possible limit on the DM mass, which we symbolized as $m_{\rm x}^{\rm g,max}$, for a large range of coupling and the inflaton EoS. To this end, let us reiterate that due to its universal nature, the gravitational contribution to DM must be added to all the additional production processes we take up in the following sections.

B. Freeze-in production via direct inflaton decay

We introduce different inflaton couplings to DM. We consider three types of possible interaction: $g_1^{\rm x}\phi S^2$, $g_2^{\rm x}\phi^2S^2$, $h^{\rm x}\phi\bar{F}F$ (see Fig. 3.11 for relevant Feynman diagrams), and corresponding decay widths are,

$$\Gamma_{\rm x}^{\phi,c}=\begin{cases}\frac{(g_1^{\rm x})^2}{8\pi m_\phi(t)}\sqrt{1-\frac{4m_{\rm x}^2}{m_\phi^2}} & \text{for}\quad g_1^{\rm x}\phi S^2\\ \frac{(g_2^{\rm x})^2}{8\pi}\frac{\rho_\phi(t)}{m_\phi^3(t)}\left(1-\frac{m_{\rm x}^2}{m_\phi^2}\right)^{1/2} & \text{for}\quad g_2^{\rm x}\phi^2S^2\\ \frac{(h^{\rm x})^2}{8\pi}m_\phi(t)\left(1-\frac{4m_{\rm x}^2}{m_\phi^2}\right)^{3/2} & \text{for}\quad h^{\rm x}\phi\bar{F}F\end{cases} \tag{3.49}$$

Using the above equation in Eq. (3.44), we have obtained the following solution of number density,

$$n_{\rm x}(A)=\frac{M_p^2H_{\rm end}}{2\pi}\begin{cases}\frac{(g_1^{\rm x})^2}{(1+3w_\phi)(m_\phi^{\rm end})^2A^3}\left(A^{\frac{3}{2}(1+3w_\phi)}-1\right) & \text{for}\quad g_1^{\rm x}\phi S^2\\ \frac{3(g_2^{\rm x}H_{\rm end}M_p)^2}{2(5w_\phi-1)(m_\phi^{\rm end})^4A^3}\left(A^{-\frac{3}{2}(1-5w_\phi)}-1\right) & \text{for}\quad g_2^{\rm x}\phi^2S^2\\ \frac{(h^{\rm x})^2}{(1-w_\phi)A^3}\left(A^{\frac{3}{2}(1-w_\phi)}-1\right) & \text{for}\quad h^{\rm x}\phi\bar{F}F\end{cases} \tag{3.50}$$

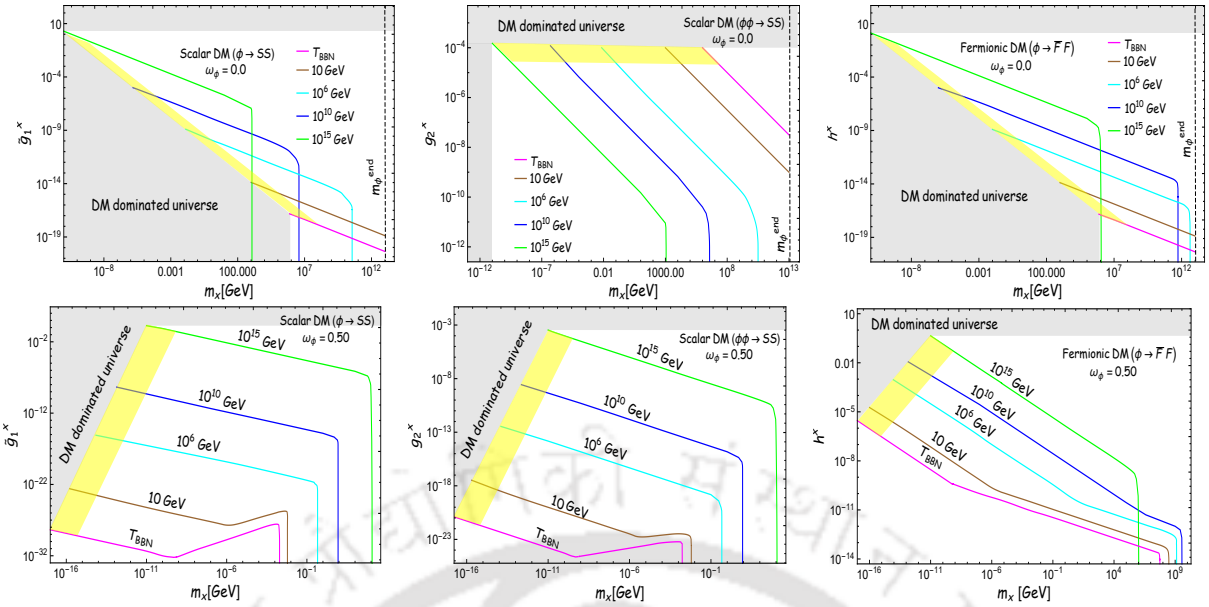

Figure 3.12: Variation of the inflaton-DM coupling against the DM mass for $w_\phi = 0.0, 0.50$ for DM production processes $\phi \to SS$ (left), $\phi\phi \to SS$ (middle) and $\phi \to \bar{F}F$ (left). The different colour lines correspond to different reheating temperatures. The yellow-shaded region is ruled out by BBN bound of $\Delta N_{\rm eff}$. The gray-shaded region corresponds to the no reheating region where the radiation domination era is impossible after inflaton domination. The vertical dashed lines (upper plot) correspond to the kinematically maximum allowed DM mass $m_\phi^{\rm end}$.

Unlike the previous gravitational production case, we now have additional coupling parameters $g_i^x, h^{\rm x}$ in the problem. Therefore, the present DM abundance will provide the constraint equation between $(m_{\rm x}, g_i^x/h^{\rm x})$ once we fix a particular reheating history by fixing $(w_\phi, T_{\rm re})$ and g_i^r/h^r.

Depending on the DM mass, we will have two different expressions for the DM abundance. If $m_{\rm x} > m_\phi(A_{\rm re})$, the DM freezes in before the end of reheating at some intermediate scale factor $A = A_{\rm re}(m_{\rm x}/m_\phi(A_{\rm re}))^{-1/3w_\phi}$ for $w_\phi \neq 0$, and, if $m_{\rm x} < m_\phi(a_{\rm re})$, the DM freezes in after the end of reheating. The contribution to the DM abundance for different direct decay channels are calculated for ($m_{\rm x} < m_\phi(A_{\rm re})$),

$$\Omega_{\rm x}^{\rm dcay} h^2 = \Omega_r h^2 \frac{M_p}{2\sqrt{3\epsilon}\pi T_{\rm now}} \frac{m_{\rm x}}{T_{\rm re}} \begin{cases} \frac{(g_1^{\rm x})^2}{(1+3w_\phi)\mathscr{M}_\phi^2} T_{re}^{\frac{-8w_\phi}{1+w_\phi}} & \text{for} \quad g_1^{\rm x}\phi S^2 \\ \frac{\epsilon(g_2^{\rm x})^2}{2(5w_\phi-1)\mathscr{M}_\phi^4} T_{re}^{\frac{4(1-3w_\phi)}{1+w_\phi}} & \text{for} \quad g_2^{\rm x}\phi^2 S^2 \ \text{ with } \ w_\phi > 0.2 \\ \frac{\epsilon(g_2^{\rm x})^2 T_{re}^{\frac{2(1-w_\phi)}{1+w_\phi}}}{2(1-5w_\phi)\mathscr{M}_\phi^4} \left(\frac{\epsilon}{3M_p^2 H_{\rm end}^2}\right)^{\frac{5w_\phi-1}{1+w_\phi}} & \text{for} \quad g_2^{\rm x}\phi^2 S^2 \ \text{ with } \ w_\phi < 0.2 \\ \frac{(h^{\rm x})^2}{1-w_\phi} & \text{for} \quad h^{\rm x}\phi\bar{F}F. \end{cases} \tag{3.51}$$

We introduce a new symbol, $\mathscr{M}_\phi = \sqrt{2n(2n-1)}\xi\Lambda^{2/n}\epsilon^{w/1+w}$ and $m_\phi(a_{\rm re}) = \mathscr{M}_\phi T_{\rm re}^{4w_\phi/(1+w_\phi)}$ is the inflaton mass defined at the end of reheating $a_{\rm re}$. Note that for $\phi\phi \to SS$ (with $w_\phi < 0.2$) DM production channel,

[5] In the final DM abundance, we also include the gravitational production of DM from the thermal bath. But for scalar DMs, which are produced from the thermal bath scattering, it has no contribution to the final DM abundance as it is always subdominant compared to the production from inflaton scattering through gravitational interaction. However, for the fermionic DM, gravitational production from the radiation bath can be dominant when reheating temperature $T_{\rm re} \geq 10^{13}$ GeV (for the details calculation, see Ref.[174])

most of the DM production happens at the initial phase of the reheating, similar to the gravitational production. On the other hand if $m_{\rm x} > m_\phi(A_{\rm re})$, we have

$$\Omega_{\rm x}^{\rm dcay}h^2 = \Omega_r h^2 \frac{M_p}{2\sqrt{3\epsilon}\,\pi T_{\rm now}}\frac{m_{\rm x}}{T_{\rm re}} \begin{cases} \frac{(g_1^{\rm x})^2}{(1+3w_\phi)\mathscr{M}_\phi^2}\left(\frac{m_{\rm x}}{\mathscr{M}_\phi}\right)^{-\frac{1+3w_\phi}{2w_\phi}} T_{re}^{\frac{2(1-w_\phi)}{1+w_\phi}} & \text{for} \quad g_1^{\rm x}\phi S^2 \\ \frac{\epsilon(g_2^{\rm x})}{2(5w_\phi-1)\mathscr{M}_\phi^4}\left(\frac{m_{\rm x}}{\mathscr{M}_\phi}\right)^{\frac{1-5w_\phi}{2w_\phi}} T_{\rm re}^{\frac{2(1-w_\phi)}{1+w_\phi}} & \text{for} \quad g_2^{\rm x}\phi^2 S^2 \text{ with } w_\phi > 0.2 \\ \frac{(h^{\rm x})^2}{1-w_\phi}\left(\frac{m_{\rm x}}{\mathscr{M}_\phi}\right)^{\frac{w_\phi-1}{2w_\phi}} T_{\rm re}^{\frac{2(1-w_\phi)}{1+w_\phi}} & \text{for} \quad h^{\rm x}\phi\bar{F}F \end{cases} \tag{3.52}$$

Since DM is produced directly from the inflaton, its origin is inherently non-thermal, and therefore its evolution and final relic abundance are insensitive to the details of the thermal history. As discussed earlier, different reheating scenarios lead to distinct thermal evolutions of the Universe. However, the resulting DM abundance only depends on the value of reheating temperature $T_{\rm re}$. This is because the DM abundance is diluted due to entropy production during reheating, and the amount of entropy production depends solely on the value of $T_{\rm re}$, not on the specific thermal evolution. Consequently, the expressions for the DM abundance, as presented in Eqs. 3.48, 3.51, 3.52, remain valid in any type of reheating scenario. This implies that the DM parameter space (Fig. 3.12) remains the same for both bosonic reheating and fermionic reheating, regardless of whether thermal effects are included.

Once the gravitationally produced DM is taken into account, the total DM abundance can be written as,

$$\Omega_{\rm x}^{\rm tot}h^2 = \Omega_{\rm x}^{\rm g}h^2 + \Omega_{\rm x}^{\rm dcay}h^2 = 0.12. \tag{3.53}$$

In order to constrain the coupling parameters, we require that the total DM abundance satisfies $\Omega_{\rm x}^{\rm tot}h^2 \simeq 0.12$.

C. Constraining the inflaton-DM couplings $(g_{\rm i}^{\rm x}, h^{\rm x})$ and DM mass $(m_{\rm x})$

Fig.(3.12) depicts the detailed allowed parameter space [6] for which the present DM abundance is satisfied. Let us emphasize again that while plotting the DM abundance, we take into account the contribution from both the direct and the universal gravity-mediated decay of inflaton. For the sake of presentation, we have considered two sample values of the inflation EoS $w_\phi = (0.0, 0.50)$ with reheating temperatures range between maximum to minimum values $T_{\rm re} = (T_{\rm BBN}, 10, 10^6, 10^{10}, 10^{15})$ GeV.

In each plot for a fixed $(T_{\rm re}, w_\phi)$ we see the maximum limit on DM mass $(m_{\rm x}^{\rm g,max})$ [174, 175] which is due to gravitational interaction as mentioned before. However, since DMs are produced from the inflaton decay, purely kinematic constraints can also set the upper limit to be $m_\phi^{\rm end}$ for some specific cases when $m_{\rm x}^{\rm g,max} > m_\phi^{\rm end}$ which is observed for $w_\phi = 0$ (see Fig. 3.12). It is natural to expect that for $m_{\rm x} < m_{\rm x}^{\rm g,max}$, the DM from the decay channel solely controls the abundance. Upon $m_{\rm x}$ approaching $m_{\rm x}^{\rm g,max}$ value, the gravitational contribution starts dominating the abundance till $m_{\rm x} = m_{\rm x}^{\rm g,max}$.

However, the lower bound on the DM mass will be fixed either from observation or theory. For example, the lower bound has been observed to be controlled by reheating temperature and the physical processes of DM production under consideration. In general, for this scenario lower the DM mass, the larger would be the inflaton-DM coupling to achieve the correct DM abundance. However, the inflaton-DM coupling should

[6] Note that the discussion of DM phenomenology is general and does not depend on the specific details of the inflationary model. It is not restricted to the E-model class, as the expression for the minimum of the potential is formulated in a generic manner.

be bounded from above so that the universe should be radiation dominated from the end of reheating ($T_{\rm re}$) to the matter-radiation equality ($T_{eq} \simeq 10^{-9}$ GeV). Hence, there exists an upper limit of the DM coupling, above which we always get the DM-dominated universe after the inflaton domination, or in other words, one never achieves the radiation-dominated universe. Since there is a one-to-one correspondence between the DM coupling and the DM mass, a lower limit of the DM mass corresponds to the upper limit of the DM coupling, and that can be obtained by equating the DM energy density and the radiation energy density at the time of matter-radiation equality. The upper limit of couplings are calculated as

$$\begin{aligned}
g^{\rm x}_{1,c} &= \left(\frac{9\pi\sqrt{\epsilon}(1+3w_\phi)\mathscr{M}_\phi}{\sqrt{3}M_p}\right)^{1/2} T_{\rm re}^{\frac{1+3w_\phi}{1+w_\phi}} \quad \text{for} \quad g^{\rm x}_1\phi S^2 \\
g^{\rm x}_{2,c} &= \left(\frac{9\pi(5w_\phi-1)\mathscr{M}^3_\phi}{\sqrt{3}\epsilon M_p}\right)^{1/2} T_{\rm re}^{\frac{5w_\phi-1}{1+w_\phi}} \quad \text{for} \quad g^{\rm x}_2\phi^2 S^2 \quad \text{with} \quad w_\phi > 0.2 \\
g^{\rm x}_{2,c} &= \left(\frac{12\pi(1-5w_\phi)\mathscr{M}^3_\phi}{\sqrt{3\epsilon}M_p}\right)^{1/2} \left(\frac{\epsilon}{3M_p^2H^2_{\rm end}}\right)^{\frac{1-15w_\phi}{12(1+w_\phi)}} T_{\rm re}^{\frac{2(3w_\phi-1)}{3(1+w_\phi)}} \quad \text{for} \quad g^{\rm x}_2\phi^2 S^2 \quad \text{with} \quad w_\phi < 0.2 \\
h^{\rm x}_c &= \left(\frac{9\pi\sqrt{\epsilon}(1-w_\phi)}{\sqrt{3}M_p\mathscr{M}_\phi}\right)^{1/2} T_{\rm re}^{\frac{1-w_\phi}{1+w_\phi}} \quad \text{for} \quad h^{\rm x}\phi\bar{F}F.
\end{aligned} \tag{3.54}$$

which does not depend on the details of the thermal history but on the nature of DM, reheating temperature, and EoS. The corresponding lower limit on the DM mass can similarly be calculated as (see Fig. 3.12)

$$m_{\rm x,\,min} = 4.3\times10^{-10}\frac{m_\phi(T_{\rm re})}{T_{\rm re}} = 4.3\times10^{-10}\mathscr{M}_\phi T_{\rm re}^{\frac{3w_\phi-1}{1+w_\phi}} \tag{3.55}$$

However, such theoretical lower bound will be further constrained by the observational BBN bound on $\Delta N_{\rm eff} \leq 0.50$ (yellow shaded region). Using this in Eq. (3.43), one readily infers that the relativistic DM energy density should be less 8% of the overall energy budget at the end of reheating. Upon incorporating such observational constraints, we arrive at the following modified expression of the lower limit of the DM mass as

$$m_{\rm x,\,min} \simeq 10^{-8}\mathscr{M}_\phi T_{\rm re}^{\frac{3w_\phi-1}{1+w_\phi}} \tag{3.56}$$

To this end, we would like to point out the fact that there exists a Lyman$-\alpha$ bound on the DM mass $m_{\rm x}^{\rm Lyman} > 5\times10^{-6}$ GeV. However, such a bound on DM depends non-trivially on the details of its phase-space distribution and EoS. Therefore, we defer this discussion in detail for our future studies.

From our discussion so far, we have obtained two broad conditions on the DM mass, say $m_{\rm x} > m_\phi(A_{\rm re})$ and $m_{\rm x} < m_\phi(A_{\rm re})$. When the DM mass satisfies the condition $m_{\rm x} < m_\phi(A_{\rm re})$, its abundance decreases with increasing reheating temperature, as shown in Eq.(3.51) (see also Fig.(3.12)). As a result, in order to achieve correct abundance for a fixed DM mass, the inflaton-DM coupling must be increased for larger reheating temperature with an exception (see Fig. 3.12) for $\phi\phi \to SS$ production channel with $w_\phi < 1/3$. The reason is that for such a situation, the $\phi\phi \to SS$ channel produces DM only during the initial stage of reheating. On the other hand, when the DM satisfies $m_{\rm x} > m_\phi(A_{\rm re})$, the slope of the figure changes (see the bottom plot of Fig. 3.12), and the co-moving DM freezes in a point during reheating due to kinematic reasons where $m_{\rm x} \sim m_\phi$. As a consequence, the mass dependency of the abundance $\Omega_{\rm x}h^2$ also changes (see Eq. (3.52)).

3.2.3 Freeze-in and Freeze-out production of DM from radiation bath

In this subsection, we will discuss DM production exclusively from the thermal bath. In addition, the universal gravitational production of DM will always be present, which can not be ignored. The associated Boltzmann equations (see, for instance, Eq. 3.5c) for the freeze-in production scenario are

$$\dot{\rho}^r_{\rm tot} + 4H\rho^r_{\rm tot} - \Gamma^r_\phi(1+w_\phi)\rho_\phi - 2\langle\sigma v\rangle\langle E_{\rm x}\rangle^r\left[(n^r_{\rm x})^2 - (n^r_{\rm x,eq})^2\right] = 0, \tag{3.57}$$

$$\dot{n}^r_{\rm x} + 3H\, n^r_{\rm x} + \langle\sigma v\rangle\left[(n^r_{\rm x})^2 - (n^r_{\rm x,eq})^2\right] = 0. \tag{3.58}$$

And for the freeze-out scenario, since the cross-section is strong enough, the gravitationally produced DM from the inflaton and radiation occurs at the initial reheating stage and reaches thermal equilibrium within a short period. Thus, the Boltzmann equations associated with DM take the following form

$$\dot{n}^r_{\rm x} + 3H\, n^r_{\rm x} + \langle\sigma v\rangle\left[(n^r_{\rm x})^2 - (n^r_{\rm x,eq})^2\right] - \frac{\Gamma_{\phi\phi\to SS/FF}\rho_\phi}{m_\phi(t)} - \frac{\gamma_{S/F}T^8_{rad}}{M_p^4} = 0. \tag{3.59}$$

Where $\Gamma^r_\phi = \Gamma^{th}_{s/f} + \Gamma^{\rm gr}_{\phi\phi\to RR}$, $\gamma_S = 1.9\times10^{-4}$ for scalar DM, $\gamma_F = 1.9\times10^{-3}$ for fermionic DM [168]. In the above expression, the fourth and last terms are associated with the DM production through gravitational scattering from the inflaton, and radiation bath, respectively (see Fig. 3.11 for relevant Feynman diagrams for gravitational scattering from the thermal bath (R)). $\langle E_{\rm x}\rangle^r = \sqrt{m^2_{\rm x} + 9\,T^2_{\rm rad}}$ is the average energy per DM particle produced from the thermal bath [41]. $\langle\sigma v\rangle$ be the thermally averaged cross section times velocity, and $n^r_{\rm x,eq}$ be the equilibrium number density of the DM, which can be expressed as

$$n^r_{\rm x,eq} = \frac{j_{\rm x}}{2\pi^2}\int_{m_{\rm x}}^{\infty}\frac{\sqrt{E^2_{\rm x}-m^2_{\rm x}}}{e^{E_{\rm x}/T_{\rm rad}}+1}E_{\rm x}dE_{\rm x} = \frac{j_{\rm x}T^3_{\rm rad}}{2\pi^2}\left(\frac{m_{\rm x}}{T_{\rm rad}}\right)^2 K_2\left(\frac{m_{\rm x}}{T_{\rm rad}}\right), \tag{3.60}$$

where, $T_{\rm rad}$ is the temperature of the radiation bath, $j_{\rm x}$ be the internal degrees of freedom of DM, and $K_2(x)$ is the modified Bessel function of the second kind. The expression of the DM relic abundance in terms of radiation abundance $\Omega_{\rm x}h^2 = (m_{\rm x}n^r_{\rm x}(A_f)\Omega_r h^2)/(\epsilon T^3_f A^3_f T_{\rm now})$, where T_f be the temperature of the radiation bath at the very late times A_f, when both the radiation and DM energy density became freezes, and $n^r_{\rm x} = n^r_{\rm x}A^3$ is the co-moving number density of DM. We constrain the DM parameter space $(m_{\rm x},\langle\sigma v\rangle)$ in terms of $(w_\phi, T_{\rm re})$. The population of the DM particles produced from the thermal bath strongly depends on the scattering cross-section $\langle\sigma v\rangle$. If the scattering cross-section is large enough, the produced DM particles reach thermal equilibrium, and when the bath temperature falls below the DM mass, the number density of DM freezes out-this mechanism is known as the freeze-out mechanism. On the other hand, if the scattering cross-section is small enough, the DM can never reach thermal equilibrium, and this mechanism is called the freeze-in mechanism [16, 204]. In this chapter, we will discuss both production mechanisms and analyze the parameter space needed to satisfy the correct relic.

A. Freeze-in from radiation bath: bosonic and fermionic reheating

For the freeze-in from the thermal bath, the DMs will never be in thermal equilibrium, and hence DM number density generically satisfies $n^r_{\rm x} \ll n^r_{\rm x,eq}$. Dynamical equation Eq. 3.58 then transformed into simplified form in terms of co-moving DM number density $N^r_{\rm x} = n^r_{\rm x}A^3$ as,

$$\frac{dN^r_{\rm x}(A)}{dA} = \frac{A^2}{H}\langle\sigma v\rangle\left(n^r_{\rm x,eq}\right)^2. \tag{3.61}$$

The above equation suggests that the production rate is simply proportional to the square of the equilibrium DM number density. In the $m_{\rm x} < T_{\rm rad}$ limit, it behaves as $\propto T_{\rm rad}^6$. Thus, freeze-in production from radiation bath naturally follows the way radiation temperature evolves up to the point $m_{\rm x} \sim T_{\rm rad}$. The production for the masses $m_{\rm x} > T_{\rm rad}$ will naturally be Boltzmann suppressed. As we have extensively discussed, the evolution of the bath temperature is conditioned non-trivially not only by the production process and its constituents, but also by the bath temperature itself. Therefore, details of the reheating history is expected to have interesting impact on DM evolution and its final abundance. Throughout our analysis, we will provide a detailed analysis of DM phenomenology and its dependence on the reheating history for the different physical situations discussed before.

♣ : Freeze-in from the bosonic radiation bath

Earlier, we discussed different possible bosonic reheating histories. In this section, we will quote our findings of the DM abundances for those different reheating histories. The detailed calculations are shown in the Addenda-C. As discussed for the bosonic reheating case, depending on the range of inflaton-scalar coupling, we have three different cases,

Case-I: Coupling strength $g_i^r > \mathscr{G}_{ci}^{1,th}$: In this regime, direct decay of inflaton into radiation controls the entire reheating process, and as discussed, we have the two broadly classified thermal histories,

When $T_{\rm rad}^{\rm max} > m_\phi^{\rm end}$: For this case, the direct inflaton decay channel controls the reheating dynamics, and the thermal effect is effective throughout the reheating period for $w_\phi > w_\phi^c$, so the temperature evolves according to Eq. 3.127,3.128. With this reheating background, we now find the DM abundance for two different mass ranges. When $m_{\rm x} < T_{\rm re}$, the present-day DM abundance can be obtained as,

$$\Omega_{\rm x} h^2 = \Omega_r h^2 \frac{6 M_p \langle\sigma v\rangle j_{\rm x}^2}{(3\epsilon)^{3/2}\pi^4 T_{\rm now}} \begin{cases} \frac{m_{\rm x} T_{\rm re}}{1+7w_\phi} & \text{for} \quad g_1^r \phi s^2 \\ \frac{m_{\rm x} T_{\rm re}}{11w_\phi - 3} & \text{for} \quad g_2^r \phi^2 s^2 \quad \text{with} \quad w_\phi > 3/11 \\ \frac{m_{\rm x} T_{\rm re}}{3-11w_\phi} \left(\frac{T_{\rm re}}{T_{\rm rad}^{\rm max}}\right)^{\frac{3(11w_\phi-3)}{3-5w_\phi}} & \text{for} \quad g_2^r \phi^2 s^2 \quad \text{with} \quad w_\phi < 3/11. \end{cases} \tag{3.62}$$

When the DM mass is lower than the reheating temperature, kinematically, DM production is expected to continue even after reheating until the point when $m_{\rm x} \sim T_{\rm rad}$. However, it is important to note that freeze-in production of DM from the radiation bath typically follows the evolution of the bath itself. In most cases, the comoving radiation energy density freezes at the end of reheating (see Fig. 3.13). Therefore, for analytical calculation, it is safe to take DM production up to the end of reheating even for $m_{\rm x} < T_{\rm re}$. On the other hand, there are some situations where radiation production happens initially, which is visible in most of the scenarios where $w_\phi < 3/11$ for $\phi\phi \to ss$ reheating process. For such case, DM production similarly happens instantaneously at the end of inflation, and its number density turned out to be independent of mass but depends on the maximum radiation temperature $T_{\rm rad}^{\rm max}$. The resulting expression for the abundance is given in the last expression of Eq. 3.62. Therefore, for this particular reheating, since maximum production happens initially, the above expression of the abundance will remain the same even for $m_{\rm x} > T_{\rm re}$. However, this should not be true in general.

Generically, if one considers the mass $m_{\rm x} > T_{\rm re}$, the DM is naturally expected to be produced during

reheating until $m_{\rm x} \sim T_{\rm rad}$, and the abundance for different decay channels are obtained as

$$\Omega_{\rm x}h^2 = \Omega_r h^2 \frac{6M_p\langle\sigma v\rangle j_{\rm x}^2}{(3\epsilon)^{3/2}\pi^4 T_{\rm now}} \begin{cases} \frac{m_{\rm x}T_{\rm re}}{1+7w_\phi}\left(\frac{T_{\rm re}}{m_{\rm x}}\right)^{\frac{3(1+7w_\phi)}{1-3w_\phi}} & \text{for} \quad g_1^r\phi s^2 \\ \frac{m_{\rm x}T_{\rm re}}{11w_\phi-3}\left(\frac{T_{\rm re}}{m_{\rm x}}\right)^{\frac{3(11w_\phi-3)}{3-5w_\phi}} & \text{for} \quad g_2^r\phi^2 s^2 \ \text{ with } \ w_\phi > 3/11 \end{cases} \tag{3.63}$$

At this point, we would like to elaborate the exceptional case for $w_\phi > w_\phi^t$, for which the reheating temperature equals the maximum radiation temperature (see, for instance, Eq. 3.127). If the EoS satisfies $w_\phi > w_\phi^t$ and $m_{\rm x} > T_{\rm re}$, the DM production remains always suppressed and the dominating contribution comes from the initial stage of reheating. On the other hand, for $w_\phi < w_\phi^t$ where maximum radiation temperature appears at the initial phase of reheating and for $m_{\rm x} > T_{\rm re}$ DM production occurs till the point $m_{\rm x} \sim T_{\rm rad}$.

As discussed earlier, when $w_\phi < w_\phi^c$, we found an intermediate temperature scale T_c (at the point A_c defined in Eq. 3.21) above which bath temperature dynamics is controlled by the thermally corrected decay width. Hence, for $m_{\rm x} > T_{\rm re}$, since the freeze-in occurs during the reheating epoch itself, two different possibilities arise. If $m_{\rm x} > T_c > T_{\rm re}$, the DM will freeze in during the early phase of reheating, where the evolution of bath temperature is controlled by thermally corrected production rate, and the abundance will take the following form,

$$\Omega_{\rm x}h^2 = \Omega_r h^2 \frac{6M_p\langle\sigma v\rangle j_{\rm x}^2}{(3\epsilon)^{3/2}\pi^4 T_{\rm now}} \begin{cases} \frac{m_{\rm x}T_{\rm re}}{1+7w_\phi}\left(\frac{T_c}{m_{\rm x}}\right)^{\frac{3(1+7w_\phi)}{1-3w_\phi}}\left(\frac{T_{\rm re}}{T_c}\right)^{\frac{2(3+5w_\phi)}{1-w_\phi}} & \text{for} \quad g_1^r\phi s^2 . \\ \frac{m_{\rm x}T_{\rm re}}{3-11w_\phi}\left(\frac{T_{\rm re}}{T_{\rm rad}^{\rm max}}\right)^{\frac{3(11w_\phi-3)}{3-5w_\phi}} & \text{for} \quad g_2^r\phi^2 s^2 \end{cases} \tag{3.64}$$

Whereas for $T_c > m_{\rm x} > T_{\rm re}$, the DM will freeze in during the later part of the reheating phase when finite temperature effect is diminished, and the abundance assumes a different form as,

$$\Omega_{\rm x}h^2 = \Omega_r h^2 \frac{12M_p\langle\sigma v\rangle j_{\rm x}^2}{(3\epsilon)^{3/2}\pi^4 T_{\rm now}} \begin{cases} \frac{m_{\rm x}T_{\rm re}}{3+5w_\phi}\left(\frac{T_{\rm re}}{m_{\rm x}}\right)^{\frac{2(3+5w_\phi)}{1-w_\phi}} & \text{for} \quad g_1^r\phi s^2 . \\ \frac{m_{\rm x}T_{\rm re}}{3-11w_\phi}\left(\frac{T_{\rm re}}{T_{\rm rad}^{\rm max}}\right)^{\frac{2(11w_\phi-3)}{3(1-w_\phi)}} & \text{for} \quad g_2^r\phi^2 s^2 \end{cases} \tag{3.65}$$

And if $m_{\rm x} < T_{\rm re}$, the DM abundance at the present time can be written as

$$\Omega_{\rm x}h^2 = \Omega_r h^2 \frac{12M_p\langle\sigma v\rangle j_{\rm x}^2}{(3\epsilon)^{3/2}\pi^4 T_{\rm now}} \begin{cases} \frac{m_{\rm x}T_{\rm re}}{3+5w_\phi} \ \text{for} \ g_1^r\phi s^2 \\ \frac{m_{\rm x}T_{\rm re}}{3-11w_\phi}\left(\frac{T_{\rm re}}{T_{\rm rad}^{\rm max}}\right)^{\frac{2(11w_\phi-3)}{3(1-w_\phi)}} & \text{for} \quad g_2^r\phi^2 s^2 \end{cases} \tag{3.66}$$

When $T_{\rm gr}^{\rm r,max} < T_{\rm rad}^{\rm max} < m_\phi^{\rm end}$: For this case, direct inflaton decay channel controls the entire reheating dynamics. Similar to the discussion above for $m_{\rm x} < T_{\rm re}$, the abundance can be written as

$$\Omega_{\rm x}h^2 = \Omega_r h^2 \frac{12M_p\langle\sigma v\rangle j_{\rm x}^2}{(3\epsilon)^{3/2}\pi^4 T_{\rm now}} \begin{cases} \frac{m_{\rm x}T_{\rm re}}{3+5w_\phi} \ \text{for} \ g_1^r\phi s^2 \ \text{with} \ w_\phi < w_\phi^c \\ \frac{m_{\rm x}T_{\rm re}}{1+7w_\phi} \ \text{for} \ g_1^r\phi s^2 \ \text{with} \ w_\phi > w_\phi^c \\ \frac{m_{\rm x}T_{\rm re}}{3-11w_\phi}\left(\frac{T_{\rm re}}{T_{\rm rad}^{\rm max}}\right)^{\frac{3(11w_\phi-3)}{3-5w_\phi}} \ \text{for} \ g_2^r\phi^2 s^2 \ \text{with} \ w_\phi < w_\phi^c \\ \frac{m_{\rm x}T_{\rm re}}{11w_\phi-3} \ \text{for} \ g_2^r\phi^2 s^2 \ \text{with} \ w_\phi > w_\phi^c . \end{cases} \tag{3.67}$$

However, for $m_{\rm x} > T_{\rm re}$ freeze-in will naturally occur during reheating, and for $w < w_\phi^c$ the abundance can be found to be the same as Eq. 3.65. On the other hand for $w > w_\phi^c$ the abundance will be same as Eq.(3.63) for $m_{\rm x} < T_c$, and for $m_{\rm x} > T_c$ is

$$\Omega_{\rm x}h^2 = \Omega_r h^2 \frac{12M_p\langle\sigma v\rangle j_{\rm x}^2}{(3\epsilon)^{3/2}\pi^4 T_{\rm now}} \begin{cases} \frac{m_{\rm x}T_{\rm re}}{3+5w_\phi}\left(\frac{T_c}{m_{\rm x}}\right)^{\frac{2(3+5w_\phi)}{1-w}}\left(\frac{T_{\rm re}}{T_c}\right)^{\frac{3(1+7w_\phi)}{1-3w_\phi}} & \text{for} \quad g_1^r\phi s^2 \\ \frac{m_{\rm x}T_{\rm re}}{11w_\phi-3}\left(\frac{T_c}{m_{\rm x}}\right)^{\frac{2(3+5w_\phi)}{1-w}}\left(\frac{T_{\rm re}}{T_c}\right)^{\frac{3(11w_\phi-3)}{3-5w_\phi}} & \text{for} \quad g_2^r\phi^2 s^2 \ , \end{cases} \tag{3.68}$$

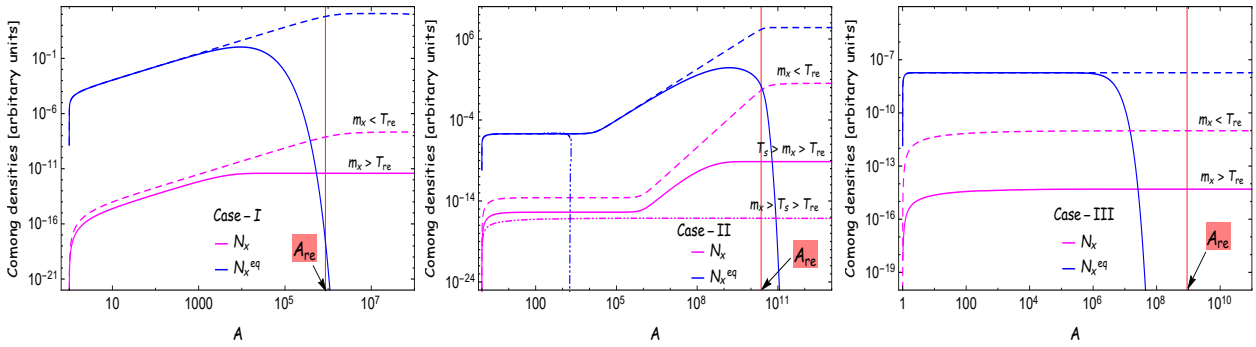

Figure 3.13: The general behavior of the evolution of the co-moving number density of DM (FIMP) as a function of the normalized scale factor A for three different cases-Case I (left), Case II (middle), and Case III (right).

Case-II: Coupling strength in between $\mathscr{G}_{ci}^{2,th} < g_i^r < \mathscr{G}_{ci}^{1,th}$: As discussed earlier, for this coupling range, the gravitational interaction drives the dynamics of reheating at the initial stage. Therefore, the maximum temperature is always controlled by the gravitational sector $T_{gr}^{r,max} = T_{\rm rad}^{\rm max}$. In this coupling range, a cross-over temperature scale T_s (at the point $A_{\rm gr\to ngr}$-see Eq. 3.27) exists across which gravitational decay dominated to non-gravitational decay-dominated reheating occurs. When $m_{\rm x} < T_{\rm re}$, the DM will be produced up to the end of reheating (except for $g_2^r\phi^2 s^2$ with $w_\phi < 3/11$), and hence the maximum production occurs at the end of reheating, and the abundance follows Eqs. 3.62, 3.66. However, if $T_s > m_{\rm x} > T_{\rm re}$ and freeze-in occurs during the decay channel-dominated phase, and the final abundance follows the same form as expressed in Eqs. (3.63), and (3.65) with T_c being replaced by T_s. However, if $m_{\rm x} > T_s > T_{\rm re}$ and freeze-in happens during the universal gravitational decay-dominated phase, and we have

$$\Omega_{\rm x}h^2 = \Omega_r h^2 \frac{6M_p\langle\sigma v\rangle j_{\rm x}^2}{(3\epsilon)^{3/2}\pi^4 T_{\rm now}} \frac{m_{\rm x}T_{\rm re}}{1-w_\phi}\left(\frac{T_{\rm rad}^{\rm max}}{T_s}\right)^{\frac{3(1-w_\phi)}{2}} \begin{cases} \left(\frac{T_{\rm re}}{T_s}\right)^{\frac{3(1+7w_\phi)}{1-3w_\phi}} & \text{for } g_1^r\phi s^2 \text{ with } w_\phi > w_\phi^c \\ \left(\frac{T_{\rm re}}{T_s}\right)^{\frac{3(11w_\phi-3)}{3-5w_\phi}} & \text{for } g_2^r\phi s^2 \text{ with } w_\phi > w_\phi^c, \end{cases} \tag{3.69}$$

and

$$\Omega_{\rm x}h^2 = \Omega_r h^2 \frac{6M_p\langle\sigma v\rangle j_{\rm x}^2}{(3\epsilon)^{3/2}\pi^4 T_{\rm now}} \frac{m_{\rm x}T_{\rm re}}{1-w_\phi}\left(\frac{T_{\rm rad}^{\rm max}}{T_s}\right)^{\frac{3(1-w_\phi)}{2}} \begin{cases} \left(\frac{T_{\rm re}}{T_s}\right)^{\frac{2(3+5w_\phi)}{1-w_\phi}} & \text{for } g_1^r\phi s^2 \text{ with } w_\phi < w_\phi^c \\ \left(\frac{T_{\rm re}}{T_s}\right)^{\frac{2(11w_\phi-3)}{1-w_\phi}} & \text{for } g_2^r\phi s^2 \text{ with } w_\phi < w_\phi^c. \end{cases} \tag{3.70}$$

The evolution of the comoving number density with the scale factor A for this case is shown in the middle panel of Fig. 3.13.

Case III: when $g_i^r < \mathscr{G}_{ci}^2$: For this case, the gravity-mediated decay of inflaton controls the entire dynamics of reheating (termed as gravitational reheating). This particular phase is realized for $w_\phi > 0.65$ (see the light-cyan region of Fig. 3.2). Similar to the previous case, $T_{\rm gr}^{\rm r,max} = T_{\rm rad}^{\rm max}$ will always holds. Since gravitational radiation production happens only at the beginning of reheating, most of the DM production is also expected to happen at the initial phase of the reheating, irrespective of DM mass (see left panel of Fig. 3.13). The DM abundance in such a scenario is given by

$$\Omega_{\rm x}h^2 = \Omega_r h^2 \frac{6M_p\langle\sigma v\rangle j_x^2}{(3\epsilon)^{3/2}\pi^4 T_{\rm now}} \frac{m_{\rm x}T_{\rm re}}{(1-w_\phi)} (T_{\rm re}/T_{\rm rad}^{\rm max})^{3(w_\phi-1)/2}. \tag{3.71}$$

♣ : Freeze-in from the Fermionic radiation bath

Details of the fermionic reheating has been discussed. In this section, we will quote our findings of the DM abundances for those different reheating histories. The detailed calculations are shown in the Addenda-C. The distinct behaviour of fermionic reheating, as opposed to bosonic one, mainly arises for the higher value of inflation EoS, say $w_\phi > 7/15\,(5/9)$ for with (without) thermal effect. In addition to that, if $w_\phi > 7/15\,(5/9)$, most of the fermionic radiation production occurs during the initial stage of reheating due to its specific behaviour of production rate from the inflaton. Similar to the bosonic one, for fermionic reheating depending on the range of inflaton-Fermion coupling we have two different possibilities,

Case-I: Coupling strength, $h^r > \mathscr{H}_c$: As discussed before, for this coupling regime, non-gravitational decay of inflaton into radiation controls the entire reheating process. In the following subsection consider different temperature regimes

When $T_{\rm rad}^{\rm max} > m_\phi^{\rm end}$: For this case, the thermal correction in the decay rate will be dominant from the beginning. Depending upon the EoS we have two different possibilities of evolution of the radiation component: (i) $1 > w_\phi \geq 7/15$, the radiation production mainly takes place at the initial stage, (ii) $0 \leq w_\phi < 7/15$, radiation production happens throughout the reheating phase (see, for instance, Eq. 3.33).

- $1 > w_\phi \geq 7/15$: As just pointed out, radiation production occurs at the initial stage and hence the comoving radiation density becomes constant early. Following the radiation evolution, the DMs are also produced at the beginning of reheating. As a result the abundance (see, Eq. 3.72), naturally be controlled by the $T_{\rm rad}^{\rm max}$, as follows

$$\Omega_{\rm x} h^2 = \Omega_r h^2 \frac{6 M_p \langle\sigma v\rangle j_{\rm x}^2}{(3\epsilon)^{3/2}\pi^4 (1-w_\phi) T_{\rm now}} m_{\rm x} T_{\rm re} \left(\frac{T_{\rm re}}{T_{\rm rad}^{\rm max}}\right)^{\frac{3(w_\phi-1)}{2}}, \tag{3.72}$$

- $0 \leq w_\phi < 7/15$: For this range of EoS, the ratio $T_{\rm rad}/m_\phi$ varies as $A^{-\frac{3}{10}(1-5w_\phi)}$ which indicates that the thermal effect is dominant throughout the entire reheating phase when $7/15 > w_\phi > 1/5$. However, for $0 \leq w_\phi < 1/5$, there exists an intermediate temperature scale T_c with the scale factor A_c (see Eq. 3.1.5) above which the thermal effects drops down drastically. Let us discuss two possible scenarios in this context:

  1.*Dominant finite temperature effect during entire reheating period for EoS* $1/5 < w_\phi < 7/15$: We found two different sub-possibilities depending on EoS.

  a) When EoS is in the range of $9/25 < w_\phi < 7/15$, comoving DM freezes at the initial stage of reheating, and due to that, there is an explicit maximum temperature dependence in the DM abundance. Henceforth, for both $m_{\rm x} > T_{\rm re}$ and $m_{\rm x} < T_{\rm re}$, we have the same DM abundance expression, and that is,

$$\Omega_{\rm x} h^2 = \Omega_r h^2 \frac{30 M_p \langle\sigma v\rangle j_{\rm x}^2}{(3\epsilon)^{3/2}\pi^4 T_{\rm now}} \frac{m_{\rm x} T_{\rm re}}{(25w_\phi - 9)} \left(\frac{T_{\rm re}}{T_{\rm rad}^{\rm max}}\right)^{\frac{9-25w_\phi}{1+5w_\phi}}, \tag{3.73}$$

  b) When EoS lies between $1/5 < w_\phi < 9/25$, the expression for DM abundance will be different for $m_{\rm x} < T_{\rm re}$ (comoving DM freezes at the end of reheating) and $m_{\rm x} > T_{\rm re}$ (comoving DM freezes at any intermediate point during reheating where $m_{\rm x} \sim T_{\rm rad}$). For $m_{\rm x} < T_{\rm re}$, DM abundance is found to be,

$$\Omega_{\rm x} h^2 = \Omega_r h^2 \frac{30 M_p \langle\sigma v\rangle j_{\rm x}^2}{(3\epsilon)^{3/2}\pi^4 T_{\rm now}} \frac{m_{\rm x} T_{\rm re}}{9 - 25w_\phi}, \tag{3.74}$$

and for $m_{\rm x} > T_{\rm re}$ we have,

$$\Omega_{\rm x} h^2 = \Omega_r h^2 \frac{30 M_p \langle\sigma v\rangle j_{\rm x}^2}{(3\epsilon)^{3/2}\pi^4 T_{\rm now}} \frac{m_{\rm x} T_{\rm re}}{9-25w_\phi} \left(\frac{T_{\rm re}}{m_{\rm x}}\right)^{\frac{9-25w_\phi}{1+5w_\phi}} . \tag{3.75}$$

2. *Finite temperature effect will not be dominant during the entire reheating period for EoS* $0 \le w_\phi < 1/5$*:* As already discussed earlier, for this range of EoS, there exits an intermediate temperature scale T_c across which thermal effect drops down (see discussion around Eq. 3.35). Therefore, for $m_{\rm x} > T_{\rm re}$ (comoving DM freezes in during reheating), we have two different possibilities:
i) When $m_{\rm x} > T_c > T_{\rm re}$, the DM freezes in before thermal to non-thermal domination crossover, and we get

$$\Omega_{\rm x} h^2 = \Omega_r h^2 \frac{30 M_p \langle\sigma v\rangle j_{\rm x}^2}{(3\epsilon)^{3/2}\pi^4 T_{\rm now}} \frac{m_{\rm x} T_{\rm re}}{9-25w_\phi} \left(\frac{T_c}{m_{\rm x}}\right)^{\frac{(9-25w_\phi)}{1+5w_\phi}} \left(\frac{T_{\rm re}}{T_c}\right)^{\frac{2(3-7w_\phi)}{1+3w_\phi}} . \tag{3.76}$$

ii) When $T_{\rm re} < m_{\rm x} < T_c$, the comoving DM freezes after thermal to non-thermal domination crossover, and abundance assumes,

$$\Omega_{\rm x} h^2 = \Omega_r h^2 \frac{4 M_p \langle\sigma v\rangle j_{\rm x}^2}{(3\epsilon)^{3/2}\pi^4 T_{\rm now}} \frac{m_{\rm x} T_{\rm re}}{3-7w_\phi} \left(\frac{T_{\rm re}}{m_{\rm x}}\right)^{\frac{2(3-7w_\phi)}{1+3w_\phi}} . \tag{3.77}$$

when $m_{\rm x} < T_{\rm re}$, the Comoving DM freezes at the end of reheating, and the abundance can be expressed as

$$\Omega_{\rm x} h^2 = \Omega_r h^2 \frac{4 M_p \langle\sigma v\rangle j_{\rm x}^2}{(3\epsilon)^{3/2}\pi^4 T_{\rm now}} \frac{m_{\rm x} T_{\rm re}}{3-7w_\phi} . \tag{3.78}$$

$T_{\rm gr}^{\rm r,max} < T_{\rm rad}^{\rm max} < m_\phi^{\rm end}$: In this case, as described earlier in detail (see, for instance, sec-3.1.5) there is no thermal effect at the beginning of reheating. Depending on the reheating background, there are two different possibilities (see, for instance, Eq. 3.38):

- $1 > w_\phi \ge 5/9$: The bath temperature always falls as A^{-1} since the radiation component is frozen at the beginning of reheating. For the freeze-in mechanism from the thermal bath, it is expected that the DM component follows the radiation and freezes at the beginning, irrespective of its mass. Thus the expression for the abundance will be exactly the same as defined earlier in Eq. 3.72.

- $0 \le w_\phi < 5/9$: In this scenario, the thermal effect is subdominant at the beginning, but there is a chance of the thermal effect being dominant at any intermediate scale where $T_{\rm rad} \sim T_c$. However, depending upon the way the finite temperature effect made its presence on the DM evolution, the EoS range is divided into three sub-ranges,

  1.*Sub-dominant finite temperature effect during the reheating for EoS* $0 \le w_\phi < 1/5$*:* If the thermal correction is not applicable throughout reheating, then the abundance follows the Eq. (3.78) for $m_{\rm x} < T_{\rm re}$ and Eq. 3.77 for $m_{\rm x} > T_{\rm re}$.

  2. *Dominant finite temperature effect at intermediate temperature* T_c *for* $1/5 < w_\phi < 3/7$ *:* Here we have two different cases depending on different EoS regimes:
  i) In the presence of the thermal effect when EoS lies within $9/25 < w_\phi < 3/7$, most of the DM

production occurs before the intermediate temperature scale T_c. Hence, for any value of $m_{\rm x} < T_c$, the DM always freezes-in its production near around the T_c, and DM abundance assumes the form,

$$\Omega_{\rm x} h^2 = \Omega_r h^2 \frac{4M_p \langle\sigma v\rangle j_{\rm x}^2}{(3\epsilon)^{3/2}\pi^4 T_{\rm now}} \frac{m_{\rm x} T_{\rm re}}{3-7w_\phi} \left(\frac{T_c}{T_{\rm re}}\right)^{\frac{-9+25w_\phi}{1+5w_\phi}} . \tag{3.79}$$

Whereas, for the same EoS range when $m_{\rm x} > T_c > T_{\rm re}$, the comoving DM will freeze in during the initial phase when the thermal effect would be subdominant, and the abundance takes the following form

$$\Omega_{\rm x} h^2 = \Omega_r h^2 \frac{4M_p \langle\sigma v\rangle j_{\rm x}^2}{(3\epsilon)^{3/2}\pi^4 T_{\rm now}} \frac{m_{\rm x} T_{\rm re}}{3-7w_\phi} \left(\frac{T_c}{m_{\rm x}}\right)^{\frac{2(3-7w_\phi}{1+3w_\phi}} \left(\frac{T_{\rm re}}{T_c}\right)^{\frac{9-25w_\phi}{1+5w_\phi}} . \tag{3.80}$$

ii) For the range of EoS $1/5 < w_\phi < 9/25$, the DM production continues up to the end of reheating, and for $m_{\rm x} < T_{\rm re}$, the abundance follows the Eq. 3.74. Whereas, when $m_{\rm x} > T_{\rm re}$, the DM production continue up to $m_{\rm x} \sim T_{\rm rad}$. Therefore, for $T_c > m_{\rm x} > T_{\rm re}$, the DM abundance will follow the Eq. 3.75 and for $m_{\rm x} > T_c > T_{\rm re}$, Eq. 3.80 will be the abundance expression.

3. For EoS $3/7 < w_\phi < 5/9$: For this case, it is observed that the comoving DM freezes immediately after the reheating begins irrespective of DM mass, and the abundance of the DM takes the following form,

$$\Omega_{\rm x} h^2 = \Omega_r h^2 \frac{4M_p \langle\sigma v\rangle j_{\rm x}^2}{(3\epsilon)^{3/2}\pi^4 T_{\rm now}} \frac{m_{\rm x} T_{\rm re}}{7w_\phi - 3} \left(\frac{T_{\rm re}}{T_{\rm rad}^{\rm max}}\right)^{\frac{2(3-7w_\phi)}{1+3w_\phi}} . \tag{3.81}$$

Case-II: Coupling strength, $h^r < \mathscr{H}_c$: As discussed before, for this coupling regime, gravitational decay of inflaton into radiation controls the entire reheating process. Therefore, $T_{\rm rad}^{\rm max} = T_{\rm gr}^{r,\rm max}$ will always be the case. Depending on the different EoS, there are the following possibilities,

- $1 > w_\phi > 0.65$: Since for this case $h^r < \mathscr{H}_c$ and $w_\phi > 0.65$, the gravitational sector is the governing reheating dynamics, termed as gravitational reheating. In gravitational reheating following the radiation component, the DM component will also freeze just at the beginning of reheating, irrespective of its mass, and the abundance will be of the same form as expressed in Eq. 3.71.

- $0 \le w_\phi < 0.65$: For this case, purely gravitational production will not be sufficient to reheat the universe. Hence, to have successful reheating, one needs to have non-gravitational production during the later stage of reheating, and the reheating temperature is defined by non-gravitational fermionic coupling. We found three interesting cases, which are as follows:

  1.*Reheating temperature $T_{\rm re} < T_{\rm BBN}$ for EoS, $5/9 < w_\phi < 0.65$:* It is observed that if the EoS lies in this range, both gravitational and non-gravitational production happen very early in reheating phase. Due to subsequent expansion, the reheating temperature turns out to be always $< T_{\rm BBN}$ (see the red shaded region of Fig. 3.7). However, from the Fig. 3.7 it is clear that for EoS between $0 \le w_\phi < 5/9$, we have non-trivial dynamics

  2.*Dominant finite temperature effect at intermediate temperature T_s for EoS, $1/5 < w_\phi < 5/9$:* In the range of EoS, the finite temperature effect start to dominate at some intermediate temperature scale T_s during reheating. Now, if $m_{\rm x} < T_{\rm re}$, the DMs are expected to freeze after the end of reheating, and consequently, its abundance is calculated to be the same as given in Eq. 3.74. If $T_s > m_{\rm x} > T_{\rm re}$, the

DMs freeze in during the later phase of reheating when non-gravitational decay dominates, and the abundance assumes the form of Eq. 3.75. Finally, if $m_{\rm x} > T_s > T_{\rm re}$, the DM will freeze during the initial part of the reheating phase when gravity-mediated decay controls the reheating, and for such case, the abundance has been calculated as

$$\Omega_{\rm x} h^2 = \Omega_r h^2 \frac{2M_p \langle\sigma v\rangle j_{\rm x}^2}{(3\epsilon)^{3/2}\pi^4(1-w_\phi)T_{\rm now}} m_{\rm x} T_{\rm re} \left(\frac{T_s}{T_{\rm rad}^{\rm max}}\right)^{\frac{3(w_\phi-1)}{2}} \left(\frac{T_{\rm re}}{T_s}\right)^{\frac{9-25w_\phi}{1+5w_\phi}} . \tag{3.82}$$

3.For EoS $0 < w_\phi < 1/5$: When $m_{\rm x} < T_{\rm re}$, the DM abundance is the same expression as Eq. 3.78 and when $T_s < m_{\rm x} < T_{\rm re}$, the abundance is same as defined in Eq. 3.77. Again, if $m_{\rm x} > T_s$, the DM will freeze in during the initial gravitational channel domination sector; in such a case, the DM abundance follows the below equation

$$\Omega_{\rm x} h^2 = \Omega_r h^2 \frac{2M_p \langle\sigma v\rangle j_{\rm x}^2}{(3\epsilon)^{3/2}\pi^4(1-w_\phi)T_{\rm now}} m_{\rm x} T_{\rm re} \left(\frac{T_s}{T_{\rm rad}^{\rm max}}\right)^{\frac{3(w_\phi-1)}{2}} \left(\frac{T_{\rm re}}{T_s}\right)^{\frac{2(3-7w_\phi)}{1+3w_\phi}} . \tag{3.83}$$

3.2.3.1 Freeze-out from the bosonic and fermionic radiation bath

For freeze in mechanism, the interaction cross-section $\langle\sigma v\rangle$ is so small that DM can never reach thermal equilibrium. However, if $\langle\sigma v\rangle$ is large enough, the DM can strongly interact with the SM bath and be in thermal equilibrium. The background expansion eventually helps the DM freeze out from the bath at a certain temperature T_f. Conventionally these DMs are called WIMP. The freeze-out temperature T_f is defined as,

$$\langle\sigma v\rangle n_{\rm x,eq}^r(T_f) = H(T_f). \tag{3.84}$$

During reheating, inflaton decays into radiation; hence, entropy is not conserved. Due to this physical situation, one can find two distinct situations:

Freeze out after reheating: If the mass of the DM $m_{\rm x} < T_{\rm re}$, it will freeze out after reheating, i.e., during the radiation-dominated era. Moreover, after the freeze out, the co-moving number density $N_{\rm x}^r = n_{\rm x}^r A^3$ will be much larger than the comoving equilibrium number density $N_{\rm x}^r$. Thus after freeze-out happens, one can neglect $N_{\rm x,eq}^r$ in comparison with $N_{\rm x}^r$ and from the Eq. 3.58, one can find[7]

$$\frac{dN_{\rm x}^r}{dA} = -\frac{\langle\sigma v\rangle}{H(A_{\rm re})}(A/A_{\rm re})^2 (N_{\rm x}^r)^2 . \tag{3.85}$$

Integrating from freeze-out point ($A = A_f$) to the present time ($A = A_0$), we get

$$N_{\rm x}^r(A_0) = \frac{H(A_{\rm re})}{\langle\sigma v\rangle} A_f A_{\rm re}^2 \implies \Omega_{\rm x} h^2 = \frac{1}{\sqrt{3\epsilon}M_p\langle\sigma v\rangle}(m_{\rm x}/T_f)(\Omega_r h^2/T_0) \tag{3.86}$$

N_0 is identified as the present day comoving number density leading to $\Omega_{\rm x} h^2 \propto 1/\langle\sigma v\rangle$. Hence, the abundance decreases with increasing $\langle\sigma v\rangle$.

[7]Near the DM thermal freezes-out temperature, the non-thermal gravitational production can become dominant as compared to thermal one. This is usually interpreted as the re-annihilation phase [205]. In our analysis, we ignored this effect. However, it is to be noted that if freeze-out occurs after reheating, such an effect turns out to be subdominant. The reason for this is that during radiation domination, the inflation energy density is negligible compared to the radiation energy density, implying $\frac{\Gamma_{\phi\phi\to SS/FF}\rho_\phi}{m_\phi} << \langle\sigma v\rangle (n_{\rm x,eq}^r)^2$ at T_f. On the other hand, for $T_f > T_{\rm re}$, such an effect can become important, particularly for the higher DM mass (when $m_{\rm x} \sim m_\phi^{\rm end}$) range, which we discussed in the Addenda-F.

Freeze out during reheating : Alternatively, DM freeze-out could occur during reheating if $m_{\rm x} > T_{\rm re}$. During reheating $H = H(A_{\rm re})(A/A_{\rm re})^{-\frac{3(1+w)}{2}}$, after utilizing this in Eq. 3.58[8]

$$\frac{dN_{\rm x}^r}{dA} = -\frac{\langle\sigma v\rangle}{H(A_{\rm re})A_{\rm re}^4}(A/A_{\rm re})^{\frac{3w_\phi-5}{2}}(N_{\rm x}^r)^2 \tag{3.87}$$

Freeze-out occurs during reheating at some intermediate scale factor $A_f < A_{\rm re}$. Therefore, integrating the above equation for the number density from A_f to $A_{\rm re}$, the comoving number density at the end of reheating is

$$N_{\rm x}^r(A_{\rm re}) = \frac{3(1-w_\phi)}{2\langle\sigma v\rangle}H(A_{\rm re})A_{\rm re}^3\left(A_{\rm re}/A_f\right)^{-3(1-w_\phi)/2} \tag{3.88}$$

Therefore, the current abundance can be written as,

$$\Omega_{\rm x}h^2 = \Omega^\dagger h^2\left(\frac{m_{\rm x}}{T_{\rm re}}\right)\left(\frac{A_f}{A_{\rm re}}\right)^{\frac{3(1-w_\phi)}{2}} \quad ; \quad \Omega^\dagger = \frac{\sqrt{3}(1-w_\phi)}{2\sqrt{\epsilon}M_p\langle\sigma v\rangle}\frac{\Omega_r}{T_{\rm now}} \tag{3.89}$$

We will evaluate the abundance for the aforementioned two cases for different reheating models discussed earlier in detail.

Freeze out temperature : The freeze-out temperature T_f in general can be computed from Eq. 3.84 by assuming $H(T_f) \propto T_f^k$ as,

$$T_f^{3/2}e^{-m_{\rm x}/T_f} = Q(T_{\rm re}, T_c)T_f^k. \tag{3.90}$$

The general solution of the above equation is expressed in terms of Lambert function $W_{-1}(q)$ of branch -1 with argument q,

$$T_f = -\frac{2m_{\rm x}}{2k-3}\frac{1}{W_{-1}(q)} \quad \text{with} \quad q = -\frac{2m_{\rm x}}{2k-3}Q^{\frac{2}{2k-3}}. \tag{3.91}$$

If freeze-out happens after the reheating, one will simply have $Q = Q_0 = \frac{\sqrt{\epsilon}}{\sqrt{3}M_{\rm p}\langle\sigma v\rangle j_{\rm x}}(2\pi/m_{\rm x})^{3/2}$, and $k = 2$. Consequently, the DM parameter space ($m_{\rm x}$ vs $\langle\sigma v\rangle$) turns out to be the same for all reheating temperatures and inflaton equations of states. However, if freeze-out happens during reheating, the expression of (Q, k) will differ. It is observed that generically we can express $Q(T_{\rm re}, T_{c/s}) = Q_0 T_{\rm re}^\mu T_{c/s}^\nu$, where (μ, ν) will assume different values for different reheating history and that will be our subject of our subsequent discussion.

♣ : **Freeze-out from the bosonic radiation bath**

Case-I: Coupling strength $g_i^r > \mathscr{G}_{ci}^{1,th}$: Similar to the freeze-in case, let us discuss two different regimes.

When $T_{\rm rad}^{\rm max} > m_\phi^{\rm end}$: If the inflaton EoS $w_\phi > w_\phi^c$, the abundance due to freeze-out can be calculated as,

$$\Omega_{\rm x}h^2 = \Omega^\dagger h^2\begin{cases}\left(\frac{m_{\rm x}}{T_{\rm re}}\right)\left(\frac{T_{\rm re}}{T_f}\right)^{\frac{3(1-w_\phi)}{1-3w_\phi}} & \text{for} \quad g_1^r\phi s^2, \ \text{and} \ \ \nu = 0, \mu = 2-k, k = \frac{3(1+w_\phi)}{1-3w_\phi} \\ \left(\frac{m_{\rm x}}{T_{\rm re}}\right)\left(\frac{T_{\rm re}}{T_f}\right)^{\frac{3(1-w_\phi)}{3-5w_\phi}} & \text{for} \quad g_2^r\phi^2 s^2, \ \text{and} \ \ \nu = 0, \mu = 2-k, k = \frac{3(1+w_\phi)}{3-5w_\phi}\end{cases} \tag{3.92}$$

where T_f is the freeze-out temperature which we already defined in Eq. (3.91).

However, if $w_\phi < w_\phi^c$, as has already been discussed for the bosonic reheating, there exists an intermediate temperature scale T_c at which the ratio $T_{\rm rad}/m_\phi$ goes less than unity, and the thermal effect becomes

[8]To find out the analytical expressions of the DM abundance, here we neglect the re-annihilation of DM.

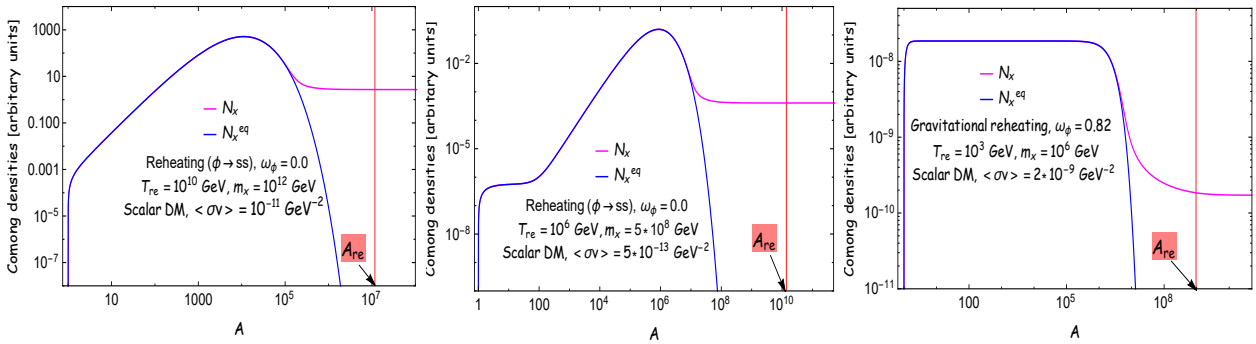

Figure 3.14: The evolution of the co-moving number density of the DM (WIMP) as a function of the normalized scale factor A for bosonic reheating ($\phi \to ss$) for three different cases-I(left),II(middle),III(right).

subdominant at the later part of the reheating phase. Therefore, if $T_f > T_c$, DM freezes out during early reheating phase and the abundance is calculated to be

$$\Omega_{\rm x} h^2 = \Omega^{\dagger} h^2 \begin{cases} \left(\frac{m_{\rm x}}{T_{\rm re}}\right)\left(\frac{T_{\rm re}}{T_c}\right)^4 \left(\frac{T_c}{T_f}\right)^{\frac{3(1-w_\phi)}{1-3w_\phi}} & \text{for} \quad g_1^r \phi s^2 \ \text{ and } \ \nu = \frac{4(1+w_\phi)}{1-w_\phi} - k, \mu = \frac{-2(1+3w_\phi)}{1-w}, k = \frac{3(1+w)}{1-3w_\phi} \\ \left(\frac{m_{\rm x}}{T_{\rm re}}\right)\left(\frac{T_{\rm re}}{T_c}\right)^{\frac{4}{3}} \left(\frac{T_c}{T_f}\right)^{\frac{3(1-w_\phi)}{3-5w_\phi}} & \text{for} \quad g_2^r \phi^2 s^2 \ \text{ and } \ \nu = \frac{4(1+w_\phi)}{3(1-w_\phi)} - k, \mu = \frac{2(1-5w_\phi)}{3(1-w_\phi)}, k = \frac{3(1+w_\phi)}{3-5w_\phi} \end{cases} \tag{3.93}$$

However, if $T_c > T_f$, the freeze-out occurs during the later phase of reheating, and the abundance assumes a different form as

$$\Omega_{\rm x} h^2 = \Omega^{\dagger} h^2 \begin{cases} \left(\frac{m_{\rm x}}{T_{\rm re}}\right)\left(\frac{T_{\rm re}}{T_f}\right)^4 & \text{for} \quad g_1^r \phi s^2 \ \text{ and } \ \nu = 0, \mu = 2 - k, k = \frac{4(1+w_\phi)}{1-w_\phi} \\ \left(\frac{m_{\rm x}}{T_{\rm re}}\right)\left(\frac{T_{\rm re}}{T_f}\right)^{4/3} & \text{for} \quad g_2^r \phi^2 s^2 \ \text{ and } \ \nu = 0, \mu = 2 - k, k = \frac{4(1+w_\phi)}{1-w_\phi} \end{cases} \tag{3.94}$$

$T_{\rm gr}^{\rm r,max} < T_{\rm rad}^{\rm max} < m_\phi^{\rm end}$: For this case, if the inflaton EoS $w_\phi < w_\phi^c$, the effective mass of inflaton remains to be greater than the radiation temperature, and the finite temperature effect will be subdominant throughout. The DM abundance for such case will be same as Eq. 3.94, and the evolution of the comoving number density is depicted in Fig.(3.14). Whereas for $w_\phi > w_\phi^c$, a new temperature scale T_c emerges as before. If DM mass happens to satisfy the condition $m_{\rm x} < T_c$, DM freezes out with radiation temperature $T < T_c$, and the abundance assumes the same form as expressed in Eq.(3.92). On the other hand if $m_{\rm x} > T_c$, freeze-out occurs during the initial non-thermal phase, and DM abundance becomes,

$$\Omega_{\rm x} h^2 = \Omega^{\dagger} h^2 \begin{cases} \left(\frac{m_{\rm x}}{T_{\rm re}}\right)\left(\frac{T_c}{T_f}\right)^4 \left(\frac{T_{\rm re}}{T_c}\right)^{\frac{3(1-w_\phi)}{1-3w_\phi}} & \text{for,} \quad g_1^r \phi s^2, \quad \nu = \frac{3(1+w_\phi)}{1-3w_\phi} - k, \mu = \frac{-(1+9w_\phi)}{1-3w_\phi}, k = \frac{4(1+w)}{1-w_\phi} \\ \left(\frac{m_{\rm x}}{T_{\rm re}}\right)\left(\frac{T_c}{T_f}\right)^{4/3} \left(\frac{T_{\rm re}}{T_c}\right)^{\frac{3(1-w_\phi)}{3-5w_\phi}} & \text{for} \quad g_2^r \phi^2 s^2, \quad \nu = \frac{3(1+w_\phi)}{3-5w_\phi} - k, \mu = \frac{3-13w_\phi}{3-5w_\phi}, k = \frac{4(1+w)}{3(1-w_\phi)} \end{cases} \tag{3.95}$$

Case-II: Coupling strength in between $\mathscr{G}_{ci}^{2,th} < g_i^r < \mathscr{G}_{ci}^{1,th}$: This reheating history is described in the bosonic reheating section. The gravity-mediated decay channel controls the initial reheating dynamic up to $T = T_s$, and then the non-gravitational decay channel controls the reheating dynamics. As a result, initially, DM production is driven by the gravity-mediated decay channel (up to $T = T_s$) and then driven by the non-gravitational decay channel (see middle Fig. 3.14). For $w_\phi > w_\phi^c$, if the DM freezes out during the late non-gravitational decay channel domination phase, i.e., $T_f < T_s$, then the DM abundance follows the Eq. 3.92, and if the DM is frozen out during gravity mediated reheating phase $T_f > T_s$, the DM has

following abundance,

$$\Omega_{\rm x}h^2=\Omega^{\dagger}h^2\begin{cases}\left(\frac{m_{\rm x}}{T_{\rm re}}\right)\left(\frac{T_s}{T_f}\right)^{\frac{3(1-w_\phi)}{2}}\left(\frac{T_{\rm re}}{T_s}\right)^{\frac{3(1-w_\phi)}{1-3w_\phi}} & \text{for,}\quad g_1^r\phi s^2,\ \ \nu=\frac{3(1+w_\phi)}{1-3w_\phi}-k,\mu=\frac{-(1+9w_\phi)}{1-3w_\phi},k=\frac{3(1+w)}{2}\\ \left(\frac{m_{\rm x}}{T_{\rm re}}\right)\left(\frac{T_s}{T_f}\right)^{\frac{3(1-w_\phi)}{2}}\left(\frac{T_{\rm re}}{T_s}\right)^{\frac{3(1-w_\phi)}{3-5w_\phi}} & \text{for}\quad g_2^r\phi^2S^2,\ \ \nu=\frac{3(1+w_\phi)}{3-5w_\phi}-k,\mu=\frac{3-13w_\phi}{3-5w_\phi},k=\frac{3(1+w)}{2}\end{cases}\tag{3.96}$$

Again for $w_\phi<w_\phi^c$, if the DM is frozen out during the late decay channel domination phase, the abundance has the Eq. (3.94), and if the DM is frozen out during the initial gravity-mediated reheating phase, the DM abundance has the following equation

$$\Omega_{\rm x}h^2=\Omega^{\dagger}h^2\begin{cases}\left(\frac{m_{\rm x}}{T_{\rm re}}\right)\left(\frac{T_s}{T_f}\right)^{\frac{3(1-w_\phi)}{2}}\left(\frac{T_{\rm re}}{T_s}\right)^{4} & \text{for,}\quad g_1^r\phi s^2,\ \ \nu=\frac{4(1+w_\phi)}{1-w_\phi}-k,\mu=\frac{-2(1+3w_\phi)}{1-w_\phi},k=\frac{3(1+w)}{2}\\ \left(\frac{m_{\rm x}}{T_{\rm re}}\right)\left(\frac{T_s}{T_f}\right)^{\frac{3(1-w_\phi)}{2}}\left(\frac{T_{\rm re}}{T_s}\right)^{4/3} & \text{for}\quad g_2^r\phi^2S^2,\ \ \nu=\frac{4(1+w_\phi)}{3(1-w_\phi)}-k,\mu=\frac{2(1-5w_\phi)}{3(1-w_\phi)},k=\frac{3(1+w)}{2}\end{cases}\tag{3.97}$$

Case-III : For this reheating scenario, the gravitational sector is the governing reheating dynamics termed as gravitational reheating (GR). The evolution of co-moving number density is shown in the left plot in Fig. (3.14). The DM abundance is

$$\Omega_{\rm x}h^2=\Omega^{\dagger}h^2(m_{\rm x}/T_{\rm re})(T_{\rm re}/T_f)^{\frac{3(1-w_\phi)}{2}},\ \text{and}\ \ \nu=0,\mu=2-k,k=\frac{3}{2}(1+w_\phi)\tag{3.98}$$

♣ : **Freeze-out from the Fermionic radiation bath**

- $w_\phi>5/9$: For $w_\phi>5/9$, the bath temperature always behaves as $T_{\rm rad}=T_{\rm re}(A_{\rm re}/A)$, and using this equation into Eq.(3.89), the abundance is,

$$\Omega_{\rm x}h^2=\Omega^{\dagger}h^2(m_{\rm x}/T_{\rm re})(T_{\rm re}/T_f)^{\frac{3(1-w_\phi)}{2}},\ \text{and}\ \ \nu=0,\mu=2-k,k=\frac{3}{2}(1+w_\phi)\tag{3.99}$$

- $0<w_\phi<5/9$: For this range of EoS, we discuss three different possibilities as follows:

  Case-I: Coupling strength $h^r>\mathscr{H}_c$:

  $T_{\rm rad}^{\rm max}>m_\phi^{\rm end}$: Depending upon the evolution of radiation, we will have different behavior of the DM abundance in terms of reheating temperature. For $7/15<w_\phi<5/9$ the radiation temperature behaves A^{-1}, and abundance follows the Eq. 3.99. On the other hand if $1/5<w_\phi<7/15$, radiation temperature behaves $T_{\rm rad}=T_{\rm re}(A/A_{\rm re})^{-\frac{3(1+5w_\phi)}{10}}$, and using this in Eq. 3.89, we get

$$\Omega_{\rm x}h^2=\Omega^{\dagger}h^2(m_{\rm x}/T_{\rm re})(T_{\rm re}/T_f)^{\frac{5(1-w_\phi)}{1+5w_\phi}}\ \text{and}\ \ \nu=0,\mu=2-k,k=5(1+w_\phi)/1+5w_\phi\tag{3.100}$$

  Finally, if the $0\le w_\phi<1/5$ similar to scalar reheating case, the intermediate temperature scale T_c, leads to two different possibilities. If $m_{\rm x}>T_c$, DM freezes out during the early reheating phase, and we have,

$$\Omega_{\rm x}h^2=\Omega^{\dagger}h^2\left(\frac{m_{\rm x}}{T_{\rm re}}\right)\left(\frac{T_c}{T_f}\right)^{\frac{5(1-w_\phi)}{1+5w_\phi}}\left(\frac{T_{\rm re}}{T_c}\right)^{\frac{4(1-w_\phi)}{1+3w_\phi}}\ \text{and}\ \ \mu=\frac{2(w_\phi-1)}{1+3w_\phi},\nu=\frac{5(1+w_\phi)}{1+5w_\phi}-k,k=\frac{5(1+w_\phi)}{1+5w_\phi}\tag{3.101}$$

  where On the other hand, if $m_{\rm x}<T_c$, DM freezes out during the late reheating phase when the finite temperature effect is subdominant, and we have

$$\Omega_{\rm x}h^2=\Omega^{\dagger}h^2\left(\frac{m_{\rm x}}{T_{\rm re}}\right)\left(\frac{T_{\rm re}}{T_f}\right)^{\frac{4(1-w_\phi)}{1+3w_\phi}}\ \text{and}\ \ \nu=0,\mu=2-k,k=\frac{4(1+w_\phi)}{1+3w_\phi}\tag{3.102}$$

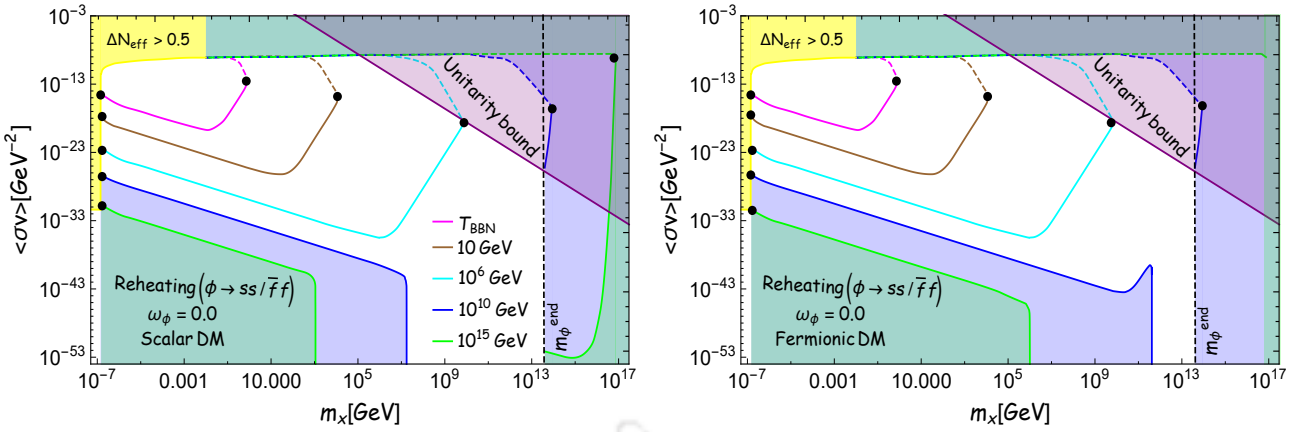

Figure 3.15: $\langle\sigma v\rangle$ vs $m_{\rm x}$ for both freeze-in and freeze-out with five different reheating temperature $T_{\rm re} = (T_{\rm BBN}, 10, 10^6, 10^{10}, 10^{15}$ GeV for $w_\phi = 0.0$. The left plot is for scalar DM, and the right plot fermionic DM. The solid (dashed) lines for freeze-in (freeze-out). The Small filled circle denotes the freeze-in and freeze-out coincidence point. The yellow-shaded region is ruled out by the $\Delta N_{\rm eff}$ bound at BBN, and purple shaded region is ruled by the unitarity bound.

$T_{\rm gr}^{r,\rm max} < T_{\rm rad}^{\rm max} < m_\phi^{\rm end}$: For this case, finite temperature correction is subdominant at the beginning. In fact, for lower EoS, namely $0 < w_\phi < 1/5$, such finite temperature effect will be subdominant throughout the reheating, and hence the abundance turned out to be same as Eq.(3.102). On the other hand, for $w_\phi > 1/5$, the finite temperature effect will become dominant after an intermediate temperature scale T_c, and if the DM freeze-out temperature satisfies $T_f < T_c$, the abundance obeys the Eq. 3.100. Conversely, if the DM freezes out during the early non-thermal phase with $T_f > T_c$, one will have

$$\Omega_{\rm x} h^2 = \Omega^\dagger h^2 \left(\frac{m_{\rm x}}{T_{\rm re}}\right)\left(\frac{T_c}{T_f}\right)^{\frac{4(1-w_\phi)}{1+3w_\phi}}\left(\frac{T_{\rm re}}{T_c}\right)^{\frac{5(1-w_\phi)}{1+5w_\phi}} \quad \text{and} \quad \nu = \frac{4(1+w_\phi)}{1+3w_\phi} - k, \mu = \frac{-3+5w_\phi}{1+5w_\phi}, k = \frac{4(1+w_\phi}{1+3w_\phi} \tag{3.103}$$

ii) **Coupling strength** $h^r < \mathscr{H}_c$: For this case, initially, the reheating phase is governed by the gravity-mediated decay channel up to a point $A_{\rm gr\to ngr}$, and the later part of the phase is dominated by direct inflaton decay. If the freeze-out happens during the later phase, the abundance will be the same as Eq. 3.100 for $w_\phi > 1/5$ and Eq. 3.101 for $w_\phi < 1/5$. If freeze-out occurs at the early phase of reheating, the abundance assumes,

$$\Omega_{\rm x} h^2 = \Omega^\dagger h^2 \frac{m_{\rm x}}{T_{\rm re}} \begin{cases} \left(\frac{T_s}{T_f}\right)^{\frac{3(1-w_\phi)}{2}}\left(\frac{T_{\rm re}}{T_s}\right)^{\frac{5(1-w_\phi)}{1+5w_\phi}} & \text{for } w_\phi > 1/5, \ \nu = \frac{5(1+w_\phi)}{1+5w_\phi} - k, \mu = \frac{-3+5w_\phi}{1+5w_\phi}, k = \frac{3(1+w)}{2} \\ \left(\frac{T_s}{T_f}\right)^{\frac{3(1-w_\phi)}{2}}\left(\frac{T_{\rm re}}{T_s}\right)^{\frac{4(1-w_\phi)}{1+3w_\phi}} & \text{for } w_\phi < 1/5, \ \nu = \frac{4(1+w_\phi)}{1-w_\phi} - k, \mu = \frac{-2+2w_\phi}{1+3w_\phi}, k = \frac{3(1+w)}{2} \end{cases} \tag{3.104}$$

3.2.4 DM Parameter space $(\langle\sigma v\rangle, m_{\rm x})$ for FIMPs and WIMPs from radiation bath

In this section, we will discuss in detail the parameter region where DM production mechanisms are at play for different reheating histories. For the sake of completeness and understanding the DM parameter space, we consider three different EoS ($w_\phi = 0.0, 0.20, 0.50$) with five different reheating temperatures $(T_{\rm BBN}, 10, 10^6, 10^{10}, 10^{15})$ GeV which includes both minimum and maximum reheating temperature. An

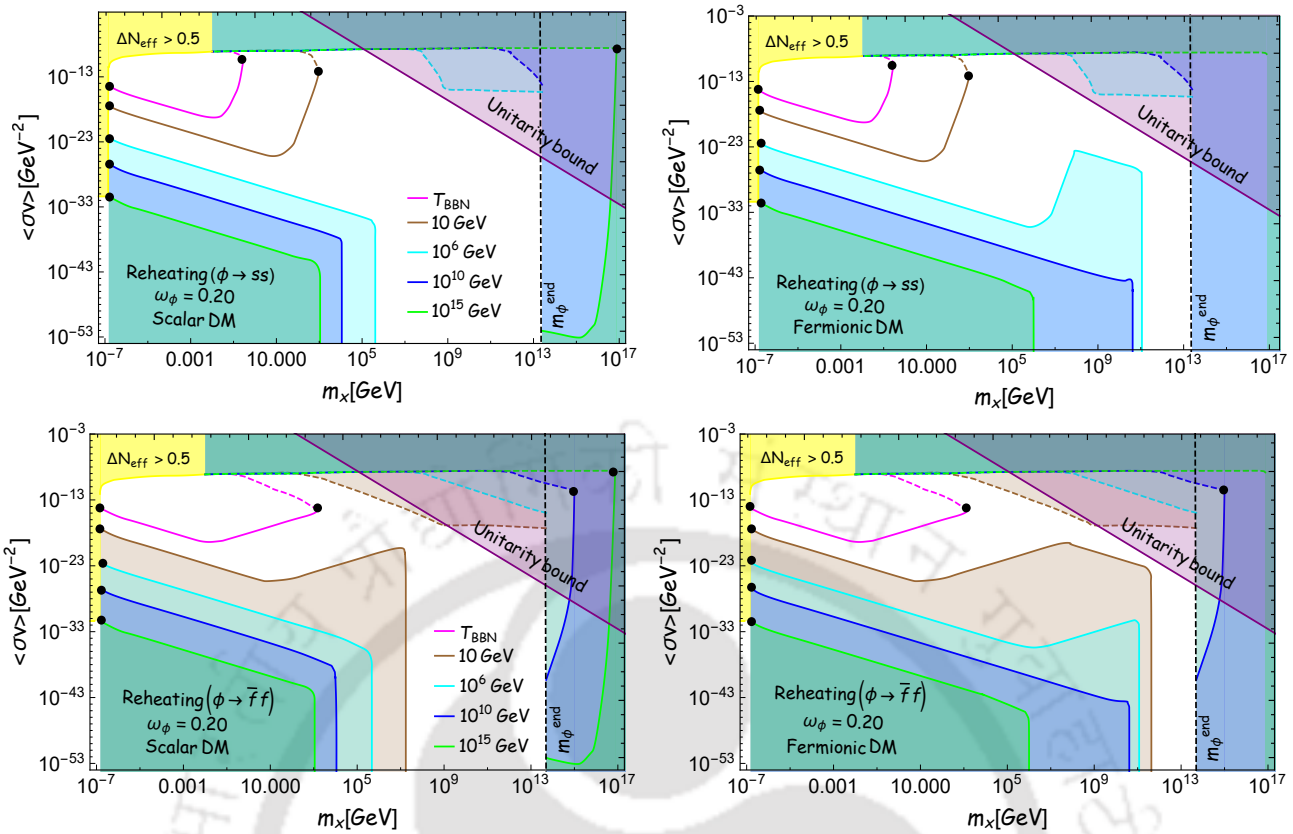

Figure 3.16: $\langle\sigma v\rangle$ vs $m_{\rm x}$ for both freeze-in (solid lines) and freeze-out (dashed lines) with five different reheating temperature $T_{\rm re} = BBN, 10, 10^6, 10^{10}, 10^{15}$ GeV for $w_\phi = 0.20$. The left plot is for scalar DM, and the right plot fermionic DM. The small filled circle is the freeze-in and freeze-out meet point. The yellow-shaded region is ruled out by the $\Delta N_{\rm eff}$ bound at BBN, and purple shaded region is ruled by the unitarity bound.

important point we want to infer is that in the final contribution to DM abundance, we ignore any possible contribution from the non-gravitational inflaton-DM coupling but include the universal gravitational production from both inflaton and radiation scattering. And as we pointed out before, such universal production has been observed to set a maximum limit on the DM mass $m_{\rm x}^{\rm g,\ max}$ ($\leq m_\phi^{\rm end}$ of course) specifically for the freeze-in production. Interestingly, for a given w_ϕ, we found a universal feature of the lowest possible DM mass within $m_{\rm x}^{\rm min} \simeq 150 - 300$ eV (see Eq. (3.163)) irrespective of its nature and the reheating histories for which freeze-in and freeze-out mechanism coincides during the radiation-dominated era. Below this mass scale, all the DM has under abundance today. However, the critical cross-section $\langle\sigma v\rangle_{crit}$ (for analytical expressions, see Addenda-D) at which this coincidence occurs depends on the reheating temperature, which is represented by filled black circles in Figs. 3.15-3.17. Moreover, another critical cross-section exists for higher DM mass ($m_{\rm x}^{\rm max}$) where the freeze-in and freeze-out mechanism coincides during reheating. Unlike the lower DM mass bound, $m_{\rm x}^{\rm max}$ has been found to have non-trivial dependence on the reheating temperature but also depends on the EoS w_ϕ, reheating background. All these features are clearly observed in Figs. 3.15, 3.16, 3.17. In some reheating temperatures, there is no meet point of freeze-in and freeze-out; it is due to the gravitational DM, which gives the overabundance for the freeze-in mechanism where we expect the meet point occurs. When $m_{\rm x}^{\rm max} < m_{\rm x}^{\rm g,max}$ condition is satisfied, then the abundance condition $\Omega_{\rm x} h^2 = 0.12$ gives rise to a closed contour in $(m_{\rm x}, \langle\sigma v\rangle)$ plane due to aforementioned

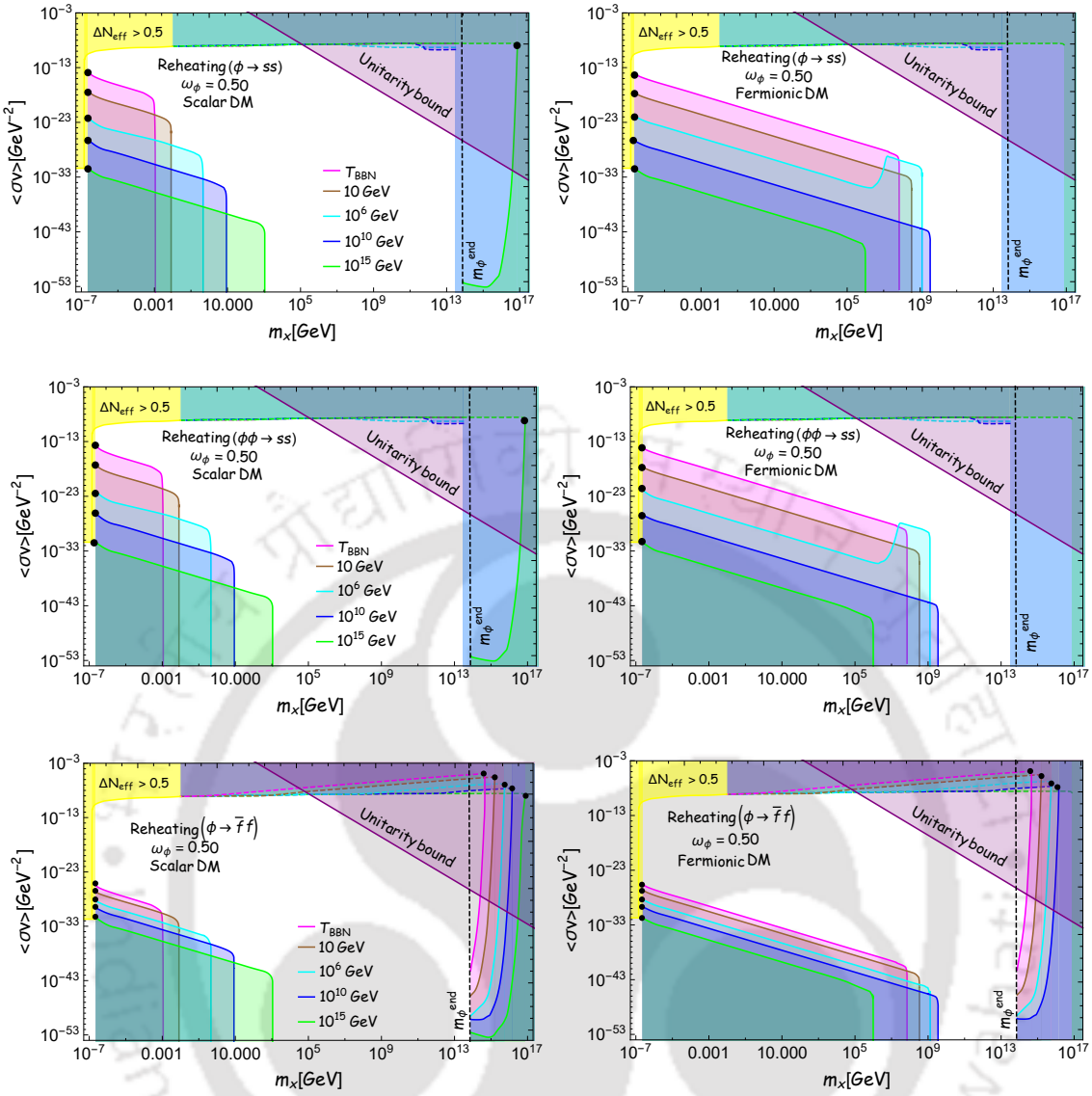

Figure 3.17: Here we have plotted the $\langle\sigma v\rangle$ as a function of DM mass $m_{\rm x}$ for $w_\phi = 0.50$ for five different reheating temperature $T_{\rm re} = BBN, 10, 10^6, 10^{10}, 10^{15}$ GeV. The plot is on the left side for scalar DM and the right side for fermionic DM. The solid lines for the freeze-in mechanism and the dotted lines for the freeze-out mechanism. The yellow-shaded region is ruled out by the $\Delta N_{\rm eff}$ bound at BBN, and purple shaded region is ruled by the unitarity bound.

two critical cross-sections for two different masses $(m_{\rm x}^{\rm min}, m_{\rm x}^{\rm max})$, where the smooth transition happens from freeze-in to freeze-out or vice versa. For example, see Fig. (3.15) where we have found close contours for $T_{\rm re} = (10^{-2}, 10, 10^6)$ GeV and in Fig. (3.16) for $T_{\rm re} = (10^{-2}, 10)$ GeV with bosonic reheating (for fermionic reheating we only have closed contour for $T_{\rm re} = 10$ GeV). On the other hand, if $m_\phi^{\rm end} > m_{\rm x}^{\rm max} > m_{\rm x}^{\rm g,\ max}$, the critical cross-section disappears for higher mass values; for such cases, the maximum allowed DM mass is turned out to be $m_{\rm x}^{\rm g,\,max}$ $(m_{\rm x}^{max})$ for freeze-in (freeze-out) mechanism. Again, when $m_{\rm x}^{\rm max} > m_\phi^{\rm end}$ (it happens for higher reheating temperatures), one can find the freeze-in and freeze-out meet point, but the close contour is not formed. To this end, we would also like to point out that DM annihilation is dominant but under-abundant in the region outside the closed contours, whereas shaded regions are under-abundant for open contours. The minimum and the maximum DM masses up to which DM can give

present abundance are 10^{-7} and 7×10^{16} GeV, respectively. But, further, some parameter space is ruled out by the $\Delta N_{\rm eff}$ at BBN (yellow shaded region) and by unitarity bound of $\langle\sigma v\rangle \leq 8\pi/m_{\rm x}^2$[41, 206, 207]. When WIMP DM has a mass scale in the order of $T_{\rm BBN}$ or below, it violates the ΔN_{eff} bound at BBN. Again for WIMP DM, freeze-out happens during RD ($m_{\rm x} < T_{\rm re}$) if the mass scale lies above 10^5 GeV, it violates the unitarity bound of $\langle\sigma v\rangle$, which is shown by the light purple color region. Using two bounds, for the freeze-in mechanism, the maximum and the minimum allowed scalar (fermionic) DM masses are $10^{-7}(10^{-7})$ GeV, $4\times10^{16}(10^{15})$ GeV, respectively.

When $m_{\rm x} < T_{\rm re}$, we obtained some generic behavior of the DM abundance specifically for freeze-in production. Moreover, in the freeze-in production mechanism, if DM freezes during the radiation-dominated era, $\langle\sigma v\rangle$ behaves as $\propto 1/m_{\rm x}$ (see Eqs. 3.62, 3.66, 3.67). On the other hand, when $m_{\rm x} < T_{\rm re}$, for the freeze-out scenario, even though we do not have such a simple relation, it turned out that $\langle\sigma v\rangle$ generically increases slowly with increasing $m_{\rm x}$.

3.2.5 WIMPs: Experimental bounds and constraints on reheating

In this section, we would like to discuss our results from the perspective of some indirect experimental constraints with their future projected sensitivity limit on the DM cross-section and its mass plane. BBN constraints on the effective number of relativistic degrees of freedom ΔN_{eff} put direct constraints on the possible lower limit on the DM mass. In all the $\langle\sigma v\rangle$ Vs $m_{\rm x}$ plots, the yellow shaded regions depict the forbidden region coming from BBN bound. For WIMP-like DM, the condition of the ΔN_{eff} at BBN sets the approximate lowest possible DM mass $m_{\rm x} \sim T_{\rm BBN}$. In addition, for $2\to2$ scattering processes, the unitarity constraints further provide a bound on the maximum possible mass $m_{\rm x} \sim 10^5$ GeV for thermally produced DMs which freeze out, particularly during the RD era ($T_{\rm re} > m_{\rm x}$). However, if freeze-out occurs during reheating era ($T_{\rm re} < m_{\rm x}$), DM mass can be large, which is observed from the pink dotted curve of the third and fourth plot of Fig. 3.18. Therefore, reheating dynamics plays a significant role in setting the possible values of maximum DM mass, and it depends non-trivially on the inflationary parameter such as inflaton EoS. In Fig.(3.18), we have shown where our WIMP DM parameter space lies with the available sensitivity curve for indirect experiments within the mass range $(0.01-10^5)$ GeV such as (i) PLANCK CMB measurement [105] labeled as CMB shown in the light yellow region in the mass range of 0.1 to 10 GeV. (ii) Alpha magnetic spectrometer (AMS)-02 experiment [106, 107] provided cosmic ray positron (e^+) and antiproton ($\bar{p}$) data with unprecedented precision in the mass range $5\to10^3$ GeV. (iii) Combined bounds (labeled as Combined) from Fermi-LAT, HAWC, HESS, MAGIC, and VERITAS experiment [108] provided a upper limit on the DM annihilation cross-section in the case of two annihilation channels $\bar{b}b$ (purple dashed) and $\tau^+\tau^-$ (red dashed). (iv) CTA experiment [109] is a ground-based gamma-ray detector that could be capable of searching the WIMP DM at the TeV scale with large sensitivity. The brown (orange) dashed line shows its expected sensitivity for WIMP annihilation to $\bar{b}b$ (W^+W^-). In the near future, CTA might be able to probe a significant portion of TeV scale WIMP DM that freeze-out during either RD or reheating era.

In order to illustrate our result, we choose $w_\phi = (0.0, 0.20, 0.50)$ with the background of both bosonic (upper plot) and fermionic reheating (lower plot). The solid and dot-dashed lines are for $T_{\rm re} = T_{\rm BBN}, 10$ GeV, respectively. The black solid lines correspond to those DMs which freeze out during the RD era and for which one requires $\langle\sigma v\rangle \sim \mathcal{O}(10^{-9})$ GeV^{-2} to get correct present-day DM relic. Moreover, most of the parts of this black line are ruled out by the experimental bound (except CTA since it is a future experiment) as it

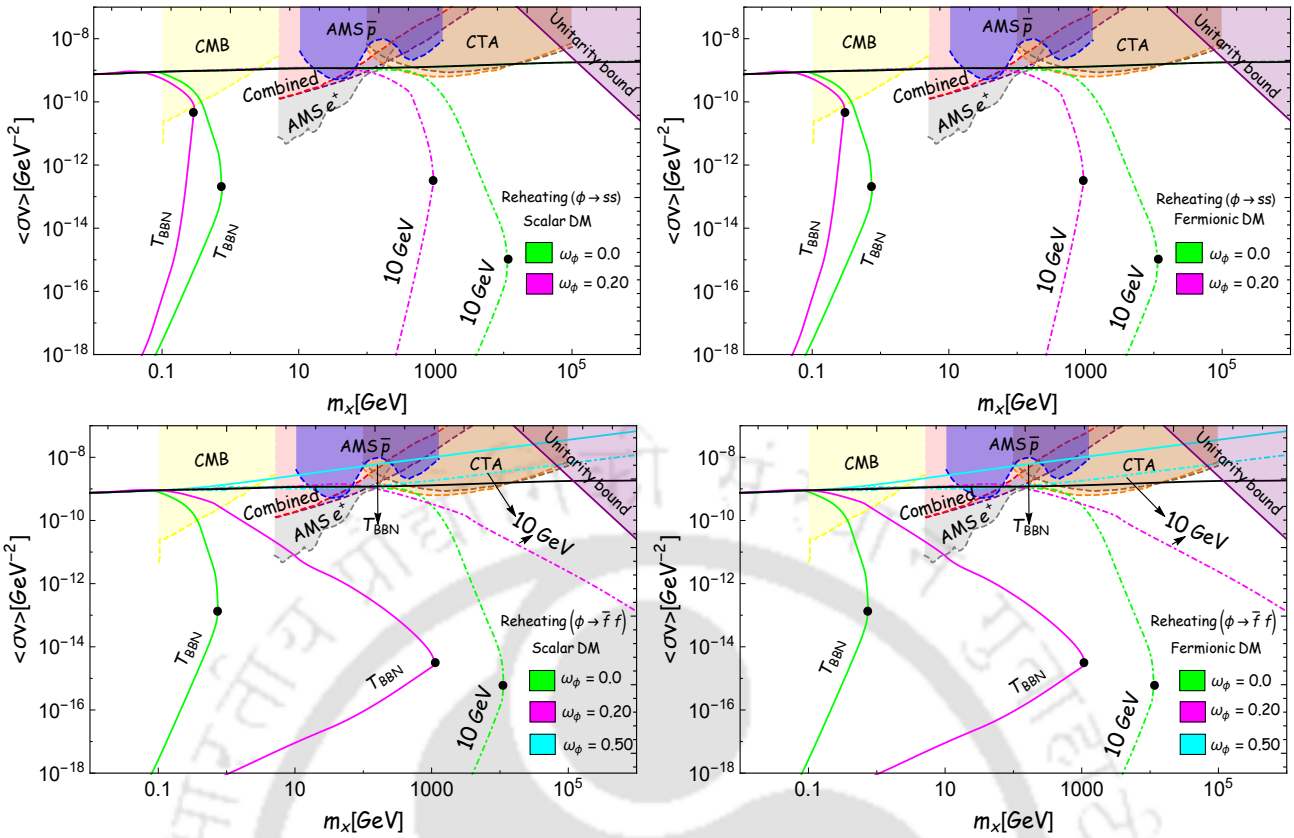

Figure 3.18: $\langle\sigma v\rangle$ Vs $m_{\rm x}$ for WIMP with experimental bound and future sensitivity for three different EoS $w_\phi = 0.0$(green), 0.20(magenta), 0.50(cyan). The upper plot for the bosonic reheating ($\phi \to ss$) and the left plot for the fermionic reheating $\phi \to \bar{f} f$. The left (right) plot for the scalar (fermionic) DM. The solid (dot-dashed) lines for $T_{\rm re} = T_{\rm BBN}(10)$ GeV and the small filled circle corresponding to the freeze-in and freeze-out meet point.

lies inside the regime of the sensitivity curves. For bosonic reheating, if $w_\phi = 0.5$, for both $T_{\rm re} = T_{\rm BBN}$ and $T_{\rm re} = 10$ GeV, the WIMPs follow the black line (see, for instance, first and the second plot of Fig. 3.18) to achieve the correct relic. For lower EoS, $w_\phi = 0.0, 0.20$ with low reheating temperature, WIMP-like DM freezes out during reheating, and one requires the lower value of $\langle\sigma v\rangle$ to obtain present-day DM relic. Therefore, the DM parameter space for freeze-out during reheating is still very much allowed. Thus in order to detect those DMs in the near future, we need to increase the sensitivity of the experiments.

3.3 Summary

The physics after the inflation is expected to play a significant role in every aspect of the late-time universe. Apart from the well-established correspondence between the physics of CMB and the early inflationary era, the intriguing effects of reheating on our present universe can not be avoided. Unlike inflation, broadly reheating is similar to the usual phases of the standard big-bang model, except for the fact that it occurs right after the end of inflation. Therefore, experimentally, it is challenging to look for its direct signatures. Further, it is generically argued that decoding any physics information is challenging because of non-linear thermalization processes during this phase. Over the years, however, the endeavor toward understanding this phase has gained significant interest due to its rich new physics content.

Reheating is the phase that naturally encodes the physics of the inflaton itself. The way inflaton decays into different fundamental fields is expected to be imprinted into different cosmological observables such as CMB anisotropy, DM, and gravitational waves in terms of new physics. Therefore, reheating could be an interesting playground for phenomenological studies of DM and inflation in a unified framework, which we have studied extensively in this thesis. We have addressed two main topics in this chapter:

Dynamics of reheating and its constraints: In the first section, we have studied in detail the dynamics of reheating separately through inflaton decaying into scalar field (bosonic reheating) and decaying into fermions (fermionic reheating). Apart from the direct decay term, we further include two important effects, namely, the universal gravity-mediated decay of the inflaton, and the finite temperature correction on different decay channels. The effects of gravitational decay have already been analyzed before [184]. It has been shown that purely gravitational reheating sets a lower bound on the reheating temperature when the inflaton EoS satisfies $w_\phi \gtrsim 0.65$. Such a lower limit on the reheating temperature further sets constraints on the inflaton direct coupling parameter below which gravity-mediated decay will be the dominant channel for the reheating process (see the cyan shaded region in Fig. 3.2, 3.7). The cyan zone of these plots is the important outcome of our present analysis. There is an EoS-dependent critical values of the coupling constant below which reheating dynamics become completely independent of direct inflaton coupling. Combining this gravitational decay with the finite temperature correction in the direct decay, we observe intriguing interplay among those different physical effects during reheating. The thermal effect is expected to influence the dynamics when radiation temperature satisfies the condition $T_{\rm rad} > m_\phi(t)$. Depending on the strength of the inflaton-radiation coupling, we observed several interesting reheating histories which have not been reported earlier. Let us outline the main interesting outcomes in the following discussion

♠ We particularly observed a new reheating history for which reheating temperature ($T_{\rm re}$) and maximum radiation temperature ($T_{\rm rad}^{\rm max}$) coincide when the EoS $w_\phi > (1/3, 3/5)$ for two different bosonic decay channels $\phi \to ss$ and $\phi\phi \to ss$ (see, Fig. 3.4 for depiction) respectively.

♠ Another interesting observation in the case of fermionic reheating is that when EoS lies above 5/9(7/15), maximum radiation production takes place at the initial stage of reheating. In this respect, therefore, fermionic reheating turns out to be qualitatively similar to gravitational reheating. The bosonic reheating through $\phi\phi \to ss$ decay process deserves special mention with regard to the fact that, if $w_\phi < 3/13(1/5)$ with (without) thermal effect, successful reheating can not be achieved (see the grey shaded region of Fig. 3.2).

♠ Thermal correction in the production rate significantly modifies the production rate (enhances for bosonic channels and diminishes for fermionic channel), which is imprinted in the radiation temperature evolution. Better visualization of how the thermal correction affects the evolution of the radiation temperature with respect to scale factor is shown in Tables-3.1, 3.3.

♠ The phenomenological constraints on the inflaton coupling are shown in Fig. 3.2 for bosonic reheating and in Fig. 3.7 for fermionic reheating. The plots depict an interesting connection between the inflaton coupling parameters (g_i^r,h^r) and inflationary parameter n (power of the inflaton potential at its minimum), which is translated into effective EoS w_ϕ through the relation $(n-2)/(n+2)$ during reheating. Contrary to the earlier claim [194], we observe that the thermal effect appeared to be most significant at low reheating temperatures for non-zero inflaton equation state, $w_\phi = (0.20, 0.50, 0.82, 0.99)$ (see solid and dotted lines in Fig. 3.6, 3.10), for which inflaton mass undergoes non-trivial evolution.

♠ For higher equation state ($w = 0.82, 0.99$), the gravitational reheating has been observed to give a lower limit on the reheating temperature $(10^3, 10^6)$ GeV, which is associated with the fixed scalar spectral index

$n_s = 0.9685$ and 0.9681, respectively. When $n_s(T_{re})$ reaches these values, the coupling parameter tends towards zero, i.e., gravitational scattering solely controls the reheating dynamics.

DM phenomenology: In the second half of the chapter, we have extensively analyzed DM phenomenology in the context of production during reheating. We have discussed all known DM production mechanisms, namely: (i) gravitational production from both the inflaton and radiation scattering, (ii) production from direct inflaton decay through various decay channels, (iii) production from the thermal bath through effective average cross-section times velocity $\langle\sigma v\rangle$ in both freeze-in and freeze-out mechanism with assuming $\langle\sigma v\rangle$ as a free parameter. The universal gravitational production of DM is always incorporated throughout our analysis. In the following, we summarize some of the main results and important outcomes of our analysis:

♠ When DMs are produced from direct decay of inflaton (see Fig. 3.12), the final abundance appears to depend only on the coupling strength, DM mass (m_x), and reheating temperature (T_{re}). We call this FIMP-like DM. For a fixed inflation EoS and reheating temperature, the minimum DM mass is fixed by the $\Delta N_{\rm eff}$ bound at BBN, and the maximum allowed DM mass is fixed by either gravitational decay or the inflaton mass.

♠ For the production of DM from the thermal bath, we have considered both freeze-in (FIMP) and freeze-out (WIMP) mechanisms. Since the DM is produced from the thermal bath, the DM production strictly depends on the evolution of the bath temperature. Due to the thermal effect, the bath temperature evolves differently during reheating, and the thermal effect directly influences DM production and its final abundance.

♠ In the context of both bosonic and fermionic reheating, we have discussed the DM production (both FIMP and WIMP) and derived the analytical expressions of the DM abundance. In Section-3.2.4, we have shown in detail the DM parameter space ($\langle\sigma v\rangle$, m_x) for both FIMP and WIMP production mechanisms. Interestingly, the lowest possible DM mass for both the mechanisms assumes a universal theoretical value $m_x \sim 10^{-7}$ GeV, which is independent of T_{re}, w_ϕ and the nature of DM. However, constraints from different physical considerations such as lyman-α, ΔN_{eff} bounds may not satisfy this universal bound. For WIMPs, the minimum allowed value of DM mass is $T_{\rm BBN}$ due to restriction from the ΔN_{eff}. Depending on the reheating parameters such as reheating temperature, inflation EoS w_ϕ, and the background reheating dynamics, a maximum allowed DM mass also exists. In most of the scenarios, the maximum allowed mass is given by a particular mass scale where there is a transition happening from freeze-in to freeze-out mechanism or vice versa (see, for instance, the black circle of Figs. 3.15-3.17).

♠ For the DM production from the radiation bath, if one incorporates the unitarity bound, the DM mass lies above 10^5 GeV is ruled out in most of the cases. However, for both fermionic and bosonic reheating, we still have some parameter space even for $m_x > 10^5$ GeV (see, for instance, the third and fourth plot of Fig. 3.18), which are consistent with the unitarity bound and satisfies the correct relic. The reason behind this is that if freeze-out happens during reheating ($m_x > T_{re}$), the freeze-out temperature shifts towards the maximum radiation temperature with the increasing mass, and we need to lower the cross-section to meet the correct relic. Such lowering of the cross-section with higher DM mass ($m_x > 10^5$ GeV), therefore, naturally evades the aforementioned unitarity bound.

♠ Important distinction of fermionic decay width from that of the bosonic one is its proportional behavior in terms of inflaton mass, which dilutes faster with increasing w_ϕ. Due to this, one finds a critical $w_\phi \simeq 7/15$ considering the thermal effect from the beginning of reheating, below which the inflaton decay process occurs throughout and above which it occurs at the beginning of the reheating. These two different reheating histories have had their distinct effects on the DM production, which is reflected on $\langle\sigma v\rangle$ Vs m_x

parameter plane (see, for instance, third and forth plot of Figs. 3.16, and fifth and sixth plots of 3.17). This phenomenon can also be explained from the Eqs. 3.99-3.102. For $w_\phi = 0.5 > 7/15$, a fixed value of $T_{\rm re} < m_{\rm x}$ and $T_f \sim m_f$, the relic abundance behaves as $\Omega_{\rm x} h^2 \propto m_{\rm x}^{1/4}/\langle\sigma v\rangle$ (see Eq. 3.99), which implies that with increasing $m_{\rm x}$, $\langle\sigma v\rangle$ increases (see, for instance, fifth and sixth plots of Fig. 3.17). However, for $w_\phi = 0 < 7/15$, for a fixed $T_{\rm re}$ if freeze-out happens during reheating one has following relation $m_{\rm x} \propto \langle\sigma v\rangle^{-3}$ (see, for instance, Eq. 3.102). This clearly suggests that with increasing DM mass above reheating energy scale, $\langle\sigma v\rangle$ decreases (see, for instance, Fig. 3.15).

♠ The oscillating inflaton condensate may be fragmented due to self-resonance (see, for instance, Refs. [13, 14]), which is expected to cause reheating dynamics non-trivial. It is observed that such an effect is not significant for $n = 1 (w_\phi = 0)$. However, for higher n, self-resonance effects turned out to be important and may lead to RD universe depending on both α and n values. When $\alpha << 1/6$, self-resonance is efficient, and the RD universe is established within less than an e-fold of expansion after inflation end. Whereas for $\alpha > 1/6$ and $n > 2$, the self-resonance effect increasingly becomes inefficient, and the inflaton condensate remains intact for a long time without any other decay channel. It is in this parlance our present study is important. In our study, we considered $\alpha = 1$ and further checked that the final results, namely the estimates of reheating temperature for different inflaton couplings and the whole DM parameters space, are not much sensitive with the increase of α within the limit set by recent Planck and BICEP/*keck* data [192, 193]. For higher α values, even though the self-resonance effect would be inefficient (as pointed out in [13, 14]), it may have a non-trivial effect on the reheating parameter space (see Addenda-E).

Addenda

A Bosonic Reheating: analytical studies

A.1 Without thermal effect

During reheating, the exponential decay term associated with the evolution of the inflaton energy density is always sub-dominant compared to the dilution due to the expansion. Thus, we can safely approximate the solution of Eq.(3.5a) as

$$\rho_\phi = \rho_\phi^{\rm end} A^{-3(1+w_\phi)} e^{-(\Gamma_s+\Gamma_{\phi\phi\to RR})(t-t_{\rm end})} \simeq \rho_\phi^{\rm end} A^{-3(1+w_\phi)} \tag{3.105}$$

where $\rho_\phi^{\rm end}$ and $t_{\rm end}$ be the inflaton energy density, and cosmic time at the inflation end. The evolution equation of radiation energy density can be written as (see, for instance, Eq. 3.5b)

$$d(\rho_s^r A^4) = \Gamma_s \rho_\phi (1+w_\phi) A^4 \frac{da}{AH} \tag{3.106}$$

In the limit of $T_{\rm rad} \ll m_\phi(t)$, finite temperature correction to the decay width [47] can be safely ignored (see, Eq. 3.2)

$$\Gamma_s = \begin{cases} \Gamma_{\phi\to ss} \simeq \frac{(g_1^r)^2}{8\pi m_\phi(t)} & \text{for } g_1^r \phi s^2 \\ \Gamma_{\phi\phi\to ss} \simeq \frac{(g_2^r)^2 \rho_\phi(t)}{8\pi m_\phi^3(t)} & \text{for } g_2^r \phi^2 s^2. \end{cases} \tag{3.107}$$

Where $m_\phi(t)$ be the time-dependent inflaton mass which is defined as $m_\phi^2(t) = V''(\phi_0(t))$. Since reheating happens near the minimum of the potential, we can expand the inflaton potential (Eq. 5.6) in the limit $\phi \ll M_p$ as

$$V(\phi) \simeq \Lambda^4 \xi^{2n} \phi^{2n} \tag{3.108}$$

where $\xi = \sqrt{\frac{2}{3\alpha}} \frac{1}{M_p}$. The field-dependent mass becomes,

$$m_\phi^2 = V''(\phi_0) \simeq 2n(2n-1)\Lambda^4 \xi^2 \left(\frac{V(\phi_0)}{\Lambda^4}\right)^{1-\frac{1}{n}}. \tag{3.109}$$

Using the envelope approximation at any instant of time, the envelope value of the field ϕ_0 must satisfy $V(\phi_0) \simeq \rho_\phi(t)$. Under this approximation, the inflaton mass at the inflation end is given by

$$(m_\phi^{\rm end})^2 \simeq 2n(2n-1)\Lambda^4 \xi^2 \left(\frac{\rho_\phi^{\rm end}}{\Lambda^4}\right)^{1-\frac{1}{n}}. \tag{3.110}$$

After utilizing Eqns.(3.109), (3.110) and (3.105), one can find the evolution of the inflaton mass as

$$m_\phi^2(t) = (m_\phi^{\rm end})^2 \left(\frac{\rho_\phi(t)}{\rho_\phi^{\rm end}}\right)^{1-\frac{1}{n}} \simeq (m_\phi^{\rm end})^2 A^{-6w_\phi}. \tag{3.111}$$

Inserting the above equation in Eqn.(3.107), we can re-write decay width in terms of the scale factor as

$$\Gamma_{\phi\to ss} = \frac{(g_1^r)^2}{8\pi m_\phi^{\rm end}} A^{3w_\phi}, \Gamma_{\phi\phi\to ss} = \frac{(g_2^r)^2 \rho_\phi^{\rm end}}{8\pi (m_\phi^{\rm end})^3} A^{-3(1-2w_\phi)}. \tag{3.112}$$

Upon substitution of the above decay width (Eq. 3.112) in Eq. 3.106, we have the evolution of the energy density associated with the bosonic non-gravitational channel as

$$d(\rho_s^r A^4) = \begin{cases} \frac{3M_p^2(1+w_\phi)H_{\rm end}}{8\pi m_\phi^{\rm end}}(g_1^r)^2 A^{\frac{3}{2}(1+w_\phi)}\,dA & \text{for } g_1^r\phi s^2, \\ \frac{9M_p^4(1+w_\phi)H_{\rm end}^3}{8\pi (m_\phi^{\rm end})^3}(g_2^r)^2 A^{\frac{3}{2}(3w_\phi-1)}\,dA & \text{for } g_2^r\phi^2 s^2, \end{cases} \tag{3.113}$$

where, $H_{\rm end} = \sqrt{\rho_\phi^{\rm end}/3M_p^2}$. Since during reheating, the background dynamics is mainly governed by the inflaton field, we approximate $H \simeq \sqrt{\rho_\phi/3M_p^2} = H_{\rm end}(a/a_{\rm end})^{-(3+3w_\phi)/2}$, which is used to determine the above equation. After straightforward integration of Eq.(3.113), we obtain,

$$\rho_s^r(A) = \begin{cases} \frac{6M_p^2(1+w_\phi)H_{\rm end}(g_1^r)^2}{8\pi(5+3w_\phi)m_\phi^{\rm end}A^4}\left(A^{\frac{5+3w_\phi}{2}}-1\right) & \text{for } g_1^r\phi s^2, \\ \frac{9M_p^4(1+w_\phi)H_{\rm end}^3(g_2^r)^2}{4\pi(9w_\phi-1)(m_\phi^{\rm end})^3A^4}\left(A^{\frac{9w_\phi-1}{2}}-1\right) & \text{for } g_2^r\phi^2 s^2. \end{cases} \tag{3.114}$$

We will follow the similar procedure to find the expression of gravitational radiation energy density, and the production width associated with the gravitational sector can be expressed as

$$\Gamma_{\phi\phi\to RR} = \frac{3M_p^2H_{\rm end}^2 m_\phi^{\rm end}}{1024\pi M_p^4}A^{-3-6w_\phi} \tag{3.115}$$

Combining Eqns.(3.5c) and (3.115), we have the following solution for the radiation energy density associated with the gravitational sector

$$\rho_{\rm gr}^r(A) = \frac{9(1+w_\phi)H_{\rm end}^3 m_\phi^{\rm end}}{512\pi(1+15w_\phi)A^4}\left(1-A^{-\frac{1+15w_\phi}{2}}\right). \tag{3.116}$$

The total energy density of the radiation bath is simply sum of the contribution from both gravitational and non-gravitational sector $\rho_{tot}^r(A) = \rho_s^r(A) + \rho_{\rm gr}^r(A)$ and the corresponding radiation temperature $T_{\rm rad} = \left(30\rho_{\rm tot}^r/(\pi^2 g_{\star r})\right)^{1/4}$. Where $g_{\star r}$ is the total relativistic degrees of freedom associated with the thermal bath. Now, let us find the maximum radiation energy density for both gravitational and non-gravitational sectors separately.

At the beginning of the reheating, the individual components of radiation (both non-gravitational and gravitational) set to be $\rho_s^r(A=1) = \rho_{\rm gr}^r(A=1) = 0$. Within a very short time, during the initial stage of reheating, both the components attain a maximum value when $\frac{d\rho_{s/gr}^r}{dA} = 0$, which is associated with a specific value of the scale factor

$$A_{\rm max} = \begin{cases} \left[\frac{8}{3(1-w_\phi)}\right]^{\frac{2}{5+3w_\phi}} & \text{for } g_1^r\phi s^2, \\ \left[\frac{9(1-w_\phi)}{8}\right]^{\frac{2}{1-9w_\phi}} & \text{for } g_2^r\phi^2 s^2, \\ \left[\frac{9+15w_\phi}{8}\right]^{\frac{2}{1+15w_\phi}} & \text{for gravitational reheating}\ . \end{cases} \tag{3.117}$$

That, in turn, fixes the maximum value of the radiation component as

$$\rho_s^{r,\max} = \begin{cases} \frac{6M_p^2(1+w_\phi)H_{\rm end}}{8\pi m_\phi^{\rm end}(5+3w_\phi)}(g_1^r)^2\left[\left(\frac{8}{3(1-w_\phi)}\right)^{\frac{3(w_\phi-1)}{(5+3w_\phi)}}-\left(\frac{8}{3(1-w_\phi)}\right)^{-\frac{8}{5+3w_\phi}}\right] & \text{for } g_2^r\phi^2 s^2, \\ \frac{9M_p^4(1+w_\phi)H_{\rm end}^3(g_2^r)^2}{4\pi(9w_\phi-1)(m_\phi^{\rm end})^3A^4}\left[\left(\frac{9(1-w_\phi)}{8}\right)^{\frac{9(w_\phi-1)}{1-9w_\phi}}-\left(\frac{9(1-w_\phi)}{8}\right)^{\frac{-8}{1-9w_\phi}}\right] & \text{for } g_2^r\phi^2 s^2, \end{cases} \tag{3.118}$$

$$\rho_{\rm gr}^{r,\rm max}=\frac{9(1+w_\phi)H_{\rm end}^3 m_\phi^{\rm end}}{512\pi(1+15w_\phi)}\left[\left(\frac{9+15w_\phi}{8}\right)^{-\frac{8}{1+15w_\phi}}-\left(\frac{9+15w_\phi}{8}\right)^{-\frac{9+15w_\phi}{1+15w_\phi}}\right]. \tag{3.119}$$

Since the gravitational scattering process is a kind of irreducible background, which will be present regardless of the coupling-dependent decay channel. However, a critical coupling exists $\mathscr{G}_{ci}^1$, above which the non-gravitational decay channel always controls the reheating dynamics. The maximum gravitational production happens initially, and the temperature associated with it falls off faster than the non-gravitational one. Thus, the critical coupling $\mathscr{G}_{ci}^1$, above which value the non-gravitational sector dominates throughout reheating, is defined from the condition $\rho_s^{r,max}=\rho_{\rm gr}^{r,\rm max}$. Since in the gravitational sector domination, the maximum radiation temperature comes out to be $10^{11}\rightarrow 10^{12}$ GeV, which is less than the inflaton mass $m_\phi(A_{\rm max})$; thermal effect not in working situation. Therefore the expression for critical coupling for with and without thermal effect be the same $\mathscr{G}_{ci}^{1,th}=\mathscr{G}_{ci}^1$ (see, for instance, Eq. 3.14). In the limit of $g_{ci}>\mathscr{G}_{ci}^1$, the maximum radiation temperature is followed by Eq. 3.118, whereas, for $g_{ci}<\mathscr{G}_{ci}^1$ gravitational sector determines the maximum radiation temperature (see, Eq. 3.119).

If the bosonic coupling strength is less than $\mathscr{G}_{ci}^1$, the gravitational sector can not reheat the universe before BBN energy scale for the EoS $w_\phi<0.65$. Therefore those (g_i^r,w_ϕ) parameter space are forbidden from BBN constraints (see, for instance, light red region of Fig. 3.2). However, for $w_\phi>0.65$, the gravitational sector can successfully reheat the universe and sets the lower bound of reheating temperature that is defined in Eq.(3.28). There exists another critical coupling parameter $\mathscr{G}_{ci}^2$, indicating below which only the gravitational sector defines the reheating temperature (see, for instance, light cyan region of Fig. 3.2). We have the expression of $\mathscr{G}_{ci}^2$ as follows

$$\mathscr{G}_{ci}^2=\begin{cases}\left[\left(\frac{3(5+3w_\phi)(H_{\rm end}m_\phi^{\rm end})^2}{128M_p^2(1+15w_\phi)}\right)\left(\frac{512\pi M_p^2(1+15w_\phi)}{3H_{\rm end}m_\phi^{\rm end}(1+w_\phi)}\right)^{\frac{5+3w_\phi}{2(3w_\phi-1)}}\right]^{1/2} & \text{for } g_1^r\phi s^2 \text{ and } w_\phi\geq 0.65\,,\\ \left[\left(\frac{(9w_\phi-1)(m_\phi^{\rm end})^4}{64M_p^4(1+15w_\phi)}\right)\left(\frac{512\pi M_p^2(1+15w_\phi)}{3H_{\rm end}m_\phi^{\rm end}(1+w_\phi)}\right)^{\frac{1-9w_\phi}{2(3w_\phi-1)}}\right]^{1/2} & \text{for } g_2^r\phi^2 s^2 \text{ and } w_\phi\geq 0.65\,.\end{cases} \tag{3.120}$$

and when the gravitational sector controls the reheating temperature, the reheating temperature can be expressed as

$$T_{\rm re}^{\rm gr}=\left(\frac{9H_{\rm end}^3 m_\phi^{\rm end}(1+w_\phi)}{512\epsilon\pi(1+15w_\phi)(A_{\rm re}^{\rm gr})^4}\right)^{1/4},A_{\rm re}^{\rm gr}=\left(\frac{512\pi M_p^2(1+15w_\phi)}{3H_{\rm end}m_\phi^{\rm end}(1+w_\phi)}\right)^{\frac{1}{3w_\phi-1}}, \tag{3.121}$$

where $A_{\rm re}^{\rm gr}$ is the normalized scale factor at the end of gravitational reheating. When the coupling parameter $g_i^r>\mathscr{G}_{ci}^2$, the decay channel controls the reheating temperature and that can be defined as

$$T_{\rm re}=\begin{cases}\left(\frac{6M_p^2(1+w_\phi)H_{\rm end}}{8\pi\epsilon(5+3w_\phi)m_\phi^{\rm end}}(g_1^r)^2\right)^{1/4}A_{re}^{-\frac{3}{8}(1-w_\phi)} & \text{for } g_1^r\phi s^2\,,\\ \left(\frac{9M_p^4(1+w_\phi)H_{\rm end}^3}{4\pi\epsilon(9w_\phi-1)(m_\phi^{\rm end})^3}(g_2^r)^2\right)^{1/4}A_{re}^{\frac{9(w_\phi-1)}{8}} & \text{for } g_2^r\phi^2 s^2\,,\end{cases} \tag{3.122}$$

where

$$A_{\rm re}=\begin{cases}\left(\frac{4\pi(5+3w_\phi)H_{\rm end}m_\phi^{\rm end}}{(1+w_\phi)(g_1^r)^2}\right)^{\frac{2}{3+9w_\phi}} & \text{for } g_1^r\phi s^2\,,\\ \left(\frac{4\pi(9w_\phi-1)(m_\phi^{\rm end})^3}{3(1+w_\phi)M_p^2H_{\rm end}(g_2^r)^2}\right)^{\frac{2}{3(5w_\phi-1)}} & \text{for } g_2^r\phi^2 s^2\,.\end{cases} \tag{3.123}$$

A.2 With thermal effect

If the radiation temperature is much smaller than the inflaton mass scale, we can safely use the zero-temperature decay width. But, for the cases where radiation temperature is much higher than the inflaton mass scale, the thermal effect becomes very efficient. In the limit $T_{\rm rad} >> m_\phi(t)$, the inflaton decay rate for different decay channels can be expressed as

$$\begin{aligned}\Gamma_{\phi\to ss} &= \frac{(g_1^r)^2}{8\pi m_\phi(t)}\frac{4T_{\rm rad}}{m_\phi(t)},\\ \Gamma_{\phi\phi\to ss} &= \frac{(g_2^r)^2\rho_\phi(t)}{8\pi(m_\phi(t))^3}\frac{2T_{\rm rad}}{m_\phi(t)}.\end{aligned} \tag{3.124}$$

When the bosonic non-gravitational channel dominates over the gravitational one, we can approximate radiation temperature as $T_{\rm rad} = \left(\frac{\rho^r_{\rm tot}}{\epsilon}\right)^{\frac{1}{4}} \simeq \left(\frac{\rho^r_s}{\epsilon}\right)^{\frac{1}{4}}$,where $\epsilon = \frac{\pi^2}{30}g_{\star r}$. And under this consideration utilizing Eq.(3.111), one can find the decay width as

$$\begin{aligned}\Gamma_{\phi\to ss} &= \frac{4(g_1^r)^2}{8\pi\epsilon^{1/4}(m_\phi^{\rm end})^2}\frac{\left(\rho^r_s(A)A^4\right)^{1/4}}{A^{1-6w_\phi}}\\ \Gamma_{\phi\phi\to ss} &= \frac{2(g_2^r)^2}{8\pi\epsilon^{1/4}(m_\phi^{\rm end})^4}\frac{\left(\rho^r_s(A)A^4\right)^{1/4}}{A^{3-9w_\phi}}\end{aligned} \tag{3.125}$$

Further Combining Eq.(3.106) and Eq. (3.125), we have

$$d(\rho^r_s(A)A^4) = \begin{cases}\frac{12(g_1^r)^2M_p^2(1+w_\phi)H_{\rm end}}{8\pi\epsilon^{1/4}(m_\phi^{\rm end})^2}A^{\frac{1+9w_\phi}{2}}\left(\rho^r_s(A)A^4\right)^{1/4}dA,\\ \frac{18(g_2^r)M_p^4(1+w_\phi)H^3_{\rm end}}{8\pi\epsilon^{1/4}(m_\phi^{\rm end})^4}A^{\frac{5(3w_\phi-1)}{2}}\left(\rho^r_s(A)A^4\right)^{1/4}dA.\end{cases} \tag{3.126}$$

Straightforward integration of the above equation, radiation energy density takes the following form

$$\rho^r_s(A) = \left[\frac{3M_p^2(1+w_\phi)H_{\rm end}}{4\pi\epsilon^{1/4}(1+3w_\phi)(m_\phi^{\rm end})^2A^3}(g_1^r)^2\left(A^{\frac{3(1+3w_\phi)}{2}}-1\right)\right]^{4/3} \quad \text{for } g_1^r\phi s^2, \tag{3.127}$$

$$\rho^r_s(A) = \left[\frac{9M_p^4(1+w_\phi)H^3_{\rm end}}{8\pi\epsilon^{1/4}(5w_\phi-1)(m_\phi^{\rm end})^4A^3}(g_2^r)^2\left(A^{\frac{3(-1+5w_\phi)}{2}}-1\right)\right]^{4/3} \quad \text{for } g_2^r\phi^2 s^2. \tag{3.128}$$

These aforementioned equations represent the modified expression of the bosonic radiation energy density when the thermal effect is functional ($T_{\rm rad} >> m_\phi(t)$). The maximum value of this radiation component associated with the scale factor $A_{\rm max}$ at which the $d\rho^r_s/dA = 0$. We have the maximum radiation energy density

$$\rho^{r,\max}_s \simeq= \begin{cases}\left[\frac{3M_p^2(1+w_\phi)H_{\rm end}}{4\pi\epsilon^{1/4}(1+3w_\phi)(m_\phi^{\rm end})^2}(g_1^r)^2\left\{\left(\frac{2}{1-3w_\phi}\right)^{\frac{3w_\phi-1}{3+9w_\phi}}-\left(\frac{2}{1-3w_\phi}\right)^{\frac{-2}{3+9w_\phi}}\right\}\right]^{4/3} & \text{for } g_1^r\phi s^2,\\ \left[\frac{9M_p^4(1+w_\phi)H^3_{\rm end}}{8\pi\epsilon^{1/4}(5w_\phi-1)(m_\phi^{\rm end})^4}(g_2^r)^2\left\{\left(\frac{2}{3-5w_\phi}\right)^{\frac{5w_\phi-3}{5w_\phi-1}}-\left(\frac{2}{3-5w_\phi}\right)^{\frac{-2}{5w_\phi-1}}\right\}\right]^{4/3} & \text{for } g_2^r\phi^2 s^2,\end{cases} \tag{3.129}$$

and the scale factor $A_{\rm max}$ associated with the maximum radiation energy density can be expressed as

$$A_{\rm max} = \begin{cases}\left(\frac{2}{1-3w_\phi}\right)^{\frac{2}{3(1+3w_\phi)}} & \text{for } g_1^r\phi s^2,\\ \left(\frac{2}{3-5w_\phi}\right)^{\frac{2}{3(5w_\phi-1)}} & \text{for } g_2^r\phi^2 s^2.\end{cases} \tag{3.130}$$

Now let us define reheating temperature in this context. For the coupling $g_1^r \phi s^2$, we have

$$T_{\rm re} = \left[\frac{3M_p^2(1+w_\phi)H_{\rm end}(g_1^r)^2}{4\pi\epsilon(1+3w_\phi)(m_\phi^{\rm end})^2} A_{\rm re}^{-\frac{3}{2}(1-3w_\phi)}\right]^{1/3}, A_{\rm re} = \left(\frac{4\pi(1+3w_\phi)(m_\phi^{\rm end})^2}{(1+w_\phi)(g_1^r)^2(\frac{\epsilon}{3})^{1/4}}\left(\frac{H_{\rm end}}{M_p}\right)^{1/2}\right)^{\frac{4}{3(1+9w_\phi)}}. \tag{3.131}$$

Whereas for the coupling $g_2^r\phi^2 s^2$

$$T_{\rm re} = \left[\frac{9M_p^4(1+w_\phi)H_{\rm end}^3(g_2^r)^2}{8\pi\epsilon(5w_\phi-1)(m_\phi^{\rm end})^4} A_{re}^{\frac{-3(3-5w_\phi)}{2}}\right]^{1/3}, A_{\rm re} = \left(\frac{8\pi(27\epsilon)^{1/4}(5w_\phi-1)}{9(1+w_\phi)M_p^{5/2}H_{end}^{3/2}}(m_\phi^{\rm end})^4\right)^{\frac{4}{3(13w_\phi-3)}}. \tag{3.132}$$

B Fermionic Reheating: analytical studies

B.1 Without thermal effect

In the absence of thermal effect, the decay width for $\phi \to \bar{f}f$ can be written as [47]

$$\Gamma_{\phi\to\bar{f}f} = \frac{(h^r)^2}{8\pi} m_\phi(t) \simeq \frac{(h^r)^2}{8\pi} m_\phi^{\rm end} A^{-3w_\phi}. \tag{3.133}$$

To derive the above equation, we utilized Eq. 3.111. Upon substitution of the above decay width in Eq. 3.5b, the evolution equation for the radiation energy density arising from the fermionic non-gravitational coupling can be expressed as

$$d\left(\rho_f^r(A)A^4\right) = \frac{3M_p^2(1+w_\phi)m_\phi^{\rm end}H_{\rm end}}{8\pi}(h^r)^2 A^{\frac{3}{2}(1-3w_\phi)}\,dA\,. \tag{3.134}$$

After integrating the above equation, we have

$$\rho_f^r(A) = \frac{6M_p^2(1+w_\phi)m_\phi^{\rm end}H_{\rm end}}{8\pi(5-9w_\phi)A^4}(h^r)^2(A^{\frac{5-9w_\phi}{2}}-1). \tag{3.135}$$

Similarly, we can find $\rho_{\rm gr}^r$, the energy density associated with the gravitational sector (see, for instance, Eq. 3.116). We can follow the Bosonic reheating section in Addenda-A for detailed derivation. The total energy density of the radiation bath is simply sum of the radiation components originated from both gravitational and non-gravitational sector, $\rho_{tot}^r(A) = \rho_f^r(A) + \rho_{\rm gr}^r(A)$

$$\rho_{tot}^r(A) = \frac{6M_p^2(1+w_\phi)m_\phi^{\rm end}H_{\rm end}}{8\pi(5-9w_\phi)A^4}(h^r)^2(A^{\frac{5-9w_\phi}{2}}-1) + \frac{9(1+w_\phi)(1+\gamma)H_{\rm end}^3 m_\phi^{\rm end}}{512\pi(1+15w_\phi)A^4}\left(1-A^{-\frac{1+15w_\phi}{2}}\right), \tag{3.136}$$

and the radiation temperature $T_{\rm rad} = \left(\rho_{tot}^r/\epsilon\right)^{1/4}$. After the end of the inflation, the energy budget associated with the thermal bath begins to increase from zero initial value and attain a maximum value when $d\rho_{f/gr}^r/dA = 0$, then starts to fall off. We obtain the maximum radiation energy density corresponding to both gravitational and non-gravitational sector as

$$\rho_{f/gr}^{r,max} = \begin{cases} \left(\frac{6M_p^2(1+w_\phi)m_\phi^{\rm end}H_{\rm end}}{8\pi(5-9w_\phi)}(h^r)^2\right)\left[\left(\frac{8}{3+9w_\phi}\right)^{\frac{-3(1+3w_\phi}{5-9w_\phi}} - \left(\frac{8}{3+9w_\phi}\right)^{\frac{-8}{5-9w_\phi}}\right] & \text{for } h^r\phi\bar{f}f\,, \\ \frac{9(1+w_\phi)H_{\rm end}^3 m_\phi^{\rm end}}{512\pi(1+15w_\phi)}\left[\left(\frac{9+15w_\phi}{8}\right)^{-\frac{8}{1+15w_\phi}} - \left(\frac{9+15w_\phi}{8}\right)^{-\frac{9+15w_\phi}{1+15w_\phi}}\right] & \text{for gravitational scattering}. \end{cases} \tag{3.137}$$

And the scale factor correlated with these maximum energy densities turns out as

$$A_{\rm max} = \begin{cases} (\frac{8}{3+9w_\phi})^{2/5-9w_\phi} & \text{for } h^r\phi\bar{f}f\,, \\ \left[\frac{9+15w_\phi}{8}\right]^{\frac{2}{1+15w_\phi}} & \text{for gravitational scattering} \end{cases}. \tag{3.138}$$

Since the gravitational scattering process is always present, there exists a critical value of coupling below which the gravitational sector always defines maximum radiation temperature $T_{\rm rad}^{\rm max}$. Equating $\rho_f^{r,max} = \rho_{\rm gr}^{r,\rm max}$, one can find the expression for the critical coupling for fermionic reheating as

$$\mathscr{H}_c = \left[\frac{3(5-9w_\phi)H_{\rm end}^2}{128M_p^2(1+15w_\phi)}\frac{\left[\left(\frac{9+15w_\phi}{8}\right)^{-\frac{8}{1+15w_\phi}} - \left(\frac{9+15w_\phi}{8}\right)^{-\frac{9+15w_\phi}{1+15w_\phi}}\right]}{\left[\left(\frac{8}{3(1+3w_\phi)}\right)^{-\frac{3(1+3w_\phi)}{5-9w_\phi}} - \left(\frac{8}{3(1+3w_\phi)}\right)^{-\frac{8}{5-9w_\phi}}\right]}\right]^{1/2} \qquad w_\phi \neq 5/9\,. \tag{3.139}$$

Therefore, in the limit of $h^r > \mathscr{H}_c$, $T_{\rm rad}^{\rm max}$ can be approximated as $T_{\rm rad}^{\rm max} \simeq \left(\rho_f^{r,max}/\epsilon\right)^{1/4}$, whereas for $h^r < \mathscr{H}_c$, $T_{\rm rad}^{\rm max} \simeq \left(\rho_{\rm gr}^{r,\rm max}/\epsilon\right)^{1/4}$.

Another interesting fact is that the behavior of the radiation component associated with the non-gravitational sector is different for $w_\phi < 5/9$ and $w_\phi > 5/9$ (see, for instance, Eq. 3.33). For $w_\phi > 5/9$, the radiation component decays as A^{-4} as the gravitational sector. Thus, if your Yukawa coupling strength $h^r < \mathscr{H}_c$ and $w_\phi > 0.65$, then reheating dynamics is governed by the gravitational sector, which is termed as gravitational reheating. Moreover, the reheating temperature is followed by Eq. 3.28. Otherwise, in all (h^r, w_ϕ) parameter space reheating end is defined via explicit coupling. In such cases, $T_{\rm re}$ and $A_{\rm re}$ is defined as :

when $w_\phi < 5/9$

$$T_{\rm re} = \left(\frac{6M_p^2(1+w_\phi)m_\phi^{\rm end}H_{\rm end}}{8\pi\epsilon(5-9w_\phi)}(h^r)^2\right)^{1/4} A_{\rm re}^{\frac{-3(1+3w_\phi}{8}} \quad ; \quad A_{\rm re} = \left(\frac{8\pi(5-9w_\phi)H_{\rm end}}{2(1+w_\phi)m_\phi^{\rm end}}(h^r)^2\right)^{\frac{2}{3-3w_\phi}}, \tag{3.140}$$

and when $w_\phi > 5/9$

$$T_{\rm re} = \left(\frac{6M_p^2(1+w_\phi)m_\phi^{\rm end}H_{\rm end}}{8\pi\epsilon(9w_\phi-5)}(h^r)^2\right)^{1/4} A_{\rm re}^{-1} \quad ; \quad A_{\rm re} = \left(\frac{8\pi(9w_\phi-5)H_{\rm end}}{2(h^r)^2(1+w_\phi)m_\phi^{\rm end}}\right)^{\frac{-1}{1-3w_\phi}}. \tag{3.141}$$

B.2 With thermal effect

Here we are mainly focused on the situation where $T_{\rm rad} > m_\phi$ and the analysis for $T_{\rm rad} < m_\phi$ will be the same as without thermal effect. In the limit, $T_{\rm rad} > m_\phi$, the thermal effect significantly impacts the reheating dynamics due to the explicit temperature dependence on the decay rate. The expression for decay rate in this limit can be written as (see, for instance, Eq. 3.2)

$$\Gamma_{\phi\to\bar{f}f} = \frac{(h^r)^2}{8\pi}\frac{m_\phi^2(t)}{4T_{\rm rad}} \simeq \frac{(h^r)^2}{8\pi}\frac{(m_\phi^{\rm end})^2}{4T_{\rm rad}}A^{-6w_\phi} \tag{3.142}$$

Inserting the above decay rate in Eq. 3.5b, one can find the evolution of the radiation energy density for fermionic coupling as

$$\rho_f^r(A) = \left[\frac{\zeta(w_\phi)(h^r)^2\epsilon^{1/4}M_P^2}{A^5}(m_\phi^{\rm end})^2H_{\rm end}\left(A^{\frac{7-15w_\phi}{2}}-1\right)\right]^{4/5}, \tag{3.143}$$

$\zeta(w_\phi) = \frac{15(1+w_\phi)}{64\pi(7-15w_\phi)}$. The aforementioned equation clearly suggests that the radiation energy density behaves differently depending on the inflaton equation state, whether it is greater than or less than 7/15.

If the coupling strength $h^r > \mathscr{H}_c$, fermionic coupling always defines reheating temperature and eventually equating $\rho_\phi = \rho_f^r$, we find reheating temperature as

$$T_{\rm re} = \left(\frac{6M_p^2(1+w_\phi)m_\phi^{\rm end}H_{\rm end}}{8\pi\epsilon(5-9w_\phi)}(h^r)^2\right)^{1/4} A_{\rm re}^{\frac{-3(1+3w_\phi}{8}} \quad ; \quad A_{\rm re} = \left(\frac{8\pi(5-9w_\phi)H_{\rm end}}{2(1+w_\phi)m_\phi^{\rm end}}(h^r)^2\right)^{\frac{2}{3-3w_\phi}} \tag{3.144}$$

The above equation is valid when $w_\phi < 7/15$. However, for $w_\phi > 7/15$ we have

$$T_{\rm re} = \left[\frac{\zeta(w_\phi)(h^r)^2M_P^2}{\epsilon}(m_\phi^{\rm end})^2H_{\rm end}A_{re}^{-5}\right]^{1/5}, A_{\rm re} = \left[\frac{\zeta(w_\phi)(h^r)^2\epsilon^{1/4}M_p^2(m_\phi^{\rm end})^2H_{\rm end}}{(3M_p^2H_{\rm end}^2)^{5/4}}\right]^{\frac{5(1-3w_\phi)}{4}}. \tag{3.145}$$

Moreover, in the limit of $h^r > \mathscr{H}_c$, the maximum radiation energy density is also defined by the non-gravitational sector, which can be expressed as

$$\rho_f^{r,max} = \left[\zeta(w_\phi)(h^r)^2\epsilon^{1/4}M_P^2(m_\phi^{\rm end})^2H_{\rm end}\left(A_{\rm max}^{\frac{-3(1+5w_\phi}{2}} - A_{\rm max}^{-5}\right)\right]^{4/5}, \tag{3.146}$$

where, $A_{\rm max} = \left(\frac{10}{3+15w_\phi}\right)^{2/7-15w_\phi}$. On the other hand, when $h^r < \mathscr{H}_c$ and $w_\phi > 0.65$, the gravitational sector drives the reheating dynamics and the reheating temperature to be the same as Eq. 3.28.

C Analytical expressions of co-moving number density for FIMP which are produced from thermal bath

For freeze in production of DM from the thermal bath, the DM can never reach thermal equilibrium i.e. $n_{\rm x}^r \ll n_{\rm x,eq}^r$, hence the co-moving number density $n_{\rm x}^r = n_{\rm x}^r A^3$ follow the following simple equation,

$$\frac{n_{\rm x}^r(A)}{dA} = \frac{A^2}{H}\langle\sigma v\rangle(n_x^{eq})^2. \tag{3.147}$$

For this case, the DM production continue to happen untill the radiation temperature equals the DM mass $T_{\rm rad} \simeq m_{\rm x}$. Therefore, in order to solve the above equation, DM can be safely assumed to be relativistic, and in the limit $m_{\rm x} < T_{\rm rad}$, the equilibrium number density becomes,

$$n_{\rm x,eq}^r = \frac{j_{\rm x}T_{\rm rad}^3}{\pi^2} \tag{3.148}$$

The Hubble parameter can also be written as

$$H(A) = H(A_{\rm re})\left(\frac{A}{A_{\rm re}}\right)^{-\frac{3}{2}(1+w_\phi)} \tag{3.149}$$

where $H(A_{\rm re}) = \frac{\sqrt{\epsilon}T_{re}^2}{\sqrt{3}M_p}$ hubble parameter at the end of reheating. So, combining the above three equations, one can get

$$\frac{n_{\rm x}^r(A)}{dA} = \frac{\langle\sigma v\rangle j_{\rm x}^2A_{\rm re}^2}{\pi^4H(A_{\rm re})}\left(\frac{A}{A_{\rm re}}\right)^{\frac{7+3w_\phi}{2}}T_{rad}^6 \tag{3.150}$$

.

C.1 Bosonic Reheating

C.1.1 Without thermal effect

From Eq. (3.114), the bath temperature can be written as

$$T_{\rm rad} = \begin{cases} T_{\rm re}(A/A_{\rm re})^{\frac{-3(1-w_\phi)}{8}} & \text{for } g_1^r \phi s^2 \\ T_{\rm re}(A/A_{\rm re})^{\frac{-9(1-w_\phi)}{8}} & \text{for } g_1^r \phi^2 s^2 \end{cases} \tag{3.151}$$

Using above equation in Eq. (3.150), one can find the below solution of $n_{\rm x}^r(A)$ at arbitrary point $A \le A_{\rm re}$

$$n_{\rm x}^r(A) = \frac{4\sqrt{3} M_p \langle\sigma v\rangle j_{\rm x}^2 T_{\rm re}^4}{3\sqrt{\epsilon}\pi^4} A_{\rm re}^3 \begin{cases} \frac{1}{(3+5w_\phi)}\left[\left(\frac{A}{A_{\rm re}}\right)^{\frac{3(3+5w_\phi)}{4}} - \left(\frac{A}{A_{\rm max}}\right)^{\frac{3(3+5w_\phi)}{4}}\right] & \text{for } g_1^r \phi s^2 \\ \frac{1}{(11w_\phi-3)}\left[\left(\frac{A}{A_{\rm re}}\right)^{\frac{3(11w_\phi-3)}{4}} - \left(\frac{A}{A_{\rm max}}\right)^{\frac{3(11w_\phi-3)}{4}}\right] & \text{for } g_2^r \phi^2 s^2 \end{cases} \tag{3.152}$$

The above equation shows that most of the production of DM happens at the beginning of reheating for $\phi\phi \to ss$ reheating process for $w_\phi < 3/11$.

C.1.2 With thermal effect

From Eq. (3.127), the bath temperature can be written as

$$T_{\rm rad} = \begin{cases} T_{\rm re}(A/A_{\rm re})^{\frac{-(1-3w_\phi)}{2}} & \text{for } g_1^r \phi s^2 \\ T_{\rm re}(A/A_{\rm re})^{\frac{-(3-5w_\phi)}{2}} & \text{for } g_1^r \phi^2 s^2 \end{cases} \tag{3.153}$$

Utilising above equation in Eq.(3.150), we have obtained following solution of $n_{\rm x}^r(A)$ at arbitrary point $A \le A_{\rm re}$

$$n_{\rm x}^r(A) = \frac{2\sqrt{3} M_p \langle\sigma v\rangle j_{\rm x}^2 T_{\rm re}^4}{3\sqrt{\epsilon}\pi^4} A_{\rm re}^3 \begin{cases} \frac{1}{(1+7w_\phi)}\left[\left(\frac{A}{A_{\rm re}}\right)^{\frac{3(1+7w_\phi)}{2}} - \left(\frac{A}{A_{\rm max}}\right)^{\frac{3(1+7w_\phi)}{2}}\right] & \text{for } g_1^r \phi s^2 \\ \frac{1}{(11w_\phi-3)}\left[\left(\frac{A}{A_{\rm re}}\right)^{\frac{3(11w_\phi-3)}{2}} - \left(\frac{A}{A_{\rm max}}\right)^{\frac{3(11w_\phi-3)}{2}}\right] & \text{for } g_2^r \phi^2 s^2 \end{cases} \tag{3.154}$$

Like earlier, most of the production of DM happens at the beginning of reheating for $\phi\phi \to ss$ reheating process for $w_\phi < 3/11$

C.2 Fermionic reheating

C.2.1 Without thermal effect

- For $w_\phi > 5/9$: The bath temperature can be written as

$$T_{\rm rad} = T_{\rm re}(A/A_{\rm re})^{-1} \tag{3.155}$$

Upon substituting the above equation in Eq. 3.150 along with Eq. (3.149), the co-moving number density at any point A during reheating takes the following form

$$n_{\rm x}^r(A) = \frac{\sqrt{3} M_p \langle\sigma v\rangle j_{\rm x}^2 T_{\rm re}^4}{\sqrt{\epsilon}\pi^4} A_{\rm re}^2 \int_{A_{\rm max}}^{A} (A/A_{\rm re})^{\frac{-5+3w_\phi}{2}} dA = \frac{2\sqrt{3} M_p \langle\sigma v\rangle j_{\rm x}^2 T_{\rm re}^4}{3\sqrt{\epsilon}\pi^4} A_{\rm re}^3 (A_{\rm max}/A_{\rm re})^{3(1-w_\phi)/2} \tag{3.156}$$

The co-moving number density is constant from the beginning of reheating.

- For $w_\phi < 5/9$: The bath temperature can be written as

$$T_{\rm rad} = T_{\rm re}(A/A_{\rm re})^{-\frac{3}{8}(1+3w_\phi)} \tag{3.157}$$

Upon substituting the above equation in Eq. 3.150 along with Eq. (3.149), the co-moving number density at any point A during reheating takes the following form

$$\begin{aligned} n^r_{\rm x}(A) &= \frac{\sqrt{3}M_p\langle\sigma v\rangle j_{\rm x}^2 T_{\rm re}^4}{\sqrt{\epsilon}\pi^4}A_{\rm re}^2\int_{A_{\rm max}}^{A}(A/A_{\rm re})^{\frac{5-21w_\phi}{4}}dA \\ &= \frac{4\sqrt{3}M_p\langle\sigma v\rangle j_{\rm x}^2 T_{\rm re}^4}{3\sqrt{\epsilon}(3-7w_\phi)\pi^4}A_{\rm re}^3\left[(A/A_{\rm re})^{\frac{3(3-7w_\phi)}{4}} - (A_{\rm max}/A_{\rm re})^{\frac{3(3-7w_\phi)}{4}}\right] \end{aligned} \tag{3.158}$$

When $w_\phi > 3/7$, the DM production happens instantaneously just at the end of inflation, as a result, the co-moving number density is constant.

C.2.2 With thermal effect :

When $w_\phi > 7/15$, the same situation will be happen as we discuss for without thermal effect for $w_\phi > 5/9$. Now for $w_\phi < 7/15$, the bath temperature is

$$T_{\rm rad} = T_{\rm re}(A/A_{\rm re})^{-\frac{3}{10}(1+5w_\phi)} \tag{3.159}$$

Upon substituting the above equation in Eq. 3.150 along with Eq. 3.149, the co-moving number density at any point A during reheating takes the following form

$$\begin{aligned} n^r_{\rm x}(A) &= \frac{\sqrt{3}M_p\langle\sigma v\rangle j_{\rm x}^2 T_{\rm re}^4}{\sqrt{\epsilon}\pi^4}A_{\rm re}^2\int_{A_{\rm max}}^{A}(A/A_{\rm re})^{\frac{17-75w_\phi}{4}}dA \\ &= \frac{10\sqrt{3}M_p\langle\sigma v\rangle j_{\rm x}^2 T_{\rm re}^4}{3\sqrt{\epsilon}(9-25w_\phi)\pi^4}A_{\rm re}^3\left[(A/A_{\rm re})^{\frac{3(9-25w_\phi)}{10}} - (A_{\rm max}/A_{\rm re})^{\frac{3(9-25w_\phi)}{10}}\right] \end{aligned} \tag{3.160}$$

When $w_\phi > 9/25$, the DM production happens instantaneously just at the end of inflation. As a result, the co-moving number density is constant.

D Analytical expressions of minimum critical mass where both freeze-in and freeze-out mechanism coincides

When the DM mass $m_{\rm x}$ is smaller than $T_{\rm re}$, the DM abundance follows simple relation $\Omega_{\rm x}h^2 \propto m_{\rm x}\langle\sigma v\rangle$ for the freeze-in scenario for a fixed $T_{\rm re}$. Therefore, the cross-section becomes inversely proportional to the DM mass. This suggests the existence of a critical $\langle\sigma v\rangle$ and the associated mass for which the DM equilibrates with the thermal bath, and freeze out happens. At that critical $\langle\sigma v\rangle_{crit}$, DM number density must equate with the equilibrium number density at the end of reheating. Corresponding to these critical $\langle\sigma v\rangle_{crit}$, there exists a minimum critical mass $m_{\rm x,\,min}$ which satisfies present-day abundance. Below this mass, no mass will be available, which can give the correct abundance. Equating the solution of the DM number density $n^r_{\rm x}$ with the equilibrium number density $n^r_{\rm x,eq}$ at the end of reheating $A_{\rm re}$, one can find

following expressions of $\langle\sigma v\rangle_{crit}$ without thermal effect

$$\langle\sigma v\rangle_{crit} = \frac{\sqrt{3\epsilon}\pi^2}{4M_p j_{\rm x}} \begin{cases} \frac{3+5w_\phi}{T_{\rm re}} & \text{for} \quad g_1^r \phi s^2 \\ \frac{11w_\phi-3}{T_{\rm re}} & \text{for} \quad g_2^r \phi^2 s^2 \quad \text{with} \quad w_\phi > w_\phi^c \\ \frac{3-11w_\phi}{T_{\rm re}}\left(\frac{T_{\rm re}}{T_{\rm rad}^{\rm max}}\right)^{\frac{2(3-11w_\phi)}{3(1-w_\phi)}} & \text{for} \quad g_2^r \phi^2 s^2 \quad \text{with} \quad w_\phi < w_\phi^c \\ \frac{2(1-w_\phi)}{T_{\rm re}}\left(\frac{T_{\rm re}}{T_{\rm rad}^{\rm max}}\right)^{\frac{3(w_\phi-1)}{2}} & \text{for} \quad h^r \phi \bar{f} f \quad \text{with} \quad w_\phi > 5/9 \\ \frac{7w_\phi-3}{T_{\rm re}}\left(\frac{T_{\rm re}}{T_{\rm rad}^{\rm max}}\right)^{\frac{2(7w_\phi-3)}{1+3w_\phi}} & \text{for} \quad h^r \phi \bar{f} f \quad \text{with} \quad 3/7 < w_\phi < 5/9 \\ \frac{3-7w_\phi}{T_{\rm re}} & \text{for} \quad h^r \phi \bar{f} f \quad \text{with} \quad w_\phi < 3/7 \end{cases} \tag{3.161}$$

and with thermal effect

$$\langle\sigma v\rangle_{crit} = \frac{\sqrt{3\epsilon}\pi^2}{4M_p j_{\rm x}} \begin{cases} \frac{2(1+7w_\phi)}{T_{\rm re}} & \text{for} \quad g_1^r \phi s^2 \\ \frac{2(11w_\phi-3)}{T_{\rm re}} & \text{for} \quad g_2^r \phi^2 s^2 \quad \text{with} \quad w_\phi > w_\phi^c \\ \frac{2(3-11w_\phi)}{T_{\rm re}}\left(\frac{T_{\rm re}}{T_{\rm rad}^{\rm max}}\right)^{\frac{2(3-11w_\phi)}{3(1-w_\phi)}} & \text{for} \quad g_2^r \phi^2 s^2 \quad \text{with} \quad w_\phi < w_\phi^c \\ \frac{2(1-w_\phi)}{T_{\rm re}}\left(\frac{T_{\rm re}}{T_{\rm rad}^{\rm max}}\right)^{\frac{3(w_\phi-1)}{2}} & \text{for} \quad h^r \phi \bar{f} f \quad \text{with} \quad w_\phi > 7/15 \\ \frac{2(25w_\phi-9)}{T_{\rm re}}\left(\frac{T_{\rm re}}{T_{\rm rad}^{\rm max}}\right)^{\frac{(25w_\phi-9)}{1+5w_\phi}} & \text{for} \quad h^r \phi \bar{f} f \quad \text{with} \quad 9/25 < w_\phi < 7/15 \\ \frac{2(9-25w_\phi)}{5T_{\rm re}} & \text{for} \quad h^r \phi \bar{f} f \quad \text{with} \quad w_\phi < 9/25 \end{cases} \tag{3.162}$$

Above this critical $\langle\sigma v\rangle_{crit}$, the DM can produce only from the freeze-out mechanism. Using the above critical $\langle\sigma v\rangle_{crit}$ in the DM abundance expressions, one can find the following expression of minimum critical mass

$$m_{\rm x,\,min} = \frac{\Omega_{\rm x} h^2}{\Omega_r h^2}\frac{\epsilon\pi^2 T_{\rm now}}{j_{\rm x}} \simeq \frac{2\times 10^{-7}(GeV)}{j_{\rm x}} \tag{3.163}$$

The minimum mass is independent of background reheating dynamics, i.e., reheating temperature and inflation EoS.

E The effect of self-resonance in reheating parameter space

Homogeneous oscillation of the inflation condensate can be unstable, leading to self-resonance. This Addenda shows the parameter region where the self-resonance effect is important. In Figs. 3.19 and 3.20 we have shown the region in the w_ϕ Vs. coupling parameter space where self-resonance may be important. It has been pointed out that self-resonance can be sufficient to reheat the universe (except $w_\phi = 0$) without any coupling to the other fields with inflaton [13, 14], however, that strictly depends on the values of α. When $\alpha << 1/6$, self-resonance is efficient, and the RD universe is established within less than an e-fold of expansion after inflation end. However, for $\alpha > 1/6$, self-resonance is not very efficient, and it takes many e-folds to give rise to radiation dominated universe. In the reference [14], the authors provide an estimation for the number of e-folds calculated from the end of inflation to the beginning of the radiation domination for α-attractor E-model,

$$\Delta N_{sr} \simeq \begin{cases} \frac{n+1}{3}\ln\left[\frac{\sqrt{6\alpha}}{2d\delta}\frac{k}{\Delta k}\frac{|4-2n|}{n+1}\right] & \text{for} \quad n > 1\ (n \neq 2) \\ \ln\left[\frac{\sqrt{6\alpha}}{2d\delta}\right] & \text{for} \quad n = 2, \end{cases} \tag{3.164}$$

where $\Delta k/k$ is the fractional width of the resonance band and d is its dimensionless "strength." $\delta = 0.126$

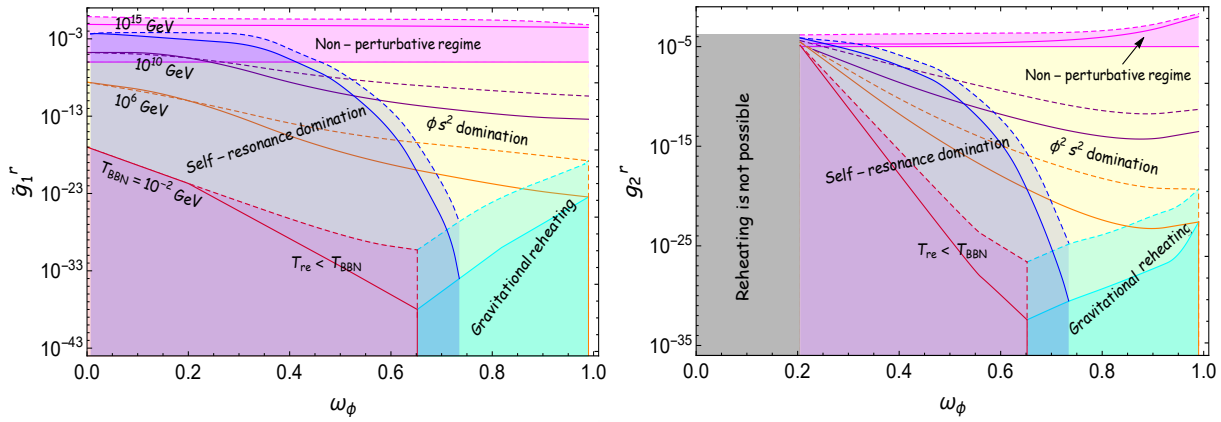

Figure 3.19: The description of this plot is the same as Fig. 3.2. Here we added the region in light blue color where the self-resonance effect is important.

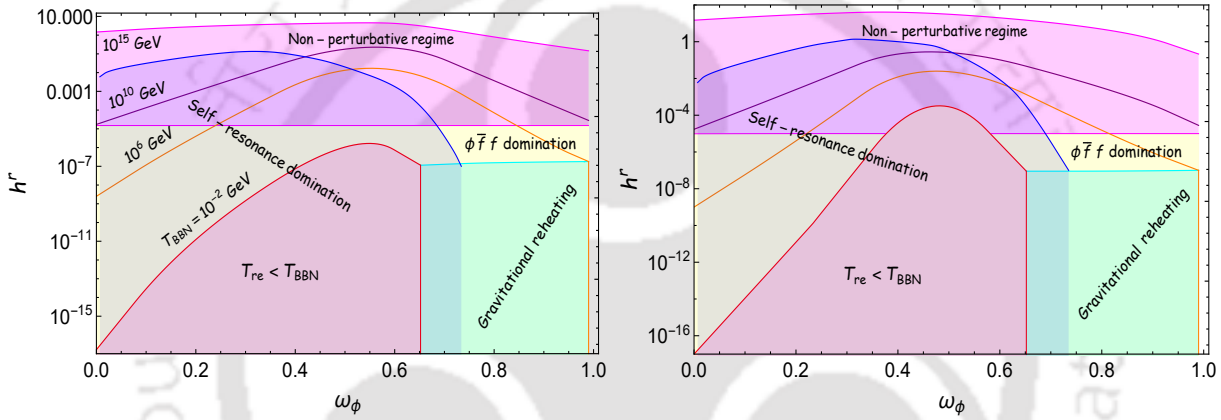

Figure 3.20: The description of this plot is the same as Fig. 3.7. Here we added the region in light blue color where the self-resonance effect is important

is a dimensionless number independent of n. This bound can be used as an upper bound on the transition duration between the inflation end and the radiation-dominated states of the universe.
Self-resonance can significantly modify the dynamics for which a comprehensive analysis is required. Here, we have shown the region where it can play its role. If the perturbative reheating is completed with e-folding number $< \Delta N_{sr}$, our analysis will not be affected. Otherwise, self-resonance will significantly affect the parameter space, which needs to be taken into account, and we defer this for our future study. Using the bound Eq. 3.164, in Fig. 3.19,3.20, we have shown regions where the self-resonance effect is important. We have found that self-resonance is effective when $0 < w_\phi \leq 0.75$ for $\alpha = 1$.

F The re-annihilation of DM and its effects on DM parameter space

Near the freeze-out temperature, the thermal production of DM receives Boltzmann suppression, and during this time, the gravitational scattering may become the dominant channel for the DM production.

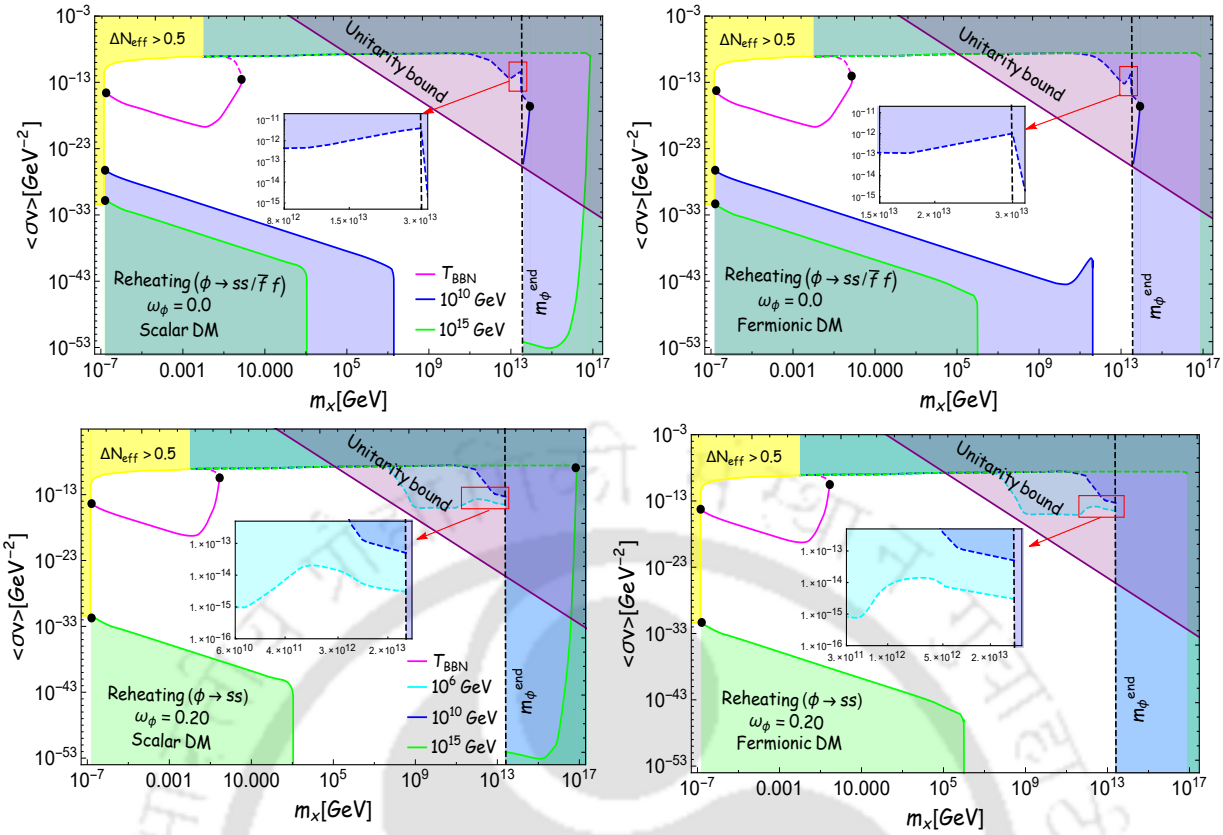

Figure 3.21: The description of this plot is the same as Fig. 3.15. Here we have shown the DM parameter space with considering the DM re-annihilation.

For such a case following conditions must be satisfied

$$\frac{\Gamma_{\phi\phi\to SS/FF}(t)\rho_\phi(t)}{m_\phi(t)} \geq \langle\sigma v\rangle(n^r_{\mathrm{x,eq}}(t))^2. \tag{3.165}$$

In our analysis, we ignored such an effect, and it is also important to note that such an effect is not important when the DMs freeze out during the RD era. However, when the DM freeze-out takes place during reheating, the DM re-annihilation turns out to be important within a very narrow DM mass range $(10^{11} - m_\phi^{\mathrm{end}})$ GeV, and its evolution till the Freeze-out point is governed by,

$$\frac{d(a^3 n^r_{\mathrm{x}})}{dt} = -a^3\langle\sigma v\rangle(n^r_{\mathrm{x}})^2 + \frac{a^3\Gamma_{\phi\phi\to xx}\rho_\phi(t)}{m_\phi(t)}. \tag{3.166}$$

From the equation, it is clear that DM re-annihilation to the thermal bath plays a crucial role along with gravitational production. Such re-annihilation is therefore expected to be important for higher reheating temperatures and large DM masses. The final DM abundance clearly becomes $\Omega_x h^2 \propto \Gamma_{\phi\phi\to xx}/\langle\sigma v\rangle$. The gravitational production rate of DM increases with DM mass. Therefore, with increasing DM mass, the cross-section has to increase to maintain the correct abundance, which is indeed observed in Fig. 3.21 for $w_\phi = 0$, for which the inflaton mass m_ϕ is constant. It turns out that most of the parameter regions we found are above the unitarity bound shown in Fig. 3.21. For $w_\phi = 0$, we observed the effect of re-annihilation for $T_{\mathrm{re}} = 10^{10}$ GeV. For this temperature, the corresponding DM mass range where this effect modifies the cross-section turns out to be within $(8\times10^{12} - m_\phi^{\mathrm{end}})$ GeV for scalar DM and $(1.5\times10^{13} - m_\phi^{\mathrm{end}})$ GeV for fermionic DM.

For the EoS other than zero, the situation becomes different due to time-varying inflaton mass. For higher DM mass possibility may arise that its gravitational production becomes kinematically suppressed due to decreasing inflaton mass. For such cases, the re-annihilation stops, and standard DM freeze-out occurs, which we discussed in detail. As an example for $w_\phi = 0.20$, we indeed see such an effect, which we have shown in Fig. 3.21. One particularly notices the curve associated with $T_{\rm re} = 10^6$ in the inset. The rising part of the curve corresponds to the re-annihilation phase for the mass range within $(6\times10^{10}, 9\times10^{11})$ GeV for scalar DM and $(3\times10^{11}, 4\times10^{12})$ GeV for fermionic DM. For higher mass values, kinematic suppression comes into play, and the cross-section needs to be reduced, as discussed before. For $T_{\rm re} = 10^{10}$, we found that the re-annihilation is not prominent due to the kinetic suppression effect.

CHAPTER 4

Inflaton phenomenology via reheating in light of latest Planck+BICEP/*Keck* Observation and Primordial GWs

In the previous chapter, we studied in detail the dynamics of reheating after inflation. We analyzed the evolution of different energy components (inflaton and radiation), as well as the thermal bath temperature, across various reheating frameworks. These frameworks were subsequently used to populate the dark sector. We constrained inflationary parameters, such as the number of e-folds N_k, along with reheating parameters including the reheating temperature and inflaton couplings, using the CMB spectral index n_s. To impose these constraints, we adopted the most conservative bounds on the reheating temperature T_{re}, ranging from 4 MeV to 10^{15} GeV. The analysis in the previous chapter focused solely on the α-attractor E-model, with $\alpha = 1$. However, a wide variety of inflationary models exist. In this chapter, we investigate whether the predictions for various cosmological parameters change when different inflationary models are considered. Furthermore, we will incorporate some direct and indirect observational constraints, along with some relevant theoretical bounds, to place tighter constraints on parameters.

Over the last decade, increasingly precise measurements of CMB have led to a new era of precision cosmology. Inflation is assumed to be a unique mechanism [7–9] in the early universe, which, apart from solving the problems of the standard big bang, has very precise predictions of large-scale inhomogeneous fluctuations. During the course of subsequent evolution, those fluctuations are translated into CMB anisotropy [4, 208, 209]. Therefore, accurate measurement of CMB anisotropies would be of fundamental importance for establishing the early inflationary phase. Two fundamental observables of interest are the scalar spectral index n_s and the tensor-to-scalar ratio r, which are directly connected to the inflation. In the realm of observations, considering the BICEP/*Keck*(BK) 15 program [66], the measurement yielded a constraint on the $r_{0.05} < 0.07$ at 95% CL, where subscript $k_\star = 0.05$ Mpc^{-1} is associated with the pivot scale. However, the latest BICEP/*Keck* 18 [54] result along with Planck 2018 [4] yields the strongest constraints in the (n_s, r) plane with $r_{0.05} < 0.036$ and scalar spectral index $0.958 < n_s < 0.975$ at 95% CL for $r = 0.004$. In this chapter, we intend to explore the impact of these latest observations on the three classes of the plateau-type inflationary model: α-attractor E-model, α-attractor T-model, and the minimal model [73]. The common feature of all these models is the plateau region in the large field limit, and that leads to quasi-de Sitter expansion consistent with observation.

Lack of direct observation evidence of reheating phase leads to a wide possible range of these parameters, reheating temperature within (10^{15} GeV, $T_{\rm BBN} = 4$ MeV), and EoS within $(0,1)$. While observable $(n_{\rm s}, r)$ typically encodes only the intrinsic nature of inflaton to the leading order, reheating encodes much more. Inflaton is naturally thought to be a part of beyond the SM of particle physics. Therefore, from the model-building perspective inflaton field can play an outstanding role in constructing a unified framework of cosmology and particle physics [16, 18, 41, 47, 167, 174, 175, 177, 184, 210, 211]. Towards this goal recently few studies have been done considering matter like reheating [192, 212, 213]. In the previous chapter, we were mostly focused on the connection between the inflaton and reheating parameter with the CMB. In this chapter, we explore phenomenological constraints on the parameters of the inflaton potential and its couplings and derive the bound on reheating parameters in light of the aforementioned combined data of Planck18, BK18, and BAO.

Primordial gravitational waves (PGWs) are one of the profound predictions of inflation [214, 215]. Because of weak coupling, it carries not only the imprints of its own origin through inflationary observable r but also of the post-inflationary evolution, particularly the reheating phase. The evolution of PGWs during the reheating phase and CMB observation is observed to set severe constraints on the inflation and reheating parameters. Around the CMB pivot scale the PGW spectrum, $\Omega^k_{\rm GW}h^2$ is constrained by $r < 0.036$ with typical dimensionless amplitude $\Omega^k_{\rm GW}h^2 \sim 10^{-18}$. However, PGW of sub-horizon scale during reheating develops a w_ϕ-dependent spectral tilt $\Omega^k_{\rm GW}h^2 \propto 10^{-18}k^{-n_{w_\phi}}$, with $n_{w_\phi} = 2(1-3w_\phi)/(1+3w_\phi)$, which greatly enhances the magnitude of $\Omega^k_{\rm GW}h^2$ for equation $w_\phi > 1/3$. Such enhancement will be observed to set a lower limit on the reheating temperature, which we defined as $T^{\rm GW}_{\rm re}$ though BBN constraint on total GW amplitude $\Omega^k_{\rm GW}h^2 \leq 1.7\times10^{-6}$ obtained from the Planck18 [31]. We used this PGWs constraint to constrain the parameter space. To put final bounds on the inflaton and reheating parameters, we further take into account perturbative and nonperturbative limits on the inflaton-radiation coupling.

This chapter is organized as follows: In Sec.4.1, we have started our discussion by demonstrating the inflation model. In Sec.4.2, we briefly revisit the dynamics of reheating for two different decay channels, as previously discussed in the last chapter. PGWs are known to be an interesting cosmological observable that can significantly restrict the possible lower limit of reheating temperature through the BBN constraint. We discuss this in detail in Sec.4.3, and show the impact of such a limit on the inflaton-radiation coupling. In Secs.4.4 and 4.5, we illustrate different theoretical constraints, particularly on the inflaton-radiation coupling and its potential impact on the inflaton phenomenological parameter space. In Sec.4.6, we discuss in detail the resulting constraints on the parameters of the inflaton and associated inflationary and reheating observables. Finally, summarize in Sec. 4.7.

4.1 Model of inflation

As pointed out earlier, in this chapter, we explore three different single-field inflation models and left multifield models for our future work. The associated potentials are

$$V(\phi) = \begin{cases} \Lambda^4\left[1-e^{-\sqrt{\frac{2}{3\alpha}}\frac{\phi}{M_{\rm p}}}\right]^{2n}, & \text{E-model}, \\ \Lambda^4\tanh^{2n}\left(\frac{\phi}{\sqrt{6\alpha}M_{\rm p}}\right), & \text{T-model}, \\ \Lambda^4\frac{\phi^{2n}}{\phi^{2n}+\phi_*^{2n}}. & \text{Minimal-model}, \end{cases} \tag{4.1}$$

In the large field limit, all the potential becomes constant $V(\phi) \simeq \Lambda^4$, setting the scale of inflation. The remaining parameters (n, α, ϕ_*) parametrize the shape of the potential near their minimum. Near the minimum at $\phi \simeq 0$, all the potential takes the power-law form,

$$V(\phi) \simeq \Lambda^4 \left(\frac{\phi}{\alpha_1 M_{\rm p}}\right)^{2n}, \tag{4.2}$$

where $\alpha_1 = (\sqrt{3\alpha/2}, \sqrt{6\alpha}, \phi_*)$ for α-attractor E, T and minimal model respectively. We can express the scale of inflation Λ in terms of $n_{\rm s}$ and r, using the same slow-roll approximation method,

$$\Lambda = \begin{cases} M_{\rm p}\left(\frac{3\pi^2 r A_{\rm s}}{2}\right)^{1/4}\left[\frac{2n(2n+1)+\sqrt{4n^2+6\alpha(1+n)(1-n_{\rm s})}}{4n(1+n)}\right]^{n/2}, & \text{E-model}, \\ M_{\rm p}\left(\frac{3\pi^2 A_{\rm s} r}{2}\right)^{1/4}\left(\frac{4n^2+3\alpha(1-n_{\rm s})+\sqrt{9\alpha^2(1-n_{\rm s})^2+8n^2(2+3\alpha(1-3n_{\rm s}))}}{4n(n+1)}\right)^{n/4}, & \text{T-model}, \\ M_{\rm p}\left(\frac{3\pi^2 A_{\rm s} r}{2}\right)^{1/4}\left[1+\left(\frac{(1-n_{\rm s})}{4n(2n+1)}\left(\frac{\phi_\star}{M_{\rm p}}\right)^2\right)^{\frac{2n}{2n+2}}\right]^{1/4}, & \text{Minimal-model}. \end{cases} \tag{4.3}$$

However, it is important to note that the expression for Λ in the case of the minimal model is approximate and not exact. The precise value of Λ can only be obtained through a numerical computation. For the detailed derivation of inflationary parameters for all these model see the section-2.9.1, 2.9.2, 2.9.3.

The post-inflationary dynamics, which we call reheating, will be controlled by the energy of the inflaton (ρ_ϕ), and its value at the end of inflation can be found as,

$$\rho_\phi^{\rm end} \sim \frac{3}{2} V(\phi_{end}) \sim \frac{\Lambda^4}{\alpha_1^{2n}}\left[\frac{\phi_{\rm end}}{M_{\rm p}}\right]^n = \frac{4.1\times 10^{64}}{\alpha_1^{2n}}\left[\frac{\phi_{\rm end}}{M_p}\right]^{2n}\left[\frac{\Lambda}{5.8\times 10^{-3} M_{\rm p}}\right]^4, \tag{4.4}$$

which is in unit of GeV^4.

4.2 Reheating dynamics and constraints

Once inflation ends, the inflaton field coherently oscillates around the minimum of its potential $V(\phi) \sim \phi^{2n}$. The coherently oscillating inflaton can be mode decomposed into, $\phi(t) = \phi_0(t).\mathscr{P}(t)$, with $\phi_0(t)$ representing the decaying amplitude of the oscillation and $\mathscr{P}(t) = \sum_\nu \mathscr{P}_\nu e^{i\nu\Omega t}$ encoding the oscillation of the inflaton with the fundamental frequency calculated to be [47],

$$\Omega = m_\phi(t)\gamma = m_\phi(t)\sqrt{\frac{\pi n}{(2n-1)}}\frac{\Gamma\left(\frac{1}{2}+\frac{1}{2n}\right)}{\Gamma\left(\frac{1}{2n}\right)}. \tag{4.5}$$

For the computation of angular frequency Ω, refer to Appendix-A. The effective mass of the inflaton is defined as $m_\phi^2 = \partial^2 V(\phi)/\partial\phi^2|_{\phi_0}$, and we have

$$m_\phi^2 \simeq \frac{2n(2n-1)\Lambda^4}{\alpha_1^{2n} M_{\rm p}^2}\left[\frac{\phi_0}{M_p}\right]^{2n-2} \simeq \frac{2n(2n-1)\Lambda^4}{\alpha_1^2 M_{\rm p}^2}\left[\frac{V(\phi_0)}{\Lambda^4}\right]^{(n-1)/n} \simeq (m_\phi^{\rm end})^2\left[\frac{a}{a_{\rm end}}\right]^{-6w_\phi}, \tag{4.6}$$

where, used $V(\phi_0) \simeq \rho_\phi = \rho_\phi^{\rm end}(a/a_{\rm end})^{-3(1+w_\phi)}$, and m_ϕ^{end} is the inflaton mass defined at the end of the inflation

$$m_\phi^{\rm end} \simeq \frac{\sqrt{2n\,(2n-1)}}{\alpha_1}\frac{\Lambda^{\frac{2}{n}}}{M_{\rm p}}\left(\rho_\phi^{\rm end}\right)^{\frac{n-1}{2n}}. \tag{4.7}$$

Table 4.1: Numerical values of the Fourier sums in the effective couplings:

$n(w_\phi)$	$\sum \nu\lvert\mathscr{P}_\nu\rvert^2$	$\sum \nu^3\lvert\mathscr{P}_\nu\rvert^2$	$\frac{g_{\rm eff}}{g}$	$\frac{h_{\rm eff}}{h}$
1 (0.0)	$\frac{1}{4}$	$\frac{1}{4}$	1	1
2 (1/3)	0.229	0.241	1.42	0.71
5 (0.67)	0.205	0.256	2.13	0.49
10 (0.82)	0.191	0.286	2.92	0.38
200 (0.99)	0.174	0.358	12.5	0.10

As an example, for $n=6$ and setting $\alpha_1 \sim \mathcal{O}(1)$, one can obtain,

$$m_\phi^{\rm end} \sim 4.5\times 10^{14}\left[\frac{\Lambda}{1.4\times 10^{16}}\right]^{\frac{4}{3}}\left[\frac{\rho_\phi^{\rm end}}{4.1\times 10^{64}}\right]^{\frac{2}{3}}, \tag{4.8}$$

measured in GeV.

Radiation fields coupled with the inflaton will be produced during the reheating period quantum mechanically. The inflaton is decaying into radiation, and we consider two phenomenological decay processes governed by the following interaction Lagrangian,

$$\mathscr{L}_{\rm int} \supset \begin{cases} h\phi\bar{f}f & \phi\to\bar{f}f \\ g\phi b^2 & \phi\to bb \end{cases} \tag{4.9}$$

with $f\,(b)$ standing for fermionic (bosonic) particle. h is the dimensionless Yukawa coupling, and g is a dimensionful bosonic coupling. Incorporating the inflaton oscillation effect, the effective inflaton decay rate Γ_ϕ associated with these two processes has been computed [47, 211], and can be expressed as

$$\Gamma_\phi = \begin{cases} \frac{h_{\rm eff}^2}{8\pi}m_\phi(t), & \phi\to\bar{f}f \\ \frac{g_{\rm eff}^2}{8\pi m_\phi(t)}, & \phi\to bb, \end{cases} \tag{4.10}$$

For the detailed derivation of the decay rate, refer to the Appendix-C.1. In this chapter, we have not included the thermal correction in the decay rate. The constraints on all the inflationary and post-inflationary parameters (except couplings) in light of Planck+BICEP/*Keck* observation are not sensitive to the thermal correction. These aspects will be discussed in more detail later.

The ratio of the oscillation induced effective coupling parameters $h_{\rm eff}$ and $g_{\rm eff}$ over their respective tree level values are calculated to be [47]

$$\left(\frac{g_{\rm eff}}{g}\right)^2 = (2n+2)(2n-1)\gamma\sum_{\nu=1}^{\infty}\nu\lvert\mathscr{P}_\nu\rvert^2 \tag{4.11}$$

$$\left(\frac{h_{\rm eff}}{h}\right)^2 = (2n+2)(2n-1)\gamma^3\sum_{\nu=1}^{\infty}\nu^3\lvert\mathscr{P}_\nu\rvert^2. \tag{4.12}$$

In the table-5.1, we have tabulated the effective coupling constant with respect to tree label one. It is interesting to observe that the oscillation with a higher n value effectively enhances the bosonic production rate but significantly diminishes the fermionic production rate. For example, going from $n=1.0$ (matter like) to $n=5.0$ ($w_\phi=0.67$) for inflaton, the tree-level bosonic coupling gets doubled $g_{\rm eff}\simeq 2g$, whereas that of the fermionic coupling reduced by half $h_{\rm eff}\simeq 0.5h$.

In order to solve reheating dynamics, the Boltzmann equations for the energy density of radiation (ρ_r) and inflaton (ρ_ϕ) supplemented with the Hubble equation are,

$$\dot{\rho}_\phi + 3H(1+w_\phi)\rho_\phi = -\Gamma_\phi \rho_\phi (1+w_\phi), \tag{4.13a}$$

$$\dot{\rho}_r + 4H\rho_r = \Gamma_\phi \rho_\phi (1+w_\phi), \tag{4.13b}$$

$$H^2 = \frac{\rho_\phi + \rho_r}{3M_p^2}. \tag{4.13c}$$

With all these ingredients, we have solved the coupled Boltzmann Eqs. 4.13 numerically with the appropriate boundary conditions; $\rho_\phi(a_{\rm end}) = 3V(\phi_{\rm end})/2$, $\rho_r(a_{\rm end}) = 0$. For analytical estimation, we also obtain the approximate analytical solution for different energy density components as

$$\rho_\phi \simeq \rho_\phi^{\rm end}\left(\frac{a}{a_{end}}\right)^{-3(1+w_\phi)}, \tag{4.14}$$

$$\rho_r \simeq \begin{cases} \frac{\rho_\phi^{\rm end}(1+w_\phi)m_\phi^{end}h_{\rm eff}^2}{4\pi(5-9w_\phi)H_{\rm end}}\left[\left(\frac{a}{a_{\rm end}}\right)^{\frac{-3-9w_\phi}{2}} - \left(\frac{a}{a_{\rm end}}\right)^{-4}\right] \\ \frac{\rho_\phi^{\rm end}(1+w_\phi)g_{\rm eff}^2}{4\pi(5+3w_\phi)m_\phi^{end}H_{\rm end}}\left[\left(\frac{a}{a_{\rm end}}\right)^{\frac{-3+3w_\phi}{2}} - \left(\frac{a}{a_{\rm end}}\right)^{-4}\right] \end{cases}.$$

Here, $H_{\rm end}$ and $m_\phi^{\rm end}$ are the Hubble constant and the inflaton mass calculated at the end of the inflation. The detailed procedure for the analytical solution we have discussed in the earlier chapter A.1, B.1. With this solution, we can identify important physical quantities, namely, reheating temperature $T_{\rm re}$, defined at the end of reheating $a_{\rm re}$ where $\rho_\phi(a_{\rm re}) \simeq \rho_r(a_{\rm re})$,

$$T_{\rm re} \simeq \left(\frac{30\rho_\phi^{\rm end}}{\pi^2 g_{\star r}^{\rm re}}\right)^{\frac{1}{4}} e^{-\frac{3}{4}N_{\rm re}(1+w_\phi)} \tag{4.15}$$

$$= 6\times 10^{15} e^{-\frac{3N_{\rm re}}{4}(1+w_\phi)}\left[\frac{\rho_\phi^{\rm end}}{4.1\times 10^{64}}\right]^{\frac{1}{4}} \tag{4.16}$$

From the above equation, it is clear that we have an upper limit on the reheating temperature $T_{\rm re}^{\rm max} \sim 10^{15}$ GeV, for $N_{\rm re} = 0$, dubbed as instantaneous reheating, and as expected that does not depend on the w_ϕ. As there exists a naive lower limit on the temperature $T_{\rm re}^{\rm min} = T_{\rm BBN} = 4$ MeV [50, 51], which can immediately give us the relation between the maximum reheating e-folding number associated with BBN constraint as,

$$N_{\rm re}^{\rm max} \simeq \frac{4}{3(1+w_\phi)}\ln\left[2.5\times 10^{18}\left[\frac{\rho_\phi^{\rm end}}{4.1\times 10^{64}}\right]^{\frac{1}{4}}\right]. \tag{4.17}$$

This clearly suggests that the maximum reheating e-folding number decreases with the EoS. Now as an example, for $\rho_\phi^{\rm end} \sim 4.1\times 10^{64}$ GeV^4, $N_{\rm re}^{\rm max}$ simply turns out as $\sim 56.5/(1+w_\phi)$. $N_{\rm re}^{\rm max} \sim 56.5$ for a matter like inflaton EoS ($w_\phi = 0$) and it reduces to half $N_{\rm re}^{\rm max} \sim 28.2$ for kination like state ($w_\phi = 1$).

Post-reheating history is also important in order to put constrain on the inflationary e-folding number. The generic assumption after the reheating phase is that the comoving entropy density remains conserved, and such conservation law starting from reheating end to the present day imposes an additional relation among the parameters ($N_k, N_{\rm re}, T_{\rm re}$) as follows [11, 12],

$$T_{\rm re} = \left(\frac{43}{11 g_{\star r}^{\rm re}}\right)^{1/3}\left(\frac{a_0 H_k}{k_\star}\right) e^{-(N_k+N_{\rm re})} T_0, \tag{4.18}$$

Considering $H_k \sim H_{\rm end}$ (which may not true for higher values of $\alpha(\phi_*)$), expression for $N_{\rm re}$ can be expressed in more simplified manner,

$$N_k = \ln\left[1.2\times10^{40}\left[\frac{\rho_\phi^{\rm end}}{4.1\times10^{64}}\right]^{\frac{1}{2}}\frac{1}{T_{\rm re}}\right] - N_{\rm re}\,. \tag{4.19}$$

From the above relation, if we consider $\rho_\phi^{\rm end} \sim 4.1\times10^{64}$ GeV^4 and $N_{\rm re} \sim 0$ (instant reheating) that immediately sets the maximum probable reheating temperature $T_{\rm re}^{\rm max} \sim 10^{15}$ GeV and the inflationary e-folding number for the CMB pivot scale as $N_k \sim 57.8$. The most important aspect of Eq. 4.18 is that it establishes a connection between the post-inflationary reheating parameter $T_{\rm re}$ and the inflationary quantities N_k and H_k, which themselves depend on the CMB observables $\eta_{\rm s}$ and r, as well as the potential parameters α and n. Therefore, to constrain both inflationary and reheating parameters, we need to relate Eq. 4.18 with the reheating temperature formula given in Eq. 4.15.

For the special case, $w_\phi = 1/3$, N_k turns out to be independent of the reheating temperature $T_{\rm re}$ (see Fig. 4.7). For a fixed inflation model N_k solely depends on inflation parameter as follows, [11, 177]

$$N_k = 40.26 - \ln\left(\frac{\sqrt{H_{\rm end}}}{H_k}\right). \tag{4.20}$$

The above equation implies that N_k is only sensitive to the H_k and $H_{\rm end}$ value, which is regulated by the potential parameter $\alpha(\phi_*)$. The limiting value of $\alpha(\phi_*)$, $H_{\rm end}$ and N_k are shown in Table 4.4.

So far, our discussions are on two main points, the nature of large-scale inflationary fluctuations imprinted into $(n_{\rm s}, r)$ and the background reheating dynamics constraining the reheating parameters. However, the dynamics of high-frequency modes, particularly of PGWs, turn out to offer a stronger bound on lower reheating temperatures than $T_{\rm BBN}$, particularly for a stiff EoS $w_\phi \gtrsim 0.6$.

4.3 PGWs and constraints

Because of its naturally weak coupling, GWs prove to be an outstanding probe to look into the early universe, which can be as early as inflation and reheating. We wish to probe the reheating phase particularly and see how PGWs play out, yielding stronger constraints on the inflaton-radiation coupling by raising the lower limit of reheating temperature. However, to probe the reheating phase's typical frequency range, one requires a wide span of $10^{11} > f > 10^{-10}$ Hz, which is way outside the window of the CMB spectrum. Here, the frequency, f associated with a particular mode k is related by $f = 2\pi/k$. Therefore, along with the constraints on the large-scale fluctuation by Planck, BICEP/*Keck*, we consider high-frequency PGWs to obtain further constraints on the inflaton model. Interesting to note that a large number of proposed/ongoing GW detectors are designed within this wide range of frequencies, and there is a growing anticipation that the stochastic GW background may provide us hints about the physics operating in the early universe, including reheating. PGWs generated from the quantum vacuum during inflation evolve through the different phases of the universe, including the epoch of reheating, until we observe them today [23, 153, 216, 217]. The amplitude and the evolution of the PGWs spectrum are sensitive to the energy scale of the inflation and the post-inflationary reheating EoS w_ϕ. For those modes between $k_{\rm re} < k < k_{\rm end}$ which become sub-Hubble at some time during reheating, the PGW spectrum at the present

time assumes the following form, (see [23] for detailed calculation)

$$\Omega^{k}_{\rm GW}h^2 \simeq \Omega^{\rm inf}_{\rm GW}h^2\frac{\mu(w_\phi)}{\pi}\left(\frac{k}{k_{\rm re}}\right)^{-\frac{(2-6w_\phi)}{(1+3w_\phi)}} \tag{4.21}$$

Where, $\mu(w_\phi)=(1+3\omega_\phi)^{\frac{4}{1+3w_\phi}}\,\Gamma^2\left(\frac{5+3w_\phi}{2+6w_\phi}\right)$, which typically $\mathcal{O}(1)$ value. Therefore, the above equation contains two main components. The scale-invariant part, controlled by the inflationary energy scale,

$$\Omega^{\rm inf}_{\rm GW}h^2=\frac{\Omega_r h^2 H^2_{\rm end}}{12\pi^2 M_p^2}=3.5\times10^{-17}\left(\frac{H_{\rm end}}{10^{-5}M_{\rm p}}\right)^2. \tag{4.22}$$

The second part is the scale-dependent one, which encodes crucial information about reheating. $k_{\rm re}=a_{\rm re}H(a_{\rm re})$ is the mode that enters the horizon at the end of reheating, and its value naturally depends on $T_{\rm re}$. On the other hand, $k_{\rm end}$ enters the reheating phase at the beginning and is fixed by $H_{\rm end}$ and $T_{\rm re}$, which is defined as

$$k_{\rm end}=a_{\rm end}H_{\rm end}=e^{N_k}\left(\frac{k_\star}{a_0}\right)\left(\frac{H_{\rm end}}{H_k}\right). \tag{4.23}$$

Using the entropy conservation Eq. 4.18, the above equation can be written as follows

$$k_{\rm end}=H_{\rm end}\left(\frac{43}{11g^{\rm re}_{\star r}}\right)^{1/3}\frac{T_0}{T_{\rm re}}\,e^{-N_{\rm re}}, \tag{4.24}$$

Using the expression of $N_{\rm re}$ from Eq. 4.15, $k_{\rm end}$, can therefore be expressed as,

$$k_{\rm end}=H_{\rm end}T_0\left(\frac{43}{11g^{\rm re}_{\star r}}\right)^{1/3}\left(\frac{\pi^2 g^{\rm re}_{\star r}}{30\,\rho^{\rm end}_\phi}\right)^{\frac{1}{3(1+w_\phi)}}T_{\rm re}^{\frac{1-3w_\phi}{3(1+w_\phi)}} \tag{4.25}$$

Similarly, $k_{\rm re}$ can be written as,

$$k_{\rm re}=\left(\frac{43}{11g^{\rm re}_{\star r}}\right)^{1/3}\left(\frac{\pi^2}{90\,g^{\rm re}_{\star r}}\right)^{1/2}\frac{T_0\,T_{\rm re}}{M_{\rm p}}. \tag{4.26}$$

We can clearly see from Eq. 4.21 that modes entering during reheating become red tilted for $w_\phi<1/3$, and blue tilted for $w_\phi>1/3$ (see left Fig. 5.43). Thus, the amplitude of the GW energy $\Omega^{k}_{\rm GW}h^2$ is an increasing function of k for $w_\phi>1/3$. In the next part, we will discuss the calculation part of the BBN constraints in the context of PGWs

The effective number of additional relativistic degrees of freedom quantified by $\Delta N_{\rm eff}$ at the time of BBN places tighter constraints on the reheating temperature. High-frequency GWs can be thought of as an effective relativistic degree of freedom during reheating. Therefore, if the reheating phase is long enough to correspond to low reheating temperature, $k_{\rm end}>>k_{\rm re}$, the GW energy puts a tighter constraint. The constraint equation is expressed as,

$$\Delta N_{\rm eff}\geq\frac{1}{\Omega_r h^2}\frac{8}{7}\left(\frac{11}{4}\right)^{4/3}\int_{k_0}^{k_{\rm end}}\frac{dk}{k}\Omega^{k}_{\rm GW}h^2 \tag{4.27}$$

The combination of the latest Planck 2018+ BAO data provides $\Delta N_{\rm eff}\leq0.284$ (within 2-σ) [31]. The straight forward's calculation with the above equation yields the following bound on the total GW energy density $\Omega^{k}_{\rm GW}h^2<1.7\times10^{-6}$, and that is depicted by the solid red line in Fig. 5.43. However, we wish to translate this bound into the associated reheating temperature. In the above expression, it is the maximum

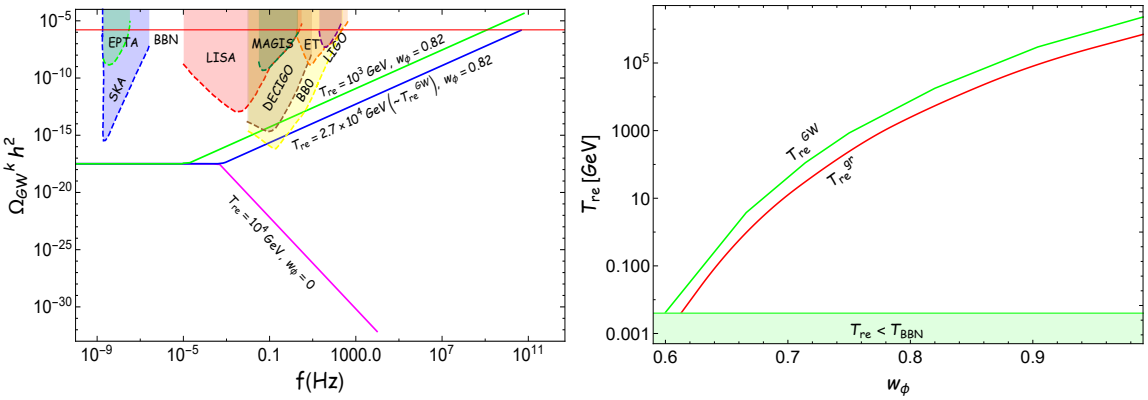

Figure 4.1: Left panel: Variation of the dimensionless energy density of PGWs observed today, viz $\Omega_{\rm GW}^k h^2$ as a function of frequency over a wide range. Right panel: Comparison between gravitational reheating temperature $T_{\rm re}^{\rm gr}$ (red curve) and $T_{\rm re}^{\rm GW}$ (green curve). For both panel, we have taken α-attractor E model with $\alpha = 1$

$k \sim k_{\rm end}$ which contributes the most to the total GW energy, and one obtains the following constraint relation,

$$2.1 \times 10^{-11} \frac{\mu(w_\phi)(1+3w_\phi)}{\pi(6w_\phi - 2)} \left[\frac{H_{\rm end}}{10^{-5} M_{\rm p}}\right]^2 \leq \left(\frac{k_{\rm end}}{k_{\rm re}}\right)^{\frac{(2-6w_\phi)}{(1+3w_\phi)}} \tag{4.28}$$

The relation between the two scales $(k_{\rm end}, k_{\rm re})$ can be further expressed in terms of reheating temperature as follows:

$$\left(\frac{k_{\rm end}}{k_{\rm re}}\right) = \left(\frac{15\,\rho_\phi^{\rm end}}{\pi^2\, g_{\star r}^{\rm re}}\right)^{\frac{1+3w_\phi}{6(1+w_\phi)}} T_{\rm re}^{\frac{-2(1+3w_\phi)}{3(1+w_\phi)}}. \tag{4.29}$$

Finally, using the above relations in Eq. 4.28, we obtain a lower limit on the reheating temperature, particularly when the inflaton EoS $w_\phi > 1/3$,

$$\begin{aligned} T_{\rm re} &> 0.35 \left(\frac{45.6\, M_{\rm p}^4}{\mu(\phi)}\right)^{\frac{3(1+w_\phi)}{4(1-3w_\phi)}} \left(\rho_\phi^{\rm end}\right)^{-\frac{1}{2}\frac{(1+3w_\phi)}{(1-3w_\phi)}} \\ &= T_{\rm re}^{\rm GW}. \end{aligned} \tag{4.30}$$

Setting the above temperature with BBN energy scale $T_{\rm re}^{\rm GW} \sim T_{\rm BBN} = 4$ MeV, we can see that the BBN bound of PGWs is only important when $w_\phi \gtrsim 0.60$. We symbolize this new lower limit on reheating temperature from PGW as $T_{\rm re}^{\rm GW}$. As an example for $w_\phi = 0.82$ $(n = 10)$ the expression for $T_{\rm re}^{\rm GW}$ can be expressed as

$$T_{\rm re}^{\rm GW} \sim 2.1 \times 10^6 \left(\frac{\rho_\phi^{\rm end}}{4.1 \times 10^{64}}\right)^{\frac{19}{16}}. \tag{4.31}$$

Now for $H_{\rm end} = 10^{13}$ GeV, $T_{\rm re}^{\rm GW}$ simply turns out as 5×10^4 GeV, and that will set the lower limit on the reheating temperature. In Fig. 5.43, we showed blue tilted behavior for $w_\phi = 0.82$, for two different sample reheating temperature $(10^4, 10^3)$ GeV. For $T_{\rm re} = 10^3$ GeV, $\Omega_{\rm GW}^k h^2 \sim 10^{-4}$ at $k = k_{\rm end}$, and it clearly violates the BBN constraints discussed just above. However, for $T_{\rm re} \sim 2.7 \times 10^4$ GeV, we see $\Omega_{\rm GW}^{k_{\rm end}} h^2$ marginally satisfies the BBN constraints, and that is consistent with our above estimation of $T_{\rm re}^{\rm GW}$.

Fixing the same $H_{\rm end}$, the numerical values of $T_{\rm re}^{\rm GW}$ for different EoS are shown in Table-4.2. Since $T_{\rm re}^{\rm GW}$ is a function of both $H_{\rm end}$ and w_ϕ, for a fixed value of w_ϕ, it can restrict the inflationary energy scale,

Table 4.2: Numerical values of the $T_{\rm re}^{\rm GW}$ for a fixed value of $H_{\rm end} = 10^{13}$ GeV

$n(w_\phi)$	$T_{\rm re}^{\rm GW}$ (GeV)
4 (0.60)	4.2×10^{-3}
5 (0.67)	13.4
6 (0.71)	3.6×10^{2}
10 (0.82)	5.0×10^{4}
25 (0.92)	1.2×10^{6}
200 (0.99)	5.7×10^{6}

which in turn puts a constraint on the potential parameter, such as α and ϕ_*, for the attractor and minimal model, respectively. Another interesting point is that this $T_{\rm re}^{\rm GW}$ also sets bounds on the inflaton coupling to other fields, which we will discuss in more detail in the subsequent sections for $\phi \to \bar{f}f/bb$ decay processes.

Note that in the previous chapter, we observed that when $w_\phi \gtrsim 0.65$, the universal gravitational production of radiation from the inflaton imposes a lower bound on the reheating temperature, denoted as $T_{\rm re}^{\rm gr}$ (see Eq. 3.28). However, this lower bound is weaker than the one set by the gravitational wave constraint $T_{\rm re}^{\rm GW}$, as illustrated in the right panel of Fig. 5.43. Therefore, for $w_\phi \geq 0.60$, we adopt $T_{\rm re}^{\rm GW}$ as the lower bound for the reheating temperature. Since in this chapter, our primary motivation is to constrain reheating parameters, not to study the reheating dynamics, that's why we do not include the gravitational reheating in this chapter.

4.4 One-loop effective potential and perturbative constraints during inflation

In the previous section, we discussed the possible lower bound on $T_{\rm re}$ through PGWs. Purely from the perturbative reheating point of view, the existence of maximum $T_{\rm re}$ is typically attributed to the instant reheating process with $N_{\rm re} \to 0$. In this regard, one should remember that the upper limit on $T_{\rm re}$ is directly related to the upper limit on inflaton-radiation coupling. During inflation, such coupling can naturally modify the effective inflaton potential through loop correction, which may modify the aforesaid upper bound so that inflation is not disturbed. In this section, we investigate the upper bound of the coupling parameters, below which the inflationary scenario is not affected by the inflaton-radiation coupling. We follow Coleman and Weinberg's (CW) 1-loop radiative correction formalism to determine the bound. The 1-loop corrected inflaton-potential is given by [218]

$$V_{\rm CW}(\phi) = \sum_i \frac{n_i}{64\pi^2}(-1)^{2s_i}\, m_i^4(\phi) \left[\ln\left(\frac{m_i^2(\phi)}{\mu^2}\right) - 3/2\right], \tag{4.32}$$

where summation, i runs over the radiation fields (f, b). (n_i, s_i) represents the total internal degrees of freedom and spin. μ is the renormalization scale, which we have taken ϕ_k. $m_i(\phi)$ corresponds to the inflaton field induced mass. The field-dependent mass of the fermionic (f) and the bosonic (b) fields can be written as

$$m_i^2(\phi) = \begin{cases} h^2\phi^2 & \text{for } \phi\bar{f}f \\ 2g\phi & \text{for } \phi bb \end{cases} \tag{4.33}$$

For the stability of the inflation potential, the coupling parameter (g, h) should be such that the following

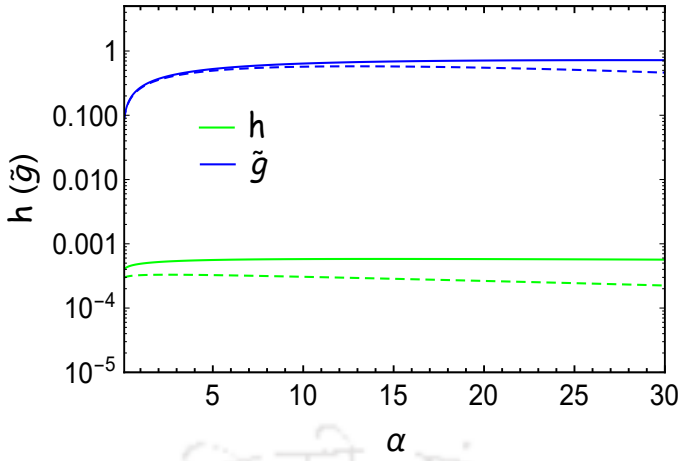

Figure 4.2: Here we plot the variation of the upper limit of the coupling parameter (from Eq. 4.37) as a function α for $w_\phi = 0.0$ (solid) and $w_\phi = 0.99$ (dashed) for α-attractor E model.

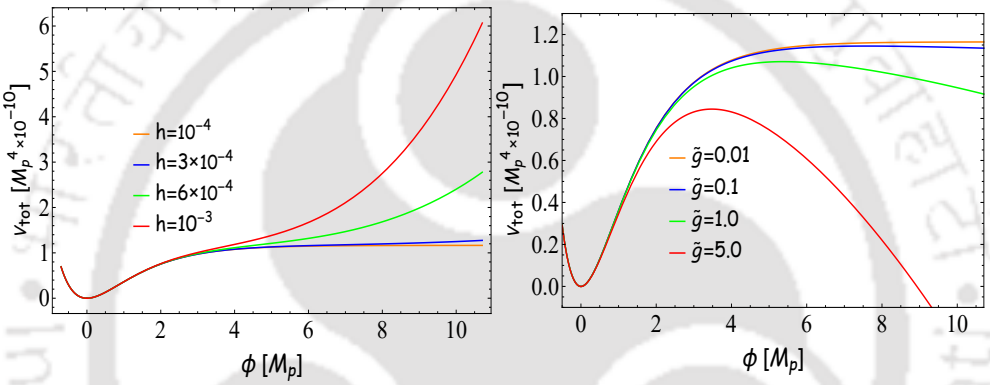

Figure 4.3: Sum of the tree level potential and CW 1-loop corrected potential, $V_{\rm tot} = V_{\rm tree} + V_{\rm CW}$ as a function of filed value ϕ for α-attractor E-model ($\alpha = 1, n = 2$) with two different interactions $h\phi\bar{f}f$ (left panel) and $g\phi bb$ (right panel).

inequality must hold,

$$\left|V_{\rm tree}(\phi)\right| > \left|V_{\rm CW}(\phi)\right|, \tag{4.34}$$

where, $V_{\rm tree}$ is the tree level potential defined in Eq. 5.70. Utilizing the above condition (Eq. 4.34), one can find the following analytical expressions for the upper bound of the coupling parameters,

$$g < \frac{8i\sqrt{2}\pi|V_{\rm tree}(\phi)|^{1/2}}{\phi^2 \mathcal{W}_{-1}\left[-\frac{128\pi^2\phi^2}{e^3\mu^4}|V_{\rm tree}(\phi)|\right]^{1/2}} \tag{4.35}$$

$$h < \frac{(-2)^{1/4}\sqrt{\pi}|V_{\rm tree}(\phi)|^{1/4}}{\phi \mathcal{W}_{-1}\left[-\frac{32\pi^2}{e^3\mu^4}|V_{\rm tree}(\phi)|\right]^{1/4}} \tag{4.36}$$

where $\mathcal{W}_{-1}$ is the Lambert function of branch -1 and the above expressions are only for E and T model, so $V_{\rm tree}$ is different for different models. For the minimal model, we could not obtain such an analytical expression. The Eq. 4.37 seems to suggest a complicated dependence of the couplings on the inflaton parameters. However, Fig-4.2 indicates that the lower limit on the couplings is indeed insensitive to α or

w_ϕ, and approximately we, therefore, estimate,

$$\begin{aligned} g &< 8\times 10^{13}\left[\frac{\Lambda}{1.4\times 10^{16}}\right]^2\left[\frac{M_p}{\phi}\right], \\ h &< 5.8\times 10^{-3}\left[\frac{\Lambda}{1.4\times 10^{16}}\right]\left[\frac{M_p}{\phi}\right], \end{aligned} \tag{4.37}$$

We have checked numerically that this bound is also the same for the E, T, and minimal models. We define all the inflationary observables at the pivot scale with a field value, ϕ_k. In Fig. 4.3, we have shown how a strong coupling parameter modifies the original potential through CW one-loop radiative correction, and violation of the above condition Eq. 4.37 always leads to a deviation from the original potential. Therefore, any coupling violating Eq. 4.37 will not be allowed. In all the plots, we shaded it in blue color and mentioned it as not allowed. For example, the upper bound of the dimensionless bosonic coupling parameter $\tilde{g} = g/m_\phi^{end}$ assumes $\mathcal{O}(10^{-1})$ value, and this bound is nearly model-independent. Corresponding $T_{\rm re}^{\rm max}$ value appears to be the same as that of the instantaneous reheating temperature ($\sim 10^{15}$ GeV). Hence, for bosonic reheating, no parameter space is ruled out by the radiative CW correction. On the other hand, for fermionic reheating, the upper bound on the Yukawa coupling parameter (h) assumes nearly model-independent value $\sim 10^{-4}$, and that can be observed from all the Figs. 4.9,4.10 and 4.11 (shaded in blue color). For the sake of brevity, we call these as Coleman-Weinberg constraints (CWc).

As discussed above, the CWc constraints are about the perturbative correction to the inflaton potential, particularly during inflation. This limit should be assumed as the strict upper limit of the inflaton coupling constant with the radiation. However, during reheating, the process through which inflaton decays into radiation may be non-perturbative in nature. We now turn to discuss another bound on the coupling parameters coming from the effect during reheating.

4.5 Non-perturbative Constraints during reheating

Radiation can be produced resonantly during reheating if the inflaton-radiation coupling is strong enough. However, our present analysis is perturbative. Therefore, it is imperative to identify the constraints (NPc) on the coupling for which our conclusion may not be strictly valid. For this, one usually solves the radiation field equation in the oscillating inflaton background and identifies the coupling region where broad parametric resonance occurs. The mode equation for the radiation field assumes a general Hill-type equation as follows,

$$\frac{1}{(m_\phi^{\rm end})^2}\frac{d^2X_k}{dt^2} + Q(t)^2 X_k = 0 \tag{4.38}$$

Where, X_k is a particular field mode for fermion (f), or boson (b), and the associated time-dependent frequencies are

$$\mathrm{Q}(t)^2 = \begin{cases} \frac{k^2}{(m_\phi^{\rm end})^2 a^2} + q^2(t)\mathscr{P}^2(t) - i\frac{q(t)\dot{\mathscr{P}}(t)}{m_\phi^{\rm end}} & \text{for } \phi\bar{f}f \\ \frac{k^2}{(m_\phi^{\rm end})^2 a^2} + q^2(t)\mathscr{P}(t) & \text{for } \phi bb \end{cases} \tag{4.39}$$

Given the inflaton-radiation coupling of our interest Eq. 4.9, the resonance parameter q is identified as

$$q(t) = \begin{cases} \sqrt{\frac{h^2\phi_0^2(t)}{(m_\phi^{\rm end})^2}} & \text{for } \phi\bar{f}f \\ \sqrt{\frac{g\phi_0(t)}{(m_\phi^{\rm end})^2}} & \text{for } \phi bb \end{cases} \tag{4.40}$$

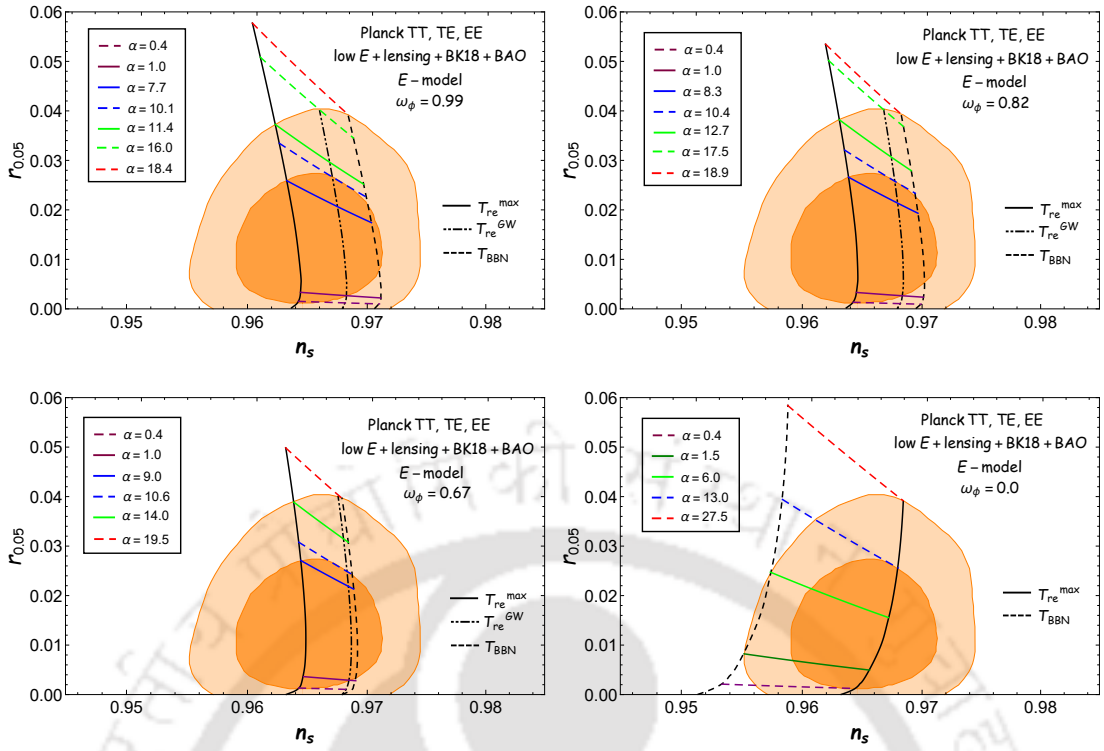

Figure 4.4: Prediction of α-attractor E-model for different (α, w_ϕ) projected on the recent Planck + BICEP/*Keck* constrained on (n_s, r) plane Ref.[55]. Deep orange and light orange shaded regions correspond to 1σ region at 68% CL and 2σ region at 95% C.L., respectively. Reheating temperature varies from $T_{\rm BBN} \to T_{\rm re}^{\rm max}$, showing in solid and dashed black lines. Another important temperature scale, $T_{\rm re}^{\rm GW}$, is shown in a dot-dashed black line.

In the literature, conditions of resonance is usually derived in Minkowski background [43, 144, 196], and the resonance is broadly classified into $q > 1$ called the broad resonance regime and $q \lesssim 1$ called the narrow or no resonance regime. However, in reality, the resonance parameter q depends non-trivially on time through inflaton oscillation amplitude $\phi_0(t)$, and hence the naive Minkowski approximation has been observed to be insufficient. Particularly, with increasing reheating EoS, the inflaton amplitude dilutes very fast, $\phi_0(t) \propto \phi_{\rm end}(a(t)/a_{\rm end})^{-3/(n+1)}$ depending on different n values. The details solution for ϕ_0 is provided in Appendix-A. Using decaying inflaton amplitude in $H^2 \simeq V(\phi_0)/3M_p^2$, we get the leading order behavior of post-inflationary scale factor as

$$a(t) = a_{\rm end}\left(\frac{t}{t_{\rm end}}\right)^{\frac{n+1}{3n}}. \tag{4.41}$$

Using above equation and Eq. 4.40 the resonance parameter $q(t)$ evolves as,

$$q(t) = \begin{cases} \sqrt{\frac{h^2\phi_{\rm end}^2}{(m_\phi^{\rm end})^2}}\left(\frac{t}{t_{\rm end}}\right)^{-\frac{1}{n}} & \text{for } \phi\bar{f}f \\ \sqrt{\frac{g\phi_{\rm end}}{(m_\phi^{\rm end})^2}}\left(\frac{t}{t_{\rm end}}\right)^{-\frac{1}{2n}} & \text{for } \phi b\,b. \end{cases} \tag{4.42}$$

In this dynamical scenario, we propose resonance condition as follows:
Resonant particle production is strongly related to the violation of adiabaticity condition, and that occurs when the background crosses zero during oscillation. To have significant resonant production within a certain period, one needs to satisfy two essential conditions. The first one is to have the oscillatory

background, executing few oscillations within the period of interest. The second condition is that within that period, the resonance q-parameter should remain greater than unity. Combining these aforesaid conditions, we state that for broad resonance to take place while the resonance parameter q evolves from its initial value to unity, it must complete at least one oscillation. Having this dynamical condition of broad resonance, we derive the lower bound of the inflaton-radiation couplings for general background EoS.

To compute the number of oscillations required for q-parameter to change from its large initial value $q_{\rm in}$ at the end of inflation to unity, we measure the dimensionless time-period of the oscillating inflaton as $T^{(\Omega)} = 2\pi m_\phi^{\rm end}/\Omega_0$, where Ω_0 is the background oscillation frequency calculated at $\phi_0 = M_p$(see Eq. 4.5 and Eq. 4.6). On the basis of these, the number of oscillations $N_{\rm osc}$ becomes,

$$N_{\rm osc} = \frac{t - t_{\rm end}}{T^{(\Omega)}} = \begin{cases} \frac{t_{\rm end}}{T^{(\Omega)}}\left(\left(\frac{h\phi_{\rm end}}{m_\phi^{\rm end}}\right)^n - 1\right) & \text{for } \phi\bar{f}f \\ \frac{t_{\rm end}}{T^{(\Omega)}}\left(\left(\frac{\sqrt{g}\phi_{\rm end}}{m_\phi^{\rm end}}\right)^{2n} - 1\right) & \text{for } \phi b b \end{cases}, \tag{4.43}$$

Where

$$\frac{t_{\rm end}}{T^{(\Omega)}} = \frac{\sqrt{2n(2n-1)}(n+1)M_{\rm p}\,\Omega_0}{2\pi\sqrt{3}\,n\,m_\phi^{\rm end}\phi_{\rm end}}.$$

Therefore, the minimum criterion that has to be met to achieve efficient resonance is $N_{\rm osc} > 1$. This yields the lower bound of the coupling strength for two decay channels as

$$\begin{aligned} h &> \frac{m_\phi^{\rm end}}{\phi_{\rm end}}\left[1 + \frac{2\pi\sqrt{3}\,n\phi_{\rm end}m_\phi^{\rm end}}{\sqrt{2n(2n-1)}(n+1)M_{\rm p}\Omega_0}\right]^{\frac{1}{n}} \\ g &> \frac{(m_\phi^{\rm end})^2}{\phi_{\rm end}}\left[1 + \frac{2\pi\sqrt{3}\,n\phi_{\rm end}m_\phi^{\rm end}}{\sqrt{2n(2n-1)}(n+1)M_{\rm p}\Omega_0}\right]^{\frac{1}{n}} \end{aligned} \tag{4.44}$$

The first term on the right-hand side of the above expressions is the one that comes from the standard analysis in Minkowski space. The new bracketed correction term originates from our dynamical definition. Considering the attractor model, the typical upper limit on the dimensionless coupling parameter $\tilde{g}, h \sim (10^{-4}, 10^{-3})$ with the allowed range of $w_\phi = (0, 1)$. To this end, we would like to stress that, unlike CWc discussed before, NPc only suggests that above this coupling, the reheating dynamics will be modified by the non-perturbative effect.

4.6 Results and discussions

So far, we have analyzed different sources of constraints from observation and theory and their possible direct and indirect impacts on inflation. We considered three plateau types of inflation models, namely α-attractor E, T, and minimal models, and two possible reheating scenarios depending on the inflaton-radiation coupling. Before we embark on discussing the results, let us summarize the main inputs we are considering:

- The combined observation data of the latest Planck 2018 and BICEP/*Keck* put stringent constraints on inflationary large-scale observables, namely, scalar spectral index $n_{\rm s}$ and tensor-to-scalar ratio r. Such constraints directly impact the possible range of inflationary parameters, such as the potential height (Λ), inflationary energy scale (H_k , $H_{\rm end}$), and the potential's nature at the end of the inflation through the potential parameter like n , α , $\phi_\star$.

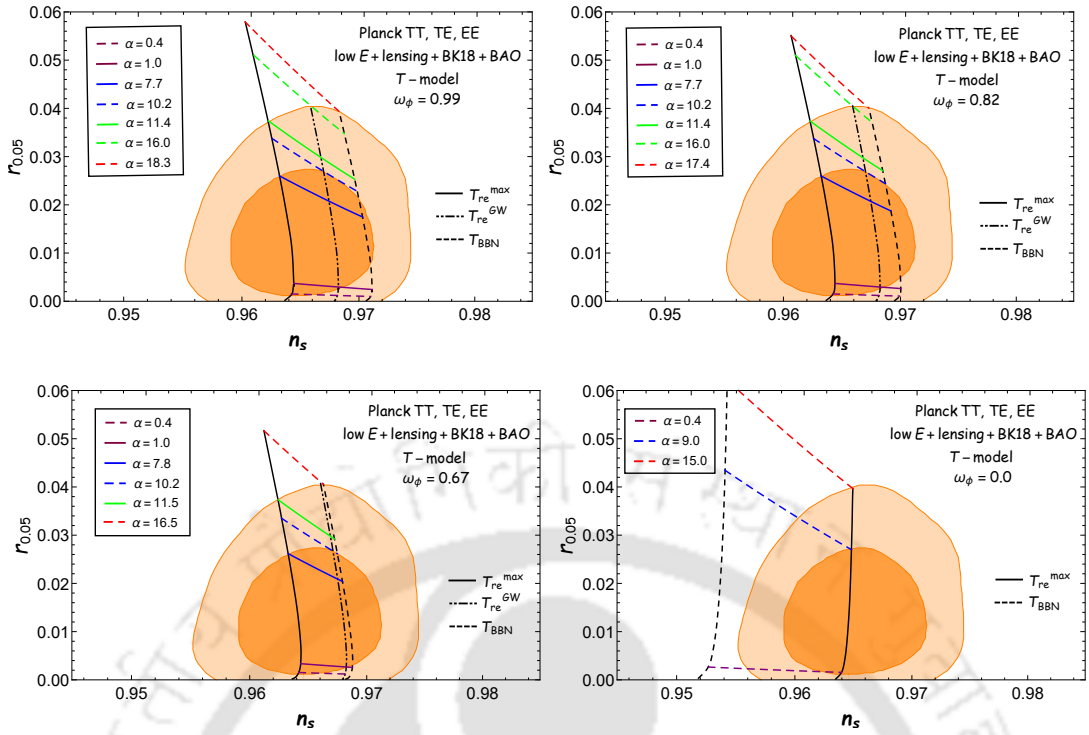

Figure 4.5: Prediction of α-attractor T-model for different (α, w_ϕ). Detailed descriptions are the same as illustrated in Fig. 4.4

Table 4.3: Limiting values of $(N_k, H_{\rm end}, \alpha)$: attractor model

E-model

w_ϕ	1 σ+ PGWs			2 σ+ PGWs		
	$\alpha_{\rm max}$	$H_{\rm end}^{\rm min}$ (GeV)	N_k	$\alpha_{\rm max}$	$H_{\rm end}^{\rm min}$ (GeV)	N_k
0.99	10.2	2.6×10^{12}	64.7,55.6	16.0	1.6×10^{12}	65.4,55.1
0.82	10.4	3.5×10^{12}	64.5,55.6	17.5	2.1×10^{12}	65.1,55.1
0.67	10.6	4.4×10^{12}	64.2,55.7	19.5	3.1×10^{12}	64.8,55.1

T-model

w_ϕ	1 σ+ PGWs			2 σ+ PGWs		
	$\alpha_{\rm max}$	$H_{\rm end}^{\rm min}$ (GeV)	N_k	α max	$H_{\rm end}^{\rm min}$ (GeV)	N_k
0.99	10.2	2.9×10^{12}	64.7,55.7	16.0	1.9×10^{12}	65.3,55.1
0.82	10.2	3.0×10^{12}	64.6,55.6	16.0	2.0×10^{12}	65.2,55.1
0.67	10.2	3.3×10^{12}	64.5,55.6	16.5	2.3×10^{12}	65.1,55.1

- Subsequent reheating causes inflaton to decay into radiation through different decay channels are under consideration. Non-trivial reheating dynamics supplemented with the post-reheating entropy conservation relates different observable and the reheating parameters though Eq. 4.18, and that immediately gives us additional constraints on the inflaton model through the maximum ($T_{\rm re} \sim 10^{15}$ GeV) and minimum ($T_{\rm re} \sim 4$ MeV) reheating temperature in the $(n_{\rm s}, r)$ plane. The bound on reheating temperature will lead to bound on the inflaton-radiation couplings $(h, \tilde{g} = g/m_\phi^{\rm end})$.

- Planck, BICEP/*Keck* usually measures large-scale inflationary fluctuations. Interestingly, the small-scale inflationary tensor fluctuations (PGWs) have been observed to play an interesting role in

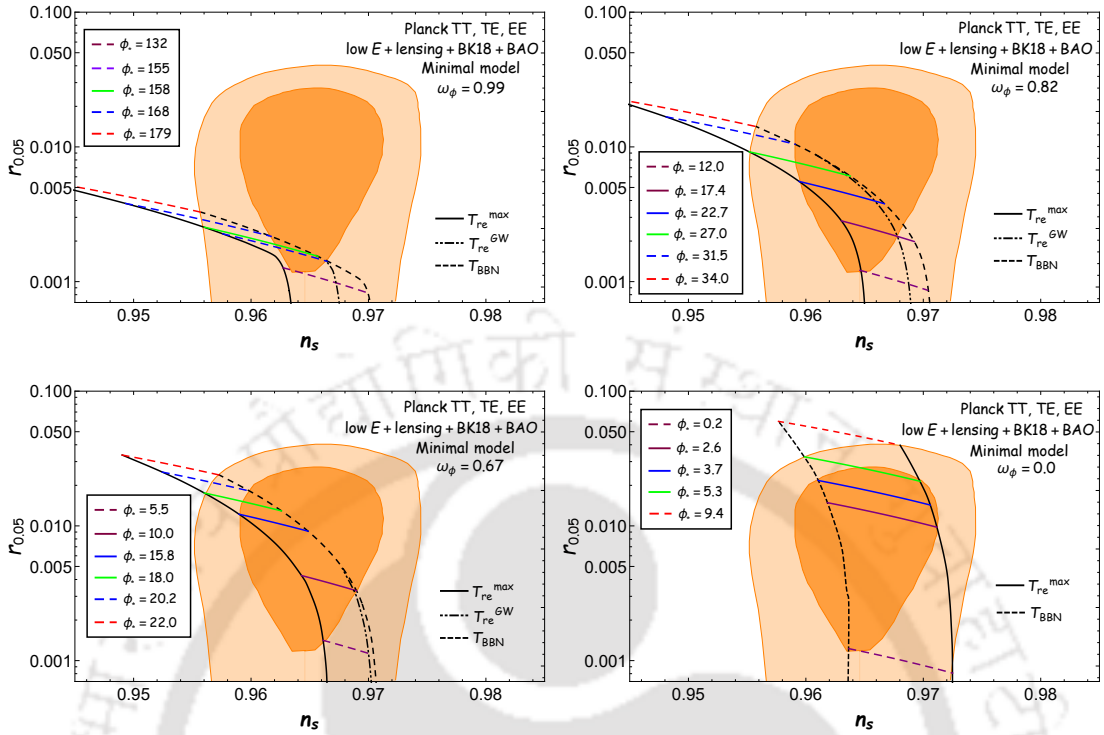

Figure 4.6: Prediction of minimal model for different values of (ϕ_*, w_ϕ). Detailed descriptions are the same as illustrated in Fig. 4.4

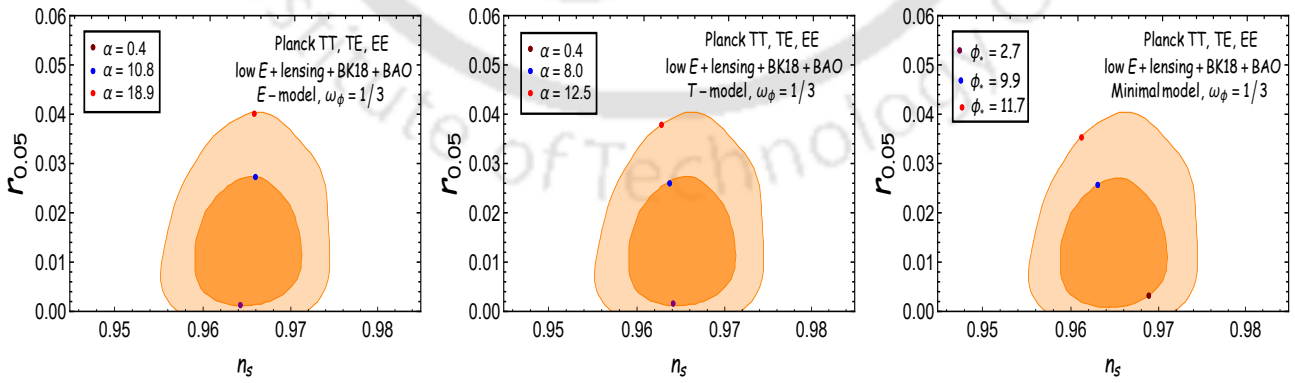

Figure 4.7: Illustrations of the restriction on the different inflationary models from recent BICEP/*Keck* data for a specific value of $w_\phi = 1/3$.

Table 4.4: Limiting values of $(N_k, H_{\rm end}, \alpha, \phi_*)$

For $w_\phi = 0.0$

Model	$1\,\sigma$			$2\,\sigma$		
	α, ϕ_* (max)	$H^{\rm min}_{\rm end}$ (GeV)	N_k	α, ϕ_* (max)	$H^{\rm min}_{\rm end}$ (GeV)	N_k
E	13.0	1.1×10^{13}	56.2,41.8	27.5	1.1×10^{13}	56.4,41.5
T	9.0	8.6×10^{12}	56.4,41.5	15	8.7×10^{12}	56.6,41.5
Minimal	5.3	1.0×10^{13}	56.1,41.5	9.4	9.5×10^{12}	56.5,41.5

For $w_\phi = 1/3$

Model	$1\,\sigma$			$2\,\sigma$		
	α, ϕ_* (max)	$H^{\rm min}_{\rm end}$ (GeV)	N_k	α, ϕ_* (max)	$H^{\rm min}_{\rm end}$ (GeV)	N_k
E	10.8	7.6×10^{12}	56.7,55.3	18.9	6.7×10^{12}	56.9,54.9
T	9.0	5.7×10^{12}	56.8,55.4	12.5	5.1×10^{12}	57.0,54.9
Minimal	9.9	4.0×10^{12}	57,55.6	11.7	4×10^{12}	57.0,54.2

Table 4.5: Limiting values of $(N_k, H_{\rm end}, \phi_*)$ for Minimal model

w_ϕ	$1\,\sigma + T^{\rm max}_{\rm re}$			$1\,\sigma$+ BBN+PGWs			$2\,\sigma$+ BBN+PGWs		
	$\phi^{min}_\star$	$H^{\rm max}_{\rm end}$ (GeV)	N_k	$\phi^{\rm max}_\star$	$H^{\rm min}_{\rm end}$ (GeV)	$N^{\rm max}_k$	$\phi^{max}_\star$	$H^{\rm min}_{\rm end}$ (GeV)	N_k
0.99	132.0	2.4×10^{12}	74.5,57.4	168.0	4.0×10^{5}	74.5,57.4	179.0	8.6×10^{2}	76.7,51.0
0.82	12.0	1.4×10^{12}	67.5,56.8	31.5	5.8×10^{10}	67.5,56.8	34.0	5.2×10^{10}	67.7,52.6
0.67	5.5	5.1×10^{12}	66.2,55.6	20.2	1.9×10^{11}	66.2,55.6	22.0	1.4×10^{11}	66.4,53.3

further constraining the possible range of reheating temperature. If the reheating period is prolonged, and reheating EoS $w_\phi > 1/3$, the high-frequency gravitational waves acquire blue tilted spectrum $\Omega^k_{\rm GW} \sim k^{n_{w_\phi}}$, where n_{w_ϕ} is the index of the spectrum and that may lead to larger lower bound on reheating temperature $T^{\rm GW}_{\rm re} > T_{\rm BBN}$. Such lower bounds naturally lead to tighter bounds on the inflaton-radiation couplings.

- In the perturbative framework, instantaneous reheating gives a natural upper bound on the inflaton-radiation coupling. However, generically, such coupling modifies the inflaton potential at the loop level during inflation (CW constraints (CWc)). The loop-corrected inflaton potential should not disturb the inflation (see Fig. 4.3), which may modify the maximum reheating temperature and, consequently, the inflaton-radiation coupling parameter. We consider those bound throughout our analysis.

- We further identify the non-perturbative constraints (NPc) on the inflaton-radiation coupling by employing the broad parametric resonance condition, taking into account the dynamical nature of resonance parameter $q(t)$ (see Eq. 4.40). These constraints will also be incorporated into our final results.

Planck + BICEP/Keck + BBN + PGWs + CWc + NPc constraints on inflation:
First, we display our theoretical prediction of $n_{\rm s}, r$ in $(n_{\rm s} - r)$ plane and compare it with the latest observational data (see Figs. 4.4-4.7) for the three different inflationary models with five reheating EoSs $w_\phi = (0, 1/3, 0.67, 0.82, 0.99)$. The predictions for $n_{\rm s}$ and r are the same for both reheating frameworks, $\phi \to \bar{f} f$ and $\phi \to b b$. In the previous chapter, we showed that the relation between $T_{\rm re}$ and $n_{\rm s}$ is insensitive to the choice of reheating framework (see Eq. 3.30). Similarly, the predictions for $n_{\rm s}$ and r are also

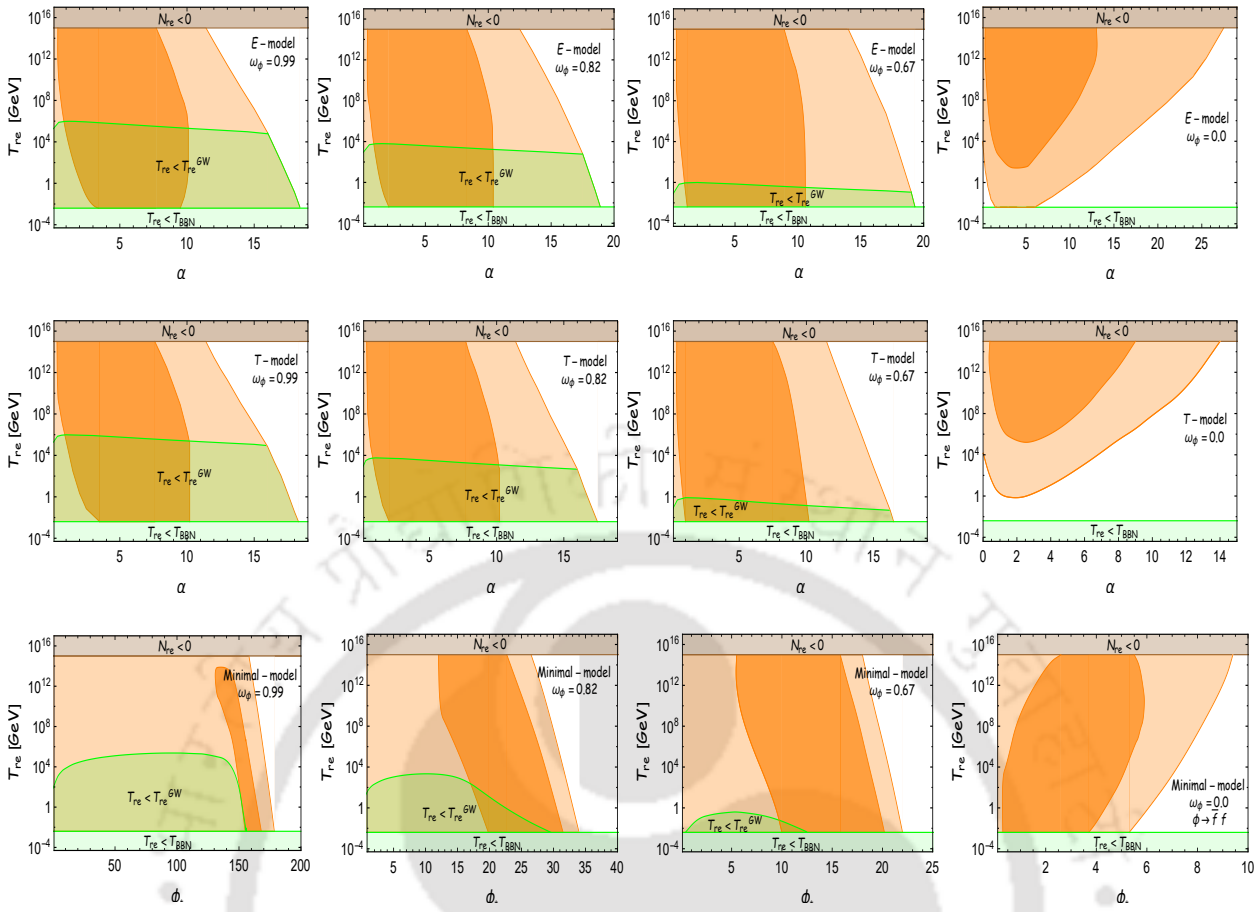

Figure 4.8: The impact of Planck 2018 + BICEP/Keck + PGW + BBN on $T_{\rm re}$ with respect to $\alpha(\phi_\star)$ for α-attractor E-model (top), T-model (middle), and minimal model (bottom). We take $w_\phi = (0, 0.67, 0.82, 0.99)$. Deep orange shaded regions correspond to 1σ and light orange shaded regions correspond to 2σ bound imported from $(n_{\rm s} - r)$ plane. The deep and light green region indicates $T_{\rm re} < T_{\rm BBN}$ and $T_{\rm re} < T_{\rm re}^{\rm GW}$, respectively. Gray-shaded region implies no reheating.

Table 4.6: Bounds on $(T_{\rm re}, \tilde{g}, h)$ from PGWs+BBN+CWc+NPc with recent BICEP/*Keck* data for E-model

I) Fermionic reheating ($\phi \to \bar{f} f$)

w_ϕ	1σ+BBN+PGWs+CWc		1σ+BBN+PGWs+CWc+NPc		2σ+BBN+PGWs+CWc		$2\,\sigma$+BBN+PGWs+CWc+NPc	
	$T_{\rm re}$(GeV)	h	$T_{\rm re}$ (GeV)	h	$T_{\rm re}$ (GeV)	h	$T_{\rm re}$ (GeV)	h
0.99	$10^{11}, 10^5$	$3\times10^{-4}, 10^{-6}$	$10^{12}, 10^5$	$10^{-3}, 10^{-6}$	$10^{11}, 7\times10^4$	$3\times10^{-4}, 7\times10^{-7}$	$10^{12}, 7\times10^4$	$10^{-3}, 8\times10^{-7}$
0.82	$10^{9}, 10^3$	$3\times10^{-4}, 10^{-6}$	$10^{8}, 10^3$	$7\times10^{-5}, 10^{-6}$	$10^{9}, 7\times10^2$	$3\times10^{-4}, 10^{-6}$	$10^{8}, 7\times10^2$	$7\times10^{-5}, 10^{-6}$
0.67	$10^{7}, 0.3$	$3\times10^{-4}, 5\times10^{-7}$	$5\times10^{5}, 0.3$	$6\times10^{-5}, 5\times10^{-7}$	$10^{7}, 0.1$	$5\times10^{-4}, 4\times10^{-7}$	$5\times10^{5}, 0.1$	$6\times10^{-5}, 4\times10^{-7}$
1/3	$10^{6}, 0.004$	$3\times10^{-4}, 10^{-9}$	$10^{5}, 0.004$	$6\times10^{-5}, 10^{-9}$	$10^{6}, 0.004$	$3\times10^{-4}, 10^{-9}$	$10^{5}, 0.004$	$6\times10^{-5}, 10^{-9}$
0.0	$10^{11}, 10$	$5\times10^{-4}, 10^{-14}$	$10^{10}, 10$	$6\times10^{-5}, 10^{-14}$	$10^{11}, 0.004$	$5\times10^{-4}, 10^{-17}$	$10^{10}, 0.004$	$6\times10^{-5}, 10^{-17}$

II) Bosonic reheating ($\phi \to bb$)

w_ϕ	1σ+BBN+PGWs+CWc		1σ+BBN+PGWs+CWc+NPc		2σ+BBN+PGWs+CWc		2σ+BBN+PGWs+CWc+NPc	
	$T_{\rm re}$(GeV)	$\tilde{g}$	$T_{\rm re}$ (GeV)	$\tilde{g}$	$T_{\rm re}$ (GeV)	$\tilde{g}$	$T_{\rm re}$ (GeV)	$\tilde{g}$
0.99	$10^{15}, 10^5$	$10^{-2}, 10^{-21}$	$10^{14}, 10^5$	$10^{-3}, 10^{-21}$	$10^{15}, 7\times10^4$	$10^{-2}, 10^{-22}$	$10^{14}, 7\times10^4$	$10^{-3}, 10^{-22}$
0.82	$10^{15}, 10^3$	$0.3, 10^{-23}$	$10^{13}, 10^3$	$7\times10^{-5}, 10^{-23}$	$10^{15}, 7\times10^2$	$0.3, 3\times10^{-24}$	$10^{13}, 7\times10^2$	$7\times10^{-5}, 3\times10^{-24}$
0.67	$10^{15}, 0.3$	$0.4, 10^{-29}$	$4\times10^{12}, 0.3$	$6\times10^{-5}, 10^{-29}$	$10^{15}, 0.1$	$0.5, 3\times10^{-29}$	$4\times10^{12}, 0.1$	$6\times10^{-5}, 3\times10^{-29}$
1/3	$10^{15}, 0.004$	$0.5, 10^{-27}$	$10^{11}, 0.004$	$6\times10^{-5}, 10^{-27}$	$10^{15}, 0.004$	$0.5, 10^{-27}$	$10^{11}, 0.004$	$6\times10^{-5}, 10^{-27}$
0.0	$10^{15}, 10$	$0.5, 10^{-14}$	$10^{10}, 10$	$6\times10^{-5}, 10^{-14}$	$10^{15}, 0.004$	$0.5, 10^{-17}$	$10^{10}, 0.004$	$6\times10^{-5}, 10^{-17}$

insensitive to the reheating framework; however, they are sensitive to the choice of inflationary potential

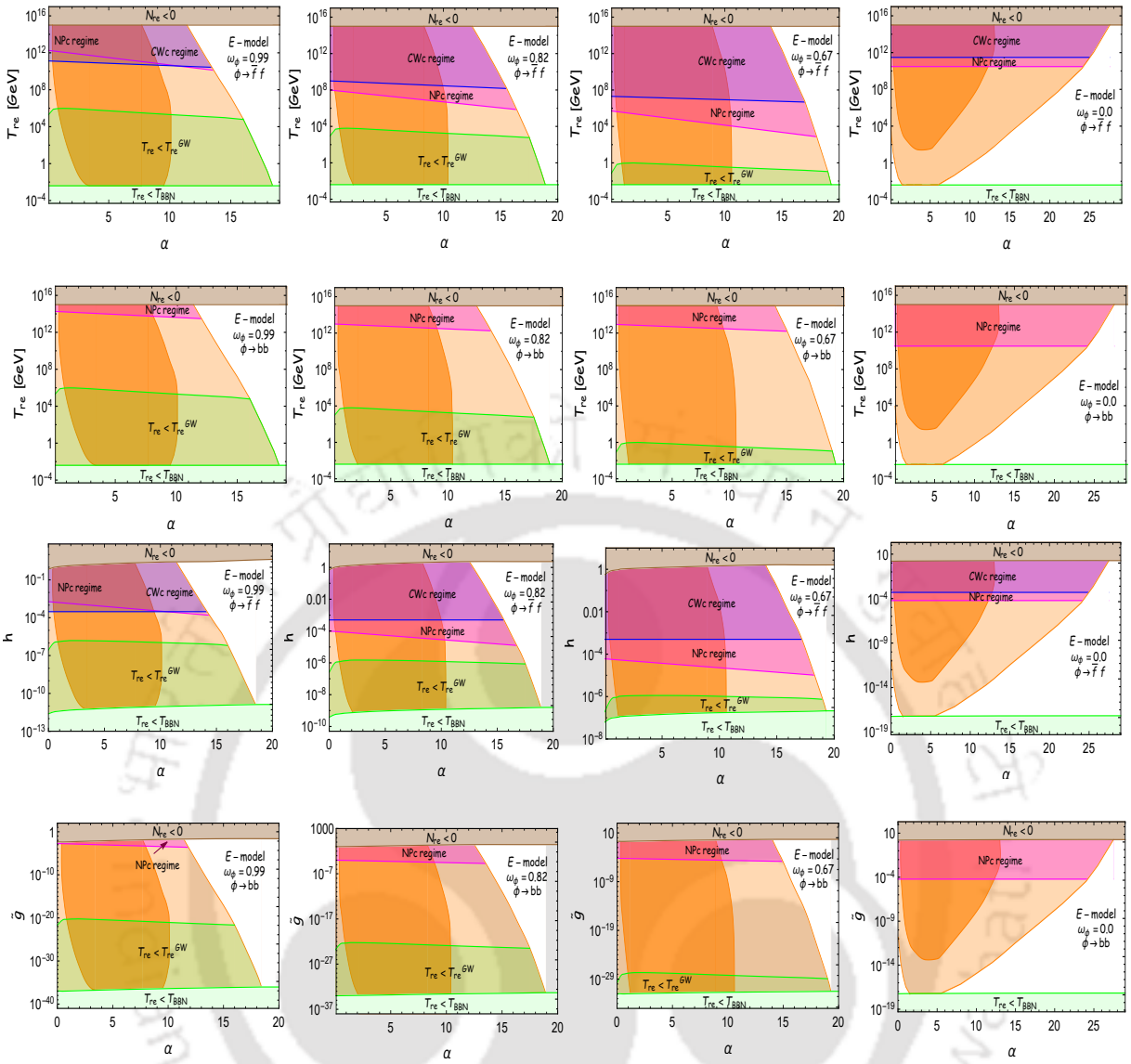

Figure 4.9: The impact of Planck 2018 + BICEP/Keck + PGW + BBN + CWc + NPc on $T_{\rm re}$ and dimensionless inflaton-radiation coupling $(h, \tilde{g})$ with respect to α for α-attractor E-model. We take $w_\phi = (0, 0.67, 0.82, 0.99)$. Deep orange shaded regions correspond to 1σ and light orange shaded regions correspond to 2σ bound imported from $(n_{\rm s} - r)$ plane. The deep and light green region indicates $T_{\rm re} < T_{\rm BBN}$ and $T_{\rm re} < T_{\rm re}^{\rm GW}$, respectively. Blue and magenta-shaded regions depict CWc and NPc. Gray-shaded region implies no reheating.

model. In conclusion, the constraints on inflationary parameters $(N_k, H_k, H_{\rm end})$ and the CMB parameters $(n_{\rm s}, r)$ depend on the choice of the inflationary model, not the post-inflationary reheating framework. [1] Therefore, the predictions for $n_{\rm s}$, r in Figs. 4.4-4.7 and the temperature in Fig. 4.8 are the same for both reheating frameworks. Even if thermal corrections are included in the decay, the results will remain the same.

In those plots, the color code for 1σ (deep orange) and 2σ (light orange) regions are given by the

[1] Note that this is true only when the inflaton governs the expansion history of the universe throughout the reheating period. If, before the end of reheating, the dominant component changes to something other than the inflaton, this condition will no longer hold. One such example is gravitational neutrino reheating (which will be discussed in the next chapter), where the parameter constraints will differ for different reheating scenarios.

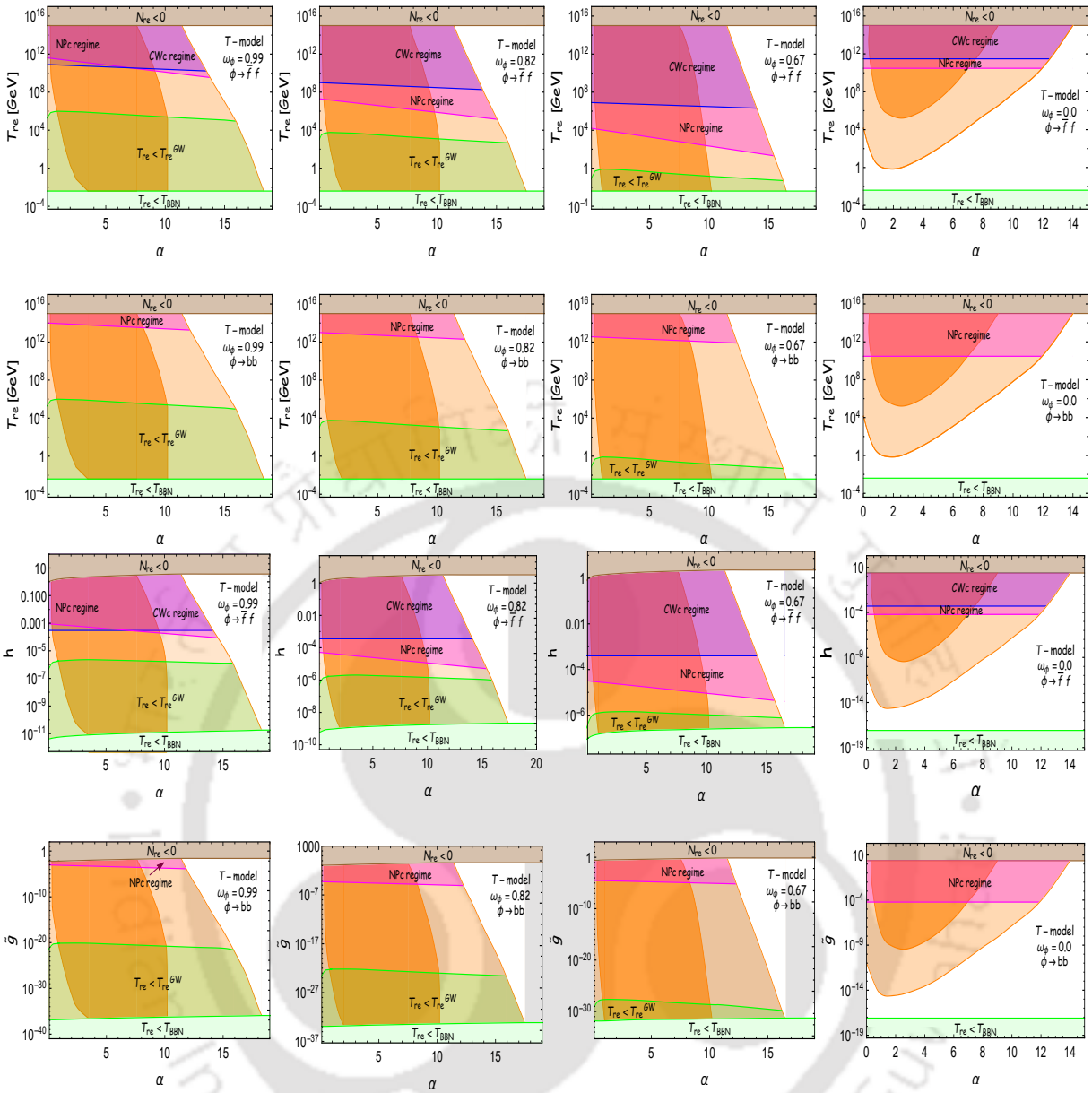

Figure 4.10: The impact of Planck 2018 + BICEP/Keck + PGW + BBN + CWc + NPc on $T_{\rm re}$ and dimensionless inflaton-radiation coupling $(h, \tilde{g})$ with respect to α for α-attractor T-model. We take $w_\phi = (0, 0.67, 0.82, 0.99)$. Deep orange shaded regions correspond to 1σ and light orange shaded regions correspond to 2σ bound imported from $(n_{\rm s} - r)$ plane. The deep and light green regions indicate $T_{\rm re} < T_{\rm BBN}$ and $T_{\rm re} < T_{\rm re}^{\rm GW}$, respectively. Blue and magenta-shaded regions depict CWc and NPc. Gray-shaded region implies no reheating.

combined data of Planck and BICEP/*Keck*. We use the same color code in subsequent plots to estimate the model parameters' 1σ and 2σ bounds. To make our representation clear, in Figs. 4.4-4.8, we did not include CW-perturbative and non-perturbative constraints but incorporated them in all the subsequent plots. Lower limits on the $T_{\rm re}$ are set by either $T_{\rm BBN}$ or $T_{\rm re}^{\rm GW}$, depending on the model and w_ϕ. The $T_{\rm re}^{\rm max}$ value differs depending on the decay channel for both perturbative and nonperturbative considerations. For example, if we ignore both CW-perturbative bound and non-perturbative effect, for $\phi \to \bar{f} f$ reheating, instantaneous reheating sets the maximum reheating temperature $T_{\rm re}^{\rm max} \sim 10^{15}$ GeV. Otherwise, it gets modified. However,

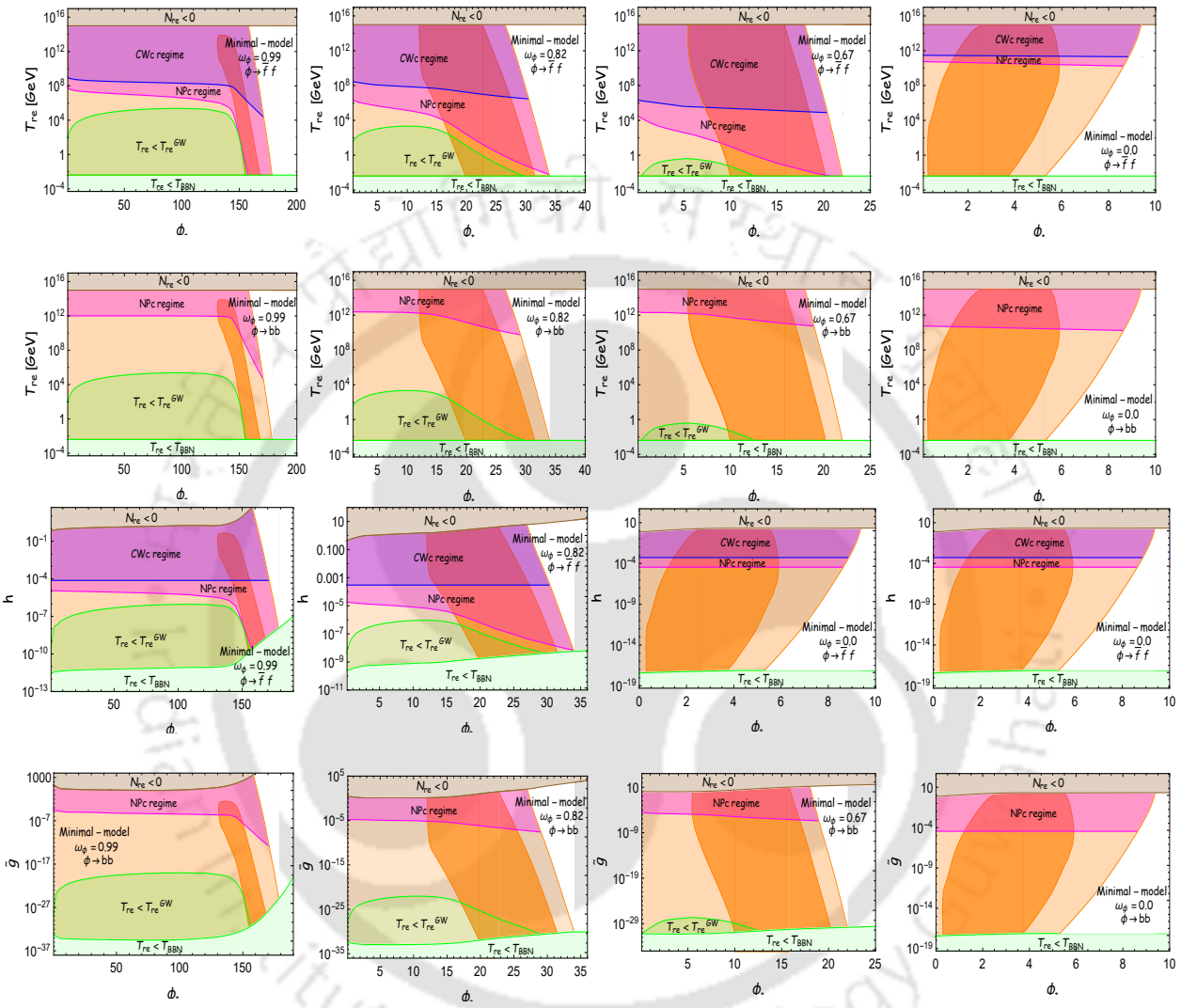

Figure 4.11: The impact of Planck 2018 + BICEP/Keck + PGW + BBN + CWc + NPc on $T_{\rm re}$ and dimensionless inflaton-radiation coupling $(h, \tilde{g})$ with respect to $\phi_\star$ for the minimal model. We take $w_\phi = (0, 0.67, 0.82, 0.99)$. Deep orange shaded regions correspond to 1σ, and the light orange shaded regions correspond to 2σ bound imported from $(n_{\rm s} - r)$ plane. The deep and light green regions indicate $T_{\rm re} < T_{\rm BBN}$ and $T_{\rm re} < T_{\rm re}^{\rm GW}$, respectively. Blue and magenta-shaded regions depict CWc and NPc. Gray-shaded region implies no reheating.

Table 4.7: Bounds on $(T_{\rm re}, \tilde{g}, h)$ from PGWs+BBN+CWc+NPc with recent BICEP/*Keck* data for T-model

I) Fermionic reheating ($\phi \to \bar{f}f$)

w_ϕ	1 σ+BBN+PGWs+CWc		1 σ+BBN+PGWs+CWc+NPc		2 σ+BBN+PGWs+CWc		2 σ+BBN+PGWs+CWc+NPc	
	$T_{\rm re}$ (GeV)	h	$T_{\rm re}$ (GeV)	h	$T_{\rm re}$ (GeV)	h	$T_{\rm re}$ (GeV)	h
0.99	$10^{11}, 10^{5}$	$3\times10^{-4}, 10^{-6}$	$10^{12}, 10^{5}$	$10^{-3}, 10^{-6}$	$10^{11}, 7\times10^{4}$	$3\times10^{-4}, 7\times10^{-7}$	$10^{12}, 7\times10^{4}$	$10^{-3}, 8\times10^{-7}$
0.82	$10^{9}, 10^{3}$	$3\times10^{-4}, 10^{-6}$	$10^{8}, 10^{3}$	$7\times10^{-4}, 10^{-6}$	$10^{9}, 7\times10^{2}$	$3\times10^{-4}, 10^{-6}$	$10^{8}, 7\times10^{2}$	$7\times10^{-5}, 10^{-6}$
0.67	$10^{7}, 0.3$	$3\times10^{-4}, 5\times10^{-7}$	$5\times10^{5}, 0.3$	$6\times10^{-5}, 5\times10^{-7}$	$10^{7}, 0.1$	$5\times10^{-4}, 4\times10^{-7}$	$5\times10^{5}, 0.1$	$6\times10^{-5}, 4\times10^{-7}$
1/3	$10^{6}, 0.004$	$3\times10^{-4}, 10^{-9}$	$10^{5}, 0.004$	$6\times10^{-5}, 10^{-9}$	$10^{6}, 0.004$	$3\times10^{-4}, 10^{-9}$	$10^{5}, 0.004$	$6\times10^{-5}, 10^{-9}$
0.0	$10^{11}, 10^{5}$	$5\times10^{-4}, 10^{-10}$	$10^{10}, 10^{5}$	$6\times10^{-5}, 10^{-10}$	$10^{11}, 0.6$	$5\times10^{-4}, 10^{-15}$	$10^{10}, 0.6$	$6\times10^{-5}, 10^{-15}$

II) Bosonic reheating ($\phi \to bb$)

w_ϕ	1σ+BBN+PGWs+CWc		1σ+BBN+PGWs+CWc+NPc		2σ+BBN+PGWs+CWc		2σ+BBN+PGWs+CWc+NPc	
	$T_{\rm re}$ (GeV)	$\tilde{g}$	$T_{\rm re}$ (GeV)	$\tilde{g}$	$T_{\rm re}$ (GeV)	$\tilde{g}$	$T_{\rm re}$ (GeV)	$\tilde{g}$
0.99	$10^{15}, 10^{5}$	$10^{-2}, 10^{-21}$	$10^{14}, 10^{5}$	$10^{-3}, 10^{-21}$	$10^{15}, 10^{5}$	$0.02, 10^{-21}$	$10^{14}, 10^{5}$	$10^{-3}, 10^{-22}$
0.82	$10^{15}, 10^{3}$	$0.3, 10^{-23}$	$2\times10^{13}, 10^{3}$	$5\times10^{-5}, 10^{-23}$	$10^{15}, 4\times10^{2}$	$0.3, 3\times10^{-24}$	$10^{13}, 4\times10^{2}$	$7\times10^{-5}, 10^{-24}$
0.67	$10^{15}, 0.1$	$0.4, 10^{-29}$	$4\times10^{12}, 0.1$	$6\times10^{-5}, 10^{-29}$	$10^{15}, 0.05$	$0.5, 10^{-29}$	$4\times10^{12}, 0.05$	$6\times10^{-5}, 10^{-29}$
1/3	$10^{15}, 0.004$	$0.5, 10^{-27}$	$10^{11}, 0.004$	$6\times10^{-5}, 10^{-27}$	$10^{15}, 0.004$	$0.5, 10^{-27}$	$10^{11}, 0.004$	$6\times10^{-5}, 10^{-27}$
0.0	$10^{15}, 10^{5}$	$0.5, 10^{-10}$	$10^{10}, 10^{5}$	$6\times10^{-5}, 10^{-10}$	$10^{15}, 0.6$	$0.5, 2\times10^{-15}$	$4\times10^{10}, 0.6$	$6\times10^{-5}, 10^{-15}$

Table 4.8: Bounds on $(T_{\rm re}, \tilde{g}, h)$ from PGWs+BBN+CWc+NPc with recent BICEP/*Keck* data for Minimal model

I) Fermionic reheating ($\phi \to \bar{f}f$)

w_ϕ	1 σ+BBN+PGWs+CWc		1 σ+BBN+PGWs+CWc+NPc		2 σ+BBN+PGWs+CWc		2 σ+BBN+PGWs+CWc+NPc	
	$T_{\rm re}$ (GeV)	h	$T_{\rm re}$ (GeV)	h	$T_{\rm re}$ (GeV)	h	$T_{\rm re}$ (GeV)	h
0.99	$10^{9}, 0.004$	$7\times10^{-4}, 10^{-10}$	$10^{8}, 0.004$	$3\times10^{-5}, 10^{-10}$	$10^{9}, 0.004$	$7\times10^{-5}, 10^{-10}$	$10^{8}, 0.004$	$3\times10^{-5}, 10^{-10}$
0.82	$10^{9}, 0.004$	$3\times10^{-4}, 10^{-9}$	$10^{6}, 0.004$	$2\times10^{-5}, 10^{-9}$	$10^{9}, 0.004$	$3\times10^{-4}, 10^{-9}$	$10^{6}, 0.004$	$2\times10^{-5}, 10^{-9}$
0.67	$10^{5}, 0.004$	$3\times10^{-4}, 10^{-9}$	$20, 0.004$	$2\times10^{-6}, 10^{-9}$	$10^{6}, 0.004$	$3\times10^{-4}, 10^{-9}$	$10^{4}, 0.004$	$2\times10^{-5}, 10^{-9}$
1/3	$10^{6}, 0.004$	$3\times10^{-4}, 10^{-9}$	$10^{5}, 0.004$	$6\times10^{-5}, 10^{-9}$	$10^{6}, 0.004$	$3\times10^{-4}, 10^{-9}$	$10^{5}, 0.004$	$6\times10^{-5}, 10^{-9}$
0.0	$10^{11}, 0.004$	$4\times10^{-4}, 10^{-17}$	$10^{10}, 0.004$	$4\times10^{-5}, 10^{-17}$	$10^{11}, 0.004$	$4\times10^{-4}, 10^{-17}$	$10^{10}, 0.004$	$4\times10^{-5}, 10^{-17}$

II) Bosonic reheating ($\phi \to bb$)

w_ϕ	1 σ+BBN+PGWs+CWc		1 σ+BBN+PGWs+CWc+NPc		2 σ+BBN+PGWs+CWc		2 σ+BBN+PGWs+CWc+NPc	
	$T_{\rm re}$ (GeV)	$\tilde{g}$	$T_{\rm re}$ (GeV)	$\tilde{g}$	$T_{\rm re}$ (GeV)	$\tilde{g}$	$T_{\rm re}$ (GeV)	$\tilde{g}$
0.99	$10^{14}, 0.004$	$10^{-3}, 10^{-32}$	$10^{12}, 0.004$	$4\times10^{-5}, 10^{-32}$	$10^{15}, 0.004$	$2\times10^{3}, 10^{-32}$	$10^{12}, 0.004$	$4\times10^{-5}, 10^{-32}$
0.82	$10^{15}, 0.004$	$30, 10^{-31}$	$10^{12}, 0.004$	$2\times10^{-5}, 10^{-31}$	$10^{15}, 0.004$	$10^{2}, 10^{-31}$	$10^{12}, 0.004$	$2\times10^{-5}, 10^{-31}$
0.67	$10^{15}, 0.004$	$0.1, 10^{-31}$	$10^{12}, 0.004$	$2\times10^{-5}, 10^{-31}$	$10^{15}, 0.004$	$0.1, 10^{-31}$	$10^{12}, 0.004$	$2\times10^{-5}, 10^{-31}$
1/3	$10^{15}, 0.004$	$0.5, 10^{-27}$	$10^{11}, 0.004$	$6\times10^{-5}, 10^{-27}$	$10^{15}, 0.004$	$0.5, 10^{-27}$	$10^{11}, 0.004$	$6\times10^{-5}, 10^{-27}$
0.0	$10^{15}, 0.004$	$0.5, 10^{-17}$	$10^{10}, 0.004$	$4\times10^{-5}, 10^{-17}$	$10^{15}, 0.004$	$0.5, 10^{-17}$	$10^{10}, 0.004$	$4\times10^{-5}, 10^{-17}$

ignoring the non-perturbative effect, CW-perturbative bound does not give additional constraint for bosonic reheating, and for that instantaneous reheating ($N_{\rm re} \to 0$) sets the value of $T_{\rm re}^{\rm max} \sim 10^{15}$ GeV. It can be further observed that for stiff EoS $w_\phi > 1/3$, $T_{\rm re}^{\rm min}$ set the maximum bound on the inflaton potential parameters α, ϕ_*, and for $w_\phi < 1/3$, it is $T_{\rm re}^{\rm max}$ which sets the bound.

As an example, $w_\phi = 0$, the upper limit of the potential parameters α, ϕ_* are (13.0, 9.0, 5.3) (1σ bound) and (27.5, 15.0, 9.4) (2σ bound) for attractor E, T, and minimal model respectively (see Table-4.4). For higher EoS $w_\phi = (0.67, 0.82, 0.99)$, the restriction of $\alpha(\phi_*)$ are given in Tables-4.3 and 4.5.

Once the maximum values of (α, ϕ_*) are fixed, the associated prediction of inflationary energy scale and the e-folding number N_k can be computed. For the attractor models with stiff inflaton EoS $w_\phi > 1/3$, the predicted value of $(H_{\rm end}^{\rm min} \sim 10^{12}\ GeV, N_k^{\rm max} \sim 65)$ (both E and T-model) turned out to be nearly independent of w_ϕ and the minimum possible e-folding number correspond to instantaneous reheating $N_k^{min} \sim 55$ which is also independent of w_ϕ. On the other hand, for the minimal plateau model, however, $H_{\rm end}^{\rm min}$ varies within the range $(10^{11} - 10^{5})$ GeV (1σ bound) and $(10^{11} - 10^{3})\}$ GeV (2σ bound) for w_ϕ varying from $0.67 \to 0.99$. For the same range of w_ϕ, $N_k^{\rm max}$ value varies from $66 \to 77$. On the other hand if, $w_\phi = 0$, $H_{\rm end}^{\rm min} \sim 10^{13}$ GeV, and $N_k^{\rm max} \sim 56$ irrespective of the models under consideration. We summarize all the bounds of inflationary parameters in Tables-4.3, 4.4, and 4.5.

In the above, we discussed mainly the constraints on macrophysical parameters, such as the inflationary parameters N_k, H_k, and the reheating temperature $T_{\rm re}$. These discussions are largely independent of the microphysics of reheating (reheating framework). However, from a particle physics perspective, it is interesting to derive constraints on microphysical parameters, such as the inflaton's coupling to radiation. Notably, the constraints on $T_{\rm re}$ can be converted into constraints on the inflaton couplings $(h, \tilde{g})$, since there exists a one-to-one correspondence between them. Along with this, we include all the theoretical bounds obtained from both CWc and NPc discussed before. The constraints on $T_{\rm re}$ from the combined Planck+BICEP/*Keck* data are independent of the microphysics of reheating. However, once we incorporate the CWc and NPc constraints on the couplings, they further constrain $T_{\rm re}$, which we will discuss next. Let us briefly describe the color codes we used in our subsequent plots: 1) Deep green region is for $T_{\rm re} < T_{\rm BBN}$, 2) Light green region is associated with BBN constraints from PGWs, $T_{\rm re} < T^{\rm GW}_{\rm re}$, 3) Gray region depicts $N_{\rm re} < 0$, 4) Blue region termed as the CWc regime which indicates the restriction from CWc, 5) Magenta regime is associated with NPc, 6) Deep orange region indicates allowed coupling parameter space satisfying 1σ bound of latest $(n_{\rm s} - r)$ data, and 7) Light orange region indicates allowed coupling parameter space satisfying 2σ bound of latest $(n_{\rm s} - r)$ data.

4.6.1 α-attractor E & T models and constraints

Constraints on the entire parameter space for attractor models can be summarized from Figs. 4.4, 4.5, 4.7, 4.9, 4.10, and Tables 4.3, 4.4, 4.6, 4.7. As stated earlier, we have discussed reheating scenarios described by two types of decay channels $\phi \to \bar{f}f$ and $\phi \to bb$. As argued before, the upper limit of the inflaton-radiation coupling should always be constrained by the fact that its quantum effect will not disturb the inflationary dynamics. If the bosonic channel dominates reheating, one loop-effective potential sets the upper bound on coupling $g \sim \mathcal{O}(10^{-1})$ and that fixes the $T^{\rm max}_{\rm re}$ value close to that of instantaneous reheating 10^{15} GeV. On the other hand, for the fermionic channel, such perturbative correction sets the upper bound on the coupling $h_{\rm max} \sim \mathcal{O}(10^{-4})$ and that leads to an upper limit on the reheating temperature, which depends on w_ϕ. For instance, if $w_\phi = 0$, $T^{\rm max}_{\rm re} \sim 10^{11}$ GeV for both the attractor models which is independent of α (see, for instance, the fourth plot of Figs. 4.9,4.10). Similarly, for stiff inflaton EoS $w_\phi \geq 1/3$, $T^{\rm max}_{\rm re}$ turns out to be nearly independent of α with the following values $T^{\rm max}_{\rm re} = (10^6, 10^7, 10^9, 10^{11})$ GeV for $w_\phi = (0.33, 0.67, 0.82, 0.99)$ respectively.

Unlike the upper limit, the lower limit on the inflaton-radiation coupling arises indirectly from the lower bound of the reheating temperature. If $w_\phi \gtrsim 0.60$, $T^{\rm GW}_{\rm re}$ always sets the lowest reheating temperature, and the lowest allow value of $T^{\rm GW}_{\rm re} \sim (10^{-1}, 10^3, 10^5)$ GeV for EoS $w_\phi = (0.67, 0.82, 0.99)$ respectively. Corresponding limiting values of couplings are tabulated in Tables-4.6,4.7. When there is no restriction from PGWs ($w_\phi < 0.6$), we expect $T^{\rm min}_{\rm re} \sim T_{\rm BBN}$, but that may not be true once we incorporate the PLACNK+BICEP/*Keck* constraints. For sample value, for $w_\phi = 0$ the T-model, $T^{\rm min}_{\rm re} \sim 10^5$,(1) GeV for the 1σ,(2σ) confidence levels. For $w_\phi = 0$ and $w_\phi = 1/3$, all numerical estimation of $T^{\rm min}_{\rm re}$ as well as $\tilde{g}_{\rm min}/h_{\rm min}$ shown in Tables-4.6,4.7.

As stated earlier, $T^{\rm max}_{\rm re}$ generally can be obtained by CWc (Eq. 4.37); however, that may be restricted by NPc (Eq. 4.44) depending upon the reheating framework under consideration. As an example, for bosonic reheating ($\phi \to bb$ process) considering NPc the dimensionless coupling must be $10^{-4} < \tilde{g} < 10^{-3}$, with the allowed range of $w_\phi = (0, 1)$, and for $\phi \to \bar{f}f$ we have more or less same range, $(10^{-4} < h < 10^{-3})$. As an example for $w_\phi = 0$, all reheating temperature above $T_{\rm re} > 10^{10}$ GeV lies in the non-perturbative regime.

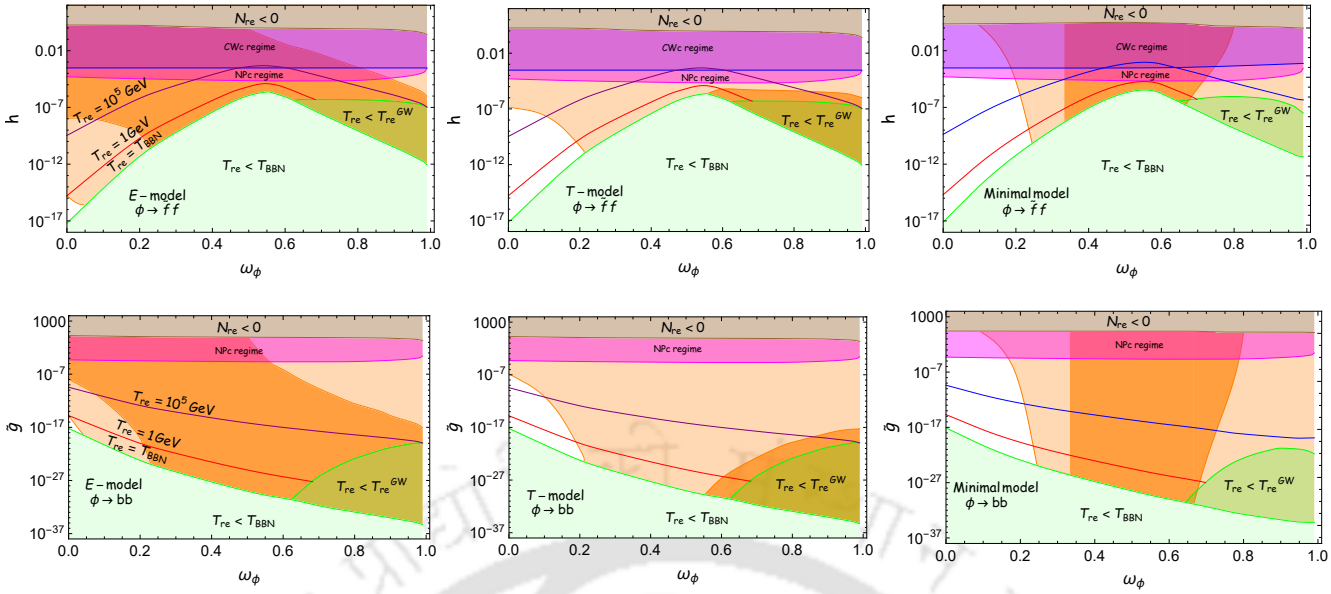

Figure 4.12: The impact of Planck 2018 + BICEP/Keck + PGW + BBN + CWc + NPc on dimensionless inflaton-radiation coupling (h,$\tilde{g}$) with respect to w_ϕ for three different models. The color codes are the same as before. For these plots, we have taken $(\alpha, \phi_*) = 10$.

This non-perturbative bound is sensitive to both (α, w_ϕ); for better visualization, see, Figs. 4.9, 4.10 and details numerical values given in Tables-4.6, 4.7.

For a complete understanding of the reheating parameter space, finally, in Fig. 4.12, we plotted the parametric dependence of inflaton-radiation coupling with respect to reheating EoS. The left two column plots are for E and T-models corresponding to $\alpha = 10$. Interestingly, if one confines within the 1σ region of Planck, for T-model inflaton-radiation couplings are tightly bound. As an example, for $w_\phi = 0.82$, one obtains $10^{-7} > h > 10^{-6}$, and $10^{-23} > \tilde{g} > 10^{-22}$.

4.6.2 Minimal model and constraints

Detailed phenomenological constraints of the minimal inflation can be observed from Figs. 4.6, 4.7 and 4.11, and are summarized in Tables-4.4, 4.5, 4.8. CWc sets the upper limit on inflaton-radiation coupling as $\tilde{g}_{\rm max} \sim \mathcal{O}(10^{-1})$ and $h_{\rm max} \sim \mathcal{O}(10^{-4})$. These available bounds on couplings thereafter set restrict $T_{\rm re}^{\rm max} \sim 10^{15}$ GeV for bosonic reheating, which is close to instantaneous reheating. However, for inflaton-fermion coupling, $T_{\rm re}^{\rm max}$ is noticeably sensitive to the inflaton parameter (ϕ_*, w_ϕ) value and detailed numerical values are provided Table-4.8 and Fig. 4.11.

Unlike attractor models, the lower bound on $T_{\rm re}$ for this model has non-trivial dependence on the potential parameter ϕ_*. For a given EoS, one observes that there exists a critical value of ϕ_* above which value lower bound decreases from $T_{\rm re}^{\rm GW}$ to $T_{\rm BBN}$. For instance in the first plot of Fig. 4.11, one clearly see that for $\phi_* > 155$, $T_{\rm re}^{\rm min} \sim 10^4$ GeV drops to $T_{\rm BBN}$. This essentially suggests that as on increase ϕ_*, the lower possible inflation-fermion coupling decreases from $h_{min} \sim 10^{-6}$ to 10^{-10}. In Table-4.8, we provide maximum and minimum values of coupling parameters and reheating temperature for different EoS $w_\phi = (0, 1/3, 0.67, 0.82, 0.99)$. For specific model parameters, bounds on the reheating parameters will

always be within the bounds provided in Table-4.8.
If one considers the nonperturbative bound, the upper limit on the coupling parameter is further modified (see Fig. 4.11). Additionally, it depicts the fact that compared to the bosonic coupling $\tilde{g}$ nonperturbative bounds on the fermionic coupling h is much more sensitive to ϕ_* when $w_\phi > 1/3$. Finally, in Fig. 4.12, the right column figures depict the parametric variation of inflaton-radiation coupling with respect to the w_ϕ for the minimal model with $\phi_* = 10$. Interestingly, the minimal model is non-viable for the lower EoS dictated by Planck together with BICEP/*Keck* data, which corresponds to white regions. This can also be observed from Fig. 4.11. As an example, 2σ $(n_s - r)$ bound ruled out $\phi_* \gtrsim 9.4$, whereas if we consider 1σ bound ruled out $\phi_* \gtrsim 5.5$.

4.7 Summary

In this chapter, we have analyzed in detail the phenomenological implications of the latest Planck 2018 and BICEP/Keck data on the physics of inflaton. We analyzed three different plateau inflation models along with two different reheating scenarios. We particularly discussed two different channels of inflaton, inflaton decaying into fermions through $\phi \to \bar{f}f$ and bosons through $\phi \to bb$. Along with the observations, we further employ bounds from PGWs and both perturbative and non-perturbative constraints on the inflaton-radiation coupling.

At the first step, considering the most conservative bound on the reheating temperature ($T_{\rm BBN}$ ($T_{\rm re}^{\rm GW}$) to 10^{15}GeV), we project our results onto the $(n_s - r)$ plane and compare them with the Planck+BICEP/*Keck* 2018 data to to fix the limit on the potential parameter $\alpha(\phi_*)$ at 1σ and 2σ C.L. Once we fixed $\alpha(\phi_*)$ for five different sets of inflaton EoS $w_\phi = (0, 1/3, 0.67, 0.82, 0.99)$, that in turn fixes inflationary parameters such as the range of N_k, $H_{\rm end}$ and also post-inflationary parameter like reheating temperature $T_{\rm re}$. The limiting values of inflationary parameters and reheating temperature for different inflation models are shown in Tables-4.3, 4.4, 4.5. Interestingly, these discussions are largely independent of the microphysics of reheating (reheating framework).

However, from a particle physics perspective, it is crucial to derive constraints on microphysical parameters, such as the inflaton's coupling, which plays a key role in the energy transfer process from the inflaton to radiation. Therefore, in the second step, we analyze the constraints on the inflaton's couplings h, $\tilde{g}$, taking into account the bounds on inflationary parameters and the reheating temperature. The upper bound on inflaton-radiation coupling $h, \tilde{g} \sim \mathcal{O}(0.1)$, is derived from the $T_{\rm re}^{\rm max} \sim 10^{15}$ GeV value corresponding to instantaneous reheating. However, once CWc and NPc are employed, the upper bound of coupling significantly drifted from the aforementioned value, and it will further constrain the reheating temperature. The detailed quantitative values of different bounds arising from the theory constraints are displayed in Tables 4.6, 4.7, and 4.8 for three different plateau-type inflationary model attractors E, T, and minimal model respectively. The lower bound on reheating temperature is conventionally fixed by $T_{\rm BBN}$ (deep green shaded region in all the plots). However, if we incorporate Planck+BICEP/Keck+PGWs constraints, such a possibility is no longer generic. If $w_\phi < 1/3$, in most of the parameter region for the E and T model, $T_{\rm BBN}$ lies outside the 1σ region (see fourth column of Fig. 4.9 and 4.10). However, for those models PGWs bound on $T_{\rm re}^{\rm min} = T_{\rm re}^{\rm GW}$ is large by several decade above $T_{\rm BBN}$ for $w_\phi > 0.6$. As an example for $w_\phi = 0.99$, $T_{\rm re}^{\rm min} = T_{\rm re}^{\rm GW} \sim 10^5$ GeV. For the minimal model, however, the lower bound on reheating temperature is noticeably dependent on ϕ_*, specifically for the higher EoS.

Apart from direct and indirect observational bounds, we further utilized the theoretical bounds coming from CWc and NPc. CWc strictly restricts the maximum allowed value of (h,g), above which inflation will be jeopardized. However, if we assume the fact that the reheating process itself is perturbative in nature, it is NPc that plays a wider role in setting the upper limit on both the reheating temperature and inflaton-radiation couplings for all the models under consideration. If nature chooses the coupling to be within the non-perturbative regime, some of the present conclusions may be affected, which we defer to our future study.

To the end, we wish to note that future experiments such as CMB-S4 [219] and LiteBIRD [220] will be able to put stronger bound in (n_s,r) plane which will certainly improve our understanding the precise nature of beyond standard model physics such as inflaton (see, for instance, the recent works [212, 213]).

Indian Institute of Technology Guwahati

CHAPTER 5

Gravitational Neutrino Reheating: A Framework for Reheating, Leptogenesis and Dark Matter

Inflatons are the dominant energy component right after the termination of inflation [6, 34]. The current observable universe, however, demands a mechanism of transferring inflaton energy into SM particles dubbed as reheating [142, 143]. Conventional reheating models primarily rely on arbitrary coupling between the inflaton and radiation, which lacks robust predictions, and hence, makes direct observational verification challenging. To address this arbitrariness, recent studies [156, 175, 184, 211, 221–224] have explored whether reheating could be primarily driven by gravitational interactions. That is, can the universe be successfully populated with radiation if the inflaton decay is mediated mainly by gravity? Many investigations in the recent past [156, 175, 184, 211, 221–224] suggest that the answer is indeed affirmative. The recently proposed gravitational reheating (GRe) [184] is one such interesting example. However, it has several limitations, as discussed earlier. To reheat the universe above the BBN energy scale, GRe requires an EoS parameter $w_\phi \gtrsim 0.65$. Moreover, the bound on the total PGW energy density, $\Omega^k_{\rm GW}h^2 \lesssim 1.7\times10^{-6}$ [23, 31, 153, 225, 226], which arises from constraints on the extra relativistic degrees of freedom during BBN, completely rules out the GRe scenario.

Recently, PBH reheating has been proposed to relax such constraints, which renders the scenario viable for any inflaton equation of state $w_\phi > 1/3$ [227, 228]. In spite of its attractive nature and recent interest in the community, the PBH formation mechanism itself is still under active investigation, let alone its observational prospects, which are still not confirmed.

Keeping all these aspects into consideration, in this thesis, we propose a novel reheating scenario [229, 230] governed by the RHNs in the well-known Type-I seesaw framework embedded in the SM. We call this scenario gravitational neutrino reheating, abbreviated as νGRe. The crucial aspects of such consideration are that, apart from successfully explaining the observed light neutrino masses and the matter-antimatter asymmetry, it can also successfully reheat the universe, satisfying all the aforementioned constraints [229, 230].

In our proposed νGRe scenario, RHNs are produced from the inflaton via purely gravitational interactions. The subsequent decay of these RHNs into SM particles not only drives the transition to a radiation-dominated era but also generates the baryon asymmetry of the universe via leptogenesis. Thus,

νGRe simultaneously addresses the origin of active neutrino masses, the baryon asymmetry, and the origin of the thermal bath. In this sense, our scenario represents the most minimal possible framework, as it does not introduce any new interactions beyond the SM, except for gravity. The only new fields involved are the RHNs. The only model dependence arises from the choice of the inflaton potential. However, our results are primarily sensitive to the shape of the potential near its minimum, i.e., to the inflaton EoS. So, this potential dependency is also relatively weak[1]. This chapter has two sections. In the section 5.1, we discuss how νGRe serves as a minimal framework for reheating and leptogenesis. In the section 5.2, we explore the implications of νGRe for the DM production.

5.1 Gravitational neutrino reheating: A minimal framework for reheating and leptogenesis

In this section, we discuss the neutrino reheating scenario in detail and show how the νGRe framework offers a minimal platform for reheating and leptogenesis. The section is organized as follows:
In subsection 5.1.1, we provide a detailed discussion of the νGRe framework. Subsection 5.1.2 is devoted to the gravitational production of the RHNs via inflaton scattering. In subsection 5.1.4, we analyze the phenomenology of νGRe, determine the reheating temperature, and identify the viable parameter space. In subsection 5.1.5, we show how constraints from extra relativistic degrees of freedom during BBN, considering PGWs, put restrictions on νGRe. In subsection 5.1.6, we discuss the impact of νGRe on the inflationary parameters (n_s, r). In subsection 5.1.7, we analyze the potential constraints on the leptogenesis scenario within this framework.

5.1.1 The framework of νGRe

Type-I seesaw [130–132] is the simplest extension of the SM, which can generate active neutrino mass along with its potential application to resolve the matter-antimatter asymmetry. The extension contains three additional right-handed SM singlet massive Majorana neutrinos $\nu_R^i (i = 1,2,3)$ with the following lepton number violating Lagrangian

$$\mathscr{L} = \mathscr{L}_\phi + \mathscr{L}_{\rm SM} - \frac{1}{2} M_{\rm i} \overline{\nu_{\rm R}^{ci}} \nu_{\rm R}^i - y_{\alpha i} \bar{L}_\alpha \tilde{H} \nu_{\rm R}^i + h.c., \tag{5.1}$$

where $\tilde{H} = i\sigma_2 H^*$ and $H(L)$ is the SM Higgs (lepton) doublet. The first two terms are the Lagrangian for the inflaton (ϕ) and the SM, respectively. Therefore, except for the usual inflaton parameters, the Yukawa coupling matrix $y_{\alpha i}$ and the Majorana mass $M = \text{diag}(M_1, M_2, M_3)$ are the only ones beyond the SM parameters in the theory. The inflaton to satisfy the approximate shift symmetry, its couplings with any other fields are assumed to be negligibly small. After the termination of inflation, all the particles will be produced quantum mechanically via gravitational interaction from the inflaton condensate (see Fig. (5.1)), and they will subsequently be diluted due to expansion. Since the gravitational production rate strictly depends on the inflaton energy density, the dominating contribution in such production is at the beginning of reheating. The relevant Boltzmann equations for different density components for these

[1] By this, we refer to the weak dependence on different classes of potentials, such as the α-attractor E-model, T-model, minimal model, etc.

processes would then be,

$$\dot{\rho}_\phi + 3H(1+w_\phi)\rho_\phi + \Gamma_\phi^{\rm tot}(1+w_\phi)\rho_\phi = 0, \tag{5.2a}$$

$$\dot{\rho}_r + 4H\rho_r - \Gamma_{\phi\phi\to hh}(1+w_\phi)\rho_\phi - \langle E_i\rangle \Gamma_i\, n_{\rm i} = 0\,, \tag{5.2b}$$

$$\dot{n}_i + 3Hn_i - R_\phi^i + \Gamma_i\, n_i = 0\,, \tag{5.2c}$$

$$H^2 = \frac{\rho_\phi + \rho_r + \langle E_i\rangle n_i}{3M_{\rm p}^2} \tag{5.2d}$$

where ρ_ϕ, ρ_r are the energy densities of the inflaton and the radiation, respectively. n_i is the number density of the RHNs. R_ϕ^i is the gravitational production rate associated with the RHNs. Note that gravitational production of RHNs mostly occurs at the beginning of the reheating. Hence, its momentum redshifts as $p = p_{\rm in}/a$ starting from its initial momentum $p_{\rm in} \sim m_\phi^{\rm end}$ (inflaton mass at the end of inflation). The average energy of the RHNs is, therefore, defined as $\langle E_i\rangle = \sqrt{p_i^2 + M_i^2}$. $\Gamma_\phi^{\rm tot}$ is the total inflaton decay width considering $\Gamma_{\phi\phi\to hh}$, the gravitational decay width for the SM Higgs production from scattering of inflaton, and the decay width associated with the production of RHN gravitationally. Γ_i's are the decay width of the RHNs $\Gamma_i = (y^\dagger y)_{\rm ii}\, M_{\rm i}/(8\pi)$.

Type-I seesaw model considers three copies of RHNs, two RHNs (namely $\nu_{\rm R}^1, \nu_R^2$) are sufficient to explain both the light neutrino mass and baryon asymmetry of the universe through their out-of-equilibrium non-thermal decay [136, 141, 231–233]. Therefore, the third RHN (ν_R^3) stands out, and we consider it to be long-lived such that its decay rate is suppressed compared to the other two RHNs. Therefore, out of all the parameters, the following three parameters

$$\{\beta = \sqrt{(y^\dagger y)_{33}}\,, M_3, w_\phi\}, \tag{5.3}$$

related to ν_R^3 and inflaton will be shown to control the reheating dynamics. The remaining parameters will give rise to active neutrino mass and baryogenesis.

We show that it is the weak decay width, $\Gamma_3 \simeq \beta^2 M_3/(8\pi) \ll \Gamma_1, \Gamma_2$ of ν_R^3, with $\beta^2 \simeq (m_1 M_3/v^2)$ compared to the other two RHNs (see Addenda-A for the construction of $y_{\alpha i}$), that plays crucial role for successful reheating to occur in present scenario. Since $\beta^2 \propto {m_1}^2$, the non-vanishing Γ_3 immediately sets the mass of the lightest active neutrino mass m_1. In other words, to have a neutrino to control the reheating process along with the successful baryogenesis, we indeed require the lightest active neutrino mass to be non-vanishing. This shows a clear correlation between the neutrino parameter and the reheating parameter.

5.1.2 Production of RHNs from inflaton

All the RHNs are assumed to be unstable in terms of their respective decay width. In the absence of decay, the evolution of RHN number density (n_i) is expected to be governed by the Boltzmann equation,

$$\dot{n}_i + 3Hn_i = R_\phi^i = \frac{\rho_\phi^2}{4\pi\gamma^2 M_p^4}\frac{M_i^2}{m_\phi^2}\Sigma_i\,, \tag{5.4}$$

where, R_ϕ^i the production rate for $\nu_{\rm R}^i$ from inflaton scattering mediated by gravity [168, 175] and

$$\Sigma_i = \sum_{\nu=1}^{\infty}\frac{1}{\nu^2}|\mathscr{P}_\nu^{2n}|^2\left(1 - \frac{4M_i^2}{\nu^2\gamma^2 m_\phi^2}\right)^{3/2}, \tag{5.5}$$

[2]Since we use the normal hierarchy of active neutrino masses here, $\beta^2 \propto m_1$. However, νGRe is also possible if one considers the inverted hierarchy, in which case $\beta^2 \propto m_3$. See Addenda-A, where we construct the Yukawa coupling using both hierarchies.

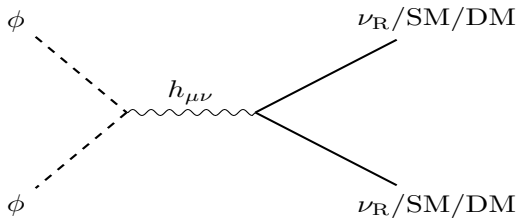

Figure 5.1: Feynman diagram for the production of RHN/SM/DM through the gravitational scattering of the inflaton condensate.

Table 5.1: Numerical values of the Fourier coefficients:

$n(w_\phi)$	$\sum \frac{1}{\nu^2}\lvert\mathscr{P}_\nu^{2n}\rvert^2$	$\sum \nu\lvert\mathscr{P}_\nu^{2n}\rvert^2$	$\sum\lvert\mathscr{P}_\nu^{2n}\rvert^2$
2 (1/3)	0.014	0.141	0.063
3 (0.50)	0.011	0.145	0.056
4 (0.60)	0.008	0.148	0.049
10 (0.82)	0.002	0.149	0.027

accounts for the sum over the Fourier modes of the inflaton potential, and its numerical values are given in Table-5.1. In this chapter, as a reference inflation model, we consider the α-attractor E-model. Again, note that our discussion is general, except CMB (n_s, r) prediction in Fig. 5.6. It is not restricted to the E-model class, as the expression for the minimum of the potential is formulated in a generic manner,

$$V(\phi) = \Lambda^4\left(1 - e^{-\sqrt{\frac{2}{3\alpha}}\frac{\phi}{M_p}}\right)^{2n} \simeq \Lambda^4\left(\frac{2}{3\alpha}\right)^n\left(\frac{\phi}{M_p}\right)^{2n}. \tag{5.6}$$

During the initial period of reheating, inflaton is the dominant energy component, and neglecting the inflaton decay rate compared to the Hubble rate H from Eq.(5.2a) ρ_ϕ evolves as,

$$\rho_\phi(a) = \rho_\phi^{\rm end}\left(\frac{a}{a_{\rm end}}\right)^{-3(1+w_\phi)}, \tag{5.7}$$

where $\rho_\phi^{\rm end} = 3M_p^2H_{\rm end}^2$ is the inflation energy density at the end of inflation. Using Eq. 5.7 in Eq. 5.4 one obtains,

$$n_i(a) \simeq \frac{3H_{\rm end}^3M_i^2\Sigma_i}{2\pi(1-w_\phi)(\gamma m_\phi^{\rm end})^2}\left(\frac{a}{a_{\rm end}}\right)^{-3}. \tag{5.8}$$

Where the effective initial number density of RHNs at the end of inflation is

$$\begin{aligned} n_i^{\rm end} &= \frac{3H_{\rm end}^3M_i^2\Sigma_i}{2\pi(1-w_\phi)(\gamma m_\phi^{\rm end})^2} \\ &= \left(10^{37}\,{\rm GeV}^3\right)\frac{3\Sigma_i}{2\pi(1-w_\phi)\gamma^2}\left(\frac{H_{\rm end}}{10^{13}\,{\rm GeV}}\right)^3\left(\frac{M_i}{10^{12}\,{\rm GeV}}\right)^2\left(\frac{10^{13}\,{\rm GeV}}{m_\phi^{\rm end}}\right)^2. \end{aligned} \tag{5.9}$$

Immediately after the inflation ends, we can observe that approximately 10^{37} number of neutrinos of mass 10^{12} GeV are produced per unit volume for a standard high-scale inflationary model.

5.1.3 GRe: Estimating critical β_ϕ^c for νGRe

To facilitate our discussion forward, we begin by stating a few basic results of the standard gravitational reheating scenario [184]. If we put $\Gamma_3 = 0$ in Eq. 5.2b, then it simply decodes the standard GRe scenario

where reheating is purely gravitationally driven with the decay width[3]

$$\Gamma_{\phi\phi\to hh} = \frac{\gamma\, m_\phi(t)\,\rho_\phi(t)}{2\pi(1+w_\phi)M_p^4}\Sigma_h\,, \tag{5.10}$$

where $\Sigma_h = \sum_{\nu=1}^{\infty} \nu\,|\mathscr{P}_\nu^{2n}|^2$ and its numerical values given in Table-5.1. During this, the radiation production from inflton via gravitational scattering can be obtained from Eq.(5.2b) as,

$$\rho_r(a) \simeq \frac{9\gamma\, H_{\rm end}^3\, m_\phi^{end}\,\Sigma_h}{4\pi(1+15w_\phi)}\left(\frac{a}{a_{\rm end}}\right)^{-4}. \tag{5.11}$$

In the present scenario where $\Gamma_3 \neq 0$, radiation can also be produced from neutrino decay. However, if the neutrino decay width is very large, the radiation produced from neutrino decay will never surpass the radiation produced by the inflaton. This is due to the mass suppression of the right-handed neutrino production. Therefore, one finds a critical value of the neutrino coupling parameter β, below which we found neutrino to control the reheating process,

$$\beta_\phi^c \simeq \left(\frac{9\gamma\Sigma_{\rm R}}{3\pi(1+15w_\phi)}\frac{m_\phi^{\rm end}}{M_{\rm p}}\right)^{\frac{-3(1+w_\phi)}{4}}\left(\frac{M_{\rm p}}{H_{\rm end}}\right)^{\frac{7+9w_\phi}{4}}\left(\frac{n_3^{end}}{M_p^3}\right)^{\frac{3(1+w_\phi)}{4}}\left(\frac{M_{\rm p}}{M_3}\right)^{\frac{-(1+3w_\phi)}{4}}\delta^{3w_\phi-1}, \tag{5.12}$$

where

$$\delta = \left(\frac{5+3w_\phi}{1+w_\phi}\right)^{\frac{3(1+w_\phi)}{4(1-3w_\phi)}}\left(\frac{1}{12\pi(1+w_\phi)}\right)^{\frac{1}{2(1-3w_\phi)}}. \tag{5.13}$$

If $\beta \gg \beta_\phi^c$, neutrino, after being produced from the inflaton will immediately decay and cannot control the reheating dynamics anymore. In such a case, reheating is predominantly controlled by gravitational scattering $\phi\phi \to h\,h$, which is the usual gravitational reheating scenario first proposed in [184]. Therefore, we will consider the $\beta < \beta_\phi^c$ throughout.

As stated earlier, this reheating scenario is completely ruled out from the $\Delta N_{\rm eff}$ constraints, considering extra relativistic degrees of freedom accounted for from the PGWs [184]. Nevertheless, for our later purpose, let us quote the expression of the reheating temperature $T_{\rm re}$ for the GRe scenario

$$T_{\rm re}^{\rm gr} \simeq 0.5\,M_{\rm p}\left(\frac{9\gamma\,\Sigma_R}{3\pi(1+15w_\phi)}\frac{m_\phi^{\rm end}}{M_{\rm p}}\right)^{\frac{3+3w_\phi}{4(3w_\phi-1)}}\left(\frac{H_{\rm end}}{M_{\rm p}}\right)^{\frac{9w_\phi+1}{4(3w_\phi-1)}} \tag{5.14}$$

5.1.4 Two possible scenarios of νGRe

Out of the three heavy right-handed neutrinos, we have assumed the decay width of the third one $\Gamma_3 \ll \Gamma_2, \Gamma_1$. Therefore, due to its longer survival probability, and its subsequent decay into radiation will compete with the inflaton decay. Therefore, during reheating, we will discuss about three major players; inflaton and $\nu_{\rm R}^3$ and radiation. Before it decays into the SM particles, $\nu_{\rm R}^3$ will evolve as non-relativistic matter,

$$\rho_3(a) = n_3 M_3 \simeq \frac{3H_{end}^3 M_3^3\Sigma_3}{2\pi(1-w_\phi)(\gamma\, m_\phi^{\rm end})^2}\left(\frac{a_{\rm end}}{a}\right)^3 \tag{5.15}$$

[3]Here, thermal correction is not significant, as gravitational production is only active at the beginning of reheating. For this νGRe scenario, the maximum achievable bath temperature is 10^{12} GeV, where the initial inflaton mass is $\sim 10^{13}$ GeV. So, the thermal effect condition ($T \gg m_\phi$) is not satisfied initially, meaning that thermal effects do not play a significant role.

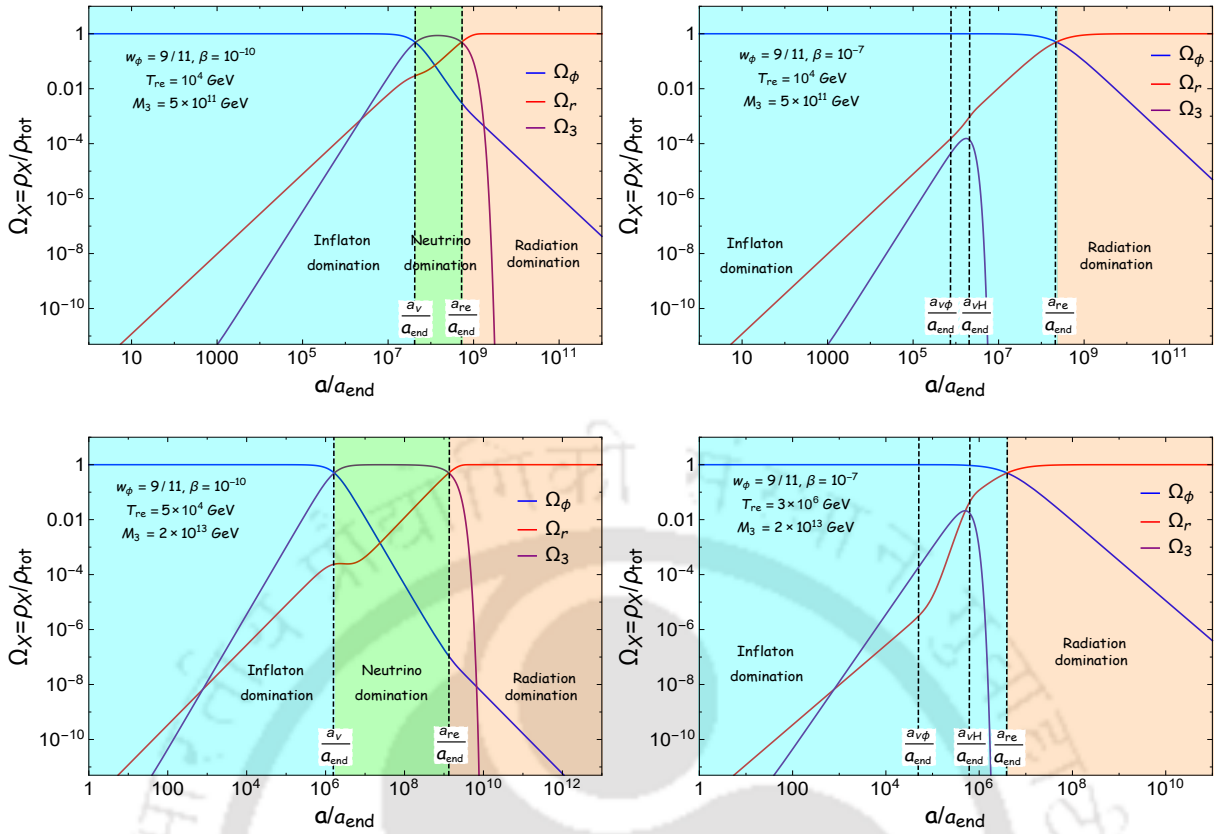

Figure 5.2: The evolution of the normalized energy densities $\Omega_X = \rho_X/\rho_{tot}$ as a function of the scale factor for the different combinations of (β, M_3) with $w_\phi = 9/11$. The left plot corresponds to the neutrino dominating case ($\beta < \beta^c_\nu$) and the right plot corresponds to the neutrino heating case ($\beta > \beta^c_\nu$).

Hence, for any value of $w_\phi > 0$, inflaton $\rho_\phi = a^{-3(1+w_\phi)}$, dilutes faster than the $\nu^3_{\rm R}$, it can dominate at $a = a_\nu$ where $\rho_\phi \sim \rho_3$.

$$\frac{a_\nu}{a_{\rm end}} \simeq \left(\frac{2\pi(1-w_\phi)\gamma^2}{\Sigma_3}\right)^{1/3w_\phi} \left(\frac{M_{\rm p}}{H_{\rm end}}\right)^{1/3w_\phi} \times \left(\frac{m^{\rm end}_\phi}{M_{\rm p}}\right)^{2/3w_\phi} \left(\frac{M_{\rm p}}{M_3}\right)^{1/w_\phi}. \tag{5.16}$$

Once $\nu^3_{\rm R}$ dominates over the inflaton, its subsequent decay into SM fields would populate the universe. One, therefore, expects a new critical value of $\beta = \beta^c_\nu$ below which $\nu^3_{\rm R}$ would survive long, and the universe becomes neutrino-dominated over the inflaton at some intermediate period before the conclusion of the reheating. If $\Gamma_3 = \beta^2 M_3/(8\pi) \sim H(a_\nu)$, one obtains following expression for the new critical value as,

$$\begin{aligned}\beta^c_\nu &= \left(\frac{8\pi H(a_\nu)}{M_3}\right)^{1/2} \\ &\simeq 22.3 \left(\frac{H_{\rm end}}{10^{13}\,{\rm GeV}}\right)^{1/2} \left(\frac{5\times10^{11}\,{\rm GeV}}{M_3}\right)^{1/2} \left(\frac{a_\nu}{a_{\rm end}}\right)^{-\frac{3(1+w_\phi)}{4}}.\end{aligned} \tag{5.17}$$

Therefore, for any value of $\beta \le \beta^c_\nu$, the ν^3_R will survive long enough such that the universe becomes neutrino (matter) dominated, say at the scale factor $a = a_\nu$. Then, after its subsequent decay into SM particles will complete the reheating process. For example, we get $\beta^c_\nu \simeq 10^{-9}\,(10^{-8})$ for $M_3 = 5\times10^{11}\,(2\times10^{13})$ GeV for $w_\phi = 9/11$. In the right plot in Fig.(5.2), we indeed see that $\nu^3_{\rm R}$ domination ceases to exist when $\beta = 10^{-7} > \beta^c_\nu$. On the other hand, for $\beta = 10^{-10} < \beta^c_\nu$, the universe undergoes a neutrino-dominated phase after inflaton domination as depicted in the left panel of the Fig. (5.2).

Depending on β, interesting possibilities arise for $\beta_\phi^c \geq \beta \geq \beta_\nu^c$. For this condition, inflaton still dominates throughout the entire reheating period. However, neutrinos can populate the thermal bath more efficiently than the inflaton.

In summary, if the coupling is very large $\beta \gg \beta_\phi^c$, neutrinos produced from inflaton will decay immediately, leaving no traces during the entire reheating process. This is what a GRe scenario is all about and has been studied before [184].

In this paper, we advocate two remaining possibilities depending on the $\nu_{\rm R}^3$ decay width: (1) **Neutrino dominating**: Heavy neutrinos can dominate the universe as a matter-like component over inflaton at some point during reheating and then decay to complete the reheating process, (2) **Neutrino heating**: Inflaton is the dominant energy component during the entire reheating process; however, the neutrino decay controls the reheating temperature.

5.1.4.1 Neutrino dominating: $\beta \leq \beta_\nu^c$

After the end of inflation, the gravitationally produced neutrino $\nu_{\rm R}^3$ will start to populate the universe. It is the long-lived that dominates over the inflaton after $a = a_\nu$, and the universe turned into matter-dominated with $\rho_3 \propto a^{-3}$ (see Eq. 5.15), then the Hubble parameter evolves as

$$H(a) = H_{\rm end}\left(\frac{a_\nu}{a_{\rm end}}\right)^{-\frac{3}{2}(1+w_\phi)}\left(\frac{a}{a_\nu}\right)^{-\frac{3}{2}} \qquad a \geq a_\nu\,. \tag{5.18}$$

During this period, radiation will naturally be populated by the $\nu_{\rm R}^3$ decay, and reheating will be completed at $\Gamma_3 \sim H(a_{\rm re})$. Considering neutrino dominated universe and utilizing Eq.(5.2b), radiation evolves as

$$\rho_r(a \geq a_\nu) \simeq \frac{\beta^2 M_3^2\, n_3(a_\nu)}{20\,\pi H(a_\nu)}\left(\frac{a}{a_\nu}\right)^{-3/2}, \tag{5.19}$$

which is independent of w_ϕ as expected. However, it is important point to remember that during pre-neutrino domination ($a < a_\nu$), the radiation was controlled by inflaton via its gravitational decay, and hence, the maximum radiation temperature lies at the beginning of reheating and determined by inflaton. In our subsequent discussion we will see this will play an interesting role in the context of dark matter production during reheating. The maximum radiation temperature will be,

$$T_{\rm rad}^{\rm max} \simeq (10^{11}\,{\rm GeV})\left(\frac{H_{\rm end}}{10^{13}\,{\rm GeV}}\right)^{3/4}\left(\frac{m_\phi^{\rm end}}{10^{13}\,{\rm GeV}}\right)^{1/4}, \tag{5.20}$$

which is of the order of $\sim 10^{11} - 10^{12}$ GeV. However, the final reheating temperature is determined by $\nu_{\rm R}^3$ decay, as indeed can be seen in the left plot in Fig. (5.2). Since $\rho_\phi \sim a^{-3(1+w_\phi)}$, for successful reheating, one must have $w_\phi \geq 1/3$; otherwise, due to slow dilution of inflaton compared to radiation, the universe will become inflaton dominated at a later stage, which we want to avoid. As stated earlier, the reheating ends at $a = a_{\rm re}$ where $\Gamma_3 = (3/2)H(a_{\rm re})$ leading to,

$$\frac{a_{\rm re}}{a_\nu} = \left(\frac{\beta^2}{12\,\pi}\frac{M_3}{H(a_\nu)}\right)^{-2/3}. \tag{5.21}$$

In equilibrium the radiation temperature $T_{\rm rad}$ relates to its energy density as $\rho_r = \epsilon\, T_{\rm rad}^4$, with $\epsilon = \pi^2 g_{\star r}^{\rm re}/30$. Where $g_{\star r}^{\rm re}$ is the relativistic degrees of freedom associated with the thermal bath. Utilizing this the radiation temperature evolves during $a_\nu \leq a \leq a_{\rm re}$, as [cf. Eq. 5.19]

$$T_{\rm rad}(a) \simeq T_{\rm re}\left(\frac{a}{a_{\rm re}}\right)^{-3/8} \tag{5.22}$$

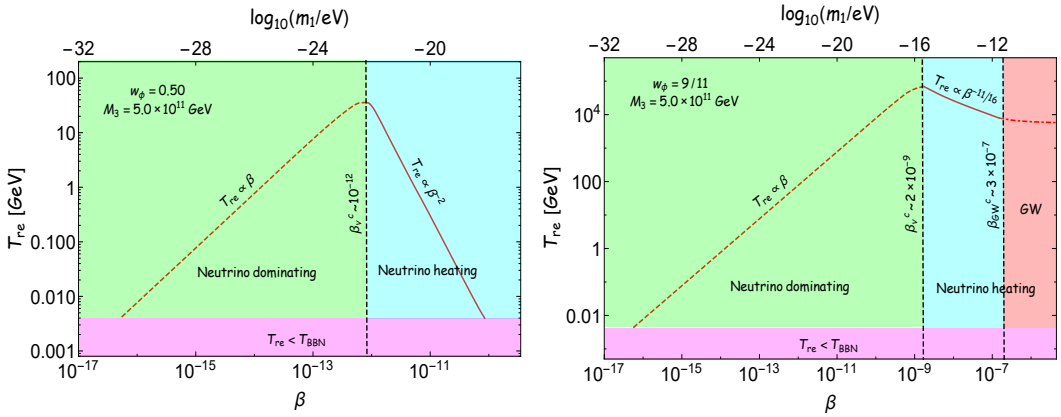

Figure 5.3: Variation of reheating temperature $T_{\rm re}$ as a function of β (bottom x-axis) and lightest active neutrino mass m_1 (top x-axis) for two different $w_\phi = 1/2$ (right plot) and $w_\phi = 9/11$ (left plot) with $M_3 = 5\times10^{11}$ GeV. BBN bounds exclude the magenta-shaded regions, and red-shaded regions (left plot) are excluded by an excess of gravitational waves.

where the reheating temperature $T_{\rm re}$,

$$\begin{aligned} T_{\rm re} &= \beta\left(\frac{2}{3\epsilon}\right)^{1/4}\left(\frac{M_3 M_{\rm p}}{8\pi}\right)^{1/2}, \\ &\simeq 10^{14}\beta\left(\frac{M_3}{5\times10^{11}\,\text{GeV}}\right)^{1/2}\text{GeV}. \end{aligned} \tag{5.23}$$

We observed that reheating temperature behaves as $T_{\rm re}\propto\beta M_3^{1/2}$. For the lowest possible reheating temperature $T_{\rm re}=T_{\rm BBN}=4$ MeV, one gets $\beta\simeq4\times10^{-17}$ for $M_3=5\times10^{11}$ GeV. On the other hand for the neutrino dominating case, the maximum reheating temperature could be achieved at $\beta=\beta_\nu^c$ for a given M_3 as

$$T_{\rm re}(\beta_\nu^c) = 10^{14}\,\beta_\nu^c\left(\frac{M_3}{5\times10^{11}\,\text{GeV}}\right)^{1/2}\text{GeV}. \tag{5.24}$$

For example given $w_\phi = 9/11\,(1/2)$ and $M_3 = 5\times10^{11}$ GeV, one obtains the the maximum reheating temperature as 10^5 (34) GeV. We indeed recover these values with $T_{\rm re}\propto\beta$ relation numerically as shown in Fig. 5.3 with the dashed line.

In summary, for the neutrino-dominated case, before it decays, the universe will go through inflaton domination (ID) → RHN domination → radiation domination (RD) era (see left plot in Fig. 5.2). The evolution of the radiation energy density in those phases can be written as

$$\rho_r\propto\begin{cases} a^{-4} & \text{for } a_{\rm end}<a<a_\nu & :\text{ID}\\ a^{-3/2} & \text{for } a_\nu<a<a_{\rm re} & :\text{ RHN domination}\\ a^{-4} & \text{for } a>a_{\rm re} & :\text{RD}. \end{cases} \tag{5.25}$$

5.1.4.2 Neutrino heating : $\beta_\nu^c\le\beta\le\beta_\phi^c$

This is the most interesting case we have encountered. Despite neutrinos being a subdominant component, the decay of RHNs is the primary source of the thermal bath than the inflation. Neutrinos to

become the dominating source of radiation the condition $M_3\Gamma_3 n_3 > \Gamma_{\phi\phi\to hh}(1+w_\phi)\rho_\phi$ must be satisfied, and that happens at $a = a_{\nu\phi}$ satisfying

$$\left(\frac{a_{\nu\phi}}{a_{\rm end}}\right)^{3+9w_\phi} \simeq \frac{48(1-w_\phi)\pi\gamma^3}{\beta^2}\frac{\Sigma_h}{\Sigma_3}\frac{H_{\rm end}}{M_3}\left(\frac{m_\phi^{\rm end}}{M_3}\right)^3 \tag{5.26}$$

Therefore, after $a > a_{\nu\phi}$, ignoring the inflaton contribution, the radiation components solely coming from the neutrino ($\nu_{\rm R}^3$) decay, and it is computed as (solving Eq.(5.2b)

$$\rho_r(a > a_{\nu\phi}) \simeq \frac{2\beta_3^2 M_3^2 n_3^{end}}{8\pi(5+3w_\phi)H_{\rm end}}\left(\frac{a}{a_{\rm end}}\right)^{-\frac{3(1-w_\phi)}{2}}. \tag{5.27}$$

This evolution will continue till the instant, say at $a = a_{\nu H} \le a_{\rm re}$, for which $\Gamma_3 \sim H$ is satisfied. We have

$$a_{\nu H}/a_{\rm end} = \left(\frac{\beta^2}{12\pi(1+w_\phi)}\frac{M_3}{H_{\rm end}}\right)^{\frac{-2}{3(1+w_\phi)}}. \tag{5.28}$$

Therefore, within $a_{\nu\phi} < a < a_{\nu H}$ the radiation temperature will evolve as

$$T_{\rm rad} \simeq \left(\frac{15\beta_3^2 M_3^2 n_3^{\rm end}}{2g_{\star r}^{\rm re}\pi^2(5+3w_\phi)H_{\rm end}}\right)^{\frac{1}{4}}\left(\frac{a}{a_{\rm end}}\right)^{-\frac{3(1-w_\phi)}{8}} \tag{5.29}$$

Such EoS-dependent temperature evolution will continue till the neutrinos decay completely into radiation. After this instant $a_{\nu H}(< a_{\rm re})$, there will be no additional entropy injected into the thermal bath, and hence the radiation component simply falls as a^{-4} with $T \propto a^{-1}$. Finally the reheating temperature will set by the condition at $\rho_\phi(a_{\rm re}) \sim \rho_r(a_{\rm re})$ (see right plot in Fig. (5.2)). However, it is important to note that such possible arises only for the inflaton EoS $w_\phi > 1/3$. The endpoints of reheating $a_{\rm re}$ and the reheating temperature $T_{\rm re}$ are expressed as,

$$\begin{aligned}\frac{a_{\rm re}}{a_{\rm end}} &= \left(\frac{8\pi(5+3w_\phi)}{\beta^2}\frac{H_{\rm end}^3 M_p^2}{n_3^{end}M_3^2}\right)^{1/3w_\phi-1}\left(\frac{a_{\nu H}}{a_{\rm end}}\right)^{\frac{-(5+3w_\phi)}{2(3w_\phi-1)}},\\ T_{\rm re} &\simeq 0.5 M_{\rm p}\,\beta^{\frac{-1}{3w_\phi-1}}\left(\frac{M_{\rm p}}{H_{\rm end}}\right)^{\frac{3}{2(3w_\phi-1)}}\left(\frac{n_3^{\rm end}}{M_p^3}\right)^{\frac{3(1+w_\phi)}{4(3w_\phi-1)}}\left(\frac{M_{\rm p}}{M_3}\right)^{\frac{1+3w_\phi}{4(1-3w_\phi)}}\delta\,.\end{aligned} \tag{5.30}$$

Reheating temperature depends non-trivially on the neutrino coupling and the mass of the $\nu_{\rm R}^3$, $T_{\rm re} \propto \beta^{\frac{-1}{3w_\phi-1}} M_3^{\frac{7+9w_\phi}{4(3w_\phi-1)}}$. As an example, once we fixed M_3, for $w_\phi = 1/2$, the $T_{\rm re} \propto \beta^{-2}$, and for $w_\phi = 9/11$, we got $T_{\rm re} \propto \beta^{-11/16}$ which we also confirm numerically and represented in the the Fig. 5.3 by solid lines. For this neutrino heating case, the maximum $T_{\rm re}$ is associated with $\beta = \beta_\nu^c$, and it is the same as the neutrino dominating case. The minimum value of $T_{\rm re}$ is set by either the BBN energy scale or the purely gravitational reheating case, which is only applicable for $w_\phi \gtrsim 0.65$.

In summary, for the neutrino heating case, the universe will go through ID → RD. However, as discussed during the inflaton domination, radiation is initially sourced by the inflaton decay and then controlled by the decay of RHNs, leading to the following evolution history of the thermal bath (see the right plot in Fig. 5.2),

$$\rho_r \propto \begin{cases} a^{-4} & \text{for } a_{\rm end} < a < a_{\nu\phi} \quad : \text{ID} \\ a^{-\frac{3(1-w_\phi)}{2}} & \text{for } a_{\nu\phi} < a < a_{\nu \rm H} \quad : \text{ID} \\ a^{-4} & \text{for } a_{\nu H} < a < a_{\rm re} \quad : \text{ID} \\ a^{-4} & \text{for } a > a_{\rm re} \quad : \text{RD}. \end{cases} \tag{5.31}$$

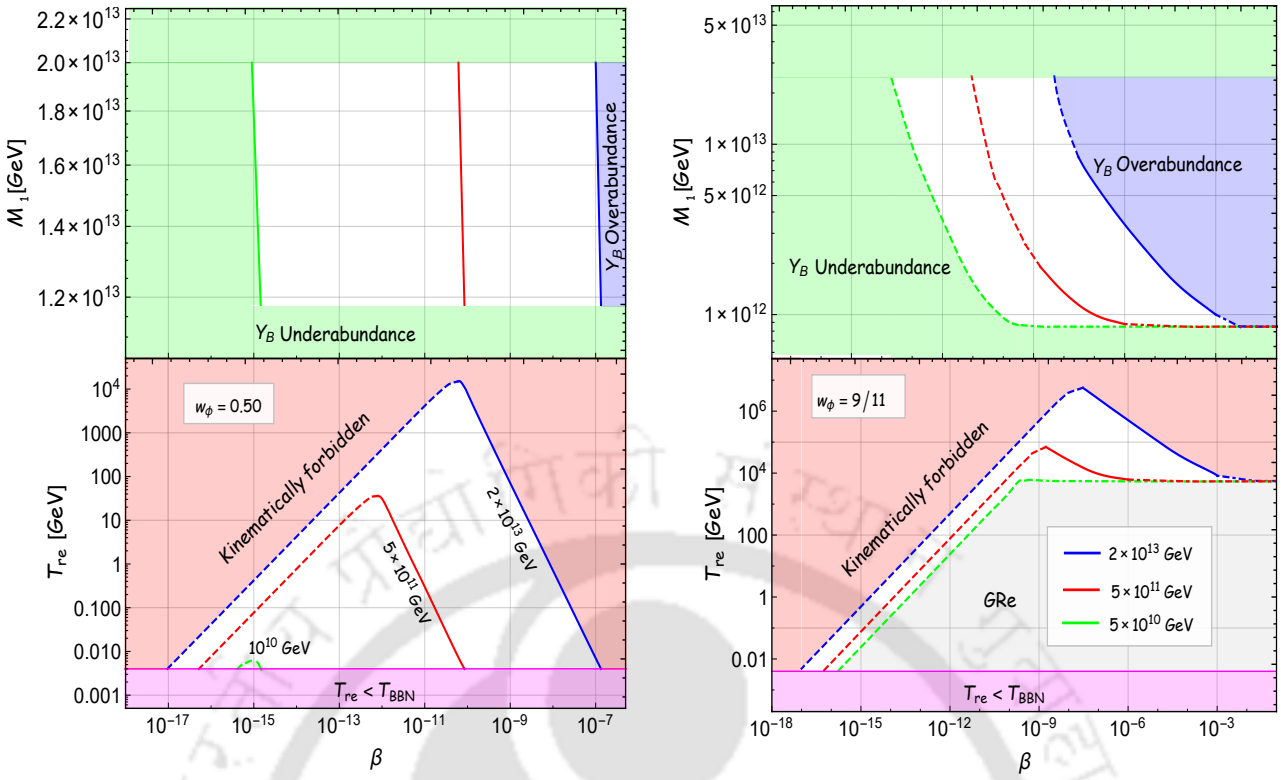

Figure 5.4: ***Lower panel*** : $T_{\rm re}$ as a function of β for different $\nu_{\rm R}^3$ mass M_3. The dashed line corresponds to the neutrino-dominating case, and the solid line corresponds to the neutrino-heating case. The dot-dashed lines are excluded by an excess production of gravitational waves from $\Delta N_{\rm eff}$ constraints. The magenta-shaded region corresponds to $T_{\rm re} < T_{\rm BBN}$. The red-shaded region is kinematically forbidden. ***Upper panel*** : we have plotted the contour of the observed baryon asymmetry $Y_{\rm B} \simeq 8.7 \times 10^{-11}$ in β-M_1 plane. The different color line corresponds to different M_3, the same as the bottom plot. The white regions are the allowed regions where the observed baryon asymmetry is possible, the blue-shaded regions are the overabundance regions, and the green-shaded regions correspond to the underabundance regions.

Considering details of the different reheating histories discussed above, we now depict the parameter regions of $\{\beta, M_3, w_\phi, T_{\rm re}\}$ where different histories are realized. In the bottom panel of Fig. 5.4, we have plotted $T_{\rm re}$ as a function of β within the allowed range of M_3. The different color lines correspond to different values of M_3. The corresponding mass range is taken within $(10^{10}, 2\times10^{13})$ GeV for $w_\phi = 1/2$ and, $(5\times10^{10}, 2\times10^{13})$ GeV for $w_\phi = 9/11$. From Fig. 5.4, for a given β, $T_{\rm re}$ increases with increasing mass of $\nu_{\rm R}^3$ M_3, due to its increase of entropy injection. However, it worth remembering that the gravitational production rate of neutrino is $\propto \left(1 - \frac{4M_3^2}{k^2\gamma^2 m_\phi^2}\right)^{3/2}$. As a result, for $M_3 \approx \gamma\, m_\phi^{\rm end} \simeq 2\times10^{13}$ GeV kinetic suppression leads to negligible neutrino production, and consequently reheating would not be possible due to significant kinematic suppression (depicted by red shaded region). On the other hand, the lowest possible mass M_3 can be determined from the condition $T_{\rm re}(\beta_\nu^c) \sim T_{\rm re}^{min}$, and the final expression of $M_3^{\rm min}$ is

$$M_3^{\rm min} \simeq M_{\rm p}\left(\frac{2\pi\,(1-w_\phi)\gamma^2}{\Sigma_3}\right)^{1/3}\left(\frac{m_\phi^{\rm end}}{M_{\rm p}}\right)^{2/3}\left(\frac{M_{\rm p}}{H_{\rm end}}\right)^{\frac{3w_\phi+1}{3(1+w_\phi)}}\left(\frac{T_{\rm re}^{\rm min}}{M_{\rm p}}\right)^{\frac{4w_\phi}{3(1+w_\phi)}}. \tag{5.32}$$

Using $w_\phi = 0.50\,(9/11)$, one can find $M_3^{\rm min} \simeq 1(5)\times10^{10}$ GeV.

The primary gravitational waves are the evolution of the tensor perturbation without any source term, and they can act as a good probe of the early universe. Once the tensor perturbations are generated due to vacuum fluctuation during inflation, they pass through different phases until we observe them today and put imprints of the background evolution on the spectrum. In the following section, we show how constraints from extra relativistic degrees of freedom at the point of BBN, considering PGWs, put restrictions on our proposed model of reheating.

5.1.5 Constraints from $\Delta N_{\rm eff}$ considering PGWs

PGWs is one of the profound predictions of inflationary paradigm [214, 215, 234]. Due to extremely weak coupling, it can pass through the universe almost unhindered and hence acts as a unique probe of the very early universe such as reheating phase [23, 153, 216, 217, 235]. The PGW amplitude and its spectral evolution are expected to be sensitive to the energy scale of the inflation and the post-inflationary phases. Particularly during the reheating phase, it has been observed that the modes between $k_{\rm re} < k < k_{\rm end}$ which re-enter the horizon during reheating, PGW spectrum shows a tilt depending on the background equation of state. Once we fixed the inflationary energy scale and w_ϕ, $T_{\rm re}$ regulates the duration of the tilted spectrum. The tilted spectrum's duration extends as we reduce $T_{\rm re}$. Nonetheless, if one considers the extra relativistic degrees of freedom arising from the GWs, the lesser value of $T_{\rm re}$ for a stiff equation can be constrained. We are going to discuss how small $T_{\rm re}$, after we fix the EoS and the inflation's energy scale, we can consider being consistent with the $\Delta N_{\rm eff}$. The additional relativistic degrees of freedom at the moment of BBN or CMB decoupling are denoted by $\Delta N_{\rm eff}$. The expression for $\Delta N_{\rm eff}$ in the case of the GWs takes the following form [202]

$$\Delta N_{\rm eff} = \frac{\rho_{\rm GW}}{\rho_\nu} = \frac{8}{7}\left(\frac{11}{4}\right)^{\frac{4}{3}} \frac{\rho_{\rm GW}}{\rho_\gamma}, \tag{5.33}$$

where ρ_γ and ρ_ν represent the photon energy density and energy density of single SM neutrino species, accordingly. One can use the relation between the neutrino and photon temperature, $T_\nu = (4/11)^{1/3}\, T_\gamma$ and find the restriction on the current GW energy density as

$$\int_{k_{\rm re}}^{k_{\rm end}} \frac{dk}{k} \Omega_{\rm GW}^k h^2 \leq \frac{7}{8}\left(\frac{4}{11}\right)^{4/3} \Omega_\gamma h^2\, \Delta N_{\rm eff}, \tag{5.34}$$

where $\Omega_\gamma h^2 \simeq 2.47 \times 10^{-5}$ is the present day photon relic density. $k_{\rm re}$ and $k_{\rm end}$ represent the wave number that reenters at the end of reheating and inflation, respectively.

5.1.5.1 Neutrino dominating: $\beta \leq \beta_\nu^c$

As the name suggests, for this scenario, ν_R^3 dominated phase emerges after the initial inflaton domination and finally the universe becomes radiation-dominated by the decay of the neutrinos. Depending upon the effective inflaton equation of state, this early neutrino domination ((matter) domination) leads to a spectral break in the GW spectrum. Such a break occurs for a particular scale $k_\nu = a_\nu H(a_\nu)$, which enters the horizon at the inflaton and neutrino equality point a_ν. The expression of k_ν can be written as

$$k_\nu = k_{\rm end}\left(\frac{a_\nu}{a_{\rm end}}\right)^{-(1+3w_\phi)/2}, \tag{5.35}$$

where $k_{\rm end}$ is the mode that enters the horizon at the beginning of reheating, which is different for different $T_{\rm re}$,

$$k_{\rm end} = H_{\rm end}\left(\frac{43}{11 g_{\star r}^{\rm re}}\right)^{1/3} \frac{T_0}{T_{\rm re}} \frac{a_{\rm end}}{a_{\rm re}}, \tag{5.36}$$

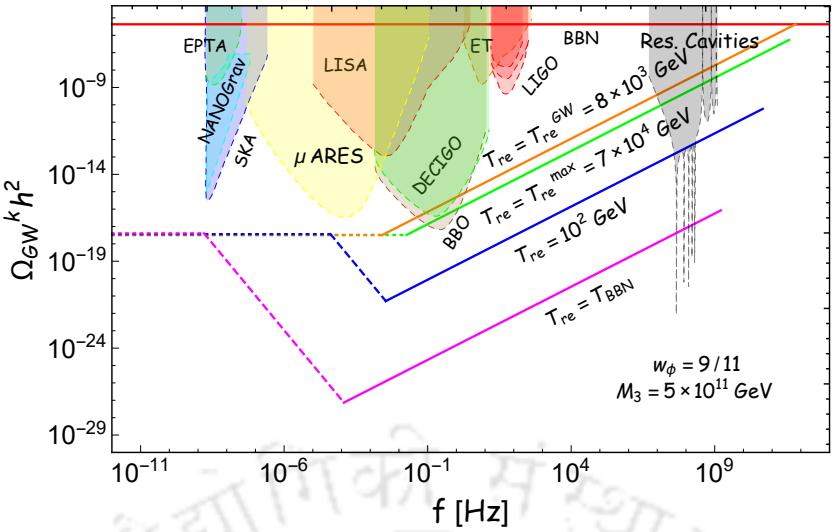

Figure 5.5: Behavior of $\Omega_{\rm GW}^{\rm k} h^2$ over a wide range of frequency $f = k/2\pi$.. Here we have considered $w_\phi = 9/11$ and $M_3 = 5\times10^{11}$ GeV.

Combining the Eqs. 5.21 and 5.23, one can find the following relation between $a_{\rm re}$ and $T_{\rm re}$ for this case,

$$\frac{a_{\rm re}}{a_{\rm end}} = \left(\frac{H_{\rm end}}{4.7\,M_p}\right)^{2/3}\left(\frac{M_p}{T_{\rm re}}\right)^{4/3}\left(\frac{a_\nu}{a_{\rm end}}\right)^{-w_\phi} \tag{5.37}$$

Utilizing Eq. 5.37 in Eq. 5.36, we have

$$k_{\rm end} \simeq (10^3\,{\rm Hz})\left(\frac{H_{\rm end}}{10^{13}\,{\rm GeV}}\right)^{1/3}\left(\frac{T_{\rm re}}{4\,{\rm MeV}}\right)^{1/3}\left(\frac{a_\nu}{a_{\rm end}}\right)^{w_\phi} \tag{5.38}$$

For example, for $w_\phi = 9/11$, $M_3 = 5\times10^{11}$ GeV, and $a_\nu/a_{\rm end} \simeq 4\times10^7$, if we consider $T_{\rm re} = 4$ MeV (10^2 GeV), the values of $k_{\rm end}$ and k_ν assume 2×10^9 (5×10^{10}) Hz and 10^{-4} (3×10^{-3}) Hz respectively. The modes within $k_\nu \geq k \geq k_{\rm re}$ that enter the horizon during the intermediate ν_R^3-dominated phase will perceive the matter with the equation of state $w = 0$ in the background. Hence, the present-day PGWs spectrum corresponding to those modes will be,

$$\Omega_{\rm GW}^k h^2 \simeq \Omega_{\rm GW}^{\rm inf} h^2 \frac{\Gamma^2(5/2)}{\pi}\left(\frac{k}{k_{\rm re}}\right)^{-2}. \tag{5.39}$$

where $k_{\rm re} = a_{\rm re} H(a_{\rm re})$ is the mode that enters the horizon at the end of reheating, and its value naturally depends on $T_{\rm re}$. In terms of $T_{\rm re}$, $k_{\rm re}$ can be written as (using Eq. 5.37),

$$\begin{aligned} k_{\rm re} &= k_{\rm end}\left(\frac{H_{\rm end}}{4.7\,M_p}\right)^{-1/3}\left(\frac{M_p}{T_{\rm re}}\right)^{-2/3}\left(\frac{a_\nu}{a_{\rm end}}\right)^{-w_\phi}, \\ &\simeq 1.2\times10^{-9}\left(\frac{T_{\rm re}}{4\ {\rm MeV}}\right){\rm Hz}. \end{aligned} \tag{5.40}$$

The scale-invariant part $\Omega_{\rm GW}^{\rm inf} h^2$, is fixed by the inflationary energy scale as follows,

$$\Omega_{\rm GW}^{\rm inf} h^2 = \frac{\Omega_R h^2 H_{\rm end}^2}{12\pi^2 M_p^2} = 6\times10^{-18}\left(\frac{H_{\rm end}}{10^{13}\,{\rm GeV}}\right)^2. \tag{5.41}$$

Due to the matter phase, the PGWs spectrum acquires a red-tilted spectrum with k^{-2}. This feature is depicted in Fig. 5.5, where $\Omega_{\rm GW}^k h^2$ is plotted as a function of frequency $f = k/2\pi$. The magenta and blue

lines correspond to the neutrino-dominating scenario. The dashed portions indicate the intermediate regime $k_\nu \geq k \geq k_{\rm re}$, where the PGW spectrum exhibits the k^{-2} scaling due to the intermediate matter-like phase.

On the other hand, modes within $k_{\rm end} \geq k \geq k_\nu$ enter the horizon during the early inflaton-dominated phase, and the PGWs spectrum assumes the following form,

$$\Omega^k_{\rm GW} h^2 \simeq \Omega^{\rm inf}_{\rm GW} h^2 \frac{\Gamma^2(\frac{5}{2})}{\pi} \left(\frac{k_\nu}{k_{\rm re}}\right)^{-2} \frac{\mu(w_\phi)}{\pi} \left(\frac{k}{k_\nu}\right)^{-\frac{(2-6w_\phi)}{(1+3w_\phi)}}, \tag{5.42}$$

where, $\mu(w_\phi) = (1+3\omega_\phi)^{\frac{4}{1+3w_\phi}} \Gamma^2\left(\frac{5+3w_\phi}{2+6w_\phi}\right)$, which typically assumes $\mathcal{O}(1)$ value. PGW spectrum is always shown blue tilted as reheating happens for $w_\phi \geq 1/3$. For $w_\phi = 9/11$, the $\Omega^k_{\rm GW} h^2$ behaves as $k^{16/19}$, as shown in the solid portions of the magenta and blue lines.

$k_{\rm end}$ is the largest frequency mode that reenters the horizon at the end of the inflation, which typically contributes to the $N_{\rm eff}$. Note that if there is no intermediate neutrino (matter) domination, such as the case of usual GRe, the form of the above spectrum Eq. 5.42 would be the same with k_ν replaced by $k_{\rm re}$. This essentially suggests that due to late matter domination, the spectrum in Eq. 5.42 acquires a large suppression factor $(k_{\rm re}/k_\nu)^{\frac{12w_\phi}{(1+3w_\phi)}} << 1$ for high frequency modes. For example taking $w_\phi = 9/11$, we obtain $T^{\rm gr}_{\rm re} \sim 4 \times 10^3$ GeV and $k_{\rm re} \sim 10^{-3}$ Hz. Whereas taking $M_3 = 5 \times 10^{13}$ GeV and keeping the same $w_\phi, T_{\rm re}$ as above, νGRe yields $k_\nu \sim 10^{-2}$ Hz. Utilizing those values, we obtain the suppression factor to be $\sim 10^{-3}$. Therefore, the neutrino-dominating case always abides by the $\Delta N_{\rm eff}$ constraint for all EoS $w_\phi > 1/3$. Furthermore, in Fig. 5.5, we presented the projected sensitivity reach of several proposed future GW experiments, including μ-ARES [236], LISA [237], Einstein Telescope (ET) [238–241], the Big Bang Observer (BBO) [242, 243], DECIGO [244, 245], and resonant cavities [246]. A significant portion of the parameter space remains accessible within the resonant cavities.

5.1.5.2 Neutrino heating: $\beta^c_\nu \leq \beta \leq \beta^c_\phi$

However, the situation gets strikingly different for the neutrino heating case ($\beta^c_\nu \leq \beta \leq \beta^c_\phi$). For this neutrino decay controls the reheating temperature, and inflation controls the background during the entire reheating period. For such cases, all the modes that enter the horizon during reheating, the PGWs spectrum we have [23, 193]

$$\Omega^k_{\rm GW} h^2 \simeq \Omega^{\rm inf}_{\rm GW} h^2 \frac{\mu(w_\phi)}{\pi} \left(\frac{k}{k_{\rm re}}\right)^{-\frac{(2-6w_\phi)}{(1+3w_\phi)}}. \tag{5.43}$$

One can observe that the spectrum is blue tilted for $w > 1/3$, and therefore, its magnitude would be maximum for the mode $k = k_{\rm end}$. This is where the BBN bound related to the effective number of relativistic degrees of freedom comes into play, and this translates into the bound on PGW spectrum as $\Omega^{k_{\rm end}}_{\rm GW} h^2 \leq 1.7 \times 10^{-6}$ [31, 225, 226] considering $\Delta N_{\rm eff} = 0.28$ [31]. Utilizing the Eqs. 5.34 and 5.43, we obtain the following contraint,

$$\left(\frac{k_{\rm end}}{k_{\rm re}}\right)^{-\frac{2(1-3w_\phi)}{1+3w_\phi}} \leq \frac{4.85\pi}{\mu(w_\phi)} \left(\frac{M_{\rm p}}{H_{\rm end}}\right)^2. \tag{5.44}$$

The relation between the two scales $(k_{\rm end}, k_{\rm re})$ for this case can be expressed in terms of reheating temperature $T_{\rm re}$, as follows

$$\frac{k_{\rm end}}{k_{\rm re}} = \frac{a_{\rm end} H_{\rm end}}{a_{\rm re} H(a_{\rm re})} = \left(\frac{H_{\rm end}}{3.3 M_{\rm p}}\right)^{\frac{1+3w_\phi}{3(1+w_\phi)}} \left(\frac{M_{\rm p}}{T_{\rm re}}\right)^{\frac{2(1+3w_\phi)}{3(1+w_\phi)}}, \tag{5.45}$$

where we have used the following relation between $a_{\rm re}$ and $T_{\rm re}$,

$$\frac{a_{\rm re}}{a_{\rm end}} = \left(\frac{H_{\rm end}}{3.3\,M_{\rm p}}\right)^{\frac{2}{3+3w_\phi}} \left(\frac{M_{\rm p}}{T_{\rm re}}\right)^{\frac{4}{3+3w_\phi}}, \tag{5.46}$$

Using the above equation, for the neutrino heating case, the expressions of $k_{\rm end}$ in terms of $T_{\rm re}$ can also be written as,

$$\begin{aligned} k_{\rm end} &= 3.3\,M_{\rm p}\left(\frac{43}{11\,g^{\rm re}_{\star r}}\right)^{1/3}\left(\frac{T_0}{T_{\rm re}}\right)\left(\frac{H_{\rm end}}{3.3\,M_{\rm p}}\right)^{\frac{1+3w_\phi}{3+3w_\phi}}\left(\frac{T_{\rm re}}{M_{\rm p}}\right)^{\frac{4}{3+3w_\phi}}, \\ &\simeq (3\times 10^{\frac{3(8+w_\phi)}{1+w_\phi}}\ {\rm Hz})\left(\frac{H_{\rm end}}{10^{13}\,{\rm GeV}}\right)^{\frac{1+3w_\phi}{3+3w_\phi}}\left(\frac{T_{\rm re}}{\rm GeV}\right)^{\frac{1-3w_\phi}{3+3w_\phi}}. \end{aligned} \tag{5.47}$$

Using the last form of the above equation and Eq. 5.45, one can find

$$k_{\rm re} \simeq 1.2\times 10^{-9}\left(\frac{T_{\rm re}}{4\ {\rm MeV}}\right){\rm Hz}. \tag{5.48}$$

Finally, upon substitution of Eq. 5.45 into Eq. 5.44, we obtain a lower bound on the reheating temperature, particularly when the inflaton equation of state $w_\phi > 1/3$ as,

$$T_{\rm re} > 0.5 M_{\rm p}\left(\frac{4.85\pi}{\mu(w_\phi)}\right)^{\frac{3(1+w_\phi)}{4(1-3w_\phi)}}\left(\frac{H_{\rm end}}{M_{\rm p}}\right)^{\frac{1+3w_\phi}{3w_\phi-1}} = T^{\rm GW}_{\rm re}. \tag{5.49}$$

We symbolize this new lower limit on reheating temperature from PGW as $T^{\rm GW}_{\rm re}$. Setting the above temperature with the BBN energy scale $T^{\rm GW}_{\rm re} \sim 4\,$MeV, we can see that the BBN bound of PGWs is only important when $w_\phi \geq 0.60$. To this end, let us remind ourselves that such bounds also exist for purely gravitational reheating cases, which completely ruled out the gravitational reheating [184, 247]. However, for the present case, due to an additional source of radiation from RHNs, we achieve a much higher reheating temperature compared to that of the GRe. As we already mentioned, increasing reheating temperature for a fixed w_ϕ and $H_{\rm end}$ reduces the duration of the tilt and makes our presented scenario consistent in the domain $1/3 < w_\phi \leq 1$. Therefore, a large region in the parameter space with $T_{\rm re} < T^{\rm GW}_{\rm re}$ GeV can be probed by future GW detectors (see Fig. 5.5).

We further point out that this lower bound on the reheating temperature naturally sets a critical value of the coupling parameter β by equating Eqs. 5.49 and 5.30,

$$\beta^c_{GW} \simeq \delta^{3w_\phi-1}\left(\frac{4.85\pi}{\mu(w_\phi)}\right)^{\frac{3(1+w_\phi)}{4}}\left(\frac{n_3^{end}}{M_p^3}\right)^{\frac{3(1+w_\phi)}{4}}\left(\frac{M_{\rm p}}{H_{\rm end}}\right)^{\frac{5+6w_\phi}{2}}\left(\frac{M_3}{M_{\rm p}}\right)^{\frac{1+3w_\phi}{4}}, \tag{5.50}$$

which turned out to be $\beta^c_{\rm GW} < \beta^c_\phi$. As an examples for $w_\phi = 9/11$ and $M_3 = 5\times 10^{11}$ GeV, we numerically obtained $\beta^c_{\rm GW} \simeq 10^{-7} < \beta^c_\phi \simeq 10^{-6}$. Further, the reheating temperature is $T^{\rm GW}_{\rm re} \simeq 8\times 10^3$ GeV, which is an order of magnitude larger than the prediction for the usual gravitational reheating case $T^{\rm gr}_{\rm re} \sim 10^3\,$GeV. Since, $\beta^c_{GW} < \beta^c_\phi$, therefore, the upper bound of β is set by $\beta^c_{\rm GW}$ when $w_\phi > 0.60$, whereas for $w_\phi \leq 0.60$, the upper bound on β is set by $T_{\rm BBN} \sim 4\,$MeV.

From our discussion so far, let us reiterate again that in order to have successful reheating, β should be non-vanishing. As stated earlier, this predicts non-zero lowest active neutrino mass ($m_1 = (\beta v)^2/M_3$). In Table-5.2, 5.3, we have provided the allowed range of β along with its predicted lowest active neutrino mass. In the next section, we will discuss where our proposed model stands in light of the recent BICEP/Keck 2018 data combined with Planck observations.

Table 5.2: Prediction of β and the lightest neutrino mass m_1 (in eV) successive reheating for EoS $w_\phi = 0.5$

M_3(GeV)	$T_{\rm re}(\beta_v^c)$(GeV)	$\beta_{min}(m_1^{min})$	$\beta_{max}(m_1^{max})$)
2×10^{13}	2×10^{4}	$1\times10^{-17}(10^{-34})$	$1\times10^{-7}(10^{-14})$
5×10^{11}	34.0	5×10^{-17} (10^{-31})	8×10^{-11} (4×10^{-19})
10^{10}	0.006	4×10^{-16} (5×10^{-28})	1×10^{-15} (7×10^{-27})

Table 5.3: Prediction of β and the lightest neutrino mass m_1 (in eV) successive reheating for EoS $w_\phi = 0.82$

M_3(GeV)	$T_{\rm re}(\beta_v^c)$(GeV)	$\beta_{min}(m_1^{min})$	$\beta_{max}(m_1^{max})$
2×10^{13}	6×10^{6}	6×10^{-18} (3×10^{-35})	$9\times10^{-4}(8\times10^{-7})$
5.0×10^{11}	7×10^{4}	5×10^{-17} (2×10^{-31})	1×10^{-7} (6×10^{-13})
5.0×10^{10}	5×10^{3}	2×10^{-16} (2×10^{-29})	5×10^{-10} (2×10^{-16})

5.1.6 Impact on the inflationary parameters $(N_k, n_{\rm s}, r)$

Along with the reheating phase, the post-reheating history is also important in order to put constraints on the inflationary e-folding number N_k, scalar spectral index, $n_{\rm s}$, and tensor-to-scalar ratio, r. If one assumes that after the reheating phase, the comoving entropy density remains conserved, then such a conservation law imposes an interesting relation among the parameters $(N_k, N_{\rm re}, T_{\rm re})$ as follows [11, 12],

$$\begin{aligned} T_{\rm re} &= \left(\frac{43}{11\,g^{\rm re}_{\star r}}\right)^{1/3}\left(\frac{H_k}{k_\star/a_0}\right)e^{-(N_k+N_{\rm re})}\,T_0 \\ &= (2.5\times10^{39}\ {\rm GeV})\left(\frac{H_k}{10^{13}\ {\rm GeV}}\right)e^{-N_k}\,\frac{a_{\rm end}}{a_{\rm re}}\,. \end{aligned} \tag{5.51}$$

Combining the Eq. 5.51 with Eqs. 5.46 and 5.37, we scan the $n_{\rm s}$-r parameter space in Fig. 5.6 for different values of α for $w_\phi = 0.50$ (left) and $w_\phi = 9/11$ (right). The black-dot correspond to $T_{\rm BBN}(T^{\rm GW}_{\rm re})$ point of $w_\phi = 1/2(9/11)$ for the neutrino heating case. Whereas green, red and blue dots correspond to the $T_{\rm BBN}$ for neutrino dominating case for three different masses of $M_3 = (M_3^{\rm min}, 5\times10^{11}, 2\times10^{13})$ GeV respectively. Although the reheating temperature is the same, the prediction of $(n_{\rm s}, r)$ is different for these two reheating scenarios, as the relation between $N_{\rm re}$ and $T_{\rm re}$ is different for these two cases. The segments between the black dot and any other color dot associated with a particular mass of M_3 are the allowed $n_{\rm s}$ range. For example, if one considers $M_3 = M_3^{\rm min} \simeq 5\times10^{10}$ GeV, $w_\phi = 9/11$ and $\alpha = 1$, the allowed range of $n_{\rm s}$ will lie within $0.96615 \le n_{\rm s} \le 0.96825$ (segment between black dots and green dots) which is well inside the 1σ bound. Consequently, the inflationary e-folding number within $59 \le N_k \le 64$. Interestingly, for $\alpha = 1.0$, the whole ranges of $n_{\rm s}$ lie within 1σ regions. For $w_\phi = 1/2\,(9/11)$, the prediction of $n_{\rm s}$ lying within $0.96329\,(0.96321) \le n_{\rm s} \le 0.96825\,(0.96724)$. Similar bounds can also be obtained for $\alpha = 10, 17, 19$, and that can be decoded from the Fig. 5.6.

5.1.7 Leptogenesis and constraints

RHNs are gravitationally produced from the inflaton. Therefore, all of them undergo CP-violating out-of-equilibrium decay and produce lepton asymmetry. By the well-known non-perturbative sphaleron processes, those lepton asymmetries are then converted into the baryon asymmetry. For our analysis, we considered the following mass hierarchy $M_1 \lesssim m_\phi^{\rm end} \ll M_2$. The lepton asymmetry will, therefore,

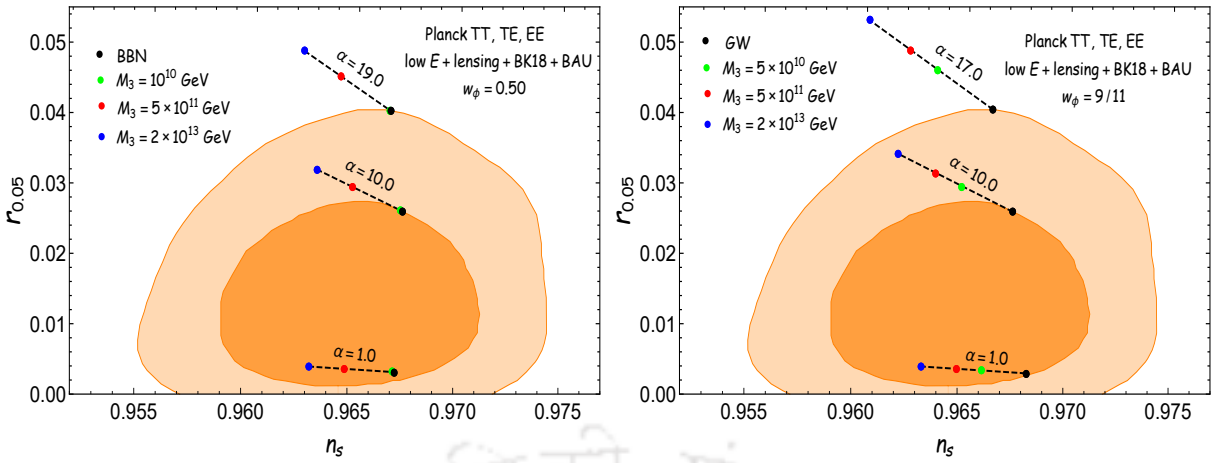

Figure 5.6: Compare our result with the observational 68% and 95% CL constraints from BICEP/Keck, in the (ns, r) plane for $w_\phi = 0.50$ (left) and $w_\phi = 9/11$ (right). The black-dot points correspond to $T_{\rm BBN}(T_{\rm re}^{\rm GW})$ point of $w_\phi = 0.50(9/11)$ for the neutrino heating case, and the different color points correspond to the $T_{\rm BBN}$ points for different mass M_3 for the neutrino dominating case.

predominantly be produced by the decays of $\nu_{\rm R}^1$ [4]. Note that due to the very small decay width of $\nu_{\rm R}^3$, $\nu_{\rm R}^3$ does not contribute a significant asymmetry. Furthermore, its suppressed Yukawa coupling ensures that the associated lepton number-violating interactions remain out of equilibrium, thereby preventing any washout of the asymmetry generated by $\nu_{\rm R}^1$. Therefore, the CP asymmetry parameter ($\epsilon_{\Delta L}$) generated from the decay of $\nu_{\rm R}^1$, using the seesaw mechanism [136, 247–249] is expressed as,

$$\begin{aligned}\epsilon_{\Delta L} &= \frac{\sum_\alpha \left[\Gamma(\nu_{\rm R}^1 \to L_\alpha H) - \Gamma(\nu_{\rm R}^1 \to \bar{L}_\alpha H^\star)\right]}{\sum_\alpha \left[\Gamma(\nu_{\rm R}^1 \to L_\alpha H) + \Gamma(\nu_{\rm R}^1 \to \bar{L}_\alpha H^\star)\right]} \\ &\simeq \frac{3\delta_{\rm eff}}{16\pi}\frac{m_{\nu,\rm max} M_1}{v^2} \\ &\simeq 9.85\times10^{-5}\left(\frac{M_1}{10^{12}\,\rm GeV}\right)\end{aligned} \tag{5.52}$$

The final lepton asymmetry depends on the out-of-equilibrium number density of $\nu_{\rm R}^1$ and the CP asymmetry ($\epsilon_{\Delta L}$). Where, $\delta_{\rm eff}$ is the effective CP-violating phase in the neutrino mass matrix, which typically assumes the value within $0 \le \delta_{\rm eff} \le 1$, and we have taken $\delta_{\rm eff} = 1$. We take the normal hierarchy of active neutrino mass with $m_{\nu,\rm max} = m_3 = 0.05$ eV [5], and the Higgs vacuum expectation value $v = 174$ GeV. As stated earlier, the above lepton asymmetry is converted into the baryon asymmetry ($Y_{\rm B}$) via the electroweak sphaleron processes [137, 138],

$$Y_{\rm B} = \frac{n_B}{s} = a_{\rm sph}\,\epsilon_{\Delta L}\frac{n_1(T_{\rm re})}{s(T_{\rm re})}, \tag{5.53}$$

where $a_{\rm sph} = \frac{28}{79}$ and $s(T_{\rm re}) = \frac{2\pi^2}{45} g_{\star s}^{\rm re} T_{\rm re}^3 = \frac{4\epsilon}{3}\frac{g_{\star s}^{\rm re}}{g_{\star r}^{\rm re}} T_{\rm re}^3$ is the entropy density at the end of reheating. Where $g_{\star s}^{\rm re}$ counts the number of entropic degrees of freedom at the end of reheating. The number density, $n_1(T_{\rm re})$ at the time of reheating from Eq. 5.8,

$$n_1(T_{\rm re}) = \frac{3H_{\rm end}^3 M_1^2 \Sigma_1}{2\pi(1-w_\phi)(\gamma m_\phi^{\rm end})^2}\left(\frac{a_{\rm re}}{a_{\rm end}}\right)^{-3}, \tag{5.54}$$

[4] Note that the three-body decay such as $\nu_{\rm R}^{1/2} \to \nu_R^3 + \nu_L + \nu_L$ is kinematically allowed. However, we checked that the associated production rate of ν_R^3, $\Gamma_{1/2\to3} \simeq \frac{\beta^2 (y^\dagger y)_{11/22}}{2M_{1/2}}\left(\frac{3}{2}p^2 + \frac{1}{2} - 2p - p^2\ln p\right), p = M_3^2/M_{1/2}^2)$ is very much suppressed compared to the gravitational contributions.

[5] For the inverted hierarchy $m_{\nu,\rm max} = m_2 = 0.05$ eV.

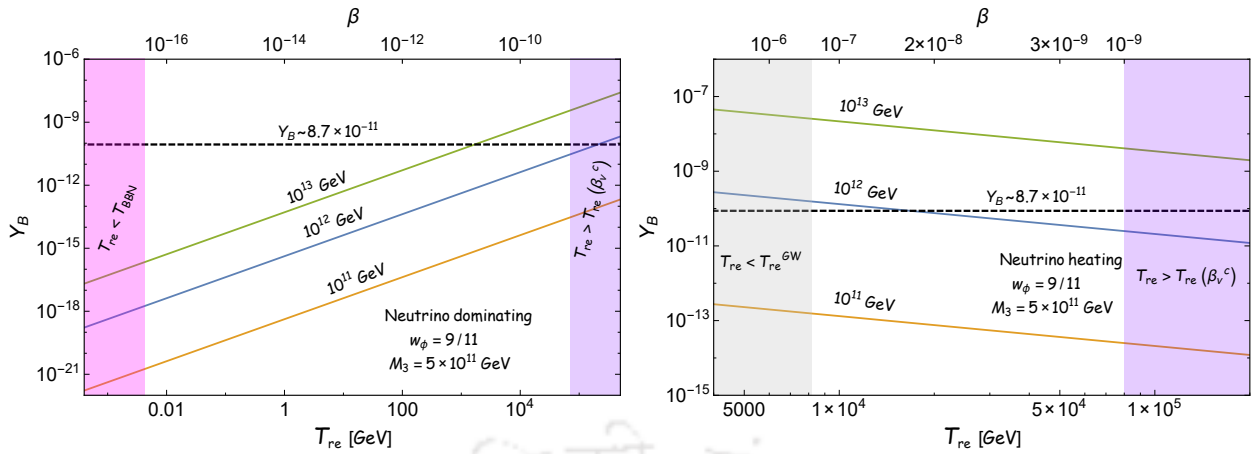

Figure 5.7: Y_B as function of T_{re} for three different choices of M_1 (different solid line) for a fixed $M_3 = 5 \times 10^{11}$ GeV and $w_\phi = 9/11$. The magenta-shaded and gray-shaded region corresponds to $T_{re} < T_{BBN}$ and $T_{re} < T_{re}^{GW}$, respectively. The purple-shaded region is correspond to $T_{re} > T_{re}(\beta_v^c)$. The horizontal dashed line corresponds to the observed baryon asymmetry $Y_B \sim 8.7 \times 10^{-11}$ GeV

We will now use this expression in Eq. 5.53 to constrain our model parameters for two different reheating cases.

5.1.7.1 Neutrino dominating: $\beta \leq \beta_v^c$

Utilizing the Eqs. 5.53, 5.54 and 5.37, Y_B can be written as in terms of T_{re},

$$\begin{aligned} Y_B &= \frac{21}{79}\frac{\epsilon_{\Delta L}}{\epsilon}\frac{g_{\star s}^{re}}{g_{\star r}^{re}}\frac{2\epsilon n_1^{end}}{3M_p^3}\left(\frac{M_p}{H_{end}}\right)^2\frac{T_{re}}{M_p}\left(\frac{a_v}{a_{end}}\right)^{3w_\phi}, \\ &\simeq 4\times 10^{-15}\frac{\Sigma_1}{\Sigma_3}\left(\frac{M_1}{10^{12}\,\text{GeV}}\right)^3\left(\frac{5\times 10^{11}\,\text{GeV}}{M_3}\right)^3\left(\frac{T_{re}}{4\,\text{MeV}}\right) \end{aligned} \tag{5.55}$$

We have also used Eq. 5.16 to find the above expression, and we assume $g_{\star s}^{re} \simeq 100$. In this scenario, the final baryon asymmetry is independent of w_ϕ but depends on the reheating temperature T_{re}. From the above equation, for a given M_3, $Y_B \propto M_1^3 T_{re} \propto M_1^3 \beta$, the baryon asymmetry increases with increasing both T_{re} (or β) and M_1. We demonstrate this behavior in Fig. 5.7 (left plot), where Y_B is plotted as a function of T_{re} for different M_1. Therefore, to find the correct baryon asymmetry, we need to decrease M_1 for increasing β (see dashed line in Fig. 5.4). Fixing the observed baryonic asymmetry, therefore, leads to $M_1 \propto \beta^{-1/3}$. This slope is also recovered numerically as shown by the dashed line in the upper part of the right Fig. 5.4 (dashed line) for $w_\phi = 9/11$.

The required T_{re} for producing the observed baryon asymmetry is not achievable for $w_\phi < 0.50$. For example, $M_1 = 10^{12}$ GeV, $M_3 = 10^{10}$ GeV, we need $T_{re} \sim 1$ GeV to satisfy the correct asymmetry. But using these M_3, $T_{re} \sim 1$ GeV is not achievable $w_\phi \leq 0.5$. For this reason, we never get a baryon asymmetry universe for $w_\phi = 1/3, 0.5$. However, for $w_\phi > 0.50$, for reasonable T_{re} and M_1, the proper asymmetry can be generated. For example, for $w_\phi = 9/11$, $M_3 = 5 \times 10^{11}$ GeV, we have found the correct asymmetry has been generated when $T_{re} \geq 100$ GeV (see left upper plot in Fig. 5.4), corresponding to a ν_R^1 mass in the range $M_1 \simeq (2-20) \times 10^{12}$ GeV.

5.1.7.2 Neutrino heating: $\beta_\nu^c \leq \beta \leq \beta_\phi^c$

For this case, using the Eqs. 5.53, 5.54 and 5.46, Y_B can be written as

$$\begin{aligned} Y_B(T_{\rm re}) &= \frac{21}{79}\frac{\epsilon_{\Delta L}}{\epsilon}\frac{g_{\star s}^{\rm re}}{g_{\star r}^{\rm re}}\frac{n_1^{\rm end}}{M_p^3}\left(\frac{\sqrt{\epsilon}M_{\rm p}}{\sqrt{3}H_{\rm end}}\right)^{\frac{2}{1+w_\phi}}\left(\frac{T_{\rm re}}{M_{\rm p}}\right)^{\frac{1-3w_\phi}{1+w_\phi}}, \\ &= 4\times 10^{\frac{30w_\phi-32}{1+w_\phi}}\frac{\Sigma_1}{(1-w_\phi)\gamma^2}\left(\frac{M_1}{10^{12}\,\text{GeV}}\right)^3\left(\frac{10^{13}\,\text{GeV}}{m_\phi^{\rm end}}\right)^2\left(\frac{H_{\rm end}}{10^{13}\,\text{GeV}}\right)^{\frac{1+3w_\phi}{1+w_\phi}}\left(\frac{T_{\rm re}}{\text{GeV}}\right)^{\frac{1-3w_\phi}{1+w_\phi}}. \end{aligned} \tag{5.56}$$

In this scenario, the final baryon asymmetry is dependent on both w_ϕ and $T_{\rm re}$ and behaves as $Y_{\rm B}\propto M_1^3 T_{\rm re}^{\frac{1-3w_\phi}{1+w_\phi}} \propto M_1^3\beta^{1/(1+w_\phi)}$, for a given M_3. As reheating happens for $w_\phi > 1/3$, the baryon asymmetry decreases (increases) with increasing $T_{\rm re}(\beta)$. We confirmed this behavior in Fig. 5.7 (right plot). Fixing the observed baryonic asymmetry leads $M_1 \propto \beta^{-1/(3+3w_\phi)}$. For example, considering $w_\phi = 9/11(1/2)$, the corresponding slope turns out to be $M_1 \propto \beta^{-11/60}(\beta^{-2/9})$. This slope also recovered numerically, as shown in the upper part of Fig. 5.4. For $w_\phi = 1/3$, the produce asymmetry is too small that we never get a baryon asymmetry universe. However, for $w_\phi \geq 0.5$, for reasonable $T_{\rm re}$ and M_1, the proper asymmetry can be generated. For $w_\phi = 1/2$, the proper asymmetry will be generated when $T_{\rm re}$ is close to BBN temperature. For $w_\phi = 1/2$, $T_{\rm re}$ range where proper asymmetry will be generated is 4 MeV to 10 MeV, the corresponding mass range $M_1 \simeq (1.2-2.0)\times 10^{13}$ GeV. If we increase w_ϕ, the relaxation of $T_{\rm re}$ and M_1 will occur. For example $w_\phi = 9/11$ and $M_3 = 5\times 10^{11}$ GeV, mass range $M_1 \simeq (8-20)\times 10^{11}$ GeV.

Combining both reheating scenarios, the viable mass range of $\nu_{\rm R}^1$ for successful leptogenesis is found to lie within $M_1 \simeq (8-200)\times 10^{11}$ GeV. Finally, in Table 5.4 and 5.5, we have provided the prediction of β (m_1) for successful reheating and leptogenesis simultaneously. Now, we have a complete picture including neutrino mass, lepton asymmetry, and reheating.

Table 5.4: Prediction of lightest neutrino mass m_1 (in eV) successive reheating and baryogenesis for $w_\phi = 0.50$

M_3 (GeV)	$\beta_{\rm min}(m_1^{\rm min})$	$\beta_{\rm max}(m_1^{\rm max}))$
2×10^{13}	$8\times 10^{-8}(9\times 10^{-15})$	$1\times 10^{-7}(1.5\times 10^{-14})$
5×10^{11}	5×10^{-11} (1.5×10^{-19})	8×10^{-11} (4×10^{-19})
10^{10}	9×10^{-16} (2.5×10^{-27})	1×10^{-15} (3.0×10^{-27})

Table 5.5: Prediction of lightest neutrino mass m_1 (in eV) successive reheating and baryogenesis for $w_\phi = 0.82$

M_3 (GeV)	$\beta_{\rm min}(m_1^{\rm min})$	$\beta_{\rm max}(m_1^{\rm max}))$
2.0×10^{13}	4×10^{-9} (1×10^{-17})	$9\times 10^{-4}(8\times 10^{-7})$
5.0×10^{11}	7×10^{-12} (3×10^{-21})	1×10^{-7} (6×10^{-13})
5.0×10^{10}	1.1×10^{-14} (7×10^{-26})	5×10^{-10} (2×10^{-16})

5.2 Thermal and Nonthermal Dark Matter with Gravitational Neutrino Reheating

In the previous section, we discussed the νGRe scenarios in detail and demonstrated how it provides a minimal framework for reheating and leptogenesis. In this section, we will examine its impact on the production of various DM models. Phenomenological studies of DM were mostly confined in the early radiation-dominated universe [250–257] with severe constraints from observation. Further, the direct probe of the reheating phase is experimentally challenging. Studying the impact of the reheating phase on DM phenomenology has, therefore, gained widespread interest in recent years [16–18, 41, 47, 174, 176–183, 190, 211, 258, 259]. Non-standard reheating histories have been shown to allow previously unexplored DM parameter regions and, therefore, opened up the intriguing possibilities of putting indirect constraints on the early universe phases, such as reheating and inflation via DM experiments. This further led to significant interest in building up a unified framework of inflaton and DM in conjunction with the reheating phase. Gravitational particle production, particularly during inflation and reheating, is universal. Hence, any phenomenological study cannot ignore such production, and that may have a significant impact on the parameter estimation of any DM model under consideration. It is in this parlance that we study the impact of gravitational neutrino reheating (νGRe) on two popular minimal DM models, namely the Higgs portal DM and QCD Axion. We study in detail both thermal and non-thermal production of DM during reheating, which is governed by gravitational neutrino production and their subsequent decay. We show how such consideration leads to an interesting correlation between the DM and Type-I seesaw parameters confronting direct observations.

This section is organized as follows: In subsection 5.2.1, we consider the production of Higgs portal scalar DM and discuss their possible constraints from the perspective of various theoretical and experimental bounds. In subsection 5.2.2, we also examine the production of the QCD axion via the misalignment mechanism and discuss the corresponding bounds on its parameter space. Finally, we conclude this chapter in section 5.3.

5.2.1 Particle dark matter phenomenology

Now, we aim to discuss how the present neutrino reheating scenario affects the DM production and constrain its parameter space. We consider both thermal and non-thermal DM production scenarios. Let us consider a real standard model singlet DM S [260–269], which is odd and all the standard model particles are even under the $\mathbb{Z}_2$ symmetry. The DM interacts with the SM via the Higgs portal interaction and also with inflaton through universal gravitational interaction. The interaction Lagrangian for DM is,

$$\mathscr{L}_{\rm int} = -\frac{h_{\mu\nu}}{M_{\rm p}}(T^{S}_{\mu\nu} + T^{\phi}_{\mu\nu}) - \lambda_{hs} S^2 H^\dagger H, \tag{5.57}$$

where $h_{\mu\nu}$ is the graviton field, $T^{\rm S}_{\mu\nu}(T^{\phi}_{\mu\nu})$ is the energy-momentum tensor of DM (inflaton) and λ_{hs} is the Higgs portal coupling.

Gravitational DM production from inflaton : Gravitational production of DM from the background inflaton field is universal and hence will always be present in any inflationary scenario. Since we have considered scalar DM, the production rate is,

$$R^{\phi}_{\rm s} = \frac{\rho^2_{\phi}}{8\pi M^4_p}\Sigma^0_s, \tag{5.58}$$

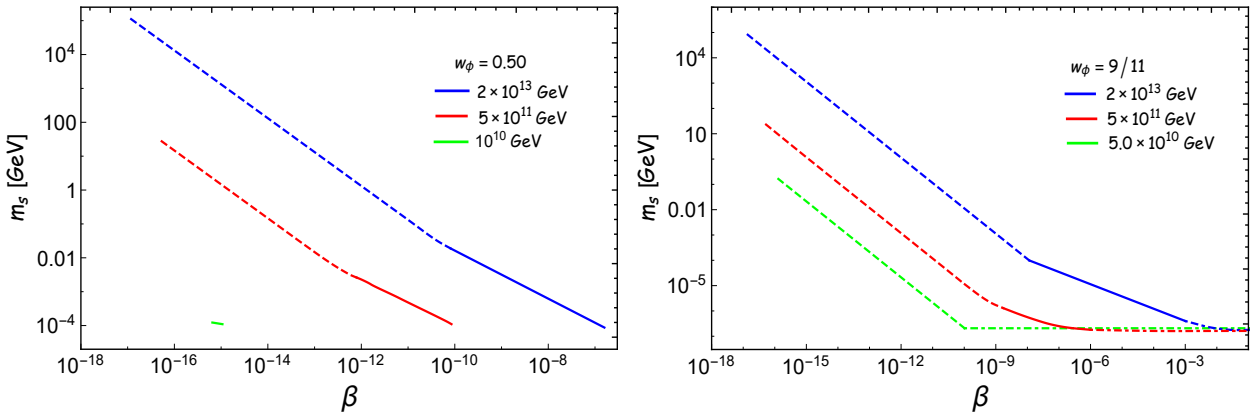

Figure 5.8: We have shown the relation between the β and the mass of DM $m_{\rm s}$, that predicts the observed DM relic abundance from purely gravitational interactions. The different color lines correspond to different M_3. The solid (dashed) lines correspond to the neutrino heating (dominating) case. The dot-dashed lines are excluded by an excess of PGWs.

where,

$$\Sigma_s^0 = \sum_{\nu=1}^{\infty} |\mathscr{P}_\nu^{2n}|^2 \left(1+\frac{2m_s^2}{\nu^2\gamma^2 m_\phi^2}\right)^2 \left(1-\frac{4m_s^2}{\nu^2\gamma^2 m_\phi^2}\right)^{1/2}. \tag{5.59}$$

accounts for the sum over the Fourier modes of the inflaton potential, and its numerical values are given in Table-5.1, and $m_{\rm s}$ is the DM mass. The evolution of DM number density ($n_{\rm s}$) is governed by the Boltzmann equation

$$\dot{n}_{\rm s} + 3H\, n_{\rm s} = R_\phi^s. \tag{5.60}$$

Using the Eq. 5.58 in Eq. 5.60, we have obtained the following solutions for the number density

$$n_{\rm s}(a) \simeq \frac{3H_{end}^3 \Sigma_s^0}{4\pi(1+3w_\phi)} (a/a_{\rm end})^{-3}. \tag{5.61}$$

The present-day DM relic abundance can be written as

$$\begin{aligned}\Omega_{\rm s} h^2 &= \Omega_r \frac{m_{\rm s}\, n_{\rm s}(a_{\rm re})}{\epsilon\, T_{\rm now}\, T_{\rm re}^3} \\ &= \Omega_r \frac{3\Sigma_s^0}{4\pi\epsilon(1+3w_\phi)} \frac{H_{end}^3 m_s}{T_{\rm now}\, T_{\rm re}^3} \left(\frac{a_{\rm re}}{a_{\rm end}}\right)^3.\end{aligned} \tag{5.62}$$

Note that the final abundance of the gravitational DM is dependent not only on the reheating temperature but also on the duration of reheating $a_{\rm re}/a_{\rm end}$. Utilizing $a_{\rm re}/a_{\rm end}$ from Eq. 5.37, the DM abundance for the neutrino dominating case turns out to be,

$$\Omega_{\rm s} h^2 \simeq 0.12 \frac{\Sigma_s^0}{\Sigma_3} \left(\frac{m_{\rm s}}{200\,{\rm GeV}}\right) \left(\frac{5\times10^{11}\,{\rm GeV}}{M_3}\right)^3 \left(\frac{m_\phi^{\rm end}}{10^{13}\,{\rm GeV}}\right)^2 \left(\frac{T_{\rm re}}{4\,{\rm MeV}}\right), \tag{5.63}$$

and similarly utilizing $a_{\rm re}/a_{\rm end}$ from Eq. 5.46 for the neutrino heating case, we have the following expression for the DM abundance,

$$\Omega_{\rm s} h^2 \simeq 10^{\frac{4(11w_\phi-4)}{1+w_\phi}} \frac{\Sigma_s^0}{1+3w_\phi} \left(\frac{m_{\rm s}}{\rm GeV}\right) \left(\frac{H_{\rm end}}{10^{13}\,{\rm GeV}}\right)^{\frac{1+3w_\phi}{1+w_\phi}} \left(\frac{T_{\rm re}}{\rm GeV}\right)^{\frac{1-3w_\phi}{1+w_\phi}}. \tag{5.64}$$

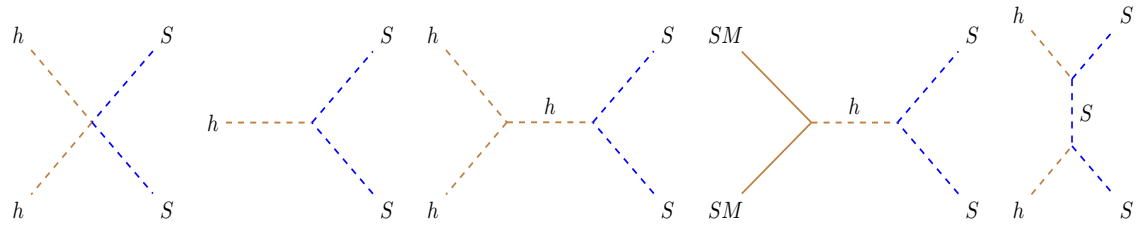

Figure 5.9: Leading diagrams for Higgs portal dark matter production

Due to their distinct reheating histories, one notes that DM abundance behaves as $\Omega_s h^2 \propto T_{re} \propto \beta$ for neutrino dominating, and $\Omega_s h^2 \propto T_{re}^{\frac{1-3w_\phi}{1+w_\phi}} \propto \beta^{1/(1+w_\phi)}$ for neutrino heating case. Once the observed DM abundance is satisfied, these two behaviors are reflected in the sudden change of the slope in the m_s vs. β curve, as shown in Fig. 5.8. This clearly depicts how the neutrino sector such as coupling parameter β is correlated with the DM sector such as mass m_s. The above production is purely gravitational and non-thermal in nature. In the following section, we discuss how neutrino reheating also controls DM production when the DM-Higgs portal coupling is taken into account.

Higgs portal DM : In the Higgs sector, the electroweak scale is an important energy scale where the phase transition occurs, and all the SM particles acquire mass. Before the electroweak symmetry breaking (EWSB), i.e., $T > T_{EW} \simeq 160$ GeV, DM particles are produced only through Higgs annihilation via the contact diagram $HH \to SS$. After EWSB i.e $T < T_{EW}$, the Higgs boson acquires VEV(v) and expanding the contact operator $S^2 H^\dagger H$ around v as $H = v + h$, we have

$$\frac{\lambda_{hs}}{2}(h^2 + 2vh)S^2 + \dots . \tag{5.65}$$

The first term represents the usual four-point interaction, and the last term generates the 3-point vertex $h \to SS$, which not only accounts for the direct Higgs decay but also enables massive SM particles to annihilate into DM through s-channel Higgs exchange, S- mediated t- and u- channel (see Fig. 5.9). In addition, the universal gravitational production of DM will always be present, which can not be ignored. Thus, the Boltzmann equations associated with DM takes the following form

$$\dot{n_s} + 3Hn_s + \langle\sigma v\rangle(n_s^2 - n_{eq}^2) + \langle\Gamma_h\rangle n_h\left(1 - \frac{n_s^2}{n_{eq}^2}\right) - R_s^\phi = 0, \tag{5.66}$$

where $n_{eq}(n_h)$ is the equilibrium DM (Higgs) number density and $\langle\Gamma_h\rangle$ is the thermally average $h \to SS$ decay width which is

$$\langle\Gamma_h\rangle = \Gamma_{h\to SS}\frac{K_1\left(\frac{m_h}{T_{rad}}\right)}{K_2\left(\frac{m_h}{T_{rad}}\right)}, \left[\Gamma_{h\to SS} = \frac{\lambda_{hs}^2 v^2}{8\pi m_h}\sqrt{1 - \frac{4m_s^2}{m_h^2}}\right] \tag{5.67}$$

where K_n is the modified Bessel function of the n-th order and $m_h = 125$ GeV is the Higgs mass. $\langle\sigma v\rangle$ is the thermally averaged annihilation cross-section [93, 267, 270] of DM for all the relevant processes discussed before (see the Appendix C where we listed the cross-section for all the process). Depending on the strength of the portal coupling λ_{hs}, DM particle production S can either be thermally or non-thermally produced. For the well-known freeze-out mechanism for the WIMPs, the portal coupling typically has to be much larger compared to the freeze-in mechanism for FIMPs. The required value of the portal coupling λ_{hs} to achieve the observed DM abundance is plotted as a function of DM mass m_s in Fig. 5.10 and 5.11 for both

FIMPs (top plot) and WIMPs (bottom plot) type DM. The different color lines correspond to different $T_{\rm re}$. In the region above (below) the $\lambda_{\rm hs} - m_{\rm s}$ lines, the predicted relic density is overproduced (underproduced) for FIMP, and for WIMP, it is the opposite. we have further shown the DM parameter space $(\lambda_{\rm hs}, m_{\rm s})$ with current and future projected experimental bounds (shown in shaded regions). Note that for the FIMP-like production in Fig. 5.10, 5.11, the dashed part of the lines is excluded due to overproduction from the gravitational contribution. The upper bound of FIMP-like DM mass can be determined from the Eq. 5.63, 5.64 after satisfying observed DM abundance and can be decoded from the solid vertical lines for different $T_{\rm re}$ values from the upper two panels of the Fig. 5.8. As indeed can be seen, if one considers $w_\phi = 1/2$ and $M_3 = 5 \times 10^{11}$ GeV, for $T_{\rm re} = 4$ MeV, the upper bound of $m_{\rm s}$ is 10 (10^{-4}) GeV for neutrino dominating (neutrino heating) case. A similar bound can also be decoded for $w_\phi = 9/11$ from Fig. 5.11. For the FIMPs production, the viable mass range for the neutrino-dominating case turned out to be within $10^2\,{\rm eV} \leq m_s \leq 10\,{\rm GeV}$ for both $w_\phi = 1/2, 9/11$. Similarly, for the neutrino-heating case, the viable mass range turned out to be within $10^2\,{\rm eV} \leq m_{\rm s} \leq 10^{-3}(10^{-6})$ GeV for $w_\phi = 1/2(9/11)$. Note that any values lower than the bound of 100 eV FIMP mass will give the under abundance today due to extremely weak production, and this bound is independent of reheating histories [211].

We performed our analysis restricting the coupling parameter $\lambda_{\rm hs} \leq \sqrt{4\pi}$ [271] in the perturbative limit, and that automatically limits the possible DM mass range as illustrated in Fig. 5.10, 5.11. For WIMPs, the mass range turned out to be within $1 \leq m_s \leq 10^{5.6}(10^{7.7})\,{\rm GeV}$ for neutrino dominating with $w_\phi = 1/2(9/11)$ and within $1 \leq m_s \leq 10^4\,{\rm GeV}$ for both $w_\phi = 1/2, 9/11$ in the neutrino heating case, while keeping fixed value of the neutrino mass $M_3 = 5 \times 10^{11}\,{\rm GeV}$. The reheating phase can affect the DM relic if the DM production is completed before the end of reheating, which happens for $m_s \gtrsim 25\,T_{\rm re}$ [211, 258, 272] for WIMP like particles. For FIMPs, it is $m_s \geq T_{\rm re}$ if $T_{\rm re}$ is larger than $m_h/2$, but if $T_{\rm re}$ is lower than $m_h/2$, all DM particles can freeze in during reheating. When the DM production is completed before reheating ends, the DM relic suffers a high entropy dilution, which demands larger DM production to achieve the current DM relic. Thus, FIMPs (WIMPs) require larger (smaller) coupling to satisfy the observed DM abundance.

In Fig. 5.10 and 5.11, we projected the DM parameter space $(\lambda_{\rm hs}, m_{\rm s})$ in two distinct reheating backgrounds with reference to various current and future projected experimental constraints. In the context of Higgs portal coupling, the Higgs decaying into DM is severely constrained by the Large Hadron Collider (LHC) experiment. For instance, if the DM mass satisfies $m_s < m_h/2$, the decay $h \to SS$ is naturally kinematically allowed and contributes to the invisible Higgs decay width $\Gamma_{h\to SS}$. The corresponding invisible branching ratio $(BR_{\rm inv} = \Gamma_{h\to SS}/(\Gamma_h + \Gamma_{h\to SS}))$ is constrained by the LHC searches to be $BR_{\rm inv} \lesssim 0.11$ at 95% CL [273–275]. Using the visible Higgs decay with $\Gamma_h \simeq 4.07$ MeV [274, 276], the bound on the portal coupling for $m_s < m_h/2$ is $\lambda_{\rm hs} \lesssim 5 \times 10^{-3}$ as depicted in orange region ((labeled as "LHC") in the figures 5.10 and 5.11. Dark matter direct detection experiments, on the other hand, impose further constraints on the model parameters. The effective spin-independent cross-section (σ_{SI}) for elastic scattering between DM and nucleons is determined by the equation

$$\sigma_{\rm SI} = \frac{\lambda_{\rm hs}^2 \mu_N^2 f_N^2 m_N^2}{4\pi m_s^2 m_h^4}, \tag{5.68}$$

$\mu_N = m_N m_{\rm s}/(m_N + m_{\rm s})$ is the reduced mass of the DM-nucleon system with nucleon mass $m_N = 1\,{\rm GeV}$ and $f_N = 0.30$. Taking $\sigma_{\rm SI}$ from various direct-detection experiments such as DarkSide-50 (DS-50) [277], XENONnT [98], LUX-ZEPLIN (LZ) [99], XLZD [100] and we have projected this on $(\lambda_{\rm hs}, m_{\rm s})$ plane. As

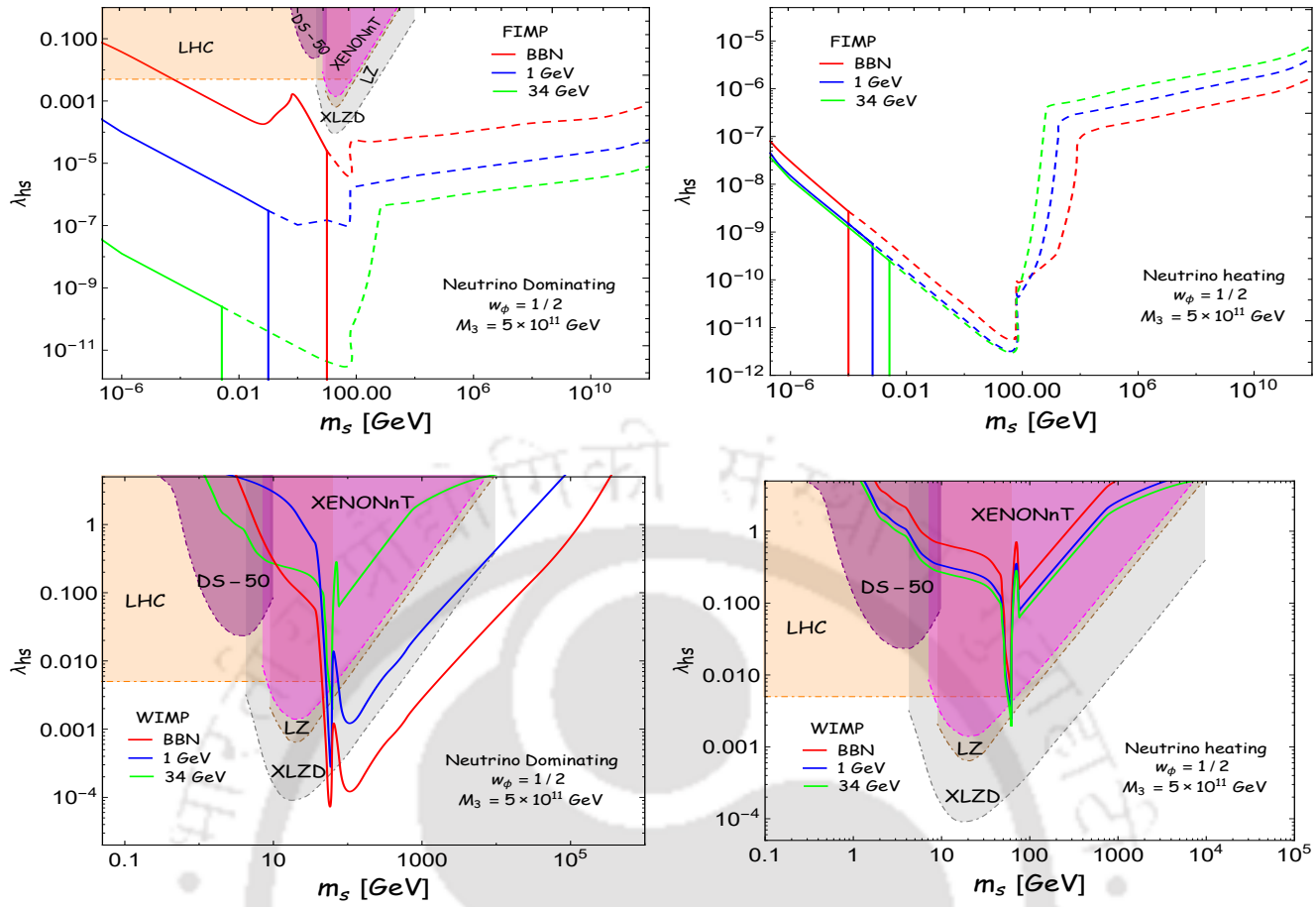

Figure 5.10: The predicted Higgs portal coupling $\lambda_{\rm hs}$ as a function of the DM mass $m_{\rm s}$ from the observed DM abundance for $w_\phi = 1/2$ for both neutrino dominating (left-column) and neutrino heating (right-column). The different color lines correspond to different reheating temperatures $T_{\rm re}$, where restricts $T_{\rm re}$ within the allowed ranges (minimum $T_{\rm re} = T_{\rm BBN}$ to maximum $T_{\rm re} = 34\ GeV$). For FIMP (top plot), the dashed part of the lines is excluded due to overproduction from the gravitational contribution. The different color-shaded regions represent the experimental constraints and projections.

indeed, one can see, some parts of the parameter space are already ruled out by the existing experimental bounds from DS-50 (purple-shaded), XENONnT (magenta-shaded), and LZ (brown-shaded). Reheating, however, provides wider allowed parameter space for WIMP-like dark matter, which may be possible to detect in the future in experiments like XLZD within the gray region. For the FIMP-like DM, however, due to extremely weak coupling, all the parameter spaces are allowed. Note that the indirect DM detection constraint in Higgs portal models is superseded by those from direct detection experiments and the LHC. Therefore, we do not consider them in our analysis.

5.2.2 QCD Axion as a DM

In the earlier section, we discussed both thermal and non-thermal DM production of DM via both gravitational and Higgs portal interaction. In this section, we discuss the impact of our new reheating scenario on another well-known non-thermal production DM, which is identified as QCD axions [42, 115, 278, 279]. We primarily focus on exploring the parameter space where axions are produced during

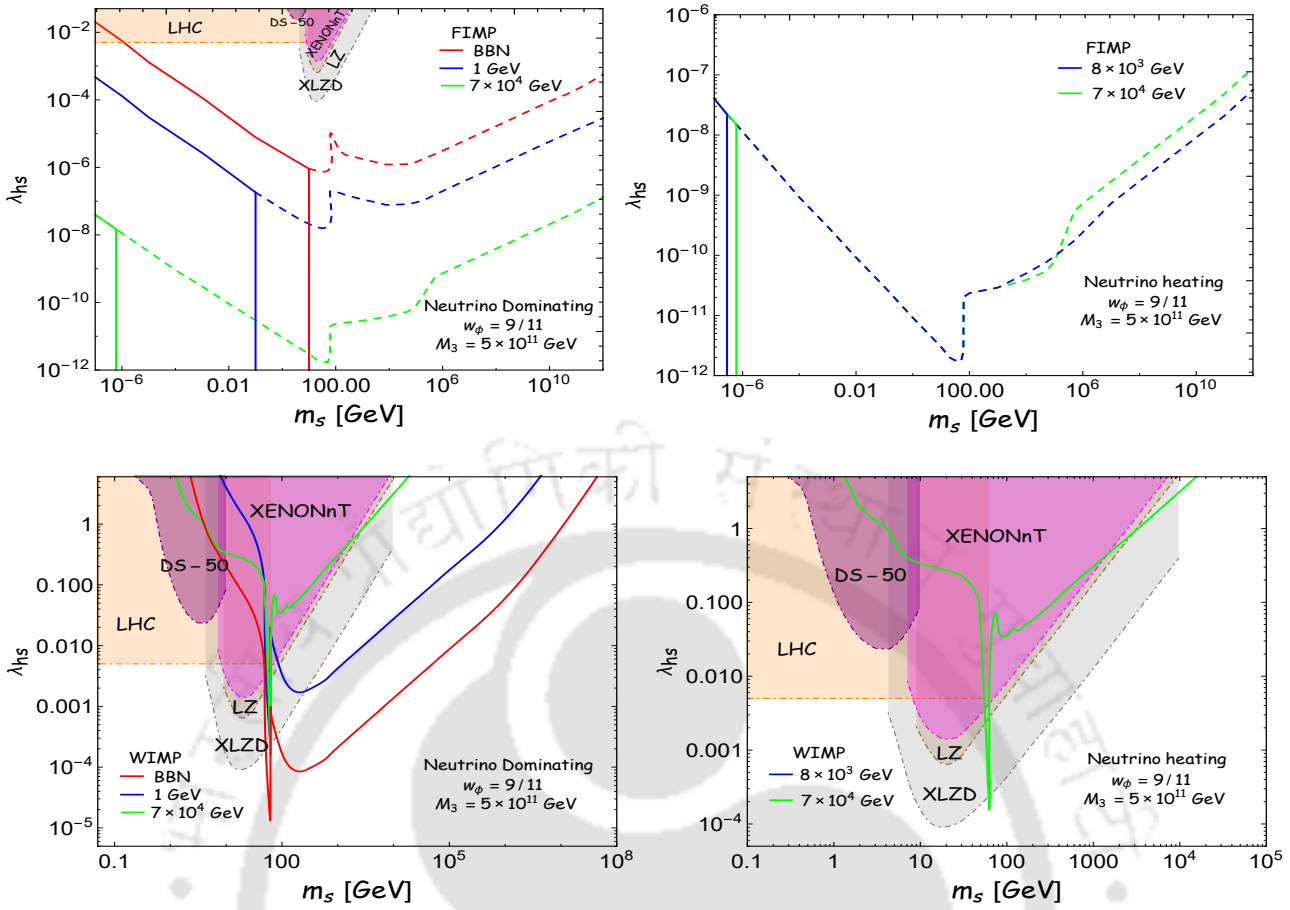

Figure 5.11: The predicted Higgs portal coupling $\lambda_{\rm hs}$ as a function of the DM mass $m_{\rm s}$ from the observed DM abundance for $w_\phi = 9/11$. The different color lines correspond to different reheating temperatures $T_{\rm re}$, where restricts $T_{\rm re}$ within the allowed ranges, minimum $T_{\rm re} = T_{\rm BBN}\,(T_{\rm re}^{\rm GW})$ to maximum $T_{\rm re} = 7\times10^4\ GeV$ for neutrino dominating (heating). Detailed descriptions are the same as Fig. 5.10.

reheating through the misalignment mechanism [116, 117], accounting for the entire observed abundance of dark matter. Before diving into this topic, let's briefly review the axion model, touching upon the key concepts and relevant parameters to be considered. The Lagrangian density for the axion field can be written as [280]

$$\mathscr{L}_{\mathfrak{a}} = \frac{1}{2}\partial^{\mu}\mathfrak{a}\,\partial_{\mu}\mathfrak{a} - \tilde{m}_{\mathfrak{a}}^2(T_{\rm rad})\left[1-\cos\left(\frac{\mathfrak{a}}{f_{\mathfrak{a}}}\right)\right], \tag{5.69}$$

where $\mathfrak{a}$ is the axion field, $f_{\mathfrak{a}}$ denotes the decay constant and $\tilde{m}_{\mathfrak{a}}(T)$ be the temperature-dependent mass of the axion, which can be written as [281–283]

$$\tilde{m}_{\mathfrak{a}}(T_{\rm rad}) \;=\; m_{\mathfrak{a}}\begin{cases}(T_{\rm qcd}/T_{\rm rad})^4 & \text{for}\ \ T_{\rm rad}\geq T_{\rm qcd}\,,\\ 1 & \text{for}\ \ T_{\rm rad}\leq T_{\rm qcd}\,,\end{cases} \tag{5.70}$$

where the QCD phase transition temperature $T_{\rm qcd} = 150$ MeV and $m_{\mathfrak{a}}$ identified as a zero-temperature axion mass which is given by

$$m_{\mathfrak{a}} \simeq 5.7\times10^{-6}\left(\frac{10^{12}\ {\rm GeV}}{f_{\mathfrak{a}}}\right){\rm eV} \tag{5.71}$$

Using the Lagrangian 5.69, one can find the following EoM for the zero-mode axion field,

$$\ddot{\theta} + 3H\dot{\theta} + \tilde{m}_{\mathfrak{a}}^2(T_{\rm rad})\sin\theta = 0\,, \tag{5.72}$$

where $\theta \equiv \mathfrak{a}/f_{\mathfrak{a}}$. When the temperature is significantly higher than the QCD transition temperature ($T \geq T_{\rm qcd}$), the Hubble parameter is much larger than the axion's mass. In this regime, the axion remains static, essentially frozen in place. Axions start to oscillate when the temperature $T_{\rm rad} \sim T_{\rm osc}$ defined by $3H(T_{\rm osc}) \equiv \tilde{m}_{\mathfrak{a}}(T_{\rm osc})$ [26]. Assuming a standard radiation Universe, the corresponding oscillation temperature can be calculated as

$$T_{\rm osc} \simeq \begin{cases} \left(\frac{1}{\pi}\sqrt{10/g_{\star r}(T_{\rm osc})}\, m_{\mathfrak{a}}\, M_{\rm p}\right)^{1/2} & T_{\rm osc} \leq T_{\rm qcd}\,, \\ \left(\frac{1}{\pi}\sqrt{10/g_{\star r}(T_{\rm osc})}\, m_{\mathfrak{a}}\, M_{\rm p} T_{\rm qcd}^4\right)^{1/6} & T_{\rm osc} \geq T_{\rm qcd} \end{cases} \tag{5.73}$$

Below $T_{\rm osc}$, the axion behaves like a non-relativistic particle. Under the assumption that both the axion number density and the Standard Model (SM) entropy are conserved, the energy density of these non-relativistic axions at present, denoted by $\rho_{\mathfrak{a}}$:

$$\rho_{\mathfrak{a}}(T_0) = \rho_{\mathfrak{a}}(T_{\rm osc}) \frac{m_{\mathfrak{a}}}{\tilde{m}_{\mathfrak{a}}(T_{\rm osc})} \frac{s(T_0)}{s(T_{\rm osc})}\,, \tag{5.74}$$

where $\rho_{\mathfrak{a}}(T_{\rm osc}) \simeq \frac{1}{2} m_{\mathfrak{a}}^2(T_{\rm osc}) f_{\mathfrak{a}}^2 \theta_i^2$, θ_i be the initial misalignment angle. Using Eq. 5.74, the axion abundance can be written as

$$\begin{aligned} \Omega_{\mathfrak{a}} h^2 &\equiv \frac{\rho_{\mathfrak{a}}(T_0)}{\rho_c/h^2} \\ &\simeq \left(\frac{\theta_i}{1.0}\right)^2 \begin{cases} 0.003 \left(\frac{m_{\mathfrak{a}}}{5.6\times10^{-6}\,\text{eV}}\right)^{-\frac{3}{2}} & m_{\mathfrak{a}} \leq m_{\mathfrak{a}}^{\rm qcd}\,, \\ 0.09 \left(\frac{m_{\mathfrak{a}}}{5.6\times10^{-6}\,\text{eV}}\right)^{-\frac{7}{6}} & m_{\mathfrak{a}} \geq m_{\mathfrak{a}}^{\rm qcd}\,, \end{cases} \end{aligned} \tag{5.75}$$

with critical energy density $\rho_c = 1.05 \times 10^{-5}\, h^2\, \text{GeV/cm}^3$, $s(T_0) \simeq 2.69 \times 10^3\, \text{cm}^{-3}$ is the entropy density at today and $m_{\mathfrak{a}}^{\rm qcd} \simeq 4.8 \times 10^{-11}$ eV. To match the observed DM abundance, the initial misalignment angle θ_i could be tuned. Assuming an initial misalignment angle $\theta_i \simeq 1.0$, the above equation indicates that an axion mass around $m_{\mathfrak{a}} \sim \mathcal{O}(10^{-5})$ eV and the decay constant $f_{\mathfrak{a}} \sim \mathcal{O}(10^{12})$ GeV is required to match the observed relic abundance.

The initial misalignment angle is deeply connected to the cosmological history of the axion. If the Peccei-Quinn (PQ) symmetry is broken before or during inflation (and not restored afterward), the initial angle θ_i will be uniform across the observable universe, and the angle is randomly chosen from the range $[-\pi, \pi]$. For $\theta_i \sim \mathcal{O}(1)$, $m_{\mathfrak{a}}$ should be in the range of μeV to avoid overproducing the DM abundance. Smaller axion masses (or equivalently, larger values of the decay constant $f_{\mathfrak{a}}$) become viable if small-tuned values of θ_i are considered. This is often referred to as the anthropic axion window [284, 285]. In this pre-inflationary scenario, large values of $f_{\mathfrak{a}}$ are constrained by isocurvature perturbations that impose $f_{\mathfrak{a}} \lesssim 10^{16}$ GeV [282]. On the other hand, if the PQ symmetry breaks after inflation, i.e, in a post-inflationary scenario, the initial value of θ_i may be different at different points in space, since we are interested in mode with zero momentum, therefore, we can safely use Eq. 5.72. When it breaks after the inflationary epoch, topological defects such as strings and domain walls could potentially contribute to axion production, affecting the mass range predictions [282, 286–288]. However, due to the persistent uncertainties regarding the extent of these contributions, our analysis has been limited to axion production through the misalignment mechanism. In this work, we primarily explore the impact of νGRe on the misalignment mechanism. Depending on the decay scale f_a, both pre-inflationary ($f_{\mathfrak{a}} \geq H_{\rm end}$) and post-inflationary ($f_{\mathfrak{a}} < H_{\rm end}$) scenarios can emerge.

Now, we consider the situation where axion oscillation begins during the reheating phase, i.e., $T_{\rm osc} > T_{\rm re}$. For such a case, the axion energy density at the present epoch is prescribed as [282, 289–293]

$$\rho_{\rm a}(T_0) = \rho_{\rm a}(T_{\rm osc}) \frac{m_{\rm a}}{\tilde{m}_{\rm a}(T_{\rm osc})} \frac{s(T_0)}{s(T_{\rm osc})} \frac{s'(T_{\rm osc})}{s'(T_{\rm re})}\,, \tag{5.76}$$

where the last factor takes into consideration the dilution of axion energy density due to entropy injection from the energy transfer between the inflaton/RHN and the thermal bath, and it can be written as

$$\frac{s'(T_{\rm osc})}{s'(T_{\rm re})} = \frac{g_{\star s}(T_{\rm osc})}{g_{\star s}(T_{\rm re})}\left(\frac{T_{\rm osc}}{T_{\rm re}}\right)^{\frac{3K-3}{K}} . \tag{5.77}$$

Here we utilize the relation $T = T_{\rm re}(a/a_{\rm re})^{-K}$, where $K = 1(3/8)$ for the neutrino heating (neutrino dominating) case. $T_{\rm osc}$ can be different for different background reheating histories. Now, we need to work out $T_{\rm osc}$, and it has two different possibilities:

Case-I :$\mathbf{T_{osc} > T_{qcd}}$

Let us suppose w is the EoS of the dominant component during reheating, so H can be written as

$$H(a) = H_{\rm re}\left(\frac{a}{a_{\rm re}}\right)^{-3(1+w)/2} \quad \left[H_{\rm re} = \frac{\pi}{3}\sqrt{\frac{g_{\star r}(T_{\rm re})}{10}}\frac{T_{\rm re}^2}{M_{\rm p}}\right] \tag{5.78}$$

Using the condition of oscillation, one can then obtain the expression for oscillation temperature as

$$T_{\rm osc} = T_{\rm re}\left(\frac{1}{\pi}\sqrt{\frac{10}{g_{\star r}(T_{\rm re})}}\frac{m_{\rm a} M_{\rm p} T_{\rm qcd}^4}{T_{\rm re}^6}\right)^{\frac{2K}{8K+3(1+w)}} . \tag{5.79}$$

Depending on the hierarchy between $T_{\rm re}$ and $T_{\rm osc}$, we have two possibilities: $T_{\rm re} < T_{\rm qcd} < T_{\rm osc}$, and that leads following inequality

$$T_{\rm qcd}^{\frac{3(1+w)}{3(1+w)-4K}}\left(\frac{1}{\pi}\sqrt{\frac{10}{g_{\star r}(T_{\rm re})}}m_{\rm a} M_{\rm p}\right)^{\frac{2K}{4K-3(1+w)}} < T_{\rm re} < T_{\rm qcd} . \tag{5.80}$$

Depending on the axion mass, we, therefore, obtained a range of reheating temperature $T_{\rm re}$ for which the oscillation temperature $T_{\rm osc}$ follows the condition $T_{\rm re} < T_{\rm qcd} < T_{osc}$. For example for neutrino dominating case ($w = 0, K = 3/8$) if we assume $m_{\rm a} = 10^{-7}$ eV, the reheating temperature should be constrained within $0.004 < T_{\rm re} < 0.15$ GeV. However, given the axion mass, the DM abundance fixes the $T_{\rm re} = 0.05, T_{\rm osc} = 0.3$ GeV and $T_{\rm re}$ is $< T_{\rm osc} = 0.3$ GeV as can be decoded from the Fig. 5.12. The second possibility $T_{\rm qcd} < T_{\rm re} < T_{\rm osc}$ leads to

$$T_{\rm qcd} < T_{\rm re} < \left(\frac{1}{\pi}\sqrt{\frac{10}{g_{\star r}(T_{\rm re})}}m_{\rm a} M_{\rm p}\right)^{1/6} . \tag{5.81}$$

Again, using the same combination of $(w, K, m_{\rm a})$, as above the bounds on reheating temperature turns out to be $0.15 < T_{\rm re} < 2$ GeV. However, to satisfy the DM abundance, $T_{\rm re}$ is required to be 0.05 GeV, which is smaller than $T_{\rm qcd} = 0.15$ GeV. As a result, this inequality is not satisfied for $m_{\rm a} = 10^{-7}$ eV.

Case-II :$\mathbf{T_{osc} < T_{qcd}}$

This is the case when the axion mass remains constant as expressed in Eq. 5.70. The analytical expressions of $T_{\rm osc}$ for this case turn out as,

$$T_{\rm osc} = T_{\rm re}\left(\frac{1}{\pi}\sqrt{\frac{10}{g_{\star r}(T_{\rm re})}}\frac{m_{\rm a} M_{\rm p}}{T_{\rm re}^2}\right)^{\frac{2K}{3(1+w)}} \tag{5.82}$$

Similar to the earlier case, using the self-consistency condition $T_{\rm re} < T_{\rm osc}$ and $T_{\rm re} < T_{\rm qcd}$, one can arrive at the following inequalities which the reheating temperature must satisfy,

$$\begin{aligned} T_{\rm re} &< T_{\rm qcd}^{\frac{3(1+w)}{3(1+w)-4K}}\left(\frac{1}{\pi}\sqrt{\frac{10}{g_{\star r}(T_{\rm re})}}m_{\rm a} M_{\rm p}\right)^{\frac{2K}{4K-3(1+w)}} , \\ T_{\rm re} &< \left(\frac{1}{\pi}\sqrt{\frac{10}{g_{\star r}(T_{\rm re})}}m_{\rm a} M_{\rm p}\right)^{1/2} . \end{aligned} \tag{5.83}$$

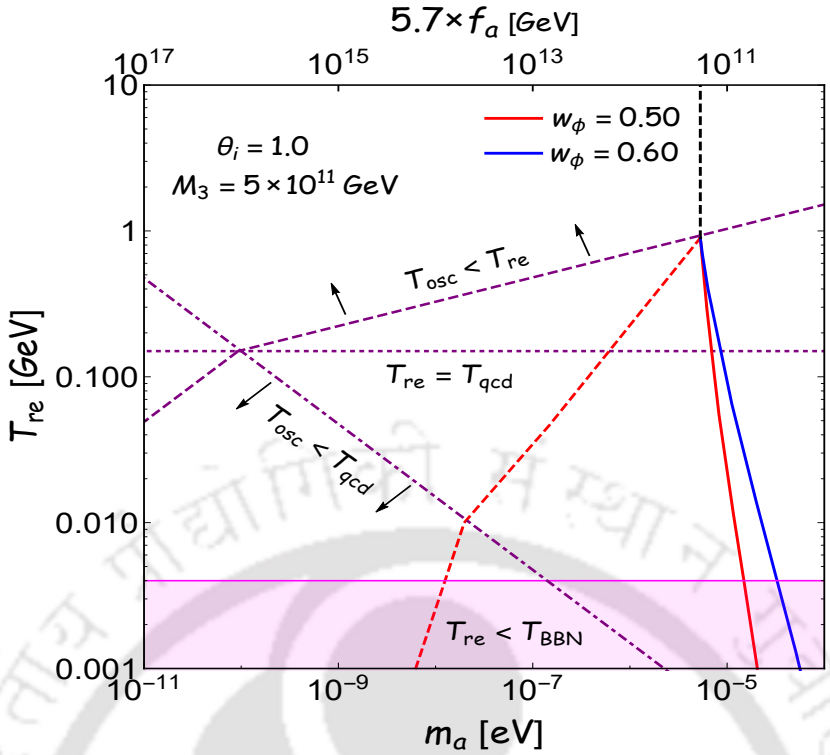

Figure 5.12: The required $T_{\rm re}$ as a function $m_{\rm a}$ or ($f_{\rm a}$) from the observed DM abundance for $w_\phi = 0.50$ (red) and $w_\phi = 0.60$ (blue) with $\theta_i = 1.0$. The purple dashed line corresponds to $T_{\rm re} = T_{\rm osc}$, which separates the parameter space into regions of $T_{\rm re} > T_{\rm osc}$ and $T_{\rm re} < T_{\rm osc}$, above and below it, respectively. The purple dot-dashed line corresponds to $T_{\rm osc} = T_{\rm qcd}$ (only for neutrino domination, i.e $w = 0.0$), which separates the parameter space into regions of $T_{\rm osc} > T_{\rm qcd}$ and $T_{\rm osc} < T_{\rm qcd}$, above and below it, respectively. The horizontal purple dotted line indicates $T_{\rm re} = T_{\rm qcd}$. The magenta-shaded regions are ruled out from $T_{\rm re} < T_{\rm BBN}$. The vertical black dashed line lies above the $T_{\rm osc} = T_{\rm re}$ lines, which indicates that oscillations occur after reheating, i.e., radiation-domination epoch and the corresponding axion mass $m_{\rm a} \simeq 6\times10^{-6}$ eV.

This is a constraint on $T_{\rm re}$ where the oscillation temperature $T_{\rm osc}$ will satisfy the both conditions above. Particular for neutrino dominating case ($w = 0, K = 3/8$) and assuming $m_{\rm a} = 1.5\times10^{-8}$ eV, observed DM abundance can be satisfied only for $T_{\rm re} = 6\times10^{-3}$ GeV and $T_{\rm osc} = 0.095$ GeV, and this satisfies the above conditions which gives $T_{\rm re} \leq 0.01$ GeV (see Fig. 5.12 for depiction).

Utilizing Eq. 5.80 and 5.82 in Eq. 5.76, we find the following expressions of the relic abundance,

$$\Omega_{\rm a}h^2 \simeq 7.9\times10^5\left(\frac{\theta_i}{1.0}\right)^2\frac{g_{\star s}(T_0)}{g_{\star s}(T_{\rm re})} \begin{cases} \left(\frac{T_{\rm qcd}}{T_{\rm re}}\right)^{\frac{3w-1}{1+w}}\left(\frac{m_{\rm a}}{93\,\text{peV}}\right)^{-\frac{2}{1+w}} & m_{\rm a} \leq m_{\rm a}^{qcd}, \\ \left(\frac{T_{\rm qcd}}{T_{\rm re}}\right)^{7+6K'}\left(\frac{m_{\rm a}}{93\,\text{peV}}\right)^{K'} & m_{\rm a} \geq m_{\rm a}^{qcd}, \end{cases} \tag{5.84}$$

where $K' = -2(4K+3)/(8K+3w+3)$.

We have summarized our results in Fig. 5.12, which is consistent with the current axion DM abundance for EoS, $w_\phi = 0.5$(red line) and $w_\phi = 0.6$(blue line). The dashed line represents the neutrino dominating, and the solid line corresponds to the neutrino heating scenario. The purple dashed line corresponds to $T_{\rm re} = T_{\rm osc}$, which separates the parameter space into regions of $T_{\rm re} > T_{\rm osc}$ and $T_{\rm re} < T_{\rm osc}$ above and below the constant line respectively. The purple dot-dashed line corresponds to $T_{\rm osc} = T_{\rm qcd}$ (only for neutrino

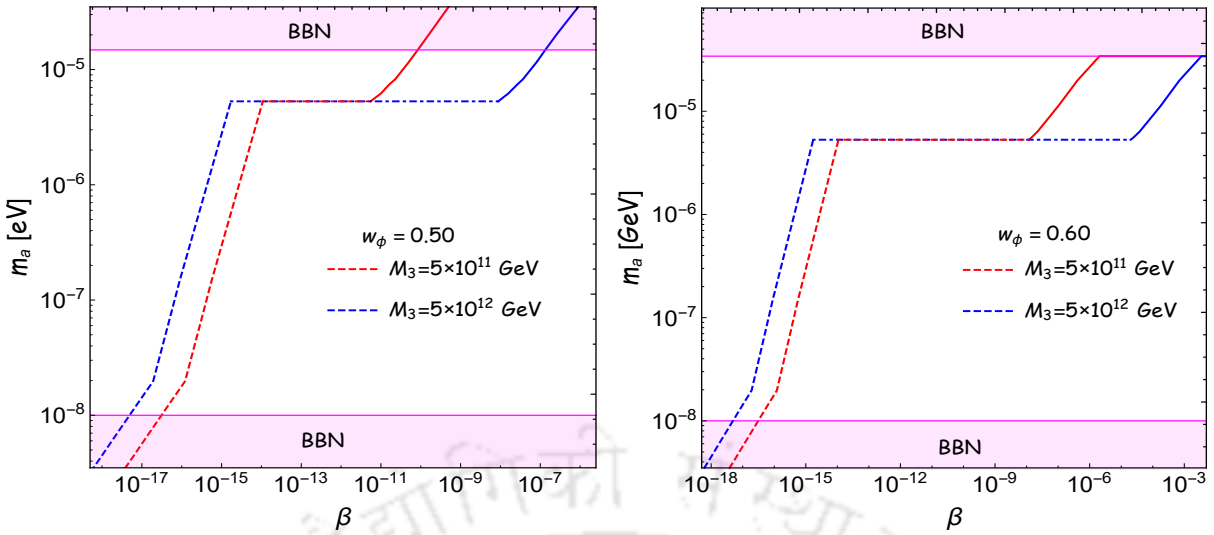

Figure 5.13: The required m_a as a function β from the observed DM abundance with $\theta_i = 1.0$ for two different choice $M_3 : \{5\times10^{11}, 2\times10^{13}\}$ GeV. The dashed (solid) line represents that misalignment occurs during the neutrino-dominating (heating) phase. The dot-dashed line represents that misalignment occurs after reheating, i.e., $T_{\rm osc} < T_{\rm re}$. The magenta-shaded regions correspond to the regions where the required $T_{\rm re}$ (for satisfying the current relic) is less $T_{\rm BBN}$.

domination, i.e $w = 0.0$), which separates the parameter space into regions of $T_{\rm osc} > T_{\rm qcd}$ and $T_{\rm osc} < T_{\rm qcd}$, above and below it, respectively. The horizontal purple dotted line indicates $T_{\rm re} = T_{\rm qcd}$. The magenta-shaded regions are ruled out from $T_{\rm re} < T_{\rm BBN}$. The vertical black dashed line lies above the $T_{\rm osc} = T_{\rm re}$ lines, which indicates that oscillations occur after reheating, i.e., radiation-domination epoch and the corresponding axion mass $m_a \simeq 6\times10^{-6}$ eV. Such tight bound has been shown to alter once the oscillation occurs during reheating [289] due to additional entropy injection. The present paper deals with the effect of gravitational neutrino reheating on the axion parameter space. The final axion abundance depends on the background EoS as well as the evolution of the bath temperature (if $T_{\rm osc} > T_{\rm qcd}$). For the neutrino dominating case, the oscillation occurs during the phase when neutrino dominates the background, i.e. $w = 0$, therefore $\Omega_a h^2$ turns out to be independent of inflaton EoS w_ϕ. For both $w_\phi = 0.50$ and 0.60, the prediction is represented by the red dashed line, and the axion mass should lie within $10^{-8}\,{\rm eV} \le m_a \le 6\times10^{-6}\,{\rm eV}$. On the other hand, for neutrino heating case, $\Omega_a h^2$ depends on the inflaton EoS w_ϕ, therefore the prediction of m_a or f_a is different for different w_ϕ, and are represented by solid blue and red lines in Fig. 5.12. The allowed mass window for $w_\phi = 0.5(0.6)$, however, is approximately within $6\times10^{-6} \lesssim m_a \lesssim 2(4)\times10^{-5}$ eV.

For both reheating scenarios, as $T_{\rm re}$ increases, each line converges toward the black dashed line. This is because, for larger $T_{\rm re}$, the misalignment tends to occur after reheating so that the reheating dynamics do not play any role. We found an upper limit of $T_{\rm re} = 1$ GeV for both reheating cases that ensures misalignment occurs during the reheating phase. We have further checked that for any values $w_\phi \ge 0.7$, the lower limit of $T_{\rm re}$ for the neutrino heating case always remains larger than 1 GeV, and hence mass bounds coincide with the black dashed line. Conversely, the neutrino reheating scenario turns out to be consistent with the axion DM scenario for $1/3 \le w_\phi \le 0.7$ and very low $T_{\rm re} \lesssim 1GeV$.

Given the axion abundance, the parameter space $(T_{\rm re}, m_a)$ is found to be nearly independent of M_3 values. As the neutrino coupling β along with its mass M_i control the value of $T_{\rm re}$, we found an interesting correlation among seemingly disconnected DM and neutrino parameters (m_a, β, M_3) as depicted in Fig. 5.13.

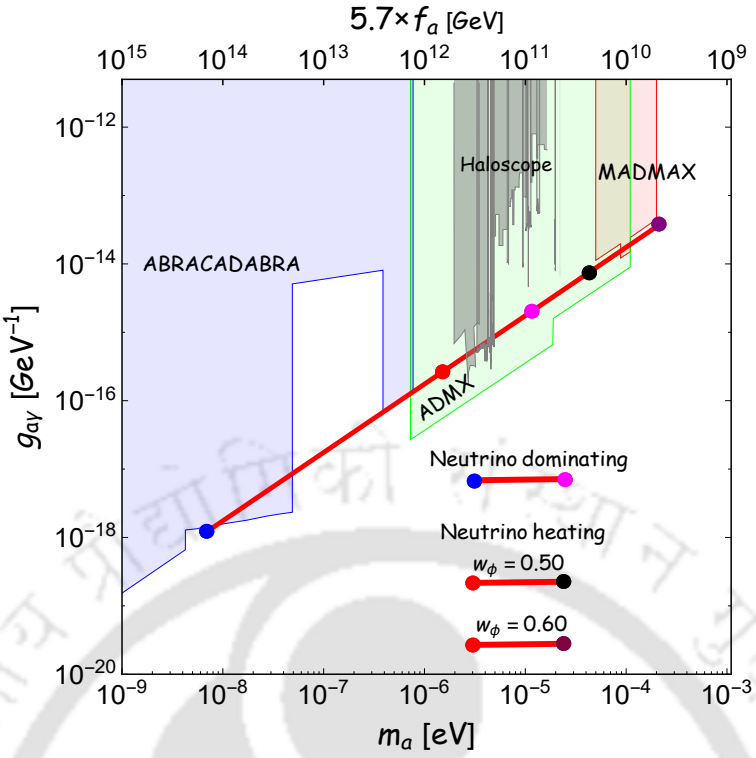

Figure 5.14: The red lines correspond to the required axion-photon coupling $g_{a\gamma}$ as a function of m_a from the observed DM relic abundance for QCD axion by considering the νGRe. The segments between blue and magenta, as well as red and purple dots, correspond to the parameter space for neutrino dominating and neutrino heating cases, respectively. The gray shaded areas correspond to excluded parameter space from cosmology, astrophysics, and laboratory experiments, and different color-shaded areas show prospects in sensitivity from various experiments.

The slanted lines correspond to neutrino dominating (dashed) and neutrino heating (solid) cases for two sample values of M_3. β independent horizontal line corresponding to $m_a \simeq 6 \times 10^{-6}$ eV which is the prediction of standard misalignment. To this end, we again reiterate that the new axion mass windows due to reheating emerge for the cases only when the reheating temperature is low $\lesssim 1$ GeV.

5.2.3 Experimental constraints on axion parameter space

In the previous section, we analyzed the relic-satisfied parameter space of axion characterized by its mass m_a and the decay constant f_a. However, such a parameter space can be further constrained from the present and proposed axion search facilities. The interaction between axions and two photons is one of the most commonly used channels in experiments and observations to detect the signature of axions. The interaction Lagrangian has taken the following form [116, 117]

$$\mathscr{L}_{a\gamma} = -\frac{1}{4} g_{a\gamma} a F_{\mu\nu} \tilde{F}^{\mu\nu}, \tag{5.85}$$

where the coupling constant $g_{a\gamma}$ is related to the decay constant f_a as [294]

$$\begin{aligned} g_{a\gamma} &\simeq 10^{-13}\,\text{GeV}^{-1} \left(\frac{10^{10}\,\text{GeV}}{f_a}\right) \\ &\simeq 1.8 \times 10^{-15}\,\text{GeV}^{-1} \left(\frac{m_a}{10^{-5}\,\text{eV}}\right) \end{aligned} \tag{5.86}$$

In Fig. 5.14, we show the parameter space $(g_{a\gamma}, m_a)$ or $(g_{a\gamma}, f_a)$ for QCD axion with current and future experimental limit. The red line corresponds to the required axion-photon coupling $g_{a\gamma}$ as a function of m_a from the observed DM relic abundance for QCD axion by considering the effects of νGRe. For finding the parameter space, we have taken $w_\phi = 0.50$ and 0.60 with initial angle in the range $\theta_i \in (1/2, \pi/\sqrt{3})$. The segments between blue and magenta, as well as red and purple dots, correspond to the parameter space for neutrino dominating and neutrino heating cases, respectively. So, viable parameter space for $w_\phi = 0.50(0.60)$ is $7 \times 10^{-9} \leq m_a \leq 5 \times 10^{-5}(3 \times 10^{-4})$eV. Further, some portions of the viable parameter space are already constrained by the Haloscope experiments like ADMX [295–299] and CAPP [300–302], as shown by gray-shaded regions. We have also shown the parameter space with future projections, such as MADMAX [303], which is shown by red-shaded, ADMX [304] (green), and broadband axion-search experiment ABRACADABRA [305] (blue). All these experiments are capable of constraining the parameter space in further.

5.3 Summary

After the inflation, the occurrence of reheating is still an unsettled issue. Primarily because observing such phenomena through cosmological experiments, even in the near future, is believed to be difficult. After realizing few existing indirect observational constraints such as BBN temperature ($T_{\rm BBN} \sim 4$ MeV) [50, 51], effective number relativistic degrees of freedom $\Delta N_{\rm eff} \sim 2.99 \pm 0.34$ at 95% CL [31, 198], dark matter abundance ($\Omega_{\rm DM} h^2 \sim 0.12$) [31], even the CMB anisotropy parametrized by scalar spectral index $n_{\rm s} = 0.9649 \pm 0.0042$ at 68% CL [31], are shown to have underlying connection with the reheating dynamics, a spate of research activity has emerged in the recent time [15–17]. Subsequently, several attempts have been made to understand this phase from the more fundamental point of view, invoking as much minimal parameters/ingredients as possible [13, 14]. Purely gravitational interaction can lead to successful reheating is one such interesting example that has recently gained significant interest in the context of gravitational reheating [184], minimal preheating [306], reheating through non-minimal gravitational coupling [156].

In this chapter, we first discussed in great detail this neutrino reheating scenario. Thanks to the well known Type-I seesaw model which is the most minimal extension of the standard model to simultaneously explain the active neutrino mass $\Delta m_{12} \sim 0.05$eV and baryon asymmetry of the universe $Y_{\rm B} \sim 10^{-10}$. The intriguing feature of this Type-I seesaw model is that apart from accounting for all the aforementioned observables, it can further reheat the universe with the following two distinct possibilities;

a) Neutrino dominating: $\beta \leq \beta^c_\nu$ :: For this case, neutrino appears to be dominating at some intermediate scale factor a_ν during reheating. After this, it is the neutrino decay that naturally dominates the radiation production and sets the reheating temperature ($T_{\rm re}$), and is found to be completely insensitive to the inflation parameter $T_{\rm re} \propto \beta M_3^{1/2}$ (see dashed lines in Fig. 5.4). $T_{\rm re}$ is observed to reach its maximum at $\beta = \beta^c_\nu$. For $w_\phi = 9/11$, the maximum temperature turned out to be as high as 10^6 GeV, which is much larger than the temperature predicted in the pure GRe case $T_{\rm re} \sim 10^3$ GeV. We found β could be as low as 10^{-18} for minimum possible reheating temperature $T_{\rm BBN}$. Because of the $\nu^3_{\rm R}$ behaving as matter, the PGW spectrum acquires a spectral break at $k = k_\nu$, where neutrino domination starts during the reheating phase. For $k_{\rm re} < k < k_\nu$, the primordial GW spectrum behaves as $\Omega^k_{\rm GW} h^2 \propto k^{-2}$, and for $k_{\rm end} < k < k_\nu$, the spectrum behaves as $\Omega^k_{\rm GW} h^2 \propto k^{-\frac{(2-6w_\phi)}{(1+3w_\phi)}}$ which is as expected inflaton parameter dependent.

b) Neutrino heating:$\beta^c_\nu \leq \beta \leq \beta^c_\phi$::. If we further increase $\beta > \beta^c_\nu$, even though neutrinos fail to dominate over inflaton, they still control the reheating through their decay. The reheating temperature is shown to behave as $T_{\rm re} \propto \beta^{\frac{-1}{3w_\phi-1}} M_3^{\frac{7+9w_\phi}{4(3w_\phi-1)}}$ acquires a negative power in β, and hence $T_{\rm re}$ decrease with β unlike the previous case. For $w_\phi \leq 0.60$, the maximum allowed value of β will be determined from the BBN bound of $T_{\rm re} \simeq 4$MeV, again for $w_\phi > 0.60$, the maximum value of β is β^c_{GW}.

νGRe can Successfully reheat the universe if the inflaton EoS w_ϕ lie within $1/3 \lesssim w_\phi \lesssim 1.0$ and $\nu^3_{\rm R}$ mass $10^{10} \lesssim M_3 \lesssim 2\times 10^{13}$ GeV. As a byproduct, we also obtain the non-vanishing lowest active neutrino mass due to non-zero β, requiring to have successful reheating. However, if one takes into account the right amount of baryon asymmetry at the present day, the reheating equation of state is further constrained to be $0.5 \lesssim w_\phi \lesssim 1.0$, and the corresponding viable mass range of $\nu^1_{\rm R}$ is $8\times 10^{11} \lesssim M_1 \lesssim 2\times 10^{13}$ GeV.

The effect of non-standard cosmology has gained significant interest in DM phenomenology. In the second part of this chapter, we explore the implications of νGRe for the production of DM. Firstly, we have considered a real scalar singlet DM, which interacts with the SM via the Higgs portal interaction and also with the inflaton through universal gravitational interaction. Depending on the strength of the portal coupling λ, the production of the DM particle S can occur either through thermal or non-thermal processes. For the well-known freeze-out mechanism for the weakly interacting massive particle(WIMP), the portal coupling typically has to be much larger compared to the freeze-in mechanism for feebly interacting massive particles (FIMP). The required value of the portal coupling $\lambda_{\rm hs}$ to achieve the observed DM abundance is plotted as a function of DM mass $m_{\rm s}$ in Fig. 5.10 and 5.11 for both FIMP (top plot) and WIMP (bottom plot) type DM. For the FIMPs production, the viable mass range turned out to be within $10^2\,{\rm eV} \leq m_s \leq 10\,{\rm GeV}$. Note that any values lower than the bound of 100 eV FIMP mass will give the under abundance today [211] due to extremely weak production. On the other, mass > 10 GeV, gives over-abundance due to strong gravitational production. Additionally the perturbativity conditions restrict the mass of the WIMP DM, within $1 \leq m_s \leq 4\times 10^5$ GeV for $w_\phi = 1/2$ and $1 \leq m_s \leq 5\times 10^7$ GeV for $w_\phi = 9/11$. Finally, we have shown the impact of direct detection experiments on our parameter space. Reheating, however, provides wider allowed parameter space for WIMP-like DM which may be possible to detect in the future in experiments like XLZD. For the FIMP-like DM, however, due to extremely weak coupling, all the parameter spaces are allowed.

Finally we investigated the impact of νGRe on the production of QCD axions as a candidate of DM via the vacuum misalignment mechanism. We analyzed the relic-satisfied parameter space (see Fig. 5.12) of axion characterized by its mass $m_{\rm a}$ and the decay constant $f_{\rm a}$. Furthermore, we analyzed the experimental constraints by comparing this parameter space with both current and upcoming axion experiments (see Fig. 5.14). We found that the current ADMX and CAPP experiments are capable of excluding small portions of the expanded parameter space, particularly within the mass range $2\times 10^{-6} \leq m_{\rm a} \leq 5\times 10^{-6}$ eV. The remaining regions of the parameter space could be explored in future experiments.

Addenda

A Construction of Yukawa coupling $y_{\alpha i}$ using Casas-Ibarra Parametrization

When the neutral component of the SM Higgs doublet acquires a VEV leading to the spontaneous breaking of the SM gauge symmetry, neutrinos in the SM acquire a Dirac mass matrix $m_D = y\,v$. Where $v = 174$ GeV is the vacuum expectation value of the SM Higgs. Using this Dirac mass m_D together with the bare Majorana mass M, the light neutrino mass matrix can be written as $m_\nu \simeq m_D^T M^{-1} m_D$. The left-handed neutrino masses are obtained by diagonalizing the mass matrix m_ν with the Pontecorvo-Maki-Nakagawa-Sakata (PMNS) unitary matrix U [307] as $m_\nu^d = \mathrm{diag}(m_1, m_2, m_3) = U^T m_\nu U$. By using this well-known Casas-Ibara (CI) parametrization [308], Yukawa coupling y can be written as

$$y = \frac{1}{v} U \sqrt{m_\nu^d}\, \mathbb{R}^T \sqrt{M}. \tag{5.87}$$

We choose the orthogonal matrix $\mathbb{R}$ as

$$\mathbb{R} = \begin{pmatrix} 0 & \cos z & \sin z \\ 0 & -\sin z & \cos z \\ 1 & 0 & 0 \end{pmatrix}, \tag{5.88}$$

where $z = a + ib$ is a complex angle. The diagonal light neutrino mass matrix m_ν^d is calculable using the best-fit values of solar and atmospheric mass obtained from the latest neutrino oscillation data [309]. The elements of Yukawa coupling matrix y for a specific value of z can be obtained for different choices of the heavy neutrino masses. For example, with $M_1 = 3 \times 10^{12}$ GeV,$M_2 = 5 \times 10^{13}$ GeV, $\{a, b\} = \{2.5, 1.4\}$, using normal hierarchy, $m_3 = 0.05$ eV,$m_2 = 0.008$ eV and taking M_3, m_1 are the free parameter, we obtain

$$y = \begin{pmatrix} -0.043 - 0.013\,i & -0.043 + 0.130\,i & 0.821\sqrt{m_1 M_3}/v \\ 0.032 - 0.087\,i & -0.315 - 0.0889\,i & (0.301 - 0.062\,i)\sqrt{m_1 M_3}/v \\ 0.079 - 0.044\,i & -0.161 - 0.220\,i & (0.477 - 0.055\,i)\sqrt{m_1 M_3}/v \end{pmatrix}. \tag{5.89}$$

In our present scenario, we need the third RHN to be the long-lived one, and its decay width should be very small. By tuning the lightest active neutrino mass (m_1), we can tune the ν_R^3 decay width as $y_{i3} \propto \sqrt{m_1 M_3}/v$. To find a small but non-vanishing decay width, the lightest active neutrino mass should be non-vanishing. For example, taking $M_3 = 5 \times 10^{11}$ GeV, $m_1 = 2.5 \times 10^{-17}$ eV, which produces the desired CP asymmetry, the coupling matrix assumes,

$$y^\dagger y = \begin{pmatrix} 0.019 & -0.0051 + 0.0616i & 6.46 \times 10^{-37} + 4.84 \times 10^{-27} i \\ -0.005 - 0.061i & 0.201 & -1.292 \times 10^{-26} i \\ 6.462 \times 10^{-27} - 4.846 \times 10^{-27} i & 1.292 \times 10^{-26} i & 4.131 \times 10^{-19} \end{pmatrix} \tag{5.90}$$

Note that the component of $(y^\dagger y)_{33}$, which is identified with β parameter, is very small compared to $(y^\dagger y)_{11}, (y^\dagger y)_{22}$. Therefore, the decay width of the third RHN is suppressed compared to the other two RHNs, and this turned out to be crucial for successful neutrino reheating.

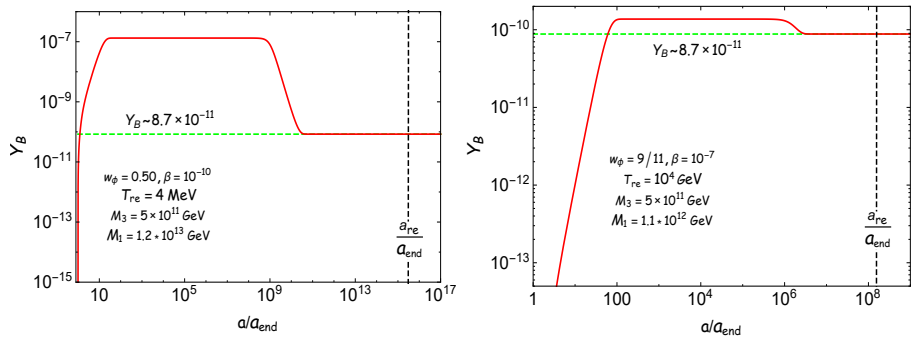

Figure 5.15: The evolution of the baryon asymmetry yield $Y_{\rm B} = n_{\rm B\text{-}L}/s$ as a function of the scale factor $a/a_{\rm end}$. $a_{\rm re}/a_{\rm end}$ corresponds to the endpoint of reheating.

Similarly, we can construct the Yukawa coupling y using the inverted hierarchy (IH). The primary distinction lies in the choice of the orthogonal matrix, where the form of orthogonal matrix $\mathbb{R}$ is,

$$\mathbb{R} = \begin{pmatrix} \cos z & \sin z & 0 \\ -\sin z & \cos z & 0 \\ 0 & 0 & 1 \end{pmatrix}. \tag{5.91}$$

For IH, the neutrino masses are given by $m_2 = 0.05$ eV, $m_1 = 0.0497$ eV, and m_3 is treated as a free parameter. Using these values, we obtain the following Yukawa coupling,

$$y = \begin{pmatrix} -0.044 - 0.112\,i & -0.402 + 0.125\,i & (0.111 - 0.100\,i)\sqrt{m_3 M_3}/v \\ 0.073 - 0.032\,i & -0.120 - 0.199\,i & 0.738\sqrt{m_3 M_3}/v \\ -0.107 + 0.024\,i & 0.086 + 0.300\,i & 0.657\sqrt{m_3 M_3}/v \end{pmatrix}. \tag{5.92}$$

Therefore, for IH, $y_{\rm i3} \propto \sqrt{m_3 M_3}/v$ i.e, $\beta^2 \propto m_3$.
To see the evolution of baryon asymmetry yield $Y_{\rm B} = n_{\rm B\text{-}L}/s$ with time, we need to solve the number density of B-L. We can calculate the $B-L$ number density (n_{B-L}) by solving the following Boltzmann equation together with Eqs. 5.2,

$$\dot{n}_{B-L} + 3H n_{B-L} = |\epsilon_{\Delta L}|\,\Gamma_1\, n_1 \tag{5.93}$$

By numerically solving Eqs. 5.2 and 5.93, we present in Fig. 5.15 the evolution of the baryon asymmetry $Y_{\rm B}$ as a function of the scale factor for $w_\phi = 0.5\,(9/11)$, with $T_{\rm re} = 0.004\,(10^4)$ GeV and $M_3 = 5 \times 10^{11}$ GeV. The required value of M_1 to reproduce the observed baryon asymmetry is found to be $1.2 \times 10^{13}\,(1.1 \times 10^{12})$ GeV. Since the decay of $\nu_{\rm R}^1$ can generate the baryon asymmetry of the universe via leptogenesis, now, we have a complete picture including neutrino mass, baryon asymmetry, and reheating.

B RG Effects in Neutrino Yukawa coupling

The one-loop renormalization group evolution (RGE) equations of the relevant parameters associated with the Seesaw-I model are :
The gauge couplings:

$$16\pi^2 \frac{dg_1}{d\ln\mu} = \frac{41}{10} g_i^3,\ 16\pi^2 \frac{dg_2}{d\ln\mu} = -\frac{19}{6} g_2^3,\ 16\pi^2 \frac{dg_3}{d\ln\mu} = -7\, g_i^3 \tag{5.94}$$

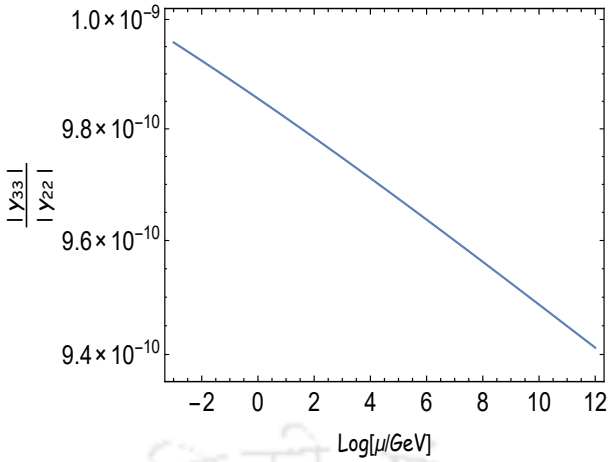

Figure 5.16: Evolution of $\frac{|y_{33}|}{|y_{22}|}$ with energy scale $\mu = T_{\rm rad}^{\rm max}$ to $\mu = T_{\rm BBN} = 4$ MeV.

The Higgs quadratic and quartic couplings:

$$16\pi^2 \frac{d\mu_H^2}{d\ln\mu} = \left(-\frac{9}{10}g_1^2 - \frac{9}{2}g_2^2 + 12\lambda + 2T\right)\mu_H^2$$

$$16\pi^2 \frac{d\lambda_H}{d\ln\mu} = \left(-\frac{9}{5}g_1^2 - 9g_2^2 + 24\lambda_H + 4T\right)\lambda_H + \frac{27}{200}g_1^4 + \frac{9}{20}g_1^2 g_2^2 + \frac{9}{8}g_2^4 - 2T1$$

The Yukawa couplings:

$$16\pi^2 \frac{dY_u}{d\ln\mu} = \left(-\frac{17}{20}g_1^2 - \frac{9}{4}g_2^2 - 8g_3^2 + T\right)Y_u + \frac{3}{2}(Y_u Y_u^\dagger Y_u) - \frac{3}{2}(Y_u Y_d^\dagger Y_d)$$

$$16\pi^2 \frac{dY_d}{d\ln\mu} = -\frac{1}{4}\left(g_1^2 + 9g_2^2 + 32g_3^2 - 4T\right)Y_d + \frac{3}{2}(Y_d Y_d^\dagger Y_d) - \frac{3}{2}(Y_d Y_u^\dagger Y_u)$$

$$16\pi^2 \frac{dY_e}{d\ln\mu} = \left(-\frac{9}{4}g_1^2 - \frac{9}{4}g_2^2 + T\right)Y_e + \frac{3}{2}(Y_e Y_e^\dagger Y_e) - \frac{3}{2}(Y_e Y_\nu^\dagger Y_\nu)$$

$$16\pi^2 \frac{dY_\nu}{d\ln\mu} = \left(-\frac{9}{20}g_1^2 - \frac{9}{4}g_2^2 + T\right)Y_\nu + \frac{3}{2}(Y_\nu Y_\nu^\dagger Y_\nu) - \frac{3}{2}(Y_\nu Y_e^\dagger Y_e)$$

The Majorana mass:

$$16\pi^2 \frac{dM_\nu}{d\ln\mu} = 2M_\nu (Y_\nu Y_\nu^\dagger)^T + Y_\nu Y_\nu^\dagger M_\nu$$

where $T = \mathrm{Tr}\left(3Y_d Y_d^\dagger + 3Y_u Y_u^\dagger + Y_e Y_e^\dagger + Y_\nu Y_\nu^\dagger\right)$ and $T1 = \mathrm{Tr}\left(3(Y_d Y_d^\dagger)^2 + 3(Y_u Y_u^\dagger)^2 + (Y_e Y_e^\dagger)^2 + (Y_\nu Y_\nu^\dagger)^2\right)$ SARAH provides with a numerical solution to the derived renormalization group equations. In the figure 5.16, we have shown ratio of running of $|y_{33}|$ and $|y_{22}|$ with the energy scale μ. Initially, $\frac{|y_{33}|}{|y_{22}|} = 9.4 \times 10^{-10}$, after taking running, $\frac{|y_{33}|}{|y_{22}|} \simeq 9.9 \times 10^{-10}$ at $\mu = 4$ MeV.

C Listed the DM annihilation cross-section

The thermally averaged cross-section $\langle\sigma v\rangle$ for any 2-2 annihilation process can be calculated using the standard formula derived in Eq. 2.172,

$$\langle\sigma v\rangle = \frac{g_s^2}{\left(n_X^{\rm eq}\right)^2}\frac{T_{\rm rad}}{32\pi^4}\int_{4m_s^2}^{\infty}\sqrt{q}\,(q-4m_s^2)\sigma(q)K_1\left(\frac{\sqrt{q}}{T_{\rm rad}}\right)dq\,, \tag{5.95}$$

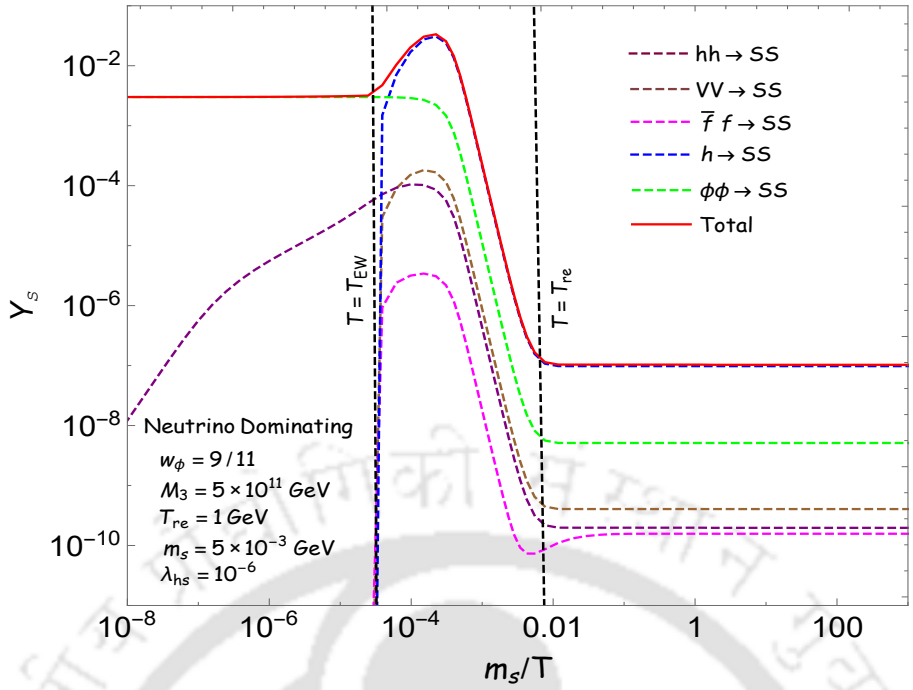

Figure 5.17: Evolution of DM yield (for freeze-in) as a function of inverse temperature with individual contributions (explained in inset) from different production processes; final yield (solid red line) corresponds to the correct DM relic.

where $g_s = 1$ is the internal degrees of freedom for the scalar dark matter. $\sigma(q)$ and q are the annihilation cross section and the squared center-of-mass energy of the DM particle respectively. The annihilation cross-section $\sigma(q)$ for different annihilation channels have the following forms:

$$\sigma_{SS\to\bar{f}f} = \sum_f n_f \frac{\lambda_{hs}^2 m_f^2}{2\pi q} \frac{\sqrt{q-4m_f^2}}{(q-m_h^2)^2+\Gamma_h^2 m_h^2} \sqrt{\frac{q-4m_f^2}{q-4m_s^2}}, \tag{5.96}$$

$$\sigma_{SS\to VV} = \sum_V n_V \frac{\lambda_{hs}^2}{4\pi s} \frac{(q^2-4q\,m_V^2+12m_V^4)}{(q-m_h^2)^2+\Gamma_h^2 m_h^2} \sqrt{\frac{q-4m_V^2}{q-4m_s^2}}, \tag{5.97}$$

$$\sigma_{SS\to hh} = \frac{\lambda_{hs}^2}{8\pi q} \sqrt{\frac{q-4m_f^2}{q-4m_s^2}} \left[\zeta^2 - \frac{16\zeta\lambda v^2}{s-2m_h^2}\frac{1}{2\xi}\log\left(\frac{1+\xi}{1-\xi}\right) + \frac{32\lambda^2 v^4}{(s-2m_h^2)^2}\left(\frac{1}{1-\xi^2}+\frac{1}{2\xi}\log\left(\frac{1+\xi}{1-\xi}\right)\right)\right], \tag{5.98}$$

where $\zeta = \left(\frac{q+2m_h^2}{q-m_h^2}\right), \xi = \frac{\sqrt{(q-4m_s^2)(q-4m_h^2)}}{q-2m_h^2}$. $(\bar{f})f$ denotes SM (anti-) fermions and $n_f = 3$ for quarks and $n_f = 1$ for leptons. $V = W^\pm, Z$ denotes the SM gauge bosons and $n_W = 1, n_Z = 1/2$.

To facilitate our understanding further into the DM evolution and identify the contribution of different production channels, in Fig. 5.17, we have shown the evolution of total DM yield $Y_s = n_s/s$ for the freeze-in mechanism as a function of inverse temperature represented by solid red line. Along with this we further plotted individual contributions from different production processes in dotted lines. The total contribution, as denoted by the solid red line, reaches an asymptotic value, resulting the correct relic abundance. Before EWSB, the DM is produced only through Higgs annihilation and gravitational interaction. If the DM mass is chosen to be below the Higgs mass, as for the case in the figure, after EWSB, the DM can also be produced from the Higgs decay $h \to SS$ and the other scattering channels namely $VV \to SS, \bar{f}f \to SS$. However, Higgs decay is the dominant production channel as expected and indeed can be seen from the

figure. Since $T_{\rm re} < m_{\rm h}/2$, most of the DM is produced during reheating, and the yield Y_s suffers from a high entropy dilution if considering the individual decay channel.

CHAPTER 6

Conclusions and Outlook

6.1 Conclusions

The reheating era, often regarded as the least understood phase in cosmic history, plays an essential role in shaping both cosmology and particle physics. The expansion history during reheating significantly influences the relation between observed CMB modes and the physical scales at the time of inflation. These effects can, in turn, modify the predictions of inflationary models for CMB observables. Again, the expansion and thermal histories of reheating also affect other key cosmological phenomena, such as DM production and matter-antimatter asymmetry production. Therefore, a detailed study of both the expansion history and thermal history is important during reheating. With these two things in mind, in this thesis, we extensively analyzed the dynamics of reheating after inflation and explored its potential implications on the inflaton and DM phenomenology. The following is a summary of the key contributions and findings of this work.

We began this thesis with a brief introduction and motivation. Then, in Chapter 2, we reviewed the foundations of FLRW cosmology and discussed the cosmological challenges that it faces, including the horizon problem, flatness problem, and monopole problem. These puzzles highlight the need for new physics in the very early universe, leading to the introduction of inflation, a period of exponential expansion that resolves many of these issues by smoothing the universe and setting the initial conditions for the standard Big Bang model. We then introduce the mechanism of reheating after inflation, which is at the core of the work pursued during this thesis. Then, we discussed some observational aspects of the early universe, such as scalar curvature perturbation, gravitational waves, DM, and Baryogenesis.

Starting from Chapter 3, we presented the core works of this thesis. In Chapter 3, we extensively analyzed the dynamics of reheating after inflation and looked into its possible implications on the inflaton and DM phenomenology. We studied reheating through various possible channels of inflaton going into massless bosons (bosonic reheating) and fermions (fermionic reheating) via non-gravitational and gravity-mediated decay processes. We further included the finite temperature effect on the decay process. This finite temperature effect strongly depends on the spin of the decay products and the inflaton EoS, which further depends on the shape of the inflaton potential near the minimum. In this chapter, we considered a typical α-attractor E-inflationary model. Since we have considered the explicit coupling-dependent interaction alongside the universal minimal gravitational interaction, we derived the inflaton's coupling versus EoS parameter space for successful reheating. As part of this, we performed a detailed comparative study to delineate the regions where each interaction channel becomes dominant, providing a clearer

understanding of their respective roles in the reheating dynamics. In particular, the universal gravitational decay of the inflaton has been observed to play a crucial role in the reheating process over a wide range of parameter spaces. Furthermore, we establish the intriguing connection between the inflationary and reheating parameters with the CMB power spectrum that can have profound implications in building up a unified model of inflation, reheating, and DM. In the second part of this chapter, we studied the effect of reheating on DM production. We analyze both fermion and scalar DM with different physical production processes being involved, such as the minimal gravitational scattering, direct inflaton decay/scattering, and the thermal bath scattering. The gravitational production can again be observed to play a crucial role in setting the maximum limit on DM mass, especially in the FIMP scenario. Depending on the DM coupling strength, we have analyzed in detail the production of both FIMPs and WIMPs-like DM during reheating and their detailed phenomenological implications from the perspective of various cosmological and laboratory experiments.

In chapter 4, we explored the phenomenological impact of the latest Planck and BICEP/$Keck$ 2018 observations on the physics of inflation and reheating. Additionally, we used the $\Delta N_{\rm eff}$ bound to constrain the overproduction of PGWs. In this chapter, we considered two more inflation models, namely α-attractor T and the minimal plateau model, along with α-attractor E-model. Using the latest constraints on $n_{\rm s}, r$ from Planck+BICEP/Keck, we derived detailed phenomenological constraints on macroscopic parameters, such as the inflationary parameters (N_k, H_k), potential parameter ($\alpha, \phi_\star$), and the post-inflationary reheating temperature $T_{\rm re}$ for all the models we considered. Interestingly, these constraints are largely insensitive to the microphysics of reheating (reheating framework), but depend on the inflation model. One can realize the reheating temperature when considering the inflaton coupling with radiation, and we considered only inflaton decays to either pairs of fermions or pairs of bosons via a trilinear interaction. So, the constraints on $T_{\rm re}$ can be converted into constraints on the inflaton couplings. From the particle physics perspective, it is essential to derive constraints on microphysical parameters like the inflaton's coupling. Apart from direct and indirect observational bounds, we further utilized the theoretical bounds coming from Coleman Weinberg constraints (CWc) and non-perturbative constraints (NPc). Coleman Weinberg constraints (CWc) strictly restrict the maximum allowed value of couplings, above which inflation will be jeopardized. However, if we assume the fact that the reheating process itself is perturbative in nature, it is non-perturbative constraints (NPc) that play a wider role in setting the upper limit of both the inflaton-radiation couplings and the reheating temperature for all the models under consideration. If nature chooses the coupling to be within the non-perturbative regime, the coupling constraints from the observation will be different, which we defer to our future study. Rather than in the laboratory, our results illustrate the potential of present and future cosmological observations to look for new physics in the sky.

In the conventional approach, arbitrary coupling between the inflaton and massless fields is introduced to reheat the universe after inflation. This coupling lacks robust predictions, as there is no direct observational probe of reheating. To circumvent this difficulty, in Chapter 5, we proposed a novel reheating mechanism (called gravitational neutrino reheating) where the particle physics model, namely the Type-I seesaw model, is shown to play a major role in the entire reheating process, and the inflaton is free from arbitrary coupling. To the best of our knowledge, it is the first reheating model of the kind that not only provides successful reheating but also solves the well-known neutrino mass and baryon asymmetry problems. This gravitational neutrino reheating constrains a large class of inflation models, RHN masses, and predicts non-vanishing lightest active neutrino mass. For successful reheating, the gravitational neutrino reheating restricted the inflaton EoS w_ϕ within $1/3 \lesssim w_\phi \lesssim 1.0$ and $\nu_{\rm R}^3$ mass $10^{10} \lesssim M_3 \lesssim 2\times 10^{13}$ GeV. However, for

both successful reheating and baryogenesis, the gravitational neutrino reheating further constrained the EoS within $0.5 \lesssim w_\phi \lesssim 1.0$, and the corresponding viable mass range of $\nu_{\rm R}^1$ is $8 \times 10^{11} \lesssim M_1 \lesssim 2 \times 10^{13}$ GeV. The gravitational neutrino reheating predicts a distinct primordial gravitational wave spectrum, and it allows a large parameter space for reheating temperature and the EoS to be probed in future gravitational wave experiments such as BBO, DECIGO, LISA, ET, and the resonance cavities. Our novel mechanism opens up a new avenue of integrating particle physics and cosmology in the context of reheating. Finally, in these neutrino reheating backgrounds, we further performed a detailed analysis of both thermal and non-thermal production of DM, invoking two minimal models, namely the Higgs portal DM and classical QCD pseudoscalar axion. An interesting correlation between seemingly uncorrelated DM and Type-I seesaw parameters has emerged when confronting various direct and indirect observations. When DMs are set to freeze-in, freeze-out, or oscillate during reheating, new parameter spaces open, which could be potentially detectable in future experiments, paving an indirect way to look into the early universe in the laboratory.

6.2 Outlook

Throughout my PhD work, several important perspectives have emerged, each with the potential for further exploration and deeper understanding. These areas represent valuable avenues for future research and can significantly contribute to advancing our knowledge in cosmology, inflation, DM, and baryogenesis. Below, I outline some of the key directions for future work.

1. Study thermalization during reheating and effect of thermalization on DM production: A crucial aspect of the post-inflationary dynamics lies in understanding the thermalization of the inflaton decay products (radiation). In most studies of reheating (also in this thesis), it is commonly assumed that the radiation produced from inflaton decay instantaneously thermalizes and creates a thermal bath. However, the detailed dynamics of how and when thermal equilibrium is established play a crucial role in determining the reheating temperature and the duration of the reheating phase [310].

In future work, I plan to systematically investigate the dynamics of thermalization during reheating for general inflaton EoS. Since the production of cosmic relics, such as DM and the matter-antimatter asymmetry, may be sensitive to whether they are generated before or after complete thermalization, I will focus on examining the implications of delayed thermalization for different particle production mechanisms. In particular, I will analyze its impact on DM production via freeze-in and freeze-out, as well as on baryogenesis and leptogenesis scenarios. The ultimate goal is to develop a more consistent framework that connects the microscopic dynamics of thermalization with macroscopic cosmological observables.

2. Study the phase transition during Reheating and GWs production: There is currently no direct experimental evidence for the reheating era, but gravitational wave astronomy offers a promising probe. One significant GW source is phase transitions, where GWs can be generated by domain wall collisions. If an early reheating phase existed, phase transitions could occur during this period, and the non-trivial evolution of the thermal bath temperature, driven by inflaton decay, could affect the nucleation and dynamics of domain walls. These effects may imprint unique features on the resulting GW spectrum, such as its amplitude and frequency, providing indirect evidence of reheating. Investigating this connection involves modeling the interplay between reheating dynamics, phase transitions, and domain wall forma-

tion, as well as predicting GW signatures. Upcoming observatories like LISA, DECIGO, and the ET could potentially detect these signals, offering new insights into the physics of reheating and the early Universe.

3. Impact of Reheating on Structure Formation: The reheating phase is very difficult to probe; till now, this phase has been ill-understood. The small-scale density perturbations can provide a probe of the early Universe. The density perturbation of DM may grow during this phase due to gravitational instability. The non-trivial evolution of the expansion history and thermal history may influence the growth of this perturbation. The early DM microholes can be formed from that enhanced perturbation if the free-streaming length is smaller than the horizon, which can open up new possibilities to learn about the reheating phase using gamma-ray observation. Then, it becomes fascinating to understand the evolution of the density perturbations in both radiation and DM for various background dynamics of reheating.
Like DM perturbation, it will also be interesting if we study Axion/ALP perturbation during reheating. Reheating can influence the evolution of axion/ALP small-scale structures, leading to the formation of dense axion/ALP miniclusters. The Pulsar timing and lensing observations can discover these minihalos over a large range of axion/ALP masses and reheating temperatures.

4. Study the Baryogenesis during Reheating : Besides leptogenesis, there are several other mechanisms for baryogenesis that could also be influenced by the dynamics of the early universe [148–150, 311]. Exploring these alternatives, such as Electroweak baryogenesis, GUT baryogenesis, and Affleck-Dine baryogenesis, in the context of non-standard cosmologies and varying reheating histories would provide a more comprehensive understanding of the generation of the baryon asymmetry. Future work in this direction could offer valuable insights into the broader landscape of baryogenesis and its connection to DM and inflationary physics.

5. Primordial Black Hole formation during Reheating: PBHs formation in the early universe is theorized to result from significant contraction during the Big Bang. PBHs are an intriguing DM candidate, as they behave as stable, cold, non-interacting massive objects. Additionally, the gravitational waves (GWs) emitted by PBHs have gained considerable attention, especially following the detection of gravitational radiation from merging black holes by LIGO. Despite the growing interest in this area, there are very few studies in the literature that focus on the impact of reheating on PBH production. Furthermore, a comprehensive study of PBH formation that fully incorporates the reheating phase is still lacking.

APPENDIX A

Calculation of Inflaton Oscillation Frequency

After the end of inflation, the inflaton field ϕ starts to oscillate around the minimum of its potential with decreasing amplitude. Moreover, the character of the oscillations strongly depends on the shape of $V(\phi)$ in the vicinity of the minimum. Note that the time scale of the inflaton oscillations is typically much shorter than the variation of its amplitude. Thus, in this phase, a generic solution to Eq. (2.38) can be written as a product of two functions [39, 47, 312],

$$\phi(t) = \phi_0(t) \cdot \mathscr{P}(t), \tag{A.1}$$

where $\mathscr{P}(t)$ is a quasi-periodic, fast-oscillating function, while $\phi_0(t)$ denotes a slowly-varying (w.r.t. the time scale of the oscillations) envelope function. Ignoring expansion within a single oscillation period, as the oscillation time scale is very short compared to redshift time-scales, from Eq. 2.52, one can numerically obtain that the average of the periodic function $\mathscr{P}$ is $\langle \mathscr{P}^{2n} \rangle = 1/(n+1)$. So, from Eq. 2.57, the average inflaton energy density and pressure can be written as a function of ϕ_0,

$$\begin{aligned} \rho_\phi &= \frac{1}{2}\langle \dot{\phi}^2 \rangle + \langle V(\phi) \rangle \simeq (n+1)\langle V(\phi) \rangle = V(\phi_0) \\ P_\phi &= \frac{1}{2}\langle \dot{\phi}^2 \rangle - \langle V(\phi) \rangle \simeq (n-1)\langle V(\phi) \rangle = \frac{n-1}{n+1} V(\phi_0). \end{aligned} \tag{A.2}$$

The rapid oscillations of $\mathscr{P}(a)$ are damped by the decreasing envelope $\phi_0(a)$ due to the expansion of the Universe. Now, our goal is to obtain approximate analytical solutions of ϕ_0 during reheating. During reheating, the inflaton decay rate is smaller than the Hubble rate, so from Eq. 2.55,

$$\frac{d\rho_\phi}{dt} + 3H(1+w_\phi)\rho_\phi = 0 \tag{A.3}$$

Again, $\rho_\phi \simeq V(\phi_0) \propto \phi_0^{2n}$, so the above equation can be written as,

$$\dot{\phi}_0 \simeq -\frac{3H(1+w_\phi)}{2n}\phi_0 = \frac{3H(1-w_\phi)}{2}\phi_0 \tag{A.4}$$

The solution of this equation can be written as,

$$\phi_0(a) = \phi_0^{\rm end}\left(\frac{a}{a_{\rm end}}\right)^{-\frac{3}{2}(1-w_\phi)}, \tag{A.5}$$

where $\phi_0(a_{\rm end})$ denotes the initial value of the envelope determined from the condition $\rho_\phi^{\rm end} = V(\phi_0^{\rm end})$.

For a general potential, the oscillations are not purely harmonic, and we can represent the periodic function as a Fourier series in terms of the oscillation frequency

$$\mathscr{P}(t) = \sum_{\nu=-\infty}^{+\infty} \mathscr{P}_\nu \, e^{-i\nu\Omega t}$$

Here, $\mathscr{P}_\nu$ represents the Fourier modes of the periodic function $\mathscr{P}(t)$. Each Fourier mode behaves as an independent classical oscillator with energy $E_\nu = \nu\Omega$. All these modes contribute to the inflaton condensate and can be calculated numerically by solving the EoM of the inflaton ϕ with the potential. The frequency of oscillations depends on the slope of the inflaton potential n. We can determine this frequency analytically, and to find it, we differentiate Eq. A.1 w.r.t. time, obtaining,

$$\dot{\phi} = \dot{\phi}_0 \mathscr{P} + \phi_0 \dot{\mathscr{P}} \tag{A.6}$$

Using Eq. A.2, this can be further written as,

$$\dot{\mathscr{P}} = \pm \frac{\sqrt{2\rho_\phi(1-\mathscr{P}^{2n})}}{\phi_0} - \frac{\dot{\phi}_0}{\phi_0}\mathscr{P} \tag{A.7}$$

ϕ_0 is constant over one oscillation, and using the relation $m_\phi = \frac{\sqrt{2n(2n-1)\rho_\phi}}{\phi_0}$ (see Eq. 4.6), we obtain,

$$\dot{\mathscr{P}} = \frac{m_\phi}{\sqrt{n(2n-1)}}(1-\mathscr{P}^{2n})^{1/2} \tag{A.8}$$

If $T = 2\pi/\Omega$ be the time period, then at $T/4$, $\mathscr{P} = 1$, so from the above equation,

$$\int_0^1 \frac{d\mathscr{P}}{\sqrt{(1-\mathscr{P}^{2n})}} = \frac{m_\phi}{\sqrt{n(2n-1)}} m_\phi \int_0^{T/4} dt \tag{A.9}$$

Directly solving this integration using Mathematica, one can obtain the following expression of oscillation frequency,

$$\Omega = m_\phi \sqrt{\frac{\pi n}{2n-1)}} \frac{\Gamma\left(\frac{1}{2}+\frac{1}{2n}\right)}{\Gamma\left(\frac{1}{2n}\right)} = \gamma\, m_\phi \tag{A.10}$$

APPENDIX **B**

Calculation of CP-violating phase $\delta_{\rm eff}$

The CP asymmetry generated from $\nu_{\rm R}^i$ decay is given by (from Eq. 2.191),

$$\varepsilon_1 \simeq -\frac{3}{16\pi (y^\dagger y)_{11}} \left({\rm Im}[(y^\dagger y)^2_{12}] \frac{M_1}{M_2} + {\rm Im}[(y^\dagger y)^2_{13}] \frac{M_1}{M_3} \right). \tag{B.1}$$

If we assume ${\rm Im}\left(y^\dagger y\right)^2_{13} \gg {\rm Im}\left(y^\dagger y\right)^2_{12}$ and $M_1 \ll M_2, M_3$, then, we have,

$$\varepsilon_1 \simeq -\frac{3\delta_{\rm eff}}{16\pi} \frac{|y_{13}|^2 M_1}{M_3}, \tag{B.2}$$

while the effective CP-violating phase is given by

$$\delta_{\rm eff} = \frac{1}{|y_{13}|^2} \frac{{\rm Im}(y^\dagger y)^2_{13}}{(y^\dagger y)_{11}},. \tag{B.3}$$

In order to simultaneously generate the active neutrino mass, one has to impose the seesaw relation

$$m_3 = \frac{|y_{13}|^2 v^2}{M_3}, \tag{B.4}$$

that leads to

$$\varepsilon_1 \simeq -\frac{3\delta_{\rm eff}}{16\pi} \frac{M_1 m_3}{v^2}. \tag{B.5}$$

If, we consider ${\rm Im}\left(y^\dagger y\right)^2_{13} \ll {\rm Im}\left(y^\dagger y\right)^2_{12}$, the CP asymmetry parameter becomes

$$\varepsilon_1 \simeq -\frac{3\delta_{\rm eff}}{16\pi} \frac{M_1 m_2}{v^2},. \tag{B.6}$$

In general, we can then write,

$$\varepsilon_1 \simeq -\frac{3\delta_{\rm eff}}{16\pi} \frac{M_1 m_i}{v^2},, \tag{B.7}$$

where $i = 2,3$ for the normal hierarchy. In a similar fashion, the CP-asymmetry parameter can be obtained for the inverted hierarchy with $i = 1,2$.

APPENDIX C

Calculation of Inflaton Decay Width

C.1 Derivation of Decay Width Formula for the Inflaton condensate

In this appendix, we derive the inflaton decay width formula by incorporating the inflaton oscillation effect. The inflaton condensate ϕ is spatially homogeneous, and its phase space distribution can be written as $f_\phi(k,t) = (2\pi)^3 n_\phi(t)\delta^{(3)}(\boldsymbol{p_\phi})$, with n_ϕ the instantaneous inflaton number density. If we consider the decay process like $\phi(p_\phi) \to X(p_X)Y(p_Y)$, from the collision Eq. 2.159, the Boltzmann equation for the inflaton number density can be written as follows [313],

$$\dot{n}_\phi + 3Hn_\phi = -\int \frac{d^3\boldsymbol{p}_\phi}{(2\pi)^3 n_\phi(t)} \frac{d^3\boldsymbol{p}_X}{(2\pi)^3 2E_X} \frac{d^3\boldsymbol{p}_Y}{(2\pi)^3 2E_Y} |\mathscr{M}^{\nu}_{\phi\to XY}|^2 (2\pi)^4 \delta^4(p_\phi - p_X - p_Y) \\ \left[f_\phi(p_\phi)(1\pm f_X(p_X))(1\pm f_Y(p_Y)) - f_X(p_X) f_Y(p_Y)(1\pm f_\phi(p_\phi))\right], \tag{C.1}$$

where (+) and (-) signs are for bosonic and fermionic species, respectively. $\mathscr{M}^{\nu}_{\phi\to XY}$ denotes the transition amplitude for n-th oscillating field mode of ϕ from the coherent state $|\phi\rangle$ to the two-particle final state $|X,Y\rangle$, which we simply denote as $\mathscr{M}_\nu$. In this case, the four-momentum of the k-th oscillation mode is given by $p_X + p_Y = p_\phi = p_\nu = (E_\nu, 0)$ where $E_\nu = \nu\Omega$ is the energy of the ν-th oscillation mode. We have assumed that the phase-space density of the inflaton quanta is large, and hence $(1\pm f_\phi(p_\phi)) \simeq f_\phi(p_\phi)$. So, integration with respect to the ϕ momentum gives

$$\dot{n}_\phi + 3Hn_\phi = -\sum_{\nu=0}^{\infty}\int \frac{d^3\boldsymbol{p}_X}{(2\pi)^3 2E_X} \frac{d^3\boldsymbol{p}_Y}{(2\pi)^3 2E_Y} |\mathscr{M}_\nu|^2 (2\pi)^4 \delta^4(p_\nu - p_X - p_Y)\left[(1\pm f_X(p_X)) \pm f_Y(p_Y))\right] \tag{C.2}$$

The evolution equation for the energy density of the inflaton can be obtained by noting that, on the right-hand side, we must introduce the energy of each oscillation mode $|\mathscr{M}_\nu|^2 \to |\mathscr{M}_\nu|^2 E_\nu$. On the left side of the equality, the adiabaticity assumption for the decay implies that only the lowest oscillation mode must be taken into account, so that $\rho_\phi = m_\phi n_\phi$, and

$$\dot{\rho}_\phi = m_\phi \dot{n}_\phi + n_\phi \dot{m}_\phi = m_\phi \dot{n}_\phi + \rho_\phi \frac{\dot{m}_\phi}{m_\phi}. \tag{C.3}$$

From the definition of m_ϕ in Eq. 3.9, $m_\phi \propto \phi_0^{(n-1)}$, and it can be written as,

$$\frac{\dot{m}_\phi}{m_\phi} \simeq \frac{2w_\phi}{1-w_\phi}\frac{\dot{\phi}_0}{\phi_0} \tag{C.4}$$

Again from the Eq. A.4, the relation between ϕ_0 and $\dot{\phi}_0$ can be written as

$$\dot{\phi}_0 \simeq -\frac{3H(1-w_\phi)}{2}\phi_0 \tag{C.5}$$

So, combining the above two equations, one can find,

$$\frac{\dot{m}_\phi}{m_\phi} = -3H w_\phi \tag{C.6}$$

Finally, substituting Eqs.C.6 and C.3 into Eq.C.2, we obtain:

$$\dot{\rho}_\phi + 3H(1+w_\phi)\rho_\phi = -\sum_{\nu=0}^{\infty}\int \frac{d^3\boldsymbol{p}_{\rm X}}{(2\pi)^3 2E_{\rm X}}\frac{d^3\boldsymbol{p}_{\rm Y}}{(2\pi)^3 2E_{\rm Y}} E_\nu |\mathscr{M}_\nu|^2 (2\pi)^4\delta^4(p_\nu - p_{\rm X} - p_{\rm Y})\left[(1\pm f_{\rm X}(p_{\rm X}))\pm f_{\rm Y}(p_{\rm Y})\right] \tag{C.7}$$

Considering the identical final states particles each have mass $m_{\rm X}$. After doing some straightforward calculations, we get

$$\dot{\rho}_\phi + 3H(1+w_\phi)\rho_\phi = -\frac{1}{8\pi}\sum_{\nu=0}^{\infty} E_\nu |\mathscr{M}_\nu|^2 \left(1-\frac{4m_{\rm X}^2}{E_\nu^2}\right)^{\frac{1}{2}}\left[(1\pm 2f_{\rm X}(E_\nu/2)\right] \tag{C.8}$$

Upon comparing with the Eq. 2.55, the decay width Γ_ϕ is,

$$\Gamma_\phi = \frac{1}{8\pi(1+w_\phi)}\sum_{\nu=0}^{\infty} E_\nu |\mathscr{M}_\nu|^2 \left(1-\frac{4m_{\rm X}^2}{E_\nu^2}\right)^{\frac{1}{2}}\left[(1\pm 2f_{\rm X}(E_\nu/2)\right] \tag{C.9}$$

For massless radiation field $m_{\rm X}=0$, it will be,

$$\Gamma_\phi = \frac{1}{8\pi(1+w_\phi)}\sum_{\nu=0}^{\infty} E_\nu |\mathscr{M}_\nu|^2 \left[(1\pm 2f_{\rm X}(E_\nu/2)\right] \tag{C.10}$$

After neglecting Bose enhancement/Pauli blocking effects $(1\pm 2f_{\rm X})\simeq 1$, we can reproduce the previous result [18]. Now, our task is to find Γ_ϕ for different production processes for the radiation.

C.2 Expression of Decay width for $\phi \to s\,s$ with $\mathscr{L}_{\rm int} \supset -g_1^r \phi s^2$

In this subsection, we derive the Feynman amplitude for the processes $\phi \to s\,s$ in the presence of the inflaton background field. In this framework, massless bosons are produced in quantum processes from the vacuum in the classical inflaton background. Thus, we consider the quantum transition from the vacuum, i.e., $|i\rangle = |0\rangle$ to two-particle final states $|f\rangle = \sqrt{4p_1^0 p_2^0}\, a^\dagger_{p_1} a^\dagger_{p_2}|0\rangle$. At the leading order, we calculate the Feynman amplitude for process $|i\rangle \to |f\rangle$ with the interaction Lagrangian $\mathscr{L}_{\rm int}$,

$$S^{(1)}_{fi} = -i\int d^4x \left\langle f\left|T\left[\mathscr{L}_{\rm int}(x)\right]\right|i\right\rangle \tag{C.11}$$

$$= -i\int d^4x \left\langle f\left|T\left[g_1^r\,\phi\hat{s}(x)\hat{s}(x)\right]\right|i\right\rangle \tag{C.12}$$

To compute these matrix elements, we first quantize the scalar field b

$$\hat{s}(x) = \int d\Pi_p \left(\hat{a}_{\vec{p}} e^{-ip_\mu x^\mu} + \text{h.c}\right) \tag{C.13}$$

where $d\Pi_p = \frac{d^3p}{(2\pi)^3\sqrt{2p^0}}$ is the phase-space factor. The polarization tensor for the spin-2 graviton field and the creation, annihilation operators of the scalar field satisfy the following relations:

$$[\hat{a}^\lambda_{\vec{p}}, \hat{a}^{\lambda'\dagger}_{\vec{k}}] = (2\pi)^3\delta^3(\vec{p}-\vec{k})\delta^{\lambda\lambda'} \tag{C.14}$$

In the case of bosonic radiation with interaction Lagrangian $\mathscr{L}_{\rm int} \supset g_1^r \phi s^2$, the lowest-order non-zero

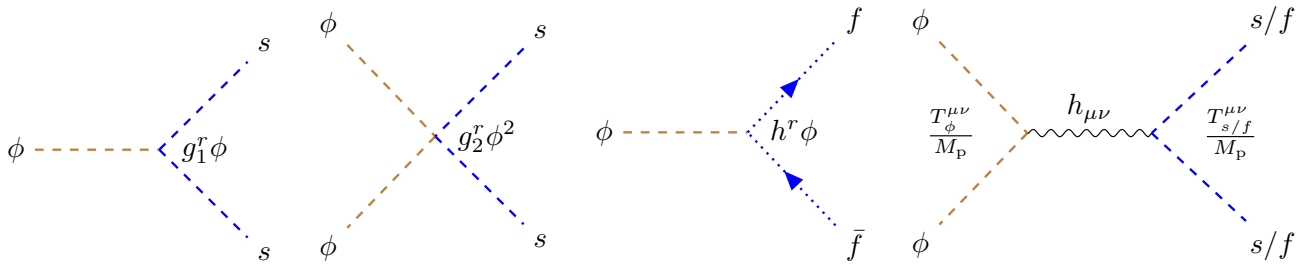

Figure C.1: Feynman diagrams for the different production processes

element of the S-matrix is given by

$$\begin{aligned}
S^{(1)}_{\phi\to b\,b} &= -i\,g_1^r\,\langle f|\int dt\int d^3x\,\phi(t)\hat{s}\,\hat{s}|0\rangle\,,\\
&= -i\,g_1^r\,\phi_0(t)\sum_k \mathscr{P}_v\int \mathrm{d}t\,e^{-iv\Omega t}\int \mathrm{d}^3x\int d\Pi_p\int d\Pi_q\,\langle 0|a(p_1)a(p_2)a^\dagger(p)a^\dagger(q)|0\rangle\sqrt{4p_1^0p_2^0}\,e^{ip\cdot x}e^{iq\cdot x},\\
&= -ig_1^r\,\phi_0(t)\sum_k \mathscr{P}_v\int dt\,d^3x\,e^{-i(v\Omega-p_1-p_2)\cdot x},\\
&= -ig_1^r\,\phi_0(t)\sum_k \mathscr{P}_v(2\pi)^4\delta(v\Omega-p_1^0-p_2^0)\delta^{(3)}(\mathbf{p}_1+\mathbf{p}_2)\\
&= i\mathscr{M}_v(2\pi)^4\delta^4(E_v-p_1-p_2)
\end{aligned}\tag{C.15}$$

The square of the Feynman amplitude can be written as,

$$|\mathscr{M}_v|^2 = (g_1^r)^2\,\phi_0^2(t)\sum_v|\mathscr{P}_v|^2\tag{C.16}$$

We can directly find out the Feynman amplitude from the Feynman diagram (1st plot in Fig. C.1) using the Feynman rule. Since we consider inflation as a classical background, it does not participate in quantization. So, the vertex is $g_1^r\phi$, and hence, the Feynman amplitude to be $\mathscr{M}_v = -i\,g\,\phi$. Using $\phi = \phi_0\sum_v\mathscr{P}_v$, the square of the Feynman amplitude can be written as,

$$|\mathscr{M}_v|^2 = (g_1^r)^2\,\phi_0^2(t)\sum_v|\mathscr{P}_v|^2\tag{C.17}$$

same as we have found in Eq. C.16. Putting $\phi_0^2 = 2n(2n-1)\rho_\phi/m_\phi^2$,

$$|\mathscr{M}_v|^2 = (g_1^r)^2\,\frac{2n(2n-1)\rho_\phi}{m_\phi^2}\sum_v|\mathscr{P}_v|^2\tag{C.18}$$

Finally, substitute $|\mathscr{M}_v|^2$ into the decay width formula, Eq. C.10 with appropriate symmetry factors, we

Table C.1: Comparison between the effective coupling and the tree-level coupling. The ratio written within the brackets is for the thermal effect.

$n(w_\phi)$	$\frac{g^r_{1,\text{eff}}}{g^r_1}$	$\frac{g^r_{2,\text{eff}}}{g^r_2}$	$\frac{h^r_{\text{eff}}}{h}$
1 (0.0)	1 (1)	1 (1)	1 (1)
2 (1/3)	1.42 (2.01)	3.64 (3.66)	0.71 (0.52)
3(1/2)	1.70 (2.93)	7.01 (8.55)	0.60 (0.38)
10 (0.82)	2.92 (8.84)	43.97 (92.01)	0.38 (0.19)

find,

$$\begin{aligned}
\Gamma_\phi &= \frac{1}{8\pi(1+w_\phi)\rho_\phi}\frac{4n(2n-1)(g^r_1)^2\rho_\phi}{m^2_\phi}\sum_\nu E_\nu|\mathscr{P}_\nu|^2\left(1+\frac{2}{e^{E_\nu/2T_{\text{rad}}}-1}\right)\\
&= \frac{1}{8\pi(1+w_\phi)}\frac{4n(2n-1)(g^r_1)^2}{m^2_\phi}\sum_\nu E_\nu|\mathscr{P}_\nu|^2\left(1+\frac{2}{e^{E_\nu/2T_{\text{rad}}}-1}\right)\\
&= \frac{1}{8\pi(1+w_\phi)}\frac{4n(2n-1)\gamma(g^r_1)^2}{m_\phi}\sum_\nu \nu|\mathscr{P}_\nu|^2\left(1+\frac{2}{e^{\nu\gamma m_\phi/2T_{\text{rad}}}-1}\right)\\
&= \frac{(2n+2)(2n-1)\gamma(g^r_1)^2}{8\pi m_\phi}\sum_\nu \nu|\mathscr{P}_\nu|^2\left(1+\frac{2}{e^{\nu\gamma m_\phi/2T_{\text{rad}}}-1}\right)\\
&= \frac{(2n+2)(2n-1)\gamma(g^r_1)^2}{8\pi m_\phi}\sum_\nu \nu|\mathscr{P}_\nu|^2\left(1+\frac{4T_{\text{rad}}}{\nu\gamma m_\phi}\right)
\end{aligned} \tag{C.19}$$

In the last line, we expand the exponential term in the limit $T_{\text{rad}} \gg m_\phi$, which is nothing but the thermal effect condition. If we put $T = 0$, we safely reproduce the vacuum decay width. Now, we can define the decay width in this manner,

$$\Gamma_{\phi\to b\,b} = \begin{cases} \frac{(g^r_{1,\text{eff}})^2}{8\pi m_\phi}\frac{4T_{\text{rad}}}{m_\phi} & \text{with thermal effect } (T_{\text{rad}} \gg m_\phi) \\ \frac{(g^r_{1,\text{eff}})^2}{8\pi m_\phi} & \text{without thermal effect} \end{cases} \tag{C.20}$$

where the oscillation induced effective coupling parameter $g^r_{1,\text{eff}}$ is now function of the tree-level coupling g^r_1,

$$(g^r_{1,\text{eff}})^2 = \begin{cases} (g^r_1)^2(2n+2)(2n-1)\sum_{\nu=1}^\infty|\mathscr{P}_\nu|^2 & \text{with thermal effect } (T_{\text{rad}} \gg m_\phi) \\ (g^r_1)^2(2n+2)(2n-1)\gamma\sum_{\nu=1}^\infty \nu|\mathscr{P}_\nu|^2 & \text{without thermal effect} \end{cases} \tag{C.21}$$

After taking care of the zero-mode inflaton oscillations, the expression of the decay width would be the same. The only difference is that our mentioned coupling parameters g^r_i in decay width (Eq. 3.2) defined in Chapter 3 behave as an effective coupling. For $w_\phi = 0\,(n = 1)$, $\sum\nu|\mathscr{P}_\nu|^2 = 1/4$, so, $g^r_{1,\text{eff}} = g^r_1$, so the effective coupling is the same as the tree-level coupling, and it is true for both cases (without and with thermal effect). Now for $w_\phi = 1/3$, $g^r_{1,\text{eff}} = 1.42(1.65)g^r_1$ for without (with) thermal effect. In Table-C.1, we have provided the ratio of $g^r_{1,\text{eff}}/g^r_1$ for other EoS w_ϕ.

C.3 Expression of Decay width for $\phi\phi \to s\,s$ with $\mathscr{L}_{\text{int}} \supset -g^r_2\phi^2 s^2$

From the 2nd plot in the Feynman diagram C.1, the square of the Feynman amplitude can be found $|\mathscr{M}_\nu|^2 = 4(g^r_2)^2\phi_0^2\sum_\nu|\mathscr{P}^2_\nu|^2$. Using this in the decay width formula Eq. C.1, and taking care of proper

Table C.2: Numerical values of the Fourier sums in the effective couplings:

$n(w_\phi)$	$\sum \nu\lvert\mathscr{P}_\nu\rvert^2$	$\sum \nu\lvert\mathscr{P}_\nu^2\rvert^2$	$\sum \nu^3\lvert\mathscr{P}_\nu\rvert^2$	$\sum\lvert\mathscr{P}_\nu\rvert^2$	$\sum\lvert\mathscr{P}_\nu^2\rvert^2$	$\sum \nu^4\lvert\mathscr{P}_\nu\rvert^2$	$\sum\lvert\mathscr{P}_\nu^{2n}\rvert^2$	$\sum \nu\lvert\mathscr{P}_\nu^{2n}\rvert^2$
1 (0.0)	0.25	0.125	0.25	0.25	0.0625	0.25	0.0625	0.125
2 (1/3)	0.229	0.1256	0.241	0.2284	0.0623	0.266	0.0635	0.141
3 (0.5)	0.218	0.124	0.244	0.2155	0.061	0.308	0.056	0.1456
10 (0.82)	0.1915	0.1141	0.2865	0.1864	0.053	0.6427	0.0266	0.1488

symmetry factors, we have,

$$\Gamma_{\phi\phi\to ss} = \frac{2n(2n+2)(2n-1)^2\gamma(g_2^r)^2\rho_\phi}{8\pi m_\phi^3}\sum_\nu \nu\lvert\mathscr{P}_\nu^2\rvert^2\left(1+\frac{2}{e^{\nu\gamma m_\phi/2T_{\rm rad}}-1}\right) \tag{C.22}$$

Now, we will write this in standard form, like,

$$\Gamma_{\phi\phi\to ss} = \begin{cases} \frac{(g^r_{2,\rm eff})^2\rho_\phi}{8\pi m_\phi^3}\frac{4T_{\rm rad}}{m_\phi} & \text{with thermal effect } (T_{\rm rad}\gg m_\phi) \\ \frac{(g^r_{2,\rm eff})^2\rho_\phi}{8\pi m_\phi^3} & \text{without thermal effect} \end{cases} \tag{C.23}$$

where the oscillation induced effective coupling parameter $g^r_{1,\rm eff}$ is,

$$(g^r_{2,\rm eff})^2 = \begin{cases} (g_2^r)^2\,2n(2n+2)(2n-1)^2\sum_{\nu=1}^\infty\lvert\mathscr{P}_\nu^2\rvert^2, & \text{with thermal effect } (T_{\rm rad}\gg m_\phi) \\ (g_2^r)^2\,2n(2n+2)(2n-1)^2\gamma\sum_{\nu=1}^\infty \nu\lvert\mathscr{P}_\nu^2\rvert^2, & \text{without thermal effect} \end{cases} \tag{C.24}$$

Like the above trilinear interaction, for the quartic interaction, the decay width is modified only by the effective coupling $g^r_{2,\rm eff}$. The ratio of the effective coupling to the tree-level coupling is shown in Table-C.1.

C.4 Expression of Decay width for $\phi\to\bar f f$ with $\mathscr{L}_{\rm int}\supset -h^r\phi\bar f f$

From the 3rd plot in the Feynman diagram C.1, the square of the Feynman amplitude can be found,

$$\lvert\mathscr{M}_\nu\rvert^2 = (h^r)^2\phi_0^2\sum_\nu\left(\sum_{s,s'}\lvert\bar u_s(p_1)v_{s'}(p_2)\rvert^2\right)\lvert\mathscr{P}_\nu\rvert^2 \tag{C.25}$$

Now, our task is to calculate the spin sum,

$$\begin{aligned}
\sum_{\rm spin} &= \sum_{s,s'}(\bar u_s(p_1)v_{s'}(p_2))^2 \\
&= \sum_{ss'}[\bar u_s(p_1)v_{s'}(p_2)][\bar u_s(p_1)v_{s'}(p_2)]^* \\
&= \sum_{ss'}[\bar u_s(p_1)v_{s'}(p_2)]_\alpha\,[\bar v_{s'}(p_2)u_s(p_1)]_\beta \\
&= \left[\sum_s u_s(p_1)\bar u_s(p_1)\right]_{\beta\alpha}\left[\sum_{s'}v_{s'}(p_2)\bar v_{s'}(p_2)\right]_{\alpha\beta} \\
&= {\rm Tr}[(\not p_1+m_s)(\not p_2-m_s)] \\
&= {\rm Tr}[\not p_1\not p_2] \quad \text{as} \quad m_s=0 \\
&= 4(p_1\cdot p_2) = 2E_\nu^2
\end{aligned} \tag{C.26}$$

So, using this in Eq. C.25, we can finally write the square amplitude,

$$\lvert\mathscr{M}_\nu\rvert^2 = 2(h^r)^2\phi_0^2\sum_\nu E_\nu^2\lvert\mathscr{P}_\nu\rvert^2 \tag{C.27}$$

Again, using it in the decay width formula Eq. C.1, we find,

$$\Gamma_{\phi\to\bar{f}f} = \frac{(h^r)^2(2n+2)(2n-1)\gamma^3}{8\pi} m_\phi \sum_{\nu=1}^{\infty} \nu^3 |\mathscr{P}_\nu|^2 \left(1 - \frac{2}{e^{\nu\gamma m_\phi/2T_{\rm rad}}+1}\right) \tag{C.28}$$

Writing it in the standard form, we have,

$$\Gamma_{\phi\to\bar{f}f} = \begin{cases} \frac{(h^r_{\rm eff})^2 m_\phi}{8\pi} \frac{m_\phi}{4T_{\rm rad}} & \text{with thermal effect } (T_{\rm rad} \gg m_\phi) \\ \frac{(h^r_{\rm eff})^2 m_\phi}{8\pi} & \text{without thermal effect} \end{cases} \tag{C.29}$$

where the oscillation induced effective coupling parameter $h^r_{\rm eff}$ is,

$$(h^r_{\rm eff})^2 = \begin{cases} (h^r)^2(2n+2)(2n-1)\gamma^4 \sum_{\nu=1}^{\infty} \nu^4 |\mathscr{P}_\nu|^2 & \text{with thermal effect } (T_{\rm rad} \gg m_\phi) \\ (h^r)^2(2n+2)(2n-1)\gamma^3 \sum_{\nu=1}^{\infty} \nu^3 |\mathscr{P}^2_\nu|^2 & \text{without thermal effect.} \end{cases} \tag{C.30}$$

C.5 Expression of Decay width for Gravitational Production

Let us first derive the gravitational Lagrangian $\mathscr{L}_{\rm int}$ in the weak field limit. In the weak field limit of gravity, we can expand the local metric around the flat Minkowski background, taking the terms up to the linear order of perturbation [155]:

$$\begin{aligned} g_{\mu\nu} &= \eta_{\mu\nu} + 2\frac{h_{\mu\nu}}{M_{\rm p}} \\ g^{\mu\nu} &= \eta^{\mu\nu} - 2\frac{h^{\mu\nu}}{M_{\rm p}} \\ \sqrt{-g} &= 1 + \frac{\eta^{\mu\nu}h_{\mu\nu}}{M_{\rm p}} \end{aligned} \tag{C.31}$$

where $\eta_{\mu\nu}$ is the flat-space metric, and $h_{\mu\nu}$ is the perturbation (graviton field) on top of the flat metric. Under this metric perturbation, the curvature scalar up to the first order metric perturbation is written as follows [155]:

$$R^{(1)} = \frac{2}{M_{\rm p}} \left(\eta_{\alpha\beta}\partial_\mu\partial^\mu h^{\alpha\beta} - \partial_\mu\partial_\nu h^{\mu\nu}\right) \tag{C.32}$$

In this thesis, we are interested in the minimal gravitational production, and the inflaton ϕ is minimally coupled with gravity, then recall it action,

$$S = \int \sqrt{-g}\, d^4x \left(-\frac{M_{\rm p}^2}{2} R + \frac{1}{2}\partial_\mu\phi\partial^\mu\phi - V(\phi)\right) \tag{C.33}$$

Under the metric perturbation Eq. C.31, we will expand the above action up to the first order. Considering only the matter Lagrangian,

$$\begin{aligned} S &= \int d^4x \left(1 + \frac{\eta^{\mu\nu}h_{\mu\nu}}{M_{\rm p}}\right)\left[\frac{1}{2}\left(\eta^{\mu\nu} - \frac{2h^{\mu\nu}}{M_{\rm p}}\right)\partial_\mu\phi\partial_\nu\phi - V(\phi)\right] \\ &= \int d^4x \left[\left(\frac{1}{2}\eta^{\mu\nu}\partial_\mu\phi\partial_\nu\phi - V(\phi)\right) - \frac{h^{\mu\nu}}{M_{\rm p}}\left(\partial_\mu\phi\partial_\nu\phi - \eta_{\mu\nu}\left(\frac{1}{2}\eta^{\mu\nu}\partial_\mu\phi\partial_\nu\phi - V(\phi)\right)\right)\right] \\ &= \int d^4x \left[\left(\frac{1}{2}\eta^{\mu\nu}\partial_\mu\phi\partial_\nu\phi - V(\phi)\right) - \frac{h^{\mu\nu}}{M_{\rm p}} T^\phi_{\mu\nu}\right] \\ &= \int d^4x (\mathscr{L}_\phi + \mathscr{L}_{\rm int}). \end{aligned}$$

Therefore, the term $\mathscr{L}_{\rm int}$ serve as the gravitational interaction Lagrangian,

$$\mathscr{L}_{\rm int} = -\frac{h^{\mu\nu}}{M_{\rm p}} T^{s}_{\mu\nu} \tag{C.34}$$

This is the most general form of the minimal gravitational interaction for any field s, and depends on the spin of the field s; the energy-momentum tensor will be different. Now, we will compute the gravitational decay rate for both bosonic and fermionic (spin-1/2) radiation. Let, do first for bosonic radiation.

C.5.1 Bosonic radiation

Suppose that the bosonic field s is produced from the inflaton field through minimal gravitational interactions. In this minimal coupling scenario, the interaction Lagrangian takes the following form, which we derived in Eq. C.34,

$$\mathscr{L}_{\rm int} = -\frac{h^{\mu\nu}}{M_{\rm p}} \left(T^{\phi}_{\mu\nu} + T^{s}_{\mu\nu} \right) \tag{C.35}$$

where $T^{\phi}_{\mu\nu}$ and $T^{s}_{\mu\nu}$ represent the energy-momentum tensors of the inflaton condensate and the bosonic field s, respectively. They are given by the following expressions:

$$T^{\phi}_{\mu\nu} = \partial_\mu\phi\partial_\nu\phi - \frac{1}{2}\eta_{\mu\nu}(\partial^\alpha\phi\partial_\alpha\phi - V(\phi)). \tag{C.36}$$

$$T^{s}_{\mu\nu} = \partial_\mu s\,\partial_\nu s - \frac{1}{2}\eta_{\mu\nu}(\partial^\alpha s\,\partial_\alpha s - m_s^2 s^2). \tag{C.37}$$

Therefore, the minimal coupling with gravity leads to a three-point vertex at the tree level (see the right-most panel of Fig.(C.1)). Since the inflaton is treated as a classical background, the transition probability turns out to be proportional to the energy-momentum tensor $T^{\phi}_{\mu\nu}$ as

$$\mathscr{M}^{\phi}_{\mu\nu} = \frac{T^{\phi}_{\mu\nu}}{M_{\rm p}} = \frac{1}{M_{\rm p}} \left\{ \partial_\mu\phi\partial_\nu\phi - \frac{1}{2}\eta_{\mu\nu}\left(\partial^\alpha\phi\partial_\alpha\phi - V(\phi)\right) \right\} \tag{C.38}$$

for $\phi\phi h_{\mu\nu}$ vertices (see 4th plot of Fig. C.1). For $s^2 h_{\mu\nu}$ vertices, however, it is,

$$\mathscr{M}^{s}_{\rho\sigma} = \frac{2}{M_{\rm p}} \left(p_{1\rho}p_{2\sigma} + p_{1\sigma}p_{2\rho} - \eta_{\rho\sigma}(p_1\cdot p_2 + m_s^2) \right), \tag{C.39}$$

where "p_1" and "p_2" are the final state s particle's four-momenta. The final scattering amplitude is expressed as,

$$\mathscr{M}^{\phi s} = \mathscr{M}^{\phi}_{\mu\nu}\,\Pi^{\mu\nu\rho\sigma}\,\mathscr{M}^{s}_{\rho\sigma}, \tag{C.40}$$

where $\Pi^{\mu\nu\rho\sigma}$ is the graviton propagator for the canonical field $h_{\mu\nu}$ with momentum $\sqrt{s}$,

$$\Pi^{\mu\nu\rho\sigma} = \frac{1}{2\,q} \left(\eta^{\mu\rho}\eta^{\nu\sigma} + \eta^{\mu\sigma}\eta^{\nu\rho} - \eta^{\mu\nu}\eta^{\rho\sigma} \right). \tag{C.41}$$

where "q" is the Mandelstam variable defined in terms of the background condensate energy. Utilizing the above expression of the propagator we obtained,

$$M^{\phi}_{\mu\nu}\,\Pi^{\mu\nu\rho\sigma} = \frac{1}{M_{\rm p}\,q} \left[\partial^\rho\phi\partial^\sigma\phi - \eta^{\rho\sigma}V(\phi) \right], \tag{C.42}$$

$$\mathscr{M}^{\phi s} = \frac{2}{M_{\rm p}^2\,q} \left(\partial^\rho\phi\partial^\sigma\phi - \eta^{\rho\sigma}V(\phi) \right) \left(p_{1\rho}p_{2\sigma} + p_{1\sigma}p_{2\rho} - \eta_{\rho\sigma}(p_1\cdot p_2 + m_s^2) \right). \tag{C.43}$$

Expanding and simplifying the above equation, we have

$$\mathscr{M}^{\phi s} = \frac{2i}{M_{\rm p}^2 q}\left[(\partial^\rho\phi\, p_{1\rho})(\partial^\sigma\phi\, p_{2\sigma}) + (\partial^\rho\phi\, p_{2\rho})(\partial^\sigma\phi\, p_{1\sigma}) - 2p_1\cdot p_2 V(\phi) + 4V(\phi)(p_1\cdot p_2 + m_s^2)\right]. \tag{C.44}$$

For a homogeneous field $\phi(t)$, $\partial_\mu\phi = \dot\phi$ and spatial derivatives vanish. Substituting this,

$$\mathscr{M}^{\phi s} = \frac{2i}{M_{\rm p}^2 q}\left[2\dot\phi^2 p_1^0 p_2^0 - \dot\phi^2(p_1\cdot p_2 + m_s^2) + 2p_1\cdot p_2 V(\phi) + 4m_s^2 V(\phi)\right]. \tag{C.45}$$

For the inflaton condensate, we can use the transition amplitude $\mathscr{M}_\nu$ for each oscillating field mode of ϕ. In this case, the four-momentum of the ν-th oscillation mode is given by $p_\nu = \sqrt{q} = (E_\nu, 0)$ where $E_\nu = \nu\Omega$ represents the energy of the ν-th oscillation mode. The four-momenta $p_1 = (E_\nu/2, \vec{p})$ and $p_2 = (E_\nu/2, -\vec{p})$, $q = (p_1+p_2)^2 = E_\nu^2$ and $p_1\cdot p_2 = E_\nu^2/2 - m_s^2$. Finally from Eq.(C.45), we obtain

$$|\mathscr{M}_\nu^{\phi s}|^2 = \frac{1}{M_{\rm p}^4}V(\phi)^2\left(1+\frac{2m_s^2}{E_\nu^2}\right)^2. \tag{C.46}$$

Using $V(\phi) = V(\phi_0)\mathscr{P}^{2n}(t) = \rho_\phi\sum_\nu \mathscr{P}_\nu^{2n} e^{-i\nu\Omega t}$ and $\rho_\phi \simeq V(\phi_0)$,

$$|\mathscr{M}_\nu^{\phi s}|^2 = \frac{\rho_\phi^2}{M_{\rm p}^4}\left(1+\frac{2m_s^2}{\nu^2\omega^2}\right)^2 |\mathscr{P}_\nu^{2n}|^2. \tag{C.47}$$

To calculate the decay width, we have used Eq. C.9, so

$$\begin{aligned}\Gamma^{\rm gr}_{\phi\phi\to ss} = &\frac{\rho_\phi}{8\pi(1+w_\phi)M_{\rm p}^4}\sum_\nu \nu\Omega\,|\mathscr{P}_\nu^{2n}|^2\left(1-\frac{4m_s^2}{\nu^2\omega^2}\right)^{\frac{1}{2}}\left(1+\frac{2m_s^2}{\nu^2\Omega^2}\right)\left(1+\frac{2}{e^{\nu\Omega/2T_{\rm rad}}-1}\right),\\ &\frac{\gamma m_\phi\rho_\phi}{8\pi(1+w_\phi)M_{\rm p}^4}\sum_\nu \nu\,|\mathscr{P}_\nu^{2n}|^2\left(1-\frac{4m_s^2}{\nu^2\gamma^2 m_\phi^2}\right)^{\frac{1}{2}}\left(1+\frac{2m_s^2}{\nu^2\gamma^2 m_\phi^2}\right)\left(1+\frac{2}{e^{\nu\gamma m_\phi/2T_{\rm rad}}-1}\right),\end{aligned} \tag{C.48}$$

For massless radiation, $m_s = 0$, and so the decay rate will be,

$$\Gamma^{\rm gr}_{\phi\phi\to ss} = \frac{\gamma m_\phi\rho_\phi}{8\pi(1+w_\phi)M_{\rm p}^4}\sum_\nu \nu\,|\mathscr{P}_\nu^{2n}|^2\left(1+\frac{2}{e^{\nu\gamma m_\phi/2T_{\rm rad}}-1}\right). \tag{C.49}$$

The gravitational decay width has also been modified by a constant factor; no extra time-dependent term has arisen.

C.5.2 Fermionic radiation

Now, we offer the detailed computations for the decay rate of inflaton annihilation to a pair of fermionic radiation via gravity. From the Feynman diagram (the right-most panel of Fig. C.1), the vertex factor for the vertex $h^{\mu\nu}\bar f f$ can be written as [166],

$$-\frac{i}{4M_{\rm p}}\left[(p_1+p_2)_\mu\gamma_\nu + (p_1+p_2)_\nu\gamma_\mu - 2\eta_{\mu\nu}(\not{p}_1 + \not{p}_2 - 2m_f)\right]. \tag{C.50}$$

The partial amplitude for this vertex will be

$$\begin{aligned}
\mathscr{M}^{f}_{\mu\nu} &= \frac{1}{4M_{\rm p}}\bar{v}(p_2)\left[(p_1+p_2)_\mu\gamma_\nu+(p_1+p_2)_\nu\gamma_\mu-2\eta_{\mu\nu}(\not{p}_1+\not{p}_2-2m_f)\right]u(p_1),\\
&= \frac{1}{4M_{\rm p}}\bar{v}(p_2)\left[(p_1-p_2)_\mu\gamma_\nu+(p_1-p_2)_\nu\gamma_\mu+2(p_{2\mu}\gamma_\nu+p_{2\nu}\gamma_\mu)-2\eta_{\mu\nu}(\not{p}_1+\not{p}_2-2m_f)\right]u(p_1)\\
&= \frac{1}{4M_{\rm p}}\bar{v}(p_2)\left[(p_1-p_2)_\mu\gamma_\nu+(p_1-p_2)_\nu\gamma_\mu+2p_{2\mu}\gamma_\nu-2\eta_{\mu\nu}(\not{p}_1-2m_f)\right]u(p_1),\\
&= \frac{1}{4M_{\rm p}}\bar{v}(p_2)\left[(p_1-p_2)_\mu\gamma_\nu+(p_1-p_2)_\nu\gamma_\mu-2\eta_{\mu\nu}(\not{p}_1-\not{p}_2-2m_f)\right]u(p_1)\\
&= \frac{1}{4M_{\rm p}}\bar{v}(p_2)\left[(p_1-p_2)_\mu\gamma_\nu+(p_1-p_2)_\nu\gamma_\mu\right]u(p_1)+\frac{1}{2M_{\rm p}}\eta_{\mu\nu}\bar{v}(p_2)\left[(\not{p}_1-\not{p}_2-2m_f)\right]u(p_1)\\
&= \frac{1}{4M_{\rm p}}\bar{v}(p_2)\left[(p_1-p_2)_\mu\gamma_\nu+(p_1-p_2)_\nu\gamma_\mu\right]u(p_1)+\frac{1}{2M_{\rm p}}\eta_{\mu\nu}\left[\bar{v}(p_2)(\not{p}_1-m_f)u(p_1)-\bar{v}(p_2)(\not{p}_2+m_f)u(p_1)\right]
\end{aligned} \tag{C.51}$$

Using the property, $(\not{p}_1-m_f)u(p_1)=0$, $\bar{v}(p_2)(\not{p}_2+m_f)=0$, we have finally,

$$\mathscr{M}^{f}_{\mu\nu} = \frac{1}{4M_{\rm p}}\bar{v}(p_2)\left[(p_1-p_2)_\mu\gamma_\nu+(p_1-p_2)_\nu\gamma_\mu\right]u(p_1) \tag{C.52}$$

Therefore, combining the above equation with Eqs. 4.6, C.41, C.42, the total scattering amplitude in Eq. C.40 is,

$$\begin{aligned}
\mathscr{M}^{\phi f} &= \frac{1}{4M_{\rm p}^2\,q}\left[\partial^\rho\phi\,\partial^\sigma\phi-\eta^{\rho\sigma}V(\phi)\right]\bar{v}(p_2)\left[(p_1-p_2)_\rho\gamma_\sigma+(p_1-p_2)_\sigma\gamma_\rho\right]u(p_1)\\
&= -\frac{V(\phi)}{2M_{\rm p}^2\,q}\bar{v}(p_2)\,(\not{p}_1-\not{p}_2)\,u(p_1).
\end{aligned} \tag{C.53}$$

Now, the square amplitude:

$$\begin{aligned}
\left|\mathscr{M}^{\phi f}\right|^2 &= \frac{V(\phi)^2}{4M_{\rm p}^4\,q^2}\sum_{s,s'}\left|\bar{v}(p_2)\,(\not{p}_1-\not{p}_2)\,u(p_1)\right|^2,\\
&= \frac{V(\phi)^2}{4M_{\rm p}^4\,q^2}\,{\rm Tr}\left[(\not{p}_1-\not{p}_2)(\not{p}_1+m_f)(\not{p}_1-\not{p}_2)(\not{p}_2-m_f)\right]\\
&= \frac{V(\phi)^2}{4M_{\rm p}^4\,q^2}\,{\rm Tr}\left[(\not{p}_1-\not{p}_2)\not{p}_1(\not{p}_1-\not{p}_2)(\not{p}_2-m_f)+m_f(\not{p}_1-\not{p}_2)^2(\not{p}_2-m_f)\right]\\
&= \frac{V(\phi)^2}{4M_{\rm p}^4\,q^2}\,{\rm Tr}\left[(\not{p}_1-\not{p}_2)\not{p}_1(\not{p}_1-\not{p}_2)\not{p}_2-m_f^2(\not{p}_1-\not{p}_2)^2\right]\\
&= \frac{V(\phi)^2}{4M_{\rm p}^4\,q^2}\left({\rm Tr}\left[(\not{p}_1-\not{p}_2)\not{p}_1(\not{p}_1-\not{p}_2)\not{p}_2\right]-m_f^2\,{\rm Tr}\left[(\not{p}_1-\not{p}_2)^2\right]\right)\\
&= \frac{V(\phi)^2}{4M_{\rm p}^4\,q^2}\left[8m_f^2(p_1\cdot p_2-m_f^2)-8(m_f^2-p_1\cdot p_2))\right]\\
&= \frac{2m_f^2V(\phi)^2}{M_{\rm p}^4\,q}\left(1-\frac{4m_f^2}{q}\right)
\end{aligned} \tag{C.54}$$

Finally, the decay for the gravitationally produced fermionic radiation will be,

$$\Gamma^{\rm gr}_{\phi\phi\to\bar{f}f} = \frac{m_\phi^2\rho_\phi}{2\pi(1+w_\phi)M_{\rm p}^4\gamma\,m_\phi}\sum_\nu\frac{1}{\nu}|\mathscr{P}_\nu^{2n}|^2\left(1-\frac{4m_s^2}{\nu^2\gamma^2m_\phi^2}\right)^{\frac{3}{2}}\left(1-\frac{2}{e^{\nu\gamma m_\phi/2T_{\rm rad}}+1}\right), \tag{C.55}$$

For massless radiation, $m_f=0$, and so the decay rate will be zero.

Bibliography

[1] P. A. R. Ade *et al.* (Planck), Astron. Astrophys. **571**, A16 (2014), arXiv:1303.5076 [astro-ph.CO] .

[2] P. A. R. Ade *et al.* (Planck), Astron. Astrophys. **594**, A13 (2016), arXiv:1502.01589 [astro-ph.CO] .

[3] P. A. R. Ade *et al.* (Planck), Astron. Astrophys. **594**, A20 (2016), arXiv:1502.02114 [astro-ph.CO] .

[4] Y. Akrami *et al.* (Planck), Astron. Astrophys. **641**, A10 (2020), arXiv:1807.06211 [astro-ph.CO] .

[5] A. H. Guth, Phys. Rev. D **23**, 347 (1981).

[6] A. D. Linde, Phys. Lett. B **108**, 389 (1982).

[7] A. H. Guth and S. Y. Pi, Phys. Rev. Lett. **49**, 1110 (1982).

[8] A. Albrecht, P. J. Steinhardt, M. S. Turner, and F. Wilczek, Phys. Rev. Lett. **48**, 1437 (1982).

[9] A. A. Starobinsky, Phys. Lett. B **117**, 175 (1982).

[10] G. Steigman, Ann. Rev. Nucl. Part. Sci. **57**, 463 (2007), arXiv:0712.1100 [astro-ph] .

[11] J. L. Cook, E. Dimastrogiovanni, D. A. Easson, and L. M. Krauss, JCAP **04**, 047 (2015), arXiv:1502.04673 [astro-ph.CO] .

[12] L. Dai, M. Kamionkowski, and J. Wang, Phys. Rev. Lett. **113**, 041302 (2014), arXiv:1404.6704 [astro-ph.CO] .

[13] K. D. Lozanov and M. A. Amin, Phys. Rev. Lett. **119**, 061301 (2017), arXiv:1608.01213 [astro-ph.CO] .

[14] K. D. Lozanov and M. A. Amin, Phys. Rev. D **97**, 023533 (2018), arXiv:1710.06851 [astro-ph.CO] .

[15] D. Maity and P. Saha, (2016), arXiv:1610.00173 [astro-ph.CO] .

[16] D. Maity and P. Saha, Phys. Rev. D **98**, 103525 (2018), arXiv:1801.03059 [hep-ph] .

[17] D. Maity and P. Saha, Phys. Dark Univ. **25**, 100317 (2019), arXiv:1804.10115 [hep-ph] .

[18] M. A. G. Garcia, K. Kaneta, Y. Mambrini, and K. A. Olive, Phys. Rev. D **101**, 123507 (2020), arXiv:2004.08404 [hep-ph] .

[19] J.-F. Dufaux, G. Felder, L. Kofman, and O. Navros, Phys. Rev. D **82**, 083518 (2010), arXiv:1006.0217 [astro-ph.CO] .

[20] D. G. Figueroa, J. García-Bellido, and F. Torrentí, Phys. Rev. D **93**, 103521 (2016), arXiv:1602.03085 [astro-ph.CO] .

[21] J. T. Giblin and E. Thrane, Phys. Rev. D **90**, 107502 (2014), arXiv:1410.4779 [gr-qc] .

[22] S. Antusch, F. Cefala, and S. Orani, Phys. Rev. Lett. **118**, 011303 (2017), [Erratum: Phys.Rev.Lett. 120, 219901 (2018)], arXiv:1607.01314 [astro-ph.CO] .

[23] M. R. Haque, D. Maity, T. Paul, and L. Sriramkumar, Phys. Rev. D **104**, 063513 (2021).

[24] G. Lemaitre, Annales Soc. Sci. Bruxelles A **47**, 49 (1927).

[25] A. Friedman, Z. Phys. **10**, 377 (1922).

[26] E. W. Kolb and M. S. Turner, *The Early Universe*, Vol. 69 (1990).

[27] D. Baumann, *Cosmology* (Cambridge University Press, 2022).

[28] A. Einstein, Sitzungsber. Preuss. Akad. Wiss. Berlin (Math. Phys.) **1915**, 844 (1915).

[29] A. Einstein, Sitzungsber. Preuss. Akad. Wiss. Berlin (Math. Phys.) **1917**, 142 (1917).

[30] S. M. Carroll, *Spacetime and Geometry: An Introduction to General Relativity* (Cambridge University Press, 2019).

[31] N. Aghanim *et al.* (Planck), Astron. Astrophys. **641**, A6 (2020), [Erratum: Astron.Astrophys. 652, C4 (2021)], arXiv:1807.06209 [astro-ph.CO] .

[32] M. Tegmark *et al.* (SDSS), Phys. Rev. D **69**, 103501 (2004), arXiv:astro-ph/0310723 .

[33] J. Frieman, M. Turner, and D. Huterer, Ann. Rev. Astron. Astrophys. **46**, 385 (2008), arXiv:0803.0982 [astro-ph] .

[34] A. H. Guth, Phys. Rev. D **23**, 347 (1981).

[35] K. D. Lozanov, (2019), arXiv:1907.04402 [astro-ph.CO] .

[36] A. Riotto, ICTP Lect. Notes Ser. **14**, 317 (2003), arXiv:hep-ph/0210162 .

[37] A. D. Linde, Phys. Lett. B **129**, 177 (1983).

[38] A. D. Linde, *Particle physics and inflationary cosmology*, Vol. 5 (1990) arXiv:hep-th/0503203 .

[39] Y. Shtanov, J. H. Traschen, and R. H. Brandenberger, Phys. Rev. D **51**, 5438 (1995), arXiv:hep-ph/9407247 .

[40] K. Ichikawa, T. Suyama, T. Takahashi, and M. Yamaguchi, Phys. Rev. D **78**, 063545 (2008), arXiv:0807.3988 [astro-ph] .

[41] G. F. Giudice, E. W. Kolb, and A. Riotto, Phys. Rev. D **64**, 023508 (2001), arXiv:hep-ph/0005123 [hep-ph] .

[42] L. F. Abbott and P. Sikivie, Phys. Lett. B **120**, 133 (1983).

[43] P. B. Greene, L. Kofman, A. D. Linde, and A. A. Starobinsky, Phys. Rev. D **56**, 6175 (1997), arXiv:hep-ph/9705347 .

[44] A. V. Frolov, JCAP **11**, 009 (2008), arXiv:0809.4904 [hep-ph] .

[45] D. Maity and P. Saha, JCAP **07**, 018 (2019), arXiv:1811.11173 [astro-ph.CO] .

[46] M. S. Turner, Phys. Rev. D **28**, 1243 (1983).

[47] M. A. G. Garcia, K. Kaneta, Y. Mambrini, and K. A. Olive, JCAP **04**, 012 (2021), arXiv:2012.10756 [hep-ph] .

[48] P. Adshead, Y. Cui, and J. Shelton, JHEP **06**, 016 (2016), arXiv:1604.02458 [hep-ph] .

[49] R. Allahverdi, R. Brandenberger, F.-Y. Cyr-Racine, and A. Mazumdar, Ann. Rev. Nucl. Part. Sci. **60**, 27 (2010), arXiv:1001.2600 [hep-th] .

[50] M. Kawasaki, K. Kohri, and N. Sugiyama, Phys. Rev. D **62**, 023506 (2000), arXiv:astro-ph/0002127 .

[51] S. Hannestad, Phys. Rev. D **70**, 043506 (2004), arXiv:astro-ph/0403291 .

[52] N. Barbieri, T. Brinckmann, S. Gariazzo, M. Lattanzi, S. Pastor, and O. Pisanti, (2025), arXiv:2501.01369 [astro-ph.CO] .

[53] P. F. de Salas, M. Lattanzi, G. Mangano, G. Miele, S. Pastor, and O. Pisanti, Phys. Rev. D **92**, 123534 (2015), arXiv:1511.00672 [astro-ph.CO] .

[54] P. A. R. Ade *et al.* (BICEP, Keck), Phys. Rev. Lett. **127**, 151301 (2021), arXiv:2110.00483 [astro-ph.CO] .

[55] M. Tristram *et al.*, Phys. Rev. D **105**, 083524 (2022), arXiv:2112.07961 [astro-ph.CO] .

[56] H. Kodama and M. Sasaki, Prog. Theor. Phys. Suppl. **78**, 1 (1984).

[57] V. F. Mukhanov, H. A. Feldman, and R. H. Brandenberger, Phys. Rept. **215**, 203 (1992).

[58] D. Baumann, in *Theoretical Advanced Study Institute in Elementary Particle Physics: Physics of the Large and the Small* (2011) pp. 523–686, arXiv:0907.5424 [hep-th] .

[59] L. Sriramkumar, Curr. Sci. **97**, 868 (2009), arXiv:0904.4584 [astro-ph.CO] .

[60] J. M. Bardeen, Phys. Rev. D **22**, 1882 (1980).

[61] V. Mukhanov, H. Feldman, and R. Brandenberger, Physics Reports **215**, 203 (1992).

[62] L. A. Boyle and P. J. Steinhardt, Phys. Rev. D **77**, 063504 (2008), arXiv:astro-ph/0512014 .

[63] J. Martin, Braz. J. Phys. **34**, 1307 (2004), arXiv:astro-ph/0312492 .

[64] J. Martin, Lect. Notes Phys. **669**, 199 (2005), arXiv:hep-th/0406011 .

[65] P. A. R. Ade *et al.* (BICEP2, Planck), Phys. Rev. Lett. **114**, 101301 (2015), arXiv:1502.00612 [astro-ph.CO] .

[66] P. A. R. Ade *et al.* (BICEP2, Keck Array), Phys. Rev. Lett. **121**, 221301 (2018), arXiv:1810.05216 [astro-ph.CO] .

[67] M. Tristram *et al.*, Astron. Astrophys. **647**, A128 (2021), arXiv:2010.01139 [astro-ph.CO] .

[68] J. Martin, C. Ringeval, and V. Vennin, Phys. Dark Univ. **5-6**, 75 (2014), arXiv:1303.3787 [astro-ph.CO] .

[69] R. Kallosh and A. Linde, JCAP **07**, 002 (2013), arXiv:1306.5220 [hep-th] .

[70] R. Kallosh, A. Linde, and D. Roest, JHEP **11**, 198 (2013), arXiv:1311.0472 [hep-th] .

[71] S. Ferrara, R. Kallosh, A. Linde, and M. Porrati, Phys. Rev. D **88**, 085038 (2013), arXiv:1307.7696 [hep-th] .

[72] Y. Ueno and K. Yamamoto, Phys. Rev. D **93**, 083524 (2016), arXiv:1602.07427 [astro-ph.CO] .

[73] D. Maity and P. Saha, Class. Quant. Grav. **36**, 045010 (2019), arXiv:1902.01895 [gr-qc] .

[74] M. Drees and Y. Xu, JCAP **09**, 012 (2021), arXiv:2104.03977 [hep-ph] .

[75] A. D. Linde, Phys. Rev. D **49**, 748 (1994), arXiv:astro-ph/9307002 .

[76] A. D. Linde and A. Riotto, Phys. Rev. D **56**, R1841 (1997), arXiv:hep-ph/9703209 .

[77] M. Yamaguchi, Class. Quant. Grav. **28**, 103001 (2011), arXiv:1101.2488 [astro-ph.CO] .

[78] M. Kawasaki, M. Yamaguchi, and T. Yanagida, Phys. Rev. Lett. **85**, 3572 (2000), arXiv:hep-ph/0004243 .

[79] K. Dimopoulos, Phys. Lett. B **735**, 75 (2014), arXiv:1403.4071 [hep-ph] .

[80] A. A. Starobinsky, Phys. Lett. B **91**, 99 (1980).

[81] E. Corbelli and P. Salucci, Mon. Not. Roy. Astron. Soc. **311**, 441 (2000), arXiv:astro-ph/9909252 .

[82] F. Zwicky, General Relativity and Gravitation **41**, 207 (2009).

[83] V. C. Rubin and W. K. Ford, Jr., **159**, 379 (1970).

[84] V. C. Rubin, W. K. Ford, Jr., and N. Thonnard, **238**, 471 (1980).

[85] D. Clowe, M. Bradac, A. H. Gonzalez, M. Markevitch, S. W. Randall, C. Jones, and D. Zaritsky, Astrophys. J. Lett. **648**, L109 (2006), arXiv:astro-ph/0608407 .

[86] E. Komatsu, J. Dunkley, M. Nolta, C. L. Bennett, B. Gold, G. Hinshaw, N. Jarosik, D. Larson, M. Limon, L. Page, *et al.*, The Astrophysical Journal Supplement Series **180**, 330 (2009).

[87] J. R. Primack, in *Midrasha Mathematicae in Jerusalem: Winter School in Dynamical Systems* (1997) arXiv:astro-ph/9707285 .

[88] M. Boylan-Kolchin, V. Springel, S. D. M. White, A. Jenkins, and G. Lemson, Monthly Notices of the Royal Astronomical Society **398**, 1150 (2009), https://academic.oup.com/mnras/article-pdf/398/3/1150/4088069/mnras0398-1150.pdf .

[89] M. Taoso, G. Bertone, and A. Masiero, JCAP **03**, 022 (2008), arXiv:0711.4996 [astro-ph] .

[90] G. Steigman and M. S. Turner, Nuclear Physics B **253**, 375 (1985).

[91] G. Arcadi, M. Dutra, P. Ghosh, M. Lindner, Y. Mambrini, M. Pierre, S. Profumo, and F. S. Queiroz, Eur. Phys. J. C **78**, 203 (2018), arXiv:1703.07364 [hep-ph] .

[92] L. Roszkowski, E. M. Sessolo, and S. Trojanowski, Rept. Prog. Phys. **81**, 066201 (2018), arXiv:1707.06277 [hep-ph] .

[93] P. Gondolo and G. Gelmini, Nucl. Phys. B **360**, 145 (1991).

[94] J. Edsjo and P. Gondolo, Phys. Rev. D **56**, 1879 (1997), arXiv:hep-ph/9704361 .

[95] N. Bozorgnia, J. Bramante, J. M. Cline, D. Curtin, D. McKeen, D. E. Morrissey, A. Ritz, S. Viel, A. C. Vincent, and Y. Zhang, (2024), 10.1139/cjp-2024-0128, arXiv:2410.23454 [hep-ph] .

[96] G. Arcadi, D. Cabo-Almeida, M. Dutra, P. Ghosh, M. Lindner, Y. Mambrini, J. P. Neto, M. Pierre, S. Profumo, and F. S. Queiroz, Eur. Phys. J. C **85**, 152 (2025), arXiv:2403.15860 [hep-ph] .

[97] G. Steigman, B. Dasgupta, and J. F. Beacom, Phys. Rev. D **86**, 023506 (2012), arXiv:1204.3622 [hep-ph] .

[98] E. e. a. X. Aprile, Phys. Rev. Lett. **131**, 041003 (2023), arXiv:2303.14729 [hep-ex] .

[99] J. e. a. L. Aalbers, Phys. Rev. Lett. **131**, 041002 (2023), arXiv:2207.03764 [hep-ex] .

[100] J. Aalbers, S. S. AbdusSalam, K. Abe, V. Aerne, F. Agostini, S. A. Maouloud, D. S. Akerib, D. Y. Akimov, J. Akshat, and A. K. A. e. a. Musalhi, J. Phys. G **50**, 013001 (2023), arXiv:2203.02309 [physics.ins-det] .

[101] X. Cui *et al.* (PandaX-II), Phys. Rev. Lett. **119**, 181302 (2017), arXiv:1708.06917 [astro-ph.CO] .

[102] D. S. Akerib *et al.* (LUX), Phys. Rev. Lett. **118**, 021303 (2017), arXiv:1608.07648 [astro-ph.CO] .

[103] E. Aprile *et al.* (XENON), Phys. Rev. Lett. **119**, 181301 (2017), arXiv:1705.06655 [astro-ph.CO] .

[104] J. Billard *et al.*, Rept. Prog. Phys. **85**, 056201 (2022), arXiv:2104.07634 [hep-ex] .

[105] R. K. Leane, T. R. Slatyer, J. F. Beacom, and K. C. Y. Ng, Phys. Rev. D **98**, 023016 (2018), arXiv:1805.10305 [hep-ph] .

[106] L. Bergstrom, T. Bringmann, I. Cholis, D. Hooper, and C. Weniger, Phys. Rev. Lett. **111**, 171101 (2013), arXiv:1306.3983 [astro-ph.HE] .

[107] F. Calore, M. Cirelli, L. Derome, Y. Genolini, D. Maurin, P. Salati, and P. D. Serpico, SciPost Phys. **12**, 163 (2022), arXiv:2202.03076 [hep-ph] .

[108] H. Abdalla *et al.* (Hess, HAWC, VERITAS, MAGIC, H.E.S.S., Fermi-LAT), PoS **ICRC2021**, 528 (2021), arXiv:2108.13646 [hep-ex] .

[109] A. Acharyya *et al.* (CTA), JCAP **01**, 057 (2021), arXiv:2007.16129 [astro-ph.HE] .

[110] L. J. Hall, K. Jedamzik, J. March-Russell, and S. M. West, JHEP **03**, 080 (2010), arXiv:0911.1120 [hep-ph] .

[111] F. Elahi, C. Kolda, and J. Unwin, JHEP **03**, 048 (2015), arXiv:1410.6157 [hep-ph] .

[112] N. Bernal, M. Heikinheimo, T. Tenkanen, K. Tuominen, and V. Vaskonen, Int. J. Mod. Phys. A **32**, 1730023 (2017), arXiv:1706.07442 [hep-ph] .

[113] B. Barman, D. Borah, and R. Roshan, JCAP **11**, 021 (2020), arXiv:2007.08768 [hep-ph] .

[114] R. Mondal, S. Mondal, and T. Yamada, (2025), arXiv:2503.20738 [hep-ph] .

[115] J. Preskill, M. B. Wise, and F. Wilczek, Phys. Lett. B **120**, 127 (1983).

[116] D. J. E. Marsh, Phys. Rept. **643**, 1 (2016), arXiv:1510.07633 [astro-ph.CO] .

[117] L. Di Luzio, E. Giannotti, E. Nardi, and L. Visinelli, Phys. Rept. **870**, 1 (2020), arXiv:2003.01100 [hep-ph] .

[118] C. A. J. O'Hare, PoS **COSMICWISPers**, 040 (2024), arXiv:2403.17697 [hep-ph] .

[119] L. Hui, Ann. Rev. Astron. Astrophys. **59**, 247 (2021), arXiv:2101.11735 [astro-ph.CO] .

[120] B. D. Fields, K. A. Olive, T.-H. Yeh, and C. Young, JCAP **03**, 010 (2020), [Erratum: JCAP 11, E02 (2020)], arXiv:1912.01132 [astro-ph.CO] .

[121] N. Aghanim *et al.* (Planck), Astron. Astrophys. **641**, A8 (2020), arXiv:1807.06210 [astro-ph.CO] .

[122] E. W. Kolb and S. Wolfram, Nucl. Phys. B **172**, 224 (1980), [Erratum: Nucl.Phys.B 195, 542 (1982)].

[123] S. Weinberg, Phys. Rev. Lett. **42**, 850 (1979).

[124] S. Dimopoulos and L. Susskind, Phys. Rev. D **18**, 4500 (1978).

[125] A. D. Sakharov, Pisma Zh. Eksp. Teor. Fiz. **5**, 32 (1967).

[126] V. A. Kuzmin, V. A. Rubakov, and M. E. Shaposhnikov, Phys. Lett. B **155**, 36 (1985).

[127] M. Fukugita and T. Yanagida, Phys. Lett. B **174**, 45 (1986).

[128] M. A. Luty, Phys. Rev. D **45**, 455 (1992).

[129] A. Pilaftsis, Phys. Rev. D **56**, 5431 (1997), arXiv:hep-ph/9707235 .

[130] M. Gell-Mann, P. Ramond, and R. Slansky, Conf. Proc. C **790927**, 315 (1979), arXiv:1306.4669 [hep-th] .

[131] R. N. Mohapatra and G. Senjanovic, Phys. Rev. Lett. **44**, 912 (1980).

[132] P. Minkowski, Phys. Lett. B **67**, 421 (1977).

[133] L. Covi, E. Roulet, and F. Vissani, Phys. Lett. B **384**, 169 (1996), arXiv:hep-ph/9605319 .

[134] C. S. Fong, E. Nardi, and A. Riotto, Adv. High Energy Phys. **2012**, 158303 (2012), arXiv:1301.3062 [hep-ph] .

[135] Y. Xu, *Polynomial Inflation and Its Aftermath*, Ph.D. thesis, U. Bonn (main) (2022).

[136] K. Kaneta, Y. Mambrini, K. A. Olive, and S. Verner, Phys. Rev. D **101**, 015002 (2020), arXiv:1911.02463 [hep-ph] .

[137] S. Y. Khlebnikov and M. E. Shaposhnikov, Nucl. Phys. B **308**, 885 (1988).

[138] J. A. Harvey and M. S. Turner, Phys. Rev. D **42**, 3344 (1990).

[139] S. Davidson and A. Ibarra, Phys. Lett. B **535**, 25 (2002), arXiv:hep-ph/0202239 .

[140] G. Lazarides and Q. Shafi, Phys. Lett. B **258**, 305 (1991).

[141] T. Asaka, K. Hamaguchi, M. Kawasaki, and T. Yanagida, Phys. Lett. B **464**, 12 (1999), arXiv:hep-ph/9906366 .

[142] L. F. Abbott, E. Farhi, and M. B. Wise, Phys. Lett. B **117**, 29 (1982).

[143] L. Kofman, A. D. Linde, and A. A. Starobinsky, Phys. Rev. Lett. **73**, 3195 (1994), arXiv:hep-th/9405187 [hep-th] .

[144] L. Kofman, A. D. Linde, and A. A. Starobinsky, Phys. Rev. D **56**, 3258 (1997), arXiv:hep-ph/9704452 .

[145] M. Kawasaki, K. Kohri, and N. Sugiyama, Phys. Rev. Lett. **82**, 4168 (1999), arXiv:astro-ph/9811437 .

[146] M. Drewes, JCAP **03**, 013 (2016), arXiv:1511.03280 [astro-ph.CO] .

[147] M. Drewes, JCAP **09**, 069 (2022), arXiv:1903.09599 [astro-ph.CO] .

[148] E. W. Kolb, A. D. Linde, and A. Riotto, Phys. Rev. Lett. **77**, 4290 (1996), arXiv:hep-ph/9606260 .

[149] S. Davidson, M. Losada, and A. Riotto, Phys. Rev. Lett. **84**, 4284 (2000), arXiv:hep-ph/0001301 .

[150] A. Megevand, Phys. Rev. D **64**, 027303 (2001), arXiv:hep-ph/0011019 .

[151] F. Hahn-Woernle and M. Plumacher, Nucl. Phys. B **806**, 68 (2009), arXiv:0801.3972 [hep-ph] .

[152] A. Dolgov, K. Freese, R. Rangarajan, and M. Srednicki, Phys. Rev. D **56**, 6155 (1997), arXiv:hep-ph/9610405 .

[153] S. S. Mishra, V. Sahni, and A. A. Starobinsky, JCAP **05**, 075 (2021), arXiv:2101.00271 [gr-qc] .

[154] Y. Tang and Y.-L. Wu, Phys. Lett. B **774**, 676 (2017), arXiv:1708.05138 [hep-ph] .

[155] B. R. Holstein, Am. J. Phys. **74**, 1002 (2006), arXiv:gr-qc/0607045 .

[156] S. Clery, Y. Mambrini, K. A. Olive, A. Shkerin, and S. Verner, Phys. Rev. D **105**, 095042 (2022), arXiv:2203.02004 [hep-ph] .

[157] E. Aprile *et al.* (XENON100), Phys. Rev. Lett. **109**, 181301 (2012), arXiv:1207.5988 [astro-ph.CO] .

[158] E. Aprile *et al.* (XENON), Phys. Rev. Lett. **121**, 111302 (2018), arXiv:1805.12562 [astro-ph.CO] .

[159] X. Cui *et al.* (PandaX-II), Phys. Rev. Lett. **117**, 121303 (2016), arXiv:1607.07400 [hep-ex] .

[160] T. Delubac *et al.* (BOSS), Astron. Astrophys. **603**, A12 (2017), arXiv:1404.1801 [astro-ph.CO] .

[161] S. Capozziello, S. Nojiri, S. D. Odintsov, and A. Troisi, Phys. Lett. B **639**, 135 (2006), arXiv:astro-ph/0604431 .

[162] S. Capozziello and M. De Laurentis, Phys. Rept. **509**, 167 (2011), arXiv:1108.6266 [gr-qc] .

[163] C. G. Boehmer, T. Harko, and F. S. N. Lobo, Astropart. Phys. **29**, 386 (2008), arXiv:0709.0046 [gr-qc] .

[164] S. Nojiri, S. D. Odintsov, and V. K. Oikonomou, Phys. Rept. **692**, 1 (2017), arXiv:1705.11098 [gr-qc] .

[165] J. F. Donoghue, Phys. Rev. D **50**, 3874 (1994), arXiv:gr-qc/9405057 .

[166] S. Y. Choi, J. S. Shim, and H. S. Song, Phys. Rev. D **51**, 2751 (1995), arXiv:hep-th/9411092 .

[167] Y. Mambrini and K. A. Olive, Phys. Rev. D **103**, 115009 (2021), arXiv:2102.06214 [hep-ph] .

[168] B. Barman and N. Bernal, JCAP **06**, 011 (2021), arXiv:2104.10699 [hep-ph] .

[169] Y. Ema, R. Jinno, K. Mukaida, and K. Nakayama, JCAP **05**, 038 (2015), arXiv:1502.02475 [hep-ph] .

[170] Y. Ema, R. Jinno, K. Mukaida, and K. Nakayama, Phys. Rev. D **94**, 063517 (2016), arXiv:1604.08898 [hep-ph] .

[171] Y. Ema, K. Nakayama, and Y. Tang, JHEP **09**, 135 (2018), arXiv:1804.07471 [hep-ph] .

[172] M. Garny, M. Sandora, and M. S. Sloth, Phys. Rev. Lett. **116**, 101302 (2016), arXiv:1511.03278 [hep-ph] .

[173] M. Garny, A. Palessandro, M. Sandora, and M. S. Sloth, JCAP **02**, 027 (2018), arXiv:1709.09688 [hep-ph] .

[174] M. R. Haque and D. Maity, Phys. Rev. D **106**, 023506 (2022), arXiv:2112.14668 [hep-ph] .

[175] S. Clery, Y. Mambrini, K. A. Olive, and S. Verner, Phys. Rev. D **105**, 075005 (2022), arXiv:2112.15214 [hep-ph] .

[176] M. A. G. Garcia, Y. Mambrini, K. A. Olive, and S. Verner, JCAP **10**, 061 (2021), arXiv:2107.07472 [hep-ph] .

[177] M. R. Haque, D. Maity, and P. Saha, Phys. Rev. D **102**, 083534 (2020), arXiv:2009.02794 [hep-th] .

[178] B. Barman, N. Bernal, Y. Xu, and O. Zapata, JCAP **07**, 019 (2022), arXiv:2202.12906 [hep-ph] .

[179] P. N. Bhattiprolu, G. Elor, R. McGehee, and A. Pierce, (2022), arXiv:2210.15653 [hep-ph] .

[180] K. Harigaya, M. Kawasaki, K. Mukaida, and M. Yamada, Phys. Rev. D **89**, 083532 (2014), arXiv:1402.2846 [hep-ph] .

[181] K. Harigaya, K. Mukaida, and M. Yamada, JHEP **07**, 059 (2019), arXiv:1901.11027 [hep-ph] .

[182] N. Okada and O. Seto, Phys. Lett. B **820**, 136528 (2021), arXiv:2103.07832 [hep-ph] .

[183] D. K. Ghosh, S. Jeesun, and D. Nanda, Phys. Rev. D **106**, 115001 (2022), arXiv:2206.04940 [hep-ph] .

[184] M. R. Haque and D. Maity, Phys. Rev. D **107**, 043531 (2023), arXiv:2201.02348 [hep-ph] .

[185] K. Mukaida and K. Nakayama, JCAP **01**, 017 (2013), arXiv:1208.3399 [hep-ph] .

[186] K. Mukaida and K. Nakayama, JCAP **03**, 002 (2013), arXiv:1212.4985 [hep-ph] .

[187] M. Drewes and J. U. Kang, Nucl. Phys. B **875**, 315 (2013), [Erratum: Nucl.Phys.B 888, 284–286 (2014)], arXiv:1305.0267 [hep-ph] .

[188] P. Adshead, P. Ralegankar, and J. Shelton, JHEP **08**, 151 (2019), arXiv:1906.02755 [hep-ph] .

[189] M. Drewes, JCAP **11**, 020 (2014), arXiv:1406.6243 [hep-ph] .

[190] A. Ahmed, B. Grzadkowski, and A. Socha, JHEP **02**, 196 (2023), arXiv:2207.11218 [hep-ph] .

[191] D. J. H. Chung, E. W. Kolb, and A. Riotto, Phys. Rev. D **60**, 063504 (1999), arXiv:hep-ph/9809453 .

[192] J. Ellis, M. A. G. Garcia, D. V. Nanopoulos, K. A. Olive, and S. Verner, Phys. Rev. D **105**, 043504 (2022), arXiv:2112.04466 [hep-ph] .

[193] A. Chakraborty, M. R. Haque, D. Maity, and R. Mondal, Phys. Rev. D **108**, 023515 (2023), arXiv:2304.13637 [astro-ph.CO] .

[194] M. Drewes, J. U. Kang, and U. R. Mun, JHEP **11**, 072 (2017), arXiv:1708.01197 [astro-ph.CO] .

[195] R. T. Co, E. Gonzalez, and K. Harigaya, JCAP **11**, 038 (2020), arXiv:2007.04328 [astro-ph.CO] .

[196] P. B. Greene and L. Kofman, Phys. Rev. D **62**, 123516 (2000), arXiv:hep-ph/0003018 .

[197] P. B. Greene and L. Kofman, Phys. Lett. B **448**, 6 (1999), arXiv:hep-ph/9807339 .

[198] R. H. Cyburt, B. D. Fields, K. A. Olive, and T.-H. Yeh, Rev. Mod. Phys. **88**, 015004 (2016), arXiv:1505.01076 [astro-ph.CO] .

[199] S. Knapen, T. Lin, and K. M. Zurek, Phys. Rev. D **96**, 115021 (2017), arXiv:1709.07882 [hep-ph] .

[200] K. M. Nollett and G. Steigman, Phys. Rev. D **91**, 083505 (2015), arXiv:1411.6005 [astro-ph.CO] .

[201] A. Paul, A. Ghoshal, A. Chatterjee, and S. Pal, Eur. Phys. J. C **79**, 818 (2019), arXiv:1808.09706 [astro-ph.CO] .

[202] R. Jinno, T. Moroi, and K. Nakayama, Phys. Rev. D **86**, 123502 (2012), arXiv:1208.0184 [astro-ph.CO] .

[203] B. Wallisch, *Cosmological Probes of Light Relics*, Ph.D. thesis, Cambridge U. (2018), arXiv:1810.02800 [astro-ph.CO] .

[204] N. Bernal, J. Rubio, and H. Veermäe, JCAP **10**, 021 (2020), arXiv:2006.02442 [hep-ph] .

[205] X. Chu, T. Hambye, and M. Tytgat, JCAP **1205**, 034 (2012), arXiv:1112.0493 [hep-ph] .

[206] K. Griest and M. Kamionkowski, Phys. Rev. Lett. **64**, 615 (1990).

[207] D. Bhatia and S. Mukhopadhyay, JHEP **03**, 133 (2021), arXiv:2010.09762 [hep-ph] .

[208] Y. Sofue and V. Rubin, Ann. Rev. Astron. Astrophys. **39**, 137 (2001), arXiv:astro-ph/0010594 .

[209] K. N. Abazajian *et al.* (CMB-S4), (2016), arXiv:1610.02743 [astro-ph.CO] .

[210] M. R. Haque and D. Maity, Phys. Rev. D **99**, 103534 (2019), arXiv:1902.09491 [hep-th] .

[211] M. R. Haque, D. Maity, and R. Mondal, JHEP **09**, 012 (2023), arXiv:2301.01641 [hep-ph] .

[212] M. Drewes and L. Ming, Phys. Rev. Lett. **133**, 031001 (2024), arXiv:2208.07609 [hep-ph] .

[213] M. Drewes, L. Ming, and I. Oldengott, JCAP **05**, 081 (2024), arXiv:2303.13503 [hep-ph] .

[214] L. P. Grishchuk, Zh. Eksp. Teor. Fiz. **67**, 825 (1974).

[215] A. A. Starobinsky, JETP Lett. **30**, 682 (1979).

[216] S. Vagnozzi, Mon. Not. Roy. Astron. Soc. **502**, L11 (2021), arXiv:2009.13432 [astro-ph.CO] .

[217] M. Benetti, L. L. Graef, and S. Vagnozzi, Phys. Rev. D **105**, 043520 (2022), arXiv:2111.04758 [astro-ph.CO] .

[218] S. R. Coleman and E. J. Weinberg, Phys. Rev. D **7**, 1888 (1973).

[219] K. Abazajian *et al.* (CMB-S4), Astrophys. J. **926**, 54 (2022), arXiv:2008.12619 [astro-ph.CO] .

[220] E. Allys *et al.* (LiteBIRD), PTEP **2023**, 042F01 (2023), arXiv:2202.02773 [astro-ph.IM] .

[221] K. Dimopoulos and T. Markkanen, JCAP **06**, 021 (2018), arXiv:1803.07399 [gr-qc] .

[222] T. Nakama and J. Yokoyama, PTEP **2019**, 033E02 (2019), arXiv:1803.07111 [gr-qc] .

[223] T. Kunimitsu and J. Yokoyama, Phys. Rev. D **86**, 083541 (2012).

[224] S. Hashiba and J. Yokoyama, JCAP **01**, 028 (2019), arXiv:1809.05410 [gr-qc] .

[225] L. Pagano, L. Salvati, and A. Melchiorri, Phys. Lett. B **760**, 823 (2016), arXiv:1508.02393 [astro-ph.CO] .

[226] T.-H. Yeh, J. Shelton, K. A. Olive, and B. D. Fields, JCAP **10**, 046 (2022), arXiv:2207.13133 [astro-ph.CO] .

[227] M. Riajul Haque, E. Kpatcha, D. Maity, and Y. Mambrini, Phys. Rev. D **108**, 063523 (2023), arXiv:2305.10518 [hep-ph] .

[228] M. R. Haque, E. Kpatcha, D. Maity, and Y. Mambrini, (2023), arXiv:2309.06505 [hep-ph] .

[229] M. R. Haque, D. Maity, and R. Mondal, Phys. Rev. D **109**, 063543 (2024), arXiv:2311.07684 [hep-ph] .

[230] M. R. Haque, D. Maity, and R. Mondal, (2024), arXiv:2408.12450 [hep-ph] .

[231] R. T. Co, Y. Mambrini, and K. A. Olive, Phys. Rev. D **106**, 075006 (2022), arXiv:2205.01689 [hep-ph] .

[232] B. A. Campbell, S. Davidson, and K. A. Olive, Nucl. Phys. B **399**, 111 (1993), arXiv:hep-ph/9302223 .

[233] N. Bernal and C. S. Fong, JCAP **06**, 028 (2021), arXiv:2103.06896 [hep-ph] .

[234] M. C. Guzzetti, N. Bartolo, M. Liguori, and S. Matarrese, Riv. Nuovo Cim. **39**, 399 (2016), arXiv:1605.01615 [astro-ph.CO] .

[235] S. Vagnozzi, JHEAp **39**, 81 (2023), arXiv:2306.16912 [astro-ph.CO] .

[236] A. Sesana *et al.*, Exper. Astron. **51**, 1333 (2021), 1908.11391 .

[237] P. Amaro-Seoane *et al.*, arXiv:1702.00786 (2017), arXiv:1702.00786 [astro-ph.IM] .

[238] S. Hild *et al.*, Class. Quant. Grav. **28**, 094013 (2011), 1012.0908 .

[239] M. Punturo *et al.*, Class. Quant. Grav. **27**, 194002 (2010).

[240] B. S. Sathyaprakash *et al.*, Class. Quant. Grav. **29**, 124013 (2012), 1206.0331 .

[241] M. Maggiore *et al.*, JCAP **03**, 050 (2020), 1912.02622 .

[242] J. Crowder and N. J. Cornish, Phys. Rev. D **72**, 083005 (2005), gr-qc/0506015 .

[243] V. Corbin and N. J. Cornish, Class. Quant. Grav. **23**, 2435 (2006), gr-qc/0512039 .

[244] S. Kawamura *et al.*, Class. Quant. Grav. **28**, 094011 (2011).

[245] S. Kawamura (DECIGO working group), PoS **KMI2019**, 019 (2019).

[246] N. Herman *et al.*, Phys. Rev. D **106**, 122001 (2022), 2203.05568 .

[247] B. Barman, S. Cléry, R. T. Co, Y. Mambrini, and K. A. Olive, JHEP **12**, 072 (2022), arXiv:2210.05716 [hep-ph] .

[248] W. Buchmuller, P. Di Bari, and M. Plumacher, Annals Phys. **315**, 305 (2005), arXiv:hep-ph/0401240 .

[249] B. Barman, N. Bernal, and J. Rubio, (2023), arXiv:2310.06039 [hep-ph] .

[250] P. Hut, **69**, 85 (1977).

[251] B. W. Lee and S. Weinberg, **39**, 165 (1977).

[252] M. I. Vysotsky, A. D. Dolgov, and Y. B. Zeldovich, **26**, 188 (1977).

[253] M. Srednicki, R. Watkins, and K. A. Olive, **310**, 693 (1988).

[254] P. Gondolo and G. Gelmini, **360**, 145 (1991).

[255] K. Griest and D. Seckel, **43**, 3191 (1991).

[256] G. Arcadi, M. Dutra, P. Ghosh, M. Lindner, Y. Mambrini, M. Pierre, S. Profumo, and F. S. Queiroz, **78**, 203 (2018), arXiv:1703.07364 [hep-ph] .

[257] Y. Hochberg, E. Kuflik, R. Mcgehee, H. Murayama, and K. Schutz, **98**, 115031 (2018), arXiv:1806.10139 [hep-ph] .

[258] N. Bernal and Y. Xu, JCAP **12**, 017 (2022), arXiv:2209.07546 [hep-ph] .

[259] N. Bernal, P. Konar, and S. Show, Phys. Rev. D **109**, 035018 (2024), arXiv:2311.01587 [hep-ph] .

[260] V. Silveira and A. Zee, Phys. Lett. B **161**, 136 (1985).

[261] C. P. Burgess, M. Pospelov, and T. ter Veldhuis, Nucl. Phys. B **619**, 709 (2001), arXiv:hep-ph/0011335 .

[262] J. McDonald, Phys. Rev. D **50**, 3637 (1994), arXiv:hep-ph/0702143 .

[263] S. Andreas, T. Hambye, and M. H. G. Tytgat, JCAP **10**, 034 (2008), arXiv:0808.0255 [hep-ph] .

[264] H. Davoudiasl, R. Kitano, T. Li, and H. Murayama, Phys. Lett. B **609**, 117 (2005), arXiv:hep-ph/0405097 .

[265] K. G. Vangsnes, (2021).

[266] O. Lebedev, Prog. Part. Nucl. Phys. **120**, 103881 (2021), arXiv:2104.03342 [hep-ph] .

[267] W. L. Guo and Y. L. Wu, JHEP **10**, 083 (2010), arXiv:1006.2518 [hep-ph] .

[268] C. E. Yaguna, JCAP **02**, 006 (2012), arXiv:1111.6831 [hep-ph] .

[269] J. M. Cline, K. Kainulainen, P. Scott, and C. Weniger, Phys. Rev. D **88**, 055025 (2013), [Erratum: Phys. Rev. D 92, no.3, 039906 (2015)], arXiv:1306.4710 [hep-ph] .

[270] N. Bernal, C. Cosme, T. Tenkanen, and V. Vaskonen, Eur. Phys. J. C **79**, 30 (2019), arXiv:1806.11122 [hep-ph] .

[271] H. Han and S. Zheng, JHEP **12**, 044 (2015), arXiv:1509.01765 [hep-ph] .

[272] J. Silva-Malpartida, N. Bernal, J. Jones-Pérez, and R. A. Lineros, JCAP **09**, 015 (2023), arXiv:2306.14943 [hep-ph] .

[273] G. e. a. A. Aad, JHEP **08**, 104 (2022), arXiv:2202.07953 [hep-ex] .

[274] A. e. a. C. Tumasyan, Eur. Phys. J. C **83**, 933 (2023), arXiv:2303.01214 [hep-ex] .

[275] G. e. a. A. Aad, Phys. Lett. B **842**, 137963 (2023), arXiv:2301.10731 [hep-ex] .

[276] A. Djouadi, Phys. Rept. **457**, 1 (2008), arXiv:hep-ph/0503172 [hep-ph] .

[277] P. e. a. D.-. Agnes, Eur. Phys. J. C **83**, 322 (2023), arXiv:2302.01830 [hep-ex] .

[278] M. Dine and W. Fischler, Phys. Lett. B **120**, 137 (1983).

[279] P. Arias, D. Cadamuro, M. Goodsell, J. Jaeckel, J. Redondo, and A. Ringwald, JCAP **06**, 013 (2012), arXiv:1201.5902 [hep-ph] .

[280] G. Grilli di Cortona, E. Hardy, J. Pardo Vega, and G. Villadoro, JHEP **01**, 034 (2016), arXiv:1511.02867 [hep-ph] .

[281] S. Borsanyi, Z. Fodor, J. Guenther, K. H. Kampert, S. D. Katz, T. Kawanai, T. G. Kovacs, S. W. Mages, A. Pasztor, and F. e. a. Pittler, Nature **539**, 69 (2016), arXiv:1606.07494 [hep-lat] .

[282] P. Arias, N. Bernal, D. Karamitros, C. Maldonado, L. Roszkowski, and M. Venegas, JCAP **11**, 003 (2021), arXiv:2107.13588 [hep-ph] .

[283] P. Arias, N. Bernal, J. K. Osiński, and L. Roszkowski, JCAP **05**, 028 (2023), arXiv:2207.07677 [hep-ph] .

[284] O. Wantz and E. P. S. Shellard, Phys. Rev. D **82**, 123508 (2010), arXiv:0910.1066 [astro-ph.CO] .

[285] M. P. Hertzberg, M. Tegmark, and F. Wilczek, Phys. Rev. D **78**, 083507 (2008), arXiv:0807.1726 [astro-ph] .

[286] M. Gorghetto and G. Villadoro, JHEP **03**, 033 (2019), arXiv:1812.01008 [hep-ph] .

[287] M. Kawasaki, K. Saikawa, and T. Sekiguchi, Phys. Rev. D **91**, 065014 (2015), arXiv:1412.0789 [hep-ph] .

[288] T. Hiramatsu, M. Kawasaki, T. Sekiguchi, M. Yamaguchi, and J. Yokoyama, Phys. Rev. D **83**, 123531 (2011), arXiv:1012.5502 [hep-ph] .

[289] Y. Xu, Phys. Rev. D **108**, 083536 (2023), arXiv:2308.15322 [hep-ph] .

[290] B. Barman and A. Datta, Phys. Rev. D **109**, 095029 (2024), arXiv:2312.13821 [hep-ph] .

[291] D. Grin, T. L. Smith, and M. Kamionkowski, Phys. Rev. D **77**, 085020 (2008), arXiv:0711.1352 [astro-ph] .

[292] L. Visinelli and P. Gondolo, Phys. Rev. D **81**, 063508 (2010), arXiv:0912.0015 [astro-ph.CO] .

[293] N. Bernal, F. Hajkarim, and Y. Xu, Phys. Rev. D **104**, 075007 (2021), arXiv:2107.13575 [hep-ph] .

[294] P. W. Graham, I. G. Irastorza, S. K. Lamoreaux, A. Lindner, and K. A. van Bibber, Ann. Rev. Nucl. Part. Sci. **65**, 485 (2015), arXiv:1602.00039 [hep-ex] .

[295] N. e. a. A. Du, Phys. Rev. Lett. **120**, 151301 (2018), arXiv:1804.05750 [hep-ex] .

[296] T. e. a. A. Braine, Phys. Rev. Lett. **124**, 101303 (2020), arXiv:1910.08638 [hep-ex] .

[297] N. Crisosto, P. Sikivie, N. S. Sullivan, D. B. Tanner, J. Yang, and G. Rybka, Phys. Rev. Lett. **124**, 241101 (2020), arXiv:1911.05772 [astro-ph.CO] .

[298] C. e. a. A. Bartram, Phys. Rev. Lett. **127**, 261803 (2021), arXiv:2110.06096 [hep-ex] .

[299] C. e. a. A. Bartram, Rev. Sci. Instrum. **94**, 044703 (2023), arXiv:2110.10262 [hep-ex] .

[300] S. Lee, S. Ahn, J. Choi, B. R. Ko, and Y. K. Semertzidis, Phys. Rev. Lett. **124**, 101802 (2020), arXiv:2001.05102 [hep-ex] .

[301] O. e. a. C. Kwon, Phys. Rev. Lett. **126**, 191802 (2021), arXiv:2012.10764 [hep-ex] .

[302] J. Jeong, S. Youn, S. Bae, J. Kim, T. Seong, J. E. Kim, and Y. K. Semertzidis, Phys. Rev. Lett. **125**, 221302 (2020), arXiv:2008.10141 [hep-ex] .

[303] S. Beurthey *et al.*, (2020), arXiv:2003.10894 [physics.ins-det] .

[304] I. Stern, PoS **ICHEP2016**, 198 (2016), arXiv:1612.08296 [physics.ins-det] .

[305] J. L. Ouellet, C. P. Salemi, J. W. Foster, R. Henning, Z. Bogorad, J. M. Conrad, J. A. Formaggio, Y. Kahn, J. Minervini, and A. e. a. Radovinsky, Phys. Rev. Lett. **122**, 121802 (2019), arXiv:1810.12257 [hep-ex] .

[306] R. Brandenberger, V. Kamali, and R. O. Ramos, (2023), arXiv:2305.11246 [hep-ph] .

[307] R. L. Workman *et al.* (Particle Data Group), PTEP **2022**, 083C01 (2022).

[308] J. A. Casas and A. Ibarra, Nucl. Phys. B **618**, 171 (2001), arXiv:hep-ph/0103065 [hep-ph] .

[309] I. Esteban, M. C. Gonzalez-Garcia, A. Hernandez-Cabezudo, M. Maltoni, and T. Schwetz, JHEP **01**, 106 (2019), arXiv:1811.05487 [hep-ph] .

[310] D. Chowdhury and A. Hait, JHEP **09**, 085 (2023), arXiv:2302.06654 [hep-ph] .

[311] D. Hooper and G. Krnjaic, Phys. Rev. D **103**, 043504 (2021), arXiv:2010.01134 [hep-ph] .

[312] K. Ichikawa, T. Suyama, T. Takahashi, and M. Yamaguchi, Phys. Rev. D **78**, 023513 (2008), arXiv:0802.4138 [astro-ph] .

[313] S. Nurmi, T. Tenkanen, and K. Tuominen, JCAP **11**, 001 (2015), arXiv:1506.04048 [astro-ph.CO] .